Large-eddy simulation and spatio-temporal analysis of internal engine aerodynamics

Zhihao Ding

To cite this version:

Zhihao Ding. Large-eddy simulation and spatio-temporal analysis of internal engine aerodynamics. Chemical and Process Engineering. Université d'Orléans, 2022. English. NNT : 2022ORLE1005 . tel-03966527

HAL Id: tel-03966527
https://theses.hal.science/tel-03966527

Submitted on 31 Jan 2023

UNIVERSITÉ D'ORLÉANS

ÉCOLE DOCTORALE ÉNERGIE, MATÉRIAUX, SCIENCES DE LA TERRE ET DE L'UNIVERS

EA 4229 - PRISME

THÈSE présentée par:

Zhihao DING

soutenue le: **9 Décembre 2022**

pour obtenir le grade de: **Docteur de l'Université d'Orléans**

Discipline/ Spécialité: **Energétique**

Simulation aux grandes échelles et analyse spatio-temporelle de l'aérodynamique interne moteur

Thèse dirigée par:

Mr. FOUCHER Fabrice	Professeur des Universités, Université d'Orléans
Mr. JAY Stéphane	Ingénieur de recherche, IFP Energies Nouvelles
Mme. TRUFFIN Karine	Ingénieure de recherche, IFP Energies Nouvelles

RAPPORTEURS:

Mr. BOUDRAA Abdel	Professeur des Universités, École Navale
Mr. FONTANESI Stefano	Associate Professor, University of Modena and Reggio Emilia

JURY:

Mr. TENAUD Christian	Directeur de recherche, CentraleSupélec, **Président du jury**
Mr. BÖHM Benjamin	Senior Researcher, TU Darmstadt
Mr. BORÉE Jacques	Professeur des Universités, ISAE-ENSMA
Mr. BOUDRAA Abdel	Professeur des Universités, École Navale
Mr. FONTANESI Stefano	Associate Professor, University of Modena and Reggio Emilia
Mr. FOUCHER Fabrice	Professeur des Universités, Université d'Orléans
Mr. JAY Stéphane	Ingénieur de recherche, IFP Energies Nouvelles
Mme. TRUFFIN Karine	Ingénieure de recherche, IFP Energies Nouvelles

To the memory of a humorous elder.
苟利国家生死以，岂因祸福避趋之。

Acknowledgements

This manuscript marks the end of my doctoral thesis, which would never be completed without the help of others. The contributions of many people in various ways have made this possible. I am most grateful for the overwhelming support of these individuals in helping me to complete this study. They have significantly shared their knowledge, time and efforts to give their best unit in completing this thesis. In particular, I would like to express my gratitude to the following:

First, I am very grateful to Dr. Christian Tenaud for presiding over the defense jury, Pr. Abdel Boudraa and Associate Pr. Stefano Fontanesi for agreeing to review my manuscript, and Pr. Jacques Borée and Dr. Benjamin Böhm for their willingness to be part of my defense jury. Their thoughts and comments on my work were invaluable guides. A special thanks to Jacques for all your suggestions and comments on my work during my Ph.D. thesis. The long meetings we had together were a great source of inspiration. I would also like to thank Benjamin for allowing me to work on the Darmstadt engine and to share my work with other researchers during the Darmstadt engine workshop. The engine configuration is simplified, while the physics inside the cylinder remains complicated.

Second, an immense thank you to my Ph.D. supervisors: Karine Truffin, Stéphane Jay, and Fabrice Foucher. Doing this Ph.D. during the Covid period was a huge challenge for me, and sometimes I lost my motivation and willingness to progress. The support and guidance from all of you during these four years have been invaluable and have finally motivated me to reach the end of this special journey. Karine in particular, you have been a fantastic supervisor and I will always have fond memories of your unwavering support (and your push at the right time). Good luck with your HDR! I know you already have everything you need to qualify.

It was an amazing experience to work with the research engineers of the R116 department. In particular, I would like to thank Gilles for welcoming me into his department and for the nice organization of Ph.D. meetings. I would like to thank Oliver for his suggestions on the use of the ECFM model, Julien and Bruno for their kind support in getting Converge to work correctly on Ener and Irene, Cédric for helping me set up my first simulation using Converge, and Damian and Guillaume for welcoming me to their office during my occasional visits over the last few months. I would also like to thank the people in the R104 department, Christian, Olivier, and especially Giampaolo.

Thanks of course to all the Ph.D. students and postdocs I've worked so closely with: Mehdi, Songzhi, Maxime, Edouard, Hassan, Outmane, Mohamed, Stéphane, Aleksandra, Sajad, Kamal, Abhijit, Paul, Hesham, Ernesto, Mathis, Pierre, Sarah, Xi, Yanzhi, Quan... We come from different countries with different cultures, I will always cherish all the wonderful moments we shared.

Thanks also to Pr. Christophe Corre of Ecole Centrale de Lyon, who introduced me to the world of CFD in 2016, developed my interest in research, and was supportive when I was considering Ph.D. application.

I would like to express my special thanks to my friends Chuhan , Chengran, and Yang for our friendship since 2015 and your support over the past few years, and also to Jiahua: no one else has ever made the delicious Swiss roll for me as you did.

Finally, I would like to thank my parents. Thank you for always supporting me and helping me every step of the way. The ten years I spent in France are a remarkable memory of my life, and a new adventure awaits me in the place where I belong.

Abstract

Among the possible use of hydrogen as a future vector for renewable energies, its combustion either as a pure compound or as an additive inside a spark-ignited engine is seen as a possible way to reach ambitious goals for road transport total reduction of emissions (greenhouse gas effects and harmful pollutants). Strategies such as ultra-lean combustion have enormous potential to improve thermal efficiency and reduce emissions of pollutants. However, lean burn is associated with problems such as cycle-to-cycle variations (CCV) in the combustion process, which weakens engine performance and can lead to misfires in some extreme cycles. Understanding and reducing CCV are one of the major research topics in automotive engineering. Previous studies have highlighted the importance of internal aerodynamics, characterized by a turbulent rotational flow called tumble, as one of the main CCV sources since both large- and small-scale flow structures present a certain level of variability. The objective of this thesis is to understand in more detail the role of internal aerodynamics on combustion variability.

In this context, we rely on Large-eddy simulation (LES) which allows to resolve the vortices up to a certain scale. It also allows the prediction of unsteady phenomena and cyclic variability. However, due to the large amount of data generated, adapted tools are needed to identify the motion of large-scale structures and the fluctuating motion associated with turbulence, both of which can be at the origin of the cycle-to-cycle variability observed in an engine. The method proposed here is based on Empirical Mode Decomposition (EMD) which allows the extraction of the low- and high-frequency components of any signal. In this study, the method has been extended to be applied in 2D and 3D on velocity fields from LES results in complex geometries. The advantages of this method are the usage of only one velocity field contrary to more classical approaches such as POD and the dispense of a priori function contrary to wavelet or Gaussian filter type approaches. We can thus treat any velocity field during an engine cycle and have access to the variability of the overall motion between cycles, which is a major contribution to the analysis and understanding of the physical mechanisms leading to the cyclic variability of combustion. In addition, it allows to define specific descriptors of high- and low-frequency components and their variability to quantify the impact of different phenomena (valve jets, interactions with the walls, tumble motion).

In terms of application, multi-cycle LES simulations of a research engine installed at TU Darmstadt have been performed on a motored case and a reactive case. The developed EMD techniques were combined with a vortex identification algorithm to show the link between the deformation of the tumble during the compression stroke and the speed of flame propagation. The role of interactions between some dominant flows during the intake phase as well as the flow deviation on the piston near the bottom dead center were also highlighted. This work has allowed the development of an innovative technique to define new descriptors of the turbulent flow in highly unsteady situations. It opens the way to further analysis of turbulent aerodynamics in order to identify mechanisms at the origin of certain undesirable phenomena (noise, emissions, ...) for energy systems.

Keywords: In-cylinder flow, Cycle-to-cycle variations, Empirical Mode Decomposition, Large-eddy simulation, Turbulence, Large-scale organized motion

Résumé

Parmi les utilisations possibles de l'hydrogène en tant que futur vecteur d'énergies renouvelables, sa combustion, soit en tant que carburant, soit en tant qu'additif dans un moteur à allumage commandé, est considérée comme un moyen possible d'atteindre les objectifs de réduction totale des émissions (gaz à effet de serre et polluants nocifs) du transport routier. Des stratégies comme la combustion ultra-pauvre ont un énorme potentiel pour améliorer l'efficacité thermique et réduire les émissions de polluants. Cependant, la combustion pauvre est associée à des problèmes tels que les variations cycle-à-cycle (CCV) dans le processus de combustion, ce qui pénalise le rendement moteur et peut conduire à des ratés d'allumage dans certains cycles extrêmes. La compréhension et la réduction des CCV sont un des principaux sujets de recherche en ingénierie automobile. Des études antérieures ont mis en évidence l'importance de l'aérodynamique interne, caractérisée par un écoulement turbulent tourbillonnaire appelé rouleau, comme l'une des principales sources de CCV puisque les structures de l'écoulement, tant à grande qu'à petite échelle, présentent un certain niveau de variabilité. L'objectif de cette thèse est de comprendre plus en détail le rôle de l'aérodynamique interne sur les variabilités de combustion.

Dans ce contexte on s'appuie sur la simulation aux grandes échelles (LES) qui permet de résoudre les tourbillons jusqu'à une certaine échelle. Elle permet également de prédire les phénomènes instationnaires et les variabilités cycliques. Cependant, au vu de la grande quantité de données générée, des outils adaptés sont nécessaires pour identifier le mouvement des grandes structures de l'écoulement et le mouvement fluctuant associé à la turbulence, les deux pouvant être à l'origine des variabilités cycle-à-cycle observées dans un moteur. La méthode proposée est basée sur la décomposition en modes empiriques (EMD) qui permet d'extraire les composantes basse et haute fréquence de n'importe quel signal. Dans cette présente étude, la méthode a été étendue pour être appliquée en 2D puis en 3D sur des champs de vitesse issue de résultats LES en géométries complexes. Les avantages de cette méthode sont de n'utiliser qu'un seul champ de vitesse contrairement aux approches plus classiques comme la POD et de ne pas nécessiter de fonction à priori contrairement à des approches de type ondelette ou filtre Gaussien. On peut ainsi traiter n'importe

quel champ de vitesse au cours d'un cycle moteur et avoir accès à la variabilité du mouvement d'ensemble entre les cycles ce qui est un apport majeur dans l'analyse et la compréhension des mécanismes physiques conduisant aux variabilités cycliques de la combustion. En outre, cela permet de définir des descripteurs propres à ces composantes haute et basse fréquence ainsi qu'à leur variabilité pour quantifier l'impact des différents phénomènes (jets de soupapes, interactions avec les parois, mouvement du rouleau).

En termes d'application, des simulations LES multi-cycles d'un moteur de recherche installé à TU Darmstadt ont été réalisées sur un cas entraîné et sur un cas réactif. Les techniques EMD développées ont été combinées avec un algorithme d'identification des tourbillons permettant ainsi de mettre en évidence le lien entre la déformation du rouleau pendant la phase de compression et la vitesse de propagation de la flamme. Le rôle des interactions entre certains écoulements dominants pendant la phase d'admission, ainsi que la déviation de l'écoulement sur le piston près du point mort bas ont également été mises en évidence. Ces travaux ont permis le développement d'une technique innovante pour définir de nouveaux descripteurs de l'écoulement turbulent dans des situations fortement instationnaires. Elle ouvre la voie à des analyses encore plus poussées de l'aérodynamique turbulente en vue d'identifier des mécanismes à l'origine de certaines phénomènes indésirables (bruit, émissions, ...) pour les systèmes énergétiques.

L'introduction présentée dans le chapitre 1 expose brièvement le contexte général de la thèse en rappelant l'intérêt du moteur à combustion interne et surtout du moteur à allumage commandé. L'accent est mis sur l'identification des principales sources des variations cycle-à-cycle (CCV) dans le processus de combustion, qui sont un frein à l'efficacité et qui pénalisent le rendement moteur. La réduction des niveaux de ces CCV est identifiée comme un verrou scientifique et technique à lever, ce qui permet de motiver la suite du travail présenté dans ce manuscrit. Enfin, le chapitre fixe les objectifs de la thèse et présente l'organisation du manuscrit.

Le chapitre 2 présente un état de l'art sur les travaux de la littérature portant sur les sources CCV du processus de combustion et en listant les sources potentielles. Les structures cohérentes rencontrées dans la chambre moteur, caractérisées par un mouvement rotationnel dit "tumble", sont présentées, suivies par les études de l'écoulement interne moteur par des approches numériques (RANS, LES et DNS) ou expérimentales dans différentes configurations de complexité croissante. On rappelle la décomposition triple des champs de vitesse dans le cylindre qui vise à séparer les structures cohérentes à grande échelle qui correspond au mouvement tumble et les fluctuations turbulentes à plus petite échelle. On liste quelques méthodes pour réaliser une telle décomposition. L'accent est mis sur les méthodes pilotées par les données qui sont les plus utilisées dans les études de l'écoulement interne moteur, la POD et l'EMD et ses extensions. Ce chapitre constitue une bonne référence pour clarifier et organiser les tâches à réaliser afin d'atteindre les objectifs fixés.

Le chapitre 3 présente la description des simulations LES et le système d'équations associé suivie des approches de modélisation pour la simulation de moteur à allumage commandé, y compris la modélisation de l'écoulement et de la combustion. Le développement numérique de la LES ne fait pas partie de la thèse, mais ce chapitre fournit des éléments théoriques pour les simulations LES réalisées dans les chapitres 5 et 6.

Dans le chapitre 4, on présente d'abord la méthode EMD à massivement appliquer dans cette thèse. On détaille l'algorithme de tamisage de l'EMD et illustre l'extraction des modes empiriques sur un signal synthétique. Limitée aux séries temporelles univariées (ou signaux 1D), l'exploitation de l'EMD pour l'analyse des champs de vitesse composante par composante n'est pas optimale (pas de concordance en termes de réponses fréquentielles des modes du même indice), on explore la version multivariée, à savoir l'EMD multivariée (Multivariate EMD ou MEMD) qui est adaptée aux signaux multivariés, qui est le cas des champs de vitesse. Comme la MEMD ne tient pas compte suffisamment de la dynamique des signaux réels où il existe un écart de puissance et/ou une corrélation inhérente entre les canaux des données, le choix s'est porté sur une version étendue de la MEMD, la méthode APIT-MEMD (adaptive-projection intrinsically transformed MEMD). Cette méthode identifie via une analyse propre de la matrice de covariance des données, la direction principale qui reflète le plus grand déséquilibre entre les composantes. Cette direction permet d'améliorer la distribution des directions de projection échantillonnées dont la densité est contrôlée par un paramètre α. Pour atténuer l'effet du mélange de modes, qui est une conséquence de l'intermittence des données signal et est connu pour l'EMD et la MEMD, le choix s'est finalement porté sur la version assistée par l'ajout d'un bruit blanc, à savoir la méthode NA-APIT-MEMD (Noise Assisted APIT-MEMD). L'ajout de NE réalisations aléatoires de bruit blanc d'écart-type σ au signal d'entrée comme une composante supplémentaire permet une meilleure séparation des différentes échelles des données sans une forte influence sur les modes extraits. Finalement la méthode NA-APIT-MEMD nécessite le réglage d'au moins trois paramètres : α, σ et NE. Le choix de la méthode NA-APIT-MEMD pour l'analyse des champs de vitesse est judicieux. L'extension de l'EMD en 2D est basée sur l'application séquentielle de l'EMD 1D à chaque direction l'une après l'autre. Ainsi les profils dans la même direction de la grille du champ de vitesse sont traités indépendamment lors du processus de tamisage. Contrairement à la version précédant de l'EMD 2D [1] où le nombre de pseudo modes doit être fixé et identique pour toutes les directions, ce qui impose une interpolation (étirement) au niveau de la grille représentant le champ de vitesse, dans la méthode proposée dans cette thèse, cette contrainte a été relaxée ce qui permet de gagner en souplesse d'autant plus que le nombre de points dans la direction verticale de la grille peut varier en fonction de la position du piston. La reconstruction de la partie de basse fréquence (mouvement à grande échelle) et celle de haute fréquence (turbulence à petite échelle) se fait aussi pendant la décomposition : la partie basse fréquence dans la direction traitée est définie comme la somme du dernier mode et le résidu extraits par l'EMD 1D et la partie haute fréquence est filtrée. La partie basse fréquence finale est obtenue à la fin de la décomposition dans toutes les directions et celle de haute fréquence est simplement l'écart entre le champ instantané et la partie basse fréquence. Ces améliorations notables de la décomposition comparées à la version précédant se font au détriment d'une décomposition complète et d'une augmentation importante de l'efficacité de calcul. Un autre apport est l'extension de la méthode de décomposition au cas 3D (spatial et spatio-temporel). En effet, l'écoulement dans un cylindre est de nature tridimensionnelle et une telle extension permet de mieux comprendre les structures du mouvement à grande échelle et la turbulence dans la chambre de combustion. On propose une extension qui exploite les trois composantes de la vitesse, et une deuxième qui est spatio-temporelle. Cette dernière permet de mesurer les fluctuations de l'écoulement dans le temps et dans l'espace (pour un plan 2D fixé). On discute aussi le problème des discontinuités présentées dans la partie basse fréquence, ce qui est causé par l'extension de l'EMD basée sur l'EMD 1D. Le nombre de réalisations NE a été testé pour diminuer le niveau de ces oscillations et les résultats montre que ce paramètre permet d'améliorer la partie basse fréquence obtenue mais le problème est loin d'être résolu. Une méthode de la détection des tourbillons dite Γ_3 est présentée dans un deuxième temps. Les méthodes Γ_1 et Γ_2 sont souvent utilisées pour détecter le centre du tumble dans un plan 2D et Γ_3 est une extension de ce type de méthode en 3D. Cette méthode permet d'extraire le noyau du tumble autour duquel la rotation tumble est organisée dans la chambre en utilisant l'isosurface de Γ_3. L'axe de rotation 3D, appelée ligne des centres du tumble, ainsi que la direction de rotation local à chaque point de l'axe de rotation sont aussi disponibles pour la description 3D du tumble. Pour compléter cette description, on propose un grandeur, le taux de rouleau local **TR**, pour quantifier l'intensité de rotation du tumble autour de son axe de rotation 3D. Ces deux outils sont ensuite combinés pour caractériser le développement de l'écoulement dans le cylindre.

Dans le chapitre 5, on présente les simulations LES d'un moteur de recherche installé à TU Darmstadt et réalisées sur un cas entraîné permettant l'analyse de l'aérodynamique interne. Le code CONVERGE, bien adapté aux applications moteur, a été utilisé pour les simulations LES. Une première simulation LES montre que l'échange thermique et celui de masse dans la crevasse ont été identifiée sous-estimés, ce qui conduit la surestimation de la pression cyclique autour de point mort haut. Un modèle de crevasse a été développé pour mieux modéliser l'écoulement dans la crevasse afin de pouvoir correctement l'évolution de la pression cylindrique. Ces dernières ont été validées et améliorées par comparaison des résultats numériques avec les résultats expérimentaux. Après cette validation, l'écoulement pendant la phase de compression a été étudié. Plus précisément, l'écoulement du rouleau pendant la phase de compression est analysé dans le plan du tumble et les fluctuations de l'aérodynamique, incluant les CCV du mouvement à grande échelle et les petits tourbillons liés à la turbulence, sont séparées et quantifiées pendant la compression et ce en exploitant les résultats de la décomposition issus de l'EMD 2D. La méthode Γ_3 et l'EMD 3D sont appliquées pour suivre le développement des structures à grande échelle et pour analyser le transfert d'énergie du mouvement à grande échelle aux fluctuations turbulentes à petite échelle. L'écoulement a été caractérisé dans la chambre de combustion en 3D à l'aides de ces deux outils ce qui a permis d'avoir un aperçu des CCV du mouvement à grande échelle. Une déformation significative du tumble est observée dans certains cycles moteurs alors que le tumble se tient sa structure même proche à la fin de compression dans les autres cycles. Le lien entre le tumble est le niveau de turbulence à la bougie est aussi investigué et on pose l'hypothèse qu'un tumble sans déformation pendant la compression est d'intensité forte, ce qui permet de maintenir le transfert d'énergie vers la turbulence à petite échelle. L'analyse de l'écoulement dans le cylindre a été réalisée avec des outils 2D et 3D, néanmoins l'écoulement 3D ne peut être obtenu que par des simulations numériques et les mesures de PIV ne sont accessibles que dans des plans 2D. On propose d'explorer s'il y a un lien entre les caractéristiques de l'écoulement en 2D et 3D. L'objectif étant de prédire les caractéristiques 3D de l'écoulement à partir de celles obtenues en 2D. L'analyse de corrélation entre les valeurs de taux de rouleau en 2D et 3D, présente un coefficient de corrélation non négligeable montrant un lien linéaire possible. A ce niveau on peut rappeler qu'un lien linéaire modeste, n'exclut pas l'existence d'une relation non-linéaire entre les variables analysées.

Le chapitre 6 est dédié à la simulation et l'analyse du moteur de recherche TU Darmstadt sur le cas réactif. Les résultats des simulations LES sont validés par rapport aux données expérimentales relatives à l'aérodynamique interne et le niveau des CCV. L'objectif est d'analyser l'aérodynamique interne du moment d'allumage et son lien avec le processus de combustion. Les caractéristiques de l'écoulement dans le cylindre lors de l'allumage ont été étudiées et des paramètres pertinents de l'écoulement ayant un impact sur la combustion ont été identifiés. Deux sources principales des CCV ont été identifiées : le niveau de la turbulence à la bougie et l'intensité du mouvement tumble à grande échelle. On montre, par application de l'EMD 2D aux champs de vitesse dans le plan du tumble et le plan horizontal passant par la bougie, que la partie basse fréquence extraite, représentant le mouvement à grande échelle, est un facteur déterminant dans le processus de combustion.

Le chapitre 7 est consacré aux relations de cause à effet ayant données lieu aux facteurs qui sont à l'origine des CCV et ce pendant le développement de l'écoulement dans le cylindre. Le but est de retracer les origines de ces facteurs de CCV en passant de la phase de compression vers la phase d'admission. Pour ce faire, on propose une méthodologie pour analyser les relations de cause à effet en exploitant la caractérisation et l'analyse de l'écoulement dans le cylindre. L'étude commence par la caractérisation du tumble pendant la phase compression. La déformation du tumble, déjà observée dans le cas entraîné, est aussi présent dans le cas réactif. Les résultats présentés montrent que la déformation du tumble est corrélée aux deux facteurs responsables des CCV. Cette déformation est en fait conditionnée par l'état de l'écoulement autour de point mort bas, plus précisément, la déviation de l'écoulement sur le piston qui est créée par l'impact de l'écoulement primaire du côté d'échappement sur le piston. On poursuit notre analyse sur la caractérisation de l'écoulement pendant la phase d'admission. L'écoulement primaire, qui est responsable pour la génération des CCV du tumble, présente déjà des variabilités cycliques à -200 CAD lorsqu'il est formé. On s'intéresse alors à la formation de cette structure dominante qui est aussi la source principale du tumble. L'EMD 3D est appliquée aux champs de vitesse 3D à -250 CAD pour l'identification des structures à grande échelle présentées dans la chambre. Quatre structures dominantes ont été mise en évidence, donc l'écoulement 4 généré par l'interaction des jets de soupape porte la plus grande variabilité. Quelques coupes 2D ont été choisi pour suivre l'évolution de ces structures dominantes ainsi que leur interaction pendant la phase d'admission. La formation des deux écoulements, primaire et secondaire, est identifiée comme la conséquence des interactions entre l'écoulement 4 dans la zone centrale et les écoulement latéraux 2 et 3. La partie basse fréquence des planes à différents instants est ensuite corrélée avec la vitesse de combustion pour mettre en évidence les zones où l'écoulement local, représentant un certain mécanisme, a un impact sur le processus de combustion. Enfin, par une analyse de régression linéaire, on ressort des résultats que l'interaction entre les écoulements dominants à grande échelle pendant la phase d'admission est responsable des CCV pendant le développement global de l'écoulements dans le cylindre. La chaîne de cause à effet est donc bien établie : les CCV de combustion sont d'origine des CCV déjà générées pendant la phase d'admission. Des essaies ont été aussi fait pour caractériser les CCV des écoulements dans la tubulure d'admission.

Dans le chapitre 8, on présente une méthodologie pour la qualification des incertitudes couplée aux simulations LES. L'objectif est la prise en compte des incertitudes associées aux mesures expérimentales et celles via des modèles physiques dans la modélisation numérique, et en particulier dans les simulations des moteurs à allumage commandé. Pour montrer l'apport de cette méthodologie, une validation a été effectuée sur un écoulement périodique turbulent dans un tube. La méthodologie consiste à évaluer les incertitudes à partir des paramètres des modèles de simulation. Ainsi, les résultats montrent que les paramètres du modèle de paroi sont plus critiques dans la simulation du cas considéré, tandis que l'impact du paramètre du modèle de sous-maille est significatif dans la zone près de la paroi. L'application de la méthodologie reste à améliorer pour son application dans le cas du moteur.

Le chapitre 9 résume les principales contributions, et dégage les perspectives pour la continuation de ces travaux de recherche, parmi les problèmes ouverts par ces travaux. Ces dernières sont nombreuses, aussi bien du point de vue des applications que des développements méthodologiques en particulier autour de l'EMD.

Mots clés : Écoulement interne, Variations cycle-à-cycle, Décomposition en modes empiriques, Simulation aux grandes échelles, Turbulence, Mouvement organisé à grande échelle

Contents

1 Introduction 1
- 1.1 General context . . . 1
- 1.2 Operation of a modern spark-ignition engine . . . 2
- 1.3 Introduction to cyclic combustion variability . . . 4
- 1.4 Objectives of the thesis . . . 5
- 1.5 Organization of the manuscript . . . 5

2 Literature review 7
- 2.1 Potential CCV sources . . . 7
- 2.2 Flow structures in a SI engine . . . 9
- 2.3 Steady-state flow configurations . . . 12
- 2.4 Aerodynamics in piston-cylinder assemblies . . . 14
  - 2.4.1 Valve-piston assembly . . . 14
  - 2.4.2 Compressed tumble . . . 16
- 2.5 Research and real engine configurations . . . 17
- 2.6 Decomposition methods of the turbulent flow field . . . 19
- 2.7 Summary of main findings . . . 22

3 Physical modeling approach 25
- 3.1 Principle of Large-Eddy Simulation . . . 25
  - 3.1.1 Concept of LES . . . 25
  - 3.1.2 Filtered governing equations . . . 26
- 3.2 Modeling approaches . . . 28
  - 3.2.1 Unresolved terms modeling . . . 28
  - 3.2.2 Combustion modeling with ECFM-LES . . . 29
  - 3.2.3 Spark ignition modeling with ISSIM . . . 34

4 Development of tools for analyzing turbulent flows in complex configurations 37
- 4.1 Empirical Mode Decomposition . . . 37
  - 4.1.1 General description of the method . . . 38
  - 4.1.2 Extension of the method for LES results of SI engine . . . 42
  - 4.1.3 2D EMD for time-varying geometry . . . 49
  - 4.1.4 Spatial 3D EMD . . . 60
  - 4.1.5 Spatio-temporal 3D EMD . . . 63
- 4.2 Vortex identification with Γ function . . . 65
  - 4.2.1 Γ_1 function in 2D plane . . . 65
  - 4.2.2 Γ_3 function in 3D volume . . . 66
- 4.3 Summary of main developments . . . 70

5 Simulation and analysis of the TU Darmstadt engine configuration: motored conditions 71
5.1 Engine characteristics . . . 72
5.2 LES methodology . . . 73
  5.2.1 Boundary conditions . . . 73
  5.2.2 Mesh . . . 74
  5.2.3 Numerical set-up . . . 75
5.3 Preliminary validation of the LES results on thermodynamics . . . 76
  5.3.1 0D simulation with GT-Power . . . 76
  5.3.2 Thermodynamic properties . . . 77
  5.3.3 Corrections on the crevice flow modeling . . . 78
5.4 Validation of the LES methodology on internal aerodynamics . . . 83
  5.4.1 Qualitative comparison with PIV measurements . . . 83
  5.4.2 Potential causes of the observed difference . . . 84
  5.4.3 Sensitivity analysis on boundary conditions of LES . . . 85
  5.4.4 Quantitative comparison of the LES results . . . 87
5.5 Analysis of the tumble flow during the compression stroke . . . 95
  5.5.1 Large-scale motion and CCV . . . 96
  5.5.2 Energy transfer between large-scale motion and small eddies . . . 98
  5.5.3 Flow characterization in 3D . . . 100
  5.5.4 The link between 2D and 3D diagnostics . . . 106
5.6 Summary of main findings . . . 109

6 Simulation and analysis of the TU Darmstadt engine configuration: fired conditions 111
6.1 Engine characteristics . . . 112
6.2 LES methodology . . . 113
  6.2.1 Boundary conditions . . . 113
  6.2.2 Mesh . . . 114
  6.2.3 Numerical set-up . . . 114
  6.2.4 Combustion modeling set-up . . . 114
6.3 Validation of the LES results . . . 116
  6.3.1 Combustion characteristics . . . 116
  6.3.2 Velocity field in tumble plane . . . 118
6.4 Identification of flow parameters at spark timing impacting the combustion process 122
  6.4.1 Global flow pattern . . . 125
  6.4.2 Local flow near the spark . . . 127
  6.4.3 Global motions in the combustion chamber . . . 131
  6.4.4 Local turbulence intensity near the spark . . . 139
  6.4.5 Thermodynamic effects . . . 141
  6.4.6 Multivariate analysis of CCV factors . . . 142
6.5 Summary of main findings . . . 143

7 Analysis of in-cylinder flow evolution and impact on CCV 145
7.1 Approach and methodology . . . 146
  7.1.1 Tumble deformation Characterization . . . 146
  7.1.2 Flow state at BDC . . . 147
  7.1.3 Intake flow . . . 147
7.2 Comprehension of the link between the compression stroke phase and the combustion phase . . . 149
  7.2.1 Tumble deformation . . . 149
  7.2.2 Spatio-temporal evolution of the large-scale motion and its CCV . . . 154

7.2.3 Impact of the energy transfer between the large-scale motion and small eddies on the combustion process . . . 156
7.3 Understanding the relation between the tumble evolution and its structure near BDC 158
7.3.1 Identification of the initial destabilization of the large-scale motion . . . 158
7.3.2 Impact and deviation of the flow over the piston . . . 159
7.4 Exploration of the CCV sources from the flow organization during the intake stroke 162
7.4.1 Characterization of the primary flow . . . 162
7.4.2 Identification and characterization of dominant flows . . . 167
7.4.3 Analysis of the combined effects of dominant flows on the CCV . . . 178
7.4.4 Exploration of CCV in the intake port . . . 185
7.5 Summary of main findings . . . 190

8 Towards uncertainty quantification in engine simulations 193
8.1 Context of the work . . . 194
8.2 LES modeling . . . 195
8.2.1 Closure of the Favre-filtered momentum equation . . . 195
8.2.2 Wall shear stress modeling . . . 195
8.3 Turbulent pipe flow . . . 196
8.3.1 Presentation of the test-case . . . 196
8.3.2 Simulation setup . . . 196
8.3.3 Results of the first run . . . 197
8.4 Uncertainty and sensitivity analysis on pipe flow simulation . . . 198
8.4.1 Methodology . . . 199
8.4.2 Design of experiments . . . 201
8.4.3 Surrogate modeling . . . 202
8.4.4 Sensitivity analysis . . . 203
8.4.5 Data calibration . . . 204
8.4.6 Final tuning of model parameters . . . 206
8.5 Summary of main findings . . . 207

9 Conclusions and perspectives 209
9.1 Conclusions . . . 209
9.1.1 Development of flow analysis tools . . . 210
9.1.2 Simulation and analysis of the motored case . . . 210
9.1.3 Simulation and analysis of the fired case . . . 211
9.2 Perspectives . . . 212

Bibliography 215

A PIV comparison of motored case 231

B PIV comparison of fired case 237

C On the application of spatio-temporal EMD to LES data 243
C.1 Arrangement of spatio-temporal data . . . 243
C.2 Results of spatio-temporal EMD on LES data . . . 244
C.3 Discussions about the usage of spatio-temporal EMD . . . 245

CHAPTER 1

Introduction

Contents

1.1 General context 1
1.2 Operation of a modern spark-ignition engine 2
1.3 Introduction to cyclic combustion variability 4
1.4 Objectives of the thesis 5
1.5 Organization of the manuscript 5

1.1 General context

The internal combustion engine (ICE) can be traced back to 1876 when Nicolaus Otto was the first engineer who applied the concept of the four-stroke cycle patented in 1862 by the French engineer Alphonse Beau de Rochas in a piston-cylinder assembly. Since then, the combustion engine has become more and more popular with continuous improvements in terms of engine power output and reduction of pollutant emissions. In 2022, 1.45 billion vehicles are running worldwide [2], most of which are powered by ICEs. However, ICEs contribute to global warming by emitting CO_2, decreasing air quality, and generating noise. In Europe, emission regulations are set [3] for automotive manufacturers to lower the CO_2 emissions with the final aim to achieve climate neutrality in Europe by 2050. More recently, the European Parliament has decided to introduce a 100% CO_2 emissions reduction target by 2035 for new cars and vans [4], which will have huge consequences across the automotive industry as automotive industry will accelerate the switch to electrical vehicles (EVs) even further. However, markets outside Europe and North America account for about 60% of annual global automotive sales [5] but may need more time to achieve fully the transition to zero-emission electrical vehicles. Shifting the epicenter of ICE innovation would help automotive industry address this demand over the long term. A recent report [6] also indicates that the global internal combustion engine market is expected to expand by 9.3% during the forecast period 2022-2030. The increasing automotive industry in developing countries also motivates automotive industry to continue with the technological advancement in ICEs in terms of pollution, fuel efficiency, and performance.

Moreover, like the usage of ICEs is impacted by petrol price, the price of EV battery cells is also crucial for the revolution of EVs. The shortage of lithium might be a major obstacle to the EV transition [7]. Also, EVs are supposed to reduce CO_2 emissions, but too few EVs are powered by clean and renewable energy, and even help extend the life of fossil fuels if they are charged primarily with fossil fuel-generated power [8]. Before the completed transition to EVs, ICEs still have strong competitiveness for future environmental improvement involving ultra-high efficiency combustion, alternative fuels, and exhaust after-treatment technology [9].

The combination of modern ICE with increased efficiency and lower emission impact with partial vehicle electrification in a hybrid mode is currently a promising candidate to decrease CO_2 and pollutant emissions in the near future. Hybridization can be seen as a transition technology until the technology for a complete electrical vehicle is mature enough and affordable. The future development of battery capacity, electricity network capacity upgrades, and electricity production decarbonization will be crucial for wider electricity usage in the transport sector. ICE, particularly the spark ignition ICE, also used in most hybrid powertrains, will continue to play a significant role in the transportation sector and requires further investments in new ICEs technologies.

One of the recent technologies, which are crucial to meet today's emission regulations and increase the combustion efficiency of ICE, is ultra-lean combustion [10]. Its combination with the usage of alternative zero-emission fuels such as hydrogen [11] is also of great interest. Nonetheless, one of the main technological challenges associated with ultra-lean engines is the capacity to maintain stable operating conditions. Ultra-lean indicates that the flame is close to the limit of being sustained in a quiescent atmosphere. To enhance flame propagation, lean-burn engines require high levels of turbulence, which leads to the need of mastering the interactions between the flame and the turbulence.

High levels of cycle-to-cycle variations of the combustion process (CCV, explained in section 1.3) are also expected in ultra-lean engines and can perturb the engine operation. They are supposed to be related to the interaction of the turbulence and the flame kernel right after the ignition. To control the undesired CCV and understand their relation with the turbulence in the combustion chamber, a precise characterization and a deep understanding of the internal engine aerodynamics are of great importance, which motivates the work presented in this thesis.

1.2 Operation of a modern spark-ignition engine

The spark-ignition engine exploits the Otto cycle for a four-stroke engine. The four stages or strokes of the revolution, shown in Figure 1.1, comprise an intake stroke when a fuel/air mixture is injected into the engine, a compression stroke when the mixture is compressed, an expansion (power) stroke when the mixture is ignited and expands and an exhaust stroke when the burnt gases are expelled from the cylinder.

Several commonly used technical terms are associated with the engine cycle. The engine's stroke is the distance travelled by the piston inside the cylinder from the top dead center to the bottom dead center. It equals twice the distance between the center of the crankshaft and the center of the bearing linking the connecting rod with the crankshaft. The position when the piston is at the top of its stroke is called top dead center (TDC), and the position at the bottom of the stroke is called bottom dead center (BDC). The volume within the cylinder is at its minimum V_c (known as clearance) when the piston is at TDC and is at its maximum V_t when the piston is at BDC. The engine displacement V_d, representing the engine's size, is the volume difference between TDC and BDC. For a multi-cylinder engine, the volume of all the cylinders is summed together to give the total engine size.

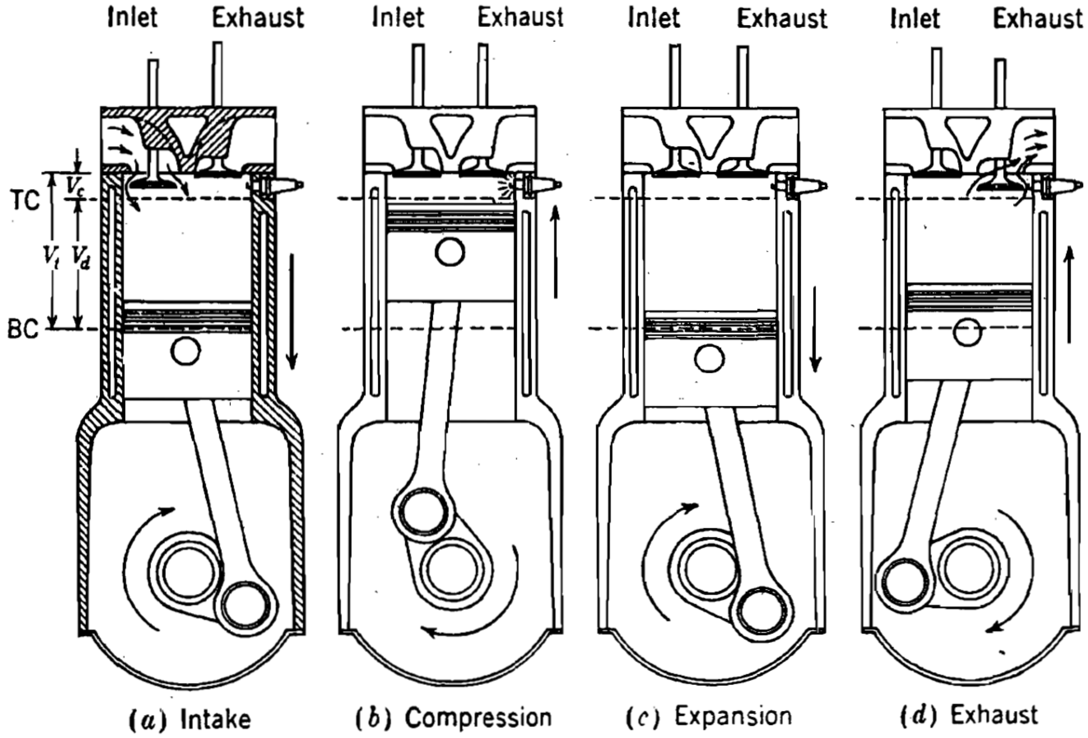

FIGURE 1.1: Schematic of the four strokes in an internal combustion engine [12].

The spark-ignition engine converts the chemical energy contained in the fuel into a mechanical output through the combustion process. The ideal Otto cycle pressure-volume diagram is schematically presented in Figure 1.2. The intake and exhaust strokes of the engine are represented between points 1 and 2 in Figure 1.2. In both strokes, the corresponding valve(s) is(are) open to inject or expel the in-cylinder gases at constant pressure and varying volume. It is assumed that no energy is produced or used.

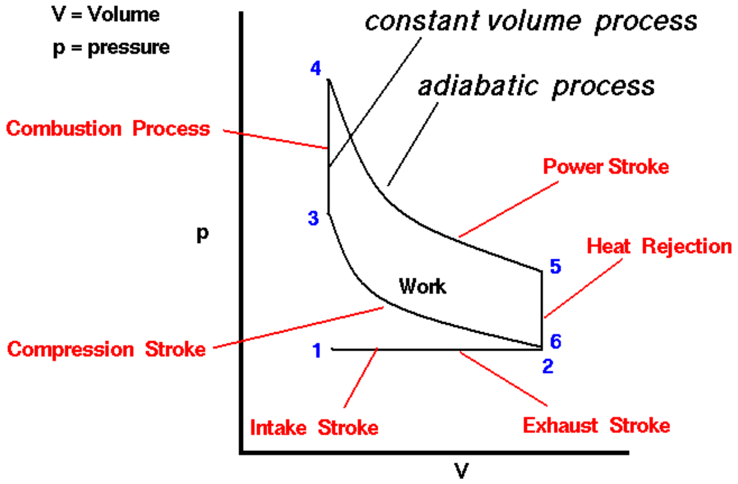

FIGURE 1.2: Ideal thermodynamic pressure-volume diagram for the Otto cycle [13].

The two remaining strokes include most changes in in-cylinder thermodynamics. During the compression stroke, 2-3 in the diagram, the fuel/air mixture is compressed in the closed combustion chamber, which decreases its volume and increases its pressure and temperature. At the end of the compression stroke, the mixture is ignited by the electrical arc released from the spark plug.

The following chemical reaction releases large amounts of heat in the chamber, which dramatically increases in-cylinder pressure (3-4). The high-pressure gases then push the piston away, expanding the volume within the cylinder as the pressure drops (4-5). At the end of the expansion stroke, the exhaust valve(s) is(are) open to release any excess heat and pressure (5-6). Finally, the exhaust stroke occurs (2-1) while the combustion gases are expelled at constant pressure. In the ideal Otto cycle, heat release during (3-4) and (5-6) is supposed to be an instantaneous process.

In this ideal form, work is done on the gas to compress it during the compression stroke, and during the expansion stroke, expanding gases force the piston to move, which generates power. The net amount of useful work that the engine provides is thus the difference between the generated power during the expansion stroke and the used energy during the compression stroke, represented graphically by the area within the cycle diagram in Figure 1.2.

1.3 Introduction to cyclic combustion variability

In the SI engine, the reciprocating motion of the piston is transformed into the circular motion of the crankshaft. Under stable operating conditions, experiments have observed that since the SI engine's combustion process is not repeated from cycle to cycle, the engine output torque in each cycle may show significant changes. This can be easily noticed in the time evolution of the in-cylinder pressure, as it is related to the heat released by combustion. Indicated average effective pressure (IMEP), defined as the average cylinder pressure during an engine cycle, can be used to quantify the intensity of combustion fluctuations.

Figure 1.3 shows the pressure curves measured in the Daimler M256 engine. It can be noticed that the peak pressure can vary from 20 to 40 bar, which leads to significant variations of IMEP. This phenomenon is called Cycle-to-cycle variations (CCV). The CCV level is usually quantified as the coefficient of variation (CoV) of IMEP.

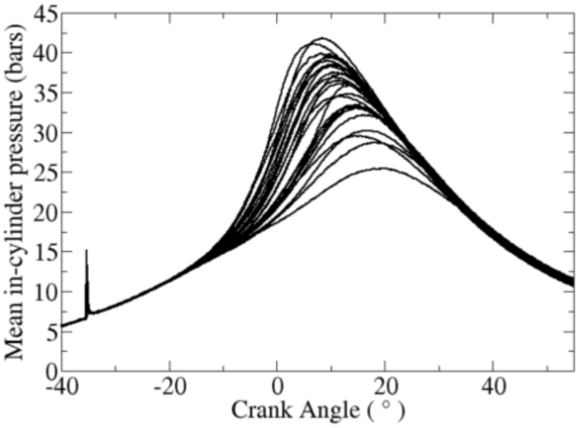

FIGURE 1.3: Experimental measurement of the in-cylinder pressure for different engine cycles on the Daimler M256 engine [14].

CCV are not desired as they can be a limiting factor for the operational range of the engine [15]. They may also reduce engine efficiency due to potential knocking phenomena [16]. For extreme cycles with globally low cylinder pressure caused by incomplete combustion, the unburnt hydrocarbon emissions are also enhanced [16, 17]. Other consequences of high CCV levels are power fluctuations (up to 10%) and an increase in fuel consumption (up to 6%) [18].

Therefore, a deep understanding of CCV sources in SI engines is a crucial step towards understanding and eventually reducing CCV levels in SI engines. Identifying the primary sources of such phenomena can be done based on experimental studies and numerical simulations, which bring more information on physical quantities that are not available from experiments.

1.4 Objectives of the thesis

The present Ph.D. thesis is a continuation of the previous work by Sadeghi [19], who demonstrated the capacity of the empirical mode decomposition (EMD) method to separate large-scale organized flow motions from random small-scale turbulent fluctuations in a given two-dimensional bivariate in-cylinder flow field.

One main objective of this thesis is to characterize the physical cause of the apparently stochastic phenomena of cycle-to-cycle variations, based on only few cycles obtained from Large-eddy simulation (LES), and to establish a cause-and-effect chain with the aim of improving the robustness of in-cylinder aerodynamics.

Another objective is to develop a numerical methodology based on several flow analysis tools including EMD for analyzing in-cylinder flow, to help characterize in-cylinder flow variations.

The present work can be divided into the following intermediate steps to achieve our objectives:

- The EMD method will be adapted to deal with velocity fields obtained by LES, which are three-dimensional trivariate in a time-varying domain.
- An appropriate LES methodology will be selected and validated against experimental data to predict in-cylinder aerodynamics and thermodynamics in a SI engine under motored and fired conditions.
- The developed numerical methodology will be used to exploit LES data obtained from the motored case to prove its capability in the in-cylinder flow characterization.
- The same methodology will then be applied to the LES results of the fired case. CCV sources related to the flow state will be identified. The investigation continues by tracing back their origins which may be associated with the in-cylinder flow evolution at different crank angles.

The present work uses the Converge solver [20] co-developed by IFPEN and Converge Science. It solves the compressible, reactive Navier-Stokes equations on Cartesian meshes. It contains various turbulent combustion models and can deal with some time-varying numerical domains with complex geometries, which CFD studies of ICE require.

1.5 Organization of the manuscript

Chapter 2 compiles a wide range of published research investigating the CCV sources, especially those related to the in-cylinder flow. It comprises experimental and numerical studies performed under various engine-like conditions.

Chapter 3 describes the LES modeling approach used in this thesis. It presents the LES governing equations to be solved and the corresponding LES models for equation closure. The combustion modeling, including ignition and flame propagation, is also introduced.

Chapter 4 is dedicated to presenting flow analysis tools developed in this thesis. The EMD method used for the flow field decomposition is first described, from its original algorithm to its extensions dealing with 2D and 3D multivariate data, combined with corresponding exemplary applications. The vortex identification algorithm based on the Γ function is then explained.

Chapter 5 presents the numerical setup and validation of the LES of the Darmstadt research engine under motored conditions. The numerical methodology of in-cylinder flow analysis, including the EMD and the Γ function, is applied to LES data to explore the CCV of in-cylinder flows.

Chapter 6 presents the numerical setup and validation of the LES of the Darmstadt research engine under fired conditions. Impacting flow factors at spark timing on the combustion process are first identified. Then their origins are investigated in Chapter 7 by a tracing back study of the flow evolution from spark timing to the intake stroke using the same numerical methodology of in-cylinder flow analysis validated in Chapter 5.

Chapter 8 includes an independent study of uncertainty quantification (UQ) in the Large-eddy simulation of a turbulent pipe flow. The developed UQ methodology based on the Gaussian process (GP) is applied to the turbulent pipe flow case with the aim of further application in engine simulations.

We conclude the thesis with a summary of main findings, and final remarks and suggestions of avenues for further study in Chapter 9.

CHAPTER 2

Literature review

Contents

2.1 Potential CCV sources 7
2.2 Flow structures in a SI engine 9
2.3 Steady-state flow configurations 12
2.4 Aerodynamics in piston-cylinder assemblies 14
  2.4.1 Valve-piston assembly 14
  2.4.2 Compressed tumble 16
2.5 Research and real engine configurations 17
2.6 Decomposition methods of the turbulent flow field 19
2.7 Summary of main findings 22

In this chapter, a state-of-the-art review of the existing studies on the investigation of CCV sources is provided. A brief presentation of commonly used decomposition methods in turbulent flow analysis is given.

First of all, potential CCV sources at different stages are listed. A brief presentation of coherent structures encountered in the engine chamber is also given. Studies of in-cylinder flow using numerical or experimental approaches in different configurations of increasing complexity are then discussed: steady-state flow benches, piston-cylinder assemblies, and finally, real engines. Suitable tools are also necessary to better understand the development of in-cylinder flow. Thus, the last section focuses on existing flow field decomposition tools that allow a deep insight into the evolution of the in-cylinder flow.

2.1 Potential CCV sources

Experimental and numerical studies have extensively investigated CCV sources impacting the combustion process. The state of the flow at spark timing, including its composition, velocity, and temperature distribution around the spark plug, has been pointed out as the critical factor leading to different combustion behavior. A fundamental problem of CCV studies is that the cause-and-effect chain, starting from cyclic variations of the intake flow and finally leading to cyclic variations of the combustion process, is not fully understood because of its non-linearity and complexity related intrinsically to the turbulent nature of the flow. Therefore, it is a challenge to propose adapted solutions to reduce CCV. To provide a basic understanding of this cause-and-effect chain, the engine cycle is divided into three consecutive phases as presented in [21]: intake flow, spray formation and mixing, and combustion. During each stage, multiple phenomena can take place. The occurrence and interaction of these phenomena constitute a complex system in which variations can be generated and evolve in space and time. Consequently, the in-cylinder flow development of consecutive cycles can result in different ignition conditions for the combustion process. Figure 2.1 schematically summarizes the phenomena mentioned above that occur within the consecutive phases of a spark-ignited four-stroke gasoline engine with direct injection.

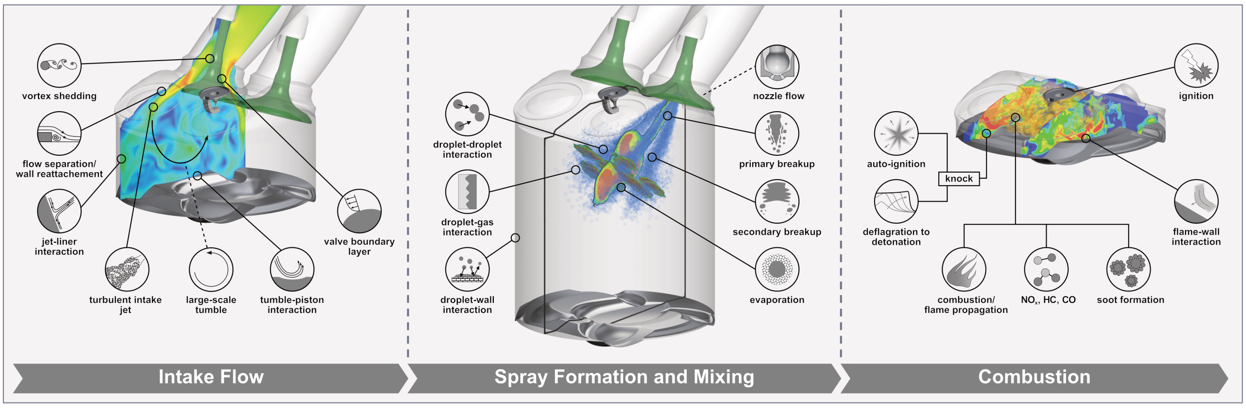

FIGURE 2.1: The engine cycle is divided into three consecutive phases: intake flow, spray formation, and mixing and combustion. Several fundamental phenomena and sub-processes are identified for each phase [21].

A series of studies focus on investigating potential CCV sources and their origins.

- Geometrical factors like the cylinder head [22], the tumble-flap [23], the spark position, orientation [24–26], and the intake port shape [27] were responsible for variations in the in-cylinder flow during the tumble formation and near the spark timing.
- Flow-spray interaction was also highlighted [27, 28] for direct-injection configurations as the resulting air-fuel mixture behaved differently, could lead to CCV in the combustion process, and could even potentially enhance or weaken the tumble motion depending on the injection direction [29].
- Variations of temperature were investigated by Koch et al. [30]. They were caused by the concentration of residuals from the previous cycle, which are at a higher temperature than the fresh mixture. Masouleh et al. [31] found that variations of the local temperature field did impact CCV but were not dominant compared with those of the local velocity field. The same conclusion was also obtained by Wadekar et al. [32].
- Thermal effect, including wall heat transfer and thermal stratification, has been investigated in [29, 33–35] using DNS in an engine-like geometry. It was found that the in-cylinder temperature fluctuations decreased during the first half of the compression stroke and increased significantly during the second half, which led to a highly stratified temperature field near top dead center (TDC). The stratification was caused by the heat transfer from the walls towards the inner part of the cylinder, which was correlated with the near-wall vortical structures generated by the intake stroke flow. Higher levels of stratification were observed near the cylinder head, suggesting that moving the spark position away from the cylinder head helps reduce the temperature impact.

- Local equivalence ratio describing the local air-fuel mixture around the spark plug was studied as well. The equivalence ratio directly impacts the laminar flame speed, and its variations were considered a critical CCV source after the variations of flow [24, 36]. A decoupling of the combined effect of the flow field and equivalence ratio field was realized [37], which proved the dominant role of the flow field in terms of CCV source. In contrast, the equivalence ratio field had minimal influence, which agreed with the conclusion [29].
- Most studies focus on the impact of the in-cylinder flow on the combustion, both its local behavior near the spark plug and its global characteristics at different phases. As pointed out in the work presented in [38, 39], the global combustion speed was discovered to be linearly correlated with the initial combustion speed, revealing the importance of the initial growth rate of the flame kernel. The local velocity was the main factor controlling the flame propagation right after ignition, and Matsuda et al. [40] later proved that CCV of the tumble motion could lead to CCV of the local flow. More results related to internal aerodynamics will be discussed later in detail.

The importance of the internal aerodynamics was revealed, especially its state at spark timing, conditioned by the overall development since the beginning of intake stroke. To enable a basic understanding, we will present the main flow structures in a SI engine in the next section.

2.2 Flow structures in a SI engine

In a SI engine, the flow structures are mainly characterized by a coherent gas motion, called tumble motion. The tumble is a rotational motion in the cylinder, whose axis of rotation is perpendicular to the piston moving axis. Figure 2.2 presents a typical tumble motion schematically.

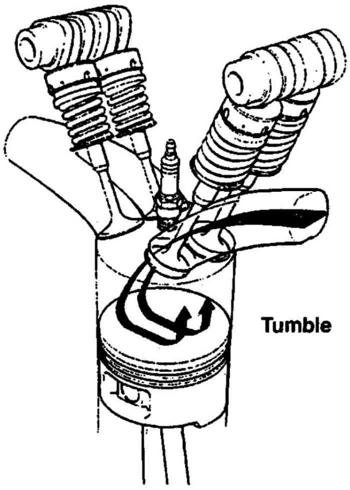

FIGURE 2.2: Tumble motion within SI engine cylinder [41].

During the intake stroke, the flow enters the cylinder through the valves, forming jets. The jets induce angular momentum creating coherent structures such as tumble. Once the intake valves are closed, and the compression starts, the decreasing available room of the chamber leads to a spatio-temporal evolution of the tumble motion, during which the tumble motion is forced to reduce its spatial scale and triggers an energy transfer from large-scale to small-scale structures by energy cascade, resulting in a high level of turbulent kinetic energy close to TDC. Figure 2.3 schematically illustrates a classical tumble breakdown scenario in the cylinder, which supposes that the large-scale tumble is largely compressed and breaks into small eddies near TDC.

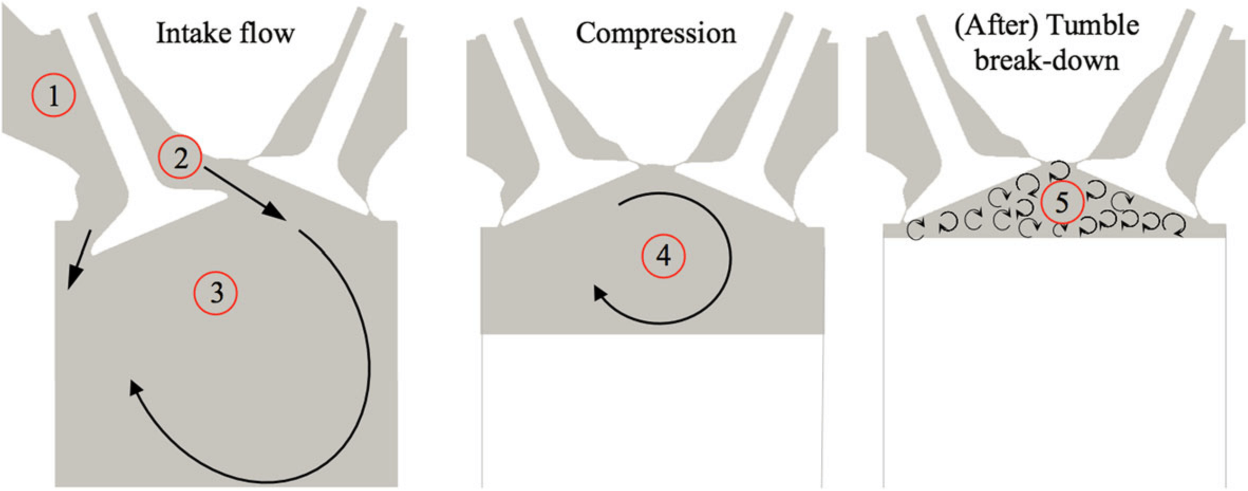

FIGURE 2.3: Sketch of the evolution of the flow: flow upstream of the intake valves (1), intake jet around the valve seat (2), tumble inside the combustion chamber during the intake stroke (3), tumble compression (4) and tumble breakdown (5) [42].

Another scenario of the tumble evolution during the compression stroke is also proposed by Lumley [43] who suggests a flow pattern switching of the tumble. The tumble motion changes its rotating axis during the compression stroke, which can be associated with elliptical instability: the rotating flow tends to rotate around the shortest axis in a closed vessel to remain stable. The resulting flow pattern is characterized by a counter-rotating vortex pair (shown in Figure 2.4) which has been observed in some experimental Particle Image Velocimetry (PIV) measurements [44–46].

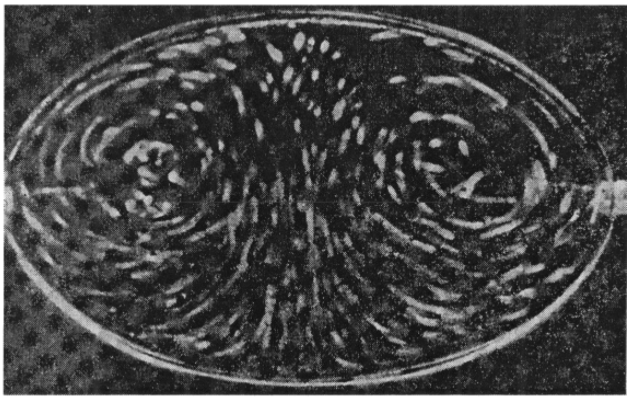

FIGURE 2.4: Multi-vortex instability is observed in an ellipsoid, similar to the scenario of a flow pattern switching: the tumble motion is transformed into a counter-rotating vortex pair because of the elliptical instability [43].

Whatever the scenario, the resulting flow plays an important role in the early flame kernel growth. After ignition, the turbulent part of the flow interacts with the flame front by stretching and wrinkling the flame surface. The large-scale residual structures impact the flame propagation by their convection effect. The mixing process of air and injected fuel is also affected by the flow, not only in large-scale structures but also in small eddies, especially during the compression stroke. Thus, the development of the large-scale organized tumble motion has considerable importance for combustion development.

The tumble motion is formed by intake valve jets. Figure 2.5 shows a velocity field of valve plan obtained in the ICAMDAC engine presented in [47]. Flow-wall interactions occur above the intake valve walls: the flow strongly deviates towards the upper part at corner 1 while it follows the form

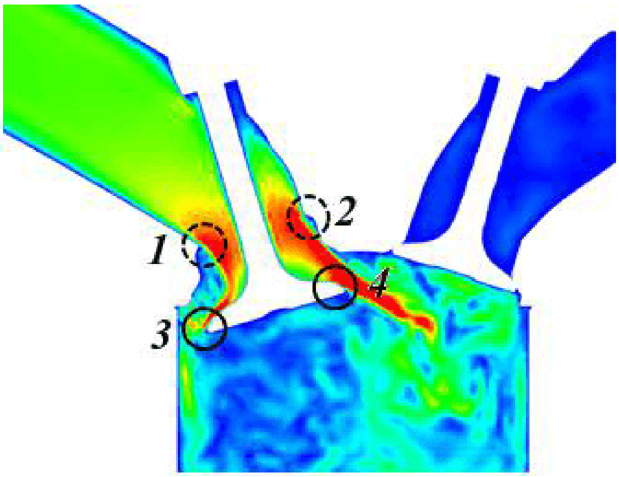

FIGURE 2.5: Flow separation during the initiation of a tumble motion [47].

of the intake port at corner 2, which results in a strong primary intake flow on the upper part and a relatively weak secondary intake flow on the down part. Both primary and secondary intake flows detach from the valve edges and then form the tumble motion. Their orientation is thus an essential ingredient for tumble development. In numerical studies, attention must be paid to the wall treatment to reproduce the internal aerodynamics.

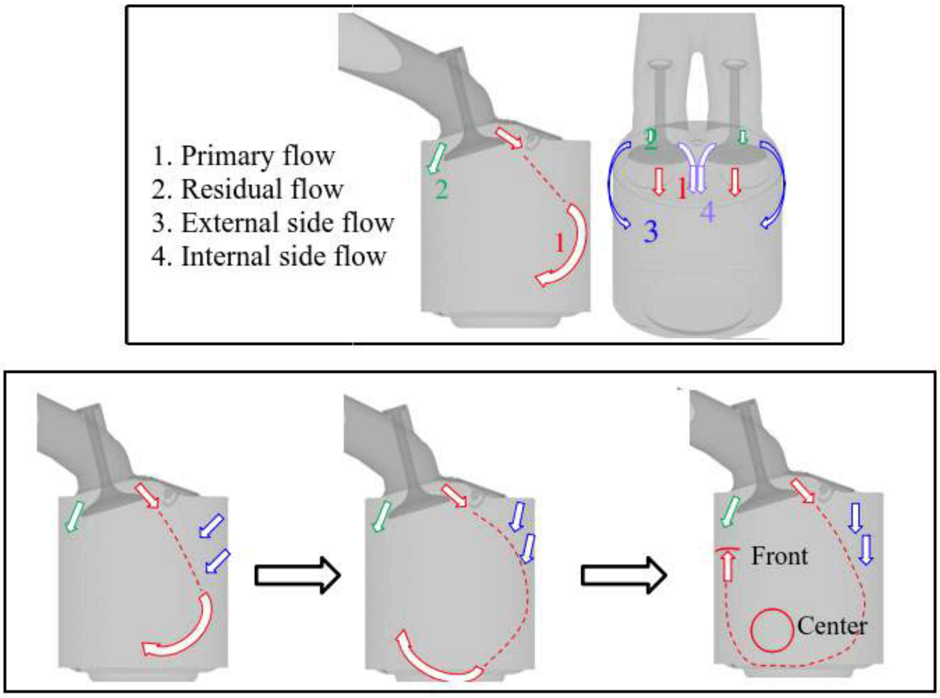

FIGURE 2.6: Sub-flows lead to a tumble motion formation in a SI engine (top). Evolution of the tumble motion (bottom) [25].

The intake flow is naturally three-dimensional and can interact with cylinder walls and even between its sub-flows. Figure 2.6 shows a decomposition of intake flow proposed in [25]. Besides the primary flow 1 and the residual flow 2, two more sub-flows can be identified: the external side flows 3, which follow the liner and move down towards the piston, and the internal side 4 flow resulting from the interaction of jets between the two valves. The primary flow 1 and these two sub-flows 3 and 4 constitute the primary intake flow which is the source of the tumble formation.

In contrast, the the residual flow 2 itself stands for the secondary intake flow entering the chamber in the intake side with much less momentum. These two intake flows can encounter each other inside the chamber. Near BDC, the tumble motion fills the whole combustion chamber and is ready for compression.

The intake flow, induced in the chamber by two conical valve jets, is undoubtedly the most important in the formation of tumble motion. A special experimental setup called flow bench for which the intake valve position is fixed can be employed to investigate their behavior. The intake flow is thus characterized in a steady state for a given valve position. The following section will present some studies on the flow bench.

2.3 Steady-state flow configurations

The momentum flux induced by the intake flow is the primary source to tumble formation. Because of this strong dependency on the intake flow, an optimal intake port is essential to obtain a well-structured tumble motion during the intake and compression strokes. Such an intake port design usually starts with numerical studies based on a simplified engine configuration on a steady-state flow bench. The flow bench setup's simplicity allows the reproduction of a highly complex flow field, as we can observe in real engine geometries.

The work presented in [48] was realized on a Volkswagen 1.6L FSI production engine. PIV and numerical simulations, including scale adaptive simulation (SAS) [49] and detached eddy simulation (DES) ,[50] were performed to conduct a comparative study, and good agreement was reported. The development of turbulent structures was also analyzed using a Q-criterion isosurface. The authors found that the largest structures introduced by intake jets, containing the highest amount of vorticity, were concentrated in the upper part of the cylinder and kept decaying as they moved towards the piston.

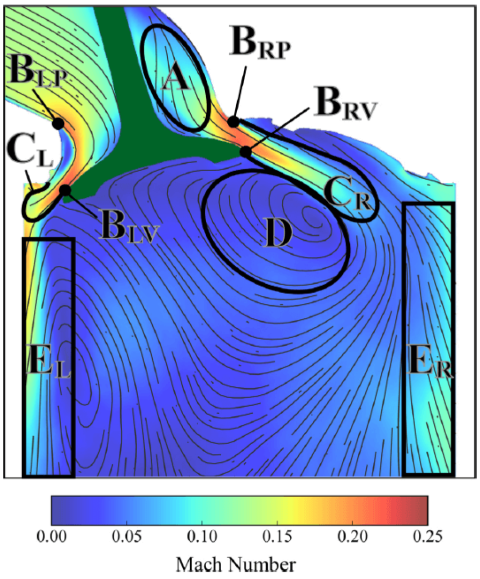

FIGURE 2.7: Ensemble-averaged Mach number and streamlines in the central valve plane of a steady-state flow bench configuration [51].

Bulh et al. studied the flow bench installed in TU Darmstadt [51]. The PIV measurement was carried out in the central valve plane. Some main flow features were identified on the time-averaged velocity field and presented in Figure 2.7. The primary and secondary intake jet flows were well captured and qualitatively similar to those in real engine configurations, despite the valve lift remaining unchanged. Other phenomena like flow detachment, reattachment, and recirculation could also be observed, revealing the flow's complexity even in a simplified geometry.

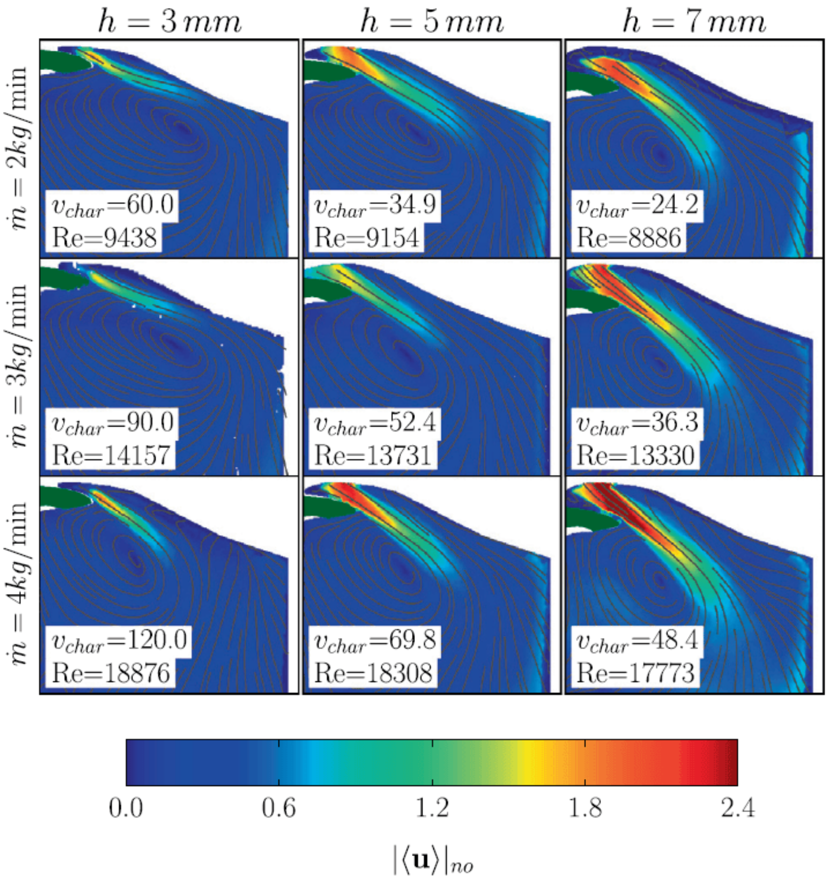

FIGURE 2.8: Normalized ensemble-averaged velocity magnitude and streamlines from PIV [52].

Different mass flow rates and valve lifts were tested in this flow bench, and Figure 2.8 shows the corresponding intake jet obtained by PIV measurement. The authors highlighted that the orientation and the penetration of the intake jet depended strongly on the local flow in the vicinity of the valve characterized by the Reynolds number computed using the valve gap and the averaged valve flow velocity: a high Reynolds number jet seemed to penetrate more deeply and oriented downward. In contrast, a low Reynolds number jet was much weaker and bent towards the cylinder head. This dependency could also explain the flapping of the jet observed in real engine configurations, in which the local Reynolds number varies with respect to the valve motion. It also revealed that for numerical simulation, an accurate prediction of the intake jet would also rely on the correct reproduction of the intake mass flow near the intake valves. The authors also performed LES of this flow configuration using Sigma sub-grid scale model [53] and the best results compared to PIV data were obtained with the most refined mesh. Nonetheless, the prediction of the penetration and orientation of the intake jet could still be improved.

Nishad et al. [54] studied the same flow bench using LES, and a particular focus was put on the generation of turbulence throughout the intake port. The intake flow anisotropy along the intake valve was identified utilizing an anisotropy map [55] and was similar to the one of a classical pipe flow. Turbulence properties along the intake port experienced a sudden change when the flow passed through the intake valves, suggesting that most turbulence was generated by the interaction between the intake flow and the valves. The turbulence length scale also increased gradually downstream of the intake flow.

The flow bench has been mainly used to validate numerical simulation results obtained with LES [51, 54] and more recently with LBM [56]. To investigate the spatio-temporal evolution of the intake flow and the resulting tumble motion, some piston-cylinder assemblies simplified compared to real engine geometries are also chosen and will be illustrated in the next section.

2.4 Aerodynamics in piston-cylinder assemblies

2.4.1 Valve-piston assembly

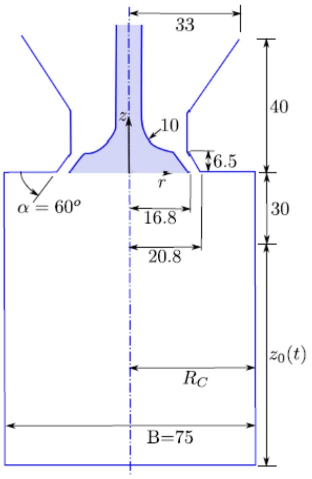

FIGURE 2.9: schematic of the single valve-piston assembly geometry [57].

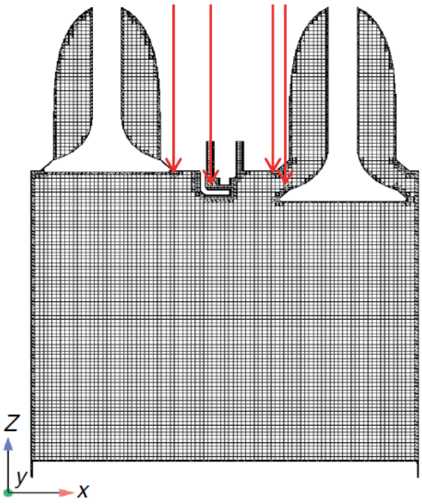

FIGURE 2.10: schematic of the two valves-piston assembly geometry [58].

A single valve-piston assembly was firstly introduced by Morse et al. [59] in 1979. Doppler laser measurements were performed to extract velocity profiles at different locations. Figure 2.9 shows the geometry of this configuration. Since then, this engine configuration has been massively studied to develop simulation techniques. El-Tahry et al. [60] performed RANS simulations on this configuration. Though the RANS approach did not permit the correct prediction of CCV, they proposed a Reynolds stress turbulence model which outplayed the standard $k - \epsilon$ model in terms of prediction of the mean flow. Haworth et al. [61] investigated the possibility of using LES to predict the flow inside this assembly to overcome issues of RANS in engine application. Acceptable accuracy was obtained, and the authors anticipated that LES would be a powerful tool in understanding and predicting in-cylinder flows. Keskinen et al. [62] studied this configuration with three LES approaches. 12 LES cycles were computed in each case, and all three methods yielded very similar results, with only slightly better prediction for the case using the standard Smagorinsky model. Two more cases were added in which the initial velocity field was zeroed either in the chamber or in the intake port. Compared to the case without manipulation of the velocity field, they concluded that the velocity structures from the intake port were more critical than those in the cylinder on the level of CCV in the in-cylinder flow, suggesting that the intake caused the variability of the in-cylinder flow flows induced into the chamber. Though very expansive to use, DNS has also been performed for this configuration by Schmitt during his Ph.D. thesis [57], which provided massive data for validation of numerical studies and wall model development.

Schmitt et al. [63] studied the intake jet structure, which created one large central and two smaller vortex rings at the corners of the cylinder liner with the cylinder head and the piston. The pressure isosurface was used to visualize the large central vortex ring, which presented significant variability. The stability of the large vortex, formed during the intake stroke, was found responsible for the generation of smaller vortical structures at TDC. The authors continued the study [64] by building a cause-and-effect chain to explain the origin of CCV observed in the in-cylinder flow, and it was found that the residual vortical structures at TDC of the current cycle could impact the intake jet and the flow pattern in the subsequent cycle. More studies were realized on the near-wall behavior of the flow. Thermal stratification increased during the second half of compression [29, 33], which was discovered to be caused by the vortical structures resulting from the remaining intake flow field. The thermal stratification at TDC was also found not related to the initial temperature distributions at BDC [34] but was generated by the local heat flux distributions during the compression stroke [65] which were determined by the wall temperature and the local flow field. The authors also highlighted that boundary layers in an engine-like geometry did not follow the logarithmic law [65].

Another two valves-piston assemblies have also been widely studied, as shown in Figure 2.10. It is called Transparent Combustion Chamber (TCC) engine [66], designed as a validation case for numerical engine simulations. This more recent configuration is closer to a real engine configuration as the exhaust valve is included. PIV measurement is also available for further validation. Liu and Haworth [67] performed LES computation for this configuration. A sensitivity analysis of the numerical schemes and model parameters was carried out, and the authors found that results were principally sensitive to mesh size and turbulence model. Abraham et al. [68] found that the intake-port pressure, or the pressure drop across the intake valve, was not correlated with the in-cylinder flow pattern. Ko et al. [69, 70] studied the LES quality and accuracy using different SGS models and numerical schemes. The authors emphasized the importance of simulation methodology in predicting intake jet of high velocity. Yang et al. [71] investigated the link between the intake valve jet and the resulted in-cylinder flow quantified by the swirl ratio (SR). The SR at the exhaust valve opening (EVO) was found highly correlated with that at the intake valve opening (IVO), indicating that the CCV of large-scale organized motion originated from the intake flow. The flow in the valve seat region was also revealed as the primary source of the generation of CCV of in-cylinder flow. Shekhawat et al. [72] studied this engine configuration under fired conditions. The local flow conditions in the spark gap at spark timing played an essential role in the early flame kernel growth. The local velocity gradient correlated with the combustion speed: higher velocity gradient magnitudes accelerated the flame growth, exposing the early kernel to a broader range of fluctuating gradients. Giannakopoulos et al. [73] performed LES of 32 cycles. They concluded that the cyclic variability of tumble motion, quantified by tumble ratio (TR), was manifested early during the intake stroke when the intake valve jet dominated the in-cylinder flow. The increase of the fluctuating kinetic energy was also observed simultaneously with the decrease of the mean kinetic energy during the second half of the compression stroke, which was considered a result of the tumble breakdown. More recent work on this configuration using LES with Conjugate Heat Transfer (CHT) modeling can also be found in [74, 75]. The logarithmic law model, which provided boundary conditions at the first grid point, failed to predict the measured velocity profiles away from the wall. Wall temperatures also showed evident variations in space and time, while in most LES approaches, wall temperatures are imposed to be constant in the current strategy. A suitable dynamic wall modeling of temperature is indeed preferred, especially for walls near the spark plug where the heat transfer is crucial for the flame kernel development at early-stage. Nevertheless, coupling CHT with LES is still of unaffordable cost for multi-cycle simulation. In most numerical studies, wall temperatures are still imposed as constant but are closed to their cycle-averaged value.

2.4.2 Compressed tumble

The square piston experiment presented in Figure 2.11 has been designed at IMFT to study the compression and the disruption of a tumbling vortex.

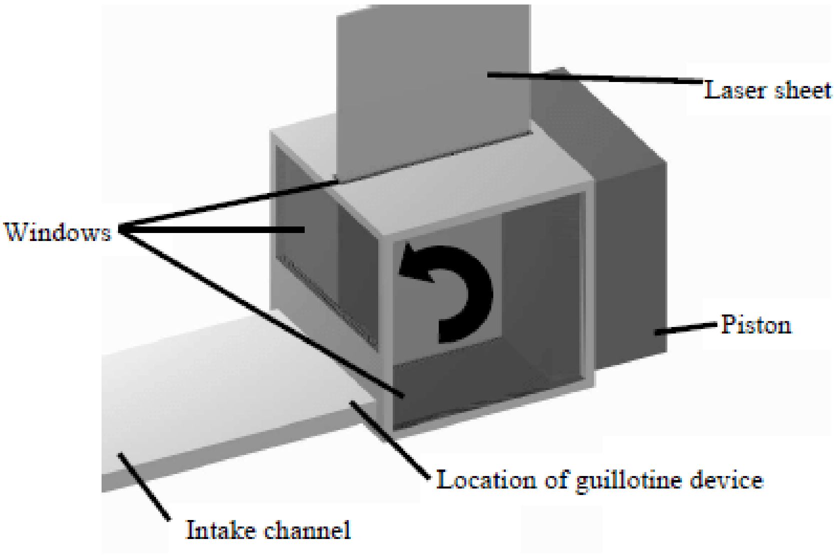

FIGURE 2.11: schematic of the square piston engine [76].

Le Roy et al. [77] performed 2D RANS of this configuration. Remarkable differences were observed between predictions of $k-\epsilon$ and Reynolds stress models, and the latter behaved much better when compared to the experiments. The existence of three-dimensional and large-scale flow was suspected in such quasi-2D configuration and could be generated by an elliptical-type instability. Maurell et al. [78] applied the Proper Orthogonal Decomposition (POD) on PIV data measured on this configuration. The first three modes were extracted to study the interactions between different flow regions. Borée et al. [76] noticed that, at a volumetric ratio of two, the mean kinetic energy was transferred from the large-scale motion to turbulence at a timescale in the order of the vortex turnover time. It was also noticed that slight deviations in the large-scale motion were amplified during compression. Moreover, Borée et al. linked the instability to elliptical and centrifugal instabilities. It was also found that the nonzero divergence of the mean flow and the spherical part of the Reynolds stress tensor had a non-negligible contribution to the energy exchange between the mean and the fluctuating flow. Moreau et al. [79] conducted a study on the same configuration with the injection to investigate the interaction between the tumble and the injection process. The injection seemed to modify the tumble characteristics and the breakdown process. Moureau et al. [80] performed the first LES of this configuration (no injection conditions) to study the tumble breakdown numerically. The 3D nature of the tumble was evidenced as only 3D simulations gave a realistic velocity field, while in the 2D case, the vortex stretching mechanism could not be considered. Devesa et al. [81] studied two similar configurations in which the injection was made in tumble counter-flow and co-flow. The injection broke the tumble in the first case. In contrast, it remained more stable in the second case despite a noticeable displacement of the tumble towards the injection direction. Toledo et al. [82] performed LES and noticed that wall interactions during compression are significant as instabilities are transported from the wall into the rotating flow. It was also observed that near the end of compression, the tumble trajectory becomes erratic and strongly dependent on initial conditions.

2.5 Research and real engine configurations

The Reynolds-average (RANS) approach has proven inappropriate for studying CCV in SI engines as it provides only ensemble- or phase-averaged mean quantities. LES is thus more and more employed given its ability to provide information about individual cycles. Some early attempts of LES application on SI engines can be found in [80, 83] which LES showed its capacity to capture cycle-to-cycle variations, though with very limited cycles. In 2007, Richard et al. [84] performed the first study on SI engine combustion using the LES code AVBP on the four-valve pent-roof PSA XU10 engine. The LES combustion model CFM and the ignition model were validated. Vermorel et al. [85] continued this work by performing multi-cycle LES on fired conditions to verify the capacity of LES to reproduce the occurrence of CCV. CCV was captured with only 10 cycles, and its causes related to the mixture and in-cylinder motion were investigated. It was found that the tumble motion and the turbulent level at the spark timing were significant causes of CCV in this engine configuration. The same conclusion was also obtained by Koch et al. [30] who highlighted the importance of the local subgrid turbulence level. Schmitt et al. [86] proved later that the local subgrid turbulence level could be associated with the decay rate of the tumble ratio during the compression stroke. Such findings suggest that CCV sources are already developed before ignition and can be traced back to an earlier phase of the engine cycle. Some experimental studies based on PIV measurements were carried out to characterize the in-cylinder flow development. Pajot [87] investigated the impact of the in-cylinder flow on the combustion process using PIV and highlighted the importance of the local flow around the spark plug at spark timing on the early flame propagation. The turbulence and the equivalence ratio were also found responsible for the flame wrinkling. Laurant [88] studied precisely the evolution of the flow during the intake stroke. The flapping instability of the intake valve jets was determined as the significant source of CCV of the flow at the end of the intake stroke. Fluctuations of the intake pressure, artificially generated during the intake stroke, were not found to impact the in-cylinder flow pattern. Voisine [46] conducted a multi-planar analysis of the in-cylinder flow to describe the formation of the tumble motion. The fusion of some sub-flows of the intake flow resulted in a descending jet which later conditioned the formation of the tumble. The tumble breakdown was also analyzed based on PIV data inside the cylinder head area. Important CCV were found during the tumble breakdown process. Cao [89] applied a cluster-based analysis of CCV to the in-cylinder flow. Based on the first two POD coefficients, all the engine cycles were classed into five sub-groups to be statistically studied.

Several studies performed at IFPEN on the SGEMAC engine are also available. Enaux et al. [90] firstly performed LES on motored conditions. With 25 cycles, good agreement was obtained compared to PIV measurements. A study on the fired condition was also conducted [38]. The 25 consecutive cycles on a stable case characterized by low CCV recovered the experimental in-cylinder pressure envelope. The initial development of the flame kernel depends on the velocity field at the spark plug and determines the overall combustion duration. Granet et al. [39] studied the same engine in fired conditions on stable and unstable operating points. The authors concluded that the variations in internal aerodynamics were the primary sources of CCV in this configuration. More recently, Truffin et al. also[91] investigated the origins of CCV in this engine. Besides a stable point considered as a reference, two unstable points were also studied. Based on multivariate analysis, it was uncovered that high local velocity magnitudes favored fast combustion in diluted and lean combustion cases, in agreement with what was found in [24, 31]. The local flow orientation was also identified as the dominant CCV source in the lean combustion case, which is in agreement with Zhao et al. [37] who confirmed the importance of the local flow on the flame kernel shape during the initial growth phase, concluding that a centered flame kernel with less elongation in piston motion direction was the most preferred for fast combustion.

The Darmstadt engine has been widely studied, involving different numerical approaches. In agreement with previous studies, LES was the most used numerical tool because of its capacity to capture CCV phenomena. The first LES studies were carried out by Baumann et al. [92] to validate their LES methodology by comparing results against experimental measurements. A qualitative comparison of the intake flow between two cycles was made using the Q-criterion, revealing an essential variability of intake flow. Freudenhammer et al. [22] compared the flow field obtained with two cylinder heads and concluded that the geometry could affect the intake flow and eventually the tumble formation. Nguyen et al. [93] also performed LES but used the immersed boundary method [94] to model moving boundaries. They also investigated the sensitivity of LES results to numerical schemes. They found that highly dissipative schemes could wipe the contribution of subgrid modeling and lead to a less resolved velocity field, undesired in predicting the combustion process. Janas et al. [42] carried out LES to investigate the evolution of the in-cylinder flow. The tumble shape was computed by a 2D vortex identification algorithm on a set of 2D slices throughout the cylinder and showed evident variations at mid-compression between different cycles. A modified integral length scale was also calculated to quantify the tumble size whose evolution was linked with the tumble breakdown. Wadekar et al. [32] used LES to identify CCV sources in a fired case. They computed the mean fluctuating part of the local flow, which proved crucial to CCV. However, the contribution of different scales was not separated. The flow vectors were primarily responsible for flame progress and confinement. Quadrant analysis also revealed that the flow instantaneous velocity and fluctuations were the significant factors affecting the flame asymmetry. Buhl et al. [52] studied the impact of port modeling strategy on DES simulation results. He et al. [95] applied the anisotropy map [55] to follow the evolution of the turbulent states during the engine cycle. The evolution of the anisotropy tensor was regarded as a good indicator of the breakdown and reorganization of turbulent structures. Iacovano et al. [96] validated their DES methodology in the simulation of operation point A of the Darmstadt engine. RANS was performed by Iacovano et al. [97] to study the mass exchange and thermal transfer in the crevice region, which were stable under motored conditions. Despite its cost in the case of engine flow modeling, DNS was carried out by Impagnatiello et al. [98]. DNS data were used as a reference for LES wall model development.

Most of the above-listed studies focused on identifying CCV sources at spark timing, and the explanation of their origins was either missing or partially attempted. A cause-and-effect chain was built in a series of studies [25, 27, 99, 100] to explain the impact of flow on CCV of combustion and its origins from flow development. Stiehl et al. [27] firstly identified the relationship between the combustion speed and the spray shape, which resulted from the interaction between the spray injection and an upward flow associated with the tumble motion near the TDC. With the help of a dual-plane analysis, Kruger et al. [99] suggested that the variations of the upward flow were the result of a 3D flow structure. An interesting hypothesis was also proposed: CCV of the upward flow results from the interaction of several dominant in-cylinder flows as presented in Figure 2.6 since the intake stroke. Experimental measurements confirmed that the upward flow disappeared, and the CCV level was vastly reduced with a modified intake port design to minimize the flow interaction. Using a pseudo-3D vortex identification algorithm, Nicollet [100] could visualize the tumble shape, which differed between fast and slow cycles. The upward flow was found related to the 3D structure of the tumble vortex as a result of the tumble deformation.

In most studies, researchers emphasized the critical role of the in-cylinder flow, located near the spark plug and in the whole chamber. However, in-cylinder flow contains multiple scales. Their impact on the combustion can not be decoupled by a simple Reynolds decomposition, as the fluctuating part could be made of contributions from different scales. The following section will discuss decomposition methods used to decompose a turbulent flow field.

2.6 Decomposition methods of the turbulent flow field

Analyses of the in-cylinder flow have shown that the in-cylinder flow exhibits cyclic variability during the engine cycle. With a Reynolds-type decomposition, the instantaneous velocity U at crank angle θ of cycle i can be expressed as follows:

$$U_i(\theta) = \overline{U}_i(\theta) + u_i(\theta) \tag{2.1}$$

where $\overline{U}_i(\theta)$ represents the mean flow of the current engine cycle and $u_i(\theta)$ the turbulent fluctuations.

As shown in Figure 2.12, the mean flow also contains some fluctuations of a larger scale than that of turbulent fluctuations. Subsequently, the mean flow can be again decomposed:

$$\overline{U_i}(\theta) = U_{EA}(\theta) + U_{c,i}(\theta) \tag{2.2}$$

where U_{EA} is the ensemble-averaged velocity of all the engine cycles at the given crank angle θ and $U_{c,i}$ cyclic variations of the velocity of large-scale motions.

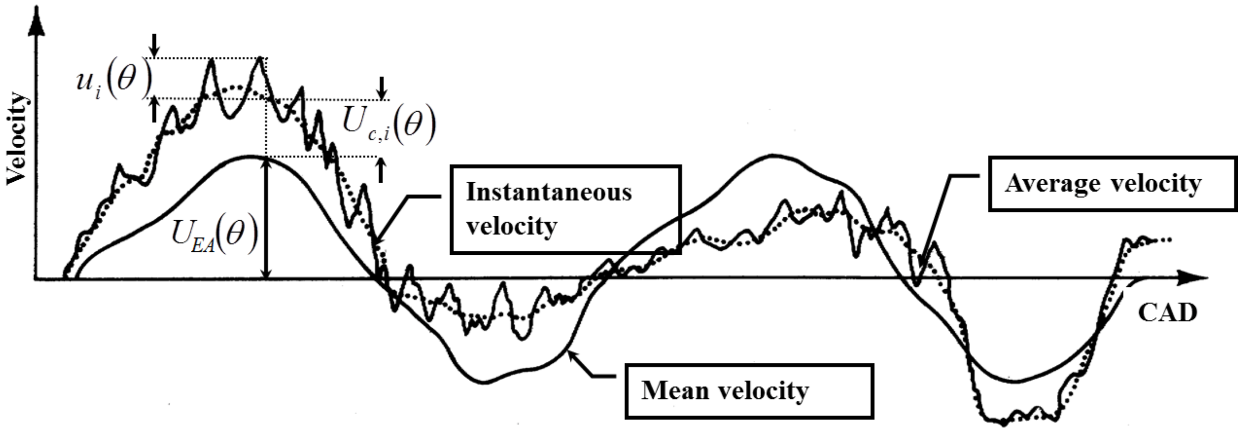

FIGURE 2.12: Triple instantaneous velocity decomposition proposed in [12].

By combining the above two expressions, the instantaneous velocity field can be decomposed into three terms:

$$U_i(\theta) = U_{EA}(\theta) + U_{c,i}(\theta) + u_i(\theta) \tag{2.3}$$

The ensemble-averaged velocity U_{EA} represents simply the averaged behavior of large-scale motions, $U_{c,i}$ gives access to cyclic variations of large-scale motions, and u_i represents variations of small-scale motions which are related to turbulence. Different decomposition methods were proposed to realize the above decomposition.

Matsuda et al. [40] applied the Gaussian filter method on the instantaneous velocity field to reduce the turbulent part, and the filter size was chosen to contain 80% of the energy of the measured velocity such that only large-scale structures are retained. Such a choice of threshold remains subjective for users, and it is difficult to find an optimal value for in-cylinder flow analysis as the fraction of kinetic energy stored in large-scale structures is variable.

Some attempts have been made to use fast Fourier transform (FFT) [101–103], but, similarly to the Gaussian filter method, the determination of a cut-off frequency to separate large- and small-scale remains difficult.

The wavelet method is suitable for the analysis of non-stationary data. It uses functions located both in real space and in Fourier space. The wavelet transform is an infinite set of transforms (wavelets) depending on the merit function used to calculate it. It is very useful for analyzing data with gradual changes in frequency. Farge [104] first proposed its application to turbulence analysis. It is then mainly used to extract coherent structures in the flow, as presented in several works [105–107]. It should be noted that the wavelet is applied to the vorticity of the flow, which is not directly available in experiments. The other drawback is that this method depends on the choice of the wavelet used for the decomposition. For example, the Morlet wavelet allows high-frequency resolution but poor temporal resolution. Conversely, a Gaussian derivative wavelet will give good temporal resolution but poor frequency resolution.

Dynamic Mode Decomposition (DMD) [108] is a data-driven, model-free decomposition technique. It is suitable for revealing spatio-temporal features of both numerically and experimentally acquired data. Conceptually, DMD performs a low-dimensional spectral decomposition of the data into a set of DMD modes representing the decomposition's spatial contribution. Their amplitudes specify their impact, and their associated eigenvalue, referred to as the DMD eigenvalue, characterizes their frequency and growth rate. Each DMD mode corresponds to a single frequency and a decay/growth rate, which can be interesting for analyzing different frequency ranges. This method is mainly applied to velocity fields for analyzing the flow evolution [109, 110] and to pressure and temperature fields for studying the combustion process [111, 112].

More studies choose proper orthogonal decomposition (POD) [113] which is a powerful tool in data analysis and was introduced in the turbulent flow analysis by Lumley [114] in 1967. The instantaneous flow field can be expressed as a linear combination of mutually orthogonal POD modes. In addition, the POD modes are optimal because most of the total kinetic energy in the flow can be captured using only the first few POD modes. These modes can be obtained by solving a Fredholm integral equation whose kernel is built from a set of data from numerical simulations or experiments. In in-cylinder flow analysis, POD is used to decompose the flow field into a series of POD modes. Each mode represents coherent structures of a specific range of spatial scales. Two categories of POD are commonly used in in-cylinder flow analysis:

- The phase-dependent POD, based on the snapshots method introduced by Sirovich [115–117], can be applied directly to velocity fields obtained from several engine cycles at a given crank angle. This process can be repeated for different crank angles of interest in an engine cycle.
- The phase-invariant POD aims at providing a single set of POD modes to represent the flow pattern over the whole engine cycle [118]. This technique is carried out using the whole dataset of the investigated phase range. The coefficients of each mode are then time-dependent, and their temporal evolution offers the possibility for rapid analysis of the in-cylinder flow structures and the energy transfer between different scales. For time-varying geometry like a piston engine, all the velocity fields at different phases are resized on a single baseline grid following the methods described in [118].

Several analyses can be found in the literature [44, 119–121] based on the phase-dependent POD. Voisine et al. [46, 122] applied the phase-invariant POD to PIV data to investigate the tumble breakdown near the TDC. Buhl et al. [123] proposed the conditional averaging method. Roudnitzky et al. [124] proposed the POD triple decomposition method and Qin et al. [125] proposed quadruple decomposition. Chen et al. [121] proposed a practical guide for using POD in in-cylinder flow analysis. The advantage of POD is that it does not require prior knowledge of the flow. The downside is that it requires a huge accumulation of data to achieve a good convergence of the projection basis. For numerical simulation, this means carrying out a very large number of cycles. Moreover, the choice of the number of modes is also subjective, and the fundamental reason is that one cannot objectively distinguish the flow variability due to CCV of the large-scale vortices from that due to turbulence. A separation criterion based on the correlation between modes was proposed by Qin et al. [125] for a quadruple POD method in which the flow field was decomposed into a mean part, a coherent part, a transition part, and a turbulent part which contained structures of different scales. They later coupled POD and DMD [126] by applying DMD in each separated component for their characterization. Rulli et al. [127] critically discussed the potential and limitations of different POD methods for the analysis of in-cylinder flow. They also proposed another quadruple decomposition using POD which was based on Kolmogorov's hypothesis for homogeneous turbulence.

A more recent method named Empirical Mode Decomposition (EMD) is also considered a promising tool to differentiate between large- and small-scale flow variations. Initially created by Huang et al. [128] to deal with 1D time series, EMD has been extended to treat multidimensional and multivariate data like the in-cylinder flow field. Foucher et al. [129] applied EMD to 1D velocity profiles measured experimentally and proved the potential of EMD in analyzing complex flow with turbulence. In the Ph.D. thesis of Sadeghi [19], the EMD method was extended to deal with the 2D velocity field by separating large-scale organized motion and small-scale fluctuations from the instantaneous velocity field. The method was later improved to reduce mode mixing [130] and to treat time-varying geometry [1]. Studies by Sadeghi et al. [1, 130] have shown that EMD can decompose the instantaneous velocity field into a limited number of modes containing structures of different scales, and the combination of these modes gives a low-frequency (LF) part and a high-frequency (HF) part. The HF part represents the turbulent fluctuations and corresponds to $u_i(\theta)$, while the LF part is associated with the large-scale motion which corresponds to $U_{EA}(\theta) + U_{c,i}(\theta)$ (in Eq. (2.2)). By removing the ensemble-averaged velocity $U_{EA}(\theta)$ from the LF part, one can easily get access to the variations of the large-scale motion $U_{c,i}(\theta)$. Compared to the widely used POD method, the advantage of EMD is that the decomposition is free of a projection basis calculated using ensemble-averaged velocity, which POD needs, and that the decomposition relies only on the instantaneous velocity. An example of EMD application result on instantaneous PIV measurements of in-cylinder flow is shown in Figure 2.13. It shows on the left the instantaneous velocity field, in the middle the low-frequency structures extracted from this same velocity field using the bivariate EMD2D technique, and high-frequency fluctuations on the right. The application of the method over several cycles makes it possible to distinguish the mean-field, the contribution of the large-scale coherent structures, and the turbulent fluctuations. A more detailed description of the EMD method will be given in Chapter 4.

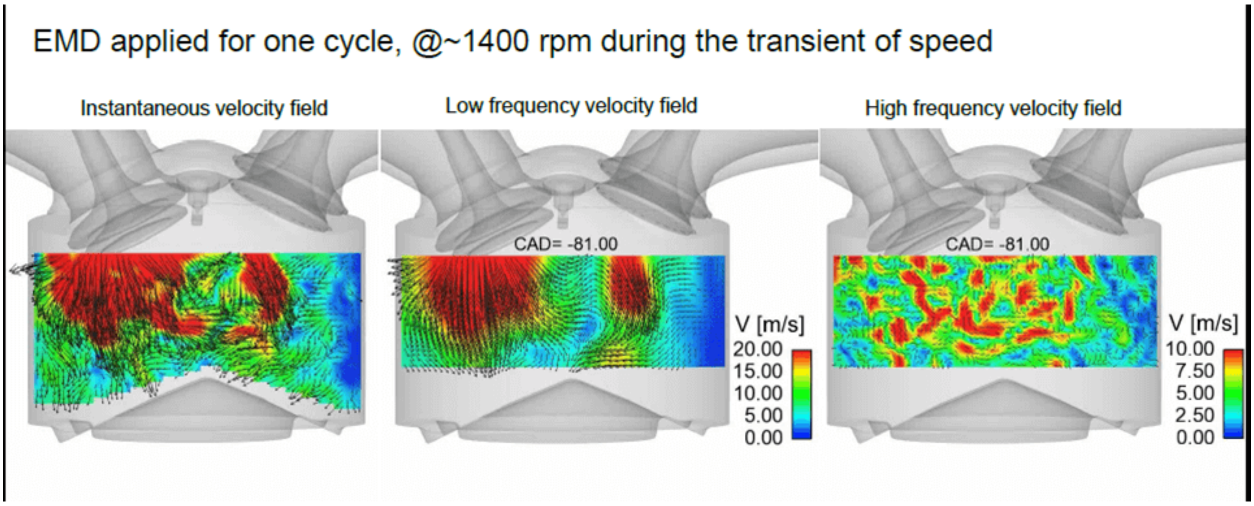

FIGURE 2.13: Example of EMD application on PIV data.

2.7 Summary of main findings

From the above literature review, some key points can be extracted as follows:

- In SI engines, CCV of the combustion process are mainly caused by the local flow state at spark timing. Local flow characteristics like velocity magnitude and orientation are critical for the flame kernel's early growth, which is crucial to the global combustion speed. Other characteristics like temperature and mixture composition are also affected by the in-cylinder flow, both by the large-scale motion and by the small-scale turbulence, during the engine cycle. The most critical CCV factor is thus the internal aerodynamics.
- The variability of the flow can originate from flow structures of different scales. Suitable decomposition tools are needed to separate turbulent fluctuations and large-scale variations so that their impact on the combustion can be decoupled. The POD method, as the most commonly used tool in in-cylinder flow analysis, has a major drawback related to global convergence, which is easily overcome by the more recent EMD method.
- The tumble motion is of 3D nature, and it seems to experience a deformation during the compression stroke, which is related to the elliptical instability. Multi-planar and even 3D analyses of the tumble motion are required to follow this evolution and to capture the 3D characteristics of the tumble correctly.
- The tumble motion presents a certain level of variability, which can be traced back to the beginning of the intake stroke. The intake flow, interacting with the valves before entering the chamber, is the primary source of the tumble formation. Its variability could be accumulated and amplified during the in-cylinder flow development. The intake flow can be divided into some dominant sub-flows, and their interaction may lead to CCVs of the flow as supposed by Krüger et al. [99], which needs further demonstration.
- A complete cause-and-effect chain is rarely built in most CCV studies and was partially done in the work of Kruger et al. [99]. A detailed description of the flow evolution using the detailed information brought by LES, including principal flow-wall interactions that occur at different stages, is still of interest and could offer potential ways of action for reducing CCV generated by the flow.

Based on this literature review, further research efforts required in the in-cylinder flow analysis are identified. In this thesis, we would like to address some central issues with our contributions to the physical comprehension of the internal aerodynamics in SI engines using advanced flow analysis tools:

- POD method has been the most used decomposition method in most in-cylinder flow analyses. Nevertheless, the more recent EMD method has similar capacities in scale separation as POD, and it does not require the statistical convergence mandatory for POD. EMD has been applied to studies on experimental PIV data, and in this thesis, we look forward to examining its capabilities in LES data processing. Some improvements to EMD may be necessary for its massive application on LES data.
- The tumble vortex was proved to be three-dimensional, while the characterization of the tumble was mainly realized by two-dimensional multi-planar analyses, especially those based on PIV data. Studies in 2D planes rely on an appropriate selection of planes which could be difficult without information from the 3D perception of in-cylinder flow. Numerical simulations allow the visualization of the tumble vortex in the whole cylinder, and the quantitative characterization of the tumble in 3D still needs suitable tools. In this thesis, we intend to develop a numerical methodology for analyzing the 3D in-cylinder tumbling flow.

The EMD technique and the vortex detection algorithm Γ will be extended to deal with 3D multivariate data like the in-cylinder flow.

- To establish the cause-and-effect chain to explain the origins of CCV, we expect to offer a quantitative description of the tumble vortex evolution during the engine cycle. All the developed analysis tools will be coupled to characterize the tumbling flow in 3D and some well-defined 2D planes.

With our contributions to the in-cylinder flow analysis methodology, both physical and technical, we hope to provide a deep insight into the in-cylinder flow evolution and its impact on combustion, which allows us to propose promising solutions for the reduction of CCV in SI engines.

CHAPTER 3

Physical modeling approach

Contents

3.1 Principle of Large-Eddy Simulation 25
  3.1.1 Concept of LES 25
  3.1.2 Filtered governing equations 26
3.2 Modeling approaches 28
  3.2.1 Unresolved terms modeling 28
  3.2.2 Combustion modeling with ECFM-LES 29
  3.2.3 Spark ignition modeling with ISSIM 34

This chapter is divided into two main parts. The first part gives a general description of the Large-Eddy simulation and the system of equations. The second part presents the modeling approaches for SI engine simulation, including flow and combustion modeling.

3.1 Principle of Large-Eddy Simulation

3.1.1 Concept of LES

Turbulent flows exist in various fields, including engineering, earth sciences, and even life sciences. The simulation of turbulent flows has been a major approach in the research, and different kinds of simulation methods have been developed thanks to the increasing computational capacities.

Simulation methods can be categorized according to the resolved scales in each method: the Direct Numerical Simulation(DNS), the Large Eddy Simulation(LES), and the Reynolds Averaged Navier Stokes(RANS).

The DNS approach resolves the turbulent flows directly without any model. Thus all the scales of the flows are resolved. However, the corresponding cost renders the DNS inapplicable to most flows, especially for highly turbulent flows characterized by high Reynold number Re. Taking the simulation of homogeneous isotropic turbulence as an example, the number of grids needed to resolve all the scales fully grows like $O(Re^{(9/4)})$.

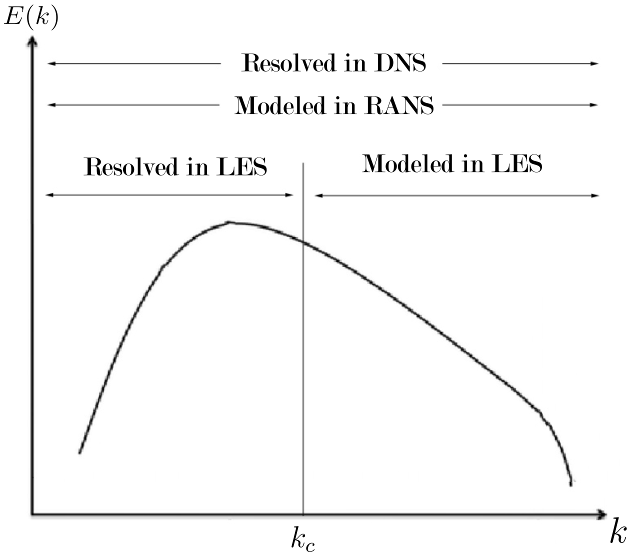

FIGURE 3.1: Resolved and modeled scales in a different type of simulation.

The RANS approach has been massively applied in all fields because of its low cost. The flow is decomposed by time-averaging into mean and fluctuating parts. The mean part is then obtained by resolving the corresponding time-averaged Navier-Stokes equations, while the fluctuating part is taken into account and fully modeled by the turbulence flow.

The LES approach is somewhat between the former two methods. In this method, spatial low-pass filtering is performed on the Navier-Stokes equations. Only large-scale flow containing most of the energy can be well captured using LES, while small-scale structures are supposed to be isotropic and need to be modeled. In practice, the filter size is chosen as the local grid size, and structures of scale smaller than it are modeled by the sub-grid scale (SGS) turbulence model.

For SI engine simulations, LES has been proved to be the most suitable one among all the three methods:

- Large-scale eddies carrying most parts of the energy are revolved, while small eddies are assumed to be relatively universal. Thus SGS models are more adapted to describe them.
- Compared to the RANS approach, well-captured large eddies can provide a more detailed description of turbulence/combustion interaction at the resolved scale, which gives access to capture combustion instabilities like CCV in SI engines. DNS can outperform LES in resolved scales, but its computational cost is not yet affordable with current HPC techniques.

3.1.2 Filtered governing equations

The Large-Eddy Simulation approach uses a filtering operation to remove scales of the flow structures which will not be resolved but modeled instead. Taking f a quantity to study, the corresponding filtered quantity $\bar{f}$ can be obtained using a convolution operation between f and the filter G_Δ:

$$\bar{f}(x) = \int f(x) G_\Delta \left(x - x'\right) dx' \tag{3.1}$$

This filtering operation allows decomposing the quantity f into a resolved part $\bar{f}$, and an unresolved SGS part f', which gives $f = \bar{f} + f'$. This decomposition is similar to the classical Reynolds decomposition for the RANS approach but only suitable for incompressible flows. In an SI engine, the flow experiences important density variations due to piston motion and combustion processes.

For such a compressible flow, the Favre filtering is proposed:

$$\widetilde{f} = \frac{\overline{\rho f}}{\bar{\rho}} \tag{3.2}$$

The associated fluctuations are noted as f'' and finally we have the new decomposition of the quantity f:

$$f = \widetilde{f} + f'' \tag{3.3}$$

This operation is not explicitly affected but implicitly because all the quantities are solved on a discretized grid. Any structures with a scale smaller than the grid size will be automatically excluded, and the resolved structures directly depend on the chosen grid size.

The Favre filtering is applied to the Navier-Stokes equations, and the resulted equations will be resolved in LES. In the following, all the equations will be presented, including the unresolved term in each one.

Filtered momentum conservation equation

$$\frac{\partial \bar{\rho} \widetilde{u}_i}{\partial t} + \frac{\partial}{\partial x_j}\left(\bar{\rho} \widetilde{u}_i \widetilde{u}_j\right) = -\frac{\partial \bar{P}}{\partial x_j} + \frac{\partial}{\partial x_j}\left[\overline{\tau_{ij}} - \bar{\rho}\left(\widetilde{u_i u_j} - \widetilde{u}_i \widetilde{u}_j\right)\right] \tag{3.4}$$

In the momentum equation, the filtered stress tensor is approximated by $\overline{\tau_{ij}} = 2\mu(\widetilde{S}_{ij} - \frac{1}{3}\delta_{ij}\widetilde{S}_{ll})$, where μ is the dynamic viscosity and δ_{ij} is the Kronecker symbol. $\tau_{ij}^{sgs} = -\bar{\rho}\left(\widetilde{u_i u_j} - \widetilde{u}_i \widetilde{u}_j\right)$ is the unresolved stress tensor for which a SGS turbulence model closure is required.

Filtered species conservation equation

$$\frac{\partial \bar{\rho} \widetilde{Y}_k}{\partial t} + \frac{\partial}{\partial x_j}\left(\bar{\rho} \widetilde{Y}_k \widetilde{u}_j\right) = -\frac{\partial}{\partial x_j}\left[\overline{V_{k,i} Y_k} + \bar{\rho}\left(\widetilde{u_i Y_k} - \widetilde{u}_i \widetilde{Y}_k\right)\right] + \widetilde{\dot{\omega}}_k \tag{3.5}$$

On the right hand of the equation, we can notice the unresolved flux $\bar{\rho}\left(\widetilde{u_i Y_k} - \widetilde{u}_i \widetilde{Y}_k\right)$ of species k, and the filtered consumption rate of species k, $\widetilde{\dot{\omega}}_k$. In the present approach, all species have identical diffusion coefficients, therefore the diffusive flux of species is estimated using Fick's law: $\overline{V_{k,i} Y_k} = -\bar{\rho} D_k \frac{\partial \widetilde{Y}_k}{\partial x_j}$, with D_k the species diffusion coefficient.

Filtered energy conservation equation

$$\frac{\partial \bar{\rho} \widetilde{e}_s}{\partial t} + \frac{\partial\left(\bar{\rho} \widetilde{e}_s \widetilde{u}_j\right)}{\partial x_j} = -\frac{\partial}{\partial x_j}\left(\tilde{u}_j\left(\bar{P}\delta_{ij} - \bar{\tau}_{ij}\right) + \bar{q}_i + q_i^{sgs}\right) + \widetilde{\dot{Q}} + \widetilde{\dot{\omega}}_T \tag{3.6}$$

In the above equation, $q_i^{sgs} = \overline{\rho e_s \widetilde{u}_j} - \bar{\rho} \widetilde{e}_s \widetilde{u}_j$ represents the unresolved flux of the sensible energy e_s. $\widetilde{\dot{\omega}}_T = -\sum_k \Delta h_{f,k}^0 \widetilde{\dot{\omega}}_k$ is the heat release rate due to combustion, where $\Delta h_{f,k}^0$ is the mass formation enthalpy of species k. $\widetilde{\dot{Q}}$ is a source term which can be attributed for instance to evaporation or heat losses at the walls. $\overline{q_i}$ is the filtered heat flux which is approximated by:

$$\overline{q_i} = -\overline{\lambda}\frac{\partial \widetilde{T}}{\partial x_j} + \bar{\rho}\sum_k D_k \widetilde{h}_{s,k}\frac{\partial \widetilde{Y}_k}{\partial x_j} \tag{3.7}$$

The filtered LES equations include unresolved terms resulting from the filtering operation. They contain contributions from the SGS level and require adequate models for the equation closure.

3.2 Modeling approaches

Inside SI engines, many physical phenomena can happen and interact between them. The modeling of such complex phenomena relies on the modeling of the flow, described by the Navier-Stokes equations, and the modeling of the combustion process, including the ignition and the flame propagation. The models used in this thesis are detailed in this section.

3.2.1 Unresolved terms modeling

The effect of the unresolved terms in Eqs. 3.4 to 3.6 on the respective filtered quantities needs to be modeled by suitable SGS closures.

In the momentum equation, the unresolved term, also referred to as subgrid stress (SGS) tensor, is generally closed using the Boussinesq eddy viscosity assumption. The SGS tensor is hereby described using the viscous tensor used for Newtonian fluids, but with a turbulent viscosity ν_t:

$$\bar{\rho}\left(\widetilde{u_i u_j} - \tilde{u}_i \tilde{u}_j\right) = -2\nu_t \widetilde{S^*_{ij}} + \frac{2}{3} k_{sgs} \delta_{ij} \tag{3.8}$$

where $\widetilde{S^*_{ij}}$ is the trace-less symmetric part of the strain rate tensor and k_{sgs} the SGS kinetic energy.

For species and total energy equations, a gradient approach is used to modeled unresolved term:

$$\bar{\rho}\left(\widetilde{Y_k u_j} - \widetilde{Y}_k \widetilde{u}_j\right) = -\bar{\rho}\frac{\nu_t}{Sc_t}\frac{\partial \widetilde{Y}_k}{\partial x_j} \tag{3.9}$$

$$\overline{\rho e_s u_j} - \bar{\rho}\widetilde{e}_s \widetilde{u}_j = -\bar{\rho} c_p \frac{\nu_t}{Pr_t}\frac{\partial \widetilde{T}}{\partial x_j} \tag{3.10}$$

The turbulent Prandtl number Pr_t and the turbulent Schmidt number Sc_t are simply fixed constant. The eddy viscosity ν_t needs further modeling using the SGS turbulence model, for instance, the Smagorinsky model[131] or Sigma model[53].

According to a simple dimensional analysis, the eddy viscosity ν_t has the dimension of a diffusion coefficient. A general expression for ν_t is thus given:

$$\nu_t = (C_m \Delta)^2 D(u) \tag{3.11}$$

where Δ is the grid size and $D(u)$ a differential operator on the velocity. The SGS turbulence model aims at giving an explicit expression of $D(u)$.

Smagorinsky model

The Smagorinsky model is the most simple model and has been proved to perform reasonably well [132].

In the Smagorinsky model, the operator $D(u)$ is defined as the filtered strain rate $\sqrt{2\tilde{S}_{ij}\tilde{S}_{ij}}$. This is the mathematical realization of the Boussinesq hypothesis that turbulent fluctuations are dissipative in the mean flow. The Smagorinsky coefficient C_s is found to be 0.18 in homogeneous isotropic turbulence.

This model is easy to implement but has some drawbacks summarized as follows:

- The coefficient C_s is an a priori input, and its value has been found to be flow-dependent.
- The eddy viscosity does not vanish for a turbulent flow over the wall and for a laminar flow.

Sigma model

The Sigma model [53] can help avoid problems introduced by the Smagorinsky model. The differential operator D_σ in this model is formed based on the three singular values of the velocity gradient tensor, noted as σ_1, σ_2 and σ_3 in their descending order, such that:

$$D_\sigma = \frac{\sigma_3 \left(\sigma_1 - \sigma_2\right) \left(\sigma_2 - \sigma_3\right)}{\sigma_1^2} \tag{3.12}$$

The coefficient C_σ is set to be 1.5 in this study.

3.2.2 Combustion modeling with ECFM-LES

In the energy equation 3.6, the source term accounts for the energy brought by chemical reactions, like the combustion inside SI engines. The energy source term $\widetilde{\dot{Q}}$ depends also on the source term $\widetilde{\dot{\omega}_k}$ in the species equations 3.5. A detailed chemistry calculation is necessary to evaluate the value of these source terms accurately but would be dominant in CPU effort in a SI engine LES. Well-established combustion models have been developed to reduce the cost while correctly representing the combustion process inside SI engines.

The choice of a suitable combustion model can be made based on the turbulent premixed combustion diagram, the Borghi-Peters diagram [133], presented in Figure 3.2.

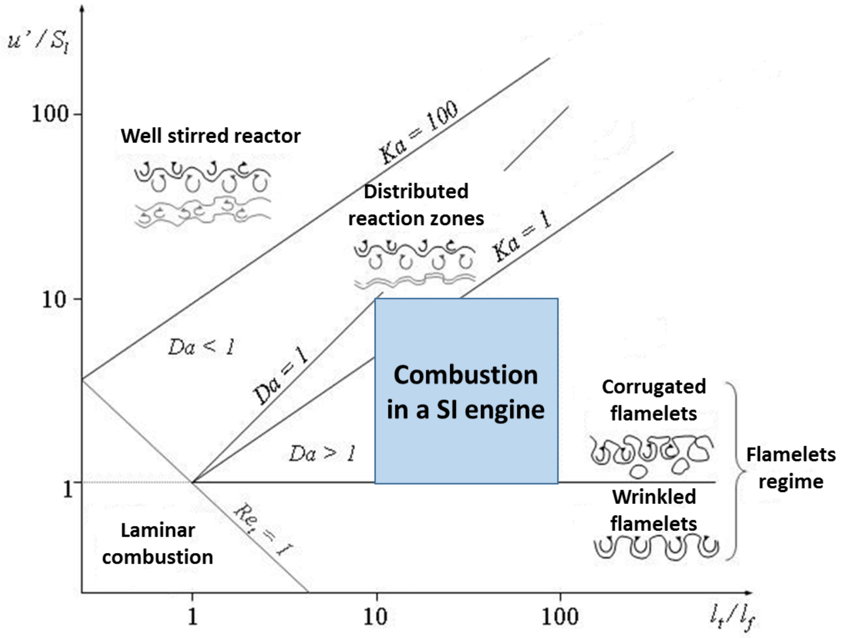

FIGURE 3.2: Premixed turbulent combustion diagram by Peters [134].

According to the ratio between the turbulence velocity and the laminar flame speed and the ratio between the integral length scale and the laminar flame thickness, the diagram indicates the corresponding regime for premixed turbulent combustion. The interaction between the flame and the turbulent eddies can also be qualitatively described based on two non-dimensional numbers:

- The Karlovitz number Ka, ratio between the chemical time scale τ_c and the Kolmogorov time scale τ_k:

$$Ka = \frac{\tau_c}{\tau_k} \tag{3.13}$$

- The Damköhler number Da, the ratio between the turbulent integral time scale τ_t and the chemical time scale τ_c:
$$Da = \frac{\tau_t}{\tau_c} \tag{3.14}$$

In SI engines, the combustion regime usually remains inside the blue box in Figure 3.2. The flame structure belongs to the corrugated flamelet regime. In this regime, the chemical time scale is relatively small compared to the turbulence time scale. Chemical reactions occur in very thin regions that can be distorted and convected by the flow. Turbulent eddies can wrinkle the flame front but cannot affect the reaction zone structures. Thus, the flame behaves like a laminar one locally. Based on the flamelet assumption, the flame front can be regarded as an interface separating the fresh and burned gases.

The Extended Coherent Flame Model (ECFM) presented hereafter will be used for this study. The ECFM model was initially developed for RANS and then adapted for LES. Compared to the CFM model from which ECFM originated, it can model partially premixed mixtures and variable fresh gases temperature.

LES combustion filter

The fresh and burned zone can be identified using the progress variable c as shown in Figure 3.3. The flame front is thus the interface between these two zones. To capture the flame front precisely, the LES grid size needs to be comparable to the flame thickness δ_L whose value varies typically around 0.01 and 0.1 mm. Such a spatial resolution is still impossible to handle with LES, for which the typical grid size used in the combustion region of engine configurations is 0.25 to 0.5 mm. Resolving the flame front at the grid-scale Δ_x can also be challenging as it involves steep gradients of filtered quantities. Therefore, the flame front is filtered again at a larger scale $\hat{\Delta} = n_{res}\Delta_x$ where n_{res} is chosen between 5 and 10. Δ_x is a typical cell size, and $nres$ is set to 8 in the present study [26, 85].

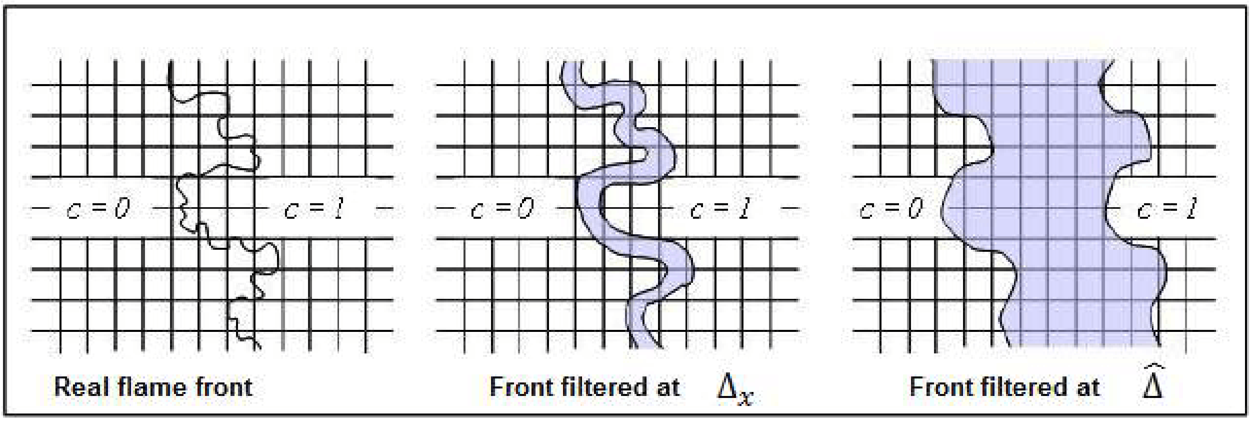

FIGURE 3.3: Flame front filtering in ECFM-LES [134].

The filtered progress variable $\tilde{c}$ is then calculated by LES to describe the filtered flame front. The ECFM model used is a modified version of the reference version, called species-based ECFM [135]. The progress variable is not transported but directly calculated as:

$$\tilde{c} = \frac{\sum_i \tilde{Y}_i^b}{\sum_i \tilde{Y}_i^u + \sum_i \tilde{Y}_i^b} \tag{3.15}$$

where $\tilde{c}$ is the filtered progress variable, $\tilde{Y}_i$ the filtered species mass-fraction with superscript u for "unburned" and b for "burned".

Species and energy equations

In ECFM-LES, the description of the air/fuel mixture is largely simplified using only seven chemical species: O_2, N_2, CO_2, H_2O, CO, H_2, C_xH_y where the latter is the fuel considered as a single component surrogate whose thermodynamic properties are known and tabulated.The filtered transport equations of species at the combustion filter scale are written following:

$$\frac{\partial \bar{\rho}\tilde{Y}_i^X}{\partial t} + \nabla \cdot \left(\bar{\rho}\tilde{u}_i^X \right) = \nabla \cdot \left(\bar{\rho}(\nu + \nu_t)\nabla \tilde{Y}_i^X \right) + \bar{\rho}\tilde{\dot{\omega}}_i^X \tag{3.16}$$

Diffusivities in species and energy equations need to be equal in the CFM approach, as this approach is based on the modeling of a progress variable transport equation. For that reason, the molecular and turbulent Prandtl and Schmidt numbers need to be equal $Pr = Sc$ and $Pr_t = Sc_t$.where^{-}and$^{\sim}$ denote Reynolds and Favre filter respectively. $\bar{\rho}$ is the filtered density and X represents either u or b. ν is the molecular kinematic viscosity and $\hat{\nu}_t$ is the subgrid-scale kinematic viscosity estimated at the combustion filter size $\hat{\Delta} = nres\Delta_x$. The source term $\tilde{\dot{\omega}}_i^X$ takes into account the reaction rate and is computed separately for burned and unburned species.

An important change on the eddy viscosity is done at the combustion filter scale:

$$\hat{\nu}_t = C_v \hat{u}' \hat{\Delta} \tag{3.17}$$

The constant C_v was estimated to be 0.12 in the work presented in [134]. Supposing that the spectral structure of turbulence follows the Kolmogorov cascade, the fluctuant velocity $\hat{u}'$ at the scale $\hat{\Delta}$ can be estimated:

$$\hat{u}' = u' \left(\frac{\hat{\Delta}}{\Delta_x} \right)^{1/3} \tag{3.18}$$

where u' is the SGS turbulent fluctuations.

To determine the local fresh gas temperature, a transport equation for the unburned enthalpy $\widetilde{h}_s^u$ is used [134, 136]:

$$\frac{\partial \bar{\rho}\widetilde{h}_s^u}{\partial t} + \frac{\partial \bar{\rho}\tilde{u}_i\widetilde{h}_s^u}{\partial x_j} = \frac{\bar{\rho}}{\bar{\rho}^u}\frac{\partial \bar{P}}{\partial t} + \frac{\partial}{\partial x_j}\left(\bar{\rho}\left(\frac{\nu}{Sc} + \frac{\hat{\nu}_t}{Sc_t} \right)\frac{\partial \widetilde{h}_s^u}{\partial x_j} \right) + \frac{\partial \tilde{u}_j}{\partial x_j}\bar{\tau}_{ij} + \tilde{\dot{Q}} \tag{3.19}$$

where $\bar{\rho}^u = (1-\tilde{c})\bar{\rho}$ is the unburned density. The filtered enthalpy is deduced from the sensible energy following:

$$\widetilde{h}_s = \widetilde{e}_s + \frac{\bar{P}}{\bar{\rho}} \tag{3.20}$$

The burned gases enthalpy can be deduced from [85]:

$$\widetilde{h}_s = (1-\tilde{c})\widetilde{h}_s^u + \tilde{c}\widetilde{h}_s^b \tag{3.21}$$

The corresponding temperature T^u and T^b can then be easily deduced based on the sensible enthalpy and the composition of unburned and burned gases, respectively. Finally, the density of unburned and burned gases can be obtained supposing gases are ideal:

$$\bar{\rho}^u = \frac{\bar{P}}{r^u Tu} \tag{3.22}$$

$$\bar{\rho}^b = \frac{\bar{P}}{r^b T^b} \tag{3.23}$$

For the above equations, the unclosed terms are the source terms related to the combustion. The modeling of these terms relies on a flame surface density(FSD) concept, which links the reaction rate of the progress variable $\overline{\dot{\omega}}_c$ to the FSD such as:

$$\overline{\dot{\omega}}_c = \bar{\rho}^u S_L \bar{\Sigma}_{\tilde{c}} \tag{3.24}$$

Its product with the FSD $\bar{\Sigma}_{\tilde{c}}$ gives the local flame surface per unit volume, and $\overline{\dot{\omega}}_c$ is thus the growth rate of the flame surface at laminar flame speed S_L.

The laminar flame speed S_L is usually obtained from existing correlation. An example is the Metghalki & Keck correlation:

$$S_L = S_L^0 \left(\frac{T^u}{T_0}\right)^{\alpha} \left(\frac{P^u}{P_0}\right)^{\beta} (1 - 2.1\chi_{EGR}) \tag{3.25}$$

where S_L^0 is the reference speed at reference conditions ($P_0 = 1atm$) and ($T_0 = 298K$), and χ_{EGR} the volume rate of exhaust gas recirculation. Coefficients α and β are fuel dependent and varies with the equivalence ratio ϕ. For iso-octane their expressions are as follows:

$$\alpha_{\text{iso-octane}} = 2.18 - 0.8(\phi - 1) \tag{3.26}$$

$$\beta_{\text{iso-octane}} = -0.16 + 0.22(\phi - 1) \tag{3.27}$$

For unburned species, without considering the auto-ignition combustion mode contribution, the source term $\tilde{\dot{\omega}}_i^u$ is computed as:

$$\tilde{\dot{\omega}}_i^u = -\frac{\tilde{Y}_i^u}{1-\tilde{c}} \left(\frac{\rho_u}{\bar{\rho}} S_l \bar{\Sigma} + \tilde{\dot{\omega}}_c^{ign}\right) \tag{3.28}$$

where ρ_u is the density of unburned gases, S_l the laminar flame speed, and $\bar{\Sigma}$ the flame surface density (FSD).

For burned species, the source term $\tilde{\dot{\omega}}_i^b$, without considering the auto-ignition combustion mode contribution, is evaluated as:

$$\tilde{\dot{\omega}}_i^b = Y_i^{b^*} \left(\frac{\rho_u}{\bar{\rho}} S_l \bar{\Sigma} + \tilde{\dot{\omega}}_c^{ign}\right) + (1 - \tilde{c})\tilde{\dot{\omega}}_i^{post} \tag{3.29}$$

where $Y_i^{b^*}$ is the burned gases composition following [136], $\tilde{\dot{\omega}}_i^{post}$ the post-oxidation reaction rate in burned gases defined by simplified kinetics [135]. In the present study, a two-step model is used to compute this term based on the equilibrium reactions of the CO_2-CO system.

The source term in the energy equation related to the enthalpy variations can be written as:

$$\overline{\dot{\omega}}_{h_s} = -\sum_k \Delta h_k^0 \overline{\dot{\omega}_k} \tag{3.30}$$

In the above two equations, two terms remain to be defined: the FSD $\bar{\Sigma}$ and the reaction rate $\tilde{\dot{\omega}}_c^{ign}$. The last one is closed by the ISSIM model accounting for the energy deposition due to spark ignition.

Flame surface density transport equation

The FSD $\bar{\Sigma}$ is the last element necessary to compute the local reaction rate. It can be expressed using the progress variable c:

$$\bar{\Sigma} = \overline{|\nabla c|} \tag{3.31}$$

A transport equation of $\bar{\Sigma}$ has been given in [137]. However, as mentioned in [84], this equation contains a non-gradient transport term which may lead to numerical instabilities. Instead, a new transport equation is proposed for $\Sigma_{\tilde{c}}$ to avoid this issue (Though $\bar{\Sigma}_{\tilde{c}}$ does not represent the real FSD as $\bar{\Sigma}$, the flame surface of each obtained from their volume integral remains the same):

$$\bar{\Sigma}_{\tilde{c}} = \bar{\Sigma} + \nabla \cdot ((\bar{c} - \tilde{c})\bar{\mathbf{N}}), \quad \bar{\mathbf{N}} = -\frac{\nabla \tilde{c}}{|\nabla \tilde{c}|}, \quad \bar{c} = \tilde{c}\frac{\bar{\rho}}{\bar{\rho}^b} \tag{3.32}$$

where $\bar{N}$ is the local vector normal to the iso-surfaces of the progress variable. The transport equation for the filtered flame surface density is modelled as follows [84, 85]:

$$\frac{\partial \bar{\Sigma}_{\tilde{c}}}{\partial t} + T_{res} = T_{sgs} + S_{res} + S_{sgs} - P_{res} + C_{res} + C_{sgs} \tag{3.33}$$

The four resolved terms T_{res}, S_{res}, P_{res} and C_{res} are respectively resolved contributions from transport, stretch, propagation and curvature. T_{sgs}, S_{sgs} and C_{sgs} are contributions of sub-grid scale from transport, stretch and curvature. Their impacts on the flame surface are resumed in Figure 3.4.

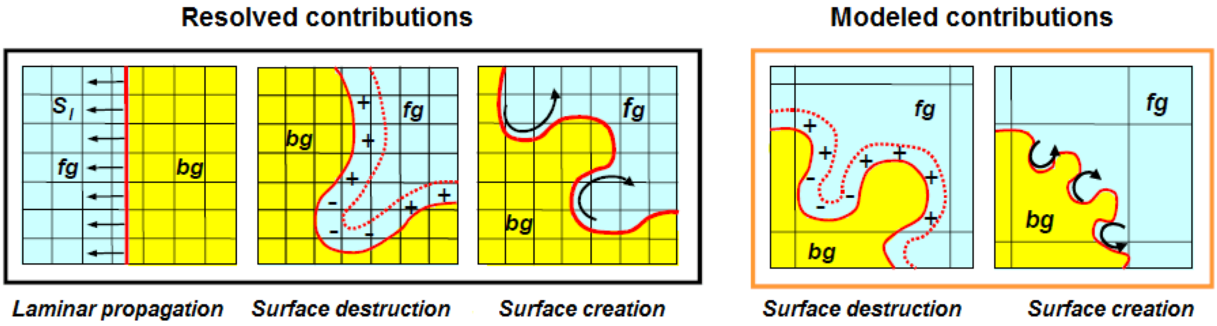

FIGURE 3.4: Resolved and sub-grid scale contributions in the FSD equation [134].

The resolved terms are detailed as follows:

- The resolved convective transport:

$$T_{res} = \nabla \cdot (\tilde{\mathbf{u}}\bar{\Sigma}_{\tilde{c}}) \tag{3.34}$$

- The resolved strain corresponding to the flame strain rate due to the resolved structures:

$$S_{res} = (\nabla.\tilde{\mathbf{u}} - \bar{\mathbf{N}}\bar{\mathbf{N}} : \nabla\tilde{\mathbf{u}})\bar{\Sigma}_{\tilde{c}} \tag{3.35}$$

- The propagation P_{res} and resolved curvature terms C_{res} are physically related and guarantee the laminar flame propagation when the SGS turbulence is close to zero. The proposed formulation of these terms is based on the normal to the iso-surface of the filtered progress variable $\tilde{c}$:

$$P_{res} = \nabla \cdot (S_D \bar{\mathbf{N}}\bar{\Sigma}_{\tilde{c}}) \tag{3.36}$$

$$C_{res} = S_D(\nabla.\bar{\mathbf{N}})\bar{\Sigma}_{\tilde{c}} \tag{3.37}$$

S_D, the propagation velocity, is defined as:

$$S_D = (1 + \tau\tilde{c})S_L \tag{3.38}$$

where τ is the thermal expansion rate across the flame front: $\tau = \bar{\rho}^u / \bar{\rho}^b - 1$.

The sub-grid terms are modeled to close the equation:

- The unresolved transport T_{sgs} is modeled using a gradient assumption and is written in the form of a turbulent diffusion:

$$T_{sgs} = -\nabla \cdot \left(\frac{\hat{\nu}_t}{Sc_t} \nabla \bar{\Sigma}_{\tilde{c}} \right) \tag{3.39}$$

- The modeling of unresolved strain S_{sgs} borrows the principle of the turbulent strain rate in RANS approach:

$$S_{sgs} = \alpha_{cfm} \Gamma \left(\frac{\hat{u}'}{S_L}, \frac{\hat{\Delta}}{\delta_L} \right) \frac{\hat{u}'}{\hat{\Delta}} \tag{3.40}$$

  The efficiency function Γ, known as Intermittent Turbulent Net Flame Stretch (ITNFS) model, considers all vortices' ability to wrinkle the flame. The work presented in [138] showed that resolved eddies smaller than the combustion filter scale $\hat{\Delta}$ would not affect the flame front. Thus their contribution should be included in the SGS part, which explains why all the parameters used are filtered at the scale of $\hat{\Delta}$. A coefficient α_{cfm} allows adjusting the combustion speed with respect to the ITNFS model used. Here the model of Meneveau and Poinsot [139] is used.

- The SGS curvature C_{sgs} is given by:

$$C_{sgs} = -\beta_0 S_L \frac{\left(\bar{\Sigma}_{\tilde{c}} - \bar{\Sigma}_{lam}\right) \bar{\Sigma}_{\tilde{c}}}{1 - \bar{c}} + \beta_c S_L (1 + \bar{\tau}) \frac{1 - \tilde{c}}{\bar{c}} \left(\bar{\Sigma}_{\tilde{c}} - \bar{\Sigma}_{lam}\right) \bar{\Sigma}_{\tilde{c}} \tag{3.41}$$

  β_0 and β_c are constants equal to 1 and 4/3 respectively. $\bar{\Sigma}_{lam}$ is the laminar part of the FSD defined as:

$$\bar{\Sigma}_{lam} = |\nabla \tilde{c}| + (\bar{c} - \tilde{c}) \nabla \cdot \bar{\mathrm{N}} \tag{3.42}$$

3.2.3 Spark ignition modeling with ISSIM

SI engines are usually designed with a relatively low compression ratio compared to Diesel engines, so the auto-ignition can be avoided. Therefore, an external energy source is needed to trigger the combustion achieved by the spark plug.

The ignition model chosen in the framework of this thesis, the ISSIM-LES model [140], decomposes the ignition process into two simplified steps. Firstly, an initial kernel of burned gases is deposited in the vicinity of the spark plug. The mass and the volume of the kernel depend on the energy released from the secondary circuit of the spark plug. The kernel will grow until its size becomes comparable to the combustion filter scale. A smooth transition between the laminar flame kernel growth and the turbulent flame propagation is ensured.

Initial burned gases kernel

At spark timing t_{spark}, an electric arc of length l_{spark} is generated in the vicinity of the spark plug. ISSIM model determines the energy $E(t_{spark})$ released by the electric arc and compares it to an estimated critical energy $E_c(t_{spark})$. Once $E(t_{spark}) > E_c(t_{spark})$, the combustion starts and an initial burned gases mass m^b_{ign} is deposited between the electrodes. The volume of the initial burned gases kernel is supposed to be equivalent to a cylinder with a radius of $2\delta_L$, δ_L being the laminar flame thickness, and a height of l_{spark}:

$$m_b^{ign} =< \rho^u l_{spark} 4\pi\delta_L^2 > \tag{3.43}$$

Brackets here represent an averaging around the spark plug.

To keep consistent with the ECFM-LES model, this initial kernel needs to be filtered at the combustion scale $\hat{\Delta}$ as well. A Gaussian profile of the initial volume fraction $\bar{c}_{ign}$ is then defined:

$$\bar{c}_{ign} = C_0 \exp\left(-\left(\frac{|x - x_{\mathrm{spark}}|}{0.6\hat{\Delta}}\right)^2\right) \tag{3.44}$$

x_{spark} is the coordinates of ignition point. The constant C_0 is chosen to guarantee that $\int \rho^b \bar{c}_{ign} dV = m_b^{ign}$. The reaction rate $\overline{\dot{\omega}}_c$ is also modified to take into account the fuel consumption caused by the ignition:

$$\bar{\dot{\omega}}_c = \max\left(\rho_u S_L \bar{\Sigma}_{\tilde{c}}, \rho_b \left(\bar{c}_{ign} - \bar{c}\right) dt^{-1}\right) \tag{3.45}$$

where dt is the simulation time step. As explained before, in ECFM-LES, the reaction rate is modeled thanks to the FSD equation. Therefore a source term related to the ignition should be added. Supposing that the initial kernel is spherical, the corresponding radius is given by:

$$r_b^{ign} = \left(3(4\pi)^{-1} \int \bar{c}_{ign} dV\right)^{1/3} \tag{3.46}$$

To match the surface of the initial kernel $4\pi\left(r_b^{ign}\right)^2$, the initial value of FSD Σ_{ign} should be $3\bar{c}/r_b^{ign}$. A wrinkling factor C_{surf} is also introduced to account for the non-perfect sphericity of the initial flame kernel such that:

$$\Sigma_{ign} = C_{surf} \frac{3\bar{c}}{r_b^{ign}} \tag{3.47}$$

The imposed source term is thus defined as:

$$\bar{\dot{\omega}}_{\Sigma}^{ign} = \max\left(0, \frac{\Sigma_{ign} - \bar{\Sigma}_{\tilde{c}}}{dt}\right) \tag{3.48}$$

In practice, the deposit of the initial kernel happens quite fast and usually lasts for several iterations in the simulation. The later growth phase is described in the next section.

Transition from kernel growth to flame propagation

After the deposit, the flame begins to propagate in the chamber. Though the initial kernel has already been filtered at the scale $\hat{\Delta}$, its size remains small compared to the filter size $\hat{\Delta}$. The growth of the flame kernel begins at the SGS level and ends at the resolved scale, and further development is charged by the ECFM-LES model. The ISSIM-LES model brings thus two significant modifications: a source term for the SGS curvature S_{ign} varying like $2/r^b$, and a transition coefficient $\alpha_{ign}(x,t)$ ensuring the transition of the ignition from the SGS level to the resolved scale. The modified FSD equation is presented below:

$$\begin{aligned}\frac{\partial \bar{\Sigma}_{\tilde{c}}}{\partial t} + T_{res} = {} & T_{\mathrm{sgs}} + \alpha_{ign}\left(S_{\mathrm{res}} + C_{\mathrm{res}}\right) - \left(\nabla . S_D \mathbf{N} \bar{\Sigma}_{\tilde{c}}\right) + S_{\mathrm{sgs}} + \alpha_{ign} C_{\mathrm{sgs}} \\ & + \left(1 - \alpha_{ign}\right) \underbrace{\frac{2}{3}\frac{(1+\tau)}{\tilde{c}} S_L \bar{\Sigma}_{\tilde{c}} \left(\bar{\Sigma}_{\tilde{c}} - \bar{\Sigma}_{lam}\right)}_{S_{ign}} + \overline{\dot{\omega}}_{\Sigma}^{ign}\end{aligned} \tag{3.49}$$

The transition coefficient is defined as:

$$\alpha_{ign}(x,t) = \frac{1}{2}\left(1 + \tanh\left(\frac{r^{b+}(t) - 1}{0.015}\right)\right), \quad r^{b+}(t) = \frac{r^b(t)}{0.65\hat{\Delta}} \tag{3.50}$$

At the beginning of the ignition, this coefficient is close to 0 to replace the resolved terms with the added source term of ignition. As the ignition process continues, its value becomes closer to 1 as the flame size is comparable to the filter size, and the source term of ignition is gradually canceled. The whole equation becomes identical to that described in the ECFM-LES model.

To evaluate the coefficient $\alpha_{ign}(x,t)$, the flame kernel radius $r^b(t)$ needs to be determined. Supposing a laminar flame kernel of spherical shape, its temporal evolution can be described as following:

$$\frac{\partial r^b}{\partial t} = (1+\tau)S_L \tag{3.51}$$

The relation is validated when only one flame kernel is presented, and thus not suiable to describe multiple spark ignitions. To resolve this problem, a new quantity Ψ is introduced:

$$\bar{\rho}\Psi = \frac{2\bar{\rho}\tilde{c}}{r^b} = \frac{2}{3}\bar{c}\Sigma_{ign} \tag{3.52}$$

A transport equation is established for Ψ. With the field of Ψ, one can easily define r^b and α_{ign} locally and simultaneously.

$$\bar{\rho}\frac{\partial \Psi}{\partial t} + \nabla\cdot(\bar{\rho}\widetilde{\mathbf{u}}\Psi) = \nabla\cdot\left(\frac{\hat{\mu}_t}{Sc_t}\nabla\Psi\right) - (1+\tau)\frac{S_L}{r^b}\bar{\rho}\Psi + \frac{2}{r^b}\bar{\omega}_c + \bar{\omega}_{\Psi}^{ign} \tag{3.53}$$

where $\overline{\dot{\omega}}_{\Psi}^{ign}$ is an additional source term at the instant of flame kernel creation.

$$\overline{\dot{\omega}}_{\Psi}^{ign} = \max\left(0, \frac{2/3\rho^b\Sigma_{ign} - \bar{\rho}\Psi}{dt}\right) \tag{3.54}$$

CHAPTER 4

Development of tools for analyzing turbulent flows in complex configurations

Contents

4.1 Empirical Mode Decomposition . . . 37
  4.1.1 General description of the method . . . 38
  4.1.2 Extension of the method for LES results of SI engine . . . 42
  4.1.3 2D EMD for time-varying geometry . . . 49
  4.1.4 Spatial 3D EMD . . . 60
  4.1.5 Spatio-temporal 3D EMD . . . 63
4.2 Vortex identification with Γ function . . . 65
  4.2.1 Γ_1 function in 2D plane . . . 65
  4.2.2 Γ_3 function in 3D volume . . . 66
4.3 Summary of main developments . . . 70

This chapter gives a detailed description of the flow analysis tools and of the new developments proposed, including the Empirical Mode Decomposition(EMD) for the characterization of flow structures of different scales and the Γ function for identifying rotational structures.

4.1 Empirical Mode Decomposition

The Empirical Mode Decomposition(EMD), introduced by Huang et al. [128] for univariate time series, is a data-driven method for analyzing nonlinear and non-stationary signals. It decomposes a signal into a finite set of amplitude and/or frequency modulated (AM/FM) components, called intrinsic mode functions (IMFs), and a residual component. It was extended for multivariate signals, firstly for complex signals [141, 142], and then for bivariate (BEMD) [143], trivariate (TEMD) [144], and finally multivariate (MEMD)[145]. The basic idea of all these approaches is to project the multivariate signal into certain directions sampled over a circle (BEMD), a sphere (TEMD), or a multidimensional sphere (MEMD) and then estimate an average signal envelop which is required in the sifting process of the EMD algorithm.

In this section, the principle of the original EMD will be described first, and then its extension for multivariate and multidimensional signals. Improvements made to consider the imbalance between different signal components and reduce the mode mixing are also presented. Finally, the EMD method is adapted for the LES results of SI engines, and possible applications are illustrated to prove the capability of the EMD in the flow analysis.

4.1.1 General description of the method

For a given time series $x[n]$, the original EMD works directly in temporal space to decompose the signal $x[n]$ into a set of intrinsic mode functions $c_i[n]$ (IMF) and a trend $r[n]$, expressed as:

$$x[n] = \sum_{i=1}^{N} c_i[n] + r[n] \tag{4.1}$$

Each IMF satisfies the following condition as specified in [128]:

- The number of local extrema and the number of zero-crossing are either equal or differ by exactly one (*i.e.*, all local maxima are positive and all local minima are negative).
- The mean value of the upper envelope defined by the local maxima and the lower envelope defined by the local minima is zero at any point (symmetric upper/lower envelope).

It is worth noting that an IMF is multi-scale as it can contain variable frequency and amplitude, unlike classical harmonic functions.

The EMD algorithm is resumed in Figure 4.1 and briefly described as follows:

1. Identification of all local maxima and minima of the signal $r_i[n]$ which initially equals to $x[n]$ with $i = 1$.
2. Building upper envelope $e_u[n]$ and lower envelop $e_l[n]$ passing through respectively all local maxima and minima using cubic spline interpolation.
3. Computation of the local mean $m[n] = (e_u[n] + e_l[n])/2$.
4. Subtraction of the local mean from the signal $r_i[n]$ to obtain modulated oscillations, written as $h_{ij}[n] = r_i[n] - m[n]$.
5. Verifying if $h_{ij}[n]$ satisfies the conditions of an IMF. If yes $h_{ij}[n]$ is exported as an IMF $c_i[n]$, else the steps 1-4 are repeated by setting $r_i[n] = h_{ij}[n]$.
6. Subtraction of the deviated IMF $c_i[n]$ from the actual residual $r_i[n]$ to continue the extraction of the next IMF from the new residual.
7. Ending of the decomposition if the residual obtained in the step 6 is monotonic as no oscillation exists.

The step 5 determines if the sifting process should stop based on the stoppage criteria proposed in [146] containing three parameters θ_1, θ_2 and α which allows to guarantee globally small fluctuations in the mean envelope $m[n]$ while take into account locally large excursions. The mode amplitude is computed as $a[n] = (e_u[n] - e_l[n])/2$ and used in the evaluation function $\sigma[n] = |m[n]/a[n]|$. The sifting is iterated until $\sigma[n] < \theta_1$ for some prescribe fraction $(1 - \alpha)$ of the total signal length while $\sigma[n] < \theta_2$ for the remaining fraction. Recommended values of $\theta_1 = 0.05$, $\theta_2 = 0.5$ and $\alpha = 0.05$ proposed in [146] are retained in this work also.

A time series is generated using the following expression for an exemplary application of EMD:

$$x[n] = A_1 \sin(2\pi f_1 t[n]) + A_2 \sin(2\pi f_2 t[n]) + 2t[n] \tag{4.2}$$

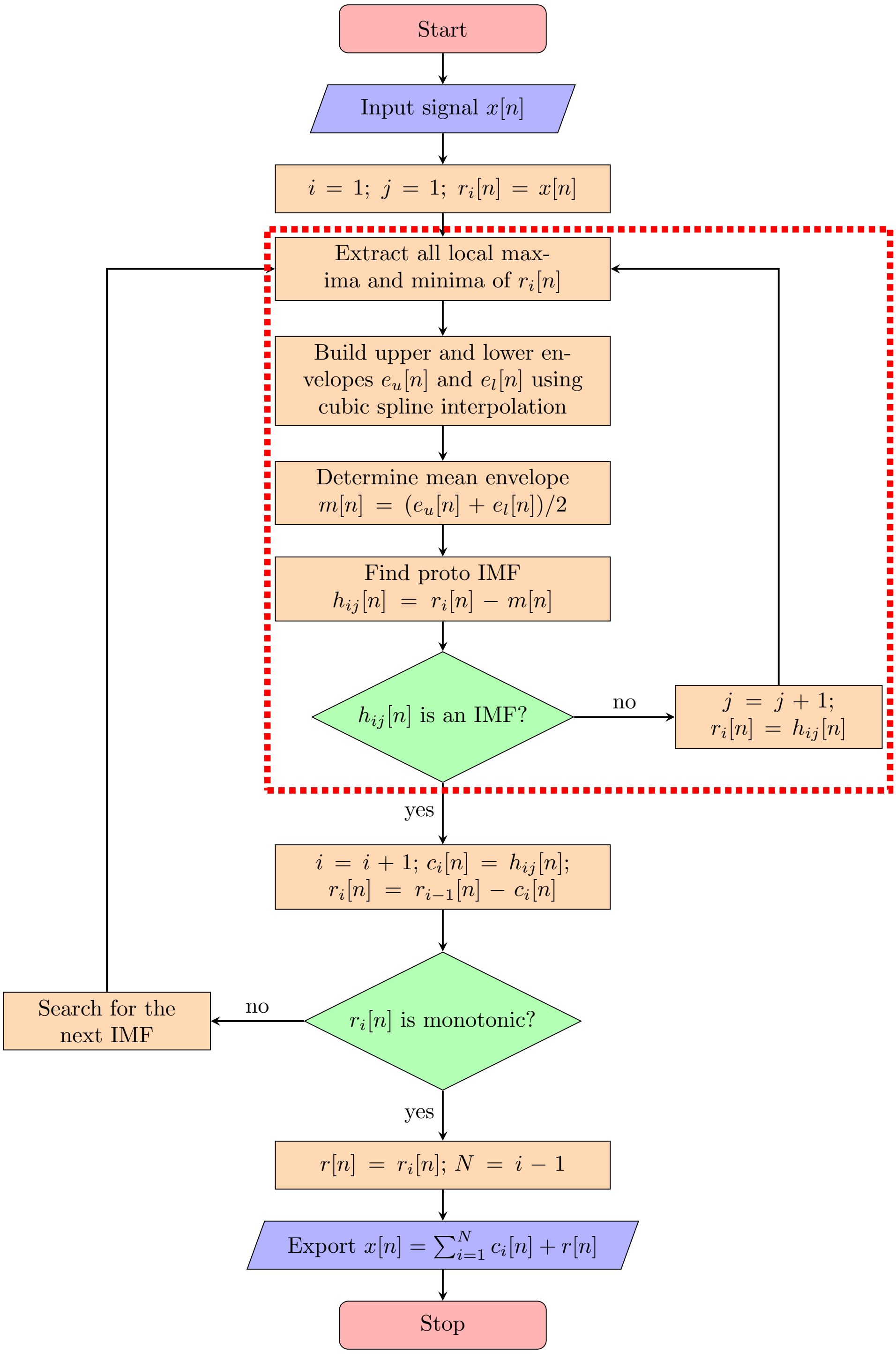

FIGURE 4.1: Flow chart of the 1D EMD. Sifting process in red dashed frame.

where $A_1 = 1$, $f_1 = 10\ Hz$ and $A_2 = 0.6$, $f_2 = 60\ Hz$, and $t[n]$ varies from 0 to 0.2s with 101 time steps. The tested series consists of a high-frequency part, a low-frequency part, and a monotonic trend. The results of EMD on the series are presented in Figure 4.2. EMD can separate different frequencies, starting from the highest and ending with a monotonic residual. Steps 1-5, included in the red dashed frame in Figure 4.1, constitute the sifting process of the IMF extraction which consists in removing the local mean of the given signal $r_i[n]$.

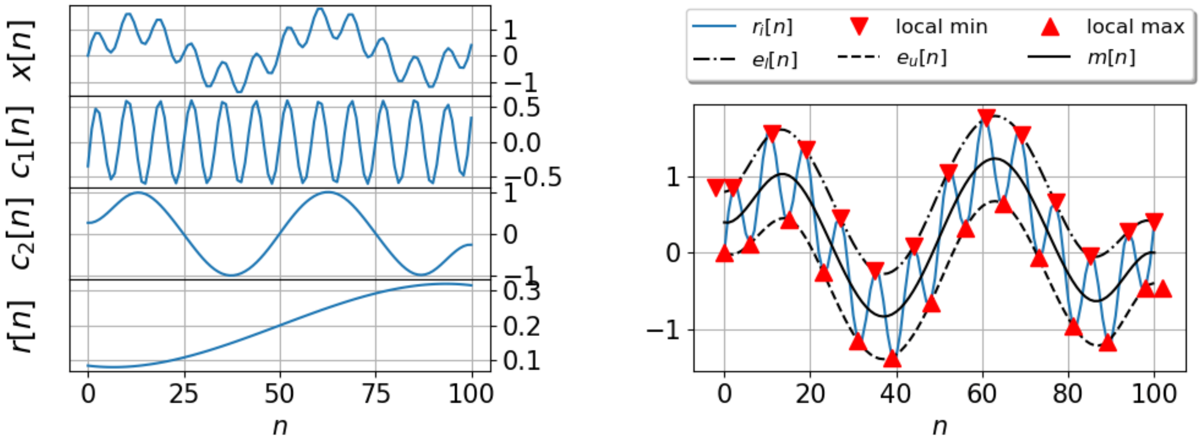

(A) IMFs and residual extracted by EMD.

(B) First iteration of the sifting process.

FIGURE 4.2: Results of EMD applied to a 1D time series.

An example of the sifting is plotted in Figure 4.2b. It needs to be noticed that the upper and lower envelopes are shorter than the series length if only local extrema identified inside the series are used for the interpolation. Extensions are thus needed by artificially adding local extrema outside the series. A classical approach is the symmetrical extension (or mirror extension) of the maxima and minima series on both borders so that the generated envelopes can cover the whole series and be used to compute the local mean at each point. The extension follows the principles described below:

- At least one local maximum and one local minimum are required outside both borders of the series, *i.e.*, $N_{sym} \geq 2$. The first (resp. last) N_{sym} local extrema are reflected about the left (resp. right) border to generate extrema on the left (resp. right) of the series.
- The values of the first (resp. last) two local extrema (one local maximum and one local minimum) are compared with that of the first (resp. last) data point:
    - If the first (resp. last) data point is compromised between the first (resp. last) two local extrema, the symmetric extension is performed normally about the left (resp. right) border, and N_{sym} extrema are inserted artificially.
    - If the first (resp. last) data point is larger than the first (resp. last) maximum, it will be considered as one of the N_{sym} local extrema to add on the left (resp. right) border.
    - If the first (resp. last) data point is smaller than the first (resp. last) minimum, it will be considered as one of the N_{sym} local extrema to add on the left (resp. right) border.

These principles are set so that envelopes of local minima and maxima can surely cover the whole series, especially the first and the last points, which can potentially pass beyond the envelopes if no precautions are taken as described above.

Such a simple extension does not allow a perfect treatment, and problems related to border effects are reported in several studies [147, 148]. The method's main drawback is that the artificially inserted extrema may not follow the series' trend near the borders, and errors can be accumulated during the sifting process. Some possible treatments are presented in [149–152], and here we present the one proposed by Sandoval et al. in [153]. In their approach, the autoregressive (AR) model [154] is utilized as both a forward and backward predictor to extend the series beyond the borders resulting in an extended series as follows:

$$x[n] = \begin{cases} \sum_{p=1}^{P} \alpha^*_{P-p} x[n+p], & -L \leq n < 0 \\ x[n], & 0 \leq n \leq N \\ \sum_{p=1}^{P} \alpha_p x[n-p], & N < n \leq N+L \end{cases} \tag{4.3}$$

where P is the order of the AR model, α_p and α^*_p are forward and backward prediction coefficients obtained by Burg's algorithm, and L is the length of the extension for each side. EMD is then performed on the extended series to mitigate border effects, and only results of EMD for $0 \leq n \leq N$ are kept. A parametric study of L is made on the test series used above and presented in Figure 4.3. The order of the AR model is set as $P = L$.

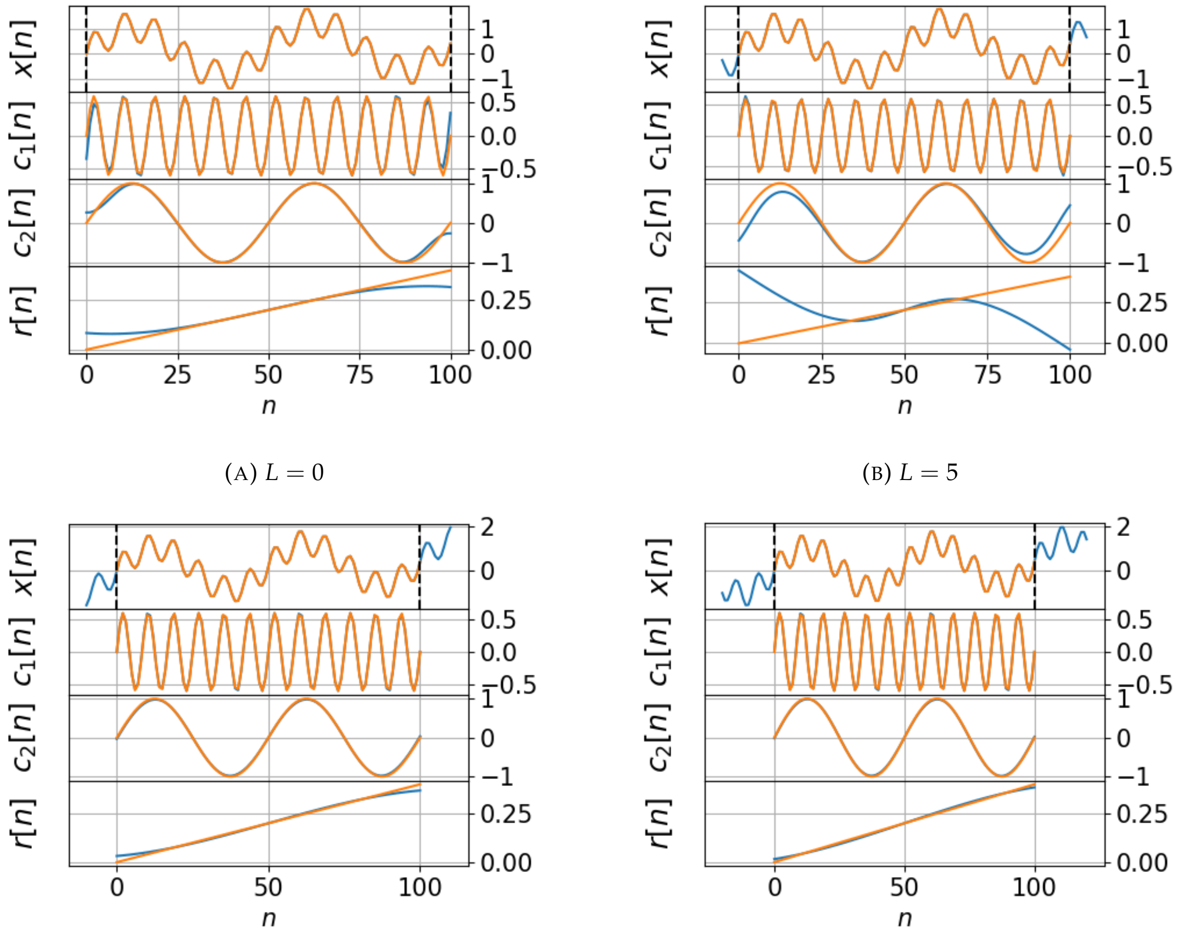

(A) $L = 0$ (B) $L = 5$

(C) $L = 10$ (D) $L = 20$

FIGURE 4.3: Comparison of EMD results on extended series with L data points added on both sides of the initial series. Blue curves represent the extended series and its decomposition, and orange curves present the initial series and its analytical decomposition described in Eq. 4.2 and considered as reference.

All the extended series seem to follow the trend of the initial series well because the test series is naturally simple in terms of frequency composition. Therefore the AR model can give an almost perfect prediction. Compared to the analytical decomposition described in Eq. 4.2 and plotted in orange curves, it can be noticed that some discrepancies locate at both borders in the two IMFs and the residual when no extension is made. By increasing L to 5, the first IMF behaves better but the second IMF and the residual have more important errors at the borders than before. With more added points 10 and 20 on each side, the decomposition results match pretty well with their analytical expression.

We note that P and L are parameters we must appropriately choose, and it is not obvious to find their optimal value for massive data analysis as they are data-dependent.

4.1.2 Extension of the method for LES results of SI engine

The classical EMD described in the previous section is suitable for 1D scalar signals. As explained before, the interest in introducing the EMD in SI engine research is using its capacity to decompose the instantaneous velocity into different spatial scales for further analysis of the evolution of different scales and their impact on the combustion process. The velocity field in SI engines is multivariate and multidimensional, which can not be treated by the original EMD algorithm and therefore needs to be extended. This section will first present the extension of the EMD for multivariate signals. Then improvements made in this thesis on the EMD for multidimensional signals will be discussed.

The algorithm of 1D multivariate EMD is presented in Figure 4.4. Compared with the original EMD algorithm (cf Figure 4.1), the major difference lies in the envelope definition. For multivariate signals, the same envelopes of scalar signals are not well-defined. An adaptation is made by the projection of the given multivariate signal $\vec{x}[n]$ into a series of chosen directions $\{\vec{v}_k\}_{k=1}^{N_{dir}}$ with N_{dir} the total number of directions. For each projected signal $p^k[n]$, the corresponding envelopes are extracted the same way as the one used for scalar signals, as well as the local mean, which is the average of the upper and lower envelopes. The local mean of the multivariate signal $\vec{m}_{ij}[n]$ is then the average of the local means obtained over all the projection directions. The following steps remain the same as those of the original EMD, except that conditions of being an IMF or monotonic must be satisfied in all the projection directions.

A suitable method must be chosen for the projection directions as their distribution can directly impact the decomposition results. An angular uniform sampling method can be employed for its simplicity, as plotted in Figure 4.5a where the sampling results correspond to a trivariate signal. However, the concentration of certain projection directions on the polar is higher. In [145], a sampling based on the Hammersley sequence is proposed, which belongs to a class of quasi-Monte Carlo methods, and provides relatively more uniform sampling in higher dimensional spaces, as illustrated in Figure 4.5b. The comparison in Figure 4.5 shows that the sampling method based on the Hammersley sequence is more suitable for generating projection directions used in the MEMD.

In [155], a modification is again proposed to improve the distribution of sampled projection directions by considering the unbalance between different components of the multivariate signals. To address this problem, the direction reflecting the largest imbalance between components is determined adaptively. For the input signal $\mathbf{s}$ with covariance matrix $\mathbf{C} = \mathbf{s}^T\mathbf{s}$, the direction of the first principal component is computed based on the eigen decomposition of the covariance matrix, $\mathbf{C} = \mathbf{V}\mathbf{\Lambda}\mathbf{V}^T$, where the matrix $\mathbf{V}$ is the matrix of eigenvectors and the entries of the diagonal matrix $\mathbf{\Lambda}$ are the corresponding eigenvalues. The first principal component $\vec{P}_1$ is simply the eigenvector with the largest eigenvalue. Subsequently, the first principal component $\vec{P}_1$ is used to construct a

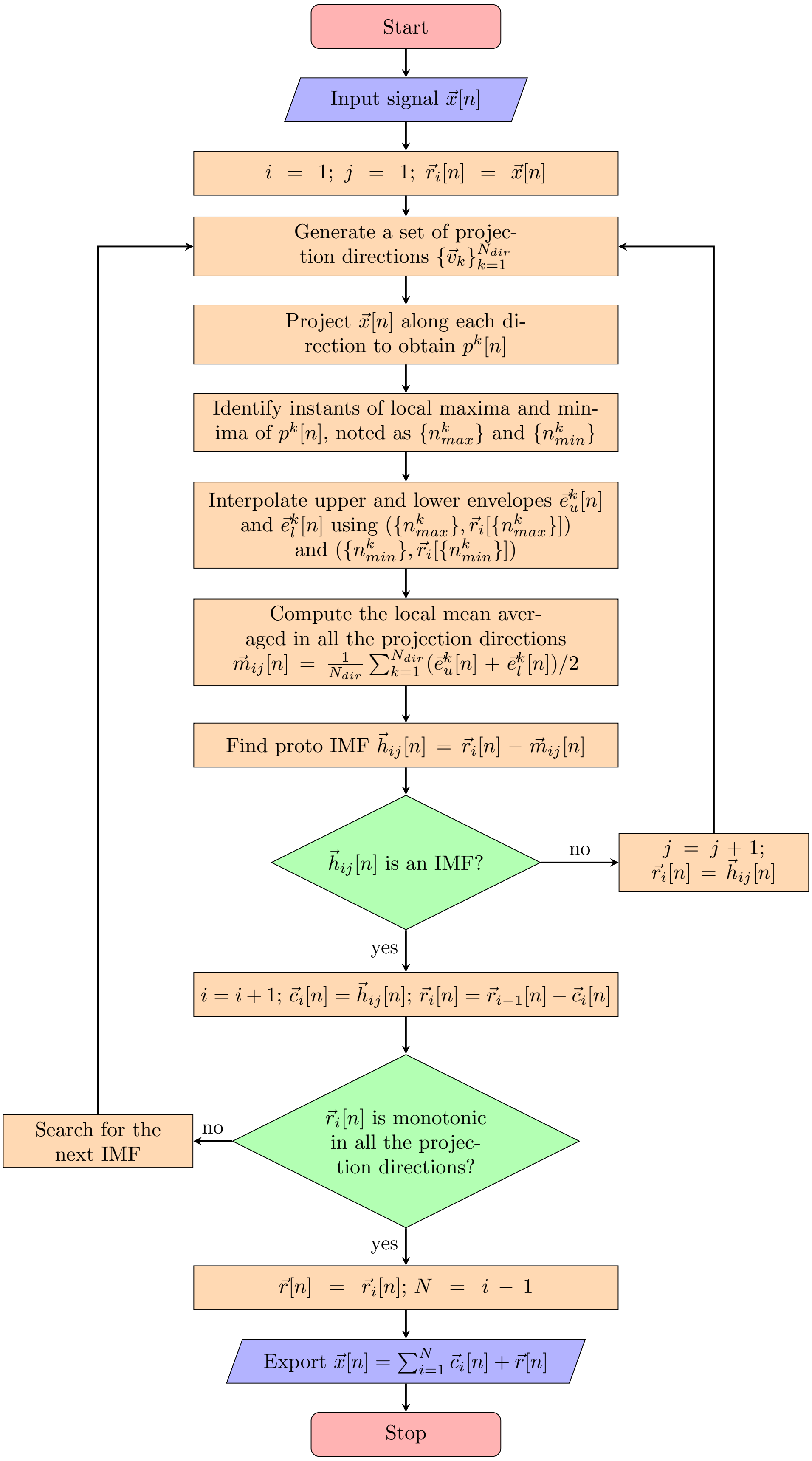

FIGURE 4.4: Flow chart of the 1D MEMD.

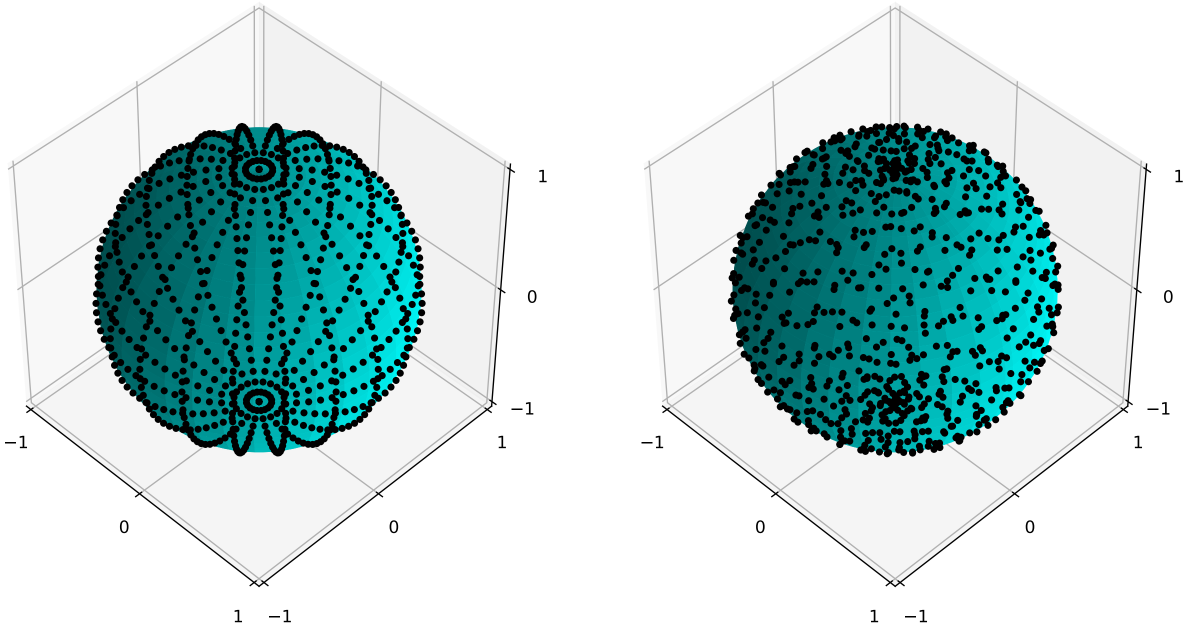

(A) Angular uniform sampling.

(B) Hammersly sequence based sampling.

FIGURE 4.5: Comparison of sampling methods for generating projection directions.

vector pointing in the diametrically opposite direction $\vec{P}_{o1}$. This pair of vectors are then used to relocate the sampled projection directions.

For the uniformly sampled direction vectors $\{\vec{v}_k\}_{k=1}^{N_{dir}}$, the Euclidean distance from each of the uniform direction vectors to $\vec{P}_1$ is computed. Half of the vectors nearest to $\vec{P}_1$, noted as $\vec{v}_k^{\vec{P}_1}$, are relocated as:

$$\vec{v}_k^{\vec{P}_1} = \frac{\vec{v}_k^{\vec{P}_1} + \alpha \vec{P}_1}{\left\| \vec{v}_k^{\vec{P}_1} + \alpha \vec{P}_1 \right\|} \tag{4.4}$$

The rest half of the vectors nearest to the opposite vector $\vec{P}_{o1}$, noted as $\vec{v}_k^{\vec{P}_{o1}}$, are relocated similarly:

$$\vec{v}_k^{\vec{P}_{o1}} = \frac{\vec{v}_k^{\vec{P}_{o1}} + \alpha \vec{P}_{o1}}{\left\| \vec{v}_k^{\vec{P}_{o1}} + \alpha \vec{P}_{o1} \right\|} \tag{4.5}$$

α is the parameter controlling the density of the relocated vectors around $\vec{P}_1$ and $\vec{P}_{o1}$ respectively, whose value is suggested to be included between 0 and 1.

As illustrated in Figure 4.6, in the case of $\alpha = 0$, no adaptive projection is performed as the imbalance between components is ignored or does not exist. On the contrary, in the case of $\alpha = 1$, vectors are strongly relocated to deal with the imbalance problem. No sensitivity analysis is carried out to evaluate the impact of this parameter on the decomposition results, and α is set to 0.5 in all the analyses to be presented in this thesis.

The mode mixing problem in the classical EMD [156], indicating that the oscillations with varying temporary scales coexist in the same IMF, or the oscillations with the same temporal scale are separated into different IMFs, is caused by the intermittency with high frequency contained in

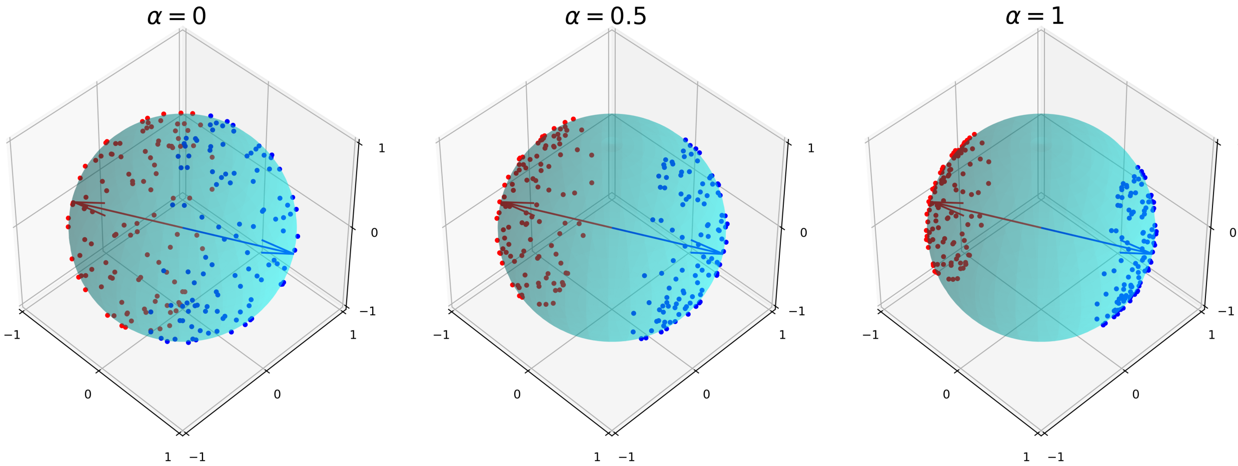

FIGURE 4.6: Relocation of projection directions with different values of α.

large-amplitude signal [157] and happens during the sifting process of EMD. The same problem comes up also in MEMD as the sifting process remains quite similar. A Noise Assisted MEMD (NA-MEMD) inspired by the ensemble EMD (EEMD) [158] was developed [159] to deal with this undesired phenomenon.

For a multivariate signal $\vec{x}$ of n components, $N_{channel}$ channels of white noise signal are inserted to form a new multivariate signal of $n + N_{channel}$ components. Each noise channel is generated randomly and independently and their variance is set to be comparable with the original signal components x_i as $\sigma_{WN}^2 = \frac{1}{n}\sum_{i=1}^{n}\sigma^2(x_i)$. The original signal is then decomposed together with the added noise components by the MEMD. The original signal is combined with the inserted noises during the projection to determine local extrema, but the local mean of each component is extracted independently. $N_{channel}$ is set to 1 in the current work as no significant improvement has been seen using $N_{channel} = 2$ in work presented in [1]. Similar to the EEMD for scalar signals, the noise-assisted MEMD also needs to be repeated to achieve statistical convergence. The total number of realizations, noted NE, is determined based on the compromise between the convergence and the computational cost. The impact of the number of realizations will be discussed later in this section.

The noise-assisted MEMD is combined with the adaptive sampling in each realization and is to be realized for NE times. This final version of MEMD is thus called "Ensemble Noise-assisted Adaptive-projection intrinsically transformed MEMD", or simply **E-NA-APIT-MEMD**, which is ready for 1D multivariate signals. To deal with velocity fields of SI engines, the method needs to be extended for 2D (even 3D if the cost is acceptable) applications. In [19], a straightforward 2D extension based on 1D MEMD is proposed and is retained in this thesis for multidimensional extension, which is schematically presented in Figure 4.7.

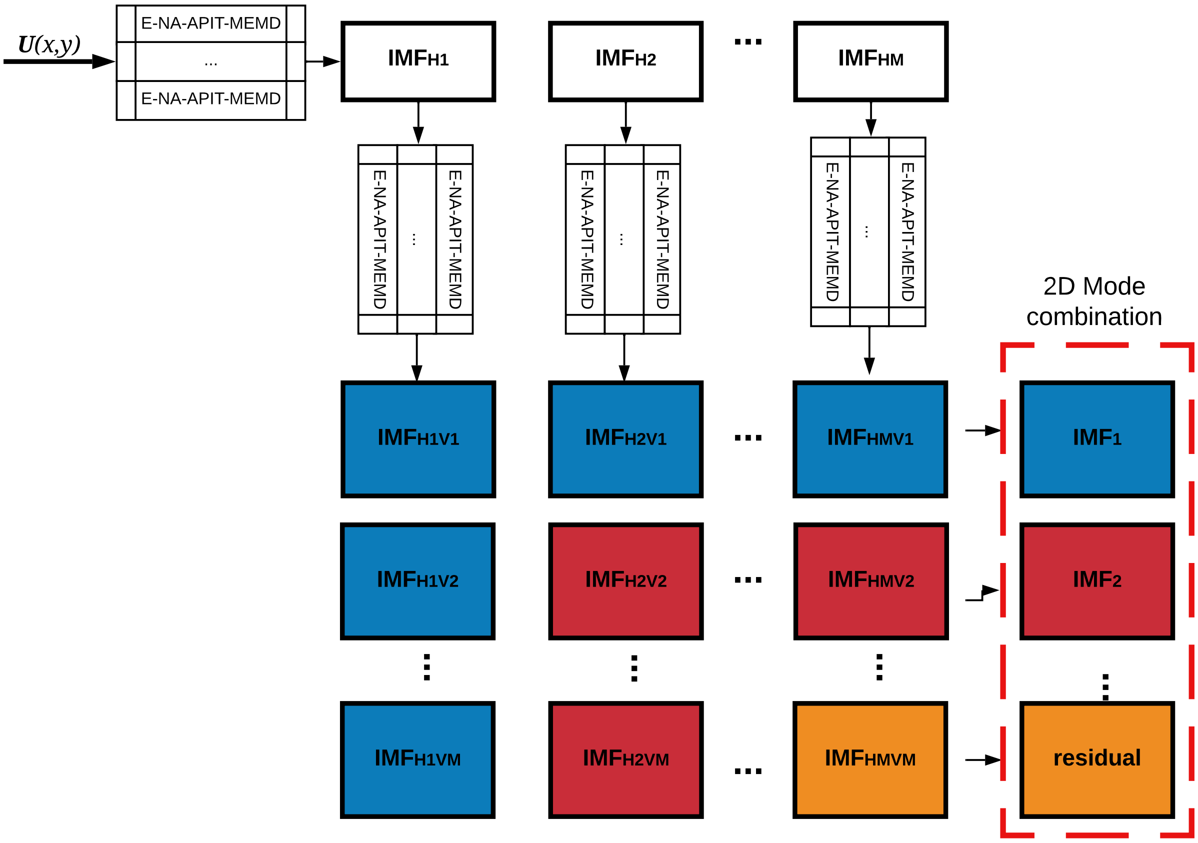

FIGURE 4.7: Extension of EMD for 2D multivariate signals based on EMD 1D.

The basic principle of the multidimensional extension of MEMD is to decompose the input signal sequentially in all directions. In the case of a 2D bivariate velocity field $U(x, y)$ organized in a regular grid, as shown in Figure 4.7, the decomposition starts along each horizontal grid row by the bivariate Ensemble NA-APIT-MEMD. IMFs of each row are then stored in the descending order in M horizontal pseudo IMFs noted as $\mathbf{IMF}_{Hi}$ with $i = 1, 2, ..., M$. The decomposition continues along each vertical grid column of all $\mathbf{IMF}_{Hi}$ and results in a $M \times M$ matrix of pseudo IMFs noted as $\mathbf{IMF}_{HiVj}$ with $i, j = 1, 2, ..., M$. 2D IMF modes and the 2D residual are then constructed using the combination strategy proposed in [158]:

$$\mathbf{IMF}_k = \sum_{i=k}^{M} \mathbf{IMF}_{HkVi} + \sum_{j=k+1}^{M} \mathbf{IMF}_{HjVk} \tag{4.6}$$

where k denotes the number of 2D IMF mode with an expectation that $\mathbf{IMF}_M$ represents the 2D residual $\mathbf{r}$. The velocity field can thus be expressed as following:

$$U(x, y) = \sum_{k=1}^{M-1} \mathbf{IMF}_k + \mathbf{r} \tag{4.7}$$

The illustration of a simple application of 2D EMD on a 2D PIV velocity field measured by TU Darmstadt [160] is given in Figure 4.8. For a predefined mode number $M = 7$, all the 49 pseudo modes are plotted.

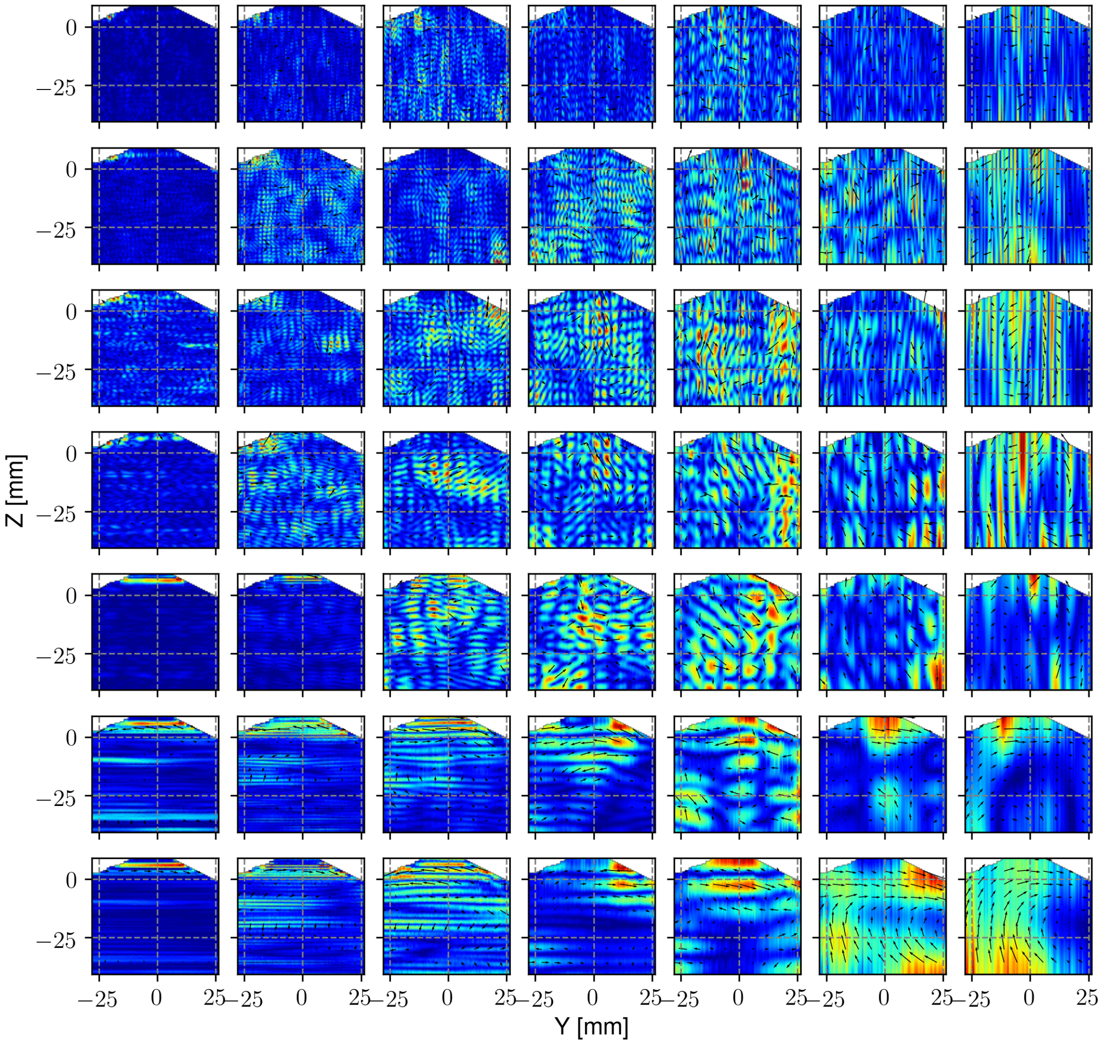

FIGURE 4.8: All IMF modes extracted by 2D EMD applied to a 2D bivariate velocity field using the method presented in [1].

Using the mode combination strategy explained previously, six 2D IMF modes and the corresponding residual can be constructed and plotted in Figure 4.9. It can be seen that small-scale motions containing spatially high-frequency oscillations are mainly present in the first few IMF modes. In contrast, large-scale motions of low-frequency oscillations are included in the last few IMF modes and the residual, which accords with the behavior of 1D EMD.

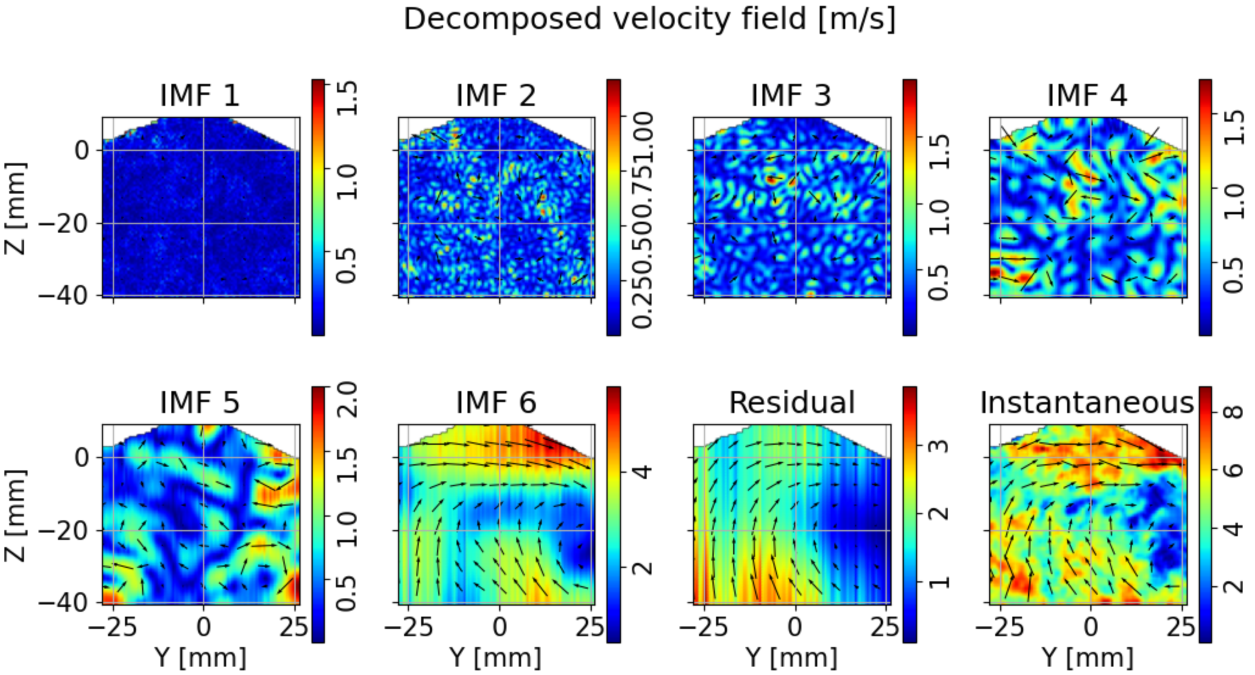

FIGURE 4.9: 2D modes combination using the method presented in [1].

As described in section 2.6, in the context of in-cylinder flow analysis, the main usage of EMD is to extract variations of large- and small-scale motions from the instantaneous velocity field $U_i(\theta)$ at a given crank angle θ of engine cycle i. The triple decomposition proposed by Heywood [12] is recalled here:

$$U_i(\theta) = U_E(\theta) + U_{c,i}(\theta) + u_i(\theta) \tag{4.8}$$

The ensemble-averaged velocity U_E represents simply the averaged behavior of large-scale motions, $U_{c,i}$ gives access to cyclic variations of large-scale motions, and u_i represents variations of small-scale motions which are related to the turbulence. EMD is here employed to distinguish the three terms for a given engine cycle i at a given crank angle θ.

The complete decomposition of the instantaneous velocity by EMD presented in Figure 4.9 shows that EMD can separate different scales into IMF modes. Understanding each mode is definitely of interest since one can investigate the temporal evolution of each mode and their interactions in energy transfer, as presented in [1, 19]. However, to achieve the triple decomposition in Equation 2.3, a combination of individual IMF modes is necessary such that the instantaneous velocity is roughly separated into a high frequency (HF) part and a low frequency (LF) part:

$$U_i(\theta) = U_{LF,i}(\theta) + U_{HF,i}(\theta) \tag{4.9}$$

In [1], the LF part was defined as the sum of the last IMF mode and the residual, and all the rest IMF modes form the HF part. Both parts are plotted in Figure 4.10 for the example case. The LF part shows clearly a large-scale tumble motion, and the HF part is instead associated with small-scale motions.

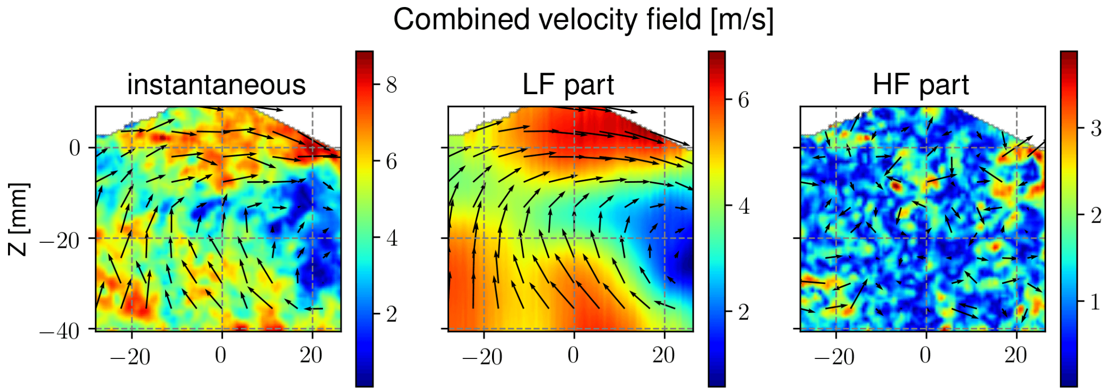

FIGURE 4.10: Separation of large- and small-scale motions.

Considering the HF part $U_{HF,i}(\theta)$ as the turbulent fluctuations $u_i(\theta)$, cyclic variations in large-scale motions can be deduced:

$$U_{c,i}(\theta) = U_{LF,i}(\theta) - U_E(\theta) \tag{4.10}$$

Therefore, the usage of EMD permits a clear separation of flow structure variations in large- and small-scale motions, which may interact and impact the combustion process in SI engines differently. However, before its general use in in-cylinder flow analysis, one last adaptation is still needed and is presented in the next section.

4.1.3 2D EMD for time-varying geometry

The number of 2D IMF modes M is determined by the direction containing less pseudo modes, *i.e.*, $M = \min(M_y, M_z)$ where M_y and M_z are respectively the number of pseudo modes in the horizontal and vertical directions. For a 1D signal of N data points, the total mode number is typically at most of the order of $\mathcal{O}(\log_2 N)$ and also depends on the complexity of the input signal. The PIV field used here is of size $98 * 90$, which corresponds to 7 modes in each direction. Nonetheless, it is highly possible that the defined mode number does not match the real one as the mode number may depend on the signal length and other factors like the signal complexity, which suggests that a predefined mode number may not be optimal. In addition, the current mode combination strategy requires an equal number of modes in all directions, which is not easy to be satisfied in in-cylinder flow analysis as the domain varies with the piston position during an engine cycle. During the compression stroke, the corresponding mode number in the vertical direction decreases as the chamber height reduces. In contrast, the one in the horizontal direction remains stable as the width is constant.

To overcome this problem, a solution is proposed in [1] for the flow analysis during the last 100 crank angle degree of the compression stroke: all the velocity fields are interpolated in the direction of fewer data points (piston moving direction in this case) to achieve a square grid with the same number of data points in all directions for all crank angles. The grid resolution in the direction of fewer points varies dynamically to keep the domain size constant. Therefore, the maximal number of pseudo modes in both directions remains unchanged despite the variation of the real domain size. A typical grid evolution during an engine cycle is presented in Figure 4.11a. EMD is then applied to all the interpolated fields, and the same mode number M is imposed for all instants. The above solution does work, but the extra step of interpolation in the pre-processing complicates the EMD analysis.

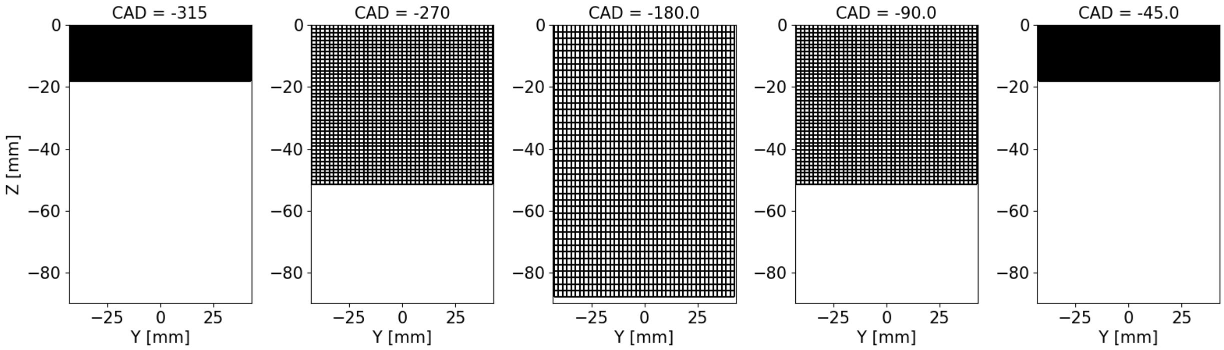

(A) Non uniform grid with variable mesh size.

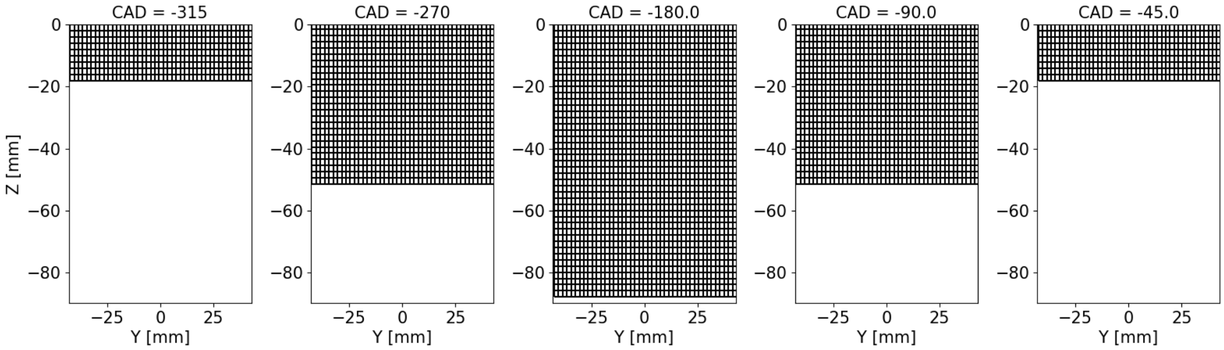

(B) Uniform grid with constant cell size.

FIGURE 4.11: (A) Topology of the grids at different instants used by the bivariate 2D EMD proposed in [1]. The total number of grid points remains the same and the vertical resolution varies dynamically to keep the real domain size. (B) Topology of the grids at different instants used in the proposed new EMD method. No interpolation is needed and EMD is applied to data stored in the LES or PIV grids of constant resolution.

In this work, an improvement is made on the mode combination strategy to get rid of the interpolation step. Inspired by the fact that a simple separation to distinguish LF and HF parts of flow is sufficient, an acceleration of the EMD calculation process is also made to facilitate the extensive usage of EMD in in-cylinder flow analysis.

The new strategy is schematically presented in Figure 4.12. EMD is applied directly to velocity fields of LES or PIV stored in their original grid of constant resolution in all the directions, and the interpolation step is not removed. An exemplary evolution of grids used in the new proposed method is shown in Figure 4.11b and compared with that used in the method of Sadeghi et al. [1]. The main difference compared to the original method is that the number of pseudo IMF modes in both directions is not a priori fixed. In practice, a maximal number of modes M_{max} is still needed but is only used to define a large enough matrix to store all the extracted pseudo modes. Using this strategy, different numbers of pseudo modes are allowed in the two directions as the number of data points in the vertical direction that varies with respect to the piston position is not imposed to be of the same order of that in the horizontal direction. For example, M in the horizontal direction and N in the vertical direction, which is often the case when the aspect ratio of the domain differs a lot from 1. All the pseudo modes are then stored in a squared pseudo mode matrix of size $M_{max} \times M_{max}$ even though it is not fully filled. To obtain the LF part of the flow field, only the last three components corresponding to the last 2D IMF and the residual in the right bottom corner of the pseudo mode matrix are needed, as shown in Figure 4.12, and the HF part is simply the sum of all the other pseudo modes. The separation criterion of the LF and the HF parts is based on the energy content of each IMF as proposed in [1, 130], where it was demonstrated that large-scale coherent structures are stored mainly in the residual. In this thesis, it was found that the residual and the last IMF provide a better reconstruction of the large-scale motions. At the same time, the rest IMF modes represent the vortex generation and dissipation process of smaller scales. Another separation criterion based on the correlation between modes is also proposed by Qin et al. in [125, 126] for a quadruple POD method.

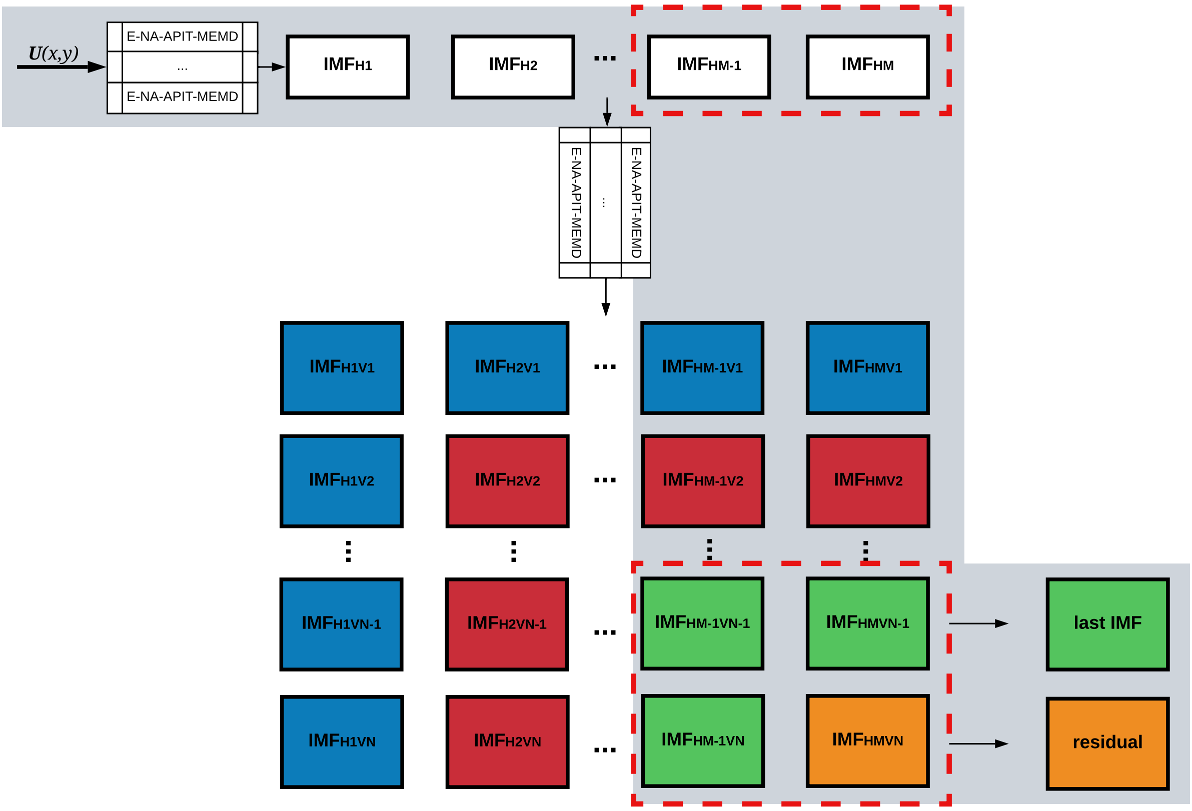

FIGURE 4.12: Modified mode combination strategy in 2D EMD decomposition.

Finally, the decomposition using this new strategy is applied to the same velocity field tested in section 4.1.2, and all the pseudo modes are listed in Figure 4.13. In this test, M_{max} is set to 15 to include all the modes, while the results show that 9 is already sufficient, but the value is still larger than 7 which was used in the original strategy. On the plot of all the pseudo modes, it can be seen that not all are complete as some lines or columns are naturally less fluctuating and thus contain less number of modes. Nonetheless, incomplete modes do not impact the construction of the LF part.

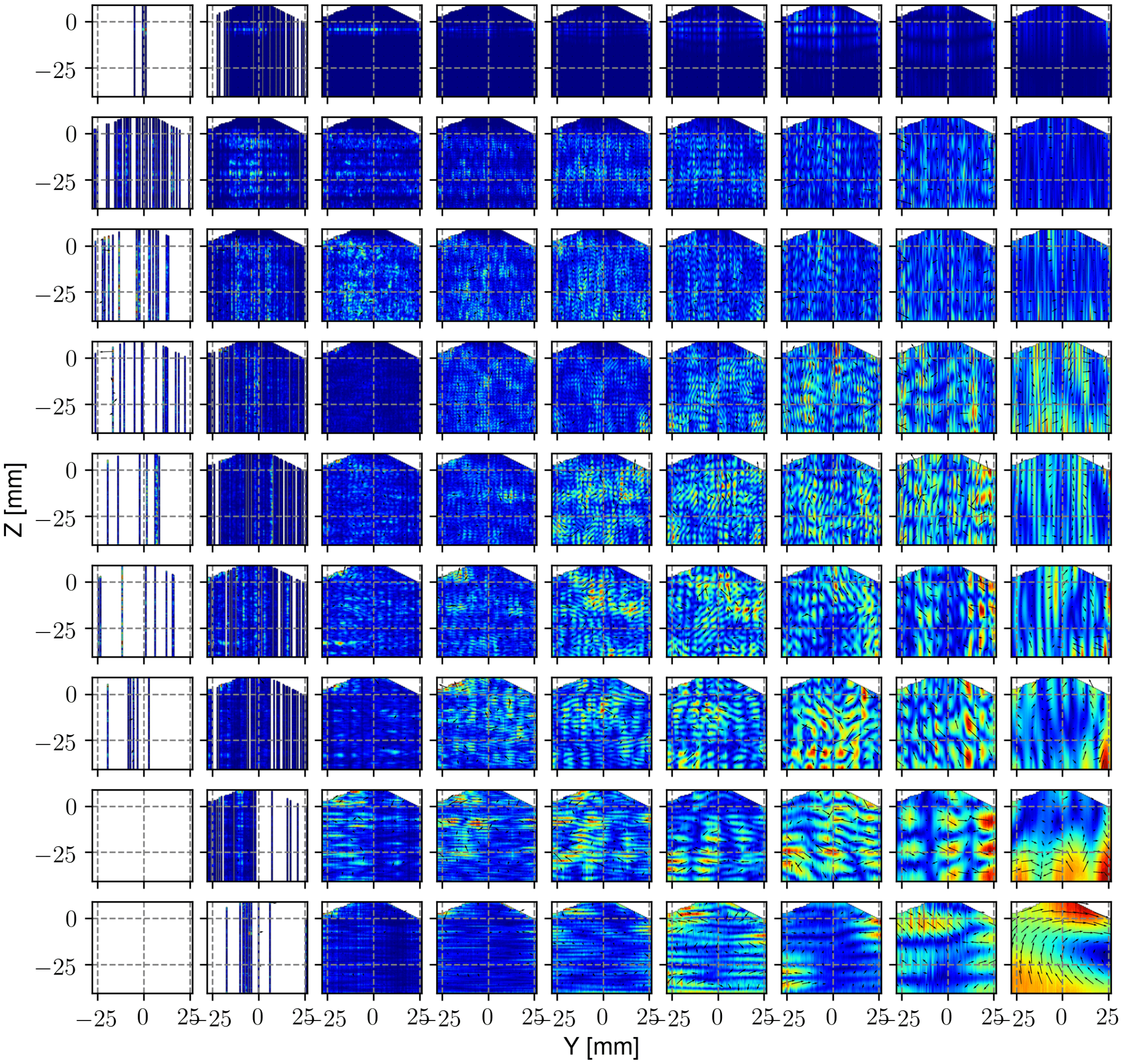

FIGURE 4.13: All IMF modes extracted by 2D EMD applied to a 2D bivariate velocity field using the method proposed in the current work.

Using the same mode combination strategy, we compare the new obtained IMF modes shown in Figure 4.14 with the old ones presented in Figure 4.8. Slight differences can be noticed in high-order modes and also the residual, which can be explained by the fact that in the original method, to match the imposed number of modes, sometimes the last modes are summed up in the residual to reduce the total number of modes, and occasionally empty modes are added as the first modes to increase the number of modes, which makes the residual and the highest order modes polluted. With the new strategy, all the extracted modes are well conserved in the pseudo mode matrix to correctly decomposition results. The complete decomposition of the velocity field gives a pseudo mode matrix of size 9 × 9.

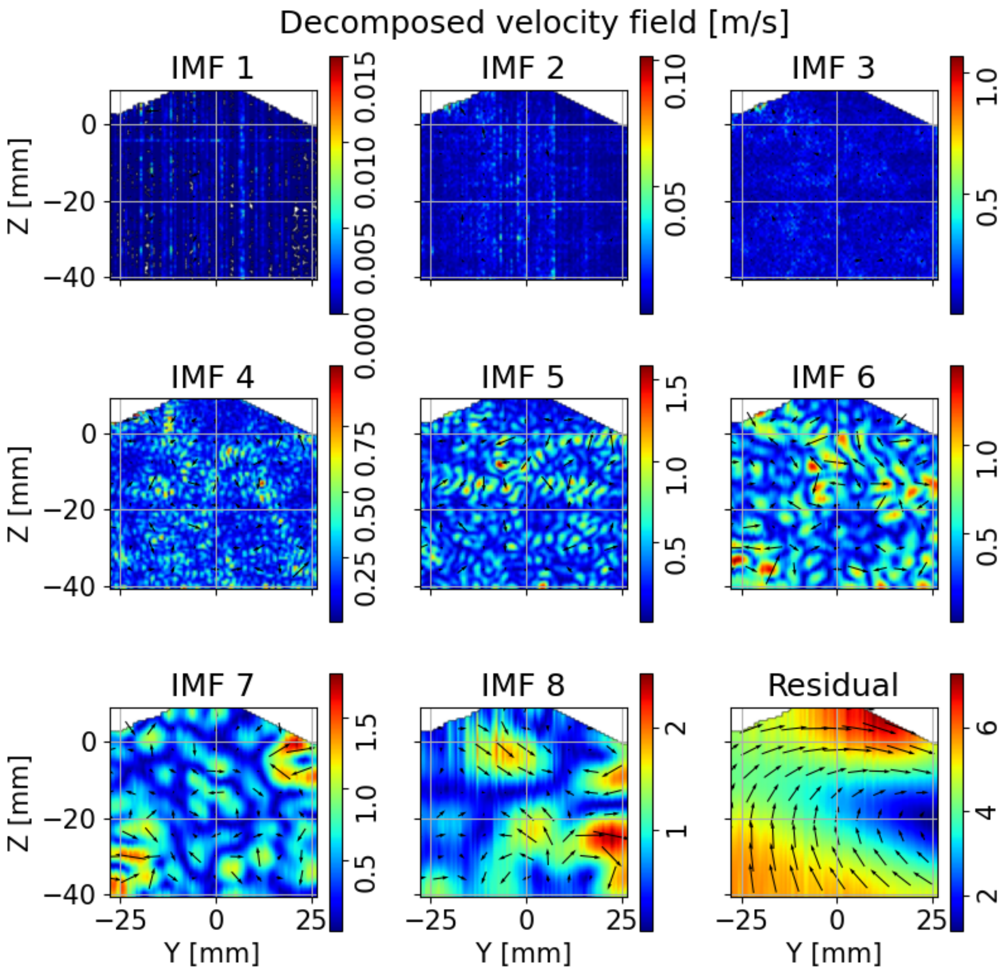

FIGURE 4.14: 2D modes combination using the same method presented in [1].

LF and HF parts are illustrated in Figure 4.15 using the same mode combination strategy.

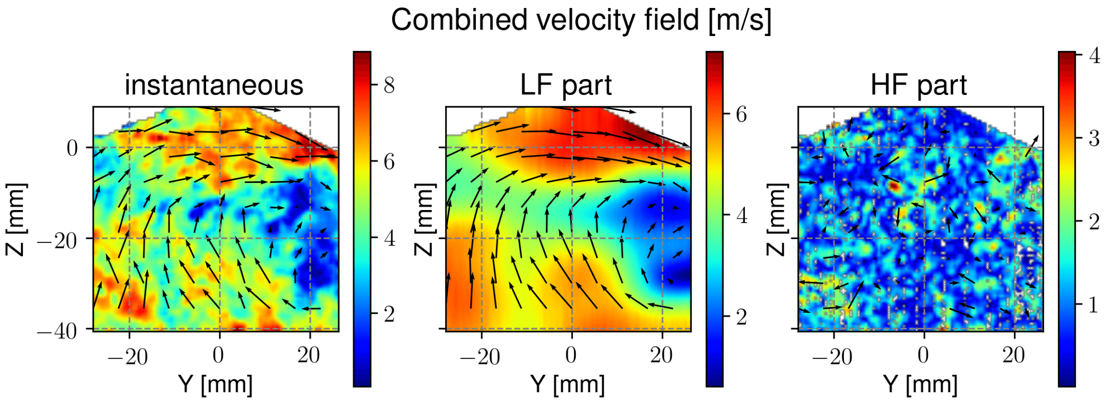

FIGURE 4.15: Separation of large- and small-scale motions using the improved EMD.

Results obtained with the method proposed in [1] and the present one for the LF part of the velocity field are compared in Figure 4.16. The residual is also plotted for comparison. It can be noticed that including the last IMF gives a slightly better representation of the large-scale motion in some local regions, though the residual alone describes it also quite well. Qualitatively, the present methodology provides a result that seems more representative of the large-scale structure observed in the instantaneous velocity field.

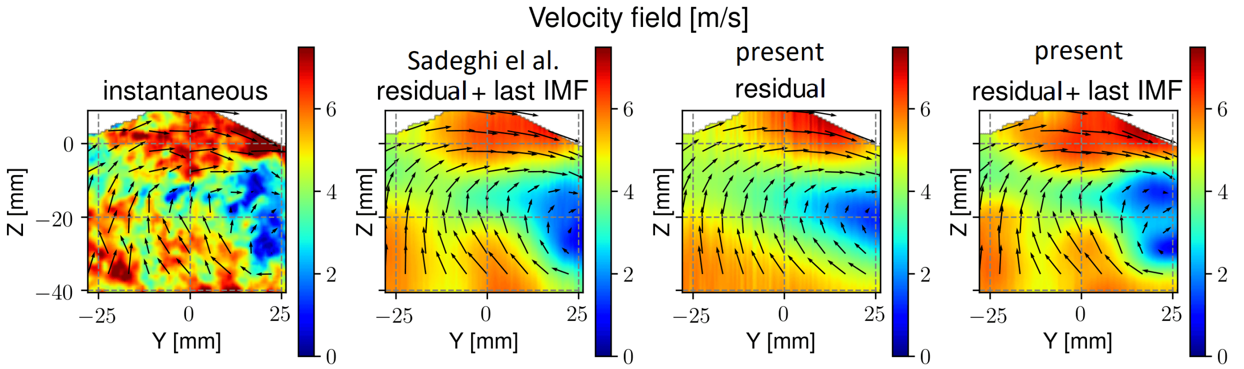

FIGURE 4.16: Comparison of the LF part of a velocity field measured by PIV at −100 CAD using the strategy of Sadeghi et al. [1] and the strategy in the present work.

The longitudinal PSD of each velocity component and their corresponding LF and HF parts obtained with the present EMD methodology are presented in Figure 4.17. They are computed by using Welch's method with 50% overlapping segments. The LF part contains energy at smaller wave numbers corresponding to large-scale structures. In comparison, the HF part is more dominant for larger wave numbers associated with small-scale turbulent structures. These two parts are decoupled, indicating that the definition of the LF part as the sum of the residual and the last IMF mode is physically reasonable.

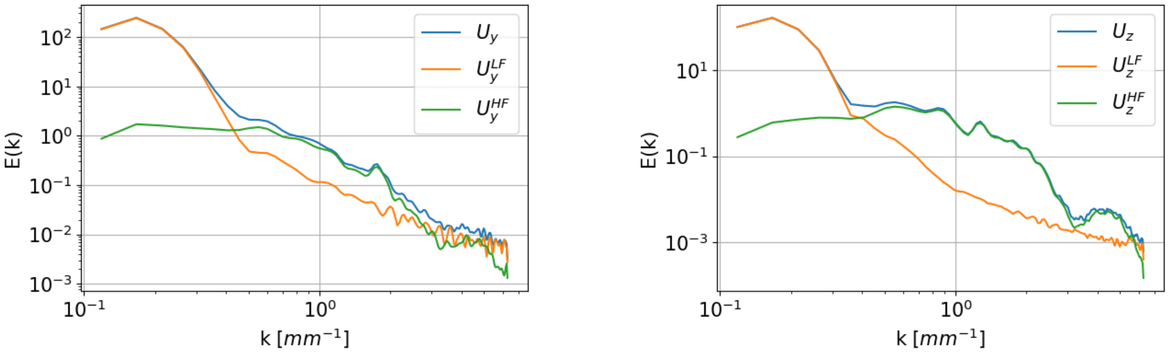

(A) U_y component.

(B) U_z component.

FIGURE 4.17: Longitudinal PSD of each component of the velocity field measured by PIV at −100 CAD and their corresponding LF and HF parts.

As mentioned before, the new strategy also allows an acceleration of the current EMD method. Knowing that the LF part contains only the last IMF and the residual, the complete decomposition is unnecessary if only a separation of LF/HF parts is of interest. The three pseudo modes and the residual needed to form the LF part, as shown in Figure 4.12, can be obtained by a two-step decomposition highlighted by gray background: a first decomposition in the horizontal direction to obtain the residual and all the horizontal pseudo modes, and a second decomposition in the vertical direction but this time only on the residual and the last pseudo horizontal mode.

We can even combine the residual and the last pseudo horizontal mode to form a pseudo LF part of the horizontal direction before the second decomposition which is carried out on the pseudo LF part only, and the final LF part is the sum of the residual and the last pseudo vertical mode obtained by the second decomposition. EMD can thus be considered as a filtering method: after each decomposition, the LF part of the current decomposition is defined as the sum of the residual and the last pseudo mode in the current direction, and the next decomposition continues on the LF part of the previous decomposition.

The same decomposition is carried out without the acceleration strategy to evaluate the speedup. It is worth noting that the decomposition in the first direction (horizontal) remains the same with or without the acceleration strategy, and the acceleration is realized in the second direction (vertical). The LF parts obtained by the complete decomposition and the accelerated decomposition are compared in Figure 4.18. Some local differences can be mainly noticed on the borders, but globally the two LF parts are almost identical.

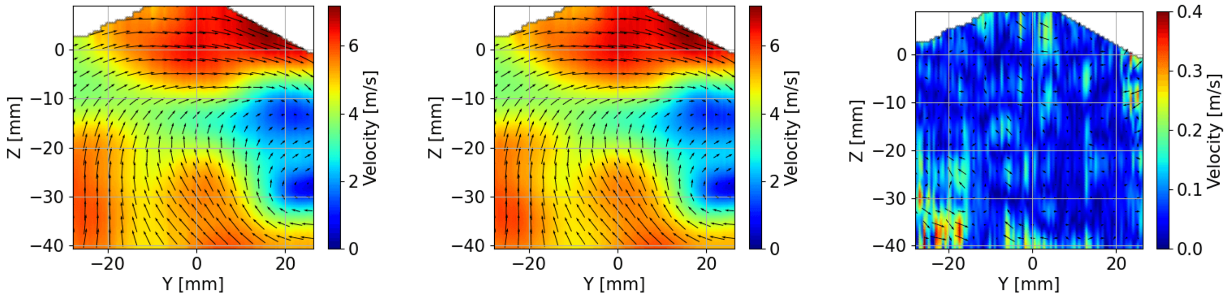

(A) Full decomposition.

(B) Accelerated decomposition.

(C) Differences in the LF part.

FIGURE 4.18: Comparison of LF part obtained with and without acceleration to validate the proposed acceleration approach.

In this test case, the decomposition in the vertical direction with the acceleration is only carried out on the sum of the residual and the last pseudo mode obtained from the decomposition in the horizontal direction, *i.e.*, only one 2D field. On the contrary, the decomposition in the vertical direction without the acceleration is required for all the pseudo-modes or the residual, *i.e.*, nine 2D fields. The theoretical gain in time in the second decomposition direction is thus equal to 9. With 108 CPUs used in both cases, our tests show that the time used for the complete decomposition is around 30.2 minutes, *i.e.*, 54.4 CPU hours, while that with the acceleration is 5.6 minutes, *i.e.*, 10.1 CPU hours. A speedup of 5.4 is obtained with the suggested acceleration strategy. Such a gain allows the extensive application of EMD in the in-cylinder flow analysis. It also inspires the extension of the EMD in 3D, which will be explained in section 4.1.4. In Table 4.1 we summarize the differences between EMD proposed in [1] and EMD with improvements proposed in the current work.

EMD version	Sadeghi et al [1]	current work
Horizontal grid resolution	constant	constant
Vertical grid resolution (direction of piston motion)	varies to keep the same number of data points	constant
Interpolation	on the stretched grids	not needed
Number of IMFs	imposed and based on the domain size	not imposed
Type of decompositon	completed	partial, only the LF part is retained during the decomposition

TABLE 4.1: Comparison between the EMD method proposed in [1] and that proposed in the current work.

The number of realizations NE was fixed as 100 in [1], and the same value is retained for the above comparisons. However, a large number of realizations lead to a considerable computational cost. Therefore, we investigate the impact of NE on the results of EMD. Three values, 10, 40, and 100, are chosen for the comparison, and the corresponding LF parts are compared in Figure 4.19. No significant differences are found between the LF parts obtained with the three numbers of realizations, except that some local discontinuities between columns can be noticed, particularly for $NE = 10$ on the top side.

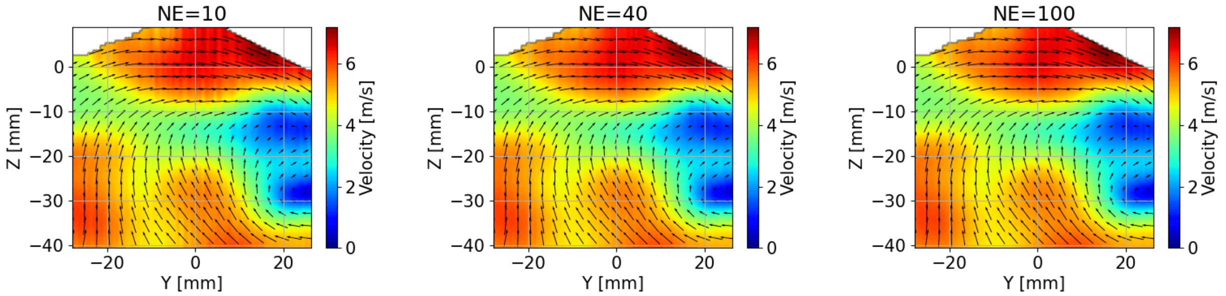

FIGURE 4.19: Comparison of LF parts obtained using the acceleration approach with $NE = 10$, 40, and 100.

A more detailed comparison is made on the velocity profile over the horizontal line at $Z = 5$ mm and is presented in Figure 4.20.

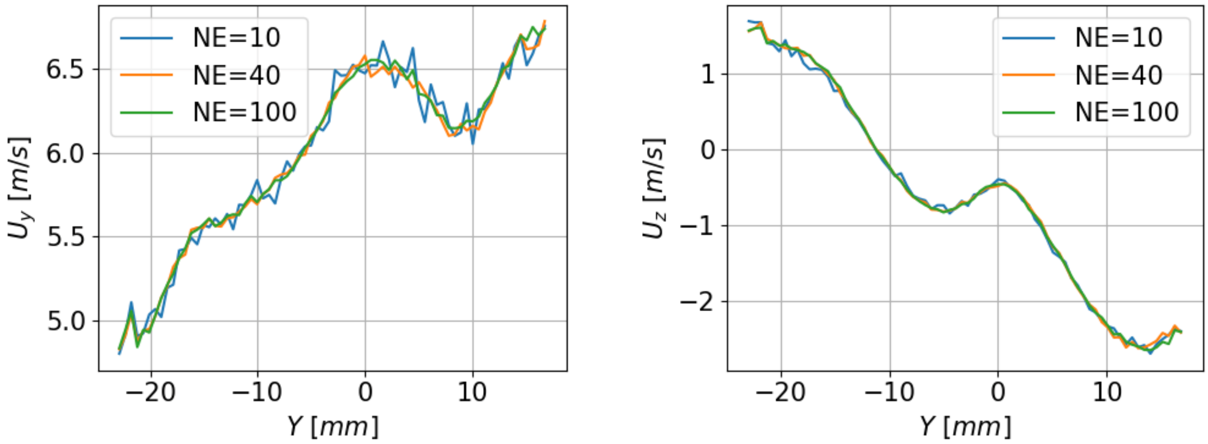

FIGURE 4.20: Comparison of LF part over the horizontal line at $Z = 5$ mm obtained using the acceleration approach with $NE = 10$, 40, and 100.

It can be seen that the three LF parts present some high-frequency fluctuations and that increasing NE leads to reducing these local discontinuities. These discontinuities are generated during the decomposition and are caused by the current 2D EMD algorithm:

- The 2D EMD is realized by the sequential application of EMD 1D in the horizontal and vertical directions.
- In the horizontal direction, all lines are decomposed independently, so continuity along the vertical direction is not guaranteed.

- In the vertical direction, the same issue can also occur and create discontinuities in the horizontal direction. However, discontinuities along the vertical direction generated during the previous decomposition are filtered during the actual decomposition.
- Discontinuities generated in the last direction of decomposition are then stored in the resulted LF part.

This issue is a major drawback of the current implemented 2D EMD, and the increase of NE is far from being a perfect solution. In this thesis, we accept the undesired effect brought by EMD, as those discontinuities remain local and do not affect the interpretation of separated LF and HF parts. For all the EMD analyses, NE is fixed at 50. Another 2D EMD implementation proposed in [161] avoids this issue by decomposing the whole 2D domain together instead of doing so sequentially in two directions.

The boundary treatment discussed in section 4.1.1 is also tested for the 2D velocity field. While decomposing each line or column, the velocity signal is extended using the vector auto-regressive (VAR) model [154] for multivariate signals. The extended signal of each line or column has $L = 5$ more data points at each side, about 5% of the total signal length, predicted by the corresponding VAR model of order $P = 5$. The resulted LF part without and with extension are compared in Figure 4.21.

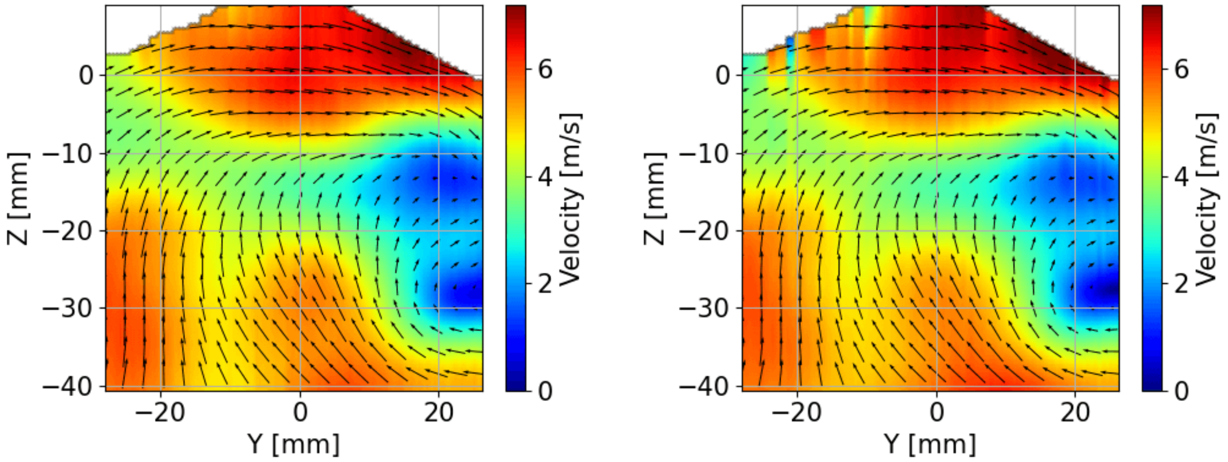

(A) Without extension.

(B) With extension.

FIGURE 4.21: Comparison of LF part obtained with and without extension to demonstrate the impact of border effect.

We do not observe significant differences between the two cases except for regions on the top-left part of the field. In the case of extension, some discontinuities are present near the cylinder head border due to the extension strategy.

The velocity of the vertical line $Y = -20.5\ mm$, which passes through the region that presents some differences, is compared in Figure 4.22. Significant differences are on the component U_y for $Y > -5\ mm$. The extended signal should have followed the trend of the initial instantaneous velocity in this part and thus leads to a more descending U_y. The resulting LF part obtained with extension also follows the same trend and therefore behaves differently compared to the one without extension.

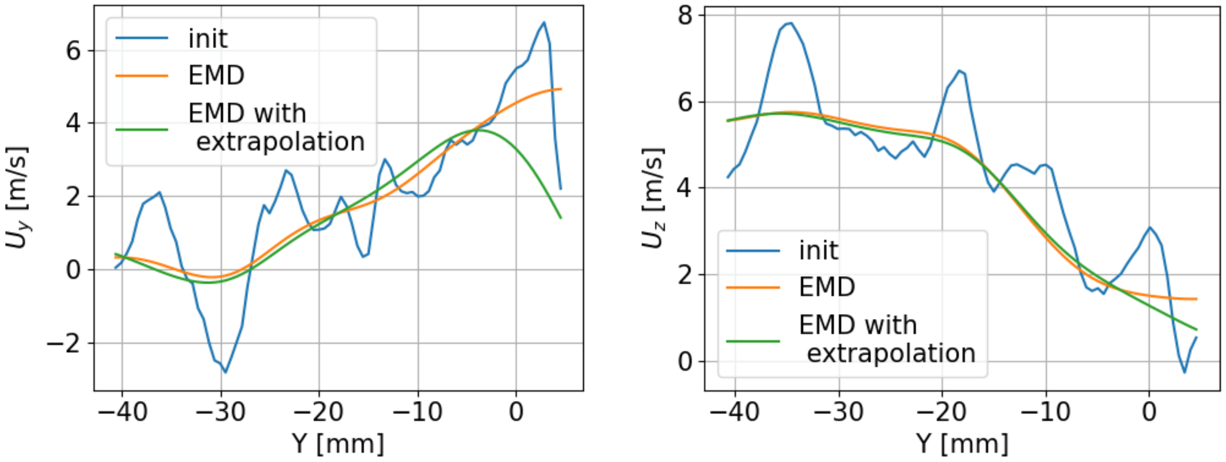

FIGURE 4.22: Comparison of the velocity profile at $Y = -20.5\ mm$ of the LF parts obtained with and without extension.

The extension strategy is supposed to reduce border effects. However, the extension depends on the prediction by the VAR model, whose accuracy is not guaranteed, especially when the original signal is complex as the velocity field. Also, as mentioned in the test of the 1D series, the choice of VAR model parameters P and L is crucial and data-dependent. It would be difficult to adjust their value for each line and column treated during the process of 2D EMD or find the most suitable pair for all the lines and columns. With the chosen values of $P = L = 5$, the LF part obtained with the extension does not outperform the one without extension. Some undesired local discontinuities are present, which are purely generated numerically. In this thesis, the extension strategy is finally not activated in in-cylinder flow analysis and is kept as an optional choice in the developed EMD tools.

For illustration, the developed 2D EMD method is applied to the LES data obtained in work presented in Chapter 5. Five instants of the individual LES cycle 3, −360 CAD, −270 CAD, −180 CAD, −90 CAD and −22.5 CAD, starting from the beginning of the intake stroke till the sparking timing, are chosen to illustrate the capacity of EMD to separate large- and small-scale motions of the in-cylinder flow.

The longitudinal PSD of each velocity component and their corresponding LF and HF parts are presented in Figure 4.23 for the five chosen instants. A clear separation of the two parts in energy content can be observed. Most energy is contained in the LF part. In contrast, the HF part includes only energy of high wave numbers, indicating that the separation criterion based on the energy content proposed in [130] is also validated for LES data. Also, the wave number which separates approximately the LF and HF parts vary with respect to the piston position, which is associated with the evolution of the in-cylinder flow.

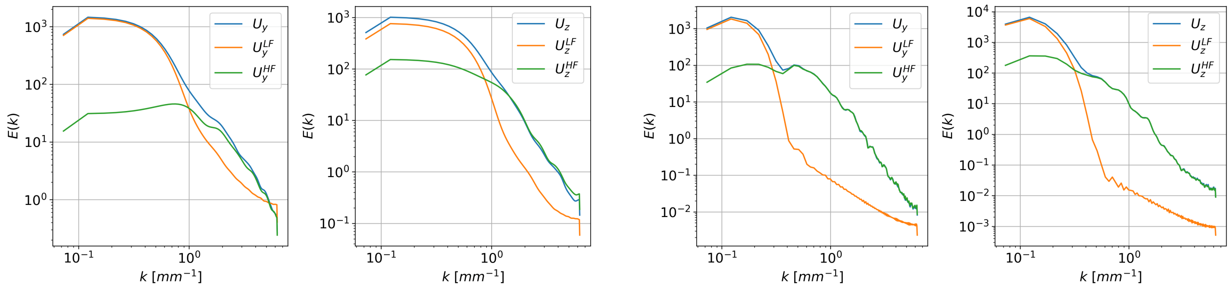

(A) −360 CAD.

(B) −270 CAD.

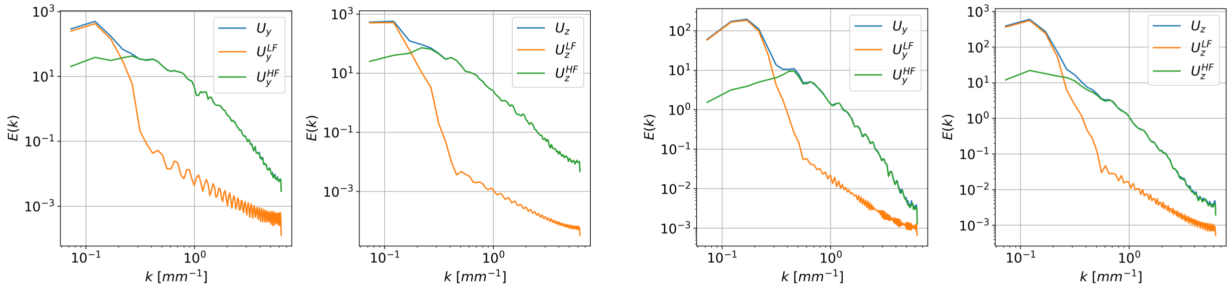

(C) −180 CAD.

(D) −90 CAD.

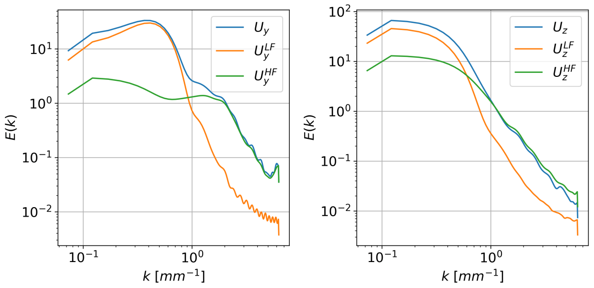

(E) −22.5 CAD.

FIGURE 4.23: Longitudinal PSD of each component of the velocity fields obtained by LES and their corresponding LF and HF parts.

The characteristic length scales of each part are also computed and compared for the chosen LES cycle 3. The normalized two-point correlation function [1, 42], defined as below, is used to estimate length scales based on the velocity field of LF and HF parts:

$$R_{ii}(r) = \frac{\langle U_i(x_i)U(x_i + r)\rangle}{\langle U_i(x_i)^2\rangle} \tag{4.11}$$

The velocity U can be the instantaneous velocity, the LF part, or the HF part extracted by 2D EMD, i denotes a velocity component in the direction i and $\langle\rangle$ represents the spatial average. The characteristic length scale is computed as the integral of $R_{ii}(r)$ from 0 to the first zero-crossing point.

The temporal evolution of the characteristic length scales in both horizontal and vertical directions for the LES cycle 3 are plotted in Figure 4.24. The length scale of the LF part follows that of the instantaneous velocity, as the large-scale motion is stored in the LF part. The length scale of the HF part remains relatively stable. The evolution in the vertical direction of the LF part seems to follow the piston motion and the tumble formation. Their evolution provides a quantitative description of the in-cylinder flow evolution.

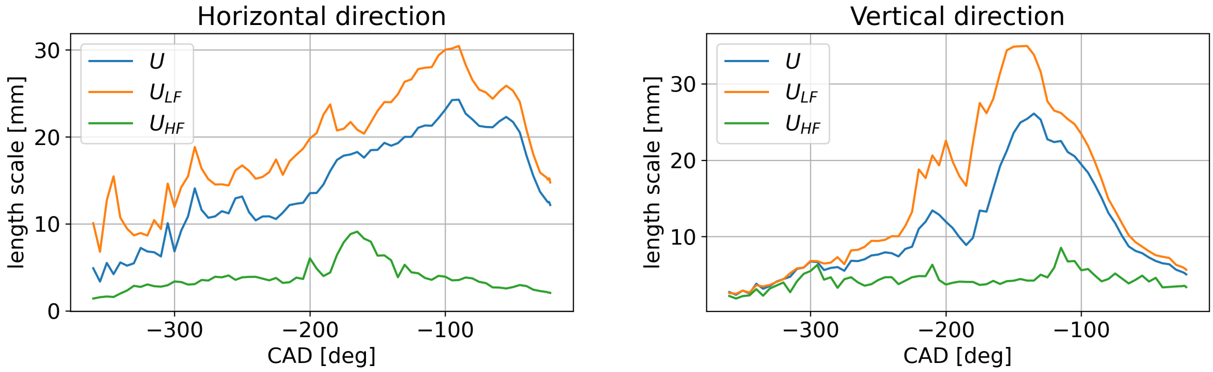

FIGURE 4.24: Evolution of characteristic length scales in both horizontal and vertical directions for the chosen LES cycle.

With the exemplary application of 2D EMD on LES data, we demonstrate that 2D EMD can be a promising tool in the multi-planar analysis of the in-cylinder flow. More discussions will be made in Chapter 5 and Chapter 6.

4.1.4 Spatial 3D EMD

The bivariate 2D EMD presented above shows its capacity in multi-planar analysis of in-cylinder flow. Nonetheless, the in-cylinder flow is naturally 3D, and an extension of EMD in the 3D spatial domain could help understand both large-scale motion structures and turbulence in the combustion chamber more clearly. The spatial 3D EMD deals with 3D data the same as 2D data, except that all the three velocity components are taken into account in the decomposition, and one additional dimension needs to be treated.

The procedure of spatial 3D EMD is schematically illustrated in Figure 4.25 with an exemplary application on the velocity field near the TDC obtained in work presented in Chapter 5. The EMD is first applied to the initial field along the X direction, then along Y and Z directions on the LF parts extracted from the decomposition in the previous direction using the acceleration strategy described in section 4.1.3.

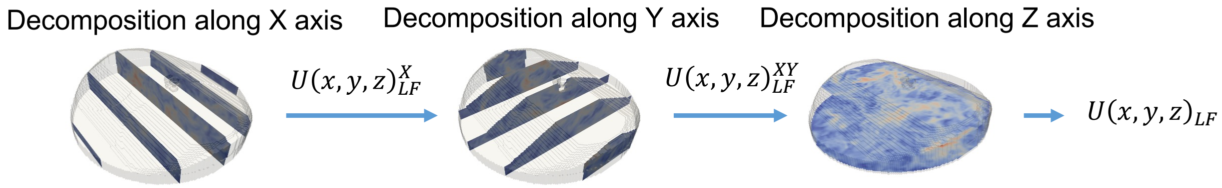

FIGURE 4.25: Extension of EMD for the 3D velocity field.

The velocity field presented in Figure 4.25 is of size 171 × 171 × 32 in X, Y and Z directions. The number of pseudo modes in one direction is of the order of $\mathcal{O}(\log_2 N)$ with N the number of data points in the corresponding direction. For the given velocity field, a total of 7 × 7 × 5 pseudo modes are expected. In case the full decomposition starts from the Z direction and ends in the X direction, the 3D EMD is carried out on 1 3D field in the Z direction, 5 3D fields in the Y direction, and $5 \times 7 = 35$ 3D fields in Z direction, while the decomposition with the acceleration methodology performs the 3D EMD only on 1 3D field in each direction. The gain in time in the case of 3D applications is even more important than in 2D. The full decomposition for spatial 3D EMD is also constrained by its potential memory usage and is not available in the current EMD tool. In the current parallelism implementation of 3D EMD, each CPU has its own pseudo mode matrix for each velocity component which are mutually communicated once the decomposition is finished in a direction. Taking the 3D velocity field presented in Figure 4.25 as an example, supposing data are of double-precision, the pseudo mode matrix of each component of size 7 × 7 × 5 to store the extracted pseudo modes in the three direction amount or a memory demand of nearly 5.1 **GB** by each CPU. For the computing node of IFPEN equipped with an Intel Skylake G-6140 processor of 36 CPUs, the total memory demand is around 183 **GB** which is already close to the maximal memory available of 192 **GB**, though the velocity field is relatively small during the engine cycle. Such a full decomposition is then surely unfeasible for larger velocity fields close to the BDC.

The obtained LF and HF parts are both presented in Figure 4.26. Concerning the spark plug region, it should be noted that the present EMD method cannot treat signals with local discontinuity. Therefore the spark plug region is filled by values generated by linear interpolation so that no discontinuity exists as it can disturb the 1D EMD on lines passing this area. Once finished, values in the interpolation region are masked to keep the real geometry.

The interest in the HF part given by the 3D EMD is that characteristics of turbulence in the chamber can be evaluated locally and globally. The turbulent level around the spark region can directly impact the combustion process, and the EMD provides the possibility to quantify the local turbulence and its impact on flame propagation.

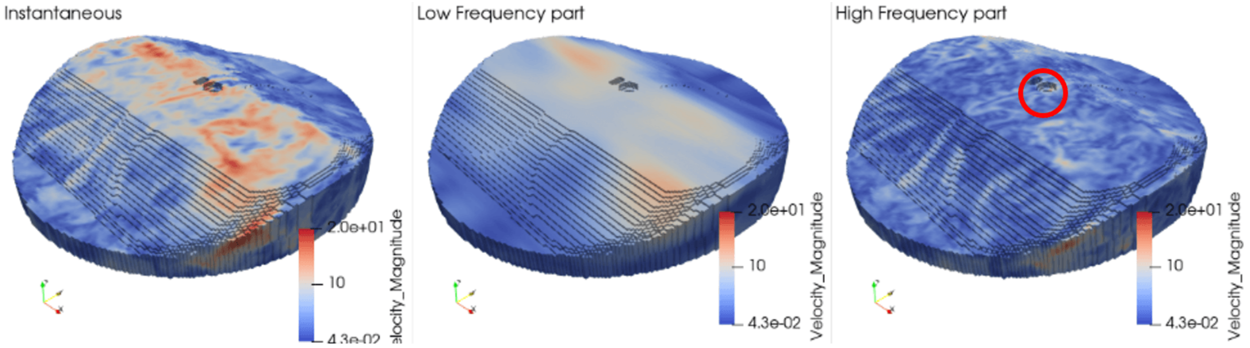

FIGURE 4.26: Application of 3D EMD on the 3D velocity field, local turbulent energy E_k^{HF} (circled in red) around spark plug is extracted.

A qualitative comparison of bivariate 2D EMD applied in the central tumble plane and trivariate 3D EMD applied to the whole domain is shown in Figure 4.27 on the same plane (the normal component of trivariate 3D EMD is excluded, and only tangential components are compared). In 2D EMD, the third component normal to the plane is not included. On the LF part, a clear difference can be observed in the central tumble plane where the tumble front extracted by 3D EMD is of lower velocity magnitude in the region of -10 mm $< Y < 0$ mm and $Z > 0$ mm on the left part of the spark plug. On the contrary, the corresponding HF part in the same region shows a higher level of velocity magnitude.

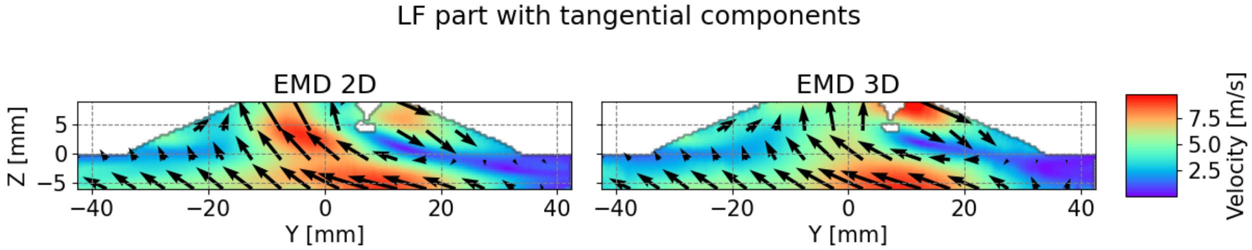

(A) LF part.

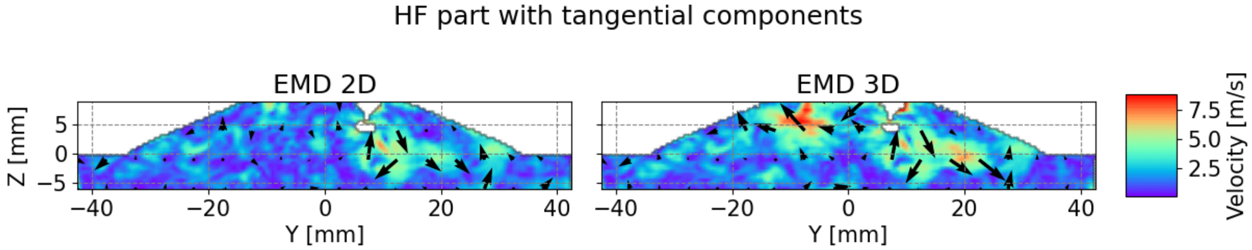

(B) HF part.

FIGURE 4.27: Comparison of results in tumble plane from bivariate 2D EMD and trivariate 3D EMD, only tangential components are included.

The observed difference comes from the missing third component U_x in 2D EMD. As shown in Figure 4.28, a transversal motion towards the negative X direction exists on the left side of the spark plug, which indicates that the residual tumble motion is not a quasi-2D rotation around the transversal axis. The impact of the third component significantly impacts the results of EMD, especially the HF part. Knowing that the turbulence is not correctly defined in 2D with 2 components, the 3D EMD is recommended to quantify it despite its cost.

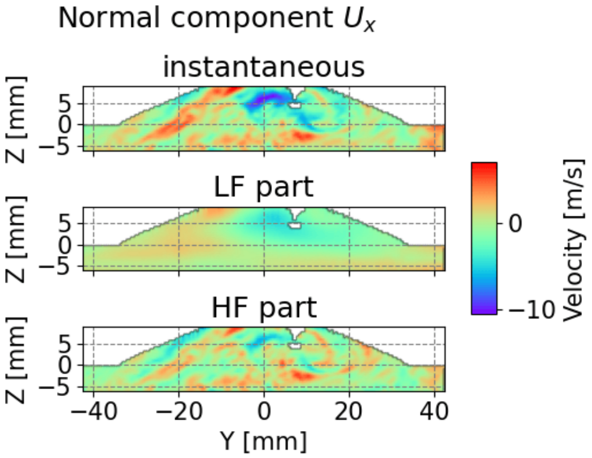

FIGURE 4.28: Decomposition of the normal component U_x with 3D EMD.

Table 4.2 compares the CPU time required by bivariate 2D EMD and trivariate 3D EMD. 108 CPUs on the IFPEN supercomputer (Intel Skylake G-6140 processors) are used for both methods. The cost of bivariate 2D EMD remains reasonable for its usage in analysis in 2D planes, while the trivariate 3D EMD requires much more resources comparable to LES simulations. Though of important interest, the general use of trivariate 3D EMD is still difficult. The trivariate 3D EMD can still be employed to deal with some selected instants representing important events during the engine cycle, like mid-admission, BDC, and mid-compression.

TABLE 4.2: Comparison on the computational cost of bivariate 2D EMD and trivariate 3D EMD.

CAD (deg)	-180	-22.5	-22.5
EMD type	2D	2D	3D
CPU time (CPU.hour)	29.3	10.9	558.4

4.1.5 Spatio-temporal 3D EMD

In this section, the 3D EMD is applied to 3D spatio-temporal data to evaluate its capability to extract spatial and temporal fluctuations.

The test case is based on the one used in [19] where 2D EMD is tested on a 2D velocity field made of a measured HIT field [162] and a synthetic Lamb-Oseen vortex, as shown in Figure 4.29. The HIT field is used as high-frequency oscillations in space, and the vortex mimics large-scale rotational motion. In this section, the data is extended in 3D with a temporal dimension, in which additional oscillations, both high and low frequency, are added.

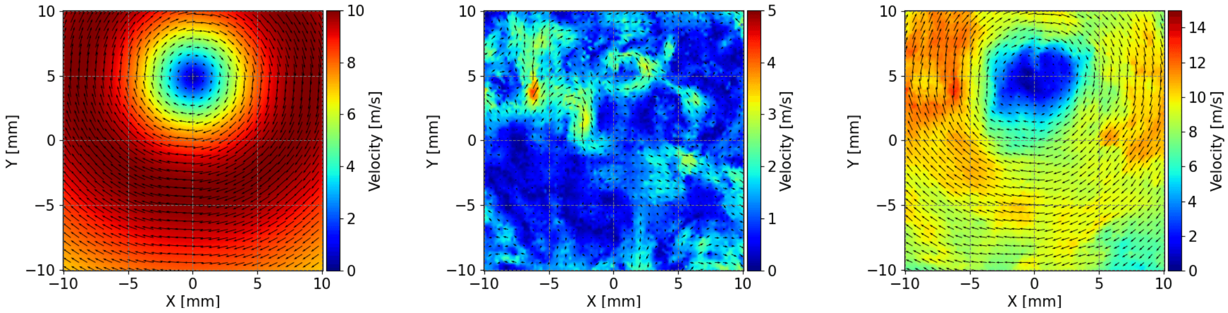

FIGURE 4.29: Combination of a large-scale moving vortex (left) and a small-scale HIT field (middle).

Compared to the test-case presented in [19], the vortex center (x_0, y_0) is not fixed but varies in time following the law described below:

$$x_0 = A_x \sin(2\pi f_x t) + \epsilon \tag{4.12}$$

$$y_0 = -A_y \sin(2\pi f_y t) + \epsilon \tag{4.13}$$

where $A_x = A_y = 5$ mm, $f_x = 25$ Hz, $f_y = 40$ Hz, and ϵ a random Gaussian noise of standard deviation $\sigma = 0.5$ mm which is generated once for both x_0 and y_0. The paths of (x_0, y_0), with and without the noise, are plotted in Figure 4.30. A total 101 time steps are generated with a total time duration of 40 ms.

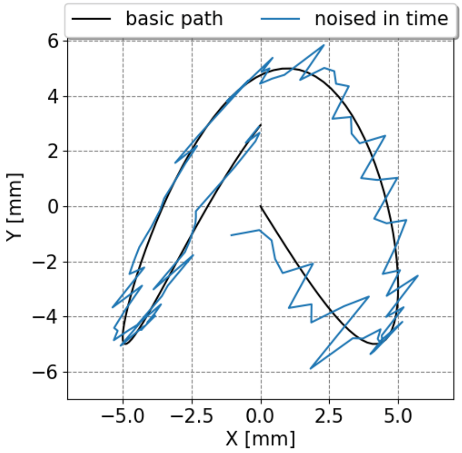

FIGURE 4.30: Path of the large-scale vortex with additional fluctuations in time.

The EMD is then applied to the 3D data. The extension of EMD for 3D or even higher dimension data is, in fact, relatively straightforward: we can easily follow the principle of sequential decomposition to start the decomposition from one direction to another till the end. It has also been found that the decomposition order does not impact the decomposition results [1]. In this test case, the decomposition starts with the two spatial dimensions and finishes with the temporal dimension. LF parts are extracted after the filtering in space and later in time. For the same time instant, the original velocity field and the corresponding LF parts after two filtering processes are presented in Figure 4.31. LF part after the spatial filtering gives already satisfying results as the rotational motion is already captured. In contrast, the LF part after the spatial and the temporal filtering changes a bit the result without significant improvement.

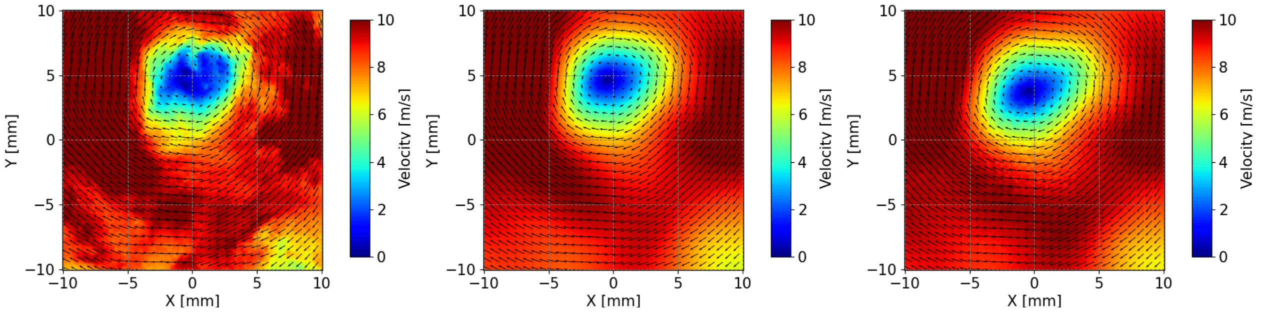

(A) Initial field.
(B) After filtering in space.
(C) After filtering in space and time.

FIGURE 4.31: Results of EMD filtering in space and in time.

To compare the two LF parts for all instants, the vortex center at each instant is extracted with the help of the Γ_1 function ,[163] which will be presented in the next section 4.2.1. The path of the vortex center is compared in Figure 4.32. The imposed path is the one without noise ϵ added in the temporal dimension and used as reference. It is worth noting that after the spatial filtering, even though the LF part at a given time step is well filtered, fluctuations between different time steps still exist, though the path detected is slightly closer to the imposed one without noise. Based on spatial filtering, temporal filtering eliminates high-frequency temporal fluctuations, as shown by the path obtained after the complete filtering in all dimensions.

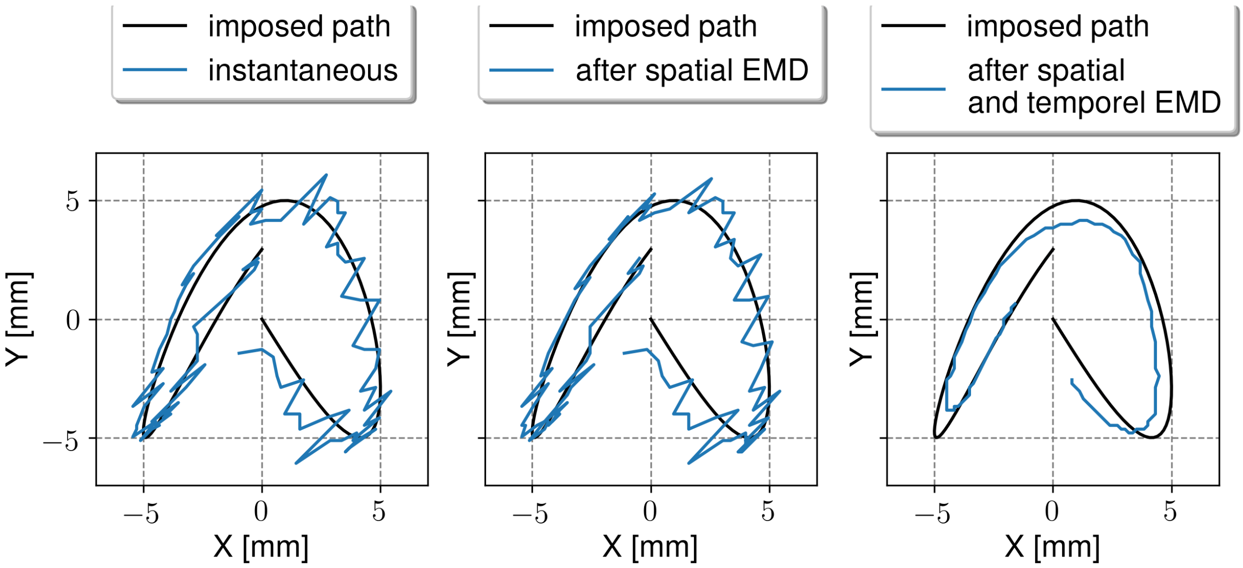

FIGURE 4.32: Comparison of the detected vortex center path.

The results of the test case presented in this section proved the capability of spatial-temporal EMD in dealing with data presenting fluctuations in space and time. The same method was also applied to LES data of engine simulation obtained in the work presented in Chapter 5. However, the physical interpretation of results after filtering in time seems difficult. This special extension of EMD was finally not used in the current thesis. More details on the application of spatio-temporal EMD to LES data are provided in Appendix C.

4.2 Vortex identification with Γ function

This section presents the Γ functions used in 2D and 3D for vortex detection. The main flow feature in a SI engine is the vortex-like tumble flow, and Γ functions are suitable tools for advanced analysis of the tumble flow.

4.2.1 Γ_1 function in 2D plane

The tumble flow is the main large-scale vortex motion in the combustion chamber of a spark-ignition engine. Algorithms called Γ_1, and Γ_2 have been developed to identify such a vortex structure by Graftieaux et al. [163]. The criterion Γ_1 is not Galilean invariant. Still, it allows a simple and robust method to identify rotational structures, while the criterion Γ_2 is Galilean-invariant as the local convection is considered. A comparison between these two criteria was made in [164] and showed that Γ_1 was much more suitable to locate vortex centers while Γ_2 could help identify the larger vortex regions. The criterion Γ_1 has been often applied to in-cylinder flow studies, though only using 2D instantaneous velocity fields, to detect and follow the tumble center location, for example, in [1].

The definition of Γ_1 is given below:

$$\mathbf{\Gamma}_1(\mathbf{x},\varphi) = \frac{1}{S}\int_{\mathbf{x}_0\in S} \frac{\mathbf{r}\left(\mathbf{x}_0\right)\times\mathbf{u}\left(\mathbf{x}_0,\varphi\right)}{\left\|\mathbf{r}\left(\mathbf{x}_0\right)\right\|\left\|\mathbf{u}\left(\mathbf{x}_0,\varphi\right)\right\|} d\mathbf{x}_0 \tag{4.14}$$

with φ the crank angle, S a sub-area centered at the point $\mathbf{x}$ of radius r and $\mathbf{r}\left(\mathbf{x}_0\right)$ the distance vector points from $\mathbf{x}$ to $\mathbf{x}_0$. $\mathbf{u}\left(\mathbf{x}_0,\varphi\right)$ is the local velocity at $\mathbf{x}_0$. It was found in [1] that the optimal r to detect the vortex center is a quarter of the total height at φ which follows the piston motion.

An exemplary application of Γ_1 on an LF velocity field at -90 CAD obtained in work presented in Chapter 5 is shown in Figure 4.33. Using the velocity field in Figure 4.33a, the corresponding field of Γ_1 is plotted in Figure 4.33b. The vortex center is defined as the point where Γ_1 is the minimal if the rotation is counterclockwise or maximal if not. In the current example, regions of negative Γ_1 represent the kernel part of the rotation, and the center lies inside (red point in Figure 4.33a).

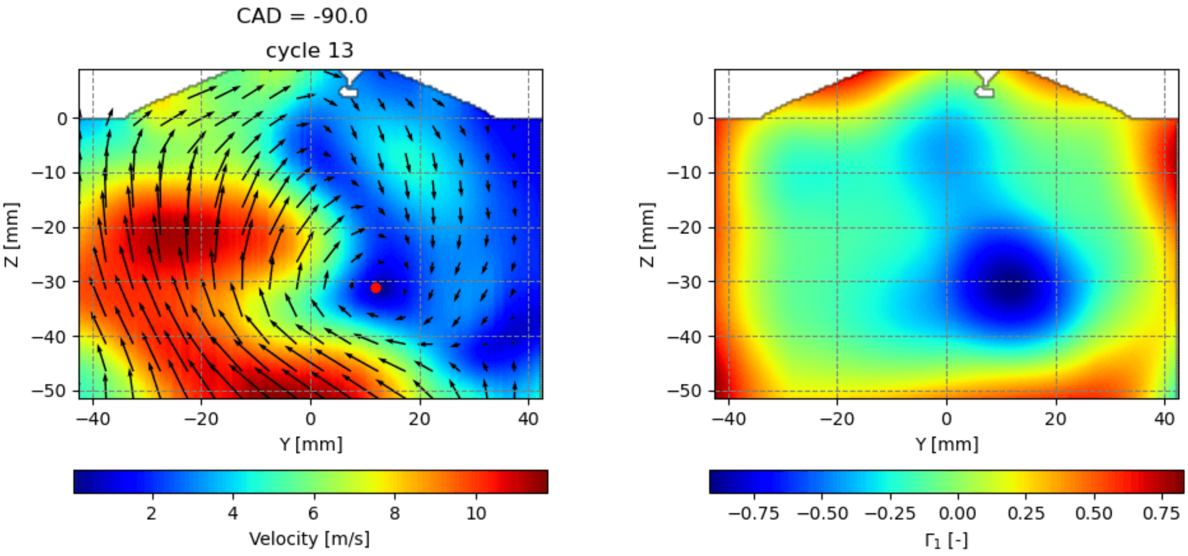

(A) Velocity field.

(B) Γ_1 distribution.

FIGURE 4.33: Vortex center detection with Γ_1 function.

4.2.2 Γ_3 function in 3D volume

For three-dimensional flows like the tumble flow, Γ_1 is limited due to its 2D nature and thus has been extended in 3D. A simple extension is to compute Γ_1 separately over several parallel 2D planes throughout the combustion chamber, as presented in [164] on PIV data and more recently in [42] on LES data. The main drawback of this type of extension is that the rotation direction can not be obtained. An improvement was made in [100] in which the author determined the local rotation direction using a sweeping method: all the possible directions were tested, and the one giving the maximal average value of $|\Gamma_1|$ over the corresponding 2D rotation plane was retained. However, this approach, not parallelized by the author, was very time-consuming and consequently only applied to two instantaneous 3D velocity fields. A real extension of Γ in 3D was realized in [165], named $\mathbf{\Gamma}_3$ and was applied to external flows to identify vortical structures in 3D volume. $\mathbf{\Gamma}_3$ was then applied to the in-cylinder flow analysis as presented in [123] with slight modifications: $\mathbf{\Gamma}_3$ was computed to obtain the rotation direction at first and then was recomputed using quantities projected into a plane normal to the rotation direction, noted as $\mathbf{\Gamma}_{3p}$. In this thesis, a modified version of $\mathbf{\Gamma}_{3p}$ will be computed to identify the tumble structure within the compression stroke.

$\mathbf{\Gamma}_3$ is first evaluated inside the combustion chamber using the following expression:

$$\mathbf{\Gamma}_3(\mathbf{x}, \varphi) = \frac{1}{V} \int_{\mathbf{x}_0 \in V} \frac{\mathbf{r}(\mathbf{x}_0) \times \hat{\mathbf{u}}(\mathbf{x}_0, \varphi)}{\|\mathbf{r}(\mathbf{x}_0)\| \, \|\hat{\mathbf{u}}(\mathbf{x}_0, \varphi)\|} d\mathbf{x}_0 \tag{4.15}$$

with φ the crank angle, V a sub-volume centered at the point $\mathbf{x}$ and $\mathbf{r}(\mathbf{x}_0)$ the distance vector points from $\mathbf{x}$ to $\mathbf{x}_0$. $\hat{\mathbf{u}}(\mathbf{x}_0, \varphi)$ is the local velocity $\mathbf{u}(\mathbf{x}_0, \varphi)$ at $\mathbf{x}_0$ without the contribution from local convection $\langle \mathbf{u} \rangle_V(\mathbf{x}, \varphi)$:

$$\hat{\mathbf{u}}(\mathbf{x}_0, \varphi) = \mathbf{u}(\mathbf{x}_0, \varphi) - \langle \mathbf{u} \rangle_V(\mathbf{x}, \varphi) \tag{4.16}$$

$\langle \mathbf{u} \rangle_V(\mathbf{x}, \varphi)$ is the average velocity inside V.

The formulation of $\mathbf{\Gamma}_3$ allows a reliable estimation of the rotation direction at the point $\mathbf{x}$ by a simple normalization of $\mathbf{\Gamma}_3$:

$$\mathbf{e}_{\Gamma_3}(\mathbf{x}, \varphi) = \frac{\mathbf{\Gamma}_3(\mathbf{x}, \varphi)}{\|\mathbf{\Gamma}_3(\mathbf{x}, \varphi)\|} \tag{4.17}$$

It should be noted that the result of $\mathbf{r}\,(\mathbf{x}_0) \times \hat{\mathbf{u}}\,(\mathbf{x}_0, \theta)$ may result in contribution to Γ_3 not aligned with the rotation direction $\mathbf{e}_{\Gamma_3}$, and thus reduce the value of $\|\Gamma_3\|$. To enhance the detection of local rotation, $\mathbf{\Gamma}_3$ is recomputed using velocity and distance vectors $\mathbf{u}_p\,(\mathbf{x}_0, \theta)$ and $\mathbf{r}_p\,(\mathbf{x}_0)$ projected into the rotational plane normal to the rotation direction and defined as follows:

$$\mathbf{r}_p\,(\mathbf{x}_o) = \mathbf{r}\,(\mathbf{x}_o) - \mathbf{e}_{\Gamma_3}(\mathbf{x}, \varphi) \cdot (\mathbf{r}\,(\mathbf{x}_o) \cdot \mathbf{e}_{\Gamma_3}(\mathbf{x}, \varphi)) \tag{4.18}$$

$$\mathbf{u}_p\,(\mathbf{x}_o, \varphi) = \hat{\mathbf{u}}\,(\mathbf{x}_o, \varphi) - \mathbf{e}_{\Gamma_3}(\mathbf{x}, \varphi) \cdot (\hat{\mathbf{u}}\,(\mathbf{x}_o, \varphi) \cdot \mathbf{e}_{\Gamma_3}(\mathbf{x}, \varphi)) \tag{4.19}$$

The final formulation of $\mathbf{\Gamma}_{3p}$ is then given by:

$$\mathbf{\Gamma}_{3p}(\mathbf{x}, \varphi) = \frac{1}{V} \int_{\mathbf{x}_0 \in V} \frac{\mathbf{r}_p\,(\mathbf{x}_0) \times \mathbf{u}_p\,(\mathbf{x}_0, \varphi)}{\|\mathbf{r}_p\,(\mathbf{x}_0)\|\;\|\mathbf{u}_p\,(\mathbf{x}_0, \varphi))\;\|} d\mathbf{x}_0 \tag{4.20}$$

Compared to the definition in [123], $\mathbf{u}_p$ is used in both the denominator and the numerator in the current study to keep a more consistent expression. The magnitude of $\mathbf{\Gamma}_{3p}$ describes whether organized rotation exists: unity values are related to a perfect vortex without deformation. In contrast, small values close to zero correspond to nearly pure convection. Based on $\mathbf{\Gamma}_{3p}$, tumble centers can be determined the same way as in the 2D case: along the main axis of the tumble motion (X-axis in this study), a local center can be determined where the magnitude of $\mathbf{\Gamma}_{3p}$ is maximized. All the local centers constitute a tumble center line (TCL) around which the tumble rotates, as illustrated in Figure 4.34.

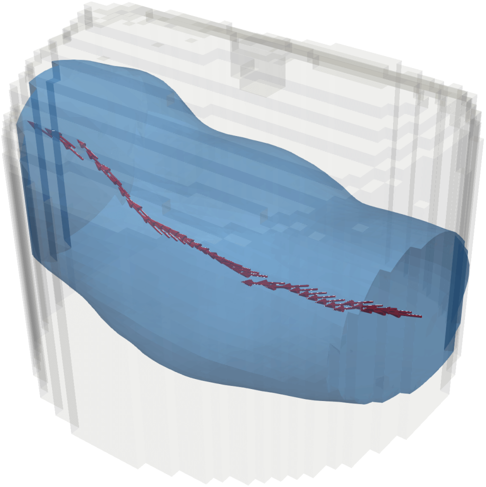

FIGURE 4.34: Tumble vortex core identified by the isosurface of $|\mathbf{\Gamma}_{3p}| = 0.5$ (blue) and Tumble Center Line (red) along X-axis around which the tumble motion is organized. Local tumble center at x_0 is of maximal value of $|\mathbf{\Gamma}_{3p}|$ for all points at $x = x_0$.

For an application to a spark-ignition engine, the following methodology is proposed: first, interpolate the velocity field on a 3D uniform grid taking into account the complex geometry of the combustion chamber; then, apply the $\mathbf{\Gamma}_{3p}$ criteria to the whole chamber. The volume V in Eq. 4.15 is set to be a sphere of radius R varying dynamically with the available chamber room height $H_c(\theta)$

such that $R = 0.3L$ as recommended in [165] where L is the characteristic scale of the searching structure, and in this study equals to $0.5H_c(\theta)$ assuming the tumble fills the chamber as a pure rotation.

The computation of $\mathbf{\Gamma}_{3p}$ in the chamber can be expensive, especially when the piston stays around the BDC. $\mathbf{\Gamma}_{3p}$ is computed inside the whole chamber, and thus a grid needs to be defined on which the computation is carried out. A uniform grid is generated with respect to the real geometry, and different resolution is tested. A small resolution provides more precision, but the cost also increases. For the same given velocity field obtained in work presented in Chapter 5, corresponding iso-surfaces of $|\mathbf{\Gamma}_{3p}|$=0.5 computed on grids of different resolutions are compared in Figure 4.35.

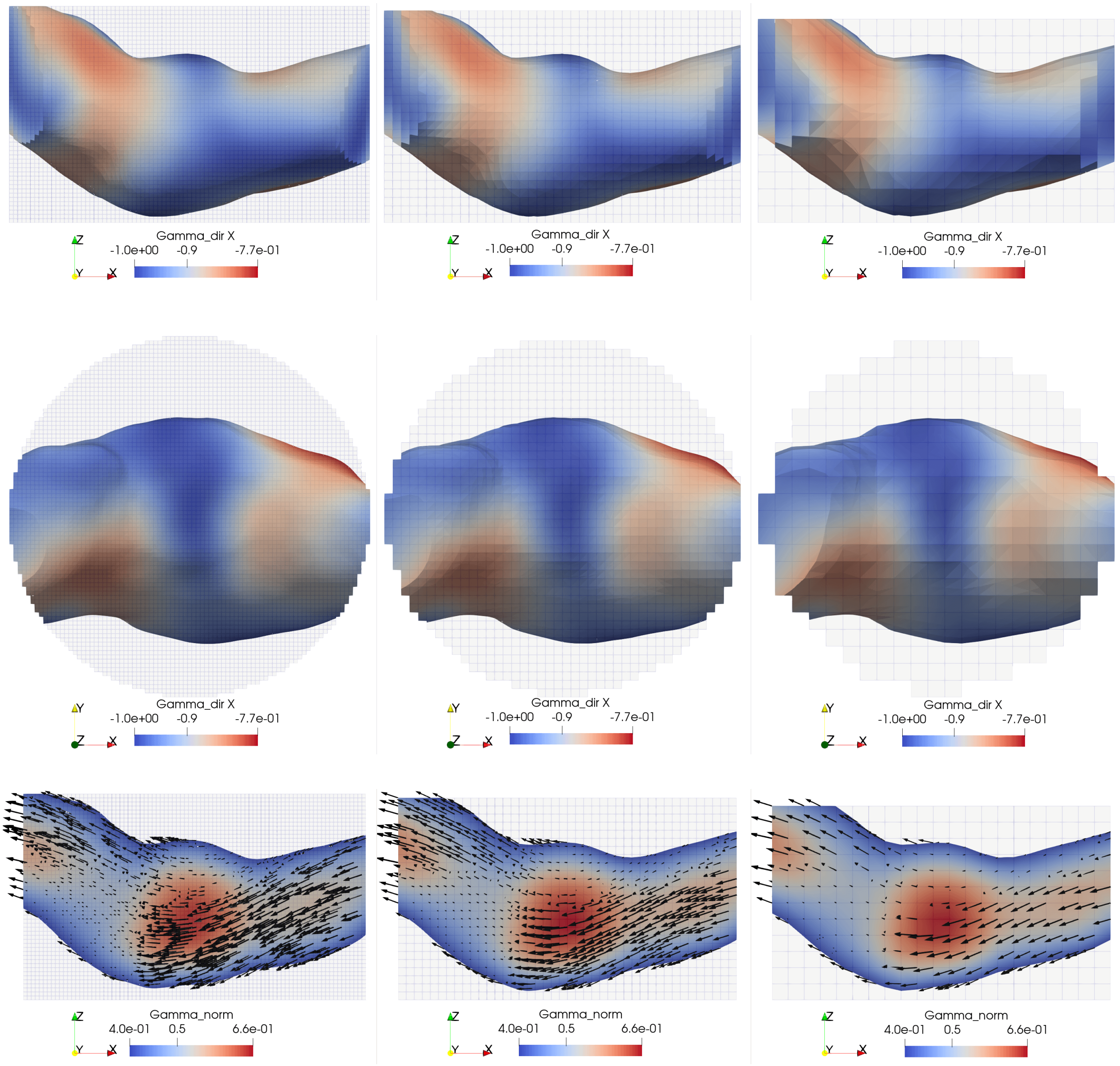

FIGURE 4.35: Effect of mesh size on the computed $\mathbf{\Gamma}_{3p}$, from left to right: 0.5 mm, 1 mm, 2 mm.

It can be concluded that even a resolution of 2 mm gives comparable results to those obtained with a resolution of 1and 0.5 mm. Knowing that the computational cost increases linearly with the grid point number, the computation on the grid of 2 mm is 64 times faster than that on the grid of 0.5 mm. Treating the velocity field at BDC using 36 CPUs on the IFPEN supercomputer (Intel Skylake G-6140 processors) takes 50 minutes, which is acceptable for a massive application on a large number of engine cycles.

$\mathbf{\Gamma}_{3p}$ does not quantify the rotation intensity. For that purpose, a local tumble ratio was defined in [123] along the TCL at each center $\mathbf{x}_c$ using average local vorticity evaluated on the circular plane with a radius of 5 mm perpendicular to the TCL. This formulation ignores the flow field outside the small circular plane where most of the tumble structure resides. Therefore, in this study, we propose another formulation named local tumble ratio **TR**, which quantifies the rotation intensity from whole local rotation planes:

$$\mathbf{TR}(\mathbf{x}_c,\theta) = \frac{1}{\omega_{ref}} \frac{\int_{\mathbf{x}_0 \in V_r} \mathbf{r}_p(\mathbf{x}_0) \times \rho(\mathbf{x}_0,\theta)\,\mathbf{u}_p(\mathbf{x}_0,\theta)\,d\mathbf{x}_0}{\int_{\mathbf{x}_0 \in V_r} \rho(\mathbf{x}_0,\theta)\left\|\mathbf{r}_p(\mathbf{x}_0)\right\|^2 d\mathbf{x}_0} \tag{4.21}$$

with V_r representing the volume which includes only points very close (whose normal distance to the plane is less than the typical mesh cell size 0.5 mm) to the rotational plane of the center $\mathbf{x}_c$. The rotational plane is the plane normal to the local rotational direction passing through the local center $\mathbf{x}_c$, as presented in Figure 4.36a. This formulation is quite similar to that of the global tumble ratio [166] except that only points close to the rotational plane are used with their projected quantities and that the tumble ratio is computed around the local center instead of the global center of gravity. **TR** here is also a vector and thus provides the rotation intensity in different directions. Its components in the X, Y and Z directions, are named classically as the tumble ratio TR, the cross-tumble ratio CTR, and the swirl ratio SR, as shown in Figure 4.36b. The X axis corresponds to the main rotation axis of the tumble motion, and the Z axis is aligned with the piston motion direction. We use the notation TR for the X component (tumble ratio) of the vector **TR**. The absolute value of TR and the norm of **TR** are therefore written respectively: |TR| and |**TR**|.

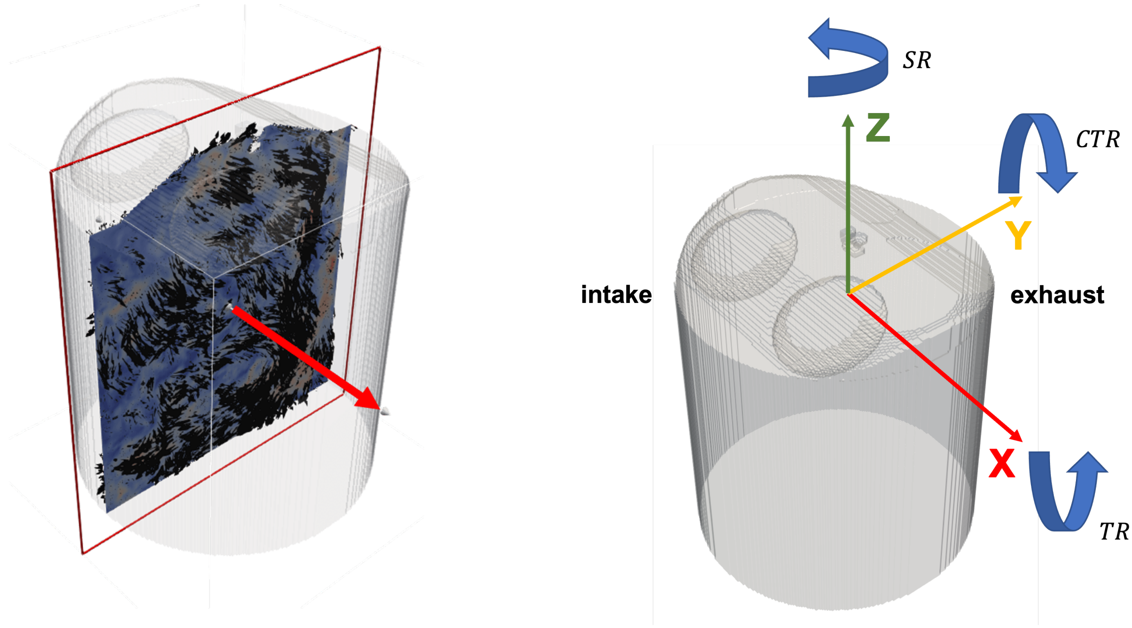

(A) Local **TR** is computed using data points in the near region of the local rotation plane normal to the local rotation axis.

(B) Decomposition of **TR** in the X, Y and Z directions gives **TR**, **CTR** and **SR**.

FIGURE 4.36: Computation of local **TR** and its decomposition.

With the criterion $\mathbf{\Gamma}_{3p}$, the tumble center line and the corresponding local tumble ratio **TR**, we can describe precisely the tumble structure in the chamber. Their evolution during the compression may provide information about the tumble's evolution during the compression stroke.

4.3 Summary of main developments

In this Chapter, we presented developments of flow analysis tools, EMD and Γ_3 function, achieved during this thesis.

EMD was previously applied to 2D bivariate velocity fields of in-cylinder flow by Sadeghi et al. [1]. We brought two major improvements for its application to LES data:

- The first modification was focused on the mode combination strategy. The improved EMD got rid of the predefined number of modes and the interpolation used in [1] to deal with time-varying geometries. The interpolation on the stretched grid was not required and EMD was applicable directly to velocity fields stored in the initial PIV or LES grid.
- The second modification was made to accelerate the decomposition to facilitate the massive application of EMD in in-cylinder flow analysis. In case of the complete decomposition, all the IMF mode and the residual were extracted and then combined to form the LF and HF parts. We proposed a strategy of acceleration with which the LF part was defined as the sum of the residual and the last IMF. Following this definition, EMD acted like a filtering tool and the decomposition in each direction amid at eliminating the HF part from the original signal. The complete decomposition was therefore unnecessary.

EMD was then extended to treat trivariate 3D data and made it possible to characterize the in-cylinder flow, both the tumble motion and the turbulence which could impact the combustion process. Its application will be presented in Chapter 5 in the motored case study, and in Chapters 6 and 7 in the fired case study. The usage of EMD to deal with spatio-temporal data was also illustrated on a simple test case. Its application to LES data from engine simulations will be discussed in Appendix C.

Γ_3 function was previously introduced to visualize the tumble vortex. We only brought a minor modification on its formulation. The computation of Γ_3 led to an important computational cost, which was the major obstacle for its extensive usage in the characterization of tumble motion. Some efforts were made in this thesis:

- The implementation of Γ_3 was made with parallelization so that the computation, naturally explicit, was much more efficient.
- The impact of the grid resolution on the results of Γ_3 was also analyzed. Results computed on the coarse grid of size 2 mm was sufficient for a qualitative visualization of the tumble vortex.

A local tumble ratio **TR** was also proposed to quantify the intensity of tumble motion along its rotational axis TCL, which completed information provided by Γ_3 function. A quantitative description of tumble motion was thus possible by combining Γ_3 function and the local tumble ratio **TR**. Such an application will also be illustrated in Chapters 5 in the motored case study, and in Chapters 6 and 7 in the fired case study.

CHAPTER 5

Simulation and analysis of the TU Darmstadt engine configuration: motored conditions

Contents

5.1 Engine characteristics . . . 72

5.2 LES methodology . . . 73

- 5.2.1 Boundary conditions . . . 73
- 5.2.2 Mesh . . . 74
- 5.2.3 Numerical set-up . . . 75

5.3 Preliminary validation of the LES results on thermodynamics . . . 76

- 5.3.1 0D simulation with GT-Power . . . 76
- 5.3.2 Thermodynamic properties . . . 77
- 5.3.3 Corrections on the crevice flow modeling . . . 78

5.4 Validation of the LES methodology on internal aerodynamics . . . 83

- 5.4.1 Qualitative comparison with PIV measurements . . . 83
- 5.4.2 Potential causes of the observed difference . . . 84
- 5.4.3 Sensitivity analysis on boundary conditions of LES . . . 85
- 5.4.4 Quantitative comparison of the LES results . . . 87

5.5 Analysis of the tumble flow during the compression stroke . . . 95

- 5.5.1 Large-scale motion and CCV . . . 96
- 5.5.2 Energy transfer between large-scale motion and small eddies . . . 98
- 5.5.3 Flow characterization in 3D . . . 100
- 5.5.4 The link between 2D and 3D diagnostics . . . 106

5.6 Summary of main findings . . . 109

This Chapter presents the LES of the optical engine disposed by TU Darmstadt performed on motored conditions. First, the LES methodology is validated and improved by comparing the numerical results with the available experimental ones.

Once the LES results are validated, the in-cylinder flow during the compression stroke is studied. The tumble motion during this stroke experiences an important evolution, and a quantitative characterization is necessary. Therefore, Γ_{3p} and EMD will be applied to precisely follow the development of large-scale structures and their variability and to investigate the energy transfer from large-scale motion to small-scale turbulent fluctuations.

5.1 Engine characteristics

The engine studied in this thesis is an optically accessible single-cylinder direct-injection four-stroke spark-ignition engine disposed by TU Darmstadt in Germany [167]. The engine has four valves (two for the intake and two for the exhaust) mounted in a pent-roof cylinder head and can be operated either with port-fuel injection (PFI) or with direct injection (DI). Experimental measurements are realized on two cylinder-head geometries, the wall-guided and the spray-guided configurations. The latter is more recent with a vast database for validating simulation results and therefore is chosen to be studied in this thesis.

The geometry of the spray-guided configuration is presented in Figure 5.1. A fuel injector is mounted centrally near the spark plug during the experiments, though in motored conditions, no injection occurs. A detailed description of the test bench can be found in [160].

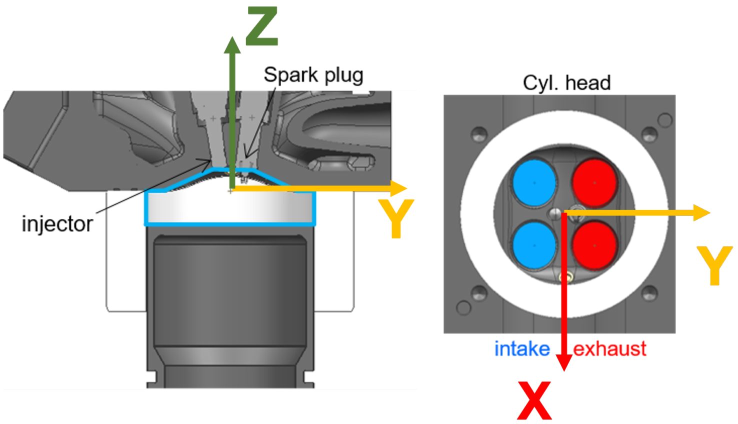

FIGURE 5.1: Engine geometry of the configuration 'Spray-guided' [160]. The coordinate system is used in the numerical modeling of this work.

Figure 5.2 shows a schematic of the engine test bench from the intake to the exhaust plenum. Locations for which fluid dynamic and thermodynamic conditions are measured during engine operation are also indicated. The measured pressure at intake and exhaust ports will be used as boundary conditions for the simulations.

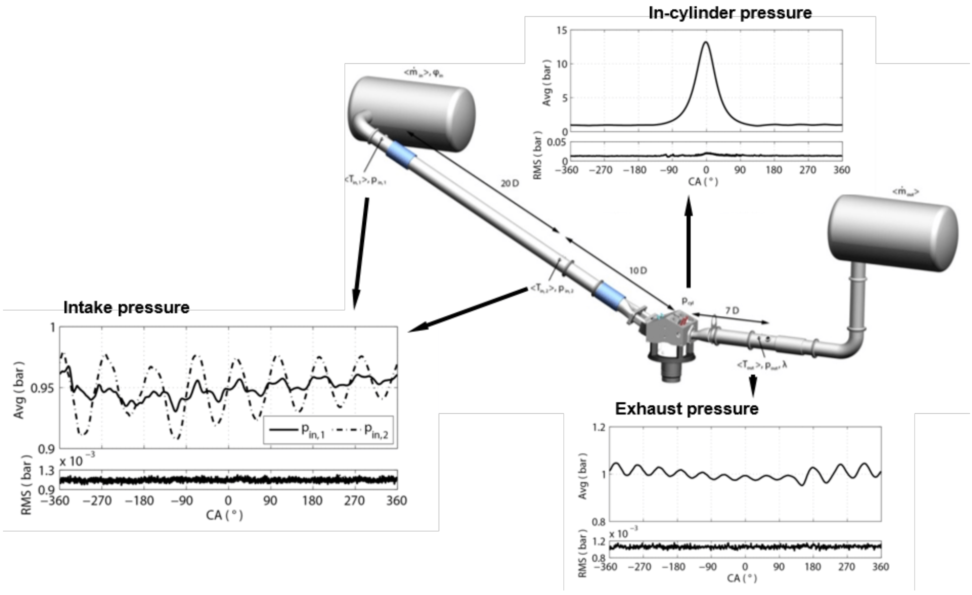

FIGURE 5.2: Schematics of the full experimental set-up [160].

Four engine operating points are available on this test bench, and only a single point (operating point C named by TU Darmstadt) has been chosen for this study. Table 5.1 summarizes the engine characteristics at this specific operating point.

Engine speed	1500 rpm
Intake/exhaust pressure	0.95/1 bar
Intake/exhaust temperature	307/310 K
Compression ration	8.7
Bore/stroke	86/86 mm
Connecting rod	148 mm
Displacement	499.6 cm^3
Intake valve opening	325 CAD
Intake valve closure	−125 CAD
Exhaust valve opening	105 CAD
Exhaust valve closure	−345 CAD

TABLE 5.1: Engine characteristics (0 CAD = top dead center of the compression stroke).

5.2 LES methodology

5.2.1 Boundary conditions

The computational domain includes only part of the whole test bench. It starts from the second probe (closer to the cylinder) located at the intake port and ends at the probe located at the exhaust port. The phase-averaged pressure at intake probe P_{MAN2} and that at exhaust probe P_{EXH} are computed based on 49 cycles and used as boundary conditions for respectively inlet and outlet of the domain. The evolution of temperatures at the intake and exhaust ports is not recorded, and only an averaged value measured by a low-frequency thermocouple is given. These two temperatures, T_{MAN2} and T_{EXH}, are imposed not only on the corresponding boundaries where they are measured but also on the intake or exhaust port boundaries, respectively. For the cylinder part, a constant wall temperature of 333 K is imposed for all the walls, including the liner and the head. A resume of used boundary conditions is presented in Figure 5.3

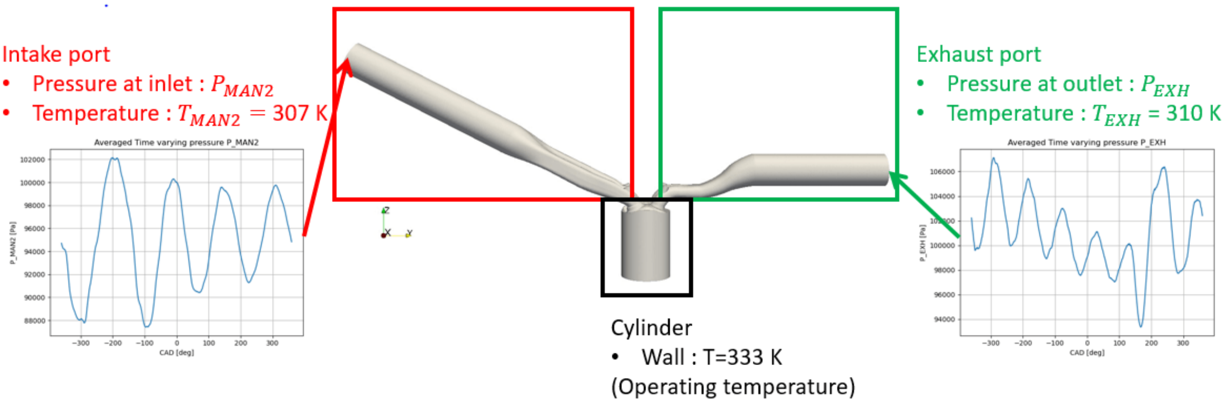

FIGURE 5.3: Boundary conditions (red: intake port; green: exhaust port; black: cylinder).

A slight modification of the engine geometry is done on the crevice region of the engine. Unlike commercial engines in which the crevice region is sealed with two or three rings, the Darmstadt engine contains only one ring to ensure the closing of the cylinder. In addition, its position is relatively low compared to the piston position, which leads to a top land region of 74.4 mm in height. The real width of the crevice is 0.5 mm, which is in the order of the typical grid size used in LES. The resolution of the flow in such a narrow region requires a finer discretization, which can increase the computational cost dramatically. To avoid grid refinement, we decided to modify the dimension of the crevice region: the modified crevice is two times larger in width and three times shorter in height. The annular volume at the bottom side is adjusted to keep the same compression ratio. A comparison of the crevice before and after modification is illustrated in Figure 5.4.

5.2.2 Mesh

A Cartesian cut-cell method is used to generate the grid and is coupled with the Automatic Mesh Refinement (AMR) strategy. During the entire engine cycle, the mesh size at different parts varies well to capture important phenomena during intake and compression strokes and save computational cost during the power and exhaust strokes which are less critical in motored conditions. A general description of the mesh size is given in Table 5.2.

	intake	compression	power	exhaust
cylinder	0.5	0.5	1	1
intake port	1	2	2	2
intake port around valves	0.5	2	2	2
exhaust port	2	2	2	1

TABLE 5.2: Mesh size (mm) variation during the engine cycle.

FIGURE 5.4: Crevice without (left) and with (right) modification.

With this mesh strategy, the number of cells varies between 1.2 to 6.2 million. An example of the mesh during the intake stroke is presented in Figure 5.5.

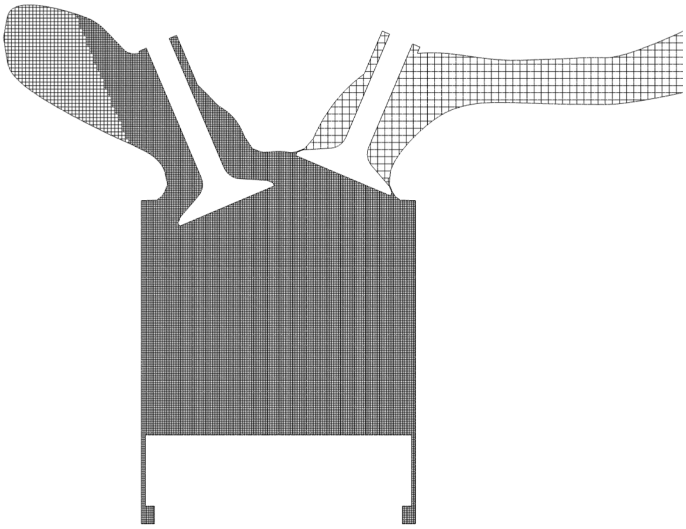

FIGURE 5.5: Mesh topology during the intake stroke at -250 CAD.

5.2.3 Numerical set-up

The commercial CFD solver CONVERGE [20] is used for the LES as it is well designed for engine application. The set of numerical parameters used in LES is summarized in Table 5.3. The wall-resolved LES is quite expensive as it requires a well-refined mesh on boundaries to resolve boundary layers. To resolve the transient in-cylinder flow with the least cost, the wall models for velocity and temperature are used in LES (wall-modeled LES).

The simulation is initialized with a uniform velocity, pressure, and temperature mapping. The first two cycles obtained with this unrealistic initialization are dropped, and results are retained from the third cycle.

Velocity-pressure coupling	PISO [168]	
Temporal scheme	Semi-Implicit 2^{nd} order	
Spatial scheme	Central scheme 2^{nd} order	
Convective CFL	$u\frac{\Delta t}{\Delta x} \leq 1$	
Fourier number	$\nu\frac{\Delta t}{\Delta x^2} \leq 2$	
Acoustic CFL	$c\frac{\Delta t}{\Delta x} \leq 10$	
SGS model	Sigma	
Wall modeling	Velocity	Log-Law
	Temperature	O'Rourke and Amsden

TABLE 5.3: Numerical set-up for Darmstadt engine simulation on motored condition.

5.3 Preliminary validation of the LES results on thermodynamics

We obtained the first useful engine cycle using the LES methodology presented above. The validation of the results is done on thermodynamic properties as it remains stable under motored conditions between different cycles. Only the in-cylinder pressure is available from experiments, and the 0D simulation with GT-Power provides other properties like the trapped mass and the in-cylinder temperature.

5.3.1 0D simulation with GT-Power

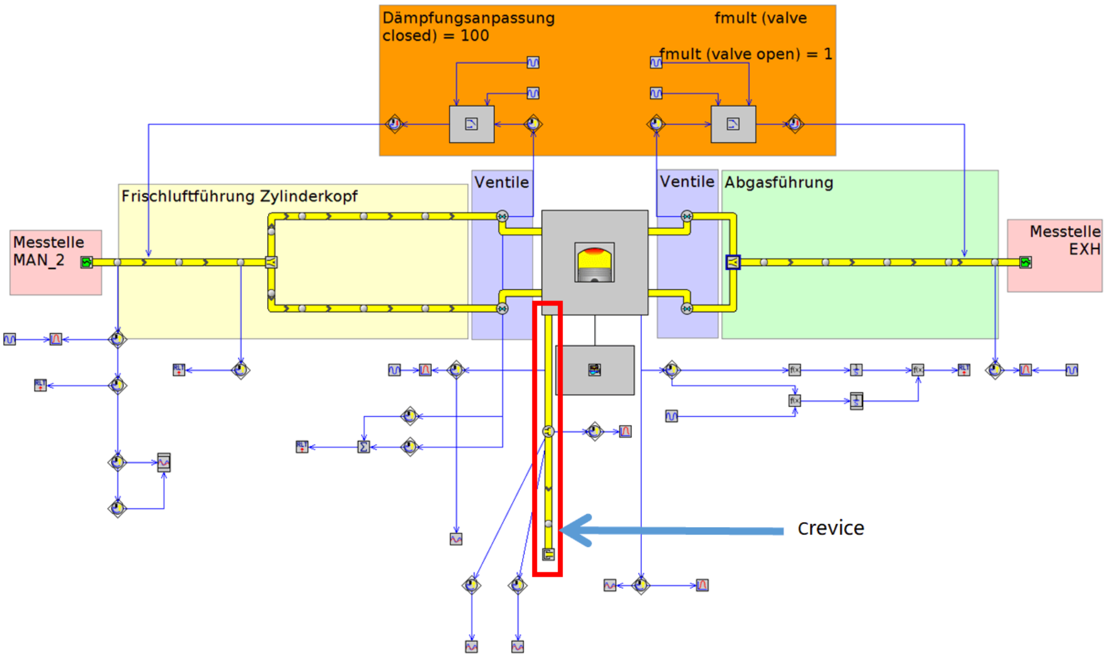

FIGURE 5.6: Workflow de la simulation 0D with GT-Power.

Figure 5.6 schematizes the 0D model built with GT-Power. In the same way as for 3D computations, the computational domain includes only part of the intake and exhaust ports. The crevice is also taken into account in the model. It is modeled by an annular volume attached to the combustion chamber (framed in red), which allows us to follow the mass exchange process between the crevice and the chamber. Results from the 0D simulation are complementary to experimental measurements which are very limited.

5.3.2 Thermodynamic properties

The pressure level at the computational domain's inlet and outlet is first validated against the experimental measurements. As shown in Figure 5.7 and Figure 5.8, the pressure conditions imposed at these two boundaries are well set in the simulation.

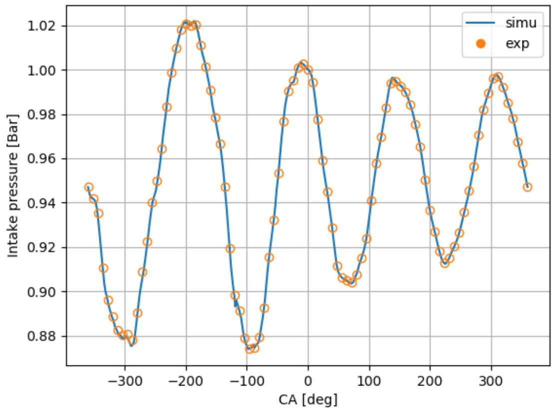

FIGURE 5.7: Pressure evolution at the inlet boundary.

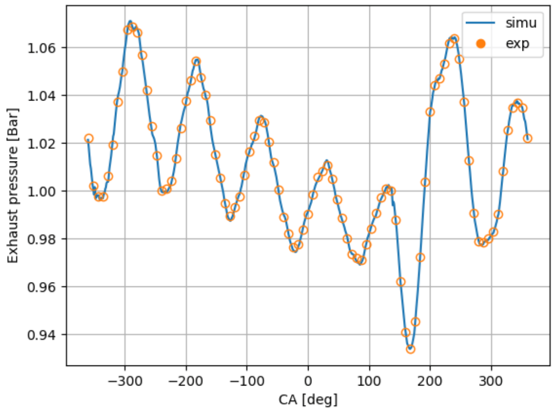

FIGURE 5.8: Pressure evolution at the outlet boundary.

The thermodynamic properties inside the cylinder are then compared to experimental and 0D simulation results. From Figure 5.9 and Figure 5.10, LES tends to over-predict the in-cylinder pressure, though the trapped mass is correctly estimated. The same problem has been reported in a study of the Darmstadt engine [42] and the authors proposed reducing the chamber volume to correct the pressure prediction.

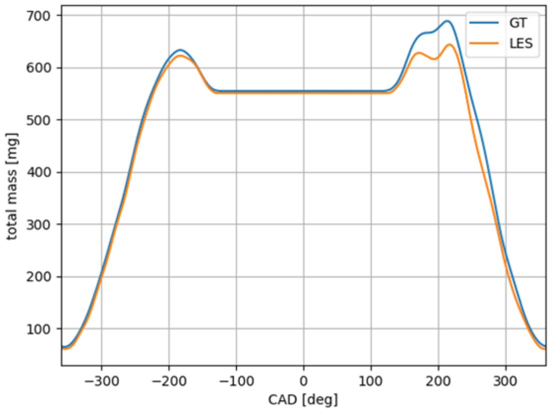

FIGURE 5.9: Trapped mass.

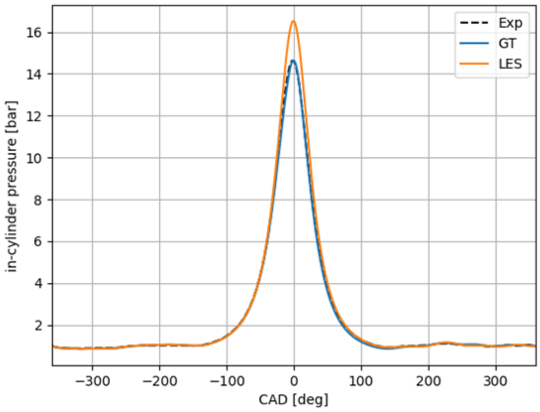

FIGURE 5.10: In-cylinder pressure.

As mentioned before, the 0D model can describe the mass exchange between the chamber and the crevice during the engine cycle. From LES results, the same information is extracted and compared to the results of the 0D model, as shown in Figure 5.11 and Figure 5.12. Interestingly, even though the total trapped mass is of the same level, the mass distribution in the chamber and the crevice shows significant differences between the LES and the 0D model. During the compression stroke, as the piston moves up, a certain quantity of mass will enter the crevice region. Later during the power stroke, the mass will be released to the chamber from the crevice. This process is quite important for the in-cylinder pressure as the mass inside the chamber determines the pressure level around the top dead center. Compared to the 0D model, LES underestimates the mass exchange and therefore overestimates the in-cylinder pressure level.

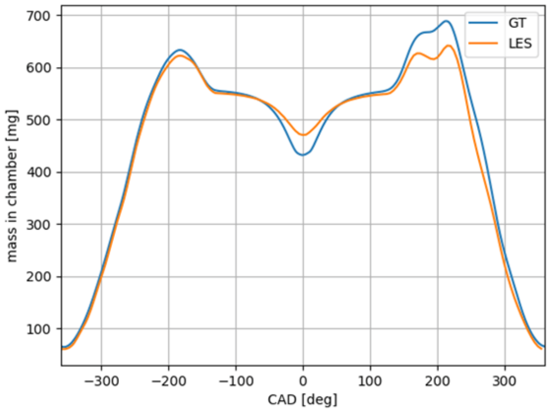

FIGURE 5.11: Mass trapped in the chamber.

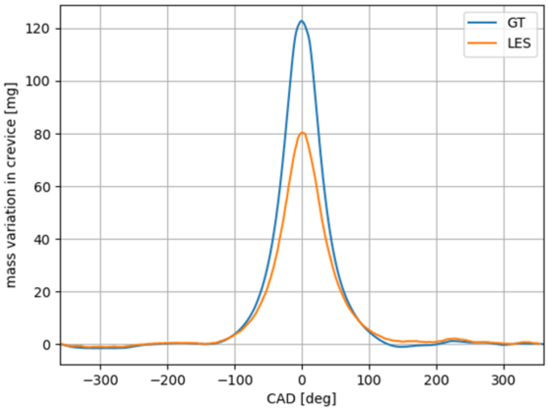

FIGURE 5.12: Mass trapped in the crevice.

5.3.3 Corrections on the crevice flow modeling

Impact of wall transfers in the crevice

The mass exchange is related to the flow modeling in the crevice region. In the LES, the number of cells in the radial direction in this part is 2 or 3, which is undoubtedly insufficient for a good flow resolution. Local refinement of the mesh leads to smaller time steps and a longer overall computational time. We chose to maintain the mesh resolution in the crevice as a compromise between the cost and the accuracy. To adjust the flow modeling in the crevice, we propose 3 test cases, listed in Table 5.4, in which the boundary conditions on the crevice walls are modified to improve the flow modeling.

case	Principal modification
0	Wall temperature at 333 K
1	Wall friction reduced to ∼ 0 Pa
2	Wall temperature decreased from 333 to 295 K
3	Heat transfer on the wall amplified by 20 times

TABLE 5.4: Wall boundary condition modification in the crevice zone in test cases 1,2,3.

The mass distribution obtained in these three test cases is presented in Figure 5.13 and Figure 5.14. In test case 1, the wall friction is set to 0 to increase the mass flow rate. However, its impact is negligible as the mass distribution remains almost the same. The modification of the wall heat transfer seems to be more crucial in the mass exchange. The slight reduction in the wall temperature in case 2 does help to amplify the mass exchange but is far from satisfactory. The amplified heat transfer in case 3 seems to perform the best as the entering flow is cooled much more efficiently in the crevice, and thus its density is largely increased.

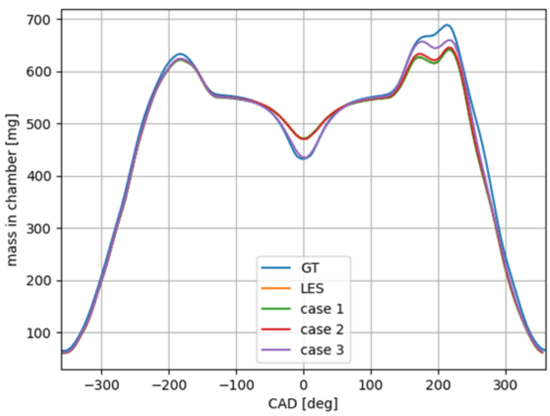

FIGURE 5.13: Mass in the chamber.

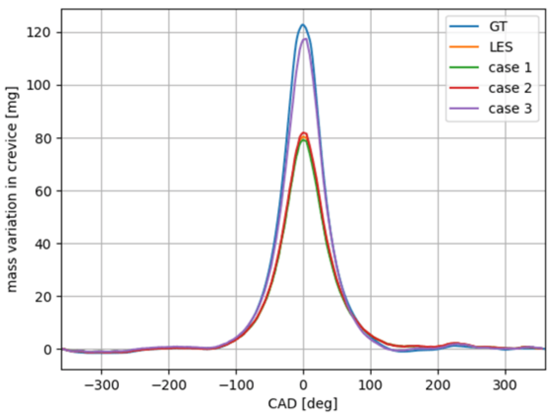

FIGURE 5.14: Mass in the crevice.

The corresponding in-cylinder pressure and temperature in the crevice are presented in Figure 5.15 and Figure 5.16. The correct mass distribution obtained in case 3 allows a correct estimation of pressure and temperature, the same as in the 0D model.

The temperature evolution in the crevice shows apparent differences between different cases. In the 0D model, the entering flow intensively exchanges heat with the wall and reaches the same temperature level as the wall. The same tendency is observed in case 3, in which the heat transfer is enhanced. In other cases, the heat transfer is relatively weak, so the entering flow stays hot compared to the wall.

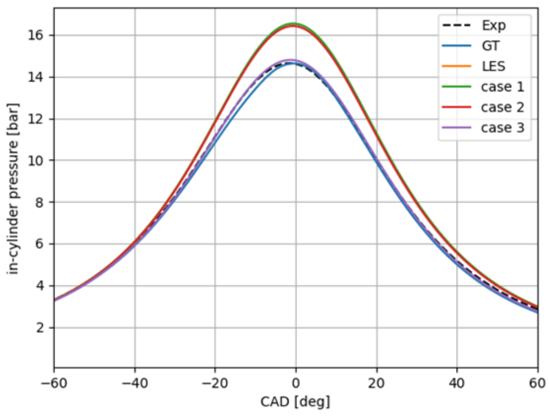

FIGURE 5.15: In-cylinder pressure.

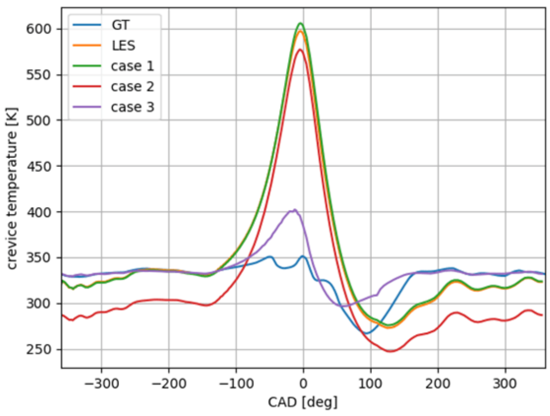

FIGURE 5.16: Temperature in the crevice.

These three test cases prove that the crevice flow is very sensitive to the wall modeling in this region. The resolution of the crevice flow is indeed difficult regarding the fact that only two/three cells are set in the radial direction, and they are bounded by the wall models.

Crevice model

To overcome the problem of crevice flow modeling, some attempts have been made to adjust the mass exchange process directly.

The first attempt is proposed in work [52]. The crevice is removed, and the left unclosed section is designed as an inlet-type boundary (cf Figure 5.17). The mass flow rate and the temperature evolution obtained from the 0D model are imposed at this boundary to model the mass exchange directly.

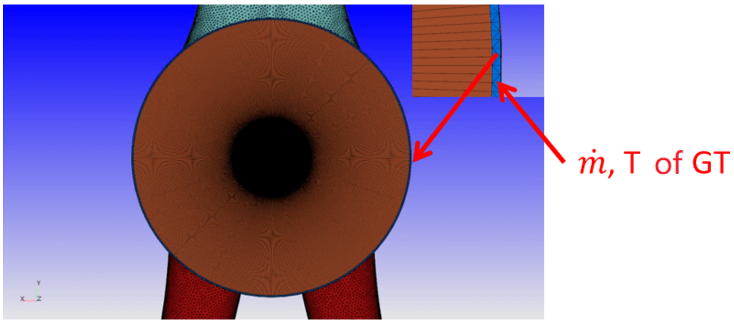

FIGURE 5.17: Mass flow rate and temperature imposed at the boundary crevice inlet.

Using this approach, test case 4 is realized. As above, the corresponding in-cylinder pressure is compared to the measured pressure, the system simulation pressure, and the reference LES (case 0) in Figure 5.18. The result is in good agreement with the experimental data. Nonetheless, as shown in Figure 5.19, the computed velocity can be tremendous in cells over the crevice inlet boundary compared to that in the whole cylinder. Its impact on the global flow is not investigated, but we consider that such a strong under-resolved gradient is not acceptable. Furthermore, this approach requires a validated 0D model to provide the in/out flow condition, which is not always available in practice.

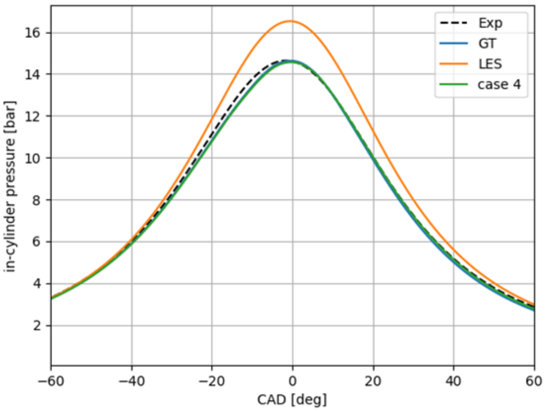

FIGURE 5.18: In-cylinder pressure.

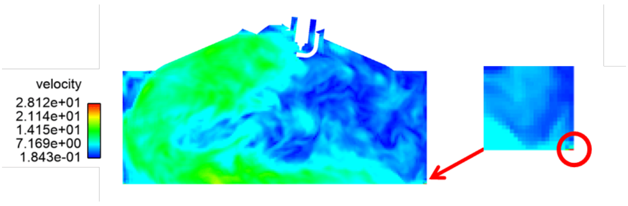

FIGURE 5.19: Local extreme velocity.

Another solution is to evaluate the mass flow rate using a crevice model instead of a system simulation. The most common crevice model is presented in [169] and built for real crevice geometry, as in Figure 5.20. The model can estimate the flow rate along the crevice region and predict the blow-by rate. The crevice of the Darmstadt engine is quite particular, and we propose a simplified crevice model based on the original one. This model will be activated for crevice cells located at the corner formed by the piston and the cylinder wall boundaries, as indicated in Figure 5.21, to model the crevice flow.

The simplified crevice model is built based on the following steps:

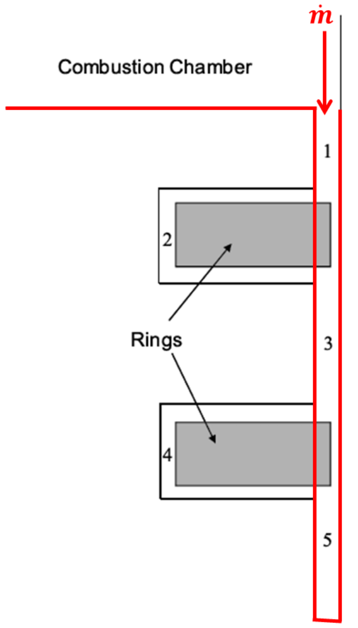

FIGURE 5.20: Crevice simplification compared to real geometry.

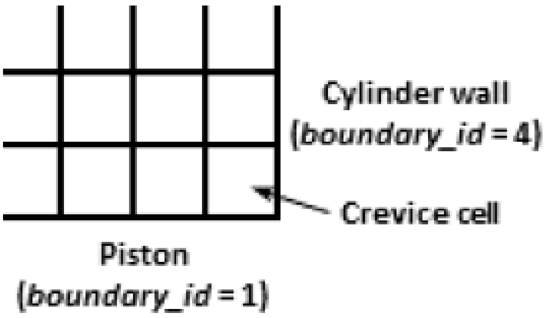

FIGURE 5.21: Crevice cell definition.

- The mass variation in the crevice m_{cre} is caused by the mass flow $\dot{m}$ between the chamber and the crevice region.

$$\dot{m} = \frac{\mathrm{d}m_{cre}}{\mathrm{d}t} \tag{5.1}$$

- m_{cre} can be expressed as the product of V_{cre} and ρ_{cre}.

$$\frac{\mathrm{d}m_{cre}}{\mathrm{d}t} = V_{cre}\frac{\mathrm{d}\rho_{cre}}{\mathrm{d}t} \tag{5.2}$$

$$\frac{\mathrm{d}m_{cre}}{\mathrm{d}t} = \rho_0 V_{cre}\frac{\mathrm{d}\rho_{cre}/\rho_0}{\mathrm{d}t} \tag{5.3}$$

- Supposing the flow remains isothermal in the crevice: $P_{cre}/P_0 = \rho_{cre}/\rho_0$.

$$\frac{\mathrm{d}m_{cre}}{\mathrm{d}t} = \rho_0 V_{cre}\frac{\mathrm{d}P_{cre}/P_0}{\mathrm{d}t} \tag{5.4}$$

- Assuming $P_{cyl} = P_{cre}$ as the pressure field is quite homogeneous, and giving $m_0 = \rho_0 V_{cre}$ the initial mass in the crevice:

$$\frac{\mathrm{d}m_{cre}}{\mathrm{d}t} = \frac{m_0}{P_0}\frac{\mathrm{d}P_{cyl}}{\mathrm{d}t} \tag{5.5}$$

Finally we obtain a simple expression of the mass flow rate between the chamber and the crevice:

$$\dot{m} = \frac{m_0}{P_0}\frac{\mathrm{d}P_{cyl}}{\mathrm{d}t} \tag{5.6}$$

The only parameter of this model is the initial mass m_0, and by adjusting its value, the model can eventually provide a correct crevice flow modeling. This model is implemented in the solver

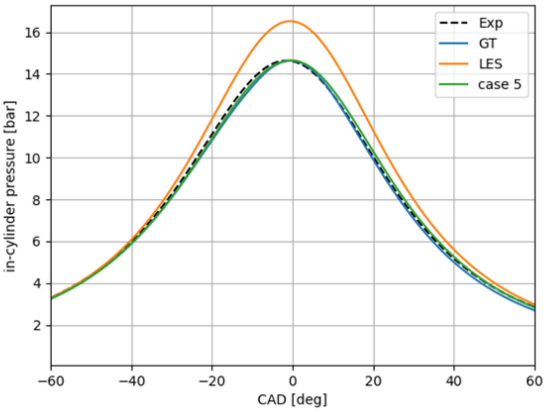

FIGURE 5.22: In-cylinder pressure.

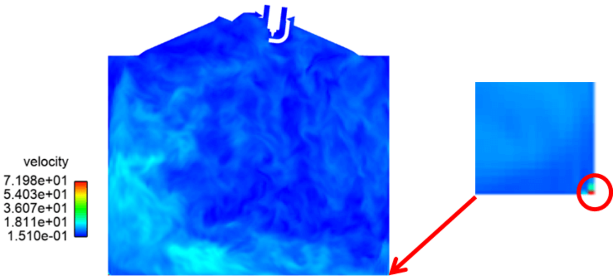

FIGURE 5.23: Local extreme velocity.

Converge and tested in test case 5. The results are presented in Figure 5.22 and Figure 5.23. With a suitable value of m_0, the in-cylinder pressure matches well the experimental data, which proves the capability of the simplified crevice model.

Nevertheless, the same problem of the local velocity is still present in this approach. The mass flow rate is uniformly distributed in crevice cells, which does not represent reality as the local flow can vary with respect to the surrounding flow state. To avoid this issue, we decided to keep the usage of this model but change the location where it is applied. The crevice is kept in the computational domain, and the crevice model is activated at the bottom side of the crevice (cf Figure 5.24). This hybrid method allows to take into account the real volume of the crevice and provide the correct mass exchange (via the source term presented in Eq. 5.6 and an ad-hoc value of m_0).

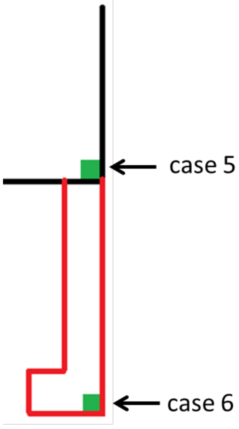

FIGURE 5.24: Application of the crevice model at the bottom of the crevice.

This approach is evaluated in test case 6, and the results are shown in Figure 5.25 and Figure 5.26. This hybrid approach provides satisfactory results. The velocity problem remains the same as before, but the related cells are far from the chamber, and their impact can be vastly reduced. Adjusting the model parameter m_0 needs some iterations in cases 5 and 6. Another reason that motivates us to choose this approach is the fact that, even though the crevice has been modified, the aspiration effect created by the crevice on the flow can still be directly captured in the simulation and be corrected by the crevice model, which remains as close to reality as possible.

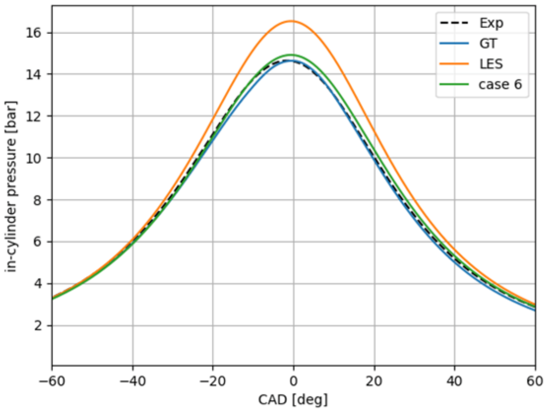

FIGURE 5.25: In-cylinder pressure.

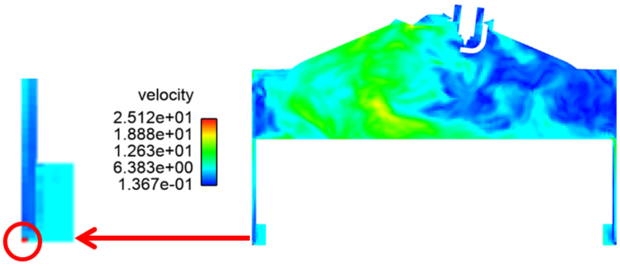

FIGURE 5.26: Local extreme velocity.

The approach of test case 6 is chosen as the final solution for the crevice flow modeling. Using this method, 15 consecutive cycles are computed, and in the next section, we will compare the obtained velocity field against PIV measurements.

5.4 Validation of the LES methodology on internal aerodynamics

5.4.1 Qualitative comparison with PIV measurements

The PIV data is available at two planes for the motored condition, the tumble plan at $X = 0$ mm and the valve plan at $X = 19$ mm, for a total of 74 cycles. We will compare the ensemble-averaged velocity field on these two planes for validation. The LES results and PIV measurements are compared for every 5 CAD during the intake and the compression strokes in both tumble and valve planes. The comparison hereafter is only for two particular instants, which already highlights the issues in the current LES methodology.

The comparison in the valve plane at −240 CAD when the intake valves are largely open is presented in Figure 5.27. The intake jet captured in LES differs significantly from PIV measurements in intensity and orientation.

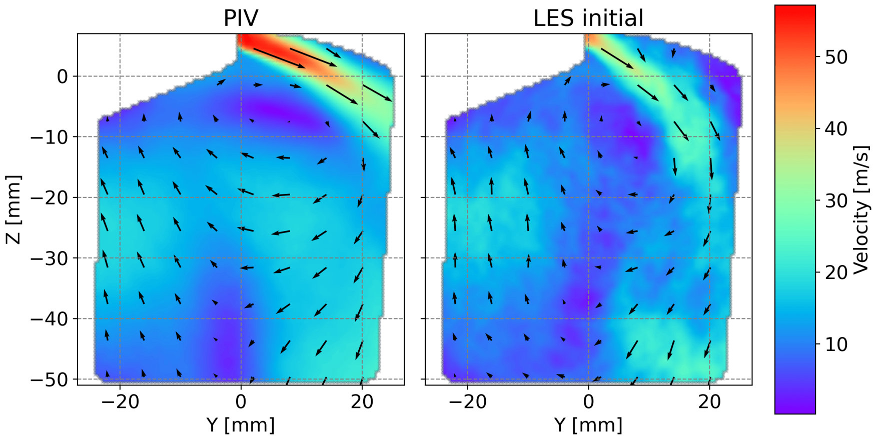

FIGURE 5.27: Comparison of the ensemble-averaged velocity field at −240 CAD in the valve plane.

We continue the validation in the tumble plane at −90 CAD during the compression stroke. As shown in Figure 5.28, a slight difference can be observed in the location of the tumble center. Moreover, the tumble intensity obtained in LES seems to be more important. Differences in the tumble during the compression stroke may come from the intake stroke, as the intake jets are the primary sources for tumble formation. The reasons for such a discrepancy are investigated in the next section.

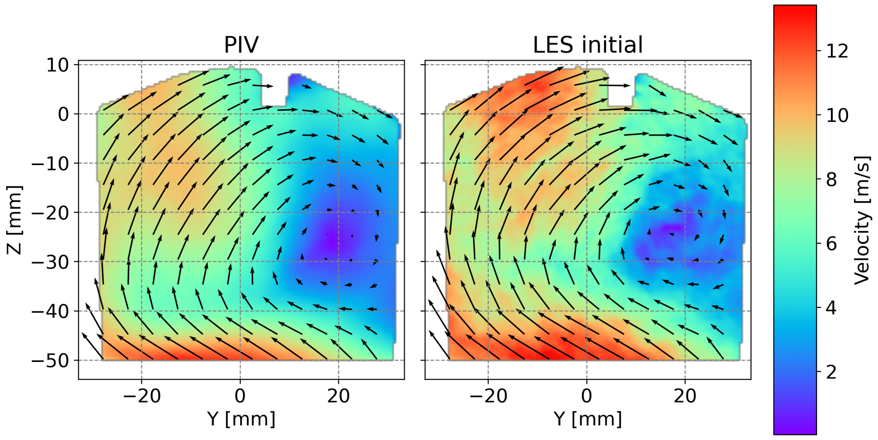

FIGURE 5.28: Comparison of the ensemble-averaged velocity field at −90 CAD in the tumble plane.

5.4.2 Potential causes of the observed difference

The prediction of the intake jets is directly related to the correct estimation of the mass flux entering the chamber. The study on the steady-state flow bench configuration [51] showed that the intake jets' orientation and penetration vary enormously according to the mass flow rate and the valve lift as they determine the local Reynolds number. The cycle-averaged mass flow rate entering the computational domain is evaluated and compared between different cases, as concluded in Table 5.5. The comparison highlights that the pressure type boundary condition at the inlet underestimates the mass flow rate of about 4.5%, both in 0D GT-Power and 3D LES simulations. The difference in the mass flow rate may further impact the prediction of the intake jets, especially their intensity.

case	Exp	GT	LES
mass flow rate [kg/s]	22.08	21.13	21.08
relative error [%]	0	−4.3	−4.5

TABLE 5.5: Cycle-averaged mass flow rate at the inlet boundary.

The orientation of the intake jets is more linked to the flow separation occurring over valves. The accurate capture of the flow separation is thus crucial but also difficult. As presented in Table 5.3, the near-wall flow is modeled by wall models, which results in a lack of accuracy. To improve the quality of the LES prediction, modifications are needed to the wall treatment.

In the next section, several test cases are prepared to correct the prediction of the intake jets by adjusting boundary conditions at the inlet and over the intake valves. A final methodology is determined based on the corresponding results.

5.4.3 Sensitivity analysis on boundary conditions of LES

Modifications to improve the LES quality based on the previous discussion are made to the inlet and intake valve boundaries.

A straightforward way to compensate for the mass flow rate underestimated by simulation is to increase the inlet pressure level. With the help of the 0D GT-Power model, an increase of 3000 Pa is needed to reach the experimental level of mass flow rate. Two choices are thus available to replace the current boundary condition at the inlet, either the increased pressure condition $P_{MAN2} + 3000$ Pa or the corresponding mass flow rate given by the 0D model $\dot{m}_{GT}$.

As presented in [14], a suitable wall treatment can help capture the flow separation over valves. The current velocity wall model is RANS based and unsuitable for transient flow like the in-cylinder flow. Therefore, the no-slip condition is applied to the intake valve boundary to directly resolve the boundary layers, which leads to a better prediction of the flow separation. This condition requires enough refined mesh locally such that the first cell center lies inside the sub-viscous layer of the turbulent boundary layer. Local refinements of the mesh are applied to the boundaries of the intake port and valves, as illustrated in Figure 5.29.

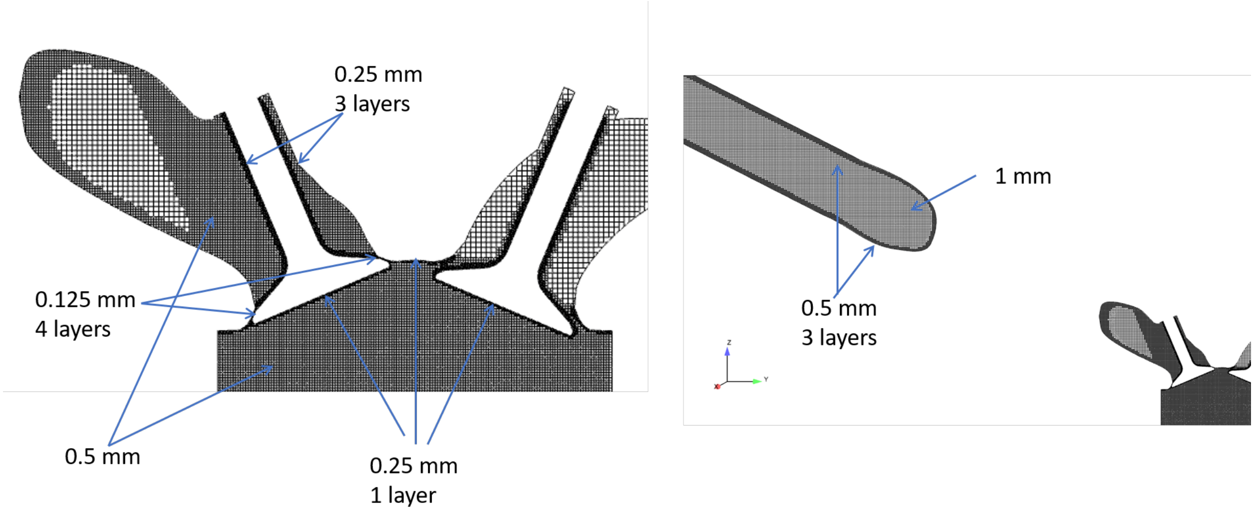

FIGURE 5.29: No-slip condition applied on refined mesh around valves.

Following the discussion above, four test cases are prepared to investigate the most suitable LES methodology, as summarized in Table 5.6. For each case, 15 consecutive cycles are launched to achieve statistical convergence. The same comparison is made as presented in Section 5.4.1 on the two planes.

case	inlet condition	wall treatment
initial set-up	P_{MAN2}	log-law
1	P_{MAN2}	no slip
2	$P_{MAN2} + 3000$ Pa	log-law
3	$P_{MAN2} + 3000$ Pa	no slip
4	$\dot{m}_{GT}$	no slip

TABLE 5.6: Test cases with different boundary conditions.

Concerning the tumble during the compression stroke at −90 CAD, as shown in Figure 5.30, the increased pressure $P_{MAN2} + 3000$ Pa (case 2) seems to intensify the tumble motion compared to case 1 as more mass enters the chamber. However, the no-slip condition also has a negative effect on the tumble intensity on this plane. A significant reduction in the tumble intensity can be seen for the three cases with the no-slip condition in the valve walls.

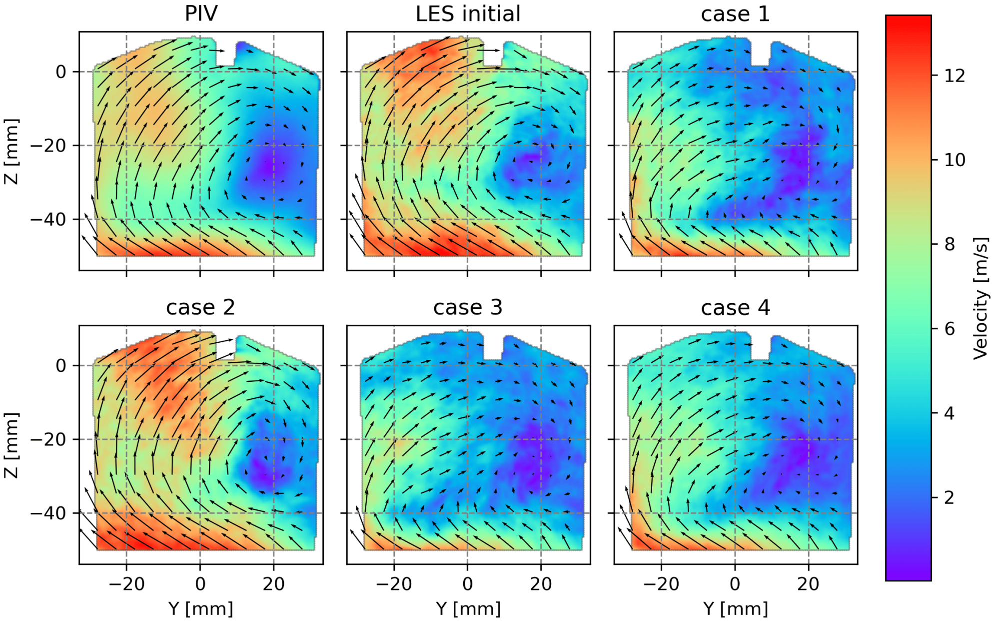

FIGURE 5.30: Comparison of the ensemble-averaged velocity field at −90 CAD in the tumble plane between test cases.

The impact on the intake jets is presented in Figure 5.31. As expected, the no-slip condition (cases 1, 3, and 4) allows a more accurate prediction of the intake jets. The angle between the jet and the vertical axis is more significant so that it licks the cylinder head wall. The correction in the inlet boundary condition also has slightly improved the intensity of intake jets, and the imposed mass flow rate $\dot{m}_{GT}$ (case 4) performs better than the increased pressure $P_{MAN2} + 3000$ Pa (case 3).

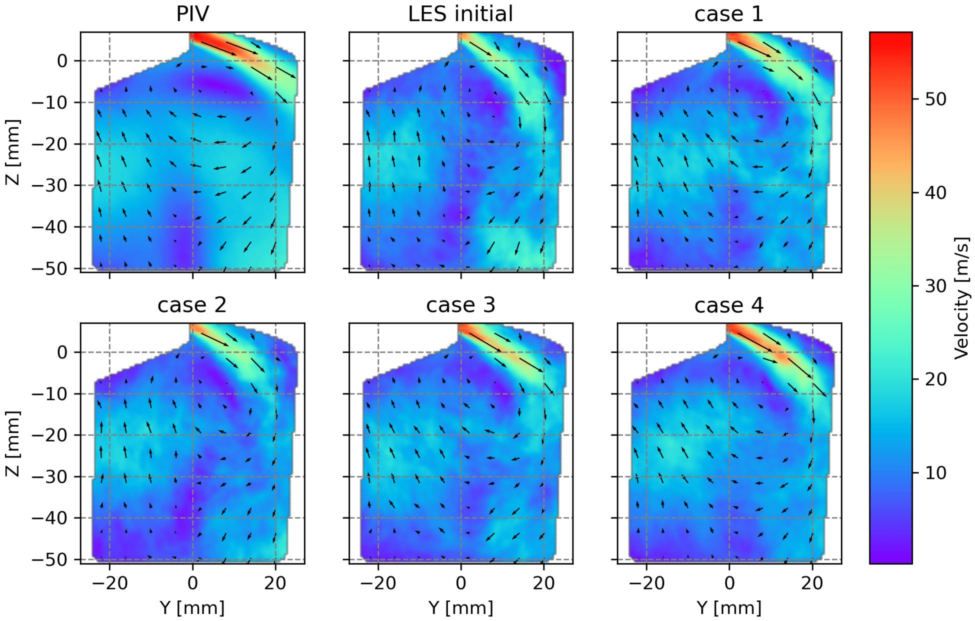

FIGURE 5.31: Comparison of the ensemble-averaged velocity field at −240 CAD in the valve plane between test cases.

A comparison of the pressure and the corresponding mass flow rate at the inlet boundary (averaged over cells at the inlet boundary) between the three types of boundary conditions at the inlet, P_{MAN2}, $P_{MAN2} + 3000$ Pa and $\dot{m}_{GT}$, is also conducted. The pressure and the corresponding mass flow rate extracted from LES are compared and plotted in Figure 5.32a and Figure 5.32b.

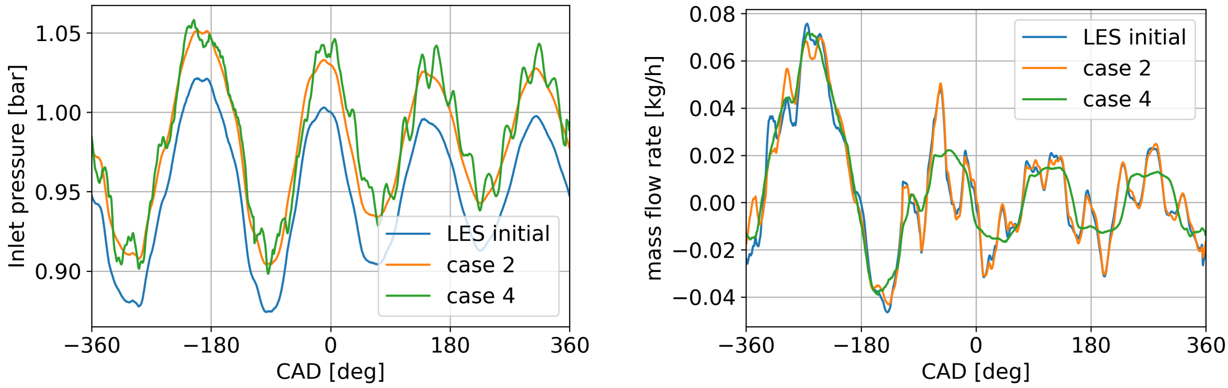

(A) Pressure at inlet.

(B) Mass flow rate at the inlet.

FIGURE 5.32: Comparison of pressure and mass flow rate at the inlet.

When imposing the mass flow rate $\dot{m}_{GT}$ at the inlet, the corresponding pressure varies almost at the same level as $P_{MAN2} + 3000$ Pa but presents more fluctuations. The same behavior can also be found in the mass flow rate in the cases where the pressure evolution is imposed as P_{MAN2} or $P_{MAN2} + 3000$ Pa. These fluctuations may come from the acoustic waves in the intake port but are not investigated in this study. The relative stable mass flow rate $\dot{m}_{GT}$ imposed at the inlet stabilizes the intake jets and enhances their intensity.

Based on the above comparison, it can be concluded that the combination of the no-slip condition and the mass flow rate $\dot{m}_{GT}$ at the inlet used in case 4 provides the best prediction of the internal aerodynamics with an important improvement on the intake jets. These two new boundary conditions and the associated mesh are updated in the LES methodology. Another 10 consecutive LES cycles are launched, resulting in a total of 25 cycles, for a further quantitative validation presented in the next section.

5.4.4 Quantitative comparison of the LES results

In this section, a quantitative comparison of the computed velocity field is carried out. The velocity field of the 25 LES cycle is averaged and compared with that of 74 cycles from PIV measurements. For simplicity, the resolved velocity $\tilde{U}$ obtained by LES is noted as U in the following.

To verify the convergence of LES results, the Coefficient of Variance (CoV) is computed using LES data. For a given quantity X, CoV is defined as:

$$CoV(X) = \frac{\sigma(X)}{\mu(X)} \tag{5.7}$$

where $\sigma(X)$ and $\mu(X)$ are respectively the standard deviation and the average of X. We propose to compute the CoV of the averaged kinetic energy in the combustion chamber $E_k(\theta)$ written as:

$$E_k(\theta) = \frac{1}{V}\int_V \frac{1}{2}\left(U_x(\theta)^2 + U_y(\theta)^2 + U_z(\theta)^2\right) dV \tag{5.8}$$

For $(\theta) = -180$ CAD, the corresponding $CoV(E_k)$ is computed using increasing number of cycles and plotted in Figure 5.33. It can be observed that CoV begins to be stable once more than 10 cycles are used. The average behavior should be captured correctly with the 25 LES cycles in total.

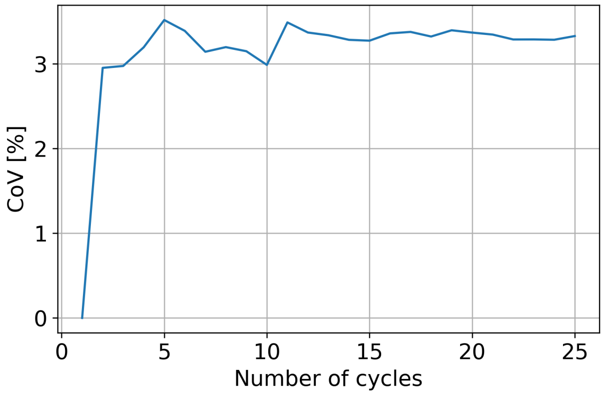

FIGURE 5.33: Evolution of the CoV(E_k).

The averaged velocity field is first qualitatively compared in the tumble and valve planes. Secondly, for a more precise comparison, the averaged velocity field is sampled over certain lines in horizontal and vertical directions on both tumble and valve planes, as plotted in Figure 5.34. The comparison of 1D velocity profiles presented below is only for the velocity field at -180 CAD. Comparisons at other instants are attached in Appendix A.

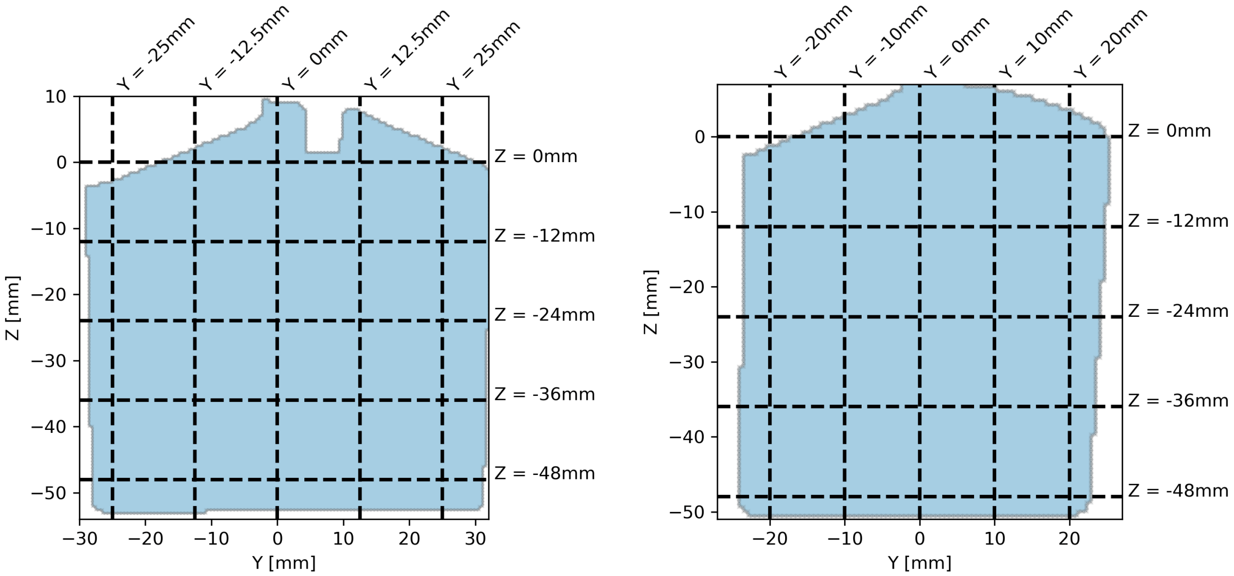

(A) Tumble plane at -180 CAD.

(B) Valve plane at -180 CAD.

FIGURE 5.34: Sampling lines for comparison with PIV measurements at -180 CAD.

The averaged velocity field is compared in Figure 5.35 in the tumble central plane at $X = 0$ mm qualitatively for instants including -300, -240, -180, -120, -90 and -60 CAD.

Figure 5.35a and Figure 5.35b compare the intake flow injected in the chamber during the intake phase. The shape and the intake flow orientation agree well between LES and PIV data. Figure 5.35c presents the ensemble-averaged velocity field in the tumble plane at BTC. The intake flow generates a strong descending flow on the exhaust side of the chamber, which is the primary source of the tumble flow. The velocity field of LES still shows some spatial fluctuations, especially in the region under the intake valves, suggesting that the phase-averaged value is statistically not fully converged. The comparison of two instants during the compression is shown in Figure 5.35d, Figure 5.35e, and Figure 5.35f. The LES seems to predict a weaker tumble front at -120 CAD, while the one measured by PIV is dominant in the chamber. At -60 CAD, differences can be identified in the tumble vortex core region. Despite local differences in some instants, LES can capture most flow features.

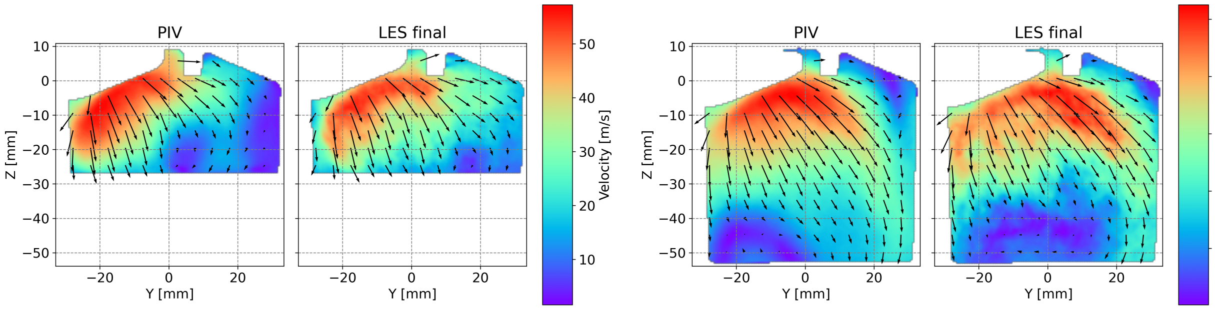

(A) -300 CAD. (B) -240 CAD.

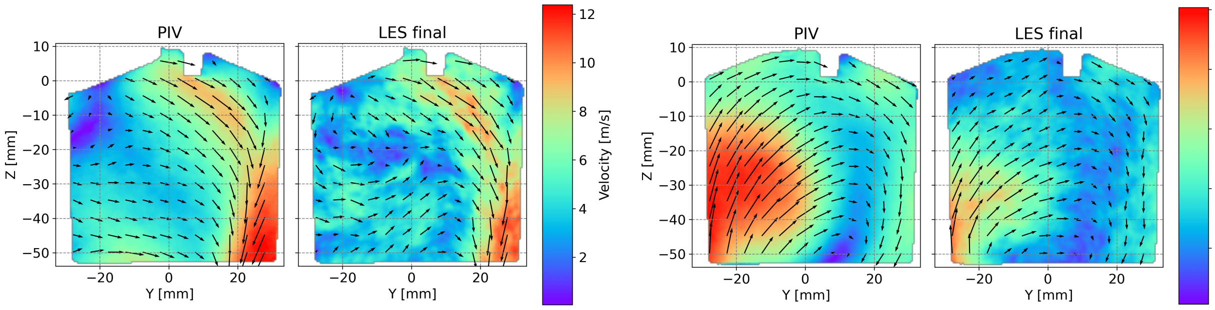

(C) -180 CAD. (D) -120 CAD.

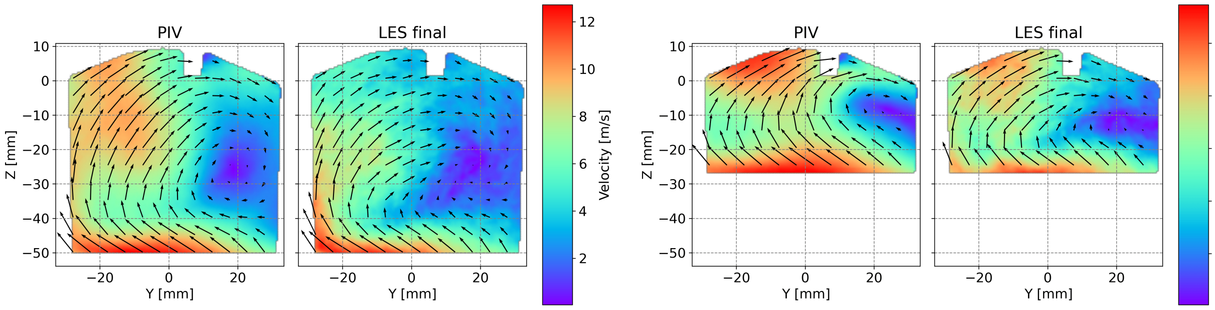

(E) -90 CAD. (F) -60 CAD.

FIGURE 5.35: Comparison of the phase-averaged velocity field in tumble plane between LES results and PIV measurements.

Figure 5.36 shows the horizontal profiles at −180 CAD. The main difference can be noted for lines located on the lower part of the tumble plane. The vertical component U_z shows more errors than the horizontal component U_y, especially in the central part, which corresponds to the central region of the tumble plane, as presented in Figure 5.35c. The flow predicted by LES shows a local recirculation zone on the left upper side, which generates an upward flow in the central region and thus creates a positive U_z.

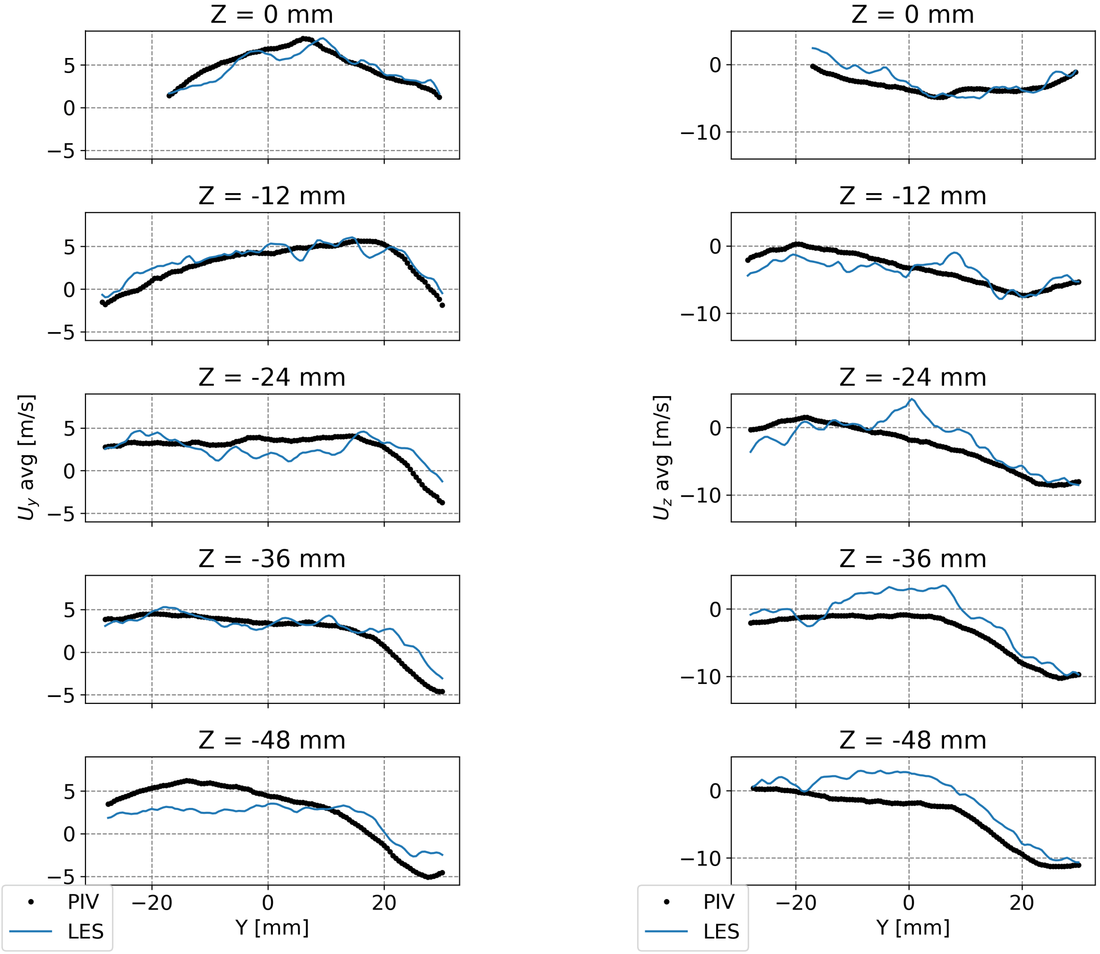

(A) U_y component.

(B) U_z component.

FIGURE 5.36: Comparison of 1D profiles over horizontal lines in tumble plane at −180 CAD.

Figure 5.37 illustrates the vertical profiles at −180 CAD. The same issue on the component U_z is also observed on the bottom part of vertical lines at $Y = -12.5$ mm, $Y = 0$ mm, and $Y = 12.5$ mm. The component U_y agrees much better with PIV measurements except on the line at $Y = 12.5$ mm, which reveals that the tumble flow predicted by LES is slightly weaker but remains acceptable.

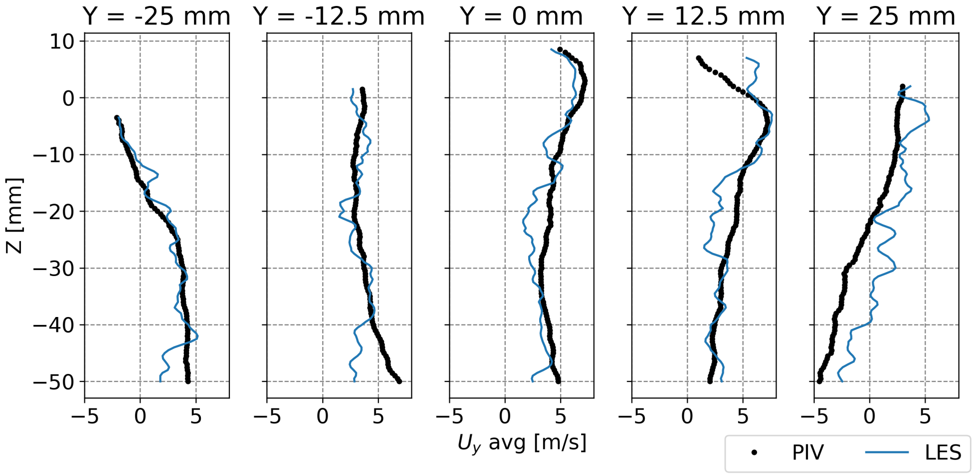

(A) U_y component.

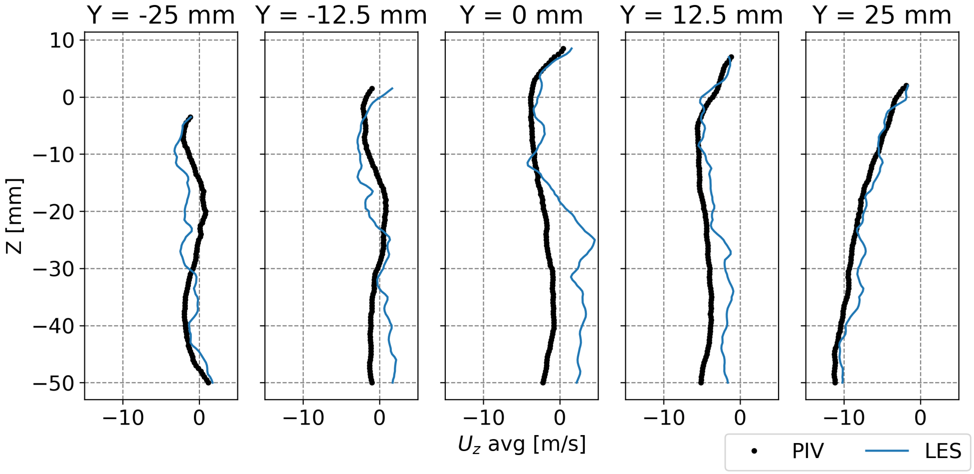

(B) U_z component.

FIGURE 5.37: Comparison of 1D profiles over vertical lines in tumble plane at −180 CAD.

The same comparison is then made in the valve plane. Figure 5.38 presents the ensemble-averaged velocity field at the six instants. For the first four instants of intake stroke (from Figure 5.38a to Figure 5.38d), a clear intake jet is captured by LES and is in good agreement with PIV measurements. At −180 CAD (Figure 5.38e), the upward flow at the left side is captured by LES but with weaker intensity. The recirculating region under the intake jets is also well reproduced by LES. The intake jet at this instant is less present in the valve plane as valves are at the half lift and are moving up. However, from PIV measurements, the lower edge of the intake jets can still be noticed, while LES predicts relatively less intense jets. At −90 CAD (Figure 5.38f), the flow pattern is of a quasi-pure rotation, which is a part of the tumble motion in the chamber. The front of the tumble predicted by LES in this plane is also slightly weaker, similar to what is observed in the tumble central plane.

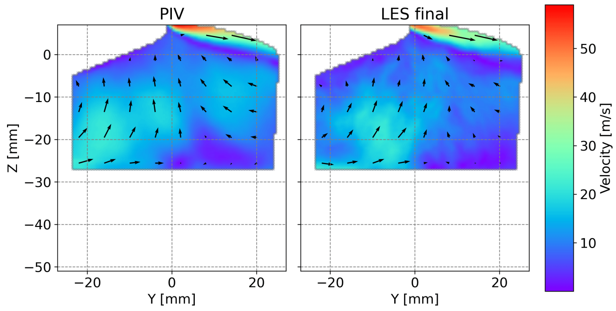

(A) −300 CAD.

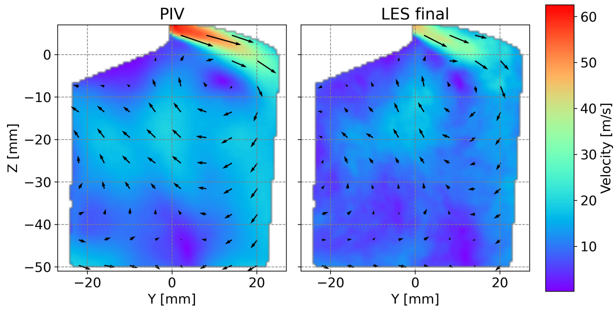

(B) −270 CAD.

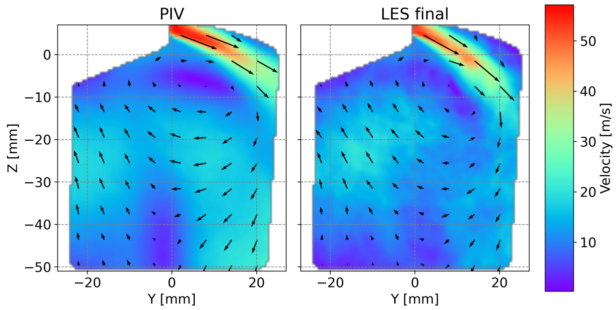

(C) −240 CAD.

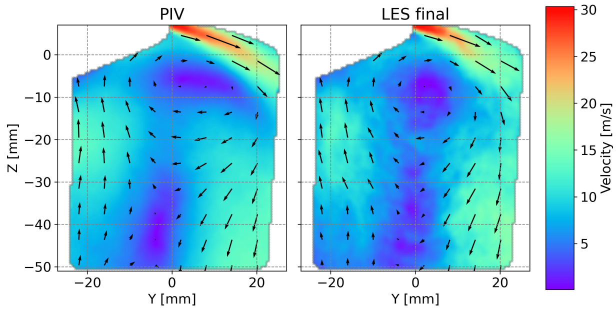

(D) −210 CAD.

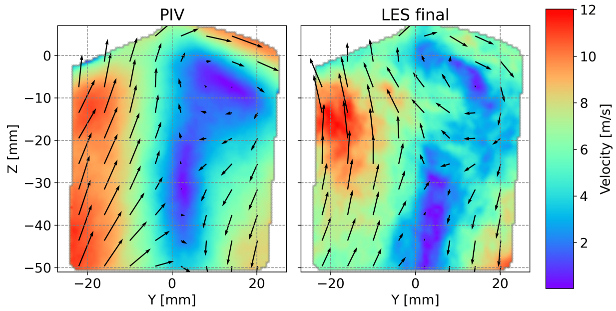

(E) −180 CAD.

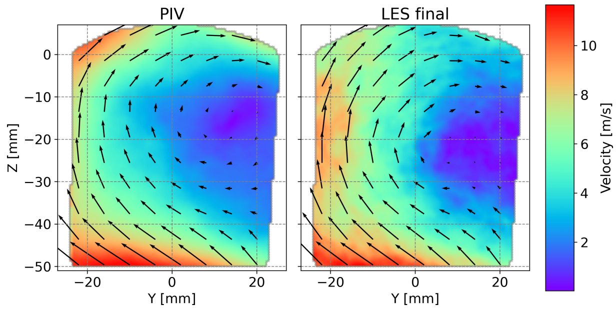

(F) −90 CAD.

FIGURE 5.38: Comparison of the phase-averaged velocity field in valve plane between LES results and PIV measurements.

Horizontal samples are shown in Figure 5.39 for −180 CAD. The difference in the component U_y is related to our previous observation in Figure 5.38e that the upward flow predicted by LES is weaker with an orientation towards the left side instead of the central region as observed in experiments. The prediction of the component U_z is much better except for the left lower region of the valve plane.

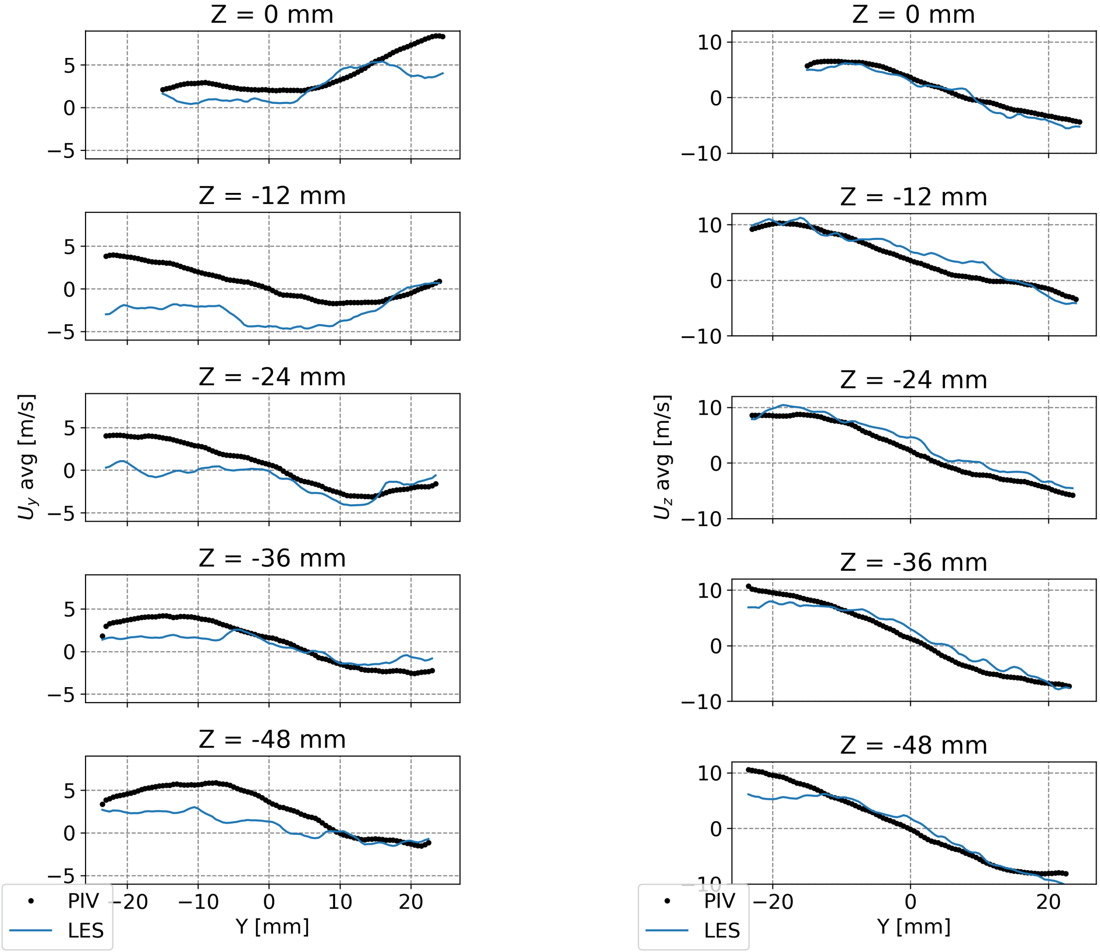

(A) U_y component.

(B) U_z component.

FIGURE 5.39: Comparison of 1D profiles over horizontal lines in valve plane at −180 CAD.

The comparison on vertical lines is plotted in Figure 5.40. Consisting with what has been concluded from the comparison over horizontal lines, vertical lines located at the left part of the valve plane show higher levels of errors compared to PIV measurements, particularly for the line at $Y = -20$ mm that lies in the region of the upward flow.

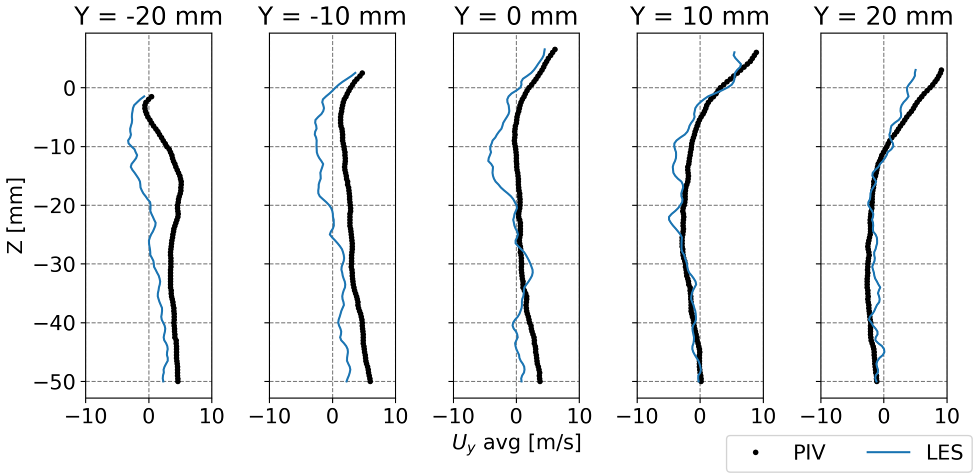

(A) U_y component.

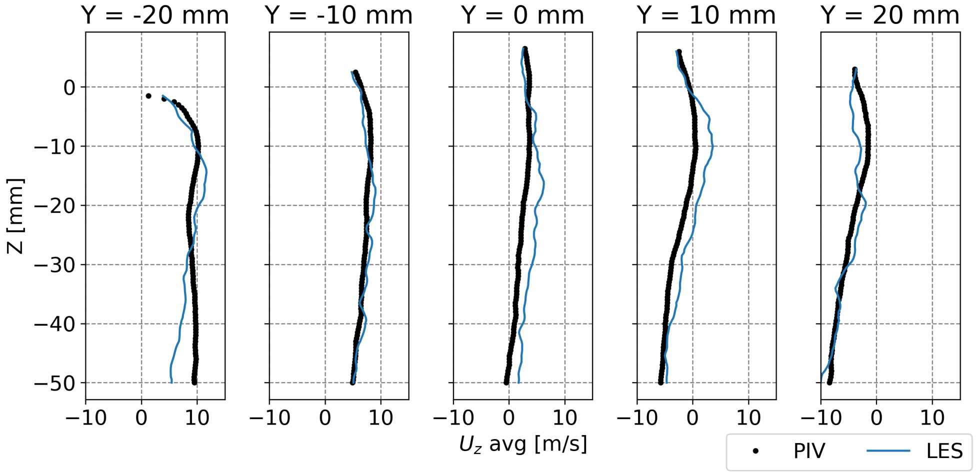

(B) U_z component.

FIGURE 5.40: Comparison of 1D profiles over vertical lines in valve plane at -180 CAD.

Considering that the phase-averaged velocity field is not statistically fully converged, only a qualitative comparison of the simulated and measured root mean square (RMS) velocity is presented hereafter in Figure 5.41 and Figure 5.42. In the tumble plane, regions of important fluctuations are well captured by LES for both the right side where the tumble flow is descending and the left side where the tumble front begins to move upwards. In the valve plane, the most fluctuating region is identified in the middle of the field by both LES and PIV.

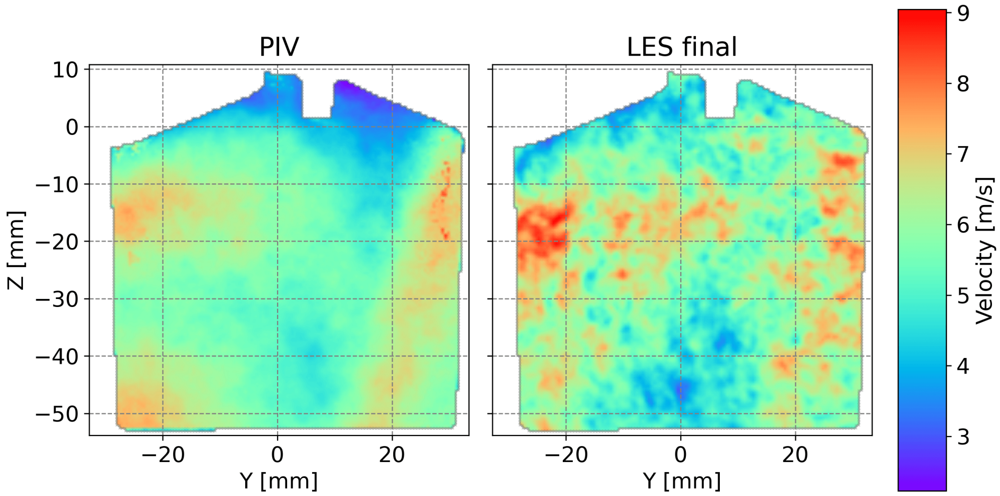

FIGURE 5.41: Comparison in tumble plane at −180 CAD.

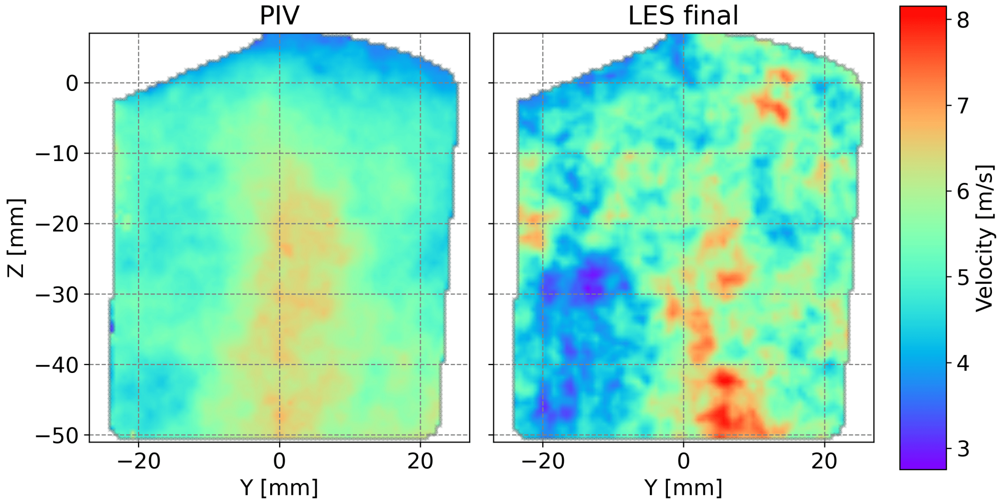

FIGURE 5.42: Comparison in valve plane at −180 CAD.

According to the above comparison, the global structures of the in-cylinder flow are well captured, despite some differences observed locally on the two planes. A good agreement is obtained. In the next section, the study will focus on the in-cylinder flow characterization. For the motored case, the analysis is only limited to the flow during the compression stroke. The Chapter on the fired case will give a more detailed analysis during the entire engine cycle.

5.5 Analysis of the tumble flow during the compression stroke

This section illustrates the application of all the analysis tools presented in Chapter 4. The tumble flow during the compression stroke is analyzed in the tumble plane as a classical approach. Fluctuations in aerodynamics, including CCV of large-scale motion and small eddies related to the turbulence, are identified and quantified during the compression based on results from 2D EMD. The second time, an investigation of the energy transfer from large-scale motion to small eddies is carried out. Finally, the flow is characterized in the combustion chamber in a 3D vision using 3D EMD and Γ_{3p}, which provides insights into the CCV of large-scale motion.

5.5.1 Large-scale motion and CCV

In this section, bivariate 2D EMD is applied on the velocity field in the central tumble plane for crank angles from -360 to 0 CAD obtained by LES. For illustration, Figure 5.43 presents the resulting decomposition for two engine cycles 10 and 12 at -180 CAD when the organization of the flow into a rotational structure is visible.

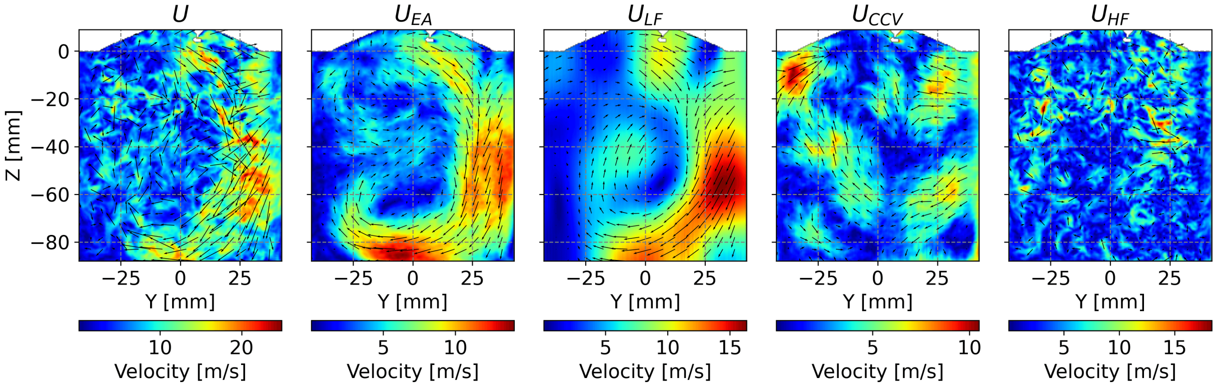

(A) cycle 10.

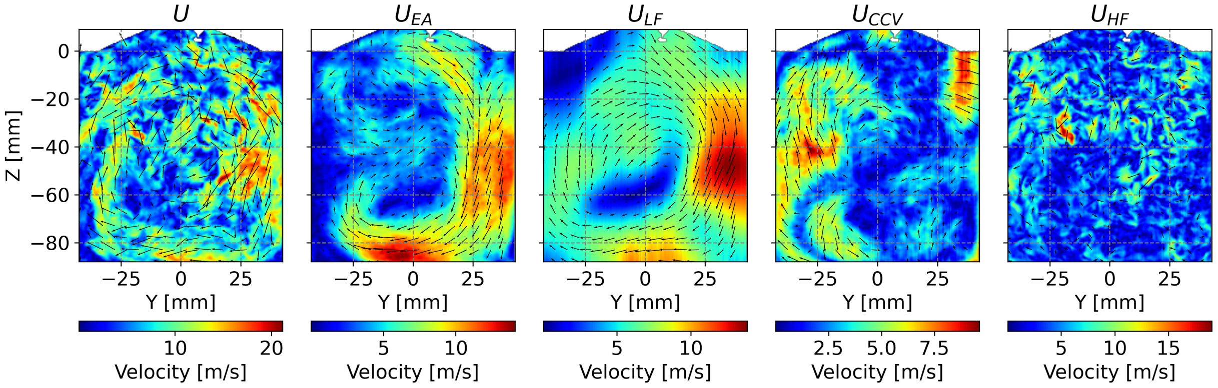

(B) cycle 12.

FIGURE 5.43: An exemplary result of bivariate 2D EMD for the instantaneous flow of engine cycles 10 and 1 at -180 CAD, the instantaneous velocity U is decomposed into an LF part U_{LF} containing the large-scale motion and an HF part U_{HF} representing turbulent fluctuation. CCV of the large-scale motion U_{CCV} is deduced by the subtraction of the ensemble-averaged velocity U_{EA} from LF part U_{LF}.

The turbulent fluctuation U_{HF} is well separated from the instantaneous velocity field U. The remaining LF part U_{LF} allows a more explicit description of the global motion. The corresponding CCV part U_{CCV}, obtained by subtracting U_{EA} from U_{LF}, indicates regions where differences are important compared to the ensemble-averaged velocity U_{EA} in the given engine cycle. By comparing these two particular cycles, apparent differences can be observed in the LF part U_{LF}: the tumble motion is more pronounced throughout the chamber in cycle 12 than in cycle 10. The corresponding CCV part U_{CCV} also indicates that compared to the averaged tumble motion of all the cycles, the tumble motion of cycle 12 differs most in the region of the tumble front.

For a more statistical description of CCV, the phase-averaged of absolute value of the CCV part U_{CCV} is computed as $\overline{U_{CCV}}(\theta) = \frac{1}{N_{cycle}} \sum_{i=1}^{N_{cycle}} |U_{CCV}(\theta, i)|$ and presented in Figure 5.44 for five different crank angle. High value of $\overline{U_{CCV}}(\theta)$ helps identify regions with significant variations in large-scale motion. The ensemble-averaged velocity U_{EA} as well as the averaged LF part $\overline{U_{LF}}$ are also plotted in Figure 5.44 to provide the flow pattern at the given instant.

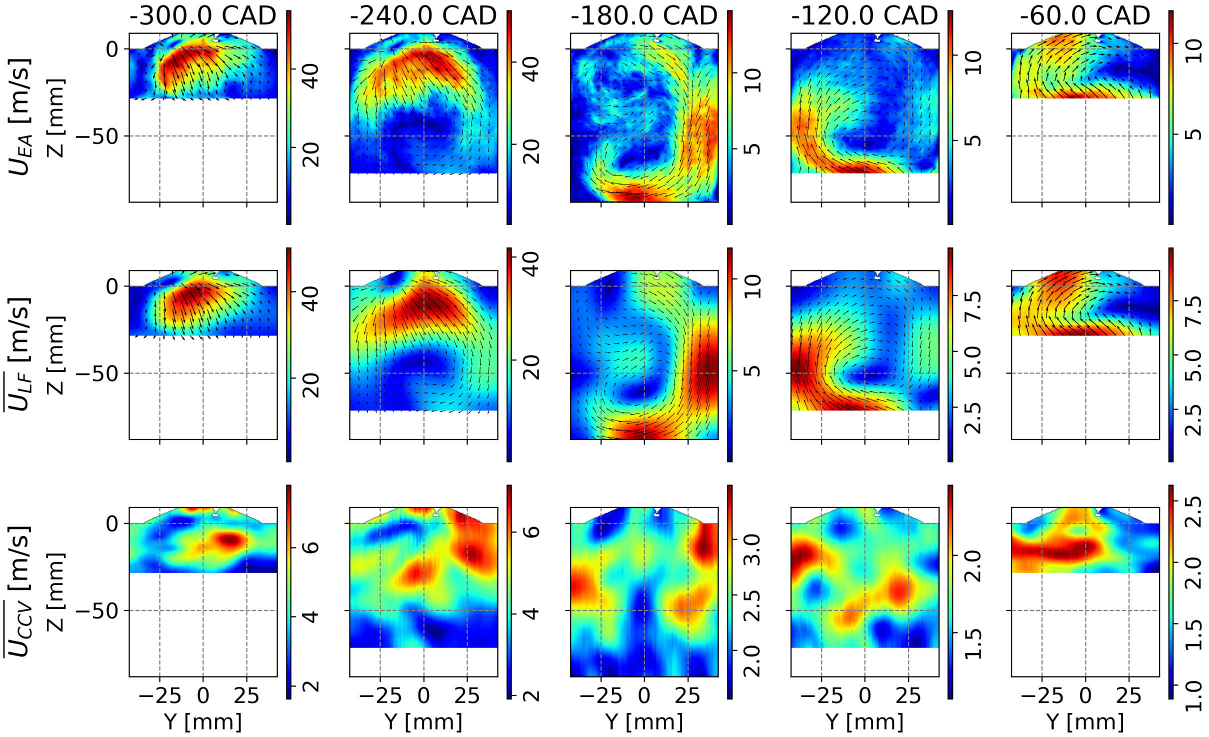

FIGURE 5.44: Evolution of the mean flow U_{EA}, the averaged LF part $\overline{U_{LF}}$ and averaged CCV part $\overline{U_{CCV}}(\theta)$.

U_{EA} and $\overline{U_{LF}}$ behave quite similarly for the given instants, as averaging operation and 2D EMD both allow for eliminating fluctuations, though, with a limited number of cycles, slight fluctuations still exist locally in U_{EA}. The magnitude of $\overline{U_{CCV}}(\theta)$ varies during the engine cycle and seems to be coherent with the actual flow pattern:

- For −300 and −240 CAD during the intake stroke, CCV of the large-scale motion remains in the region where intake jets from the two valves interact with each other, resulting in a thick shear layer.
- At BDC, the tumble is already structured in the chamber, and three regions of high CCV can be identified: the upper-right corner where a local recirculation zone is created by the intake jets; the mid-right part inside the tumble flow; the mid-left part where primary and secondary jets emerge.
- At −120 CAD during the compression stroke, the flow variability is more visible on the tumble front and around the tumble rotation center. At −60 CAD, significant CCV resides inside the tumble flow, indicating that the tumble's structure can differ significantly between different cycles when close to the end of compression.

5.5.2 Energy transfer between large-scale motion and small eddies

The flow decomposition with bivariate 2D EMD in the tumble plane has allowed us to separate the flow's mean and fluctuating parts and distinguish the large-scale variations and turbulent fluctuations in the fluctuating part. The role of internal aerodynamics is to conserve the kinetic energy introduced by the intake jets during the intake stroke to release it in the form of turbulence at the end of the compression stroke. The energy transfer during these two phases is thus crucial and is of particular interest in this section. The following analysis focuses on the second half of the compression stroke from −100 CAD to TDC.

The instantaneous resolved velocity field U can be expressed as follows using the Reynolds decomposition:

$$U(\theta, i) = \langle U \rangle (\theta) + u(\theta, i) \tag{5.9}$$

where the symbol $\langle \cdot \rangle$ denotes the phase-averaged operator and u the fluctuating velocity.

The resolved kinetic energy of the phase-averaged velocity and its fluctuating part is computed in the tumble plane for the mean and the phased-averaged fluctuating parts of the flow, noted as E_k^m and E_k^f respectively and defined as follows [1, 122]:

$$E_k^m(\theta) = \frac{1}{2S} \int_S \left(\langle U_y \rangle^2 (\theta) + \langle U_z \rangle^2 (\theta) \right) dS \tag{5.10}$$

$$E_k^f(\theta) = \frac{1}{2S} \int_S \left(\left\langle u_y^2 \right\rangle (\theta) + \left\langle u_z^2 \right\rangle (\theta) \right) dS \tag{5.11}$$

where U_y and U_z are resolved velocity obtained by LES, S the domain size and u_y and u_z defined as following:

$$u_y(\theta, i) = U_y(\theta, i) - \langle U_y \rangle (\theta) \tag{5.12}$$

$$u_z(\theta, i) = U_z(\theta, i) - \langle U_z \rangle (\theta) \tag{5.13}$$

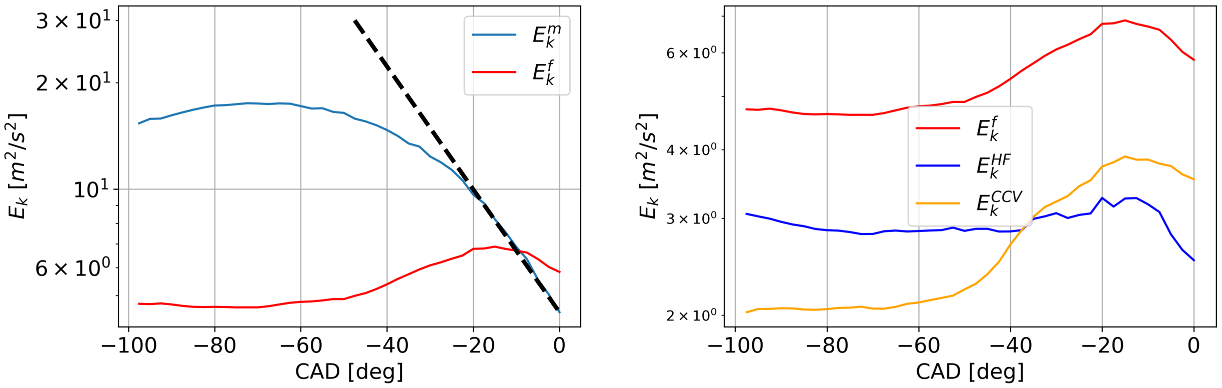

(A) The resolved kinetic energy in the mean and fluctuating part of the flow.

(B) Contribution of turbulence and CCV part in kinetic energy fluctuations.

FIGURE 5.45: Evolution of phase-averaged resolved kinetic energy obtained from LES during the engine cycle.

The evolution of E_k^m and E_k^f during the last 100 CAD of the compression is presented on a log scale in Figure 5.45a. At around −70 CAD, E_k^m reaches its maximum and begins to decline. The negative slope decreases between −70 and −20 CAD for several reasons: As the piston approaches TDC, the available room in the chamber reduces, and the tumbling flow is slowed down because of the wall friction. A significant increase of E_k^f can also be noticed after −50 CAD and may explain the drop of E_k^m observed during the same period: the kinetic energy is transferred from the mean flow to the fluctuating part, which is usually considered as the result of tumble breakdown [122]. After -20 CAD, as described by the black dashed line in Figure 5.45a, E_k^m decreases exponentially with time, and its evolution can be expressed as:

$$E_k^m(\theta) = E_k^m(\theta_0)e^{-\frac{t-\theta_0}{\tau_d}} \tag{5.14}$$

with $\theta_0 = -20$ CAD, t the time in CAD and τ_d a characteristic time scale of the decrease of E_k^m equals to 25 CAD or 2.77 ms. The turnover time scale of the tumble at -20 CAD can be estimated as $\tau_t = L/U$ where L is the available height in the chamber and U is an approximated value of the mean velocity magnitude. Taking $L = 15$ mm and $U = 5$ m/s, τ_t equals to 3 ms which is of same order of τ_d. This indicates that the rate of decay of the kinetic energy of the mean tumbling flow scales with its turnover time scale. This was also observed in [122] and is usually interpreted as the signature of tumble breakdown. During the last 10 CAD, E_k^f becomes larger than E_k^m, which means that the global motion has vanished.

Using the Reynolds decomposition, the fluctuating part obtained still contains contributions from CCV of the large-scale motion and turbulence. 2D EMD has made it possible to separate these two types of fluctuations of different scales. In Figure 5.45b, the evolution of the kinetic energy in CCV, E_k^{CCV}, and that of turbulence, E_k^{HF}, are plotted. The turbulent kinetic energy E_k^{HF} remains stable during the compression except for the last 10 CAD, during which an evident decay is present as the piston reaches almost the end of displacement. Therefore, E_k^{CCV} seems to be responsible for the increase of the kinetic energy in the fluctuating part: it raises in sync with E_k^f beyond -50 CAD. After -35 CAD, a more important part of the fluctuating kinetic energy is contained in the CCV part rather than in the turbulence. The evolution of E_k^{CCV} indicates that an important change in the large-scale evolution of the flow takes place after around -50 CAD. The averaged U_{CCV} magnitude at -60 CAD presented in Figure 5.44 also shows that significant variations of the large-scale structures appear already inside the tumble flow.

The application of bivariate 2D EMD on velocity fields in the central tumble plane gave us a deeper insight into the variations of the tumble motion in both large- and small-scale structures during the intake and the compression. Large-scale variations were noticed in the tumble motion, the tumble vortex core region, and the tumble front region. The analysis of the energy transfer between large- and small-scale showed that in this engine configuration, the main contribution to the increase of flow variations near TDC comes from the large-scale tumble motion rather than turbulent fluctuation. The classical tumble breakdown process did occur as captured by the exponential decrease of E_k^m but quite late in the cycle, indicating the existence of large-scale residual structures near TDC.

Observations of flow variations in the central tumble plane cannot be explained using only information from the same plane; the tumble motion is natural three-dimensional. In the next section, analysis tools for describing the tumble motion in the cylinder volume will be proposed to complete the analysis in 2D planes using EMD. The tumble ratio [166] is evaluated for all the cycles around the tumble center detected by Γ_1 function [163] at -22.5 CAD, which corresponds to the spark timing of the fired case at the same operating point. Evident cyclic variability can be observed in the distribution of computed $TR_{2D}(\theta_{ign})$ as shown in Figure 5.46. Cycle 10 and cycle 12, two extreme cycles with opposite behavior in tumble ratio, are chosen for the qualitative analysis in the 3D flow analysis.

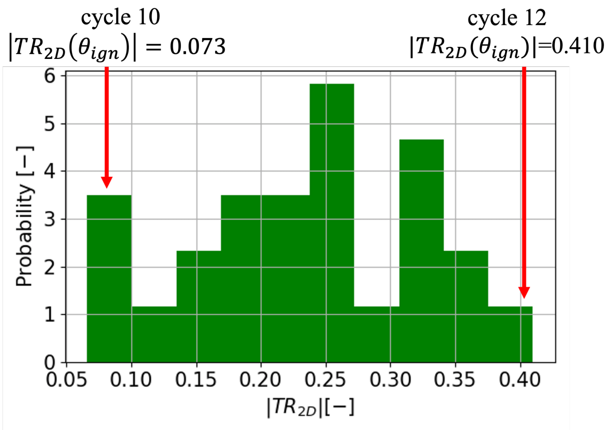

FIGURE 5.46: Distribution of tumble ratio $|TR_{2D}(\theta_{ign})|$ at −22.5 CAD computed using U_{LF} of the tumble central plane.

5.5.3 Flow characterization in 3D

The characterization of the tumble flow is classically carried out in the tumble plane where the rotational flow is visible, especially in experimental studies, as PIV measurements are usually available for 2D planes. However, analysis is limited as a complete description of the tumble is not accessible, including CCV and turbulence variations in 3D. In this section, tools presented in Chapter 4, including Γ_{3p} and 3D EMD, are applied to the velocity fields to explore their capability to characterize the 3D tumble flow motion.

Γ_{3p} is calculated for several CAD of the compression stroke during which the large-scale tumble motion is well-formed at BDC and interacts with the piston and the cylinder walls up towards TDC. With the help of Γ_{3p}, the rotation kernel of the tumble can be extracted and described quantitatively. An exemplary result of Γ_{3p} applied on two engine cycles at −22.5 CAD, which corresponds to the ignition timing of the reactive case, is presented in Figure 5.47. With a threshold of Γ_{3p} =0.5 as proposed in [165], the core part of the tumble can be visualized in Figure 5.47a.

For the given two engine cycles, the structure of the flow behaves completely differently. In cycle 12, the rotational structure has a cylindrical shape corresponding to a quasi-ideal tumbling flow motion, while in cycle 10, two vortex cores are emphasized. The associated vector field of Γ_{3p} plotted in Figure 5.47b provides an insight into the global structure of the flow: as indicated by red arrows, the rotation in cycle 12 is mainly along the X axis, while in cycle 10 a pair of counter-rotating vortices appears and tends to rotate around an inclined axis in YZ plane.

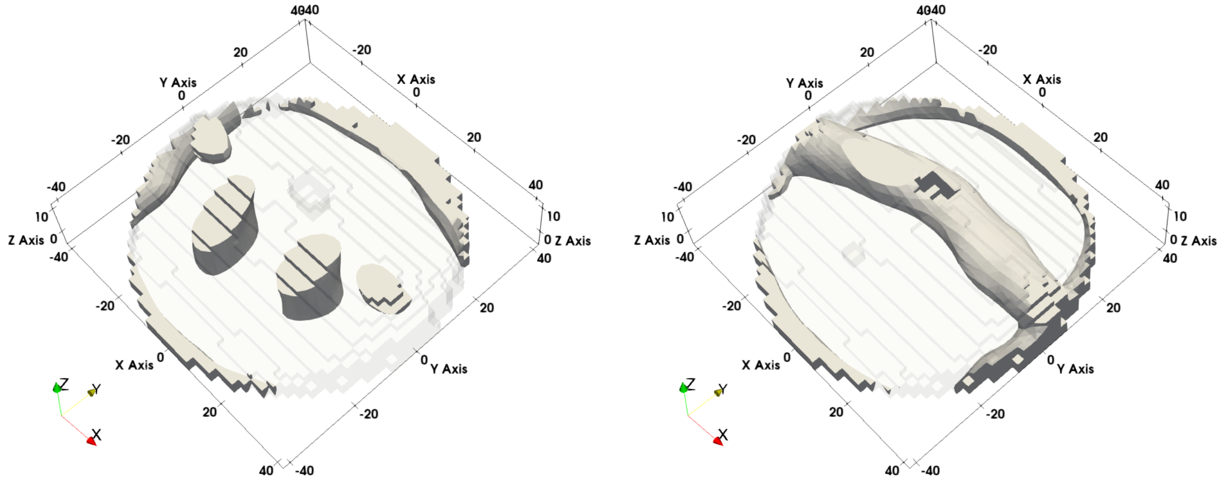

(A) Isosurface of $|\boldsymbol{\Gamma}_{3p}| = 0.5$.

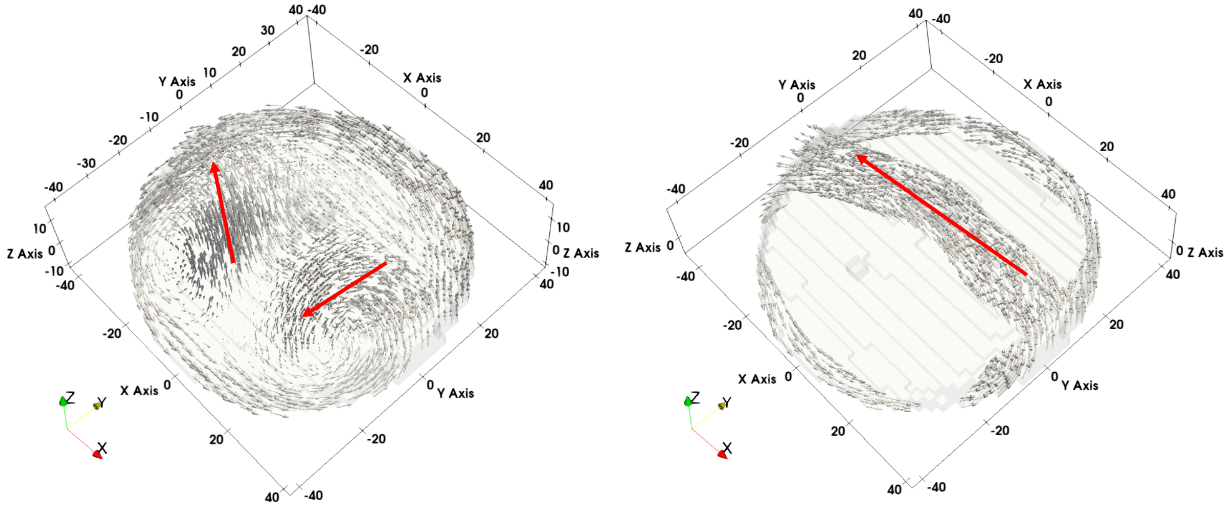

(B) Vector field of Γ_{3p}.

FIGURE 5.47: An exemplary result of the Γ_{3p} for the instantaneous flow of engine cycles 10 (left) and 12 (right) at -22.5 CAD.

The differences in the tumble can be observed even earlier during the compression. In Figure 5.48, the comparison of the vortex core is given for several crank angles, combined with the vector field of Γ_{3p} at $Y = 0$ mm, so-called cross tumble plane, which indicates the local rotation direction.

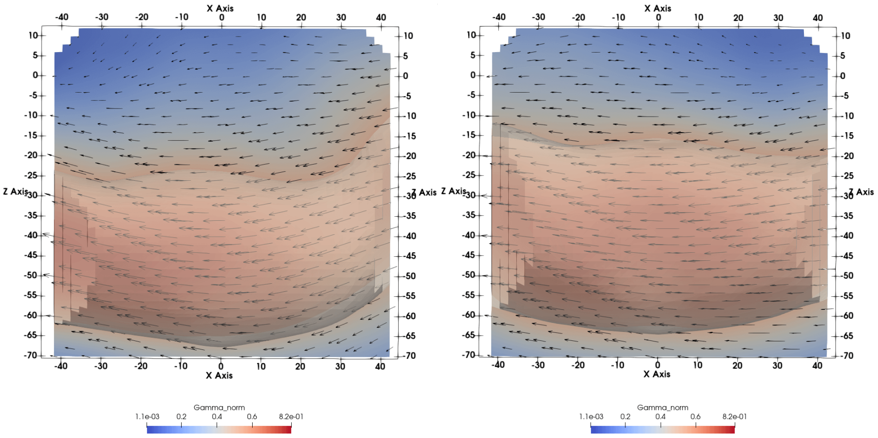

(A) −120 CAD.

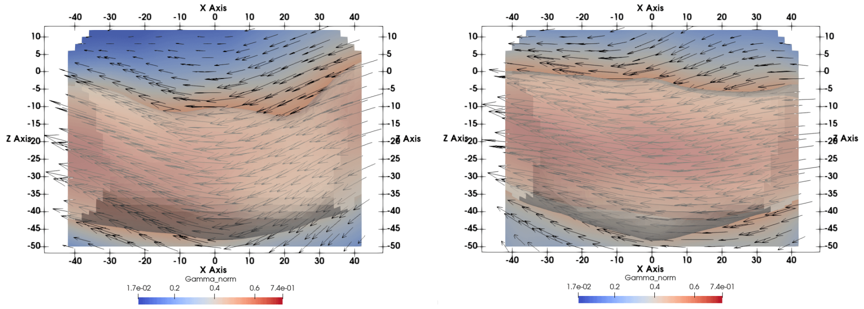

(B) −90 CAD.

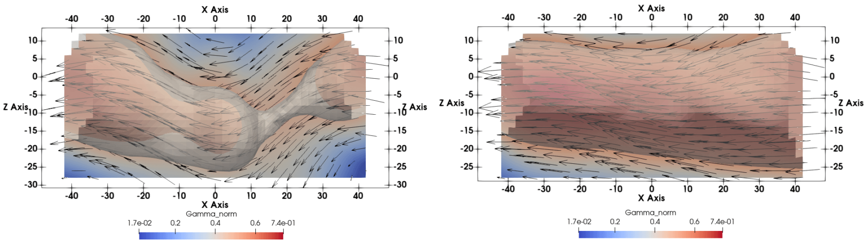

(C) −60 CAD.

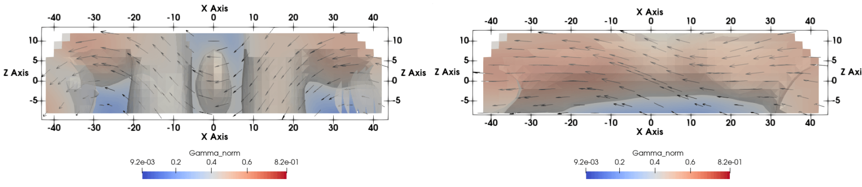

(D) −30 CAD.

FIGURE 5.48: Evolution of the tumble vortex core for cycles 10 (left) and 12 (right), combined with the vector field of Γ_{3p} at slice $Y = 0$ mm.

- At −120 CAD, the vortex core appears quite similar in both cycles though the one in cycle 12 is relatively larger.
- At mid-compression, the deformation of the vortex core in cycle 10 seems to take place as the rotation direction on both sides bends up, which indicates that a tilting of the axis of rotation of the tumble structure is observed on opposite sides (near the wall). In contrast, in cycle 12, the vortex core still keeps its cylindrical form along the X axis.

- The differences are amplified during the second half of the compression. In cycle 10, the rotation direction of the lateral parts becomes much more inclined while the middle part keeps rotating around the X axis. In cycle 12, the $|\mathbf{\Gamma}_{3p}|$ isosurface seems to fill the combustion chamber, which corresponds to a strong tumble motion along the X axis.
- Close to the end of the compression, the vortex core in cycle 10 breaks up into several vortices, which resembles what has been observed in Figure 5.47a. The rotation of the middle part remains along the X axis in cycle 10 but is much less organized than that in cycle 12.

The tumble deformation occurring in the chamber can be associated with the elliptical instability of the tumble motion, as discussed in Chapter 2. The tumble motion initially aligns with one of the two shorter axes at BTC. During the compression, as the piston moves upward, the axis of piston movement (Z axis in this case) becomes gradually the shortest axis, which causes the tumble motion to flip and break into a pair of vortices aligned with the Z axis, as shown in Figure 5.48.

The local tumble ratio **TR** is then calculated for two selected engine cycles for a more quantitative comparison of the evolution of the tumble motion. The three components of **TR** represents the rotation intensity in directions X, Y, and Z and are noted classically as TR, CTR, and SR [166]. Their definition is recalled in Figure 5.49

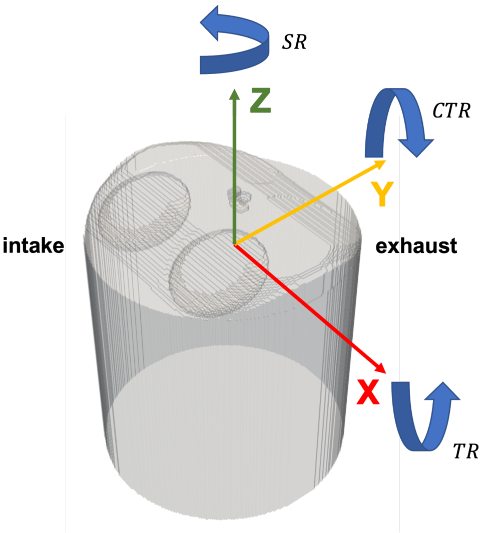

FIGURE 5.49: Decomposition of **TR** in the X (TR), Y (CTR), and Z (SR) directions.

In Figure 5.50, the tumble intensity computed along the TCL in the three directions is plotted with respect to the crank angle for the two engine cycles chosen before.

The tumble intensity in the three directions also provides information about the tumble deformation. The tumble intensity along the X axis |TR| is the main component among the three. An apparent enhancement beyond -120 CAD can be seen in its evolution. In cycle 10, which experiences a significant deformation, it can be noted that |TR| between -90 and -40 CAD is larger on the lateral parts than in the middle part, which indicates a faster rotational air motion on both sides. Near the end of the compression, |TR| decreases to almost 0 as the local rotation is no more around the X axis. In cycle 12 during the second half of the compression, |TR| is more homogeneously distributed along X and conforms to the cylindrical form of the vortex core that sustains the end of the compression.

The other two components |CTR| and |SR| also offer complementary information on the tumble deformation. The deformation occurs during the compression resulting in the change of the local rotation direction of the large-scale motion, which is no longer aligned with the X axis in this case.

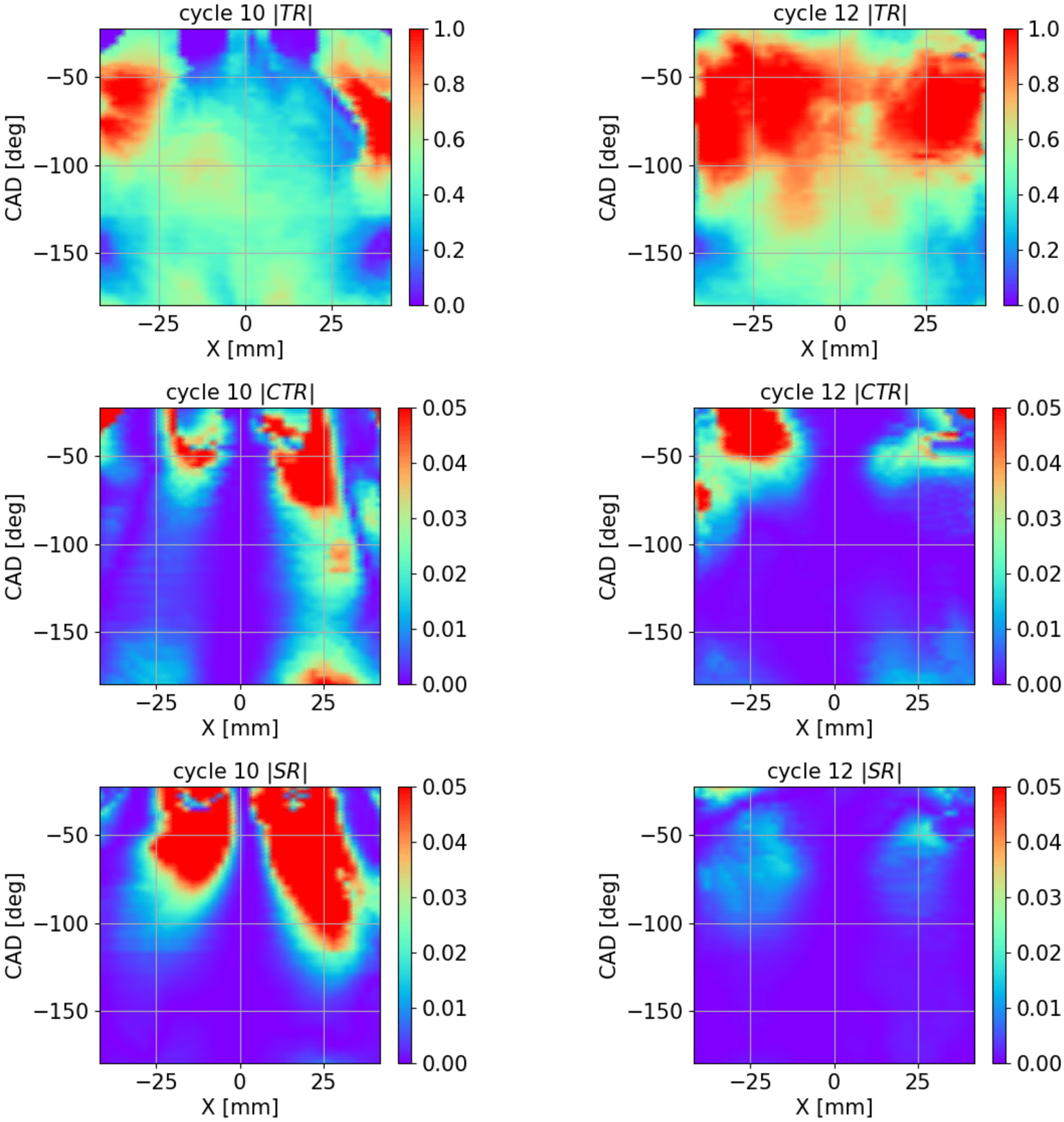

FIGURE 5.50: Comparison of tumble intensity during the compression stroke in direction X, Y, and Z for engine cycles 10 (left) and 12 (right).

Though their values are much smaller compared to |TR|, the increasing of |CTR| and |SR| during the compression allows us to identify the beginning of the deformation, which starts at around −120 CAD in cycle 10. It is also interesting to highlight that noticeable differences already exist on the component |CTR| at the beginning of the compression, which leads us to the hypothesis that the initial form of the tumble may be responsible for the tumble deformation.

The deformation of the tumble has been highlighted thanks to Γ_{3p} and the related angular momenta in different directions. It seems that the tumble does not completely break up into small eddies in the current engine as expected but, in some particular cycles, switches from a pure rotation around the X axis to a pair of counter-rotating vortices around an inclined axis in YZ plane. The large-scale motion seems to be dominant in this engine even at the end of compression, and significant differences reside in the large-scale structures, which may explain why E_k^{CCV} contributes much more than E_k^{HF} in the kinetic energy of the fluctuating part as presented in Figure 5.45b. However, it is still worth studying the energy transfer between the tumble deformation in large-scale motion and small-scale turbulence.

The turbulent part of the flow can be separated from the instantaneous velocity field with the help of 3D EMD. As we focus on the flow properties at the time corresponding to the spark-timing of the reactive case, *i.e.*, −22.5 CAD, 3D EMD is applied at this specific instant. Instead of regarding the global turbulent level, the local turbulent energy around the spark is of greater interest as it can impact the flame kernel development at the early stage of ignition, which can be determinant for the whole combustion process in SI engines.

The local turbulent energy is evaluated in a sub-volume surrounding the spark plug, whose size should be comparable to the turbulent integral length scale. The integral length scale can be estimated from the normalized two-point correlation function [1, 42] defined as:

$$R_{ii}(r) = \frac{\langle u_i(x_i)u(x_i + r)\rangle}{\langle u_i(x_i)^2\rangle} \tag{5.15}$$

In Eq. 5.15, the velocity u is the HF part extracted by 3D EMD, i denotes a velocity component in the direction i and $\langle\rangle$ represents spatial average. Cycle 3 is selected for illustration and the corresponding auto-correlation curves for each component of U_{HF} in their corresponding direction are plotted in Figure 5.51.

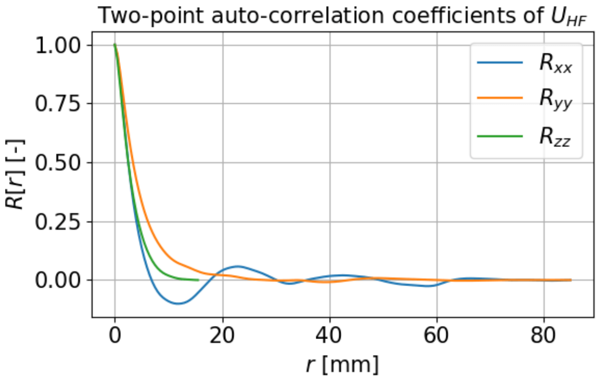

FIGURE 5.51: Two-point auto-correlation functions of U_{HF} of cycle 3 extracted by 3D EMD, computed for each component of U_{HF} in the corresponding direction using Eq. 5.15.

The integral length scales in the three directions are obtained by integrating auto-correlation functions until the first zero crossing as used in [1, 42]. The length scales, ensemble-averaged over the 25 cycles at ignition time, are equal to 3.1 mm, 4.6 mm, and 3.3 mm respectively in X, Y, and Z

directions. Therefore, the sub-volume's size should be of the order of 5 mm. This study chooses a sphere of diameter 5 mm around the spark plug, and the averaged turbulent energy is computed (see Figure 5.52a) for the following analysis.

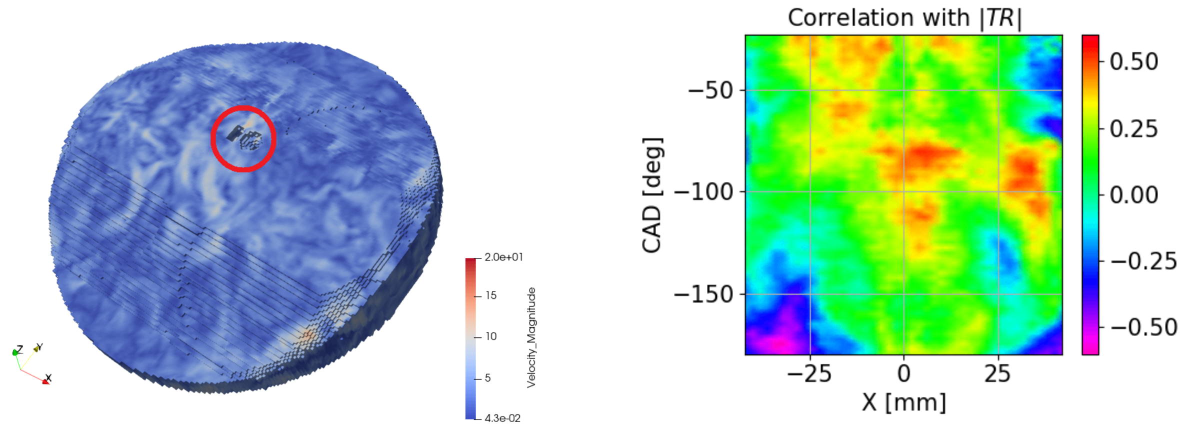

(A) HF part obtained using 3D EMD for 3D velocity field at -22.5 CAD. Evaluation of the averaged local turbulent energy E_k^{HF} (circled in red) around the spark plug.

(B) Correlation map between the averaged local turbulent energy E_k^{HF} around spark plug at -22.5 CAD and the local tumble intensity $\mathrm{TR}(X, \theta)$.

FIGURE 5.52: Relation between large-scale tumble motion and local turbulent intensity.

The component TR is representative of the tumble deformation and thus is used as a descriptor of the tumble during the compression stroke. The relation between the tumble and the resulting turbulent energy around the spark plug is investigated by computing the Pearson correlation coefficient R_{xy} between the averaged local turbulent kinetic energy at ignition $E_k^{HF}(t_{ign})$ and the tumble intensity $\mathrm{TR}(X, \theta)$ for varying crank angle θ and X coordinate. Results are plotted on a 2D map in Figure 5.52b. It can be seen that regions with significant positive correlations are located in the central part of the tumble during the entire compression stroke. It can be inferred that a well-organized tumbling flow in the chamber that sustains itself and experiences slight deformation is favorable for a high level of turbulent energy around the spark, which is preferred for fast combustion. A possible explanation is that a stronger tumble motion contains more kinetic energy and can maintain the energy transfer to small eddies by the energy cascade. In contrast, a weaker tumble motion, caused by the tumble deformation leading to a vortices pair near TDC, is supposed to release its energy faster to turbulence which also dissipates earlier.

5.5.4 The link between 2D and 3D diagnostics

The in-cylinder flow analysis was performed using both 2D and 3D analysis tools. The flow characterization in 3D provided insight into the tumble's shape and intensity and the kinetic energy distribution in different structure scales. Nonetheless, 3D flow can only be obtained with numerical simulations, and PIV measurements are available in 2D planes. In this section, we would like to explore the potential link between flow characteristics obtained from 2D and 3D analysis and investigate if 2D flow features allow predicting 3D flow ones.

In the 2D tumble central plane, the tumble motion is visible during the compression, and we choose the 2D tumble ratio computed from this 2D plane during the whole compression stroke from -180 to -22.5 CAD as the 2D flow feature. A Scatter plot of the 2D tumble ratio as a function of the averaged 3D tumble ratio along the TCL is plotted in Figure 5.53 showing a non-negligible correlation.

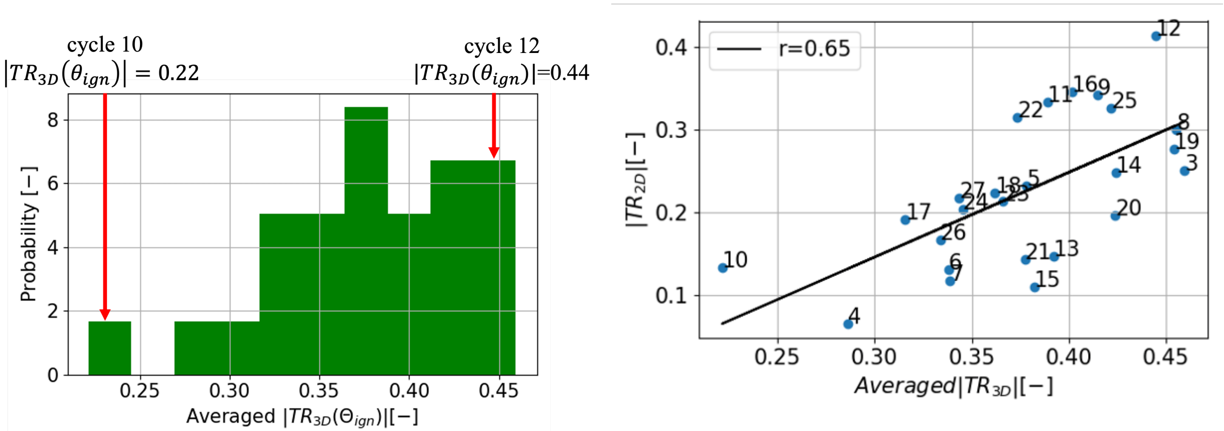

(A) Distribution of the 3D tumble ratio at −22.5 CAD.

(B) Correlation between the tumble ratio of 2D and 3D at −22.5 CAD.

FIGURE 5.53: Relation between the tumble ratio of 2D and 3D at −22.5 CAD.

The two extreme cycles 10 and 12, found different in the 2D tumble central plane, behave the same way in 3D as their 3D tumble ratios are also located in the two extreme groups. A strong correlation exists between these two flow features, which proves that the tumble ratio quantified in the 2D tumble central plane is a good descriptor of the flow state in 3D.

Coefficients of correlation are computed between several 3D flow features at spark timing like the kinetic energy of the LF and HF parts extracted by 3D EMD, both in the whole chamber and the spark plug region, and the 2D tumble ratio as a function of the crank-angle degree $TR_{2D}(\theta)$. Results are plotted in Figure 5.54.

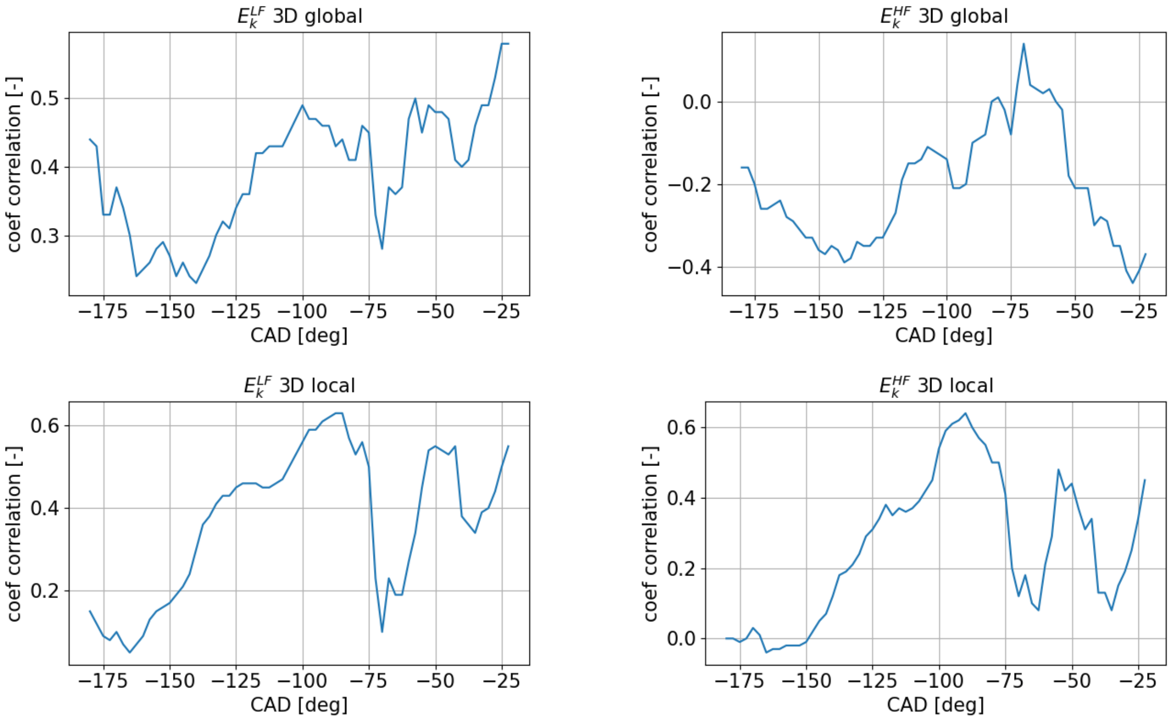

FIGURE 5.54: Evolution of the coefficient of correlation between $TR_{2D}(\theta)$ and kinetic energy $E_k(\theta_{ign})$ of the LF or HF parts in the whole chamber (global) or near the spark plug (local) at −22.5 CAD extracted by 3D EMD, for $-180 < \theta < 22.5$ CAD.

The evolution of the coefficients of correlations between the 2D and the 3D flow features shows globally no significant correlations except the one between $TR_{2D}(\theta)$ and the global $E_k^{LF}(\theta_{ign})$ for θ close to θ_{ign}, which is normal as both of them quantify the intensity of large-scale motions. From the 2D tumble ratio $TR_{2D}(\theta)$, it seems difficult to predict 3D kinetic energy $E_k(\theta_{ign})$, especially those of the HF part which is related to the turbulence.

Another attempt is made to investigate the link between the LF and the HF parts of the flow, both locally and globally. The two scatter plots, and their corresponding coefficients of correlations plotted in Figure 5.55 indicate that the global turbulent level does not depend on the intensity of large-scale motions. The local turbulent energy strongly depends on the large-scale local motion, which suggests that the local high-velocity flow motion generates the local turbulence.

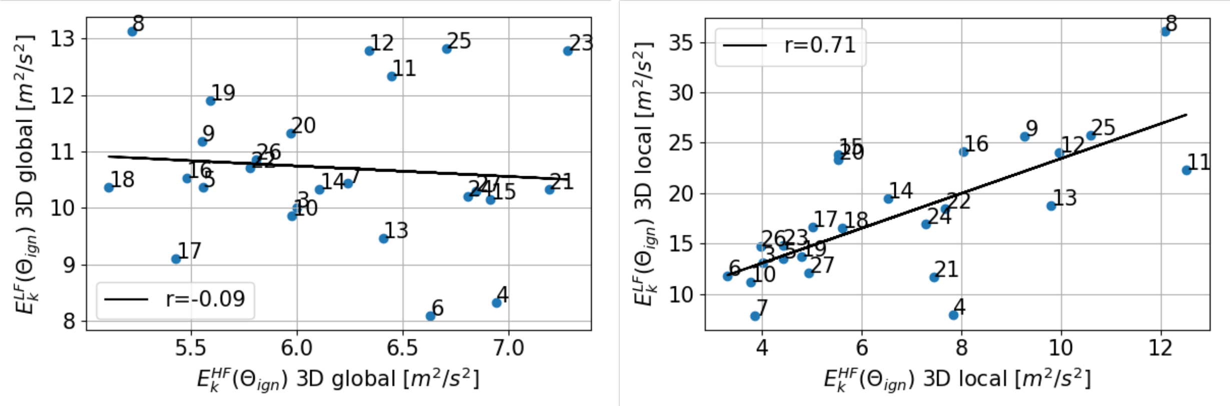

FIGURE 5.55: Correlations between LF and HF parts kinetic energy in the whole chamber or near the spark plug at −22.5 CAD.

In Figure 5.56, we present again the distribution of the averaged 3D tumble ratio at θ_{ign}, with each bar colored by the corresponding averaged 3D swirl ratio at θ_{ign} that quantifies the tumble deformation. It is worth noting that a global weak tumble motion is more likely to have a high 3D swirl ratio because of the deformation, while a strong tumble motion is resistant to such a flow structure change.

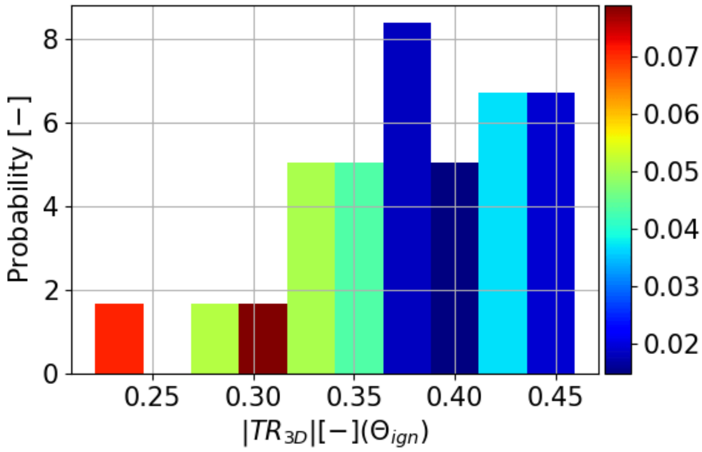

FIGURE 5.56: Distribution of 3D tumble ratio TR at −22.5 CAD, colored by the corresponding averaged 3D swirl ratio SR in each bar.

5.6 Summary of main findings

In this Chapter, the TU Darmstadt optical engine was simulated using LES on motored conditions to analyze the internal aerodynamics.

Using an initial LES methodology, a first LES cycle was launched, and the obtained results on thermodynamics presented an overestimation of the in-cylinder pressure compared to the experimental measurements. It was found that the crevice flow modeling was responsible for this issue as the heat transfer inside the crevice seemed to be too moderate compared to the 0D simulation. In consequence, the crevice flow was underestimated. To correct the crevice modeling, a simplified crevice model was integrated into the LES to adjust the mass exchange between the chamber and the crevice. For the motored case, the overestimation of the in-cylinder pressure is not crucial as its impact on the prediction of internal aerodynamics is not visible [42]. However, a correct pressure level (and the corresponding temperature) is desired for the reactive case. This model will be kept for the reactive case simulation presented in the next Chapter 6.

Once the thermodynamics was validated, the comparison with experiments continued on the prediction of aerodynamics. With the initial set-up, the prediction of the intake jets was found to lack accuracy. Based on findings from the bench flow case, a sensitivity analysis was carried out on the boundary conditions used at inlet and valve walls. Best improvements were made compared to PIV measurements from experiments, using an imposed mass flow rate at inlet and no-slip condition on valve walls with adapted mesh refinement. It evidenced the high sensitivity of the internal aerodynamics to the boundary conditions and emphasized the problem of uncertainties in the boundary conditions, especially those obtained from experiments. In Chapter 8, an attempt to introduce the uncertainty quantification techniques in LES will be presented for a pipe flow case as a prior work for further applications on SI engine simulation.

The validated LES methodology was then used to obtain 25 LES consecutive cycles. The analysis of the internal aerodynamics was then performed on these LES cycles. For the motored case, the analysis was focused on the flow during the compression stroke, and approaches of 2D and 3D were used to characterize the tumble motion. CCV in aerodynamics was first identified in the tumble plane in a 2D vision after decomposition using 2D EMD. It was noticed that CCV appeared to be strongly correlated with the tumble structure. Next, the energy transfer between different scales was also investigated. A noticeable energy transfer from the mean flow to the fluctuating part was observed beyond -70 CAD. Based on 2D EMD analysis, it was concluded that most energy transferred from the mean flow was retained in CCV of large-scale motion, and the turbulent fluctuations stayed at a stable level till the end of the compression.

The analysis was extended in 3D for a complete vision of the tumble motion. Γ_{3p} was used to describe the vortex core of the tumble at different instants during the compression. Two typical flow structures near the end of the compression were found in this engine as a result of the tumble deformation: the flow could either stay rotational around the X axis or switch to a pair of counter-rotating vortices around an inclined axis in YZ plane, which supports the existence of elliptical instability in the tumbling flow as proposed by Lumley [43]. A qualitative comparison between two engine cycles showed that differences in the vortex core existed already during the compression. The computed angular momentum in the three directions confirmed our finding with Γ_{3p}. It was observed that the flow structure at the end of the compression was related to its initial form at BDC. Especially the appearance of secondary cross-tumble and swirl motions were prone to destabilize the tumble motion.

In this optical research engine, the large-scale motion was sustained until the end of the compression despite the geometric changes during the compression and friction with the walls. An attempt was still made to link the tumble motion and the local turbulent level around the spark. Local E_k^{HF}, extracted from 3D EMD analysis, was found to be positively correlated with the tumble intensity around the X axis of the central part. The local tumble intensity around the spark plug, related to the flow pattern near TDC, was thus crucial to generating turbulent fluctuations, suggesting a potential link between large-scale motions and small-scale turbulence.

In this Chapter, analysis tools were applied and showed their potential for an extensive understanding of the internal aerodynamics in SI engines. The analysis of the tumble motion remains on two typical cycles and thus stays qualitative. In Chapter 6 and Chapter 7, more quantitative analysis will be performed on the internal aerodynamics to precisely describe the flow development during the whole engine cycle and its impact on the combustion process.

CHAPTER 6

Simulation and analysis of the TU Darmstadt engine configuration: fired conditions

Contents

6.1 Engine characteristics . . . 112
6.2 LES methodology . . . 113
  6.2.1 Boundary conditions . . . 113
  6.2.2 Mesh . . . 114
  6.2.3 Numerical set-up . . . 114
  6.2.4 Combustion modeling set-up . . . 114
6.3 Validation of the LES results . . . 116
  6.3.1 Combustion characteristics . . . 116
  6.3.2 Velocity field in tumble plane . . . 118
6.4 Identification of flow parameters at spark timing impacting the combustion process . . . 122
  6.4.1 Global flow pattern . . . 125
  6.4.2 Local flow near the spark . . . 127
  6.4.3 Global motions in the combustion chamber . . . 131
  6.4.4 Local turbulence intensity near the spark . . . 139
  6.4.5 Thermodynamic effects . . . 141
  6.4.6 Multivariate analysis of CCV factors . . . 142
6.5 Summary of main findings . . . 143

The present Chapter covers the simulation and the analysis of the optical engine supplied by TU Darmstadt and performed on fired conditions. The LES methodology for the fired case is based on that for the motored case presented in Chapter 5 and includes ignition and combustion modeling. Secondly, LES results are validated against experimental data concerning the internal aerodynamics and the CCV level. Following the validation, the analysis was carried out on the internal aerodynamics and its link with combustion. The in-cylinder flow features at spark timing were studied, and crucial flow parameters impacting the combustion process were identified.

6.1 Engine characteristics

The same engine geometry is used in the fired case as in the motored case. Figure 6.1 recalls the coordinate system used in the current work of the fired case. The engine configuration is almost the same as the one studied in motored conditions, as summarized in Table 6.1. In fired conditions, the engine is operated with a port fuel injection of stoichiometric iso-octane/air mixtures. The fuel injection takes place inside the intake port about 1.4 m upstream of the engine. The corresponding fuel-air mixtures can be considered homogeneous when they flow into the engine chamber.

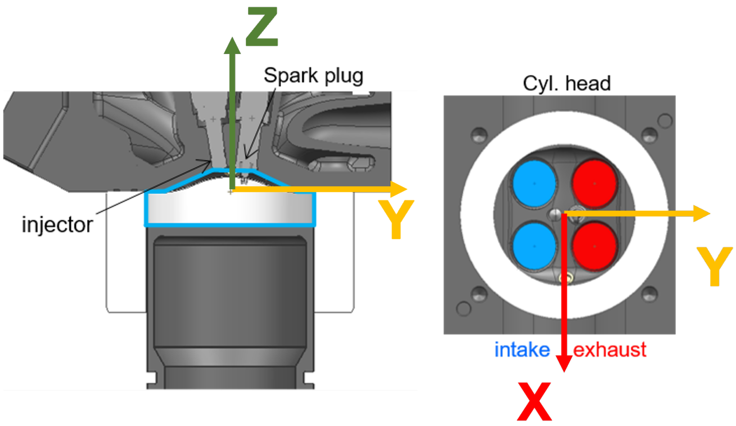

FIGURE 6.1: Engine geometry of the configuration 'Spray-guided' [160]. The coordinate system is used in the numerical modeling of this work.

Engine speed	1500 rpm
Intake/exhaust pressure	0.95/1 bar
Intake/exhaust temperature	303/797 K
Compression ration	8.7
Bore/stroke	86/86 mm
Connecting rod	148 mm
Displacement	499.6 cm^3
Intake valve opening	325 CAD
Intake valve closure	-125 CAD
Exhaust valve opening	105 CAD
Exhaust valve closure	-345 CAD
Fuel	Iso-octane
Air-fuel equivalence ratio	1
Spark timing t_{ign}	-22.2 CAD

TABLE 6.1: Engine characteristics (0 CAD = top dead center of the compression stroke) in fired conditions.

6.2 LES methodology

6.2.1 Boundary conditions

The boundary conditions of the fired case are illustrated in Figure 6.2. A pressure type condition is given at both inflow and outflow boundaries. Two major differences can be noticed compared to the set-up of the motored case.

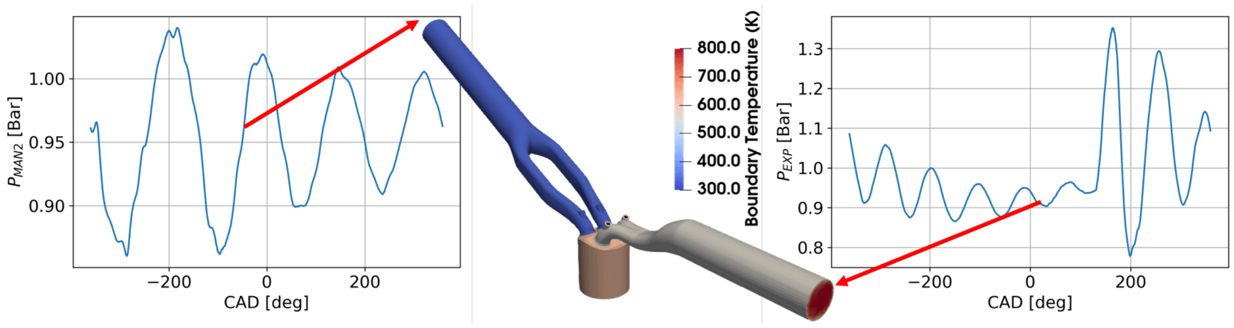

(A) Pressure condition at inlet and outlet.

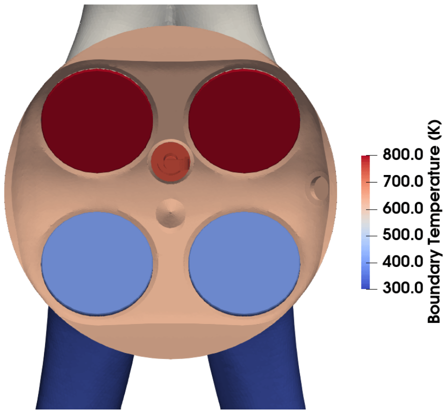

(B) Temperature distribution imposed on different walls.

FIGURE 6.2: Boundary conditions of the fired case.

The heat release generated by the combustion leads to much higher wall heat transfers than in the motored case. However, no temperature measurement is available on the walls, which makes the temperature assignment difficult and introduces uncertainties in the simulation. The values of wall temperatures are chosen by referring to studies on similar engine configurations as presented in [170] and [26]. Constant temperature values are imposed respectively on the walls of the intake port, the cylinder head, the liner, the piston, and the exhaust port, as illustrated in Figure 6.2b. The different values are summarized in Table 6.2.

As discussed in section 5.4.3, for the motored case, imposing a mass flow rate obtained from the 0D simulation at the inlet leads to fewer fluctuations in the entering mass flux and allows a slightly better prediction of intake jets. The 0D model was also built with GT-power for the fired case, but it does not predict the combustion process correctly. The combustion modeling with GT-power of our case is incompatible with the crevice flow modeling we have for the motored case. To fit the imposed in-cylinder pressure, GT tends to end the combustion earlier than expected. As the mass flow rate can not be obtained from the GT-Power simulator, the pressure type boundary condition is thus retained in the simulation of the fired case.

Intake/exhaust	303/797 K
Intake port	330 K
Exhaust port	550 K
Intake valves	400 K
Exhaust valves	800 K
Head	620 K
Spark plug	750 K
Liner	620 K
Piston	620 K

TABLE 6.2: Temperature values assigned to different walls in fired conditions.

6.2.2 Mesh

The meshing strategy remains almost unchanged, as presented in Figure 6.3, compared with the one used in the motored case. Local refinement is made around intake valves to ensure the accurate prediction of the intake flow. The Automatic Mesh Refinement (AMR) is also activated based on the unresolved (SGS) velocity (threshold of 1 m/s) and the progress variable gradient with a minimum cell size of 0.25 mm to better resolve the flow field and the flame front, respectively.

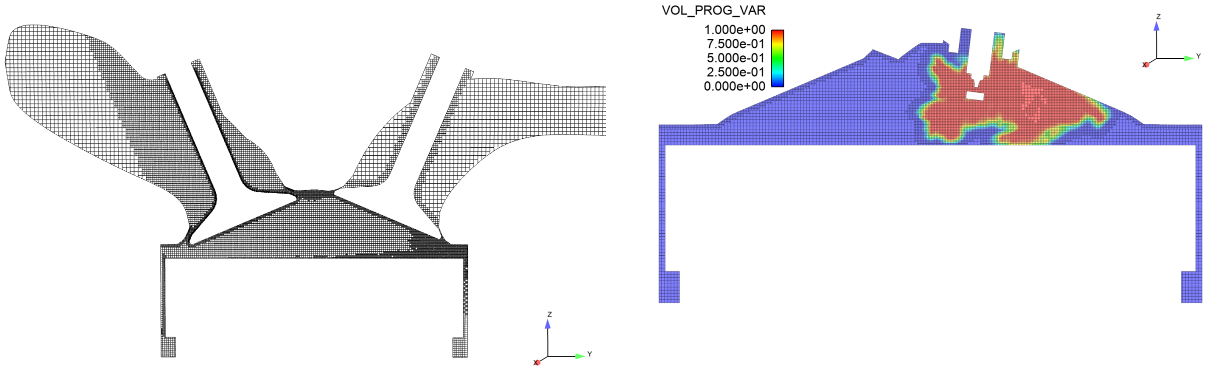

(A) AMR activated based on the unresolved velocity.

(B) AMR activated near the flame front based on the gradient of progress variable.

FIGURE 6.3: Mesh topology used in the fired case.

6.2.3 Numerical set-up

The CFD solver CONVERGE [20] is used for the LES of the fired case. The numerical set-up used in LES is summarized in Table 6.3 and remains unchanged as it was validated in the motored case. Wall models are applied for most walls except those surrounding the intake valves, for which the near-wall flow is directly resolved with locally refined mesh.

6.2.4 Combustion modeling set-up

Concerning combustion modeling, the main objective is to reproduce the combustion phenomena in the cylinder, including the average behavior and the corresponding variations between cycles.

In the motored case, the crevice flow, which is essential for correctly predicting the in-cylinder pressure, was related to the variation of the in-cylinder pressure. In the fired case, the in-cylinder pressure variation is undoubtedly more important because of the heat release from combustion. Therefore the crevice model presented in Chapter 5 should also be used. A first comparison is

<table>
<tr><td>Velocity-pressure coupling</td><td colspan="2">PISO [168]</td></tr>
<tr><td>Temporal scheme</td><td colspan="2">Semi-Implicit 2^{nd} order</td></tr>
<tr><td>Spatial scheme</td><td colspan="2">Central scheme 2^{nd} order</td></tr>
<tr><td>Convective CFL</td><td colspan="2">$u\frac{\Delta t}{\Delta x} \leq 1$</td></tr>
<tr><td>Fourier number</td><td colspan="2">$\nu\frac{\Delta t}{\Delta x^2} \leq 2$</td></tr>
<tr><td>Acoustic CFL</td><td colspan="2">$c\frac{\Delta t}{\Delta x} \leq 10$</td></tr>
<tr><td>SGS model</td><td colspan="2">Sigma</td></tr>
<tr><td rowspan="2">Wall modeling</td><td>Velocity</td><td>Log-Law/no-slip</td></tr>
<tr><td>Temperature</td><td>O'Rourke and Amsden</td></tr>
</table>

TABLE 6.3: Numerical set-up for Darmstadt engine simulation on fired condition.

made to compare a single LES cycle with the crevice model activated with the same cycle without the crevice model. The result is presented in Figure 6.4a. The impact of the crevice model can be emphasized in two aspects:

- Before the ignition, the pressure level is corrected by the model, which is crucial for the flame kernel development at the early stage: the corresponding in-cylinder temperature is also corrected, hence the viscosity and consequently the turbulence, especially in the spark region where turbulence can interact with the flame front.
- After the ignition, a large amount of mass enters the crevice region as the in-cylinder pressure increases. The crevice model enhances the mass exchange; thus, the in-cylinder pressure is lower than in the case where the crevice model is not activated.

In both cases, it is worth noting that the pressure is consistently overestimated for crank angle larger than −15 CAD, which indicates that the heat release is too important compared to the experimental one. In this region, the cycle-to-cycle variation of the pressure can be neglected, which means that the difference does not originate from the cycle-to-cycle variation of the combustion efficiency.

The width of the crevice region is 0.5 mm and has been modified to 1 mm in the simulation. In such a narrow region, flame quenching can happen [171] and consequently, the propagation of the flame can not reach deep inside the crevice. To verify this hypothesis, another test is launched in which the laminar flame speed is imposed to be 0 m/s in the crevice so that no fuel consumption takes place inside. The comparison is made in Figure 6.4b, and it can be noticed that the change made in the crevice helps significantly to capture the correct pressure evolution.

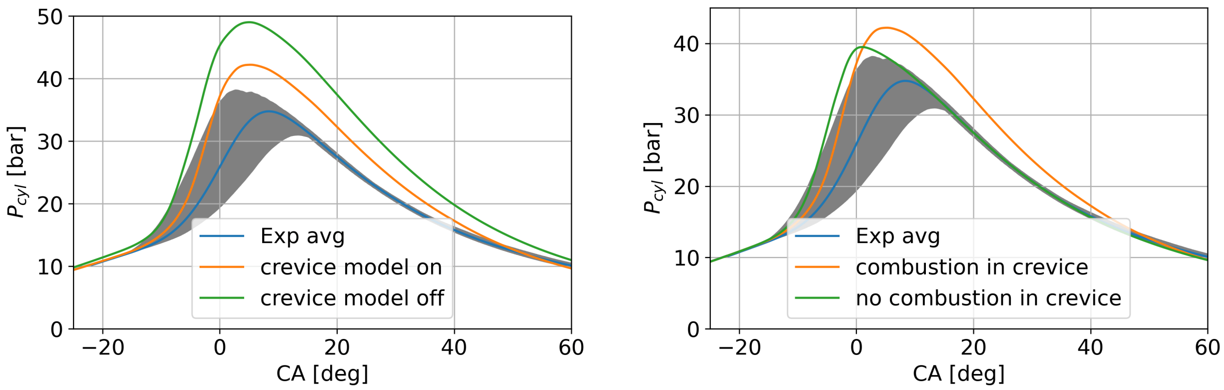

(A) Impact of the crevice flow correction.

(B) Impact of flame penetration into the crevice.

FIGURE 6.4: In-cylinder pressure with different set-up in the crevice region.

The combustion model is activated until the opening of the exhaust valves. The choice is based on the fact that the combustion duration is much longer in this specific engine configuration because of the crevice flow. When the piston moves downwards, fresh gases are released from the crevice to the chamber by the crevice flow. The combustion is thus maintained at the exit of the crevice along the liner (see Figure 6.5). Though the combustion of the fresh gases brought by the crevice flow happens much later after the ignition, it does contribute to the fuel consumption of the current cycle, which could affect the next cycle, and therefore it is also simulated.

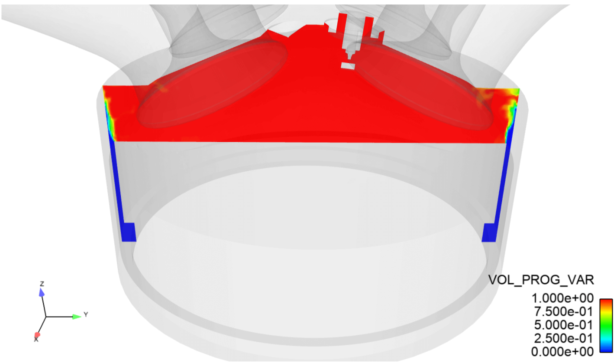

FIGURE 6.5: Distribution of progress variable $\bar{c}$ in tumble plane. Residual combustion ($0<\bar{c}<1$) is captured near the exit of the crevice at 35 CAD.

In the following, this configuration (activated crevice model and no reaction inside the crevice) is retained for multi-cycle simulations. Further calibration on the combustion speed is also needed to match the average pressure evolution and the CCV level. For the calibration, only the phase after the ignition of each engine cycle is recomputed with different values of the two calibration parameters in ISSIM C_{surf} and ECFM α_{cfm}, and the best couple of value, $\alpha_{cfm} = 1.5$ and $C_{surf} = 15$, is retained for all the cycles.

6.3 Validation of the LES results

Using the LES methodology described above, 35 consecutive cycles are obtained for the CCV analysis, though not enough to achieve full convergence. The validation of LES results against experimental measurements focuses on two parts: aerodynamics and combustion. In what follows, the results associated with the combustion are compared between the simulation and the experiments. Then, the assessment of the internal aerodynamics predicted by LES compared to PIV measurements is carried out.

6.3.1 Combustion characteristics

The in-cylinder pressure evolution reflects the combustion state and the corresponding heat release. Hence it is always used to characterize the combustion process.

In Figure 6.6a, all the LES cycles and experimental cycles are plotted. LES has succeeded in capturing most occurring cycles observed in experiments, except for extremely fast and slow cycles which appear rarely. The statistical comparison is presented in Figure 6.6b, where the averaged pressure and the envelope of variation of width equal to two times the standard deviation σ are illustrated for both numerical and experimental data. A good agreement can be found between experimental and numerical results, though the combustion speed predicted by LES is slightly slower during -10 to 10 CA with less variation.

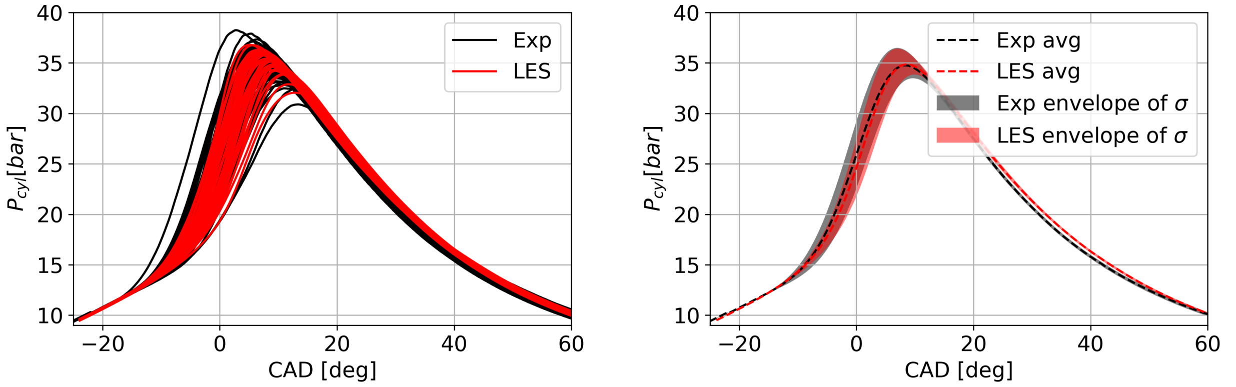

(A) Individual cycles of LES (35) and experiments (74).

(B) Phase-averaged evolution with variation envelope of LES and experiments.

FIGURE 6.6: Comparison of the in-cylinder pressure evolution.

The Matekunas diagram presented in Figure 6.7 helps to characterize cycle-to-cycle variations using in-cylinder pressure data. The diagram displays the maximum in-cylinder pressure P_{cyl}^{max} versus the crank angle CA_{max} at which it occurs for all the individual cycles. It provides direct observation of the cyclic combustion variations since mass-burning rate variations produce variations in P_{cyl}^{max} as well as in its occurring crank angle CA_{max}. Both experimental and numerical data points lie in the same region and present a similar linear behavior between P_{cyl}^{max} and CA_{max} (slope of -0.67 for experimental data and -0.56 for LES data), which indicates good agreement between LES results and experimental measurements. It is noteworthy that, although cyclic combustion variability is observed, the linear behavior featured in Figure 6.7 is representative of a stable operation. The level of CCV can be quantified to yield a more quantitative assessment.

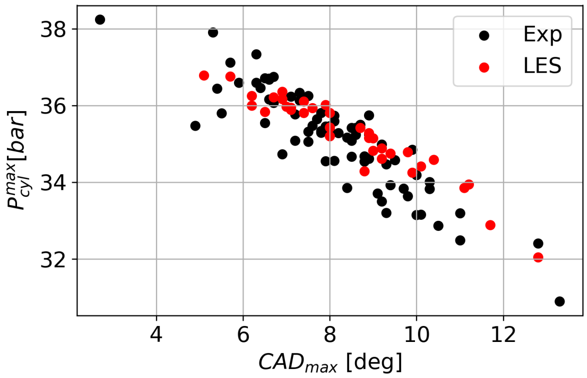

FIGURE 6.7: Matekunas diagram scattering P_{cyl}^{max} as function of CA at which P_{cyl}^{max} occurs.

The coefficient of variation (CoV) in maximum pressure P_{cyl}^{max} is one of the most commonly used variables to quantify the CCV level. In Figure 6.8, the evolution of the CCV level with respect to the number of cycles is plotted for both numerical and experimental data. In both cases, the CCV level converges after around 10 to 15 cycles. Using all the available cycles, LES predicts a CCV level of 3% compared to 3.8% measured in experiments. This slight difference can be explained by the fact that the boundary conditions are imposed in LES identically for all the cycles. In contrast, in experiments, boundary conditions indeed vary from one to another cycle. Errors from the numerical resolution caused by the use of low-order schemes and a high CFL acoustic number can also decrease the precision of our LES results. This CoV level is indeed similar to the stable operating point studied in [91] on another research engine fuel with a stoichiometric mixture of air and gaseous propane to be compared with CoV levels of the order of 12% obtained in two unstable cases (a lean and a diluted one) of the same engine.

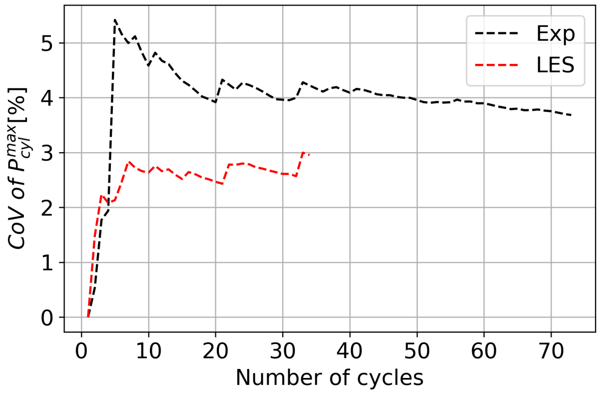

FIGURE 6.8: Evolution of the CCV level with the number of cycles considered experimentally and numerically.

6.3.2 Velocity field in tumble plane

The validation of LES results continues with the prediction of internal aerodynamics. PIV measurements were carried out only for the tumble plane for the fired case. In Figure 6.10, the ensemble-averaged velocity fields at six instants are compared between PIV measurements (74 cycles) and LES (35 cycles). A more detailed comparison for the instant −180 CAD is made over certain sampling lines uniformly located in the horizontal and vertical directions, as presented in Figure 6.9. The same comparison for more instants is available in Appendix B.

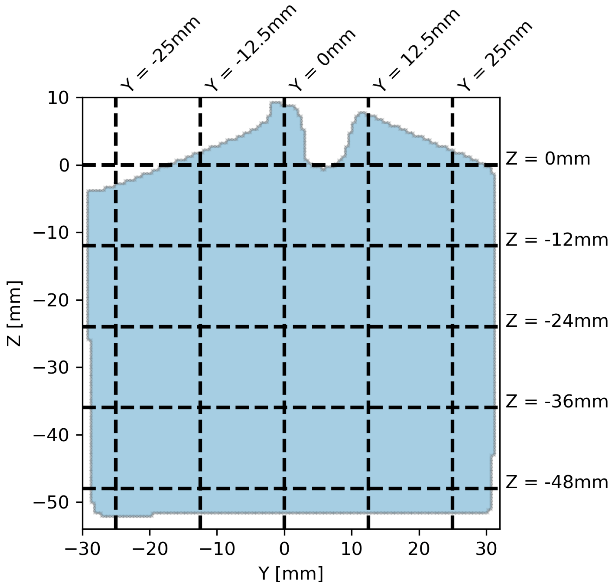

FIGURE 6.9: Sampling lines for comparison with PIV measurements at −180 CAD.

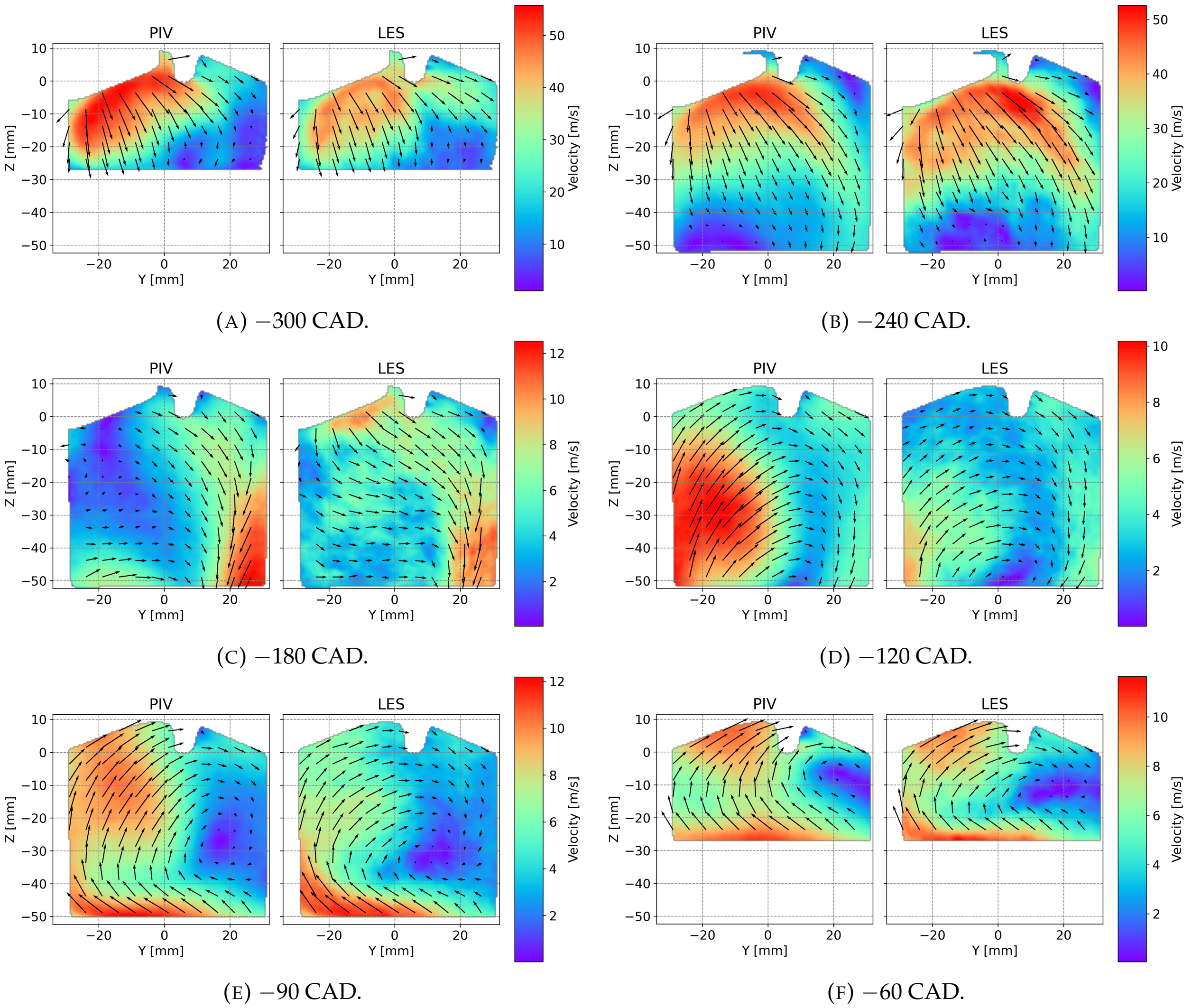

(A) −300 CAD.

(B) −240 CAD.

(C) −180 CAD.

(D) −120 CAD.

(E) −90 CAD.

(F) −60 CAD.

FIGURE 6.10: Comparison of the phase-averaged velocity field in tumble plane between LES results and PIV measurements.

In Figure 6.10a and Figure 6.10b, a high-velocity region beneath the intake valves is equally captured by LES and PIV. At −180 CAD (cf Figure 6.10c), the tumble motion begins to organize in the chamber. We observe a flow directed downwards at the exhaust side of the plane for both PIV and LES. The difference remains in the region under the intake valves, where the intake jets interact strongly after valve opening. In LES, this interaction is more important, as highlighted by the high-velocity zone under the intake valve, and hence it keeps generating the descending flow towards the exhaust side. On the contrary, the flow measured by PIV in the same region is almost at rest. Moreover, the front of the tumble begins to appear on the left lower corner of the PIV field, though very weak, while on the LES field, nothing can be observed in the same place. Figure 6.10d and Figure 6.10e compare the ensemble-averaged velocity field during the compression stroke. The front of the tumble captured by PIV advances much quicker towards the cylinder head than that predicted by LES. Near the spark timing at −60 CAD, some differences are present around the tumble core, as shown in Figure 6.10f.

Figure 6.11 shows the comparison for all the horizontal sampling lines. The major difference can be noticed on the left side of lines at $Z = 0$ mm, $Z = -12$ mm, and $Z = -24$ mm, which stays in the interaction zone of the intake jets. A global agreement is achieved on the right side, where the flow is convected downward along the liner wall.

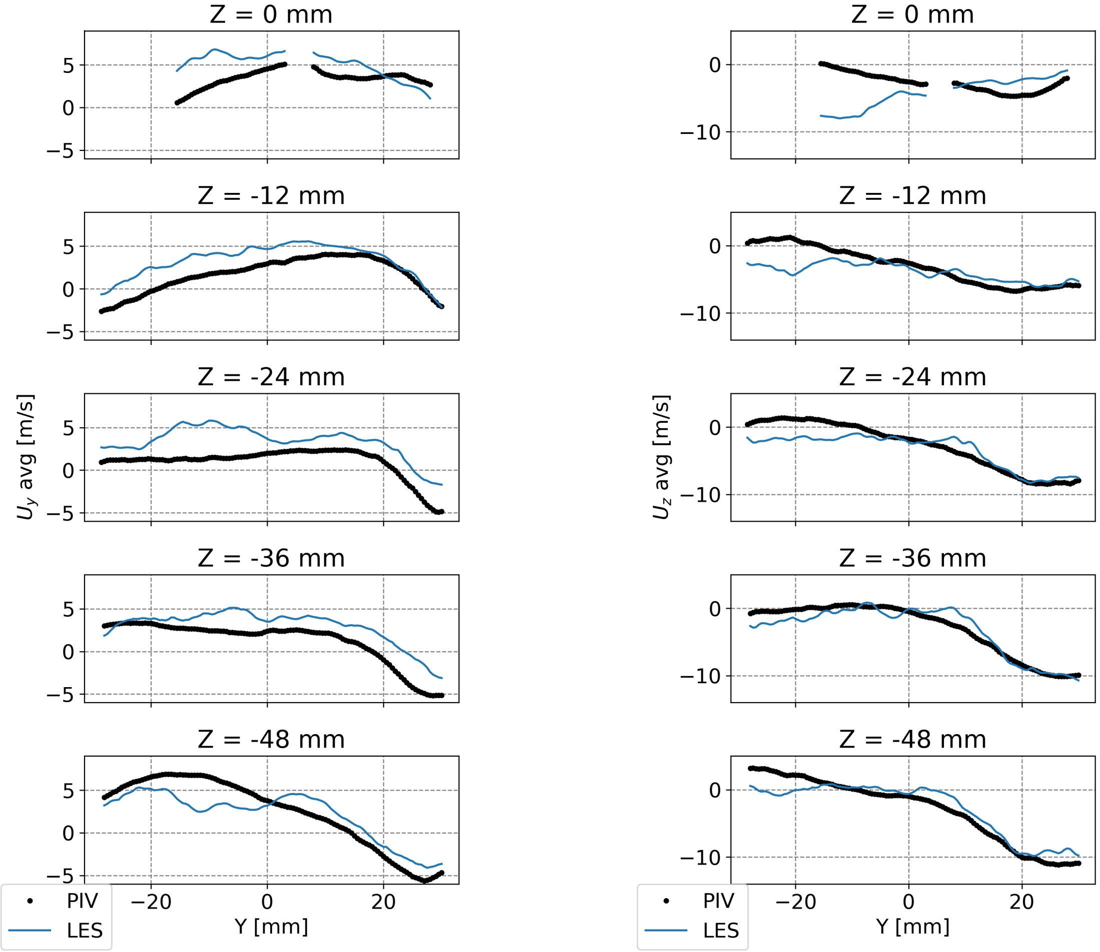

(A) U_y component.

(B) U_z component.

FIGURE 6.11: Comparison of 1D profiles over horizontal lines in tumble plane at −180 CAD.

The comparison over vertical lines results in a similar observation as the one over horizontal lines. The difference resides mainly in the lines at $Y = -25$ mm and $Y = -12.5$ mm, both on the top and bottom sides: LES predicts a higher horizontal velocity U_y on the top because the interaction between the intake jets seems to be stronger in LES; on the bottom, an upward flow representing the tumble front is captured by PIV and therefore the vertical velocity U_z is positive locally.

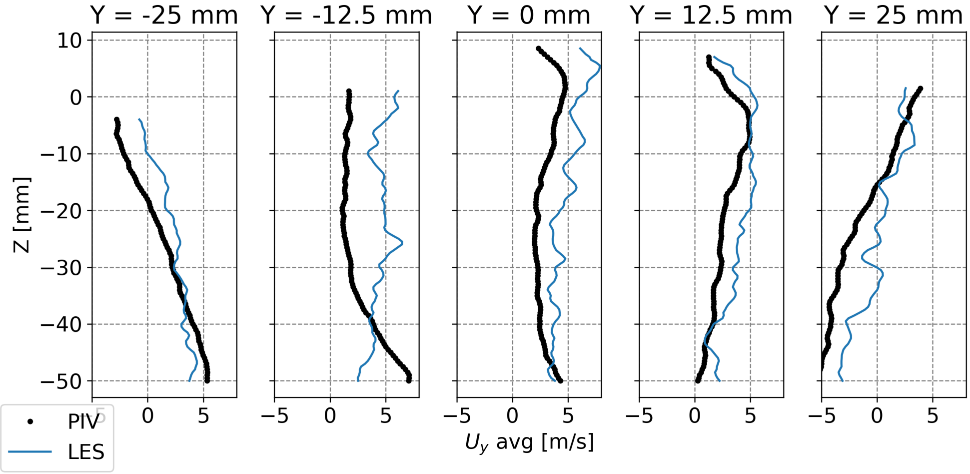

(A) U_y component.

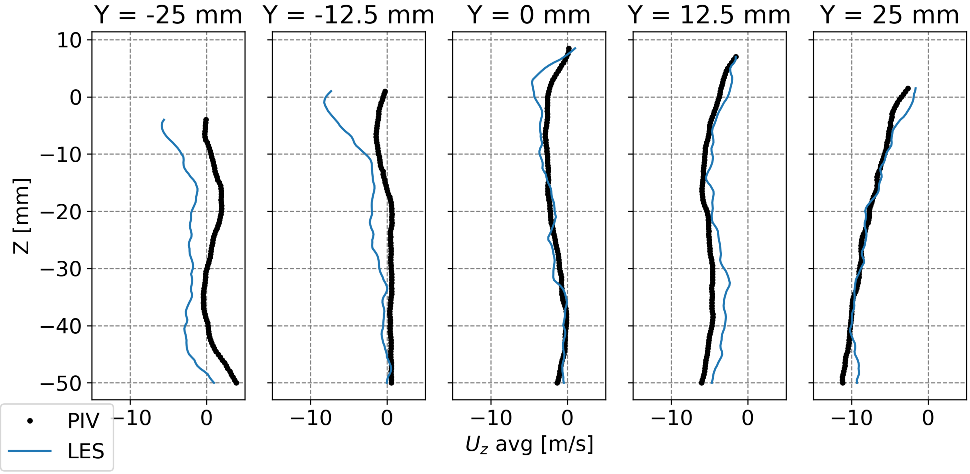

(B) U_z component.

FIGURE 6.12: Comparison of 1D profiles over vertical lines in tumble plane at −180 CAD.

The comparison of the RMS velocity is also conducted for the same instant and is plotted in Figure 6.13. 35 LES cycles are, in fact, not enough to achieve the convergence of the RMS velocity, which is the second moment of the velocity. Nevertheless, a qualitative comparison is still of interest to verify if the fluctuations level agrees with PIV data. According to Figure 6.13, LES predicts the correct level of RMS velocity globally, especially for regions near the spark plug, along the liner on the exhaust side, and in the middle of the plane.

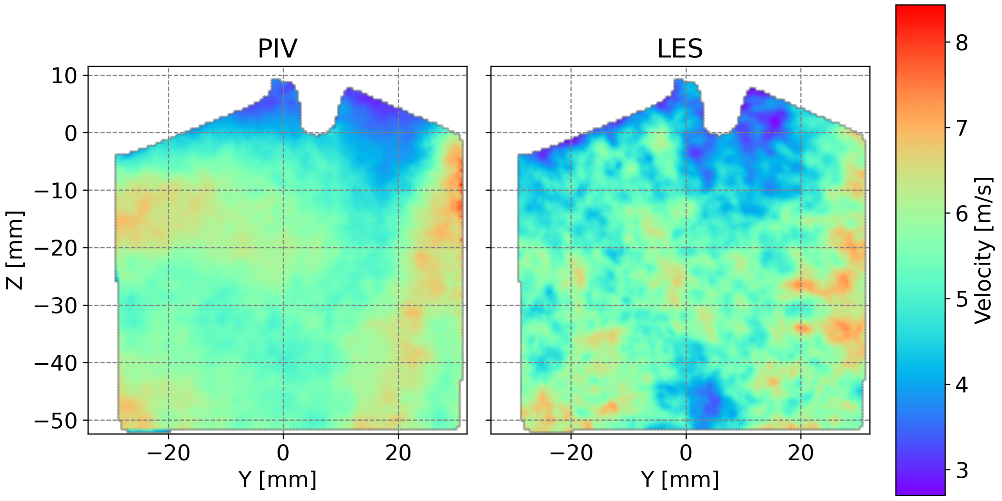

FIGURE 6.13: Comparison of RMS velocity in the tumble plane at −180 CAD.

The aerodynamics prediction by LES is validated by comparing the averaged and RMS velocity fields with the PIV data. A global agreement is obtained despite deviations in some local regions. In the next section, we will conduct a CCV analysis to identify significant CCV factors for the combustion process at spark timing.

6.4 Identification of flow parameters at spark timing impacting the combustion process

After validating LES results against experimental measurements, in this section, we start the investigation of the CCV sources originating from the flow.

In previous studies [39, 91], it was found that the early-stage development of the flame kernel is crucial for flame propagation in the combustion chamber: a fast burning rate at the beginning of the combustion leads to globally rapid combustion. To verify this, quantities noted as CA_X, representing the combustion advancement, are defined based on the fuel consumption as presented in Figure 6.14a. X indicates the percentage of consumed fuel compared to the total fuel mass at spark timing. As explained previously, the impact of the crevice flow can not be neglected: the in-cylinder mass of fuel slightly increases after about 10 CAD because of the existing crevice flow; residual combustion takes place at the exit of the crevice and consumes gradually the fuel contained in the exiting flow. Both CA_2 and CA_{50} are extracted, which characterize the crank-angle degree at which respectively 2% and 50% of the fuel has burned.

The correlation between CA_2 and CA_{50} is presented in Figure 6.14b. A strong linear correlation exists between these two indicators of combustion duration, which confirms the conclusion obtained in previous studies [38, 39] that flame propagation at the early stage is a determining factor of the global combustion speed.

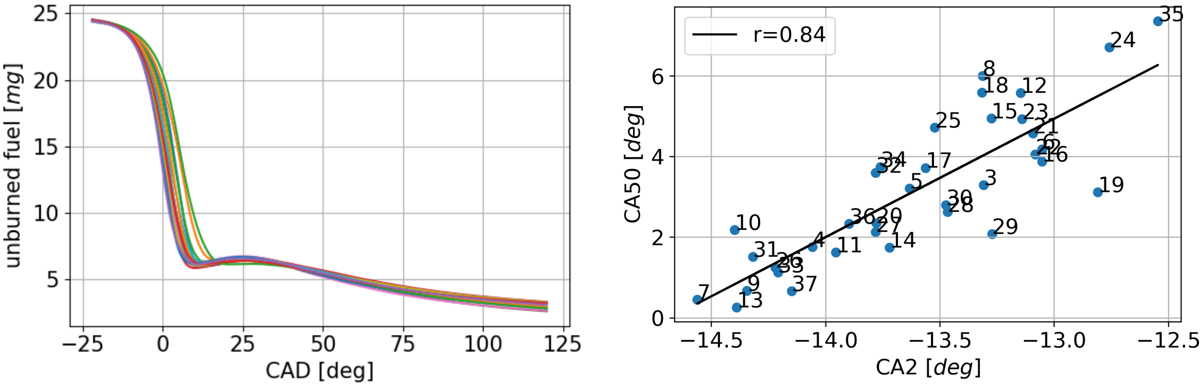

(A) Evolution of the unburned fuel in the chamber.

(B) Correlation between CA_2 and CA_{50}.

FIGURE 6.14: Definition of CA_X based on the evolution of unburned fuel mass.

To investigate the origin of the observed CCV on the combustion, we start with a qualitative analysis based on some extreme cycles to propose potential CCV factors. Quantitative descriptors are then extracted for these factors, and their relations with the combustion speed are verified using the linear correlation. In this study, 3 cycles with different combustion speeds (fast cycle 13, median cycle 20, and slow cycle 18) are selected for a qualitative comparison. The development of the flame kernel combined with the plot of the velocity field on two planes is visualized in Figure 6.15 for three chosen instants.

From the velocity field at −22.5 CAD, which is taken slightly before the ignition (cf Figure 6.15a), significant differences can be identified in the tumbling plane: in the fast cycle 13, well-organized tumble motion is still present at the end of the compression stroke, while the same tumble motion is relatively weaker in the median cycle 20, and it is not visible in the slow cycle 18 but replaced by a simple unidirectional flow. The existence of such tumble motion can also be verified on the spark plane: in the fast cycle 13, a forwarding flow from the intake to the exhaust side can be noticed along the whole X axis, especially near the spark plug, which confirms that the tumble motion in this engine cycle is well structured inside the entire combustion chamber, which is not the case neither in the median cycle 20 where the forwarding flow is only remarkable on the side of negative X, nor in the slow cycle where only a less coherent flow remains, with small velocities near the piston and near the spark plug.

The difference observed in the flow pattern before the ignition seems responsible for the preferential direction of the flame propagation, as illustrated in Figure 6.15b. At −15 CAD, the flame is convected away from the spark plug. In all three cycles, the kernel remains at the exhaust side as the global flow direction in the spark region is oriented towards the exhaust side. What differs at this instant is the flame propagation near the piston: a strong tumble motion enhances quite much the flame propagation towards the exhaust side. The flame kernel is thereby convected towards the exhaust side following the global motion, and it is also elongated and wrinkled due to the stretch effect. In the fast cycle, the high horizontal velocity allows the flame to propagate later towards the intake side. In the slow cycle 18, the flame kernel remains on the exhaust side because of the absence of a strong tumble motion on the bottom part of the cylinder.

The variation on the early stage flame propagation at −15 CA yields finally different global combustion speeds at −5 CA. The elongated flame kernel in the fast cycle 13 leads to a more homogeneous flame propagation on both sides of the chamber and thus a faster fuel consumption rate. On the contrary, in the slow cycle 18, the flame kernel is still stuck on the exhaust side, and consequently, the fuel consumption takes place firstly on the same side and later on the intake side, which slows down the combustion process.

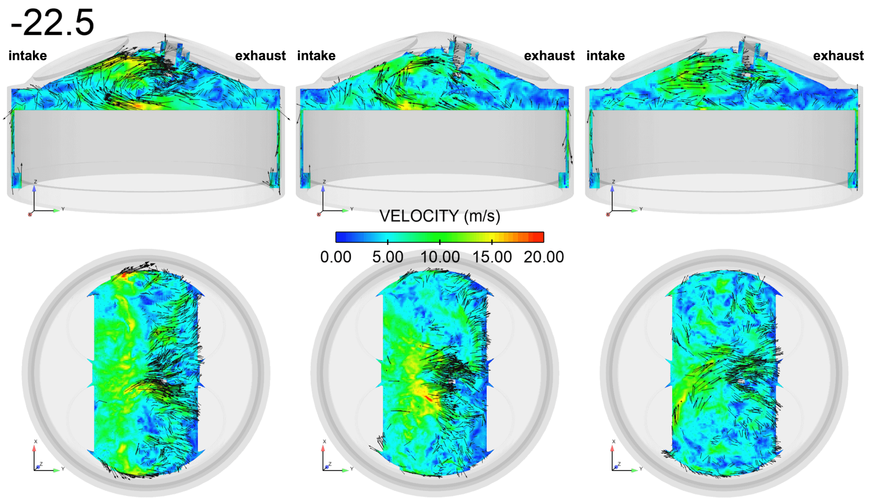

(A) −22.5 CAD.

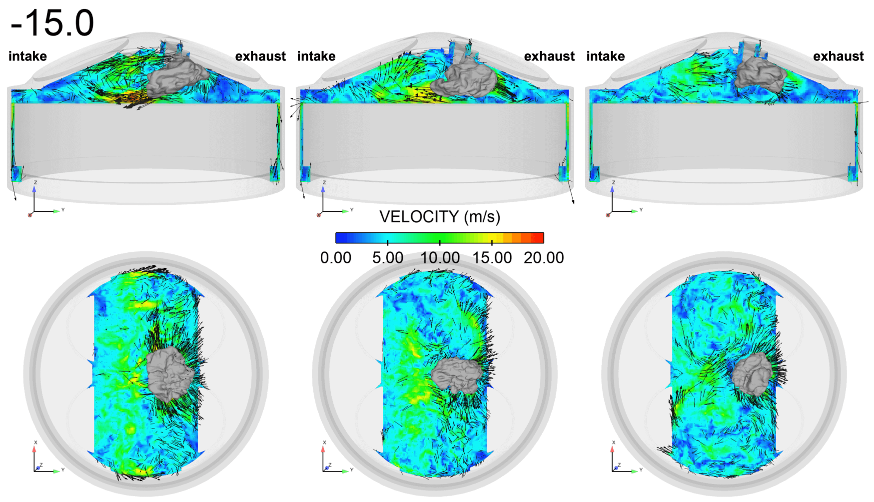

(B) −15 CAD.

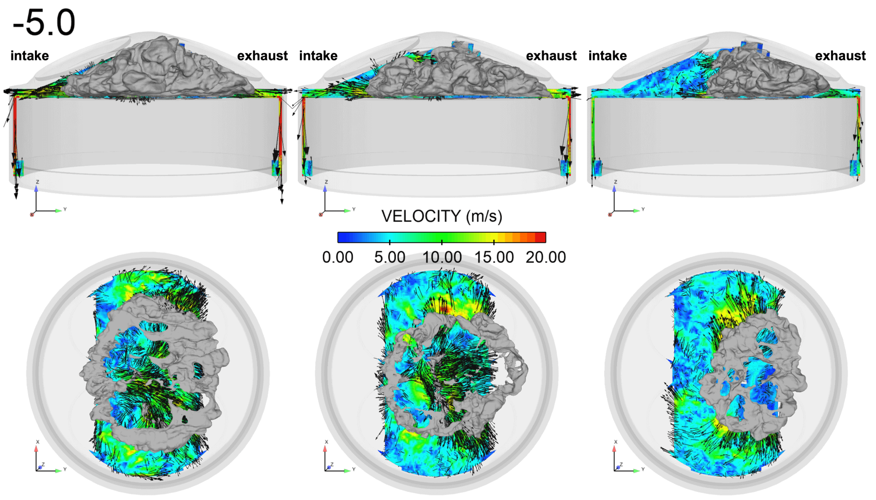

(C) −5 CAD.

FIGURE 6.15: Flame propagation in fast cycle 13 (left), median cycle 20 (middle) and slow cycle 18 (right), combined with velocity field on tumble plane($X = 5.5$ mm) and spark plane($Z = 5.5$ mm).

This qualitative analysis reveals that the flow structure before the ignition is critical and needs to be precisely analyzed quantitatively. The flow structure will be studied in the following sections, and quantitative descriptors of local and global flow features will be extracted. To quantify the importance of the flow features on combustion, the classical linear correlation is used to evaluate the relation between combustion and aerodynamics.

The total flame surface achieved at -10 CAD (red dashed line in Figure 6.16), noted as S_{-10}, is chosen to quantify the combustion speed indirectly. In the flamelet regime, which is the case of the combustion in SI engines, we have the following relation [172]:

$$\frac{S_T}{S_L} \propto \frac{A_T}{A_0} \tag{6.1}$$

where S_T is the turbulent flame speed, S_L the laminar flame speed, A_T the total flame surface, and A_0 the equivalent flame surface of a spherical flame kernel.

The total flame surface A_T is considered proportional to the turbulent flame speed as the laminar flame speed shows only slight cyclic variations, and can be used to evaluate the combustion speed.

A certain level of variability in S_{-10} is already present. The choice is based on the average CA_2 (cf Figure 6.14b), which equals -13.3 CAD. At -10 CAD, more than 2% of fuel is burnt, and the combustion state is sufficient to predict the overall combustion duration.

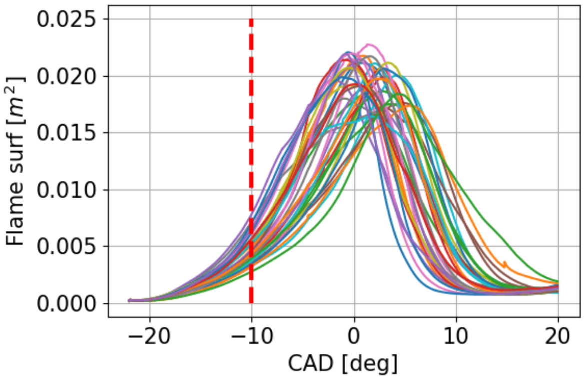

FIGURE 6.16: Evolution of flame surface for all engine cycles. The flame surface at -10 CAD is chosen to represent the combustion speed.

6.4.1 Global flow pattern

At first, the global flow pattern at -22.5 CAD is investigated. The qualitative comparison showed that the flow structure could potentially be an important factor in combustion. In this section, we would like to investigate the importance of the global flow pattern on combustion speed. A mode projection approach, inspired by the POD method, is proposed to classify the flow pattern.

For the mode projection, two modes representing two flow patterns are firstly extracted by averaging the extreme cycles using the following formula:

$$\mathbf{U}_{fast}(\theta) = \frac{1}{N_C} \sum_{i \in C_{fast}} \mathbf{U}(\theta, i) \tag{6.2}$$

$$\mathbf{U}_{slow}(\theta) = \frac{1}{N_C} \sum_{i \in C_{slow}} \mathbf{U}(\theta, i) \tag{6.3}$$

where C_{fast} and C_{slow} are respectively the subgroup of the five fastest and the five slowest cycles, $N_C = 5$ is the size of each subgroup. The resulting averaged velocity fields at -22.5 CAD are plotted in Figure 6.17.

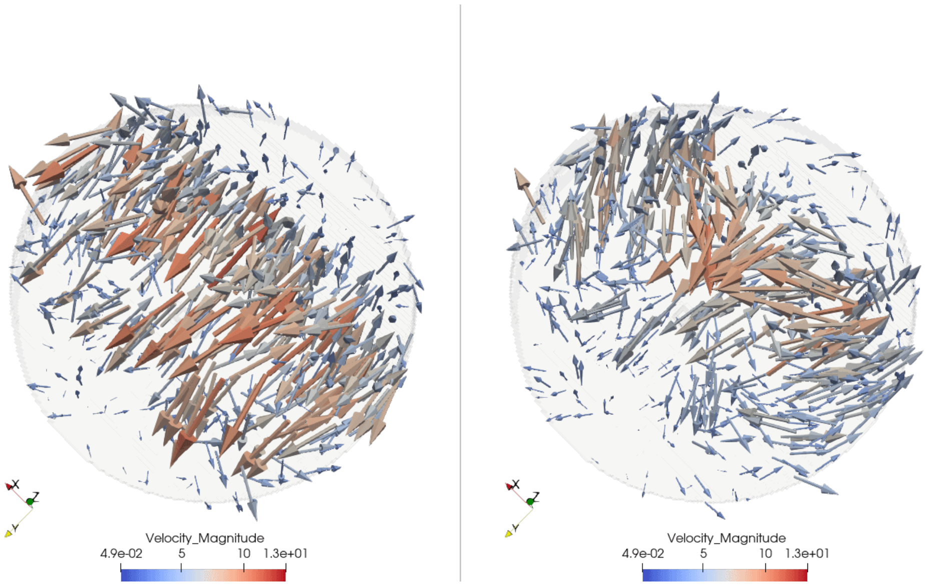

(A) 3D view.

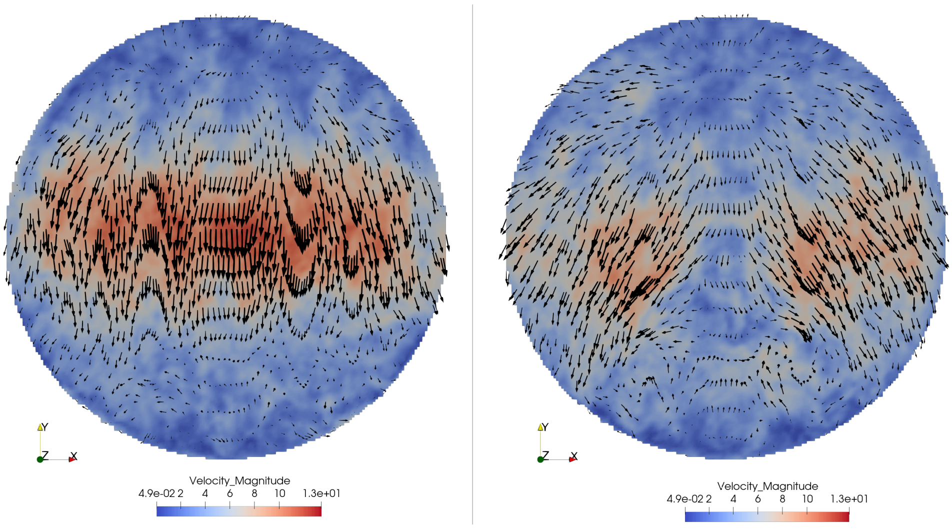

(B) 2D slice at $Z = -5$ mm.

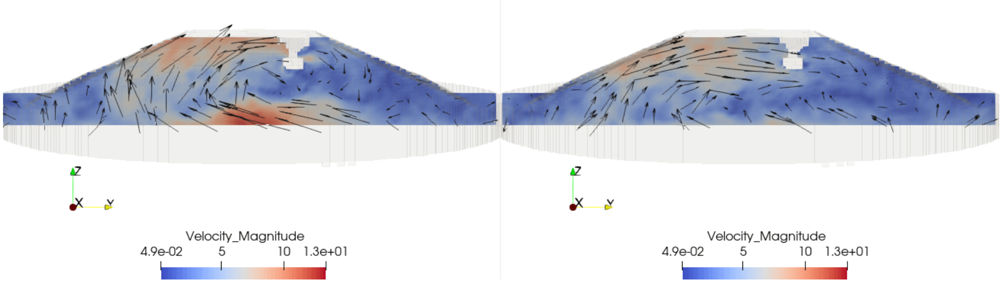

(C) 2D slice at $X = 0$ mm.

FIGURE 6.17: Fast mode (left) and slow mode (right) at -22.5 CAD obtained by averaging the extreme cycles.

It can be noticed that the flow modes representing fast and slow cycles show apparent differences between each other: the fast mode corresponds to a dominant rotation around the X axis in the counterclockwise direction, while the slow mode contains a vortex pair principally. The flow pattern of the fast mode can also be observed in cycle 13, and that of the slow mode is more similar to the one in cycle 18.

To quantify the similarity between the flow pattern of a given cycle and a flow mode, fast or slow, a coefficient of projection is computed using the following formula:

$$C_X^i = \frac{1}{V}\int \frac{\mathbf{U}_i \mathbf{U}_X}{\|\mathbf{U}_i\|\,\|\mathbf{U}_X\|} dV \tag{6.4}$$

where X denotes fast or slow mode projection and i the index number of each cycle. With the volume averaging, the coefficient of projection measures the averaged cosine of the angle between the velocity field $\mathbf{U}_i$ of cycle i and the chosen flow mode $\mathbf{U}_X$ at each point. C_X^i varies between 0 and 1: it equals 1 if the given velocity field $\mathbf{U}_i$ is identical to the mode $\mathbf{U}_X$. In contrast, it equals 0 if the given velocity field $\mathbf{U}_i$ is totally uncorrelated with the mode $\mathbf{U}_X$.

The obtained coefficients C_{fast} and C_{slow} are then used to be correlated with the flame surface S_{-10}. The results are plotted in Figure 6.18.

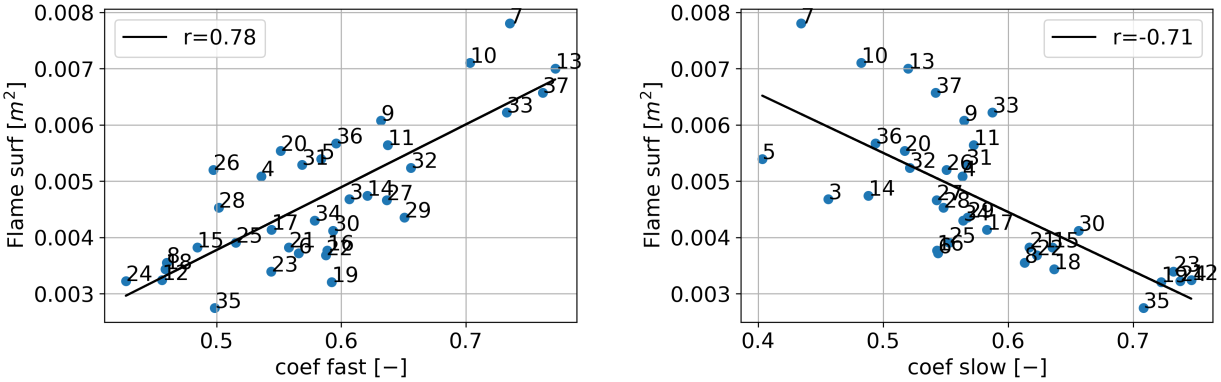

(A) Fast mode projection.

(B) Slow mode projection.

FIGURE 6.18: Correlation between the combustion speed and the coefficients of projection.

Both fast and slow coefficients are strongly correlated with S_{-10}, indicating that the global flow pattern at spark timing is crucial to the combustion process, as already observed in the qualitative analysis. It should be noticed that when realizing the projection, the velocity field used contains both large-scale structures and resolved smaller eddies which can impact the combustion process in different ways, locally or globally. Hence, in the following sections, analysis tools will be applied to the velocity fields to decouple different scales and investigate their links with the combustion speed.

6.4.2 Local flow near the spark

First, the local flow state is studied here as it is one of the classical flow descriptors in similar CCV studies [37, 91, 173]. As shown in Figure 6.19, the local flow characteristics are evaluated in a sphere of radius equal to 2.5 mm centered at the spark point. The choice of the sphere size is the same as that used in the analysis of the motored case in section 5.5.3. Averaged values of the three velocity components U_x^{mean}, U_y^{mean} and U_z^{mean} as well as the kinetic energy E_k^{mean} are all computed in the spherical volume.

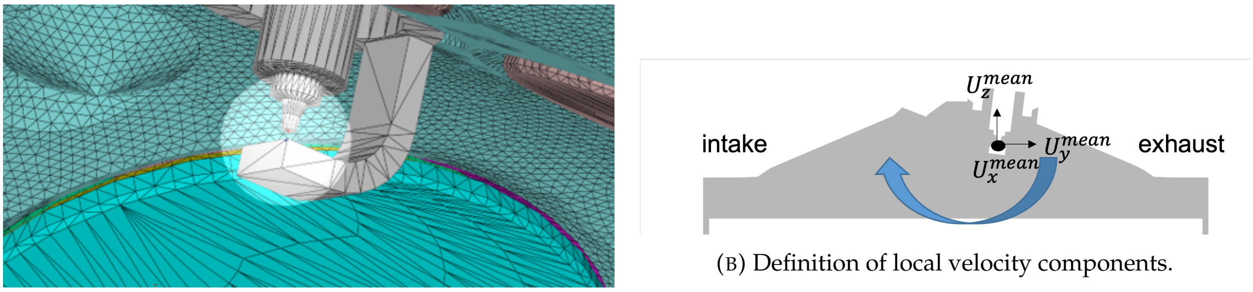

(A) Location of the sphere.

(B) Definition of local velocity components.

FIGURE 6.19: Local flow characterization in a sphere surrounding the spark plug.

The correlation between the combustion speed and the averaged local flow state is listed in Figure 6.20.

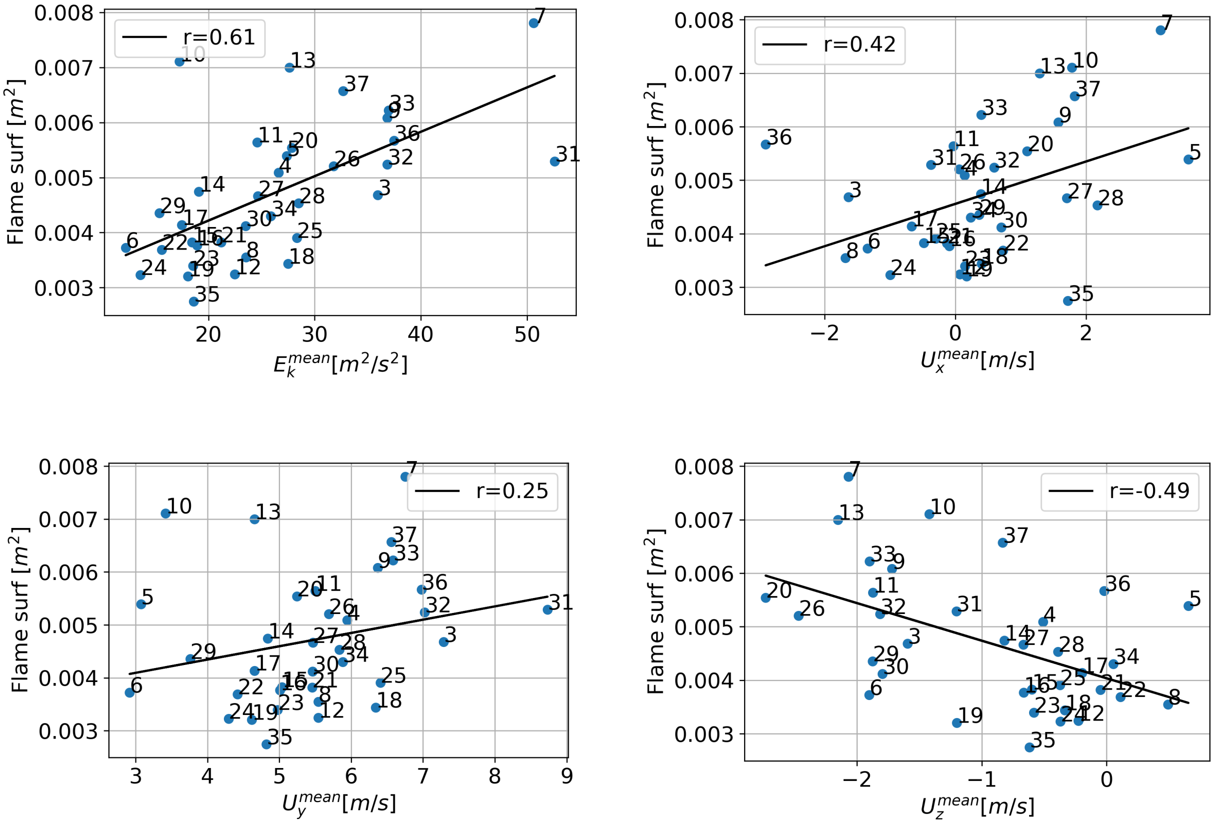

FIGURE 6.20: Correlation between local flow state at −22.5 CAD and combustion speed.

Among the four averaged quantities, the local kinetic energy is the most correlated with the combustion speed. Nevertheless, it contains contributions from large-scale motion and small-scale fluctuation, and their impact can not be decoupled without the help of scale separation tools. The three velocity components seem to only have a mild correlation with the combustion speed:

- positive U_x^{mean} is weakly correlated with fast combustion, which can be explained by the fact that the open side of the spark plug is located towards the positive X side, and therefore the flame front can propagate away from the spark plug region shortly after the ignition; We recall that the X direction is orthogonal to the tumble plane.

- U_y^{mean} is not significantly correlated with the combustion speed, possibly because the flow in this direction can be generated either by an organized tumble motion or a vortex pair, as shown in Figure 6.18. Its value remains positive in all the cycles, indicating that the flame kernel is always transported to the exhaust side at the beginning of the combustion. The later development is then determined by the global motion as revealed in the quantitative analysis;
- negative U_z^{mean} is more favorable to fast combustion, as it allows the flame front to be convected and elongated downward inside the chamber instead of a relatively modest consumption near the cylinder head.

The local velocity at spark timing is supposed to transport the early flame kernel in the local flow direction. The correlation between the local velocity and the flame kernel center is investigated at two crank angles -17 and -10 CAD shortly after spark timing at -22.5 CAD. The position of the flame kernel center x^{flame} is computed using the expression below:

$$x_i^{flame} = \frac{\int \tilde{c}\, x_i \, dV}{\int \tilde{c}\, dV} \tag{6.5}$$

The definition of the gravity center inspires the expression above, and the progress variable $\tilde{c}$ is used here instead of density. Results are presented in Figure 6.21.

At -17 CAD, about 5.5 CAD after ignition, the flame center strongly correlates with the local velocity at spark timing, indicating that the local flow mainly determines the flame propagation shortly after ignition. However, at -10 CAD, when the flame begins to expand in the chamber, the correlation in the Y direction is much less significant. The correlation in the X direction remains strong, which can be associated with the impact of the spark plug orientation. The component U_x^{mean} does not belong to the large-scale motion observed in the tumble plane, suggesting a potential 3D impact of the local flow on the flame propagation.

The importance of the local velocity on the flame propagation is revealed, while the local flow direction is not sufficient to determine the combustion speed. The local kinetic energy is also found to be responsible for the combustion speed. However, the local velocity contains the large-scale motion and the turbulent fluctuations simultaneously, and their impacts are not decoupled. In the following sections, a particular focus will be placed on decoupling impacts from structures of different scales.

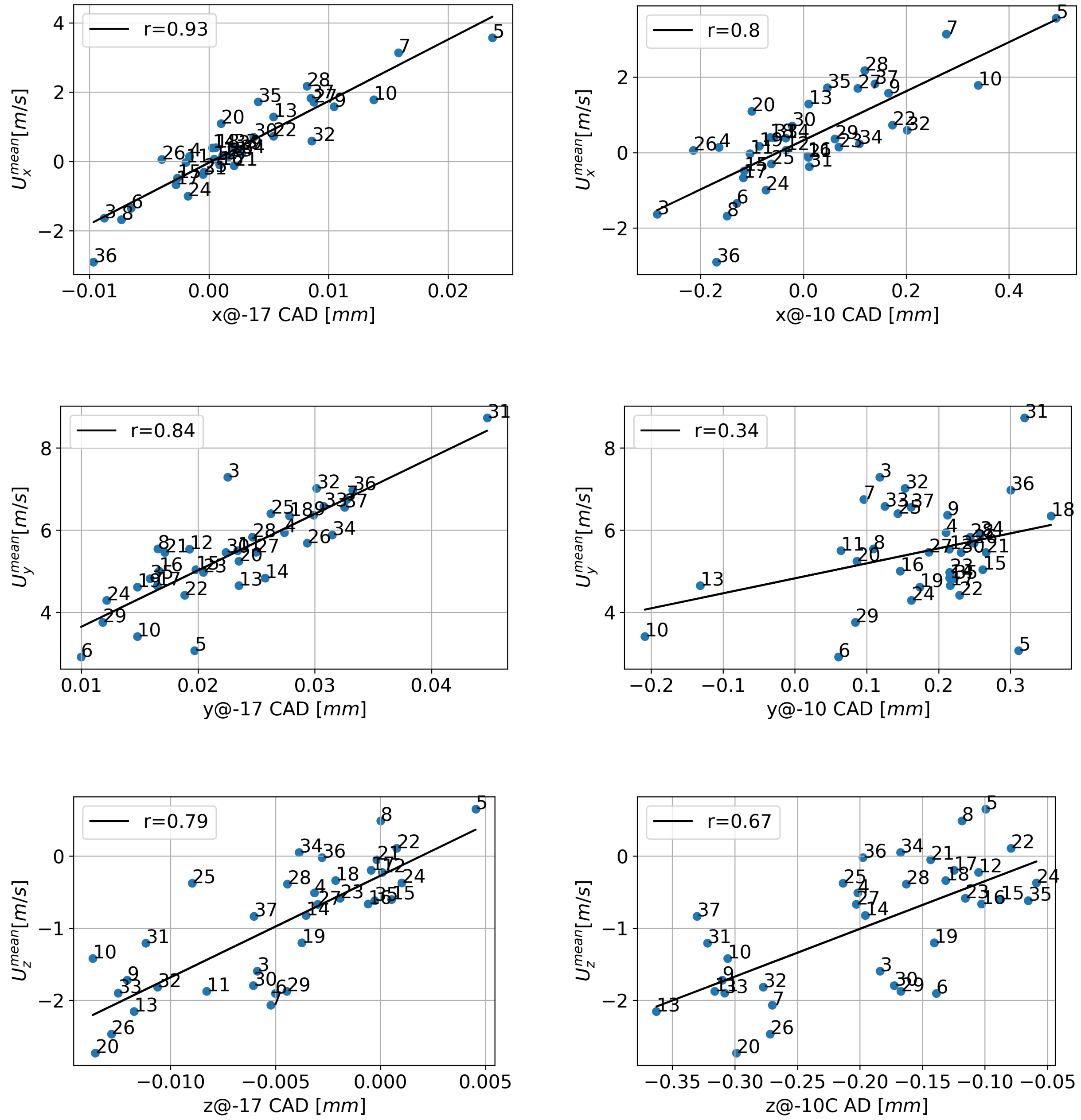

FIGURE 6.21: Correlations between the local velocity and the flame kernel position at -17 and -10 CAD.

6.4.3 Global motions in the combustion chamber

The tumble motion can generally represent global motions in the combustion chamber and can be more or less organized at spark timing, as seen previously in Figure 6.17. An analysis based on a 2D view is conducted to characterize the tumble motion.

The tumble plane at $X = 0$ mm is used to characterize the tumble flow, as the tumble motion can be visualized in this plane. As mentioned before, flow structures of different scales need to be separated to investigate their impact on the combustion process. For this purpose, bivariate 2D EMD is applied to the velocity field of the tumble plane at -22.5 CAD, and the results of the three exemplary cycles are shown in Figure 6.22, including the velocity magnitudes of different contributions and their corresponding velocity vectors.

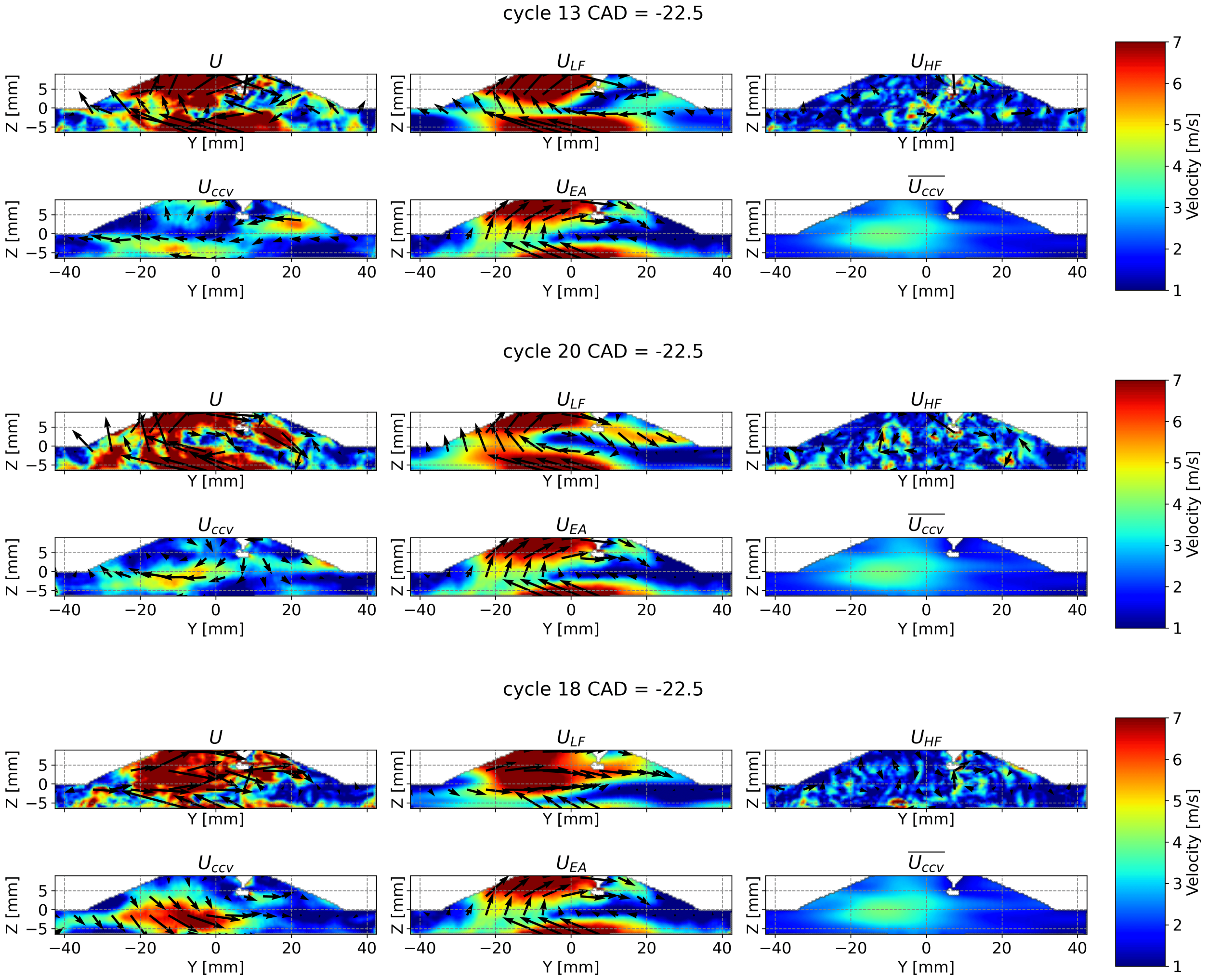

FIGURE 6.22: Application of bivariate 2D EMD in the tumble plane at -22.5 CAD.

Comparing the extracted LF part U_{LF} shown in Figure 6.22, it can be noticed that the large-scale motion behaves quite differently in fast and slow cycles in a much clearer way than what has been observed on the instantaneous field. Regarding the U_{ccv} field, it can be seen that the CCV of large-scale structures are mainly located in the tumbling flow as observed before in the flow mode analysis: in the fast and medium cycles 13 and 20, the flow is upward on the intake side which follows the rotational tumble motion; in the slow cycle 18, the flow direction of the same region is towards the exhaust side which coincides with the previous observation on the flow mode analysis (cf Figure 6.17c). The averaged CCV part $\overline{U_{ccv}}$ field also confirms that CCV in large-scale structures mainly resides on the intake side, where the local flow direction allows distinguishing the two types of flow patterns. On the contrary, the HF part U_{HF} presents differences but remains difficult to compare qualitatively.

The horizontal plane at $Z = 5.5$ mm passing the spark plug is added to complete the observation in the tumble plane. The results of bivariate 2D EMD are presented in Figure 6.23.

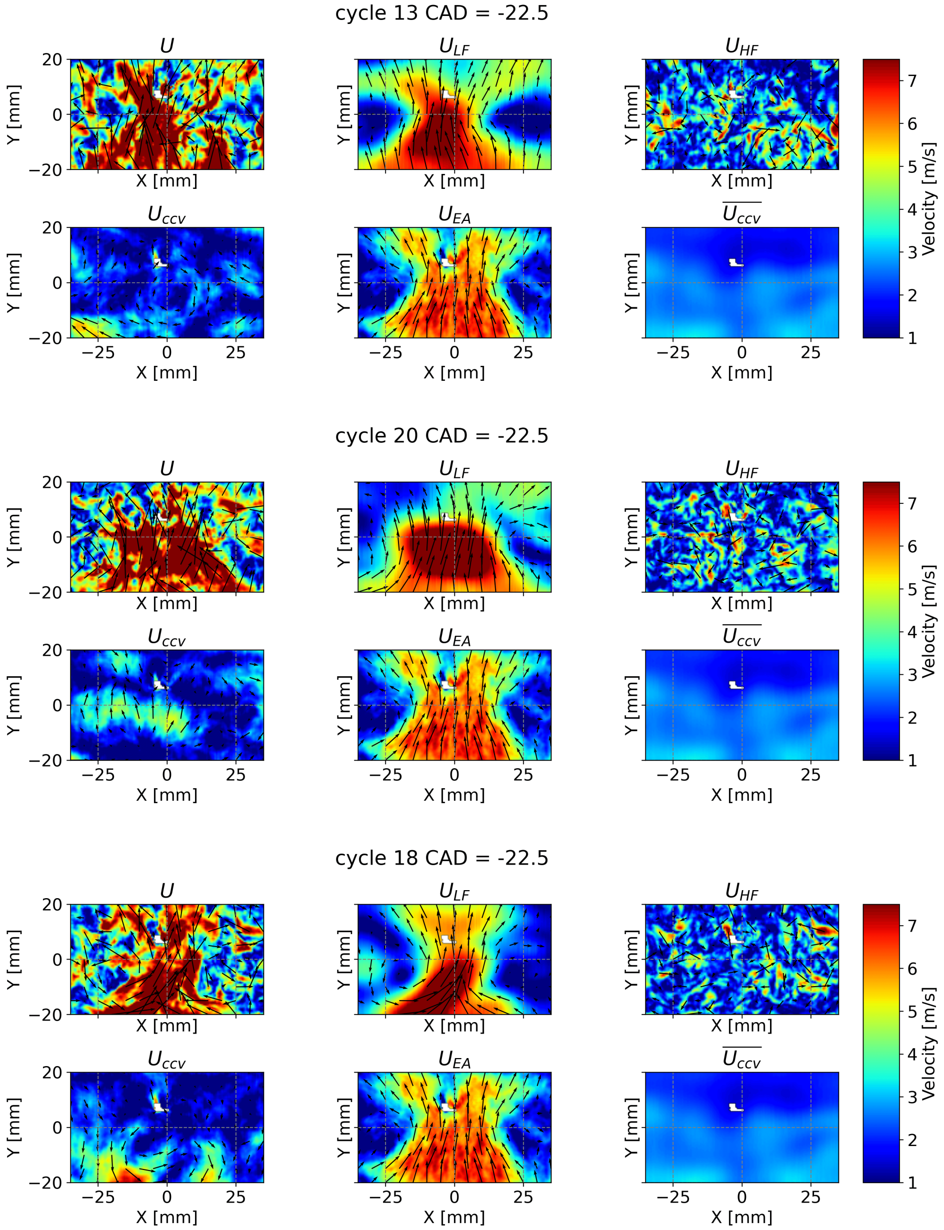

FIGURE 6.23: Application of bivariate 2D EMD in the spark plane at $Z = 5.5$ mm at -22.5 CAD.

Similar to the observation in the tumble plane, the LF part U_{LF} shown in Figure 6.23 differs a lot between the three cycles. The forwarding flow towards the exhaust side (positive Y) is much more expanded in the transversal direction in the fast cycle 13 and narrower in the slow cycle 18. The averaged CCV part is relatively more important in regions of weak motions on both sides of the central flow. The spark plane also emphasizes the 3D nature of large-scale motion.

Based on the separated LF and HF part of each cycle in the tumble plane, quantitative descriptors can be extracted, including the kinetic energy contained in each part and their characteristic scales in both horizontal and vertical directions. Correlations are then established to seek links between the combustion process and LF/HF parts of the flow at spark timing.

In Figure 6.24, correlations between the LF part and the combustion speed are shown. E_k^{LF} is the averaged kinetic energy of the LF part over the tumble plan. It quantifies the kinetic energy contained at the largest scale of the flow motion. L_y^{LF} and L_z^{LF}, estimated from the normalized two-point correlation function (cf Eq. 5.15), quantify the scales of the tumble motion in Y (horizontal) and Z (vertical) directions, respectively. The kinetic energy and the scale in the Z direction of the flow observed in the tumble plane correlate positively with the combustion speed. The scale in the Y direction seems uncorrelated, which can be interpreted as it does not allow determining the flow pattern. For the two types of flow patterns, convective (*e.g.*, cycle 18) and rotational (*e.g.*, cycle 13), their horizontal scales could be quite close. Nonetheless, the convective type flow pattern remains on the top side of the chamber while the rotational type flow pattern fills the chamber vertically. Therefore the scale in the Z direction is generally larger for cycles with an organized tumble flow and is qualified as a good indicator of the flow pattern. The total height of the chamber at this instant is equal to 16 mm, and the scale in the Z direction of some extreme cycles reaches almost 7 mm, indicating that a well-organized flow exists in these cycles. These two correlations emphasize the importance of a well-organized flow with high kinetic energy and a large scale in the Z direction for fast combustion.

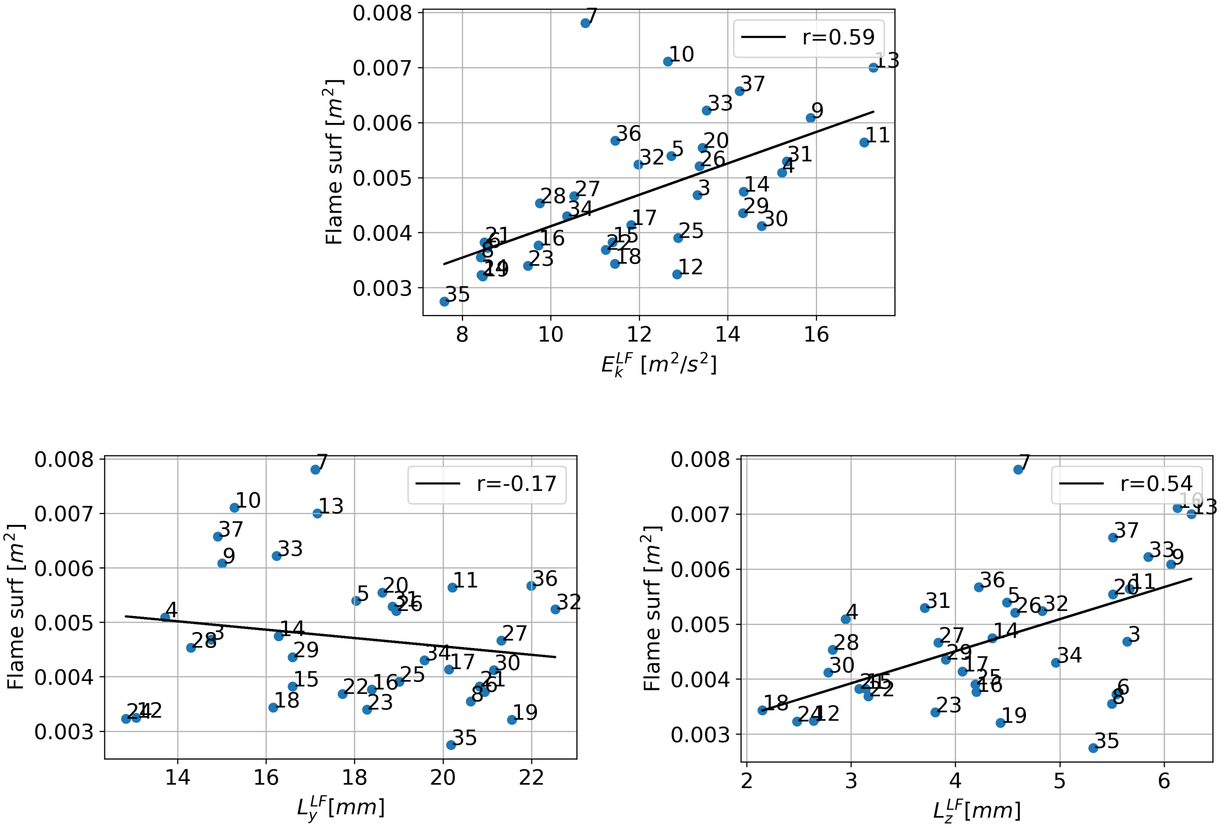

FIGURE 6.24: Correlations between the combustion speed and the LF part of the flow at −22.5 CAD.

A spatial correlation study is also conducted to investigate the link between local flow features and combustion speed. The CCV part U_{ccv} is extracted by subtracting the ensemble-averaged velocity from the LF part and then used for the correlation analysis. The correlation coefficient is computed between each point of the CCV part U_{ccv} and the combustion speed and then plotted in Figure 6.25.

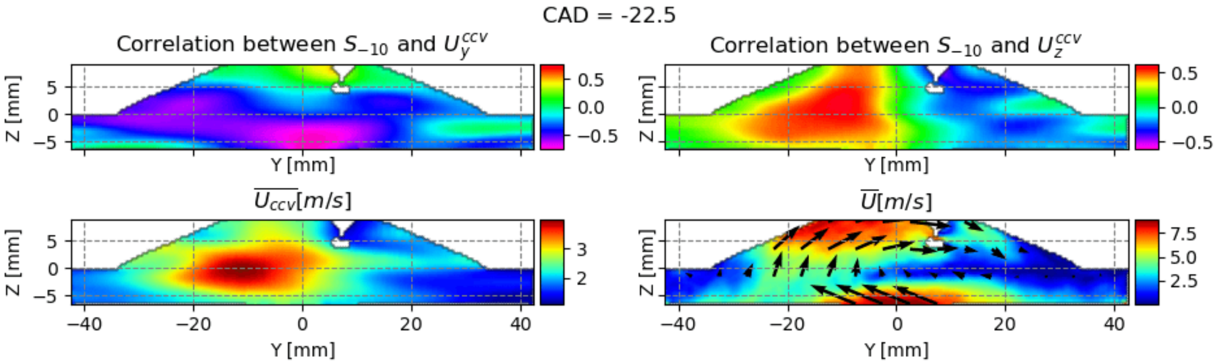

FIGURE 6.25: Correlation between the combustion speed and U_{ccv} in the tumble plane at −22.5 CAD.

Significant correlations can be marked in several regions:

- For the horizontal component U_y^{ccv}, weak positive correlations can be noted near the spark plug. In contrast, strong negative correlations are present in the lower region (left side and near the piston). These two regions correspond to the tumble motion's front and end. In the case of the strong tumble motion, the rotation is generally faster. Thus both the front and the end of the tumble motion move faster, respectively, to the positive and negative Y direction.
- For the vertical component U_z^{ccv}, positive correlations are located on the intake side and negative correlations near the spark plug. The region near the spark plug is coherent with what is observed with U_y^{ccv}: this region is part of the tumble front, and for a strong tumble, the flow direction is descending and pointing towards the exhaust side. The intake side region is related to the local flow direction: the flow is upward if the global flow pattern is rotational.

The same analysis is also made in the spark plane at $Z = 5.5$ mm and presented in Figure 6.26.

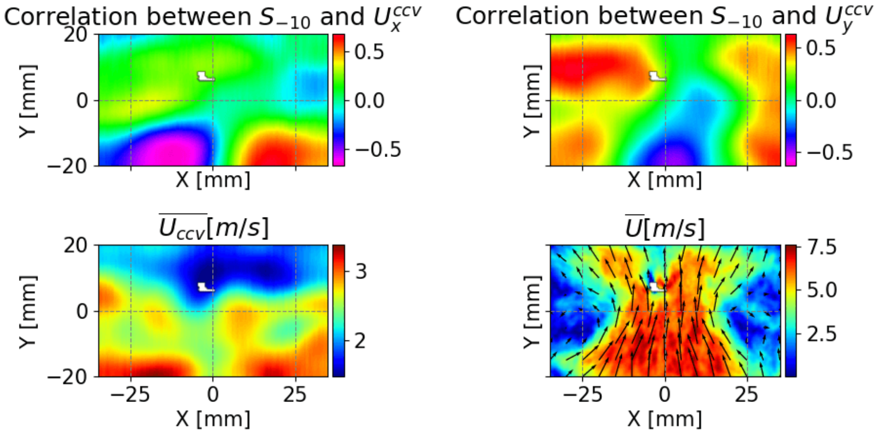

FIGURE 6.26: Correlation between the combustion speed and U_{ccv} in the spark plane at −22.5 CAD.

Significant correlations with the transversal component U_x^{ccv} are located at the bottom side of the spark plane, where the forwarding flow begins to converge to the central part. The component U_y^{ccv} also presents significant correlations on both sides of the plane and the central side where most forwarding flow passes. The two correlation maps suggest that a less concentrated flow in the X direction of higher velocity in the Y direction is favorable for fast combustion, which confirms the results of the flow mode analysis. The local U_x was found important for the flame propagation. However, U_x^{ccv} does not show any correlation in regions near the spark plug, as shown in the corresponding correlation map. The remained high-frequency turbulent part of U_x might be responsible for the impact on the combustion, which will be verified later.

In the local flow analysis based on the instantaneous velocity field, no significant link was found between the local flow direction and the combustion speed. In contrast, the analysis based on a 2D view using bivariate 2D EMD highlights the importance of the large-scale global motion (LF part) in the combustion process. However, we should remember that the tumble has its 3D features. The 2D analysis is limited as only the tumble visualized in the symmetrical tumble plane, completed by the observation in the spark plane, is characterized and linked to the combustion. Therefore, a 3D analysis is carried out to better describe the tumble's structure and complete the 2D analysis. For experimental studies, the methodology of 2D analysis is still of interest since 3D information is challenging to obtain.

The 3D analysis is essentially based on the quantity Γ_{3p} with which the rotation kernel of the tumble can be extracted and visualized, as we have seen in the study of the motored case in Chpater 5. By computing Γ_{3p} for all the cycles at spark timing, it becomes possible to bring out more clearly the structure of the tumble inside the whole combustion chamber rather than on the symmetrical plane. As presented in Chapter 4, Γ_{3p} is a vector field whose magnitude indicates if a rotation is organized around the corresponding point and whose direction represents the local axis of rotation.

The results of Γ_{3p} obtained for the three cycles (fast 13, slow 18, and medium 20) are illustrated in Figure 6.27. By choosing a threshold value of 0.5, the iso-surface of $|\Gamma_{3p}|$, considered as the tumble kernel, is visualized in Figure 6.27a. The Γ_{3p} field on the 2D slice at $Y = 0$ mm is also plotted to provide the local direction of the rotation axis inside the tumble kernel.

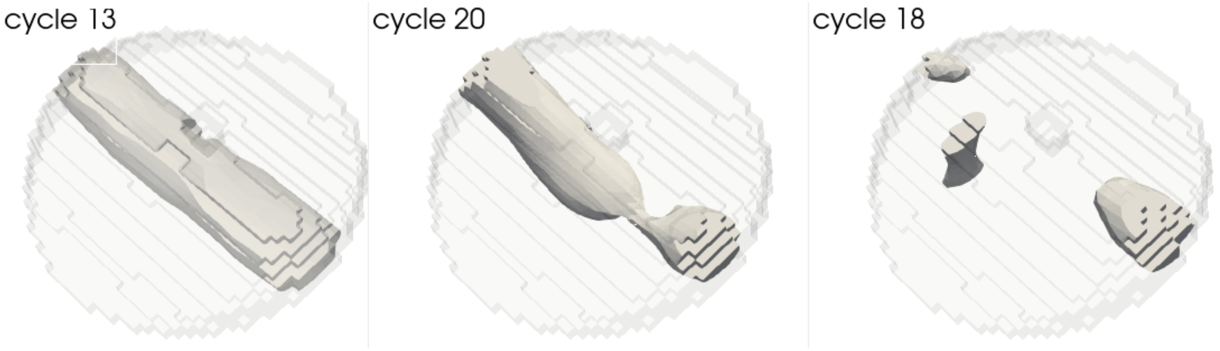

(A) Iso-surface of $|\Gamma_{3p}| = 0.5$ at -22.5 CAD.

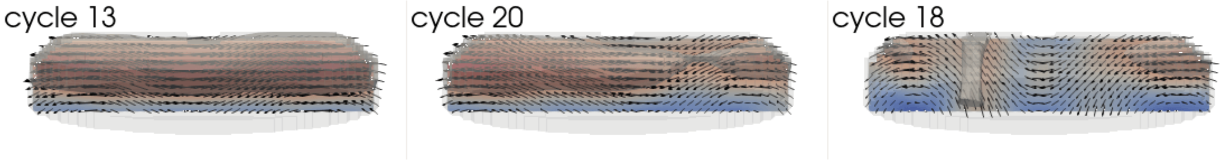

(B) 2D slice of $|\Gamma_{3p}|$ at $Y = 0$ mm.

FIGURE 6.27: Visualization of the tumble kernel with Γ_{3p}.

From the extracted tumble kernel, it is clear that a global rotation is well organized along the X direction in cycle 13, partially less organized on the right side in cycle 20, and almost disappeared in cycle 18 except in some regions of local rotation. Regarding the rotation direction presented on the 2D slice which passes through the tumble kernel, it can also be noticed that the local direction of the rotation axis is basically aligned with the X axis in cycle 13 and that the rotation axis in the restricted region on the right side in cycle 20 is no longer aligned with the X axis. The change in rotation direction is much more evident in cycle 18, in which the rotation axes are largely inclined on both sides. Thus the global rotation is no more similar to a classical tumble motion but becomes a vortex pair, which confirms previous observations on the flow pattern of the slow mode presented in Figure 6.17b. Compared to the tumble kernel of the cycle 13, the one of the cycle 18 seems to have experienced a distortion during the compression stroke. Nonetheless, it is worth noting that the global motion, either a tumble or a vortex pair, is still present in the chamber even before spark timing. Classically, a tumble breakdown is expected in SI engines, yielding an energy transfer from large- to small-scale structures and caused by the reducing room available in the chamber during the compression stroke.

The Γ_{3p} is a suitable tool to identify regions of organized rotation, but it does not help quantify the rotation speed. To complete the description of the tumble evolution, both on its spatial structure and intensity, the use of a local tumble ratio **TR** is proposed. Unlike the classical tumble ratio, which is a global scalar quantity characterizing the angular momentum around the principal axis of the tumble motion, **TR** is calculated locally along the tumble center line and quantifies the rotation intensity around the local rotation axis, as explained in Chapter 4.

The computed **TR** is then decomposed into three components, corresponding to a tumble motion TR, a cross-tumble motion CTR and a swirl motion SR by projection in the three directions. Their definition is recalled in Figure 6.28

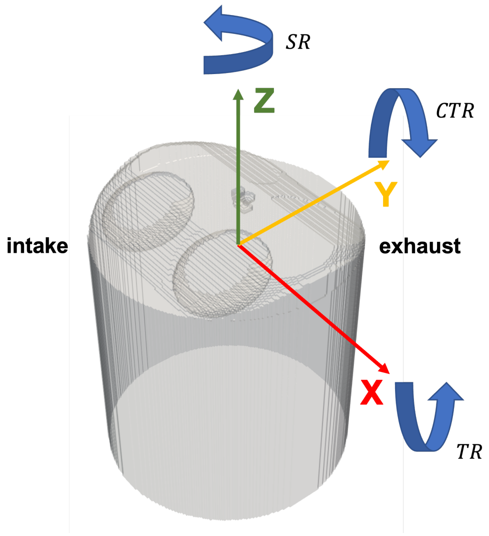

FIGURE 6.28: Components of the normalized angular momentum **TR** in the X (TR), Y (CTR), and Z (SR) directions.

Their evolution along the X axis is plotted in Figure 6.29 for the three cycles. The absolute value of TR is noted as $|\mathrm{TR}|$, which differs from that of the norm of **TR** noted as $|\mathbf{TR}|$.

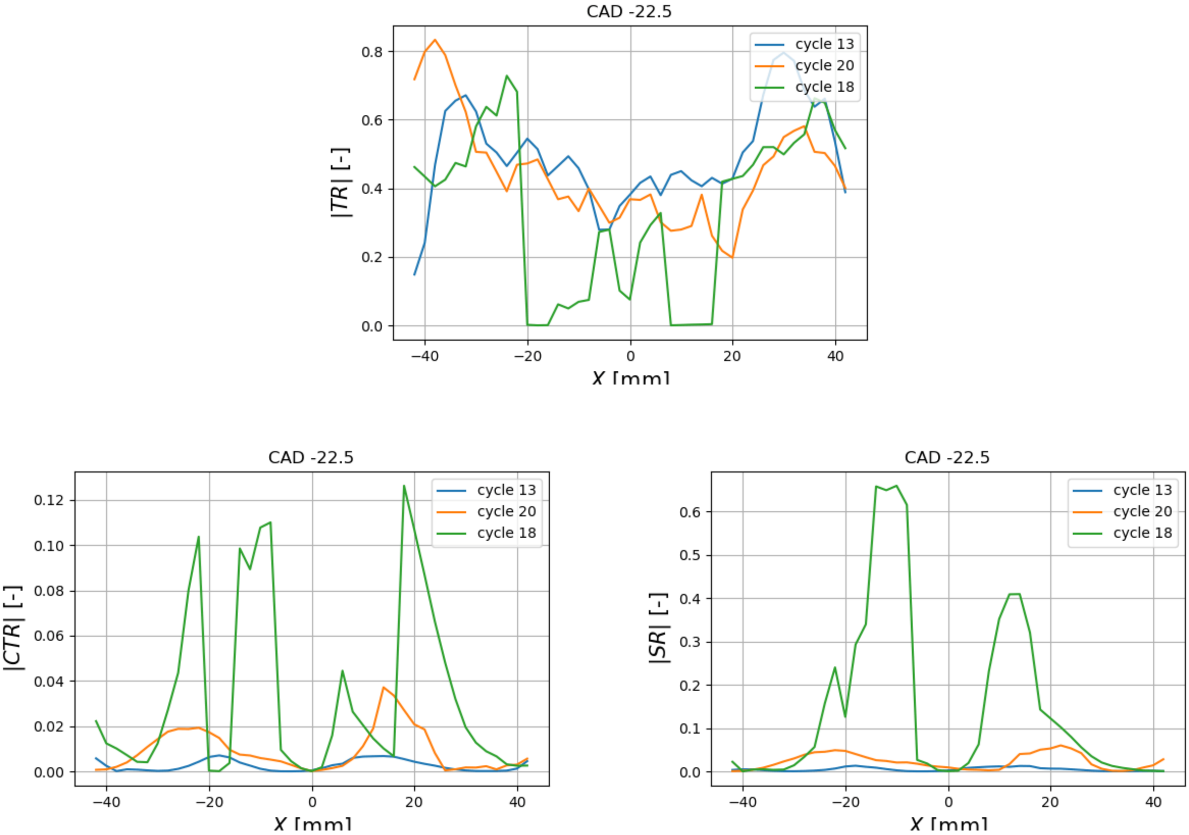

FIGURE 6.29: Evolution of the three components of the local normalized angular momentum called **TR**, computed along the tumble center line, as a function of X coordinate.

The evolution of all three components differs between the three chosen cycles:

- The component TR, similar to the classical tumble ratio definition, quantifies the rotation intensity around the X axis, which is also the principal rotation axis of the tumble. It can be seen that the major difference is located in the central part around the spark plug region: TR is globally higher in cycle 13 and cycle 20 while it drops to 0 locally in cycle 18. The behavior of TR in the spark plug region also agrees with the observation on the 2D tumble plane. In addition, compared to the evolution in cycle 13, TR decreases slightly around $X = 20$ mm, which is consistent with the restricted region that has been remarked on the tumble kernel visualization in Figure 6.27a.
- Other two components CTR and SR remain relatively small compared with TR, but their evolution shows a significant disparity between different cycles. Their values in cycle 18 are much greater than those in cycle 13 and cycle 20. Moreover, regions of high values of CTR and SR correspond to a significant inclination of the local rotation direction with respect to the X axis.

The three components are then averaged over the tumble center line and correlated with the combustion speed. Concerning TR, the global average and the local average evaluated in the region -10 mm$< X < 10$ mm are both used for the investigation. All the correlations are shown in Figure 6.30.

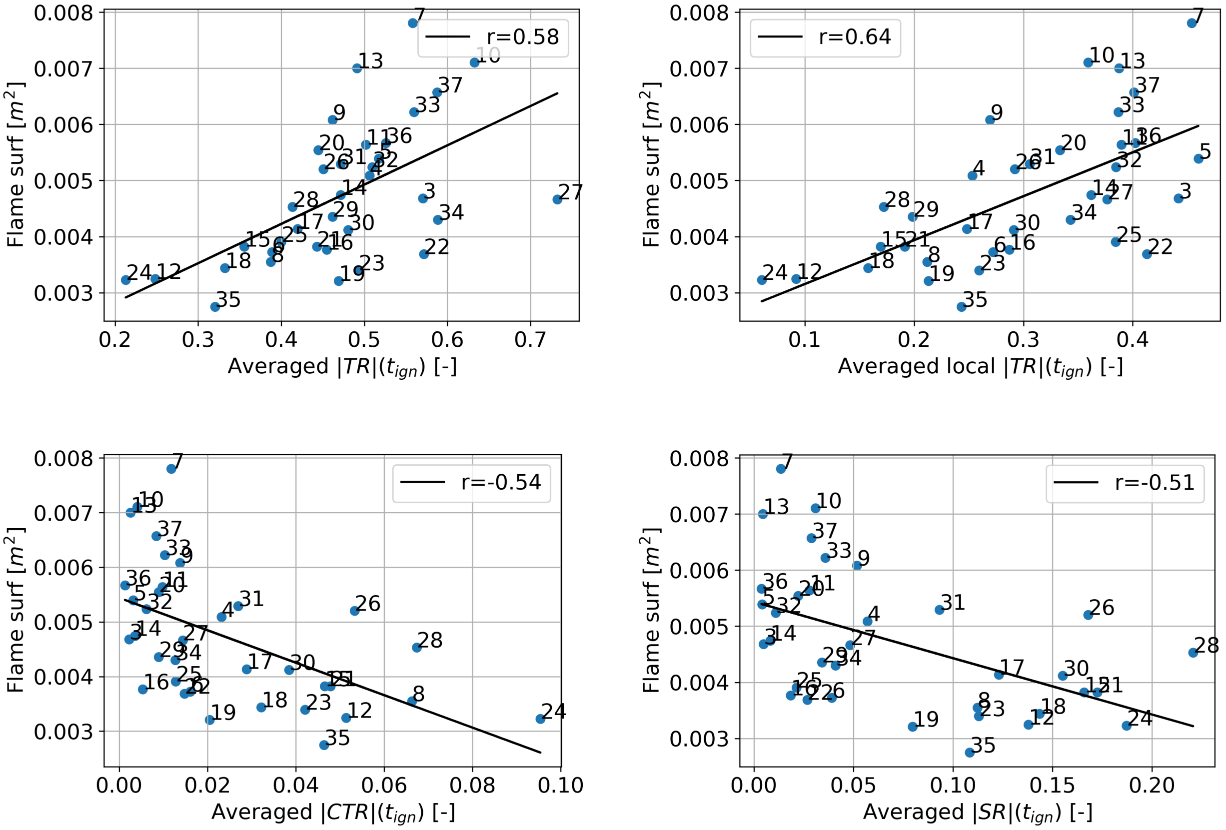

FIGURE 6.30: Correlations between the combustion speed and different components of the averaged local tumble ratio **TR**.

The results highlight a strong positive correlation between the combustion speed and the averaged TR, especially the one in the spark plug region, which supports the conclusion that a strong tumble motion is favorable for fast combustion due to convective and stretch effects on the flame propagation. The other two components CTR and SR are negatively correlated with the combustion speed. The three components of TR describe the flow structure quantitatively at spark timing: the averaged TR of high value corresponds to the flow pattern of fast mode in which a rotation around the X axis is well organized. In contrast, the averaged CTR and SR of high value are more associated with the flow pattern of slow mode in which a vortex pair is present.

Correlations are also computed between different components of TR as shown in Figure 6.31. The local averaged TR is strongly negatively correlated with averaged CTR and SR. It reveals a potential flow pattern switching: in fast cycles, the tumble motion stays dominant, and hence CTR and SR remain small; in slow cycles, the tumble is transformed into the vortex pair, which results in a relatively small TR and large CTR and SR. This flow pattern switching should occur earlier than spark timing and must be studied during the whole compression stroke. Γ_{3p} will still be a valuable tool to visualize the tumble kernel at different instants apart from spark timing.

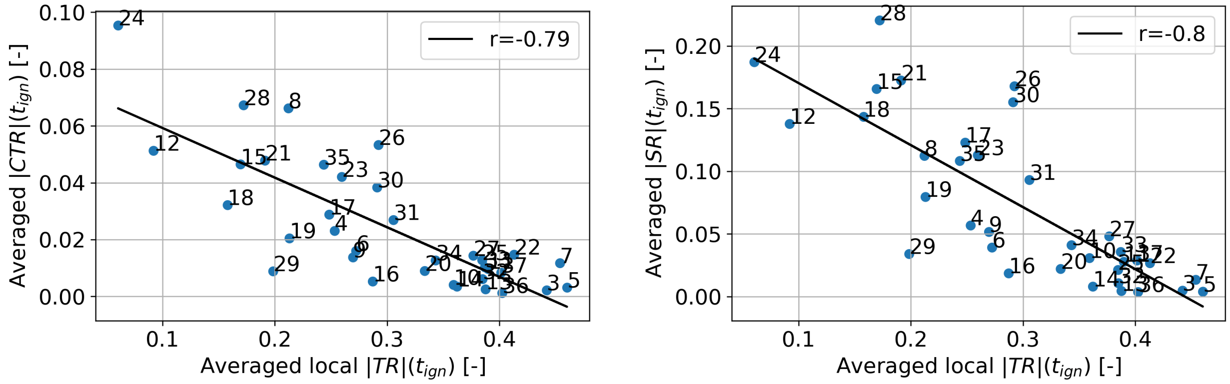

FIGURE 6.31: Correlations between different couples of **TR** components.

6.4.4 Local turbulence intensity near the spark

In the previous section, the tumble motion in the 2D tumble plane has been carefully studied using bivariate 2D EMD. The LF part has been used to quantify the tumble's scales and intensity, and the HF part was not investigated. In this section, the same analysis applied to the LF part is also conducted for the HF part, and all the correlations are presented in Figure 6.32. It should be mentioned that the velocity component normal to the tumble plane is excluded in the analysis.

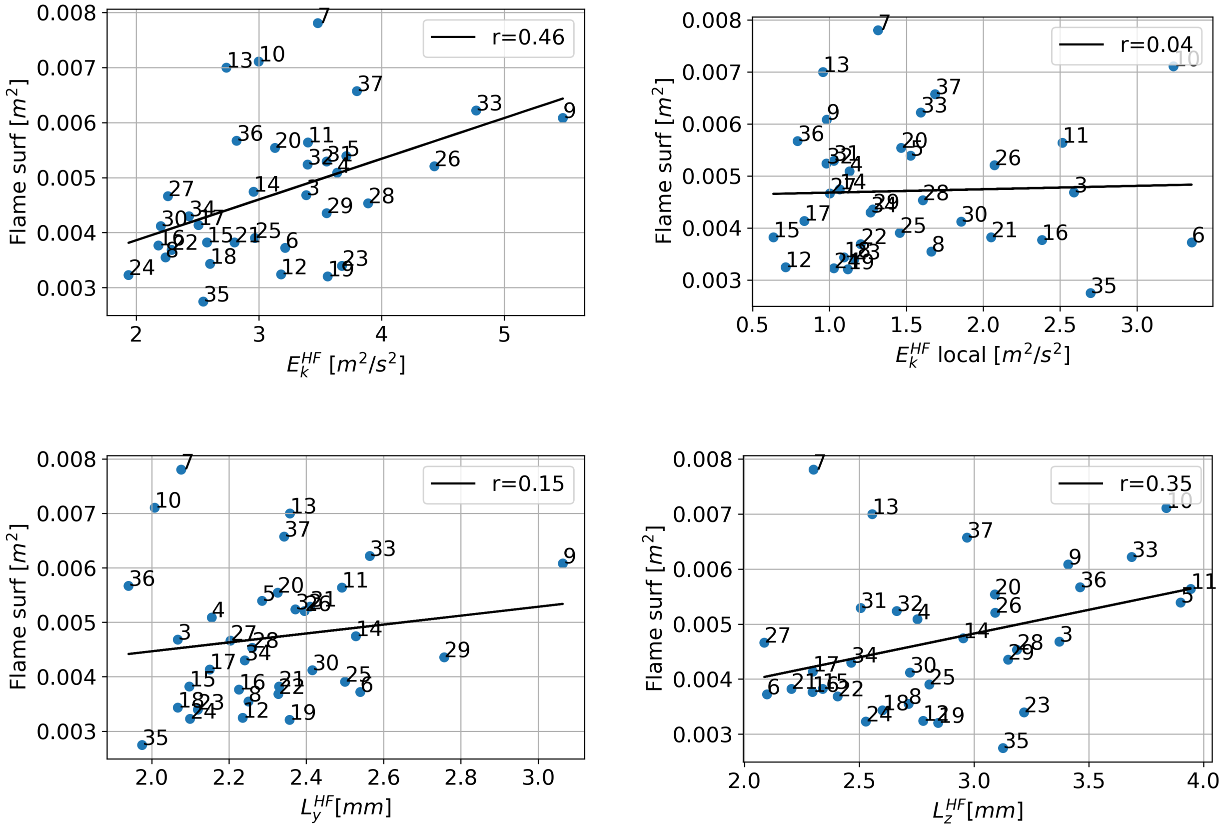

FIGURE 6.32: Correlations between the combustion speed and the HF part of the flow at −22.5 CAD.

The global averaged kinetic energy of the HF part E_k^{HF} is moderately correlated with the combustion speed, while the turbulence scales seem to be not impacting. The local averaged kinetic energy of the HF part is also evaluated (in the same volume presented in Figure 6.19a) since the local turbulence interacts with the initial flame kernel right after the ignition. However, the local E_k^{HF} is not at all correlated with the combustion speed. As a reminder, the turbulence on the 2D tumble plane is not correctly defined as only tangential components of the velocity are taken into account when doing bivariate 2D EMD. The normal component could also behave quite differently between cycles. Hence, to extract the real local turbulent energy, the spatial 3D EMD method, presented in Chapter 4, is applied to the 3D velocity field at -22.5 CAD.

The averaged 3D local kinetic energy, evaluated in the sphere of $r = 2.5$ mm around the spark plug, has proved to be correlated with the combustion speed (cf Figure 6.20). By applying trivariate 3D EMD, the flow field is decomposed into 3D LF and 3D HF parts. With the 3D HF part, we also compute the ensemble-averaged integral length scales over the 35 cycles in the three directions using the same method presented in section 5.5.3, which gives 3.0 mm, 4.6 mm, and 3.2 mm in the X, Y, and Z directions, respectively. The choice of $r = 2.5$ mm used in the motored case for the sphere to quantify the local flow state near the spark plug is thus also justified in the fired case.

The total local kinetic energy is then decomposed into a 3D local turbulent energy E_k^{HF} *3D local* and a 3D local kinetic energy of the LF part E_k^{LF} *3D local*. Their correlation with the combustion speed is illustrated in Figure 6.33.

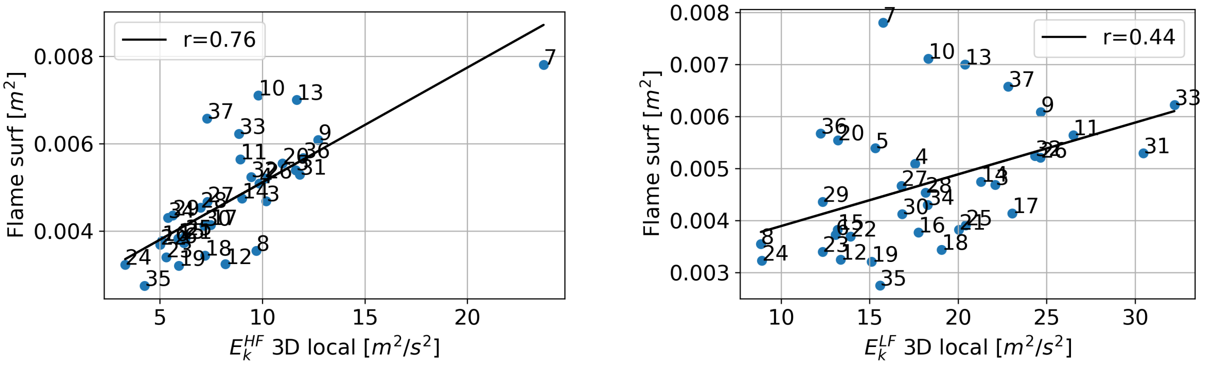

(A) E_k^{HF} *3D local*. [1]

(B) E_k^{LF} *3D local*.

FIGURE 6.33: Correlations between the combustion speed and the local kinetic energy.

The kinetic energy of the LF part E_k^{LF} *3D* does have a moderate correlation with the combustion speed. However, the local turbulent level, quantified by the E_k^{HF} *3D local*, seems to be a much more impacting factor, which implies that the local turbulent level plays an important role in the early stage of flame propagation by wrinkling the flame as the result of the action of turbulent eddies acting upon the flame surface and consequently increasing the total flame surface.

E_k^{HF} *3D local* is extracted from the resolved velocity and thus represents only the resolved turbulent level. In the ECFM, the turbulent level below the combustion filter scale $\hat{\Delta}$ is also considered by using a fluctuating velocity $\hat{u}'$. Similar to the way used to extract the averaged E_k^{HF} *3D local*, the averaged local $\hat{u}'$ in the spark plug region is also computed to represent the local modeled turbulence.

Figure 6.34 shows the impact of the local $\hat{u}'$ on the combustion speed and its relation with the resolved turbulence. Similar to the resolved turbulence, the modeled turbulence quantified by $\hat{u}'$

---

[1] r reduced to 0.7 if the cycle 7 is removed.

positively correlates with the combustion speed. The correlation between $\hat{u}'^2$ (in square to represent the kinetic energy) and $E_k^{HF}3D$ exists as well due to the energy cascade between the combustion filter scale and the resolved turbulence scale.

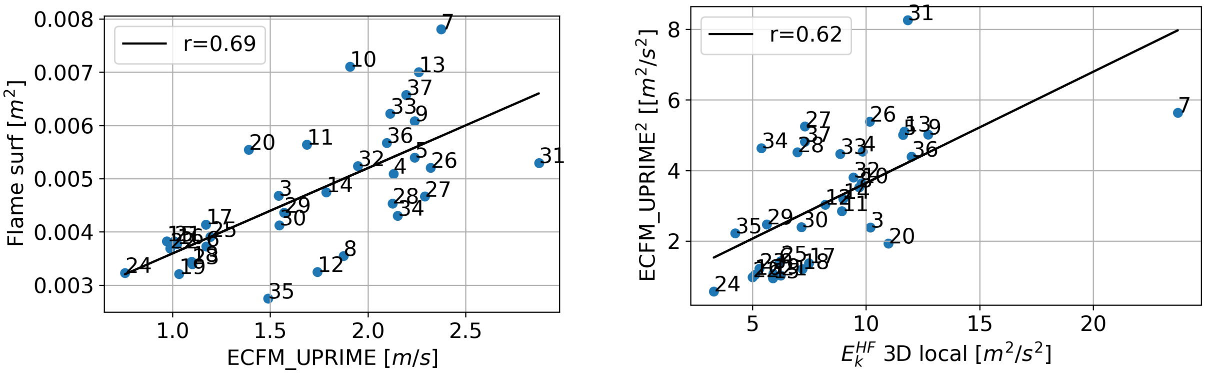

(A) $\hat{u}'$ and S_{-10}. (B) $\hat{u}'^2$ and $E_k^{HF}3D$ *local*.

FIGURE 6.34: Impact of $\hat{u}'$ on the combustion, coupled with the resolved turbulence.

6.4.5 Thermodynamic effects

Most previous analyses focused on the impact of aerodynamics, both large- and small-scale. Thermodynamic effects also need to be explored because they determine the laminar flame speed directly on the flame front.

The residual gases origin from the previous cycle is of higher temperature than the fresh gases induced in the present cycle. Their presence may lead to variations in temperature. The residual gases mass m_{res} and the contribution of unburnt fuel m_{res}^{fuel} are thus chosen for investigation. The trapped mass $m_{trapped}$ in the chamber at spark timing is also selected as it partially determines the pressure evolution. The averaged temperature T^{mean} in the near spark region, which directly impacts the local laminar flame speed, is also taken. As no direct injection occurs in the current engine configuration, the equivalence ratio is uniform at spark timing in all the 35 cycles and is not included in the analysis.

The correlation coefficient is computed between the above quantities and the combustion speed, and the results are listed in Figure 6.35. The chosen thermodynamic factors do not correlate with the

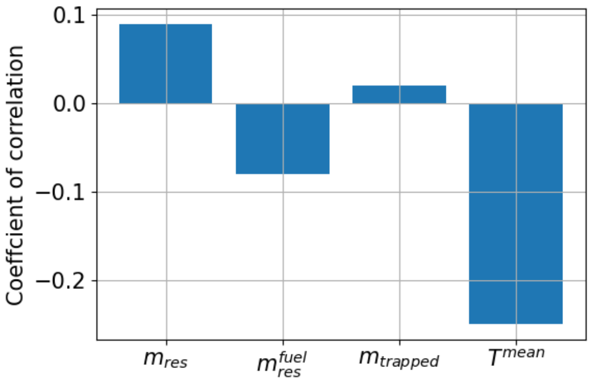

FIGURE 6.35: Correlation between the thermodynamic factors and the combustion speed.

combustion speed. It seems that aerodynamic features have more importance than thermodynamic features in the current engine configuration.

This work does not study the impact of the heat transfer between the flame kernel and the spark plug. Johansson et al. [174] investigated the relation between the heat transfer from the flame kernel to the spark plug, indicating that the interaction between the flame kernel and the spark plug leads to heat loss which impacts the laminar flame speed. In the current LES methodology, wall temperatures are fixed in time, while in the real condition, they evolve with time, which has been proved by some numerical studies using Conjugate Heat Transfer (CHT) technique [74, 175]. The coupling with CHT needs extra computational resources and is not applied in this thesis. The inaccurate modeling of heat loss makes us focus more on the impact of aerodynamic features than thermodynamic ones.

6.4.6 Multivariate analysis of CCV factors

The above analysis based on linear regression has allowed identifying multiple CCV factors. However, the univariate linear regression analysis is limited when dealing with multiple factors that act simultaneously, which is the case in the present study.

To identify the most significant CCV factors, a multivariate linear regression model is built between the flame surface S_{-10} and all the flow descriptors mentioned in the previous sections and summarized in Table 6.4, using the same methodology as in [91].

Local (spark plug region) flow descriptors		Tumble descriptors
Velocity	Kinetic energy	**TR**
$\vec{U}$, $\vec{U}_{LF}$	E_k^{LF}, E_k^{HF}	|TR|, |TR| *local*, |CTR|, |SR|

TABLE 6.4: Summary of flow descriptors used to build the multivariate linear regression model of S_{-10}.

Two models with a correlation coefficient of around 0.8 are obtained and presented in Figure 6.36.

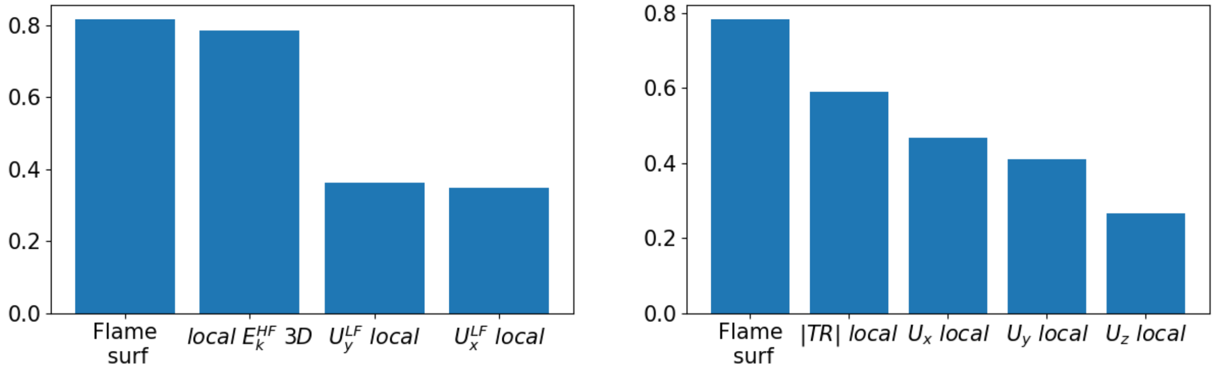

(A) Model 1.

(B) Model 2.

FIGURE 6.36: Histogram of correlation coefficients between the total flame surface at −10 CAD and the variables representing flow features at spark timing. The best two models are presented.

The model 1 that gives that best fit with a correlation coefficient $r = 0.82$ is composed of three independent variables E_k^{HF} *3D local*, U_y^{LF} *local* and U_x^{LF} *local*. E_k^{HF} *3D local* is the most critical factor in this model as its contribution to the prediction is already comparable with that of model 1. The other two variables are of a pretty weak correlation coefficient.

The second-best model 2 contains four independent variables $|\mathrm{TR}|$ $local$, U_x $local$, U_y $local$, U_z $local$. The local tumble ratio near the spark $|\mathrm{TR}|$ $local$ was previously found as an significant CCV factor as it reflects the level of the tumble deformation, which is crucial for the combustion process. The other three averaged local velocity components were not highly correlated with the combustion speed. However, information about the local turbulence is hidden inside them, which may explain why the model chooses them.

The two models highlight the two most crucial CCV factors, E_k^{HF} $3D$ $local$ and $|\mathrm{TR}|$ $local$, which will be attentively studied in Chapter 7.

6.5 Summary of main findings

In this Chapter, the Darmstadt research engine was studied under fired conditions of the same regime as the study under motored conditions presented in Chapter 5.

LES was performed, and a total of 35 LES cycles were obtained. The validation against experimental data showed a generally good agreement on the statistical behavior of the in-cylinder pressure. The correct CCV level was captured by LES, which allowed the further investigation of CCV. The comparison with PIV data also validated the prediction of LES for internal aerodynamics.

The study focused on the identification of CCV factors at spark timing. Starting with a qualitative analysis based on chosen extreme cycles, we noticed the importance of the flow state at spark timing on the flame propagation. More quantitative analyses were performed:

- The mode projection approach showed that the global flow state at spark timing was significantly correlated with the combustion speed. Two flow patterns were identified, which led to different combustion performances. The impacts from different scales were not yet distinguished.
- The local velocity field near the spark plug was also studied. The local flow direction determined the initial flame propagation direction but only moderately correlated with the combustion speed, which contradicts conclusions found in previous studies [37, 91]. The local kinetic energy impacted the combustion, and contributions from different scales were not distinguished.
- 2D EMD was applied to velocity fields in the tumble and spark planes. The extracted LF part representing the large-scale motion was recognized as an important factor in the combustion process.
- The HF part was not correctly defined in 2D, and 3D EMD was used to evaluate the impact of turbulent fluctuations on the combustion. The local kinetic energy was divided into large-scale and turbulent parts. The latter was found significantly correlated with the combustion speed, indicating the importance of the turbulence on the initial growth of the flame kernel. Coherence between the resolved turbulence and modeled turbulence was also revealed.
- The large-scale tumble motion was visualized and quantified using Γ_3 function and local tumble ratio **TR**. The tumble motion was largely distorted in the slow cycle, whereas it was well preserved in the fast cycle. The local $|\mathrm{TR}|$ near the spark plug correlated with the combustion speed, confirming our qualitative analysis observation.
- Other thermodynamic factors were studied in the end, and no significant impact was noticed in this engine configuration.

Through the multivariate analysis of CCV factors at spark timing, two main contributors to CCV of combustion were finally identified: the local (spark plug region) turbulent energy E_k^{HF} $3D$ $local$

and the local large-scale tumble motion quantified by $|\mathrm{TR}|\ local$ near the spark plug. Moreover, these two CCV factors are also partially correlated.

Characterizing flow state at spark timing allowed us to identify two major CCV factors related to the in-cylinder flow. In Chapter 7, a root-cause analysis will be performed to investigate their origins along the in-cylinder flow development.

CHAPTER 7

Analysis of in-cylinder flow evolution and impact on CCV

Contents

7.1 Approach and methodology 146
  7.1.1 Tumble deformation Characterization 146
  7.1.2 Flow state at BDC 147
  7.1.3 Intake flow 147
7.2 Comprehension of the link between the compression stroke phase and the combustion phase 149
  7.2.1 Tumble deformation 149
  7.2.2 Spatio-temporal evolution of the large-scale motion and its CCV 154
  7.2.3 Impact of the energy transfer between the large-scale motion and small eddies on the combustion process 156
7.3 Understanding the relation between the tumble evolution and its structure near BDC 158
  7.3.1 Identification of the initial destabilization of the large-scale motion 158
  7.3.2 Impact and deviation of the flow over the piston 159
7.4 Exploration of the CCV sources from the flow organization during the intake stroke 162
  7.4.1 Characterization of the primary flow 162
  7.4.2 Identification and characterization of dominant flows 167
  7.4.3 Analysis of the combined effects of dominant flows on the CCV 178
  7.4.4 Exploration of CCV in the intake port 185
7.5 Summary of main findings 190

In Chapter 6, the identification of some significant CCV factors at spark timing was made. The local turbulent level near the spark plug and the large-scale tumble motion were found as major CCV sources. However, we do not know how they are generated during the in-cylinder flow development. In this Chapter, we would like to trace their origins back to the compression and intake strokes and build a cause-and-effect chain. This analysis will give a description of the global in-cylinder flow evolution.

7.1 Approach and methodology

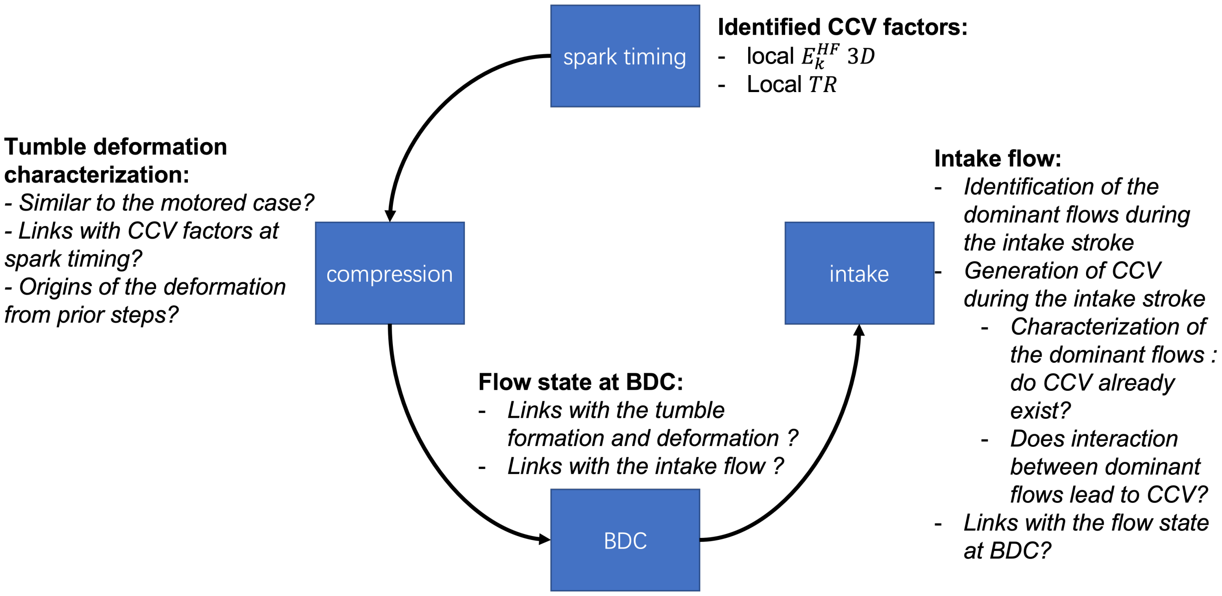

FIGURE 7.1: Cause-and-effect chain investigation and related questions to answer in Chapter 7.

A root-cause study is realized based on the characterization and analysis of in-cylinder flow. We attempt to link the flow variations at spark timing to the flow state at different stages. In this section, we present the approach and methodology that we will use to achieve our objectives.

To seek the origins of CCV factors at spark timing in the overall flow development, we divide the in-cylinder flow evolution into three phases: the compression stroke, around BDC, and the intake stroke. Figure 7.1 schematically illustrates the mentioned strategy with the related questions to answer, and the analyses we propose for each phase will be explained in the following.

7.1.1 Tumble deformation Characterization

The large-scale tumble motion at spark timing showed significant differences between fast and slow cycles, as presented in Figure 6.27. In the study of the motored case in Chapter 5, we had a similar observation on the flow at the same instant, as shown in Figure 5.47. The previous investigation in the motored case showed that (cf Figure 5.48) the tumble experienced a deformation leading to large-scale variations. Moreover, in case of an important deformation, the tumble could be highly distorted and gradually change its rotation axis near TDC during the compression. In the fired case, we would like to conduct the same analysis for characterizing the tumble motion during the compression stroke. Γ_3 function and local tumble ratio $\mathbf{TR}$ will be used to describe the tumble evolution during the compression quantitatively.

Given that both motored and fired cases are in the same engine regime (same rpm and intake pressure level), it would be interesting to compare the results of tumble characterization between these two cases. We will first qualitatively examine if a similitude exists in the tumble deformation between these two engine conditions despite the potential impacts of combustion on the tumble motion. Then, the relation between the tumble evolution and the two main factors of CCV at spark timing will be investigated. We have proved in the study of the motored case that Γ_3 and **TR** could precisely characterize the tumble evolution, and they will be used as main descriptors to establish links with CCV factors. In the present Chapter, an additional effort is made to explain the occurrence of tumbling deformation. In the motored case, we simply linked the deformation with the elliptical instability without further explication. In the fired case, we aim to identify determinant factors that trigger the deformation.

7.1.2 Flow state at BDC

BDC is the end of the intake stroke and the start of the compression stroke. As an intermediate phase, multiple events related to the intake flow and the tumble deformation, including flow/wall interactions and flow interactions, can occur simultaneously.

The flow state at BDC shows several important features, as seen in the ensemble-averaged velocity field at this instant of the fired case, presented in Figure 7.2. A global tumble motion begins to form, and the tumble front reaches the intake side liner. On the exhaust side, a descending flow carrying important momentum can also be marked (following the black dashed line in Figure 7.2), which will be noted as the primary flow in the following. It impinges almost normally on the piston surface and deviates towards the intake side. Another descending flow containing less kinetic energy can also be observed on the intake side (following the red dashed line in Figure 7.2) and will be noted as the secondary flow in the following.

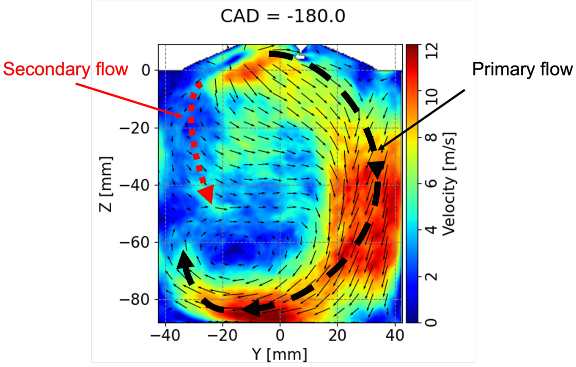

FIGURE 7.2: Ensemble-averaged velocity field from LES at −180 CAD of the fired case. The tumble front arrives at the intake side, and the descending flow at the exhaust side keeps impacting the piston. The primary flow is marked by the black dashed line, and the secondary flow is marked by the red dashed line.

A potential link between the intake flow, partially represented by the primary flow, and the tumble formation at BDC, related to the deviated flow over the piston, is likely to exist. By analyzing the flow state at BDC, we expect to extract flow descriptors that allow us to establish such a link.

7.1.3 Intake flow

The intake flow generated by intake valve jets is the primary source of the tumble motion. Nonetheless, the intake flow is not simply the fast descending flow visible in the tumble plane on the exhaust side as it is often schematized, as shown in Figure 7.2. Krüger et al. [99] proposed an intake flow division into four dominant flows based on their observation in a Daimler M256 engine, as indicated in Figure 7.3:

- The tumble flow 1: part of the intake valve jets enters the chamber from the upper side of the valves.

- The filling flow 2: part of the intake valve jets enters the chamber from the lower side of the valves. The inclined intake port design results in a less strong flow 2 than flow 1.
- The side flow 3: flow generated by the interaction between intake valve jets and the liner. It follows the liner and advances towards the exhaust side.
- The central flow 4: flow generated by the interaction between the two intake valve jets.

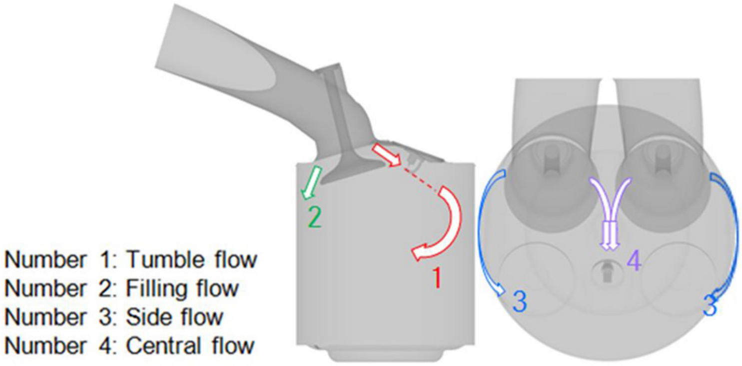

FIGURE 7.3: Intake flow division proposed in [99].

In this work, we also expect to identify dominant flows during the intake stroke in the Darmstadt engine. The engine geometry in this study differs from the one used by Krüger et al., and our proposition of intake flow division will be based on the one of Krüger et al. and be adjusted by taking into account the impact of geometry.

The identified dominant flows will be quantitatively studied. Laurant [88] found that the intake valve jets were naturally unstable. The author also highlighted that the jet impinging was of a short period compared to the duration of the intake stroke, indicating that spatio-temporal oscillations were visible on the intake valve jets. These fluctuations can be at large or small scales, so 2D EMD and 3D EMD would be appropriate tools to check whether CCV is present for each dominant flow.

Regarding the flow division in Figure 7.3, we notice that the flow 1, 3 and 4 all move in the same direction and may encounter each other in the chamber and eventually form together the primary flow observed in Figure 7.2. Krüger et al. [99] also proposed their hypothesis: *The in-cylinder cycle-to-cycle fluctuations are stronger in the presence of several dominant in-cylinder flows interacting with each other*. Therefore, in addition to the CCV of each dominant flow, CCVs resulting from interactions between dominant flows will also be characterized to verify the hypothesis of Krüger et al..

Finally, if the presence of CCV of dominant flows is amplified by their interactions, we may expect to link these CCV of the intake flow with the flow state at BDC to complete the root-cause analysis. The resulting cause-and-effect chain will eventually allow us to link the CCV of combustion to those of intake flow.

To establish the cause-and-effect chain, we will study the above three phases starting from the tumble deformation during the compression stroke and ending with the intake flow characterization. For analyzing each phase, we use the methodology summarized in Figure 7.4 and described below:

- Some extreme cycles with different combustion performances are chosen. We start with a qualitative analysis by comparing the chosen cycles.
- Flow characteristics (kinetic energy, scales, local flow features, etc.) presenting important differences will be quantified by appropriate numerical descriptors.

- Linear correlation coefficients will be computed between extracted descriptors of the current phase and those of the previous phase.
- If the correlation is significant, flow descriptors are kept for the current phase, and we continue to the next phase.

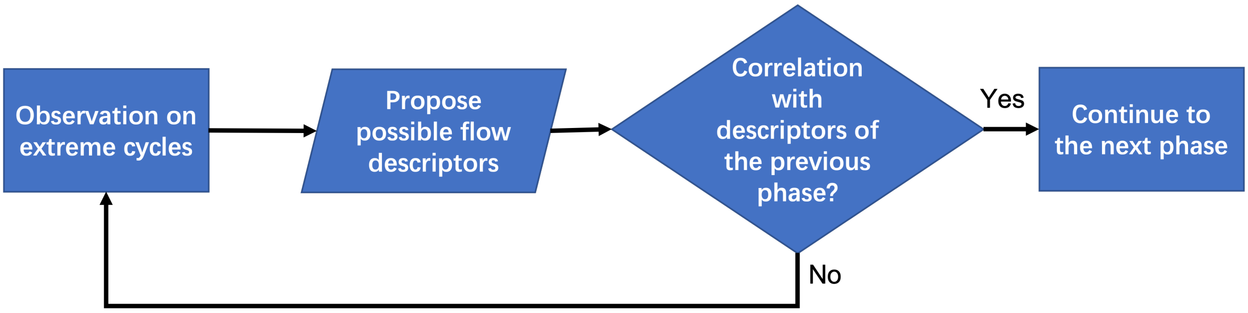

FIGURE 7.4: Methodology of the root-cause analysis in Chapter 7.

In the following sections, we will present analyses of the in-cylinder flow made in the three phases.

7.2 Comprehension of the link between the compression stroke phase and the combustion phase

The analysis of CCV sources at spark timing allows identifying two important flow parameters impacting the combustion process: the global motion and the local turbulence near the spark plug.

Regarding the global motion, two typical flow patterns are identified: tumble-type rotation around the X axis and a vortex pair around two inclined axes (with respect to the Y and Z axis). The occurrence of the vortex pair (quantified by important $|CTR|$ and $|SR|$ shown in Figure 6.29) in slow engine cycles corresponds to the tumble breakdown scenario characterized by a flow pattern switching of the tumble motion. The classical tumble breakdown scenario, supposing that the large-scale tumble is largely compressed and breaks into small eddies near TDC, is not observed in this engine configuration, as the large-scale global motion is preserved during the compression stroke. The presence of the vortex pair near TDC can also be considered as an indication of the disorganization and mitigation of the tumbling flow and, therefore, the beginning of the tumble breakdown. However, the relation between the large-scale motion and the turbulence generation, especially in the spark plug region, needs further exploration.

In this section, the deformation experienced by the large-scale tumble motion will be carefully analyzed using Γ_{3p} and the associated local tumble ratio **TR**. The CCV developed in the large-scale motions will also be pointed out with the help of bivariate 2D EMD. The link between the large-scale motions and the generated turbulence will be finally investigated.

7.2.1 Tumble deformation

The difference was already remarked on the large-scale motions at spark timing by visualizing the rotation kernel presented in Figure 6.27. Based on our findings in the motored case, it was assumed that the difference was formed during the compression stroke. To verify this hypothesis in the fired case, Γ_{3p} is computed using 35 consecutive cycles and evaluated for 33 different instants during the compression stroke with a resolution of 5 CAD, which allows following the evolution of the large-scale motions with respect to the piston movement.

The rotation kernel identified respectively in cycles 13, 20, and 18 is illustrated in Figure 7.5. An iso-surface of $|\Gamma_{3p}| = 0.5$ is superimposed to a 2D slice at $Y = 0$ mm on which the Γ_{3p} field is plotted.

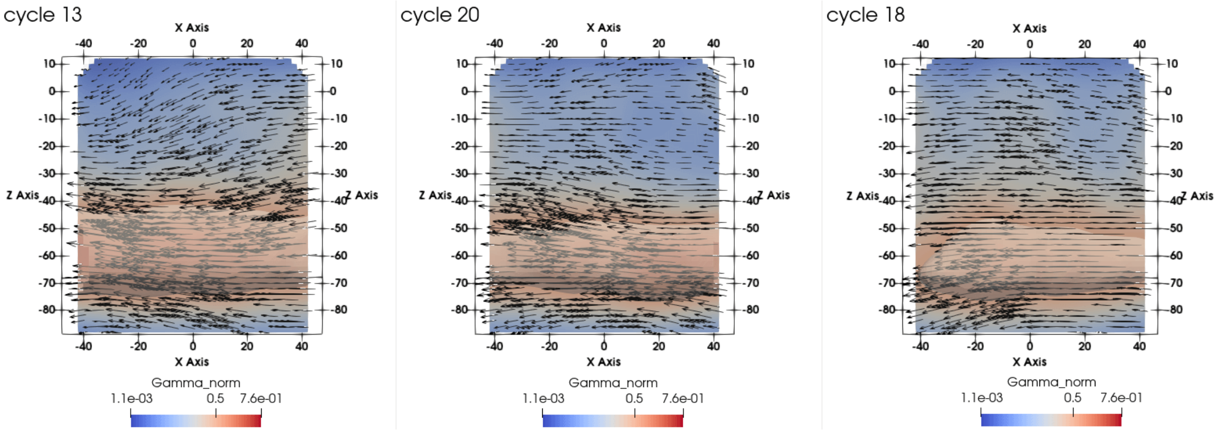

(A) −180 CAD.

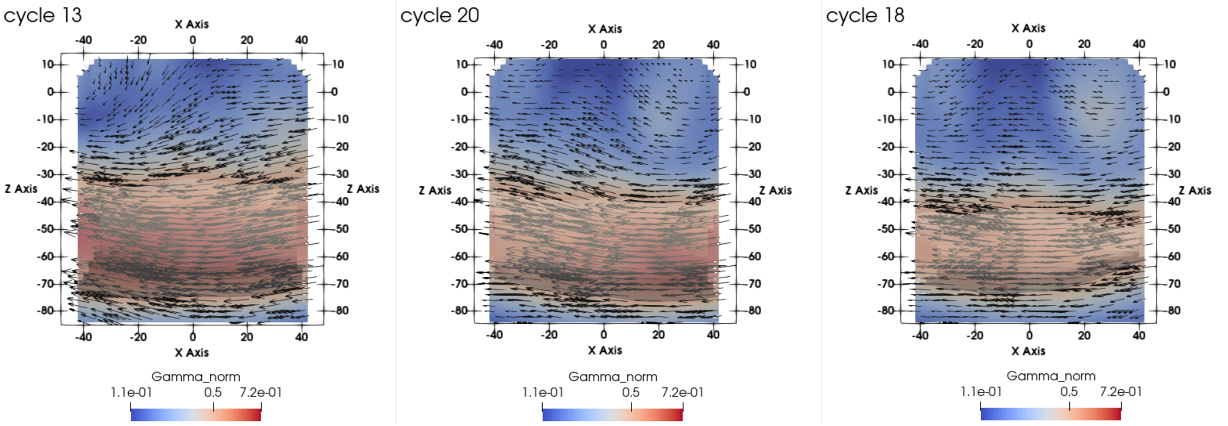

(B) −150 CAD.

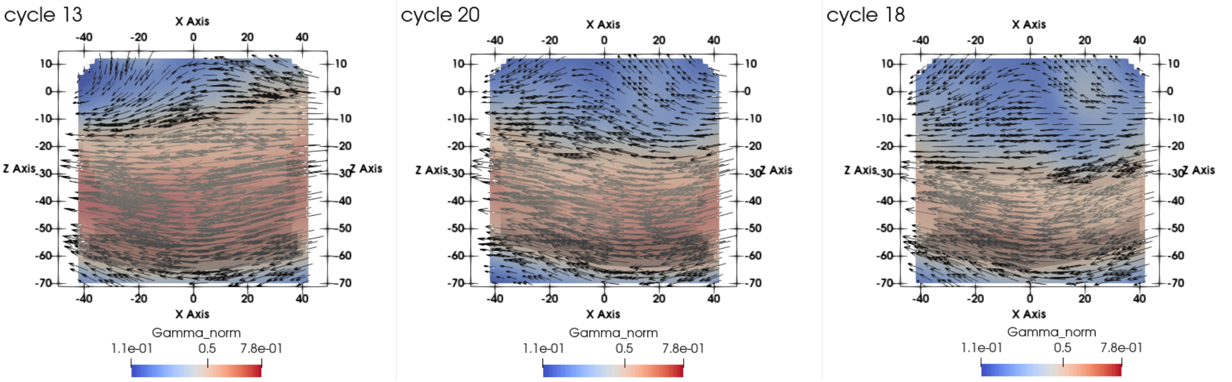

(C) −120 CAD.

FIGURE 7.5: Evolution of the rotation kernel for cycles 13, 20 and 18, combined with the vector field of Γ_{3p} at slice $Y = 0$ mm.

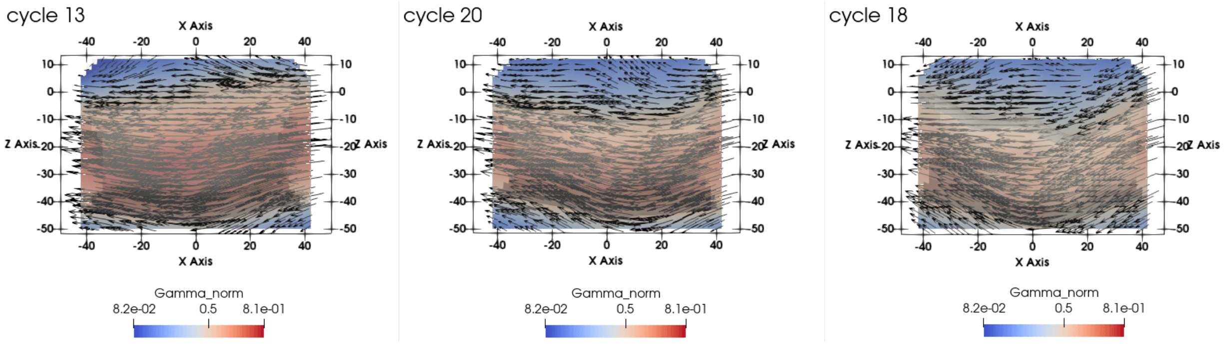

(D) −90 CAD.

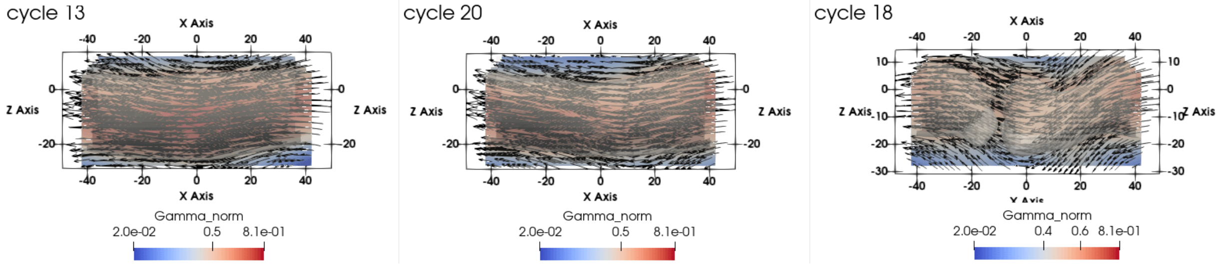

(E) −60 CAD.

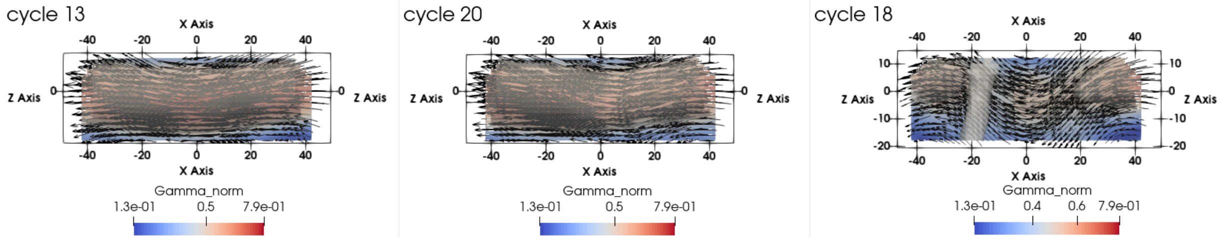

(F) −45 CAD.

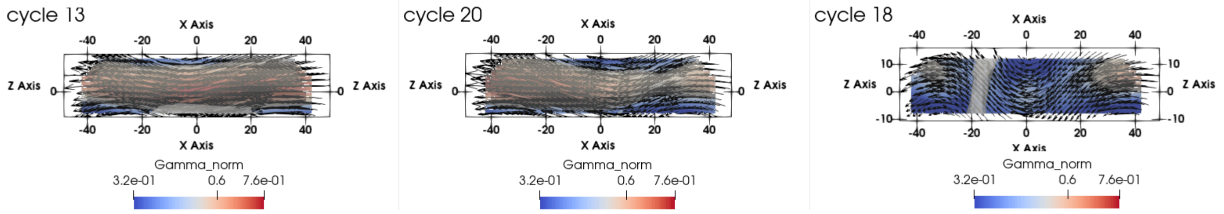

(G) −30 CAD.

FIGURE 7.5: Evolution of the rotation kernel for cycles 13, 20 and 18, combined with the vector field of Γ_{3p} at slice $Y = 0$ mm (cont.).

- It can be noticed that the initial rotation kernel at -180 CAD follows a different evolution according to the cycle: the kernel of cycle 18 is relatively less structured, in particular on the negative X side.
- At -150 CAD and -120 CAD, compared with the initial state, the rotational structure is enhanced as its size becomes larger. Between the three cycles, the kernel of cycle 13 is the most organized, filling almost the whole chamber, while the one of cycle 18 occupies only the half-height of the chamber.
- At -90 CAD, a significant change can be noticed in cycle 18: the rotation direction inside the tumble motion is no more aligned with the X axis but becomes slightly inclined; the tumble's shape is also no longer cylindrical as before and seems to be bent upwards on both sides. This trend in cycle 18 continues, and the kernel is increasingly deformed.
- At -60 CAD, the tumble vortex splits, which can be considered the beginning of the tumble 'breakdown' in the sense that the flow pattern begins to switch from a tumbling rotation around the X axis to a vortex pair. At -45 CAD, the vortical flow in cycle 18 is not even visible as the global $|\Gamma_{3p}|$ is small. The corresponding rotation direction field also tends to be much more inclined, which indicates that the flow pattern is totally different from a typical tumble motion.
- At -30 CAD, the tumble motion disappears totally in the central part near the spark plug, which agrees with what has been observed on the velocity field in the tumble plane in Figure 6.15a. Between the two relatively fast cycles 13 and 20, though the kernel remains cylindrical most of the time, the one of cycle 20 becomes less organized on the right side at -30 CAD and thus, the rotation is less structured locally. The same flow switching was also observed in the study of the motored case presented in Chapter 5, which was linked to the elliptical instability proposed by Lumley [43].

Following the rotation kernel visualization, the associated local rotation intensity **TR** is computed. The computed **TR** is projected onto the X, Y and Z directions, resulting in a tumble motion TR, a cross-tumble motion CTR and a swirl motion SR. Their definition is recalled in Figure 7.6.

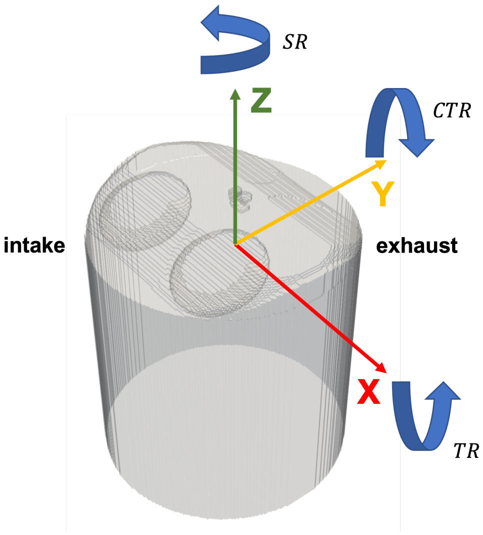

FIGURE 7.6: Components of the normalized angular momentum **TR** in the X (TR), Y (CTR), and Z (SR) directions.

The computed **TR** is compared between the three cycles in Figure 7.7. The absolute value of TR is noted as |TR|, which differs from that of the norm of **TR** noted as |**TR**|.

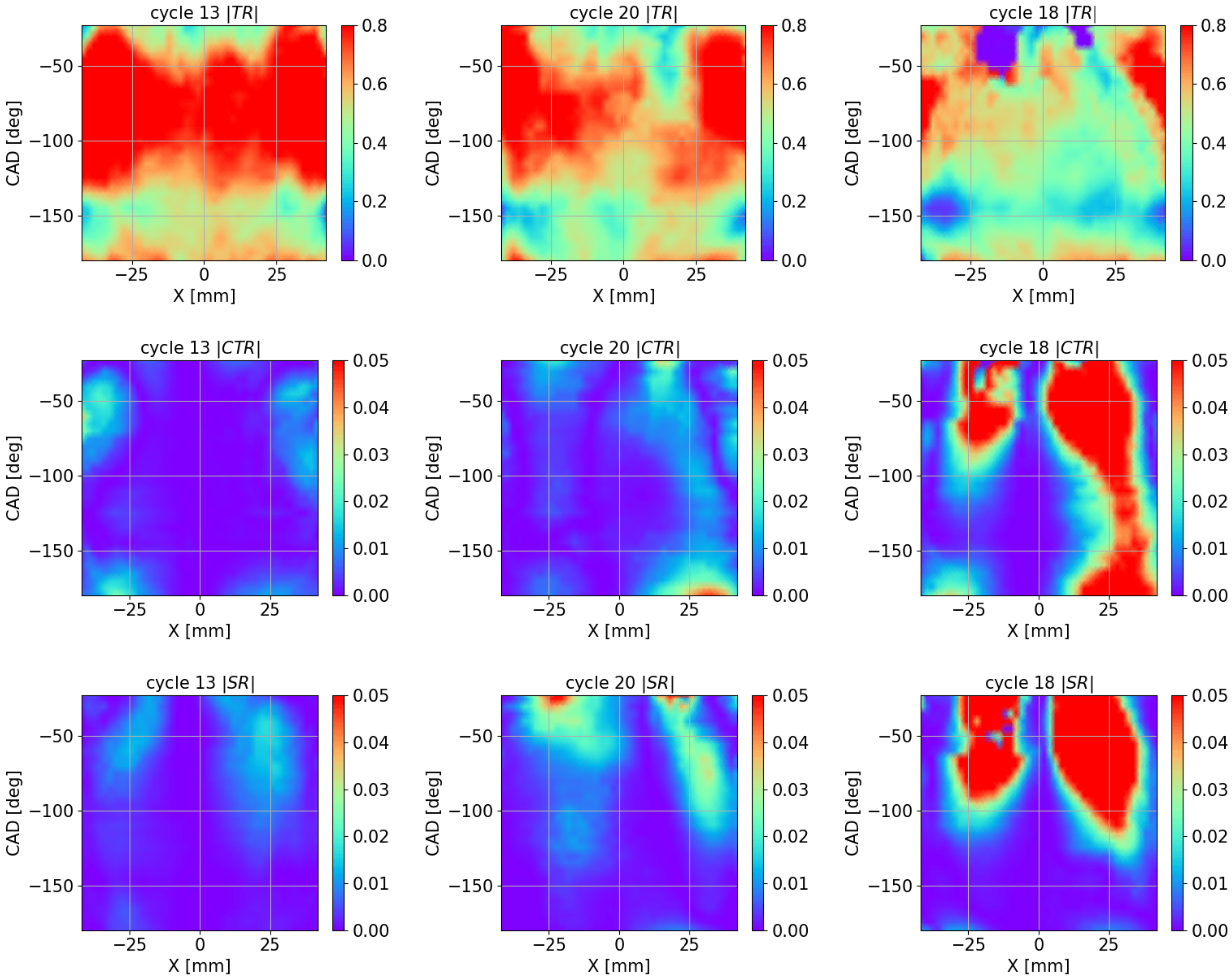

FIGURE 7.7: Comparison of tumble intensity during the compression stroke in direction X, Y and Z for engine cycles 13, 20 and 18.

Concerning the principal component |TR| which quantifies the tumbling rotation intensity, significant variations can be noticed during the whole compression stroke: around −150 CAD, |TR| remains close to 0 in cycle 18 on both sides while in cycle 13 it is almost uniform along the X axis. As the piston moves up, the level of |TR| remains high in cycle 13 since the tumbling rotation is always well conserved. Conversely, it is much smaller in cycle 18 and even decreases to 0 near spark timing. In cycle 20, its evolution is similar to that of cycle 13, except that after −90 CAD, |TR| on the right side decreases faster than on the left side.

The other two components |CTR| and |SR|, though of relatively small value compared to |TR|, do help understand and follow the tumble deformation. |CTR| differs from one cycle to another from the beginning of the compression, and it is generally more important in cycle 18 than in the other two cycles. During the compression, |CTR| stays strong in cycle 18 and generally increases after −120 CAD, which is consistent with the observation that after −90 CAD the kernel begins to deform in cycle 18 (see the evolution of the kernel rotation in Figure 7.5). Regarding |SR|, it does not appear from BDC but begins to increase after around −120 CAD. At the same time, |CTR| also begins to intensify, which coincides with the kernel deformation. At the end of the compression, both components are the most important in cycle 18, much weaker in cycle 20, and close to 0 in cycle 13.

It is also interesting to notice that |CTR| in cycle 20 is not negligible on the right side but much smaller on the left side. It may be responsible for the asymmetry of the global tumbling rotation near the end of compression.

In addition, the initial state of the local rotation intensity around Y axis |CTR| is likely to be important for the tumble deformation. Even at BDC, |CTR| is already of more significant value in cycle 18 and is amplified during the compression. The three components of TR also represent the form of the tumbling rotation kernel, and a high level of |CTR| at BDC indicates that the tumble is already partially distorted before the compression starts. A more detailed study will be given in the analysis of the flow state at BDC in section 7.3.

The evolution of **TR** allowed us to quantitatively describe the tumble deformation, which completed information provided by $|\Gamma_{3p}|$ on the tumble kernel evolution. The tumble deformation was observed and showed significant CCV. The following section will focus on characterizing large-scale CCV in the 2D tumble plane.

7.2.2 Spatio-temporal evolution of the large-scale motion and its CCV

The visualization of the tumble kernel has demonstrated that the tumble motion presents CCV in its structure that evolves with time. In this section, the CCV of large-scale structures will be quantitatively extracted with the help of bivariate 2D EMD applied to the velocity field in the tumble plane.

In Figure 7.8 the ensemble-averaged magnitude of the instantaneous velocity, that of the LF part, and the absolute magnitude of its CCV are plotted for different instants during the compression stroke.

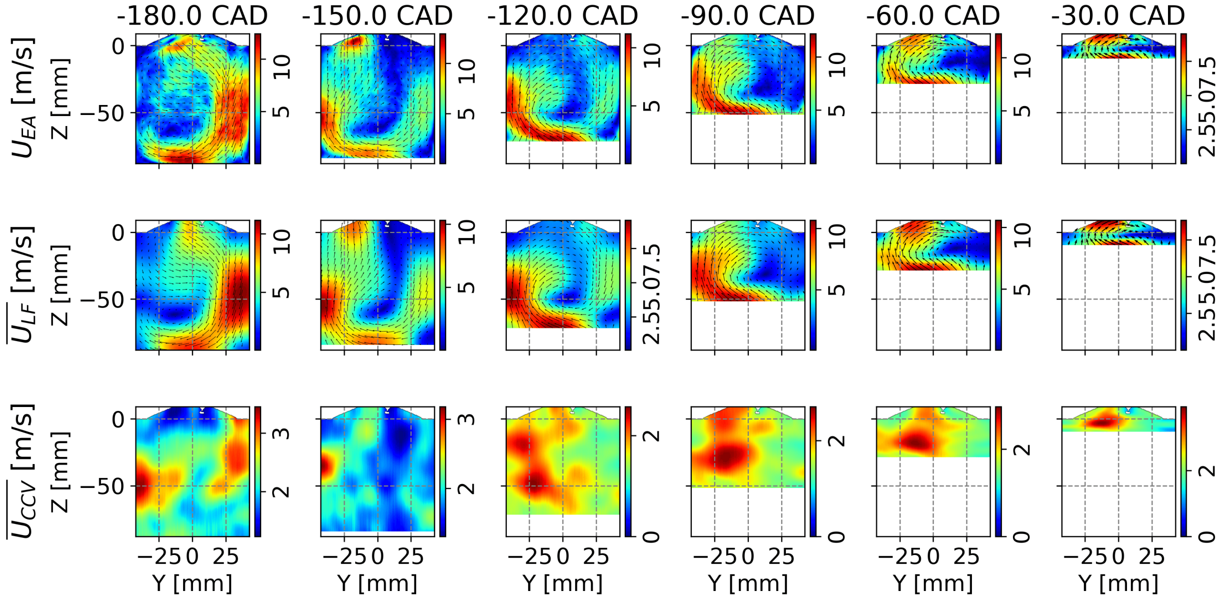

FIGURE 7.8: Evolution of ensemble-averaged flow quantities: the velocity magnitude U_{EA}, its LF part $\overline{U_{LF}}$ and the absolute magnitude of its CCV part $\overline{U_{CCV}}$ of velocity in the tumble plane during the compression stroke.

The ensemble-averaged velocity fields of 35 cycles present the global flow pattern at different instants. Local oscillations are still visible, resulting from the lack of convergence. It is apparent that the tumble motion begins forming from BDC when the tumble front reaches the intake side and starts to move up. Between BDC and −150 CAD, a high level of CCV appears essentially in the region where the tumble front and the secondary flow on the intake side interact. A high flow variability also coincides with the interaction zone between the intake flow on the exhaust side and the upper wall of the liner. Later on, CCV is always present on the intake side inside the tumble structure, which indicates that a change of the tumble flow pattern occurs during the second half of the compression stroke, even though the observation is only made in the tumble plane. Near spark timing at −30 CAD, a high level of CCV is still visible on the intake side, comparable to the local velocity intensity.

The behavior of the CCV part in the 2D view is in agreement with the previous findings obtained with the tumble kernel visualization in the 3D view: an significant variation undergoes in the tumble's structure during the compression stroke and generates CCV in large-scale structures; the CCV of the large-scale motion before spark timing become relatively significant.

Correlation maps are generated between the combustion speed and the CCV part of the velocity in the tumble plane to identify local large-scale flow features impacting the combustion process. The two components U_y^{ccv} and U_z^{ccv} are separately considered. The results are illustrated in Figure 7.9.

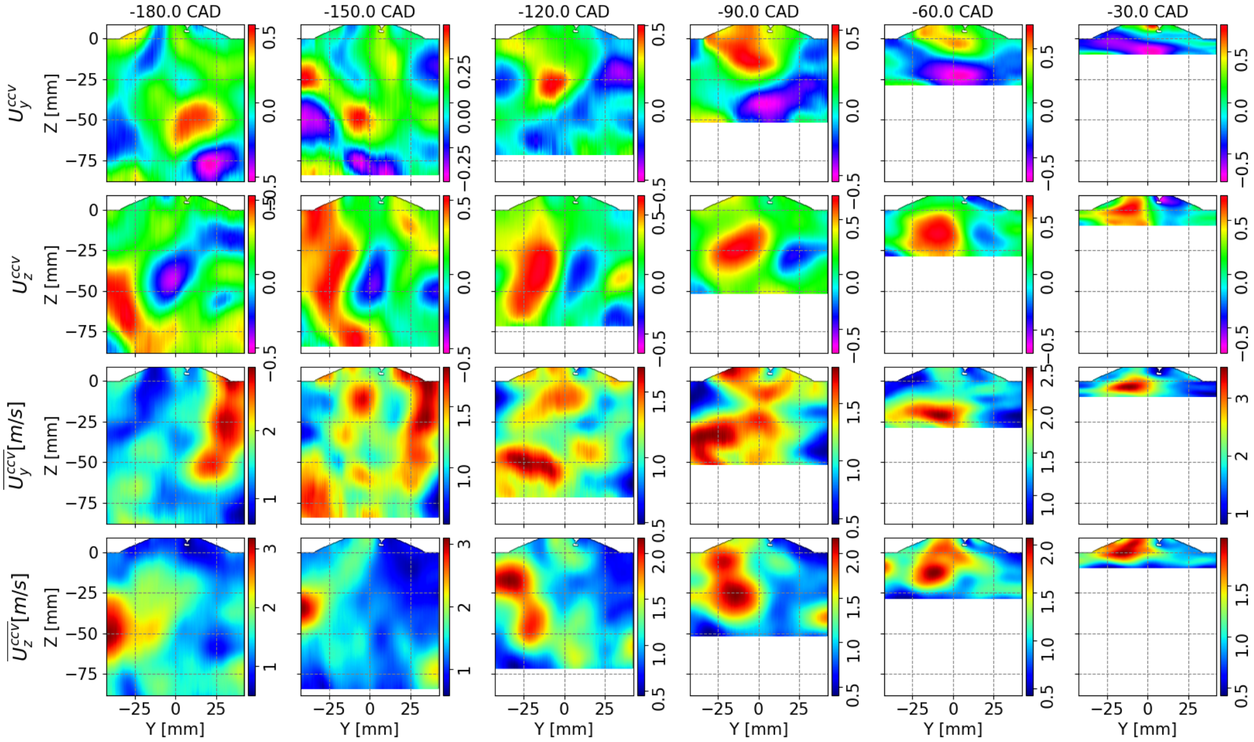

FIGURE 7.9: Correlation between the combustion speed S_{-10} and the two components U_y^{ccv} and U_z^{ccv} of the CCV part U_{ccv} in the tumble plane during the compression stroke. Averaged CCV velocity components $\overline{U_y^{ccv}}$ and $\overline{U_z^{ccv}}$ are also provided.

At BDC, significant correlations are found with U_y^{ccv} in the right lower corner where the primary flow at the exhaust side impacts the piston and deviates to the intake side, and with U_z^{ccv} in the left lower corner where the tumbling flow moves upward to the cylinder head. At −150 and −120 CAD, strong correlations with U_z^{ccv} on the left side (intake side) are noticed, indicating the positive impact of the ascending velocity on the combustion speed. For the rest three instants −90, −60, and −30 CAD, correlations maps behave similarly despite the variation of domain size: U_z^{ccv}

correlates positively on the left side and negatively on the right side with the combustion speed; U_y^{ccv} shows positive correlations near the piston, and negative ones close to the head. According to correlation maps of the last three instants and the corresponding averaged velocity field presented in Figure 7.8, the favored flow pattern for fast combustion is a tumble motion of high rotation speed.

The above analysis confirmed our previous findings at spark timing: a strong tumble motion near the spark plug is favorable for fast combustion. Moreover, this dependence seems to exist at -120 CAD, as shown by correlation maps in Figure 7.9, suggesting that CCV of large-scale flow at spark timing is probably generated at least during the compression.

In the next section, we will carefully investigate the energy transfer from large-scale structures to small eddies.

7.2.3 Impact of the energy transfer between the large-scale motion and small eddies on the combustion process

The tumble deformation, observed through the 3D visualization of the tumble kernel with the help of Γ_{3p}, led to an important flow variability. The flow decomposition with bivariate 2D EMD in the tumble plane allowed us to identify large-scale CCV in the tumbling flow. However, the small-scale turbulence was also crucial for the combustion process, and its evolution has not been quantified. In this section, a particular interest is put on the energy evolution in large- and small-scale structures and their energy transfer.

With bivariate 2D EMD, we can distinguish large-scale CCV in the LF part and small-scale fluctuations. Figure 7.10 presents the kinetic energy in different parts computed from bivariate 2D EMD in the tumble plane using Eqs.(5.9, 5.10, 5.11) presented in section 5.5.2. The following analysis focuses on the second half of the compression stroke from -100 CAD to spark timing -22.5 CAD. Statistically, the mean and the fluctuating part of the total kinetic energy can be easily extracted by a Reynolds-type decomposition, as shown in Figure 7.10a. During the second half of the compression stroke, the mean kinetic energy E_k^m indeed decreases with respect to the available room in the chamber as the tumbling flow is more and more confined. The level of fluctuation is small compared to E_k^m, and it begins to increase near -70 CAD. An energy transfer from the mean flow to the fluctuating part occurs but seems moderate.

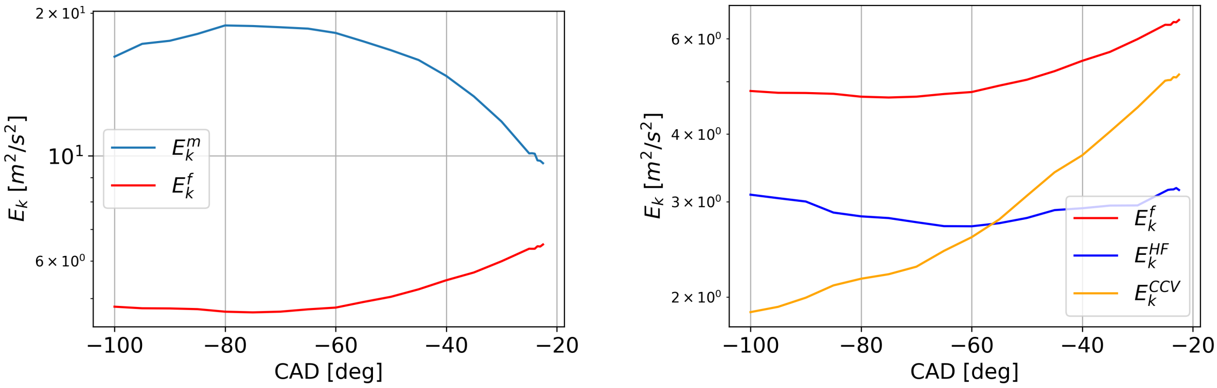

(A) Kinetic energy in the mean and fluctuating parts of the flow.

(B) Contribution of turbulence and CCV part in kinetic energy fluctuations.

FIGURE 7.10: Evolution of the phase-averaged kinetic energy during the engine cycle.

Two contributions can be distinguished in the fluctuating part: the CCV contribution related to the large-scale motion and the turbulent one related to small-scale fluctuations. The comparison between them with respect to time is shown in Figure 7.10b. The turbulent kinetic energy E_k^{HF} is relatively stable. In contrast, the kinetic energy of the CCV part E_k^{CCV} continues to increase and becomes one order of magnitude higher than E_k^{HF} before spark timing. Most of the energy of the mean flow is conserved in the large-scale movements with a variability associated with the flow pattern switching. Only a small fraction of the energy is transferred to small-scale fluctuations. Similar conclusions were also obtained in the motored case.

To seek the relation between large-scale motions and small-scale turbulence, especially the one in the spark plug region at spark timing, a correlation analysis is made between the local E_k^{HF} $3D$ extracted by 3D EMD, which was proved to be crucial to the combustion speed in section 6.4.4, and the local tumble intensity $|\mathrm{TR}|(\mathrm{X}, \mathrm{CAD})$ in the three directions. The correlation maps are plotted in Figure 7.11.

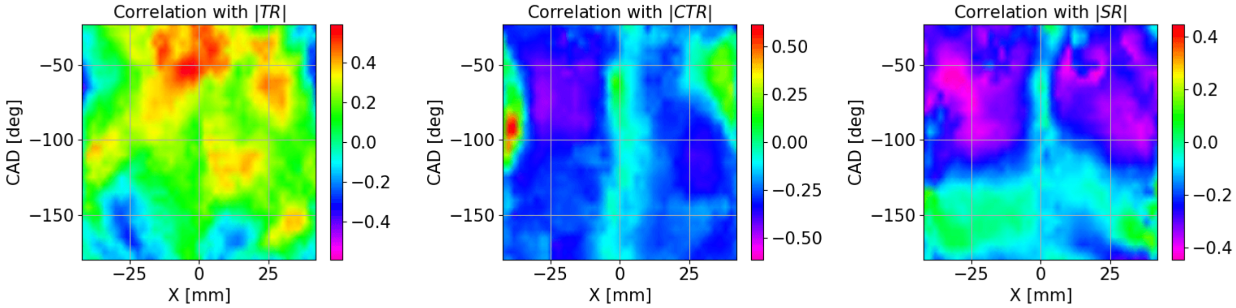

FIGURE 7.11: Correlations between the local turbulence level $E_k^{HF}(t_{ign})$ $3D$ and the local tumble intensity $\mathbf{TR}(\mathrm{X}, \mathrm{CAD})$.

On the correlation map with $|\mathrm{TR}|(\mathrm{X}, \mathrm{CAD})$, a region of positive correlation can be found in the central part of the X axis after -100 CAD when the tumble deformation begins to take place more or less in different cycles. It indicates that an organized tumble motion of high intensity in the central part leads to a high turbulence level. Negative correlation can also be identified on the correlation maps with $|\mathrm{CTR}|(\mathrm{X}, \mathrm{CAD})$ and $|\mathrm{SR}|(\mathrm{X}, \mathrm{CAD})$ in regions where both of these two components are of relatively important values if the deformation is significant. It is noteworthy that the lack of symmetry may be attributed to the lack of statistical convergence.

The results of the three correlation maps in Figure 7.11 suggest a link between the local large-scale tumble motion and the local turbulence, which were identified as the two major CCV factors at spark timing: in the case of a tumbling flow pattern, the large-scale motion conserves a high energy level during the compression and maintains the energy transfer to small-scale eddies till spark timing so that the turbulence does not dissipate quickly; in case of a vortex pair flow pattern, the locally organized rotation in the spark plug region is much less present, and hence the local turbulence production is less favored.

In section 7.2, we investigated the tumble deformation carefully during the compression stroke. Similar to what was found in the motored case, a tumble deformation was observed in the fired case, which led to an important flow variability. The large-scale motion was found responsible for most flow variations caused by the tumble deformation during the compression. It was also associated with the turbulence generation near the spark plug at spark timing. Therefore, the tumble deformation was considered the origin of the two CCV factors at spark timing. The link between the compression stroke and the combustion phase was thus built. In the next section, we will move to the analysis of the flow state at BDC to explore the origin of the tumble deformation.

7.3 Understanding the relation between the tumble evolution and its structure near BDC

The tumble deformation analyzed in the previous section has shown its important impacts on the large-scale flow CCV and the local turbulence level at spark timing. A well-organized tumble motion is thus generally favorable for fast combustion. It has been noticed in the comparison of |CTR| that the level of |CTR| near BDC seems to be decisive to the mean aerodynamic state at spark-timing, which suggests a potential dependence of the tumble deformation on the initial tumble shape at BDC.

In this section, the relation between the initial tumble structure and its final state at spark timing is analyzed; also, the phenomena responsible for the initial tumble destabilization are identified and quantified.

7.3.1 Identification of the initial destabilization of the large-scale motion

As observed in the comparison of the evolution of |CTR| between the three cycles 13, 20 and 18 presented in Figure 7.7, the high value of |CTR| at BDC is amplified during the compression stroke because of the tumble deformation. According to the evolution of the rotation kernel illustrated in Figure 7.5, the tumble deformation does not occur instantly at a specific moment but starts early and develops gradually during the compression stroke. The tumble deformation could probably be determined by the flow state even at earlier instants.

To seek potential causes of the tumble deformation during the compression stroke, correlations are computed for each component of TR between their evolution in time $\mathbf{TR}(CAD)$ and their final value at spark timing $\mathbf{TR}(t_{ign})$, both of which are averaged along the tumble center line. The evolution of the corresponding correlation coefficients is plotted in Figure 7.12.

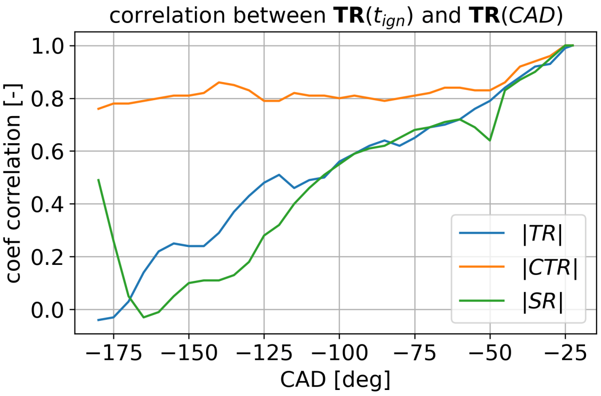

FIGURE 7.12: Correlations between the final state and the evolution of **TR**.

A strong correlation coefficient between $\mathrm{CTR}(t_{ign})$ and $\mathrm{CTR}(CAD)$ is remarkable. It is almost constant during the whole compression phase and greater than 0.75. It implies that the tumble deformation depends on the state of the tumble at BDC. Moreover, CTR helps quantify the angular momentum around the Y axis and consequently the distortion level of tumble compared to a pure rotational motion about the X axis.

TR is initially not correlated with its final state as it quantifies the principal tumble intensity and does not allow determining if the imperfection exists already in the tumble's shape at the beginning of compression. Once the tumble deformation occurs after around −120 CAD, TR starts to present a certain level of correlation with its final state, which increases with time. This can be explained by the fact that the flow pattern switching begins to impact the value of TR and its value reflects the level of deformation.

After a drop up to −165 CAD, the auto-correlation coefficient of |SR| follows a similar behavior as that of |TR| with an almost constant increase. The same drop around −165 CAD can also be noticed in the evolution of **TR** in the three directions (cf Figure 7.7 which corresponds to a slight reduction of the rotation intensity. A possible source of this decrease is the friction between the liner/piston and the tumble front. As shown by the ensemble-averaged velocity field at BDC in Figure 7.2, the tumble front starts to reach the intake side near BDC, and a strong impact is expected shortly after, which may lead to this drop. However, we did not investigate the depth of this phenomenon in this work.

Among all three components, |CTR| is a robust descriptor to quantify the deformation of the tumble's structure (compared to a pure tumbling flow around the X axis) during the compression stroke. The initial state of |CTR| at BDC depends on the flow structure and will be investigated in the next section.

7.3.2 Impact and deviation of the flow over the piston

The ensemble-averaged velocity field at BDC presented in Figure 7.2 describes an important phenomenon enduring in the chamber: the flow impacting and deviation over the piston surface. The primary flow impacts the piston on the exhaust side and then is deviated towards the intake side, which gives birth to the tumbling flow in the chamber.

Therefore, it is worth investigating if CCV exist already in the flow/piston interaction and how it impacts the tumbling flow generation. In Figure 7.13, the flow over the piston at different heights is visualized and compared between the cycles 13, 20, and 18. Among the three swirl planes at different heights, the flow deviation can be captured at $Z = -88$ mm, which is inside the second cell in the normal piston direction, and also at $Z = -85$ mm. The flow deviation in the swirl plane at $Z = -80$ mm becomes less evident as the boundary layer is below this height.

Between the three cycles, it can be seen that the impact area, characterized by low velocities on the top part (exhaust side), is more expanded in cycle 13 while it is more restricted in cycle 18. The resulted deviation also behaves differently. Qualitatively, a more expanded impact region seems to result in a more uniform flow direction distribution towards the intake side. In contrast, a more restricted impact region leads to a more important deviation, and the flow direction varies significantly. In case of an important deviation, part of the near piston flow moves towards the $X/-X$ directions and hence generates rotational movements around the $Y/-Y$ axis, which is quantified by |CTR|.

As concluded from the analysis of the tumble destabilization presented in section 7.3.1, the initial distortion of the tumble at BDC, quantified by |CTR|, is a determinant factor for the subsequent evolution of the tumble motion. To quantitatively describe the relation between the flow deviation and |CTR|, a global flow deviation angle $\overline{\Theta}_{xy}$ in the XY plane is quantified. Only the deviated flow in the near piston region under $Z = -85$ mm is included in the computation of Θ_{xy}. The angle $\overline{\Theta}_{xy}$ is computed as:

$$\overline{\Theta}_{xy} = \frac{\sum_i w_i \arctan\left|\frac{U_x}{U_y}\right|}{\sum_i w_i} \tag{7.1}$$

where the weighting factor w_i is defined as $w_i = \frac{\sqrt{U_{x,i}^2+U_{y,i}^2}}{\max(\sqrt{U_{x,i}^2+U_{y,i}^2})}$.

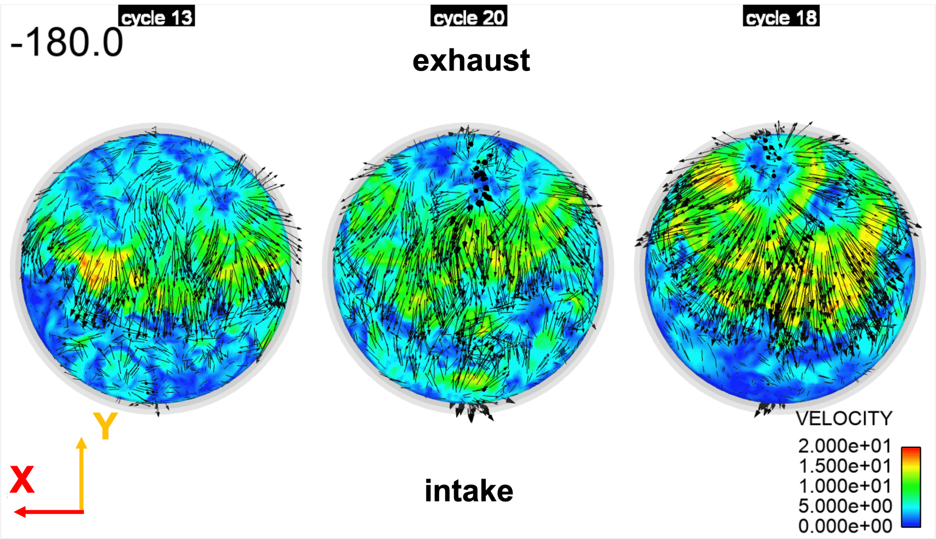

(A) $Z = -88$ mm.

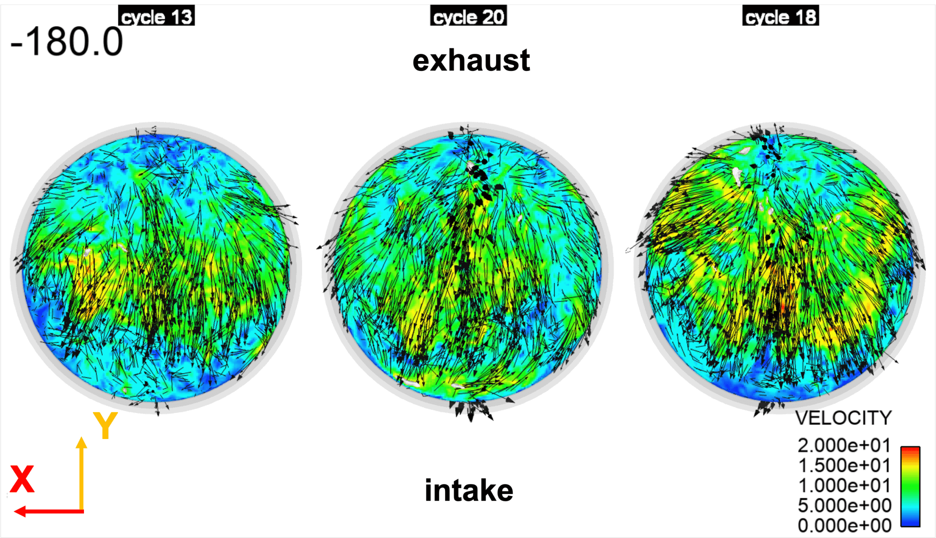

(B) $Z = -85$ mm.

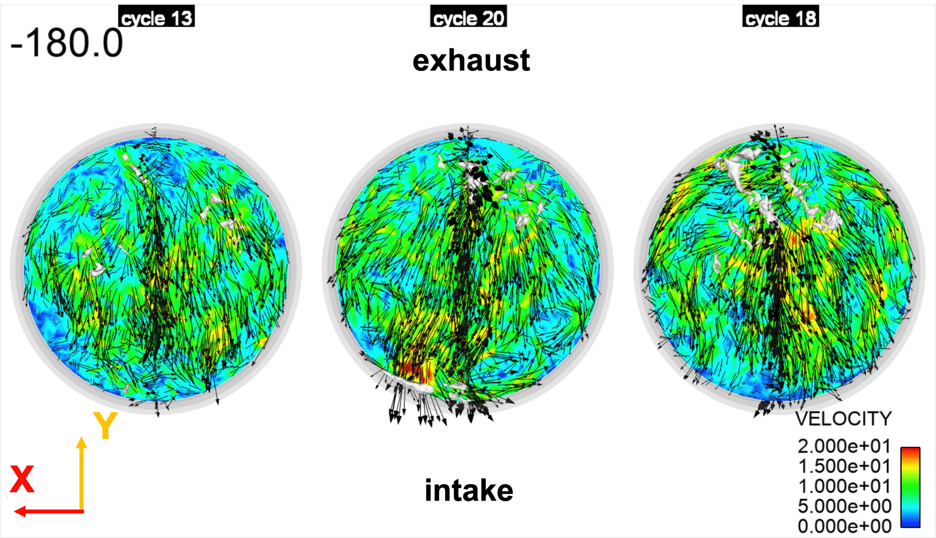

(C) $Z = -80$ mm.

FIGURE 7.13: Flow deviation over the piston surface (piston at $Z = -88.6$ mm). Intake side on the bottom, exhaust side on the top.

The global deviation angle, made between the flow direction and the $-Y$ axis, is a weighted averaged value of the local flow direction at each point i with consideration of the local velocity intensity.

The instantaneous velocity contains turbulent fluctuations and may perturb the computation of Θ_{xy}, and trivariate 3D EMD is thus applied here to facilitate the characterization of the flow deviation. The LF part of the near piston flow below $Z = -85$ mm is shown in Figure 7.14 for the three cycles. The velocity components $U_{x,i}$ and $U_{y,i}$ are thus respectively replaced by $U_{x,i}^{LF}$ and $U_{y,i}^{LF}$ in the Equation 7.1.

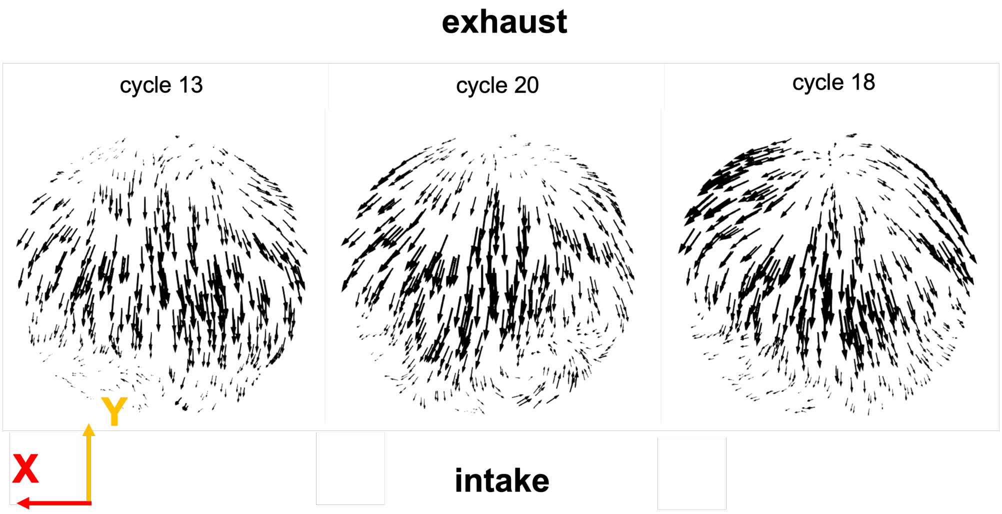

FIGURE 7.14: Filtered flow direction in the region under $Z = -85$ mm.

The correlation between the computed deviation angle $\overline{\Theta}_{xy}$ and the averaged tumble intensity around Y axis |CTR| at BDC is plotted in Figure 7.15.

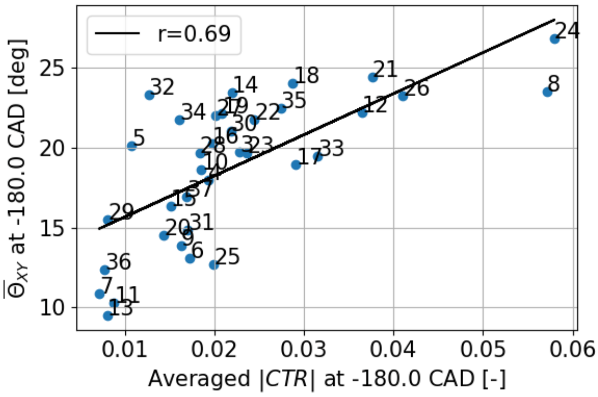

FIGURE 7.15: Correlation between the deviation angle $|\overline{\Theta}_{xy}|$ and CTR at BDC.

The direct impact of the flow deviation on the initial tumble shape can be deduced from the strong correlation between these two quantities. In section 7.3, we discovered that the tumble deformation was conditioned by the initial tumble distortion at BDC, quantified by |CTR|. The flow deviation over the piston, characterized by $|\overline{\Theta}_{xy}|$, was also found responsible for the tumble distortion. The deviation was caused by the impact of the primary flow on the exhaust side over the piston(cf Figure 7.2). The associated impacting region size differed significantly between the three extreme cycles, suggesting that the primary flow might already exhibit CCV in its structure. A potential link is thus expected to be built between the flow state at BDC and the intake flow during the intake stroke. In section 7.4, we will focus on the characterization of intake flow before BDC, which is also the most challenging part of this Chapter.

7.4 Exploration of the CCV sources from the flow organization during the intake stroke

In the previous section, the flow structure at BDC was analyzed, and the impact of the flow over the piston was found to be critical for the tumbling flow generation. The impact of the flow on the piston surface is generated by the primary flow (cf Figure 7.2) on the exhaust side, which is formed during the intake stroke. In this section, we will first attempt to characterize the primary flow on the exhaust side and link its variability to the flow deviation at BDC. As mentioned in section 7.1, the primary flow possibly results from the interaction between dominant flows. We also look forward to providing an intake flow division based on observations in the Darmstadt engine. The CCV in each dominant flow will then be quantified to explain the variability of the primary flow. Finally, we will investigate interactions between dominant flows and quantify their impact on the combustion process.

7.4.1 Characterization of the primary flow

The impact of the primary flow on the exhaust side over the piston surface has shown a significant disparity between cycles. The resulting deviation was successfully linked with the tumble deformation and the CCV of combustion. The impacting region is surely related to the structure of the primary flow, particularly its size. In Figure 7.16, the primary flow at -200 CAD is visualized for the three cycles 13, 20 and 18 using the iso-surface of $U_z = -10$ m/s. A qualitative comparison of the primary flow topology is proposed to understand the origin of the flow variability observed over the piston caused by the impact.

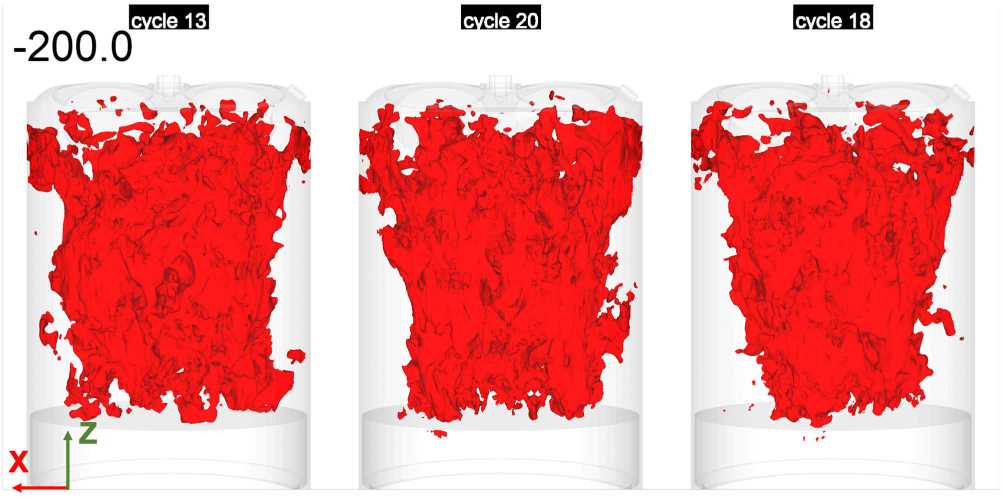

FIGURE 7.16: Intake jet at -200 CAD, visualized by iso-surface of $U_z = -10$ m/s. View from the exhaust side.

Differences can be marked in the primary flow's shape between the three chosen cycles: the primary flow of cycle 13 is almost of the same width along the vertical direction, whereas the one of cycle 18 is of conical shape with a larger size close to the cylinder head, and a smaller size near the piston. The width of the primary flow near the piston is crucial as it determines the shape of the impacting region and, therefore, could be linked to the flow deviation over the piston.

To quantify the size of the primary flow, a horizontal slice is made at $Z = -75.5$ mm at -200 CAD, which is about 9 mm above the piston. Trivariate 2D EMD is applied on this plane to filter turbulent fluctuations. The LF part of the normal component U_z^{LF} is used to identify regions where the primary flow passes. A threshold value arbitrarily set at -6 m/s allows to identify the core of the primary flow, colored in black in Figure 7.17.

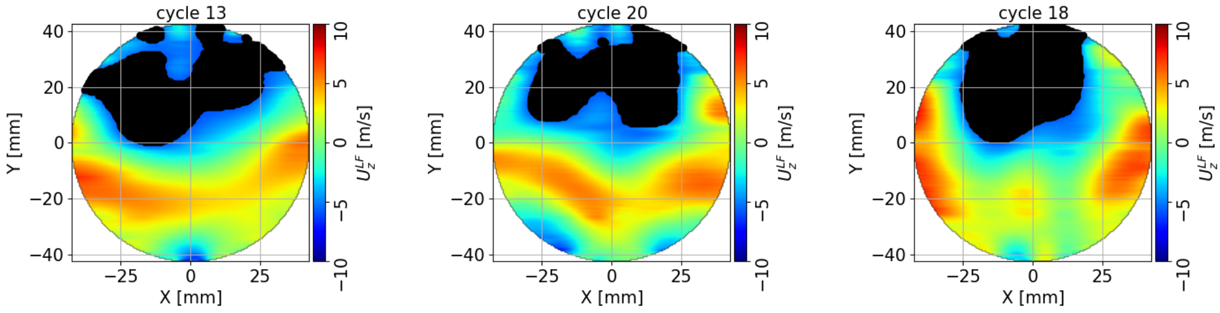

FIGURE 7.17: LF part of U_z in the horizontal plane at $Z = -75.5$ mm, regions of $U_z^{LF} \leq -6$ m/s are colored in black, representing the passage of the primary flow.

Different shapes of the primary flow region in the plane at $Z = -75.5$ mm are observed between the three cycles, which is consistent with the behavior of the flow deviation over the piston: for fast cycle 13, the primary flow region is much more expanded along the X direction and thinner along the Y direction, which leads to a less compact impact zone over the piston and consequently a weaker deviation; for slow cycle 18, the primary flow region is much more concentrated in the X direction and thicker in the Y direction, which leads to a more important deviation over the piston as the impact zone is more restricted. To characterize the shape of the primary flow zone, we propose the following definition of the flow size in the X and Y directions:

$$X_{jet} = \frac{1}{N_y} \sum_{i=1}^{N_y} X_i, \quad Y_{jet} = \frac{1}{N_x} \sum_{i=1}^{N_x} Y_i \tag{7.2}$$

where N_y and N_x represent respectively the number of lines (along X axis) and columns (along Y axis) passing through the primary flow region, and X_i and Y_i are respectively the lengths of each line and column inside the primary flow region. The quantified flow size in the X and Y directions X_{jet} and Y_{jet} are then correlated with the deviation angle $\overline{\Theta}_{xy}$, as presented in Figure 7.18.

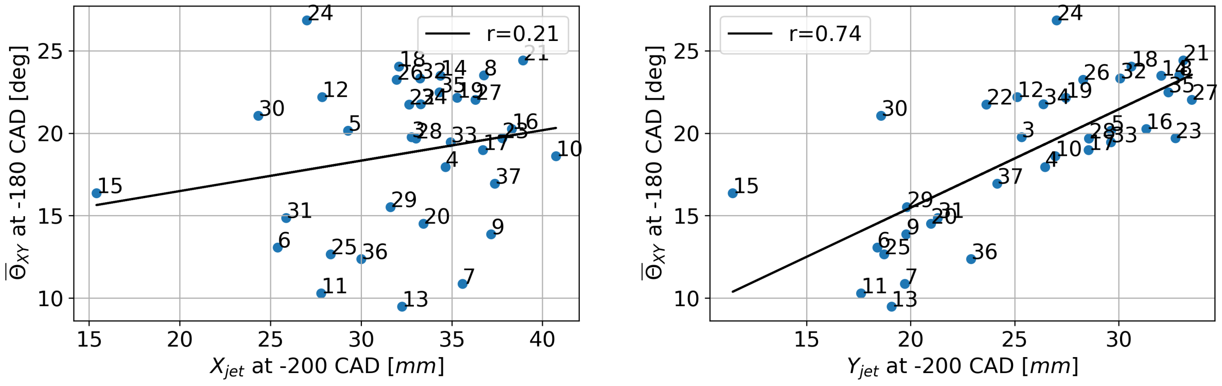

FIGURE 7.18: Correlation between the flow size and the deviation angle Θ_{xy}.

A strong correlation between the deviation angle Θ_{xy} and the primary descending flow's size in the Y direction can be seen, which allows us to link the large-scale variability of the primary flow formed during the intake stroke to the flow state at BDC. It is also worth noting that CCV of large-scale structures is at least already present in large-scale structures during the intake stroke at -200 CAD.

It is then essential to identify how the CCV of the primary flow are generated during the intake stroke. Since the primary flow can be partially observed in the tumble plane (cf Figure 7.2), we choose this plane again to follow the flow evolution during the intake stroke. Bivariate 2D EMD is applied on velocity fields in the tumble plane for every 5 CAD during the intake stroke. Results of some chosen crank angles are presented in Figure 7.19. The averaged CCV part $\overline{U_{ccv}}$ indicates regions where large-scale motions vary the most.

In this plane, we can follow the generation of the primary and secondary flows (cf Figure 7.2) and their penetration in the chamber:

- At -330 and -310 CAD, intake valve jets enter the chamber and interact with each other, resulting in forming a thick shear layer, noted as "central flow" in Figure 7.3. Regions of significant CCV are mainly located inside the interaction zone, indicating that the CCV generation occurs early during the engine cycle and is potentially caused by the intake valve jets' interaction.
- At -290 and -270 CAD, the formed central flow begins to move downwards from the exhaust and the intake sides, corresponding to respectively the primary and secondary flow, as illustrated in Figure 7.2. The CCV can be noticed in the central flow downstream, which is slightly beneath the interaction zone. It should be noted that the "tumble flow" and the "side flow" presented in Figure 7.3 are not visible in the tumble plane.
- At -250 and -230 CAD, the primary flow at the exhaust side advances much faster than the secondary one as it contains larger momentum. The tumble motion begins to fill the chamber. Significant CCV appear on the exhaust side around the corner made by the cylinder head and the liner where the primary flow deviates towards the piston. Compared to the primary flow, the secondary one seems more stable as the CCV level stays low in the corresponding region.
- At -210 and -190 CAD, the front of the primary flow arrives at the intake side and starts to encounter the secondary intake flow. Important CCV can be visualized in this interaction zone. Moreover, the same region of high CCV in the upper right corner associated with the primary flow is again observed at -250 and -230 CAD.

It can be summarized that CCV are already present in the in-cylinder flow during the intake stroke, and regions of significant CCV vary according to the flow evolution. Two important flows can be marked, the primary and the secondary flows in the central zone (cf Figure 7.2). The former brings the largest momentum in the chamber and exhibits much more variations at various instants, while the latter shows a weak level of variability. The interaction of these two main flow features also leads to local variations.

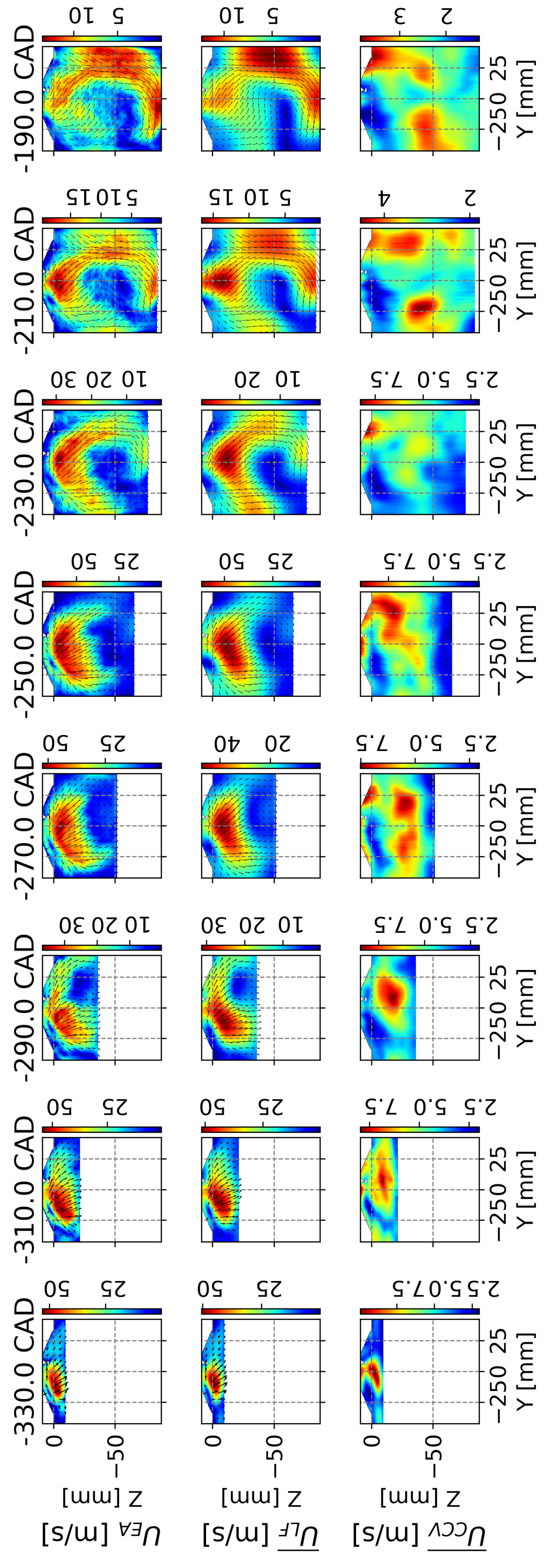

FIGURE 7.19: Evolution of the mean flow U_{EA}, the averaged LF part $\overline{U_{LF}}$ and CCV part $\overline{U_{CCV}}$ in the tumble plane during the intake stroke of the fired case.

From the primary flow visualization in Figure 7.16 and its characterization in the horizontal plane (cf Figure 7.17) and the tumble plane 7.2, we have seen that this important flow, formed during the intake stroke, presents already significant CCV. We intend to investigate the origin of these CCVs. Taking Y_{jet} as a descriptor of the primary flow at -200 CAD, we compute correlation maps between Y_{jet} and U_{ccv} in the tumble plane at earlier instants in the engine cycle to identify flow features that could cause the variability of the primary flow. Correlation maps are generated for -270, -250, -230, and -210 CAD and plotted in Figure 7.20.

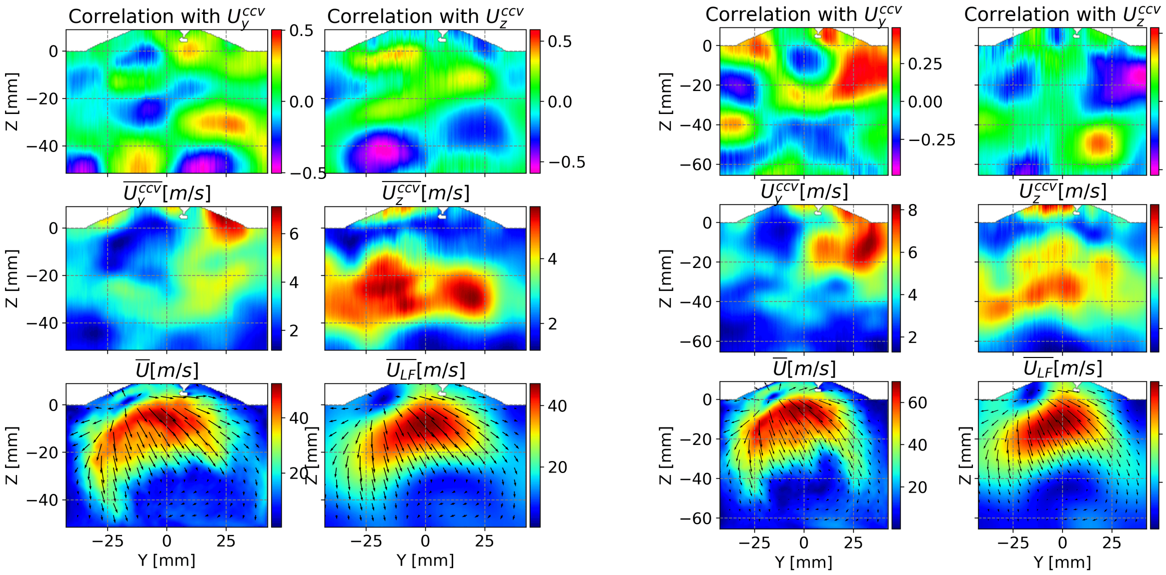

(A) −270 CAD.

(B) −250 CAD.

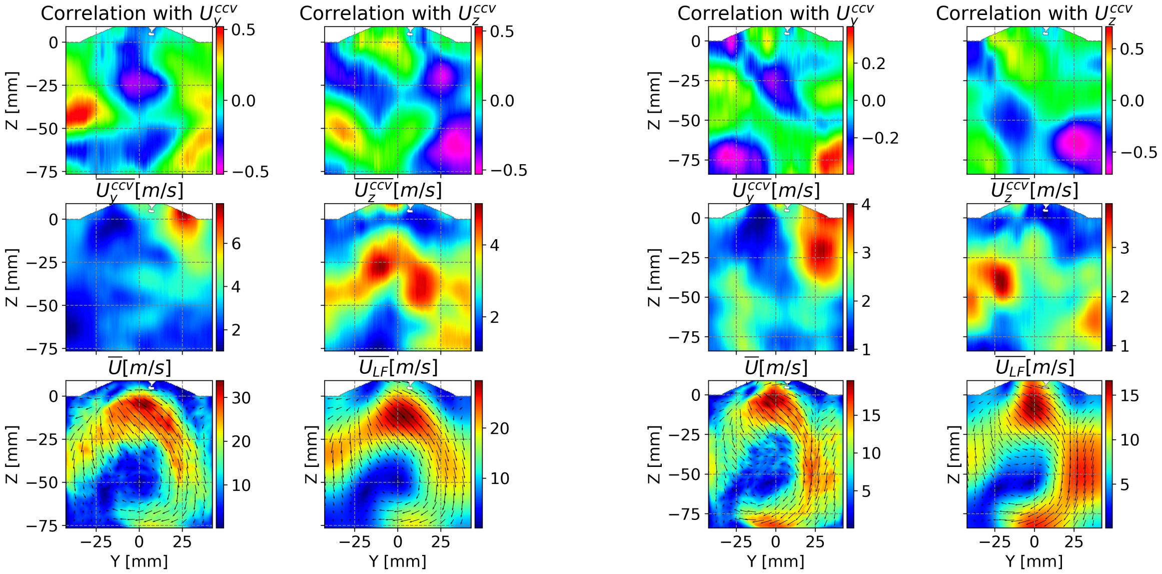

(C) −230 CAD.

(D) −210 CAD.

FIGURE 7.20: Correlation maps showing the correlation between the primary flow's size Y_{jet} and the LF part in the tumble plane.

Significant correlations can be found in primary or secondary flows in the central zone as shown in Figure 7.20:

- At −270 CAD (cf Figure 7.20a), the region above the piston, where the impact of the secondary flow on the piston takes place, shows a strong negative correlation (maximal correlation coefficient $r = -0.54$) between Y_{jet} and U_z^{ccv}, highlighting that the secondary and the primary flows are potentially coupled: The variability on the penetration of the secondary flow in the central zone at −270 CAD is correlated with the variability of the primary flow marked at −200 CAD.
- At −250 CAD (cf Figure 7.20b), regions of significant correlations (maximal correlation coefficient $r = 0.49$ with U_y^{ccv} and $r = -0.53$ with U_z^{ccv}) are concentrated around the upper right corner of the chamber, which also coincides with a high level of CCV. The primary flow's orientation in this area seems decisive for its later shape at −200 CAD.
- At −230 (cf Figure 7.20c) and −210 CAD (cf Figure 7.20d), negative correlations can be noticed in the lower part of the cylinder on the exhaust side with U_z^{ccv} (maximal correlation coefficient $r = -0.52$ at −230 CAD and $r = -0.68$ at −210 CAD), suggesting that the primary flow's shape is linked to its descending velocity. On the intake side at −230 CAD, a small area of positive correlation also exists near the front of the secondary flow where significant CCV are also present.

The above analysis is conducted in the central tumble plane corresponding to the interaction zone between both valve jets. It highlights that the primary flow's shape at −200 CAD is related to its prior advancement along the cylinder head and the liner on the exhaust side. The central secondary flow on the intake side also seems to influence the primary one on the opposite side, though no direct impact is noticed. A possible explanation is that the primary and the secondary flow are naturally coupled, as they are both generated by the intake valve jets since the beginning of intake stroke. Correlations between these two flows do not necessarily mean direct interaction but the dependence between them.

The primary flow (cf Figure 7.2) showed significant CCV in its shape at −200 CAD, which was recognized as the determinant factor for the flow deviation over the piston surface at BDC. We successfully linked the flow state at BDC to the primary flow which is only part of the global intake flow formed during the intake stroke. As discussed in section 7.1, the primary flow is possibly generated not only by the "central" flow but also by the "tumble flow" and "side flow" indicated in Figure 7.3. In the next section, similar to what was done by Krüger et al. [99], we will try to identify dominant flows formed during the intake stroke. The presence of CCV on each dominant flow will also be examined. The relation between the dominant flow and the primary flow will also be addressed.

7.4.2 Identification and characterization of dominant flows

The previous section highlighted the importance of the primary flow (cf Figure 7.2) on the flow deviation over the piston, which linked the flow state at BDC to the intake flow development. Nonetheless, the origin of the primary flow was challenging to fully explain using the only information from the tumble plane, as multiple sources could be responsible for it but were not visible in the tumble plane. In this section, we aim to precisely identify dominant flows in the 3D volume, based on the previous work of Krüger et al. [99]. CCV will also be quantified on each dominant flow. Finally, we will attempt to explain how CCV observed on the primary flow are generated.

To facilitate the identification of dominant flows, we apply spatial trivariate 3D EMD to the in-cylinder flow fields of all the LES cycles so that high-frequency fluctuations are removed. The instant −250 CAD is selected in this study based on our observation in the tumble plane (cf Figure 7.19):

- Principal flow structures are well present. The primary and secondary flows (defined in Figure 7.2) begin to penetrate the chamber towards the piston.
- The primary flow presents already high CCV as observed in the tumble plane.
- Some local flow features (*e.g.*, flow orientation in the upper right corner of the tumble plane) already indicate the future flow development.

The ensemble-averaged 3D LF part of the velocity field at −250 CAD is computed based on the LF part of the 35 LES cycles. In Figure 7.21, the ensemble-averaged LF part is visualized by its iso-surface of $|\overline{U_{LF}}| = 25$ m/s colored by U_z^{LF}.

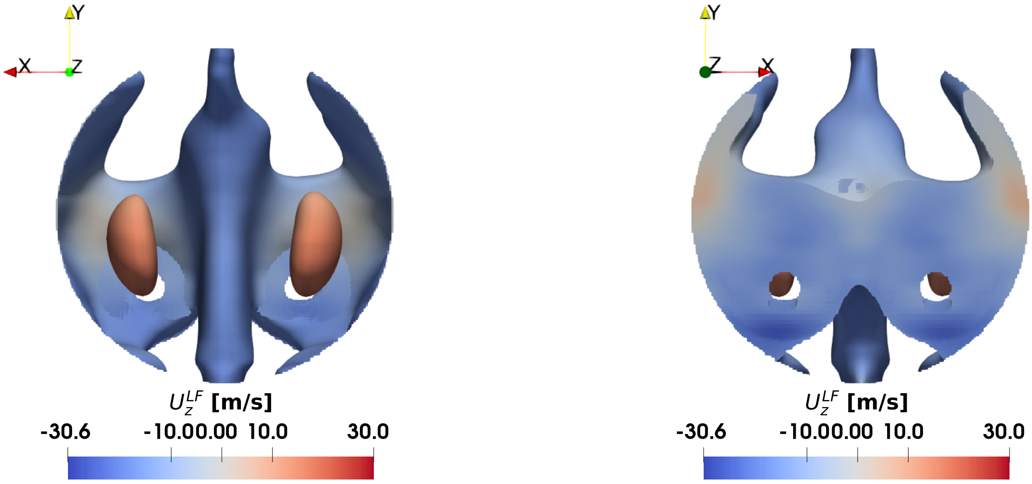

(A) Bottom.

(B) Top.

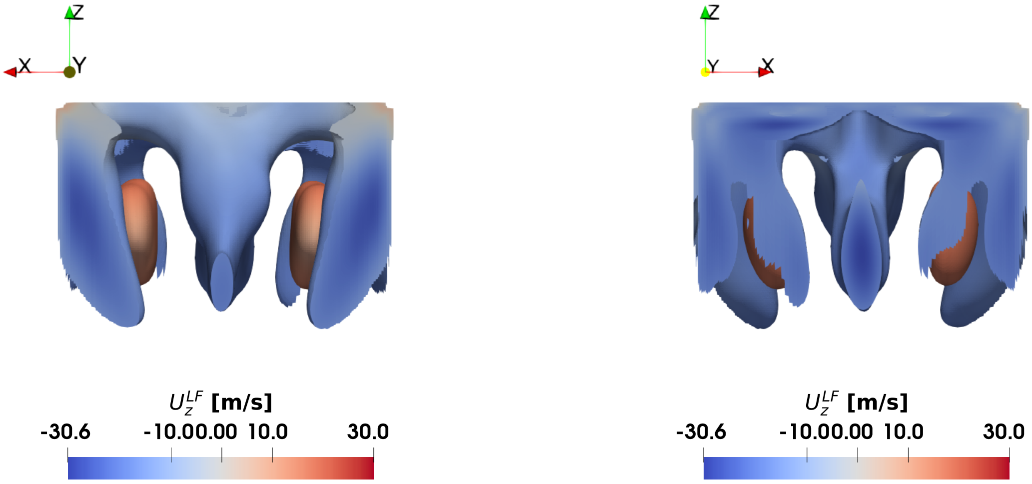

(C) Intake side.

(D) Exhaust side.

FIGURE 7.21: Iso-surface at 25 m/s of the averaged LF part $\overline{U_{LF}}$ of the in-cylinder flow at −250 CAD colored by U_z^{LF}.

The averaged behavior of the LF part at −250 CAD emphasizes that the intake flow generated during the first half of intake stroke is much more complicated than what can be visualized in the tumble plane. The primary and secondary flows we observe in the tumble plane are only a part of the intake flow structure. On the intake and exhaust sides, besides the primary and secondary flows, a lateral flow, created by the interaction between the intake valve jets and the lateral liner, is also present and corresponds to the "side flow" defined in Figure 7.3. The lateral flow tends to merge with the descending flow in the middle corresponding to the "central flow" defined in Figure 7.3. Red areas of positive vertical velocity are associated with the local flow recirculation between the "side flow" and "central flow", which is also presented in Figure 7.22 in the transversal plane $Y = 0$ mm.

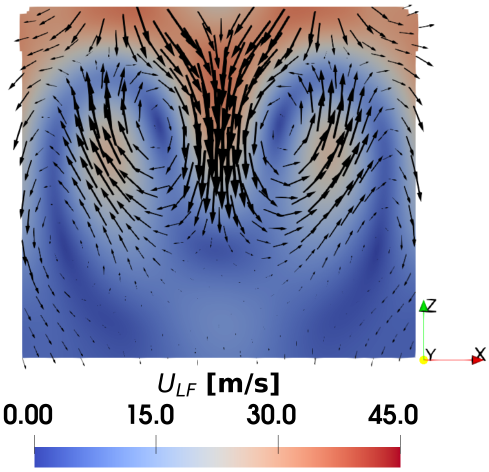

FIGURE 7.22: 2D slice at $Y = 0$ mm of the averaged 3D LF part of the velocity field at -250 CAD. Red cores are associated with the local flow recirculation between the "side flow" and "central flow".

Based on the intake flow division proposed by Krüger et al. [99] and presented in Figure 7.3, and also observations on the averaged 3D LF part presented in Figure 7.21, we propose our 3D flow division as shown in Figure 7.23.

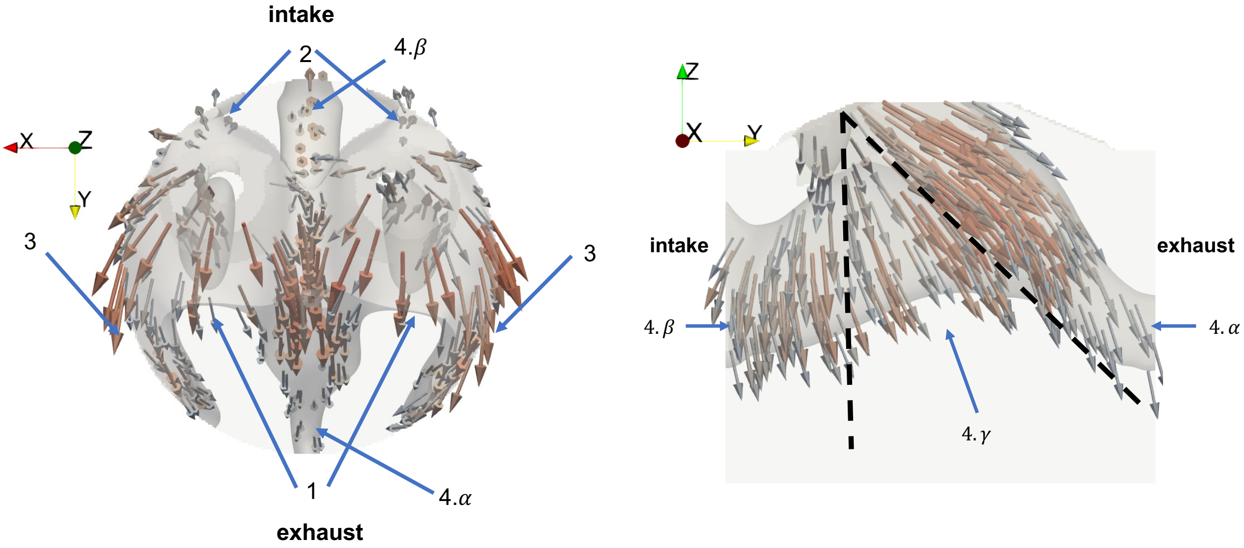

FIGURE 7.23: Iso-surface at 20 m/s of the ensemble-averaged LF part $\overline{U_{LF}}$ of the in-cylinder flow at -250 CAD, combined with velocity vectors. Dominant flows are identified: 1 - Primary jet flow; 2 - Secondary jet flow; 3 - Side flow; 4 - Central flow, 4.α towards the exhaust side, 4.β towards the intake side, and 4.γ penetrate directly towards the piston.

- Flow 1, named "primary jet flow", is part of intake valve jets towards the exhaust side, penetrating the chamber independently.
- Flow 2, named "secondary jet flow", is part of intake valve jets towards the intake side, penetrating the chamber independently.
- Flow 3, named "side flow", represents the lateral side flow resulting from the interaction between the lateral liner and intake valve jets.
- Flow 4, named "central flow", represents the internal side flow generated by the interaction between intake valve jets.

Flow 4 is again divided into 4.α, 4.β, and 4.γ, as illustrated in Figure 7.23:

- Flow 4.α is the part of flow 4 towards the exhaust side, *i.e.* the primary flow in the central zone.
- Flow 4.β is the part of flow 4 towards the intake side, *i.e.* the secondary flow in the central zone.
- Flow 4.γ is the rest part of flow 4 towards the piston.

The tumble plane passes through flow 4, and the primary and secondary flows defined in Figure 7.2 are mainly related to flow 4.α and flow 4.β, which are only part of the global intake flow according to our intake flow division. Flow 1 and 3, which move towards the exhaust side, could join flow 4.α to form the primary flow; Flow 2, which moves towards the intake side, might also merge with Flow 4.β to generate the secondary flow.

The computed 3D LF parts of all the 35 LES cycles also allow us to quantify CCV of the intake flow, but only at -250 CAD. The variability of the 3D LF part is evaluated, and the averaged 3D CCV part $\overline{U_{ccv}}$ at -250 CAD is presented in Figure 7.24.

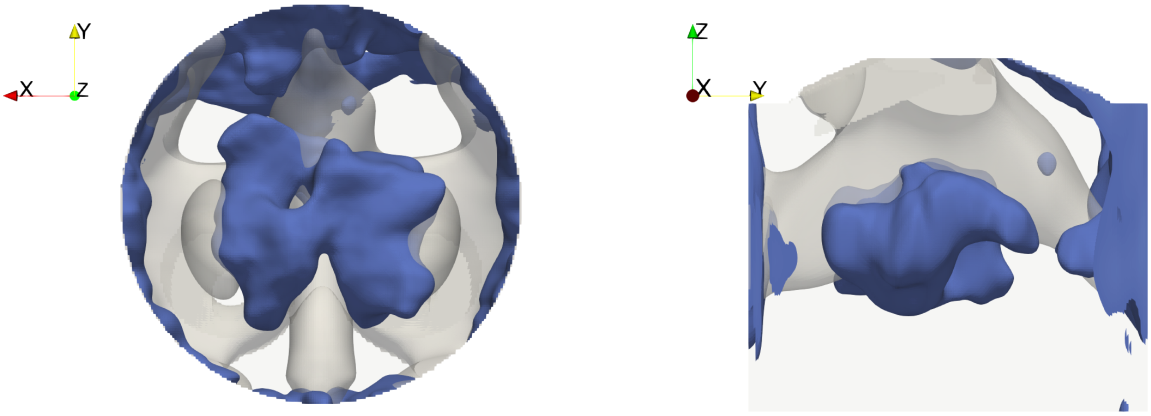

FIGURE 7.24: Iso-surface of $\overline{U_{CCV}}$ at 4.5 m/s (blue) overlaid on the iso-surface of averaged LF part $\overline{U_{LF}}$ at 25 m/s (gray). Regions of high variability are identified around the internal side flow 4.α, 4.β and 4.γ.

It can be noticed that significant CCV are mainly located around flow 4.

- An important region of high CCV is identified between the two cores, previously presented in Figure 7.22, and around the interaction zone in the middle of the chamber, corresponding to the location of flow 4.γ.

- CCV are also observed close to flow 4.α in the region where the local flow deviates towards the piston. Significant CCV were also captured by bivariate 2D EMD in the part of the tumble plane at -250 CAD (cf Figure 7.19).
- The other dominant flows exhibit much less CCV than flow 4, suggesting that the intake valve jets' interaction in the middle of the chamber brings most CCV in large-scale motions during the intake stroke.

The comparison of the LF part at -250 CAD between the three cycles 13, 20, and 18 is given in Figure 7.25. In agreement with previous observations on the averaged CCV part of the intake flow at -250 CAD, the three cycles show apparent differences in flow 4, particularly around flow 4.γ inside the interaction zone and flow 4.α towards the exhaust side. All these differences could lead to further disparities between these cycles, as observed in the primary flow in section 7.4.1.

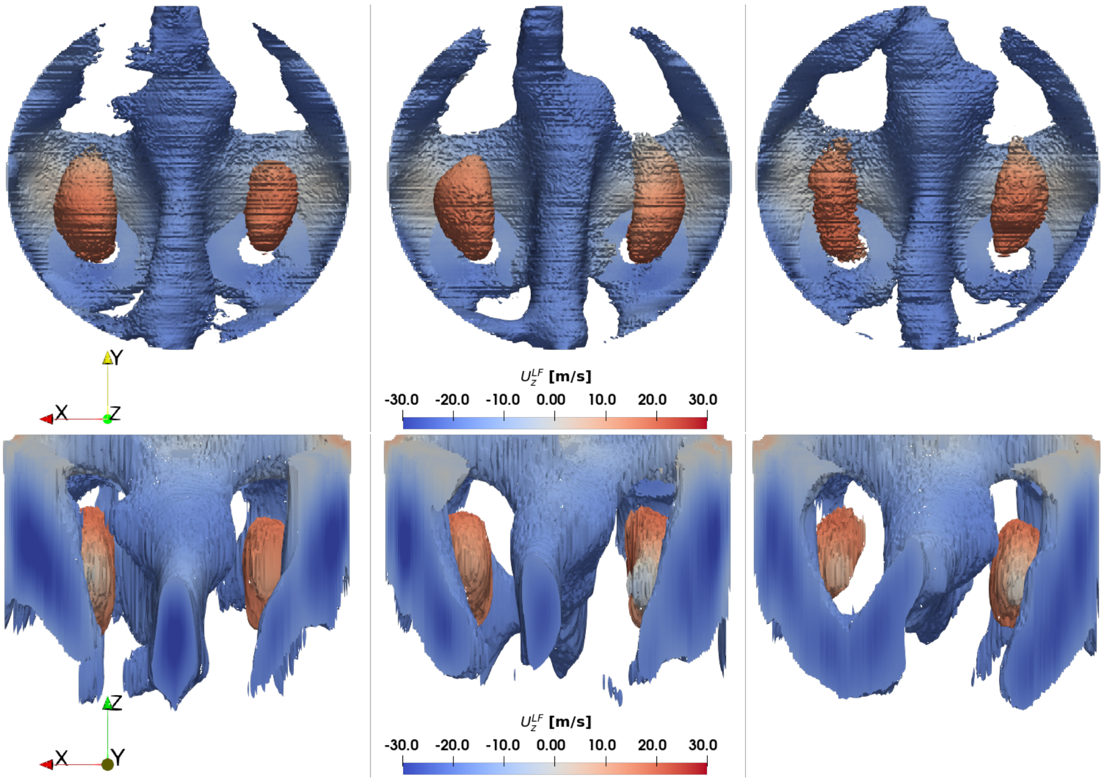

FIGURE 7.25: Comparison of the LF part between cycles 13, 20, and 18. Differences can be noticed in the structure of the central flow 4. Iso-surface of $\overline{U_{LF}}$ is at 20 m/s and colored by U_z^{LF}.

Despite the potential of spatial 3D EMD to improve the understanding of the in-cylinder flow structures, it is yet too expensive to be applied massively to follow the flow evolution in 3D. However, results at -250 CAD provide a distinct identification of dominant flows and the location of each dominant flow in the chamber. We will return to the multi-planar analysis based on 2D EMD, with a suitable choice of planes to characterize each dominant flow and its CCV. A particular focus will be put on flow 4, which was recognized as the primary CCV source during the intake stroke. In addition to the tumble plane studied previously (cf Figure 7.19), a transversal plane at $Y = 30$ mm is added to visualize flow 4.α, flow 1, and flow 3; another transversal plane at $Y = -35$ mm is also chosen to capture flow 4.β and flow 2; a horizontal plane is also used, whose position varies dynamically with the piston motion to stay in the middle of the cylinder. A schematic presentation of the chosen planes is given in Figure 7.26.

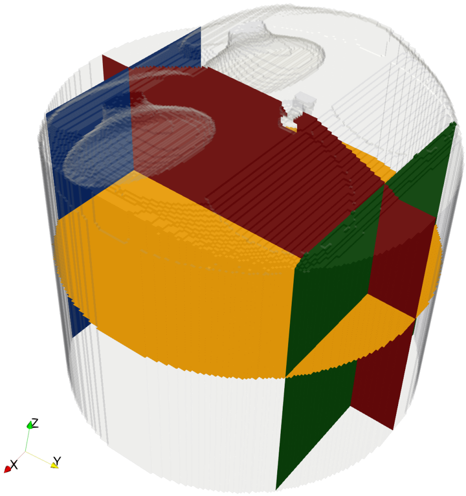

FIGURE 7.26: Planes chosen for the multi-planar analysis: transversal plane P_1 at $Y = 30\ mm$ (green), transversal plane P_2 at $Y = -35\ mm$ (blue), tumble plane P_3 at $X = 0\ mm$ (red) and swirl plane P_4 at $Z = Z_{piston}/2$ (orange).

Unlike the tumble motion visualized in the tumble plane, these dominant flows do not evolve in the tangential direction of chosen planes. Therefore, the third velocity component is considered in the EMD analysis. Trivariate 2D EMD is thus applied to velocity fields in the three added planes to complete the statistical description of the in-cylinder flow evolution during the intake stroke, which was partially achieved in the tumble plane (cf Figure 7.19).

Flow 4.α and flow 3 are captured in the plane at $Y = 30$ mm, and the results are illustrated in Figure 7.27:

- At -330 CAD, flow 4.α arrives at first in the plane, and flow 3 appears slightly later.
- Between -330 and -250 CAD, most CCV are associated with flow 4.α in the middle of the plane, confirming our previous observation on the variability of the 3D LF part at -250 CAD (cf Figure 7.24).
- The flow 3 converges towards the central area and gradually merges with flow 4.α to form the primary flow corresponding to the structure visualized in Figure 7.16.
- Starting from -230 CAD, the primary flow also presents CCV on its lateral sides in the regions where the flow presents a convergent shape, indicating an interaction between flow 4.α and flow 3 occurs and leads to CCV in large-scale structures.
- Flow 1 is not captured in this plane, possibly due to its weak penetration towards this transversal plane.

It is worth noting that the characterization of the primary flow's shape presented in Figure 7.17 is coherent with what is observed in the transversal plane at $Y = 30$ mm. The interaction and the merge between flow 4.α and flow 3 results in a variable primary flow that presents a more or less convergent shape and further leads to different behaviors of flow deviation over the piston surface. Analyses with 3D EMD at -250 CAD (cf Figure 7.24) and with 2D EMD in the plane at $Y = 30$ mm (cf Figure 7.27) demonstrate that CCV associated with flow 4.α are higher than those of flow 3. Therefore, Flow 4, recognized as the main source of flow CCV at -250 CAD, might contribute to the CCV generation in the overall intake flow development.

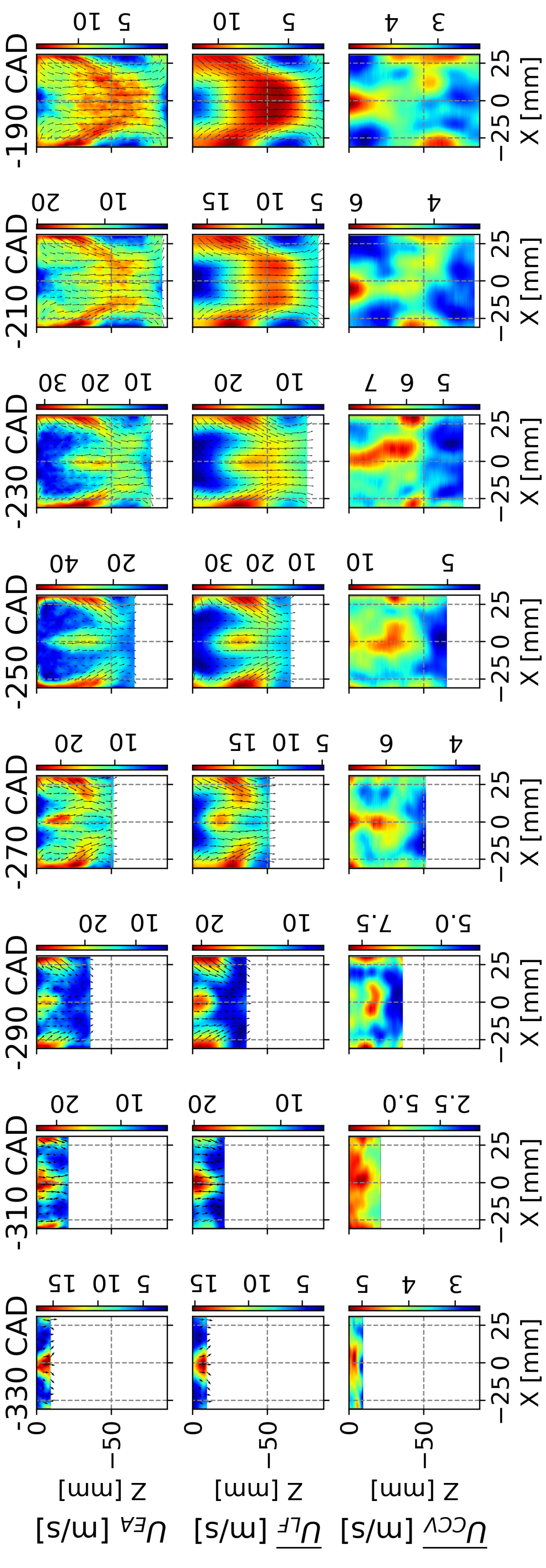

FIGURE 7.27: Evolution of the mean flow U_{EA}, the averaged LF part $\overline{U_{LF}}$ and CCV part $\overline{U_{CCV}}$ in the transversal plane at $Y = 30\ mm$.

The same analysis is performed in the transversal plane at $Y = -35$ mm to characterize flow 4.β and flow 2. The results are presented in Figure 7.28:

- Flow 2 reaches the plane earlier than flow 4.β, as the valve gap is very close to this plane. Most CCV are also related to flow 2 between -330 CAD and -290 CAD.
- A merge process between these two dominant flows can be noticed after -250 CAD, which is similar to that between flow 3 and flow 4.α. The resulting secondary flow also presents a convergent shape with a pair of low-velocity regions on its lateral sides. A high level of CCV is also present in the same regions.

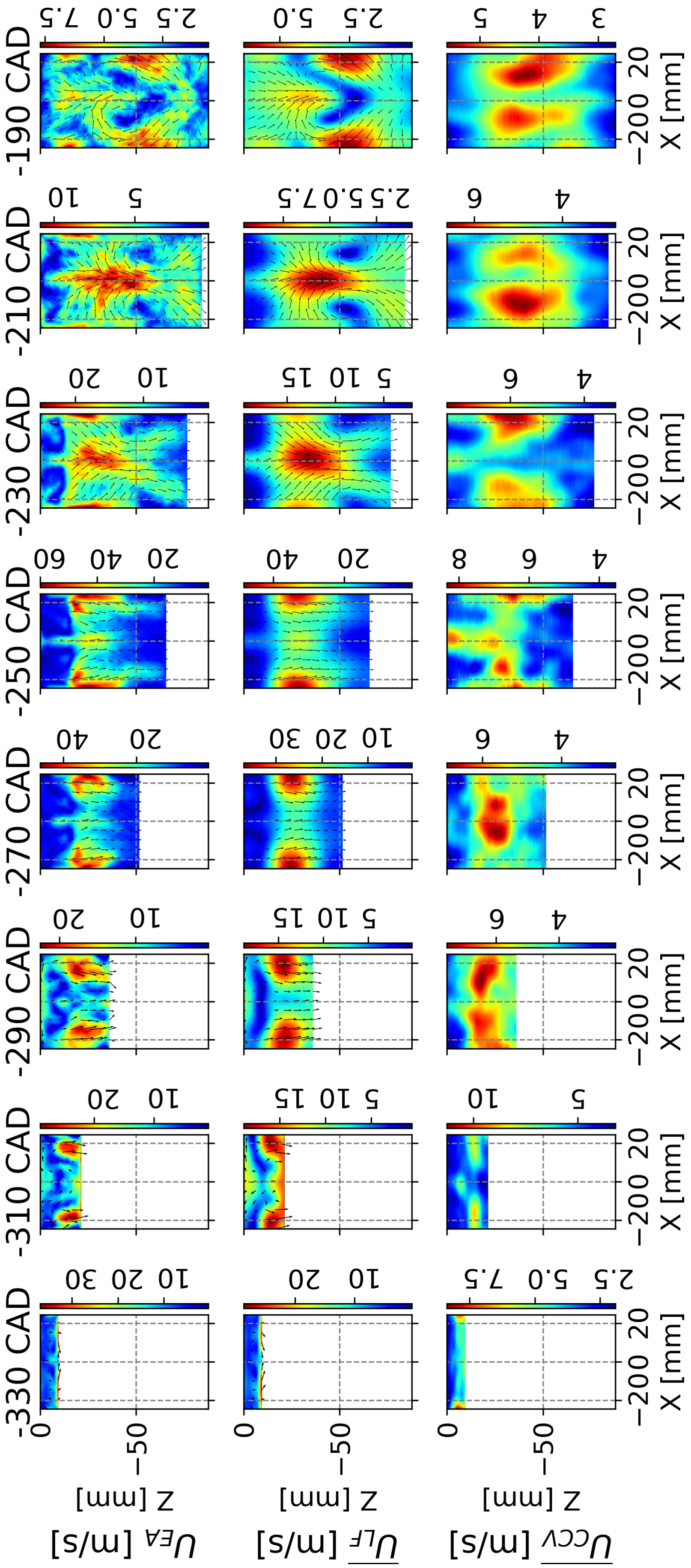

FIGURE 7.28: Evolution of the mean flow U_{EA}, the averaged LF part $\overline{U_{LF}}$ and CCV part $\overline{U_{CCV}}$ in the transversal plane at $Y = -35\ mm$.

The last plane located horizontally in the middle of the chamber is used to follow the penetration of all the dominant flows toward the piston. The results of trivariate 2D EMD are shown in Figure 7.29:

- Between -330 CAD and -290 CAD, the dominant structure in the chamber is valve jets that exit valve gaps and impact the piston directly. A ω shape distribution of the intake flow can be observed, corresponding to the intake valve jets entering from the lower side of valve gaps.
- Once the piston begins to move downwards, flow 4 is already present in the central part, and flow 4.γ starts to penetrate the chamber. Important CCV are noticed around it as shown from -310 to -250 CAD, which is coherent with our observations on the CCV of the 3D intake flow at -250 CAD (cf Figure 7.24).
- Flow 3 moves gradually along the liner towards the exhaust side to encounter flow 4.α. These two flows appear on the exhaust side at -250 and -230 CAD.
- At -210 and -190 CAD, we can not distinguish flow 4.α and flow 3 because the merge process has started, confirmed by previous observations in the plane at $Y = 30$ mm (cf Figure 7.27). The merged primary flow is strongly present on the exhaust side. The secondary flow also passes through this plane on the intake side and brings more CCV than the primary one.

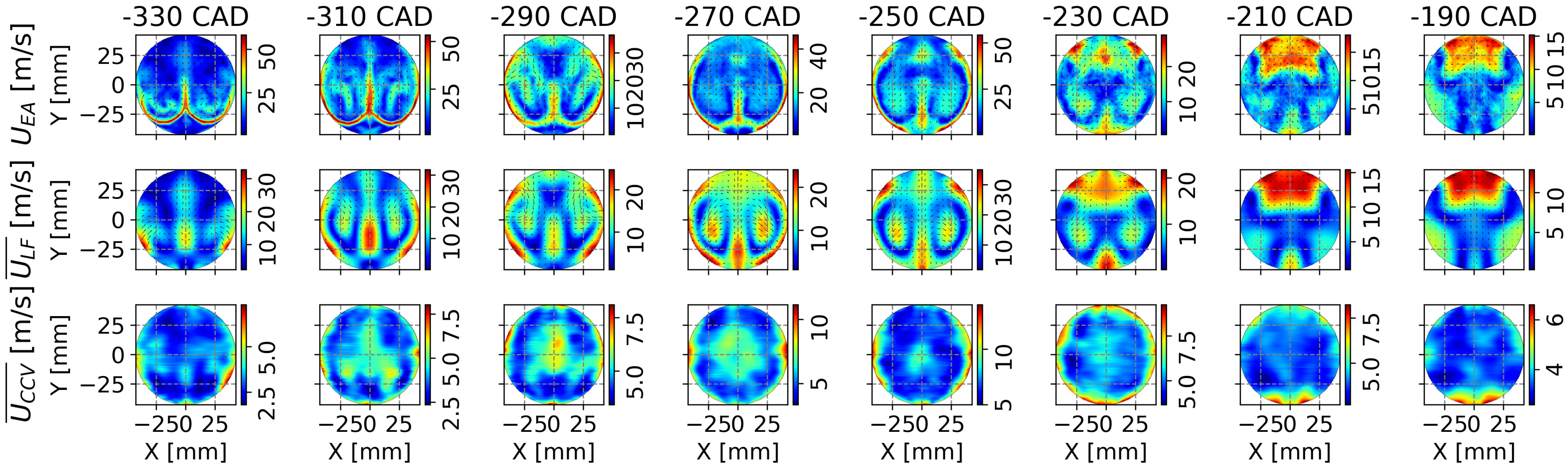

FIGURE 7.29: Evolution of the mean flow U_{EA}, the averaged LF part $\overline{U_{LF}}$ and CCV part $\overline{U_{CCV}}$ in the transversal plane at $Z = Z_{piston}/2$.

According to the multi-planner analysis, we can conclude that:

- The presence of flows 2, 3, and 4 are visualized in different planes, while flow 1 was not present. Two merge processes between dominant flows were identified: flow 3 and flow 4.α form the primary flow; flow 2 and flow 4.β form the secondary flow. Flow 1 was not seen and might be due to its weak penetration in the chamber. The application of 3D EMD to some chosen instants during the intake stroke could help follow its advancement.
- CCV can be mainly noticed on flow 4 at a very early stage of the intake stroke, suggesting that CCV are caused by the intake flow, especially by the interaction between intake valve jets since the opening of intake valves.
- CCV of flow 4 lead to those of the primary flow as observed in the transversal plane at $Y = 30$ mm. The interaction between flow 3 and flow 4.α yields a high level of CCV, which is a direct cause of the cyclic variability presented by the shape of the primary flow.

The analysis in this section allowed us to partially answer the questions summarized in Figure 7.1 concerning the intake flow:

- Four dominant flows were identified during the intake stroke, similar to what was done by Krüger et al. [99].
- Beside flow 1, all the other dominant flows were carefully studied, and the CCV of each one were quantified. Among the four dominant flows, flow 4 is the most fluctuating one.
- Two merge processes between dominant flows were identified, which gave birth to the two descending flows presented in Figure 7.2. CCV were also noticed on these two flows, especially on the primary flow, correlated to the flow deviation at BDC. The link between the intake flow development and the flow state at BDC was thus extended.

For now, most attention has been paid to the primary flow, whereas the impact of the secondary one on the combustion process was not addressed. In the next section, we will focus on the combined effects of all the dominant flows on the CCV of combustion.

7.4.3 Analysis of the combined effects of dominant flows on the CCV

In the multi-planar analysis, several in-cylinder events were identified during the intake stroke, including flow/wall interactions and interactions between dominant flows. All these interactions can potentially impact, individually or collectively, the formation of the tumble motion and the combustion speed. In this section, we propose collectively applying the univariate and multivariate linear regressions to investigate the link between important flow events and the combustion process.

We use 2D correlation maps to identify regions of interest in LF parts of different planes and then extract local flow features by computing the averaged velocity inside these regions. Two descriptors are chosen, the primary flow's size Y_{jet} at -200 CAD and the combustion speed S_{-10}, to correlate with extracted local flow features in different planes. The former was identified as an important factor for the flow deviation over the piston and the tumble formation, while the latter quantifies the variability of the combustion process that results principally from the variability of the in-cylinder flow.

Impact of valve jet interactions on CCV with a focus on flow 4.α

Correlations between the LF velocity at -250 CAD and the size Y_{jet} of the primary flow at -200 CAD in the tumble plane allow emphasizing the effect of flow 4.α, as illustrated in Figure 7.30.

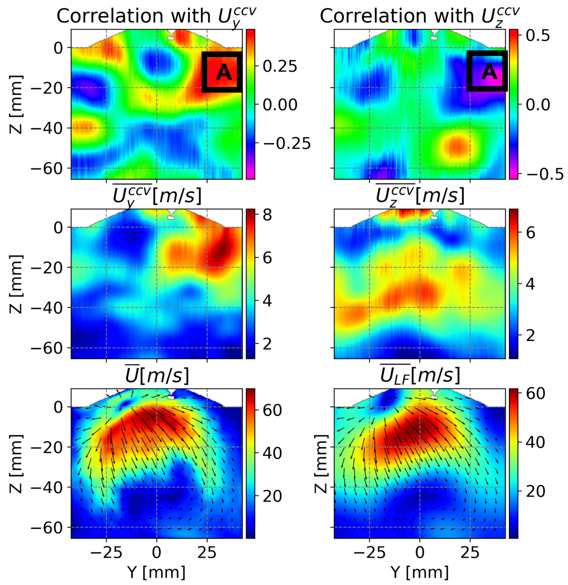

FIGURE 7.30: Correlation maps showing the correlation between the jet's size Y_{jet} and the LF part in the tumble plane at −250 CAD. Zone A stands for regions of significant correlation related to the deviation of the primary flow at the upper right corner.

The region of significant correlations is located in the upper right corner (averaged correlation coefficient $r = 0.48$ with U_y^{ccv} and $r = -0.51$ with U_z^{ccv}), which has been already discussed in section 7.4.1. A deviation of Flow 4.α is undergoing at this instant in this region where significant CCV are present, suggesting that flow 4.α presents a significant variability. The primary flow was found (cf Figure 7.27) formed by flow 3 and flow 4.α, and the variability of flow 4.α can be conserved in the primary flow, resulting in CCV in its shape.

Combined effect of the secondary flow and valve jet interactions on CCV with a focus on flow 2 and flow 4.β

The impact of dominant flow 2, flow 4.β, and the formed secondary flow, captured by the tumble plane (cf 7.19) and transversal plane at $Y = -35$ mm (cf 7.28), is studied at first. Correlation maps are generated between LF parts of these two planes and the two chosen descriptors. Three correlation maps are shown in Figure 7.31.

- In Figure 7.31a, a region of negative correlation between U_z^{ccv} and Y_{jet} is located around the front of the secondary flow near the piston, indicating that the descending velocity of the secondary flow can impact the shape of the primary flow. However, no direct interaction between these two flows occurs at this instant. Regarding the CCV distribution of U_z, it can be recognized that the penetration of flow 4 is highly variable, which can be related to the interaction between intake valve jets. The distributions of flow 4.α and flow 4.β could be naturally coupled as they are generated by the same mechanism.
- In Figure 7.31b and Figure 7.31c, the same region showing correlations with S_{-10} is identified in the two planes, which are located at the corner made by the liner and the cylinder head on the intake side. Flow 4.β experiences a deviation in the same region, and these correlations may be associated with the local orientation of flow 4.β. The tumble motion was always

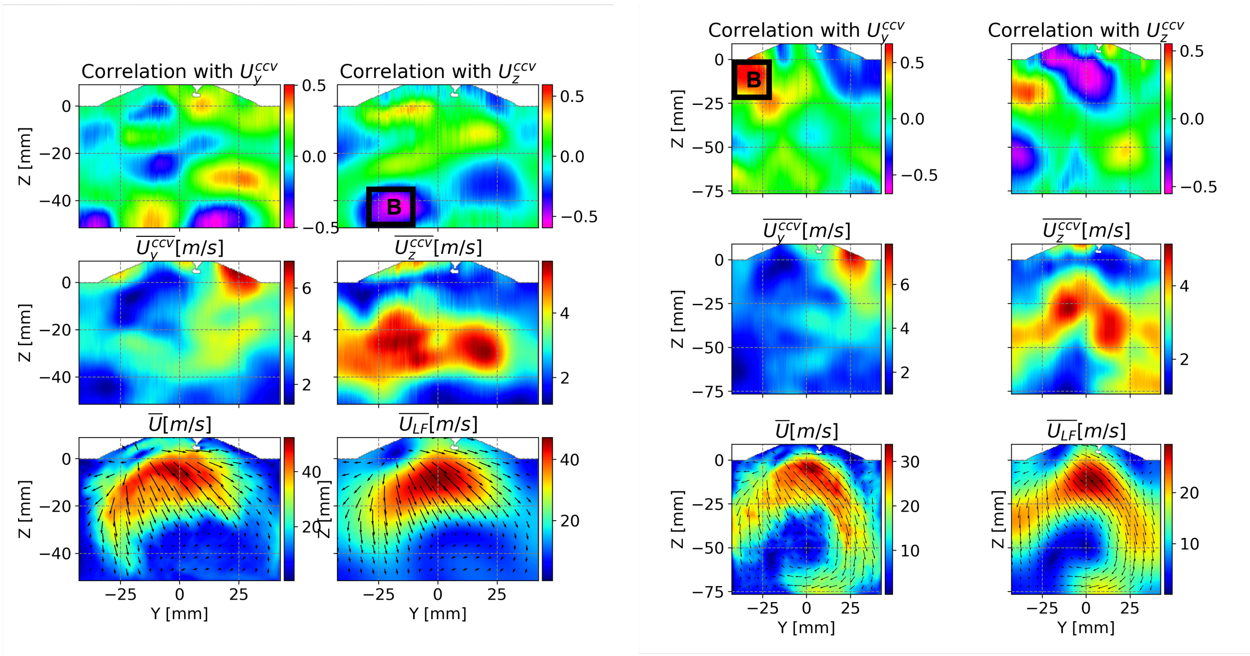

(A) with Y_{jet} in the tumble plane at −270 CAD.

(B) with S_{-10} in the tumble plane at −230 CAD.

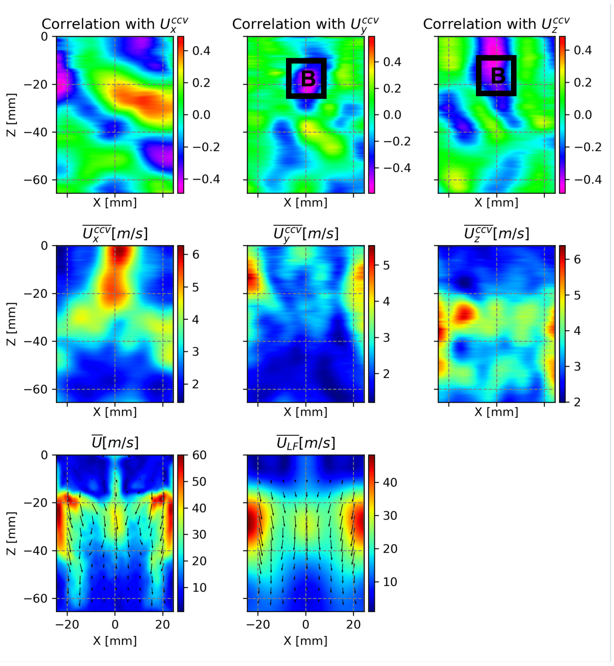

(C) with Y_{jet} in the transversal plane at $Y = -35$ mm at −250 CAD.

FIGURE 7.31: Correlation maps showing the correlation between the jet's size Y_{jet} or the combustion speed S_{-10} and the LF part of the secondary flow. Zone B stands for regions of significant correlation related to the secondary flow.

considered the major CCV factor, and it was mainly associated with the primary flow. However, the impact of the secondary flow on the tumble motion, which could help explain the observed correlations, was never explored before.

Regions of interest with significant correlations are all surrounded by a black box and noted as B for flow features related to the secondary flow.

Impact of valve jet interactions on CCV with a focus on flow 4.γ

The impact of dominant flow 4.γ, captured by the tumble plane (cf 7.19), is then investigated. Its correlation with the combustion speed S_{-10} at -250 CAD is presented in Figure 7.32.

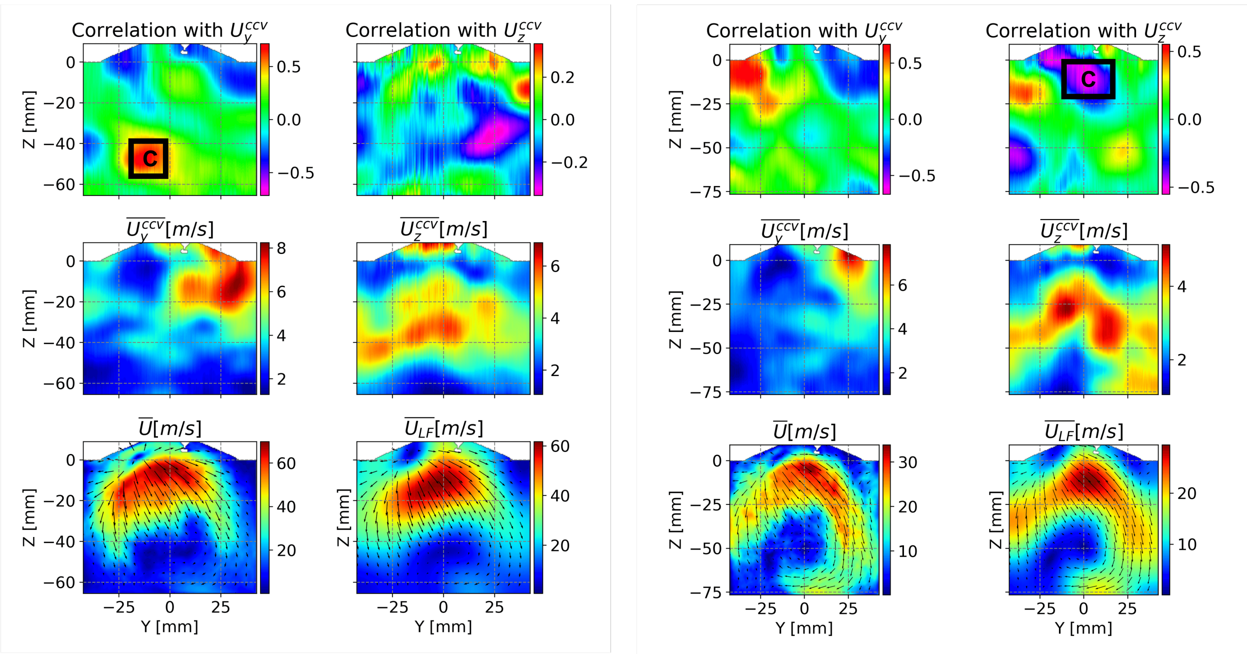

(A) with S_{-10} in the tumble plane at -250 CAD.

(B) with S_{-10} in the tumble plane at -230 CAD.

FIGURE 7.32: Correlation maps showing the correlation between the combustion speed S_{-10} and the LF part in the tumble plane. Zone C stands for regions of significant correlation related to the flow 4.γ.

- At -250 CAD, a region of significant positive correlation with U_y^{ccv} is found beneath the interaction zone, which overlaps the location of flow 4.γ. The averaged LF part in the same area is close to 0 m/s, indicating that this region is near the front of flow 4.γ. The correlation corresponds to the penetration of flow 4.γ that varies significantly between cycles.
- At -230 CAD, another region of negative correlation with U_z^{ccv} is present inside the interaction zone below the spark plug. An important level of variability of U_z^{ccv} is also visible in the same region, which is related to the penetration of flow 4.γ in the central region.

At -250 CAD, the fronts of flow 4.α and flow 4.β start to arrive in the same region where U_y^{ccv} correlates positively with S_{-10}. An interaction between the three sub-flows of flow 4 could occur in this region. We compare the LF part in the tumble plane at -250 CAD for five cycles (2 more cycles 7 (fast) and 12 (slow) are added) in Figure 7.33.

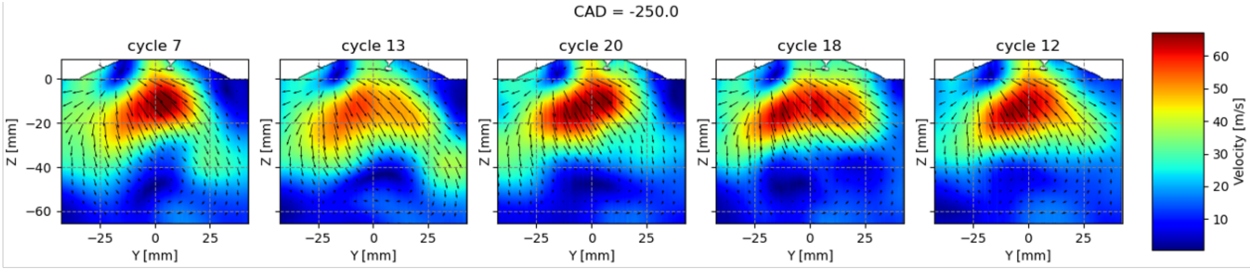

FIGURE 7.33: Comparison of the LF part in the tumble plane at -250 CAD obtained by 2D EMD for fast cycles 7 and 13, median cycle 29, and slow cycles 18 and 12.

A significant variability of flow 4 can be observed: for fast cycles, flow 4.α and flow 4.β penetrate more deeply than flow 4.γ, and the front of flow 4 is curved; for slow cycles, the global penetration of flow 4 is more balanced between the three sub-flows, and the front of flow 4 is plate.

The comparison is also made in 3D by comparing the averaged LF part obtained by 3D EMD of the five fastest cycles and with that of the five slowest cycles, as shown in Figure 7.34. The isosurface of U_{LF} presented in Figure 7.34a emphasizes the variability of flow 4, especially the shape of its front that depends on the penetration of its sub-flow 4.γ. The comparison made in the tumble plane plotted in Figure 7.34b also indicates that the local flow feature inside the red frame differs between the two groups of cycles: for fast cycles, the local flow is quite calm; for slow cycles, the local flow is towards the intake side, *i.e.* U_y^{LF} is negative. The local flow is resulted from the interaction between the three sub-flows, suggesting that the distribution of flow 4 formed during the early stage of intake stroke could already exhibit a certain level of CCV that is accumulated gradually during the development of intake flow.

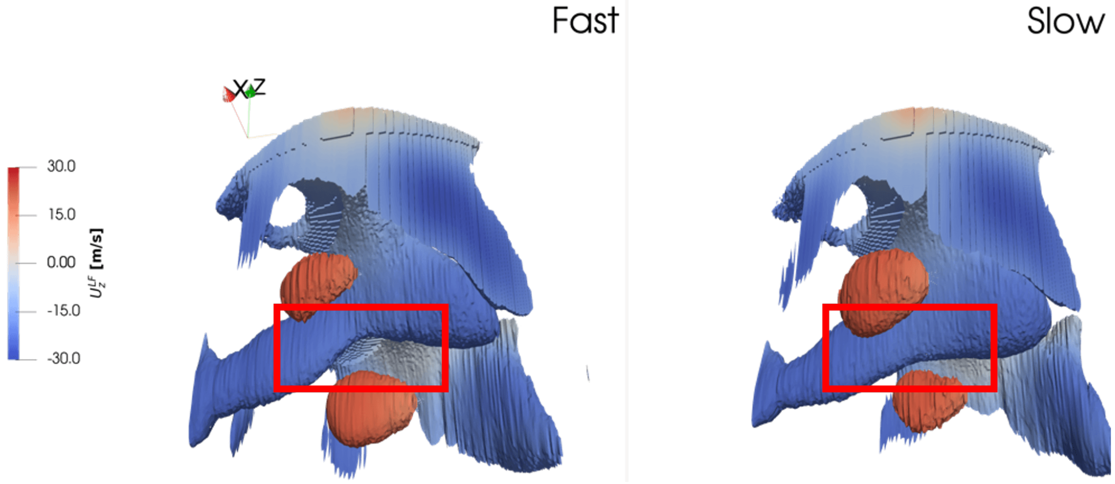

(A) Isosurface of $U_{LF} = 25$ m/s, colored by U_z^{LF}.

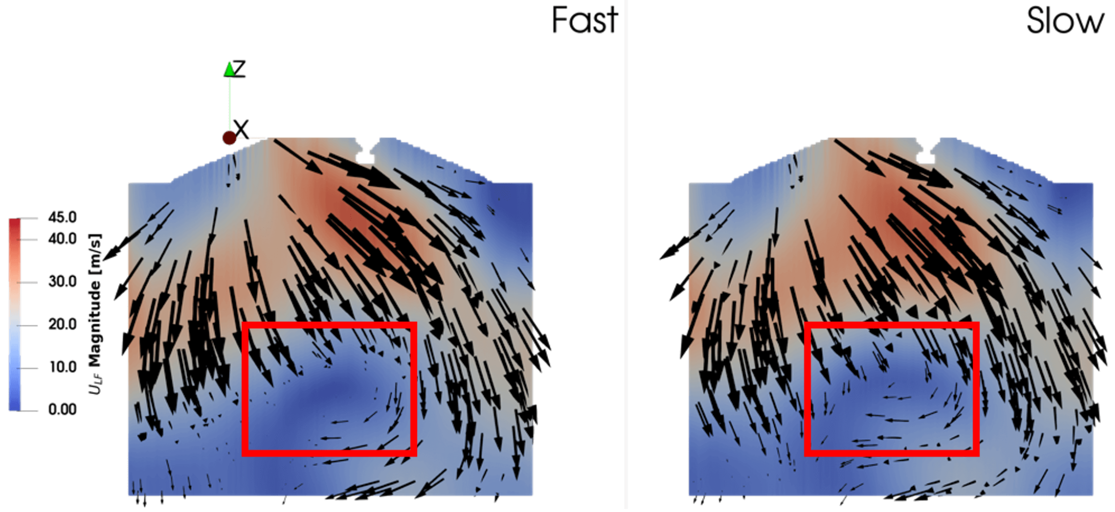

(B) U_{LF} in the tumble plane obtained by 3D EMD.

FIGURE 7.34: Comparison of the averaged LF part at -250 CAD obtained by 3D EMD between the five fastest cycles and five slowest cycles. Differences can be observed in the red frame.

We did not succeed in establishing links between the spatial distribution of flow 4 and the tumble formation, which merits further attention in future work.

Combined effects of the lateral flow, primary flow and valve jet interactions on CCV with a focus on flow 3 and flow 4.α

Last but not least, flow 3, flow 4.α, and the formed primary flow, characterized in the tumble plane (cf 7.19) and transversal plane at $Y = 30$ mm (cf 7.27), are analyzed. Two correlation maps are shown in Figure 7.35.

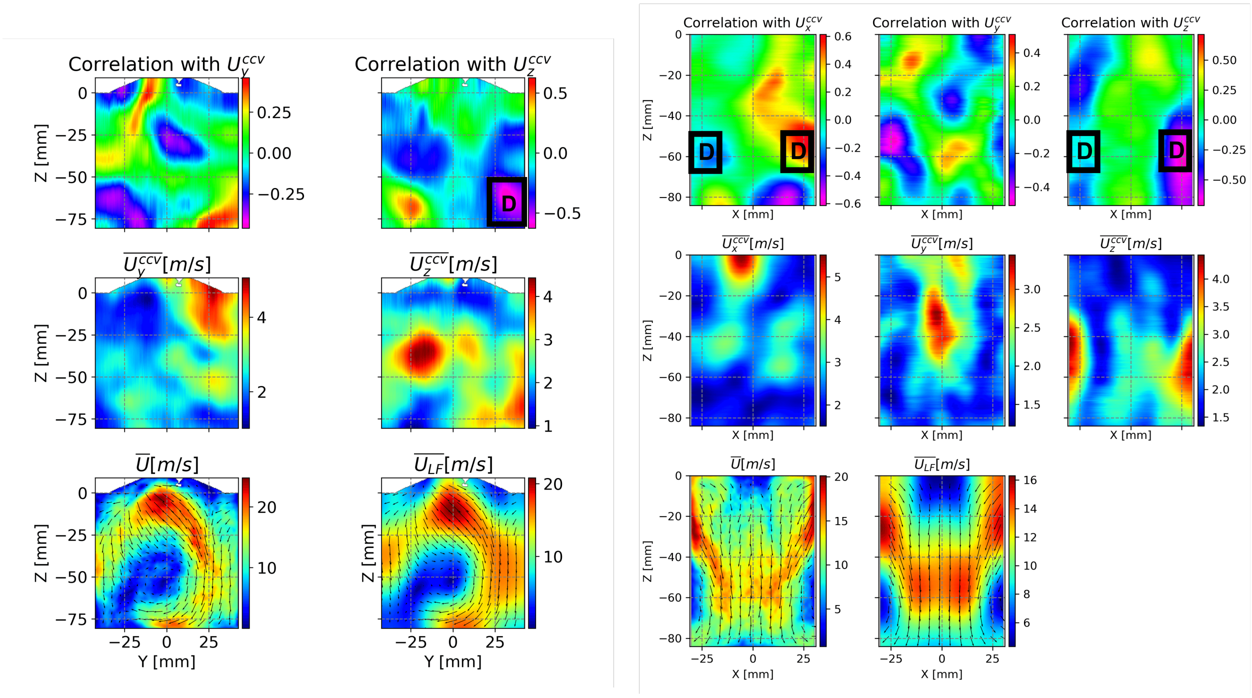

(A) with Y_{jet} in the tumble plane at -220 CAD.

(B) with S_{-10} in the transversal plane at $Y = 30$ mm at -210 CAD.

FIGURE 7.35: Correlation maps showing the correlation between the primary flow's size Y_{jet} or the combustion speed S_{-10} and the LF part of the primary flow after merging between flows 3 and 4.α. Zone D stands for regions of significant correlation related to the primary flow formed by the merge between flow 3 and flow 4.α.

Figure 7.35a shows a strong correlation (averaged correlation coefficient $r = -0.58$ with U_z^{ccv}) at -220 CAD with Y_{jet} in the right lower corner where the primary flow impacts the piston at this instant. The vertical velocity at which the primary flow advances towards the piston is related to the primary flow's shape. Significant correlations are also found between S_{10} and the velocity components on either side of the transverse plane $Y = 30$ mm parallel to the cylinder wall in Figure 7.35b. Despite the asymmetry due to a lack of convergence, both zones are highlighted (zone D). They coincide with the region where significant CCV are present for the vertical velocity component U_z, suggesting that the interaction between flow 3 and flow 4.α could generate CCV of the flow and the combustion.

In Table 7.1 we summarize all the regions representing different flow interactions mentioned above and the descriptors we compute for each region.

Zone	A	B	B	B	C	C	D	D
Plane	P_3	P_3	P_3	P_2	P_3	P_3	P_3	P_1
CAD (deg)	-250	-270	-230	-250	-250	-230	-220	-210
Descriptors	U_y U_z angle	U_z	U_y U_z angle	U_y U_z angle	U_y	U_z	U_z	U_x U_z angle

TABLE 7.1: Summary of flow features representing different mechanisms. P_1 for the transversal plane at $Y = 30\ mm$, P_2 the transversal plane at $Y = -35\ mm$ and P_3 the tumble plane P_3 at $X = 0\ mm$.

The correlation matrix showing correlations between all the flow descriptors is plotted in Figure 7.36.

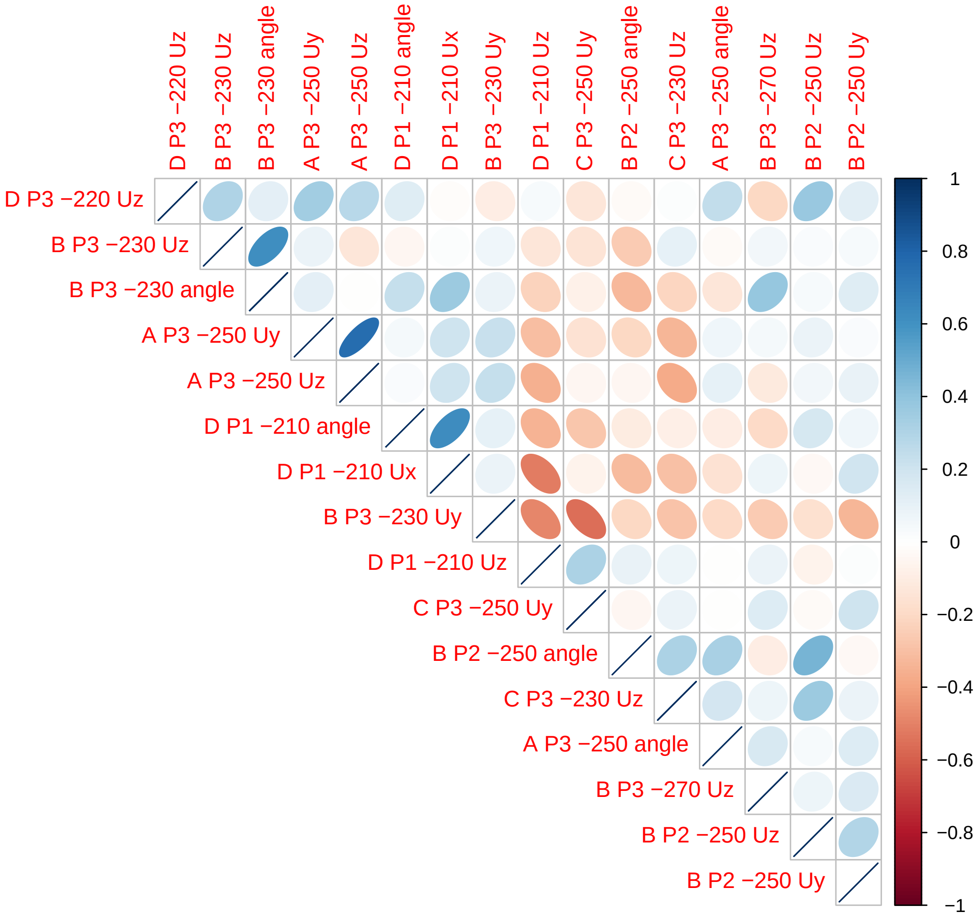

FIGURE 7.36: Correlation matrix of chosen variables representing flow features in different regions at different times. P_1 for the transversal plane at $Y = 30\ mm$, P_2 the transversal plane at $Y = -35\ mm$ and P_3 the tumble plane P_3 at $X = 0\ mm$.

Some strong correlations can be found for descriptors evaluated in the same region, for example, between U_y and U_z in zone A of plane P_3 at -250 CAD, indicating that the local flow is well-organized and the evolution of each velocity component is mutually coupled. Some correlations between zones are also obtained: U_y in zone C of plane P_3 at -250 CAD, standing for the penetration of flow 4.γ, is correlated with U_y in zone B of plane P_3 at -230 CAD, representing the deviation of the secondary flow at the upper left corner. These findings lead us to conclude that CCV of the in-cylinder flow is generated not only during the intake stroke by the intake valve jets but also by the interactions between dominant flows that occur during the intake stroke. The resulting CCV of the in-cylinder flow during the intake stroke will continue to generate new CCV at BDC and during the compression stroke, which finally leads to CCV of combustion.

To evaluate the effect of multiple flow descriptors on the CCV of combustion, a multivariate linear regression model is built between the flame surface S_{-10} and all the computed flow descriptors, using the same methodology as in [91]. Among all the 14 flow descriptors, the algorithm can identify four independent descriptors whose combination gives the best prediction of the flame surface S_{-10}.

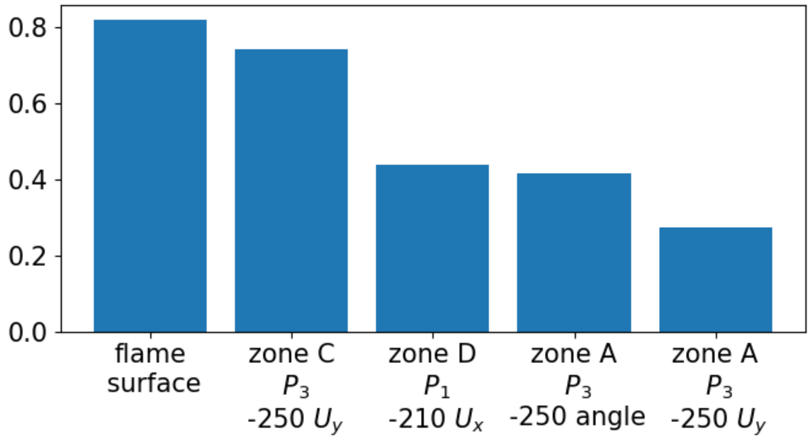

FIGURE 7.37: Histogram of correlation coefficients between the total flame surface at -10 CAD and the variables representing flow features used in the multivariate analysis.

Figure 7.37 shows the resulting correlation coefficient between the target value S_{-10} and this best-fitting model, as well as its four independent contributions. It is found that the major contribution to the response comes from the flow feature of zone C, which is associated with the penetration of flow 4.γ. The other three contributors are all associated with the primary flow, especially the flow deviation in zone A quantified by the local flow angle and the convergent shape of the primary flow formed by flow 3 and flow 4.α. Descriptors related to the secondary flow are not included in the model, suggesting that the behavior of the primary flow is relatively more dominant in the overall in-cylinder flow development.

It should be noted that the above analysis is based on linear regression. The multivariate modal supposes the existence of linearity between different flow features and the combustion process quantified by S_{-10}, which is undoubtedly not the case in in-cylinder physics. Moreover, 35 LES cycles are used in this analysis, which does not allow to ensure statistical convergence. Therefore quantitative values can not be taken as accurate, but they help provide significant tendencies.

7.4.4 Exploration of CCV in the intake port

The previous section has proved that large-scale CCV were formed during the intake stroke and were strongly present in the dominant flow 4 which resulted from the interaction between the intake valve jets. The variations in the interaction contribute to the CCV of the in-cylinder flow. In this section, we will present a simple investigation of the potential sources responsible for large-scale CCV in the intake port.

The two intake valve jets are generated by the pressure difference between the chamber and the bifurcated intake port. The asymmetrical variations of the two valve jets could potentially lead to variations in their interaction. To verify this hypothesis, we decide to evaluate the pressure level in the two separated branches of the intake port. Two slices at $Y = -55$ mm are chosen, as shown in Figure 7.38.

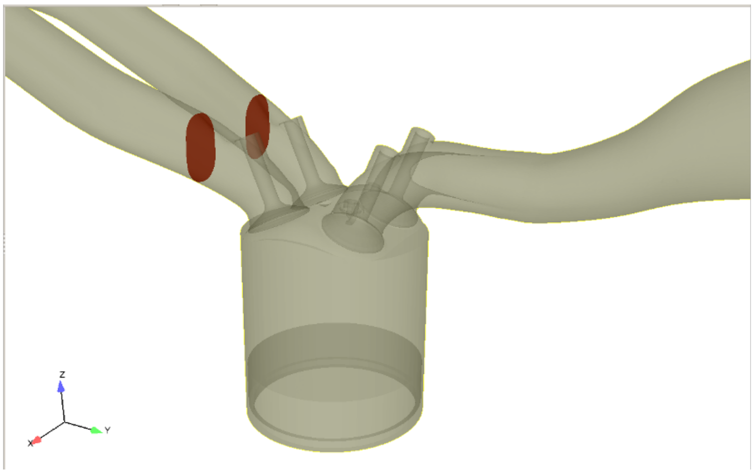

FIGURE 7.38: Slices (marked in red color) at $Y = -55$ mm in the intake port for evaluating acoustic impacts on the CCV of the primary flow.

The evolution of the pressure in the left slice $P_l(x, z, CAD)$ $(X < 0)$ and that in the right side $P_r(x, z, CAD)$ $(X > 0)$ are then averaged in each plane, noted as $\overline{P_l}(CAD)$ and $\overline{P_r}(CAD)$, respectively. Figure 7.39 compares the temporal evolution of $\overline{P_l}(CAD)$ and the pressure difference between the left and right branches, $P_{diff}(CAD) = \overline{P_l}(CAD)$-$\overline{P_r}(CAD)$, between the three cycles 13, 20 and 18.

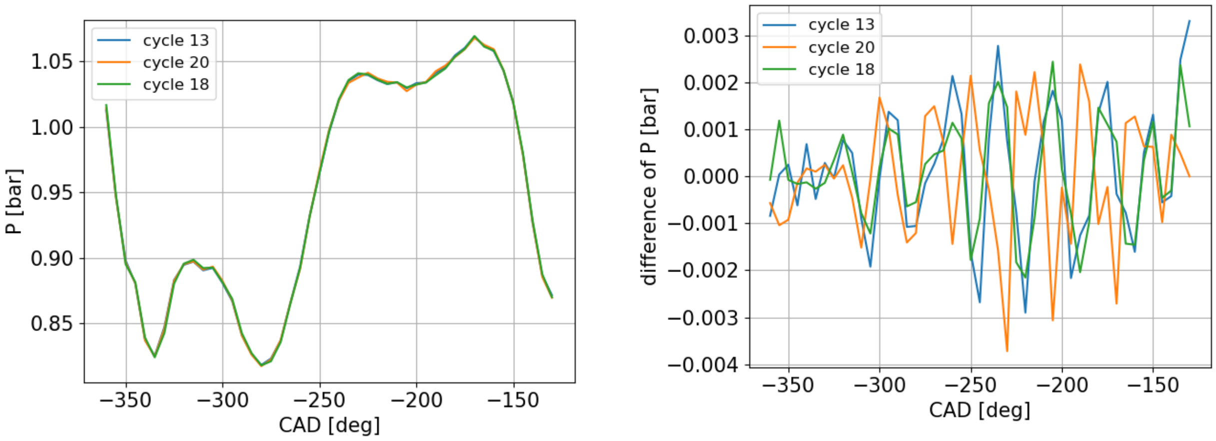

(A) Average pressure $\overline{P_l}(CAD)$ at the left $(X < 0)$ side.

(B) Pressure difference between the left and right side $P_{diff}(CAD) = \overline{P_l}(CAD)$-$\overline{P_r}(CAD)$.

FIGURE 7.39: Comparison of pressure characteristics in the intake port between the three cycles 13, 20 and 18.

It can be seen that the averaged pressure in the left side $\overline{P_l}(CAD)$ exhibits only minor differences between the three cycles and is almost identical before -250 CAD when the dominant flows are well organized. On the contrary, the pressure difference $P_{diff}(CAD)$ between the two branches presents is highly variable and behaves differently between the three cycles. The asymmetry of pressure in the two branches could result in the asymmetry of intake valve jets and later in the variations of their interaction. We can notice that the pressure difference $P_{diff}(CAD)$ is around 0.2% of the averaged pressure, which is not significant and unlikely to cause significant CCV. However, the absolute level of $P_{diff}(CAD)$ around 200 Pa corresponds to a velocity U of order 20 m/s knowing $P = 1/2\rho U^2$ with ρ of order 1 kg/m^3. Such a difference in pressure could lead to important differences in the induced momentum flux from the two branches of the intake port.

To seek the links between the pressure level in the intake port and the intake flow formed during the intake stroke, we compute again the correlation coefficients between the descriptors of pressure, the averaged pressure in the intake port $\overline{P}(CAD) = (\overline{P_l}(CAD){+}\overline{P_r}(CAD))/2$ and the pressure difference between the two branches $\overline{P}_{diff}(CAD) = \overline{P_l}(CAD){-}\overline{P_r}(CAD)$, and the primary flow descriptor Y_{jet} which was found critical for the tumble formation. We observe in Figure 7.40 that both the averaged pressure $\overline{P}(CAD)$ and the pressure difference $\overline{P}_{diff}(CAD)$ are not correlated with the formed primary flow characterized by Y_{jet}. It should be noticed that the linear correlation is a very simple approach with a strong assumption of linearity to quantify the relevance between two quantities. The impacts of pressure in the intake port on the formation of intake flow could be nonlinear and thus could not be identified by the linear correlation. Also, Y_{jet} is quantified from the flow state at -200 CAD which is quite later in the intake stroke. Descriptors extracted at earlier stages could be more appropriate to establish the links between the CCV in the intake port and those of the in-cylinder flow.

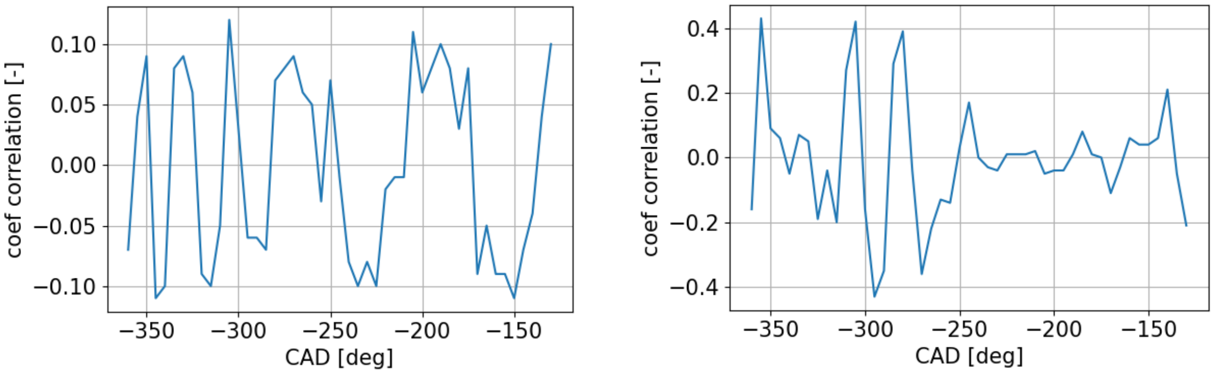

(A) With averaged pressure $\overline{P}(CAD)$.

(B) With pressure difference $\overline{P}_{diff}(CAD)$.

FIGURE 7.40: Correlation coefficients between Y_{jet} and pressure-related descriptors in the intake port.

Despite the simplicity of the linear correlation, our conclusions are in agreement with those obtained in the previous study [88] in which the pressure in the intake port was found not relevant to the CCV of the in-cylinder flow. In this thesis, we did not have time for deeper studies on the generation of intake valve jets. However, we strongly believe that the interaction between these two dominant structures is the origin of the observed CCV in the tumble motion. Future work could be focused on the characterization of the intake valve jets to complete the overall root-cause analysis presented in this Chapter.

Our last attention is paid to the intake mass flow distribution around the two valve curtains. As discussed in section 7.4.3, flow 4 formed by the interaction of intake valve jets is highly variable and contributes to the generation of CCV of the in-cylinder flow. The variability of flow 4 might be caused by the intake flow interaction which is highly fluctuating, and also by the variability of intake mass flow from the two intake valves.

To evaluate the variability of intake mass flow, we choose the two cylindrical planes surrounding the two valve curtains to quantify the intake mass flow (cf Figure 7.41). The two valve curtain planes are of radius $r = 14$ mm, and their height varies with respect to the valve lift.

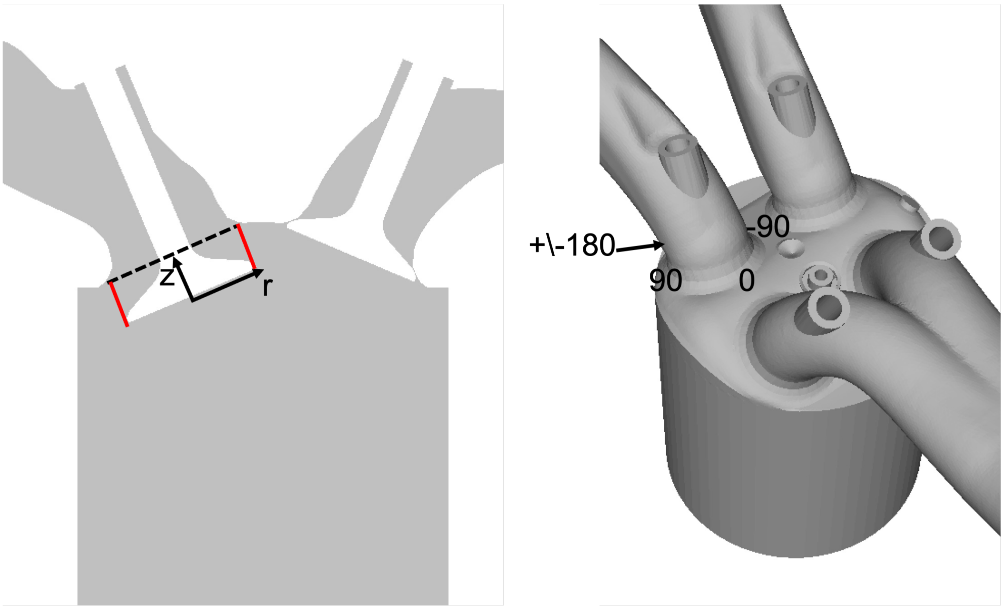

FIGURE 7.41: Definition of the right valve curtain plane (marked in red) located at $r = 14$ mm.

The instantaneous velocity field in the left valve curtain plane at -250 CAD is plotted for the three cycles 13, 20 and 18 in Figure 7.42. It can be seen that most of the mass flow enters the chamber from the central part of the plane, *i.e.* from the upper side of the valve towards the exhaust side. Differences can also be marked between the three cycles, mainly in the central part, which confirms the fluctuating nature of the intake flow.

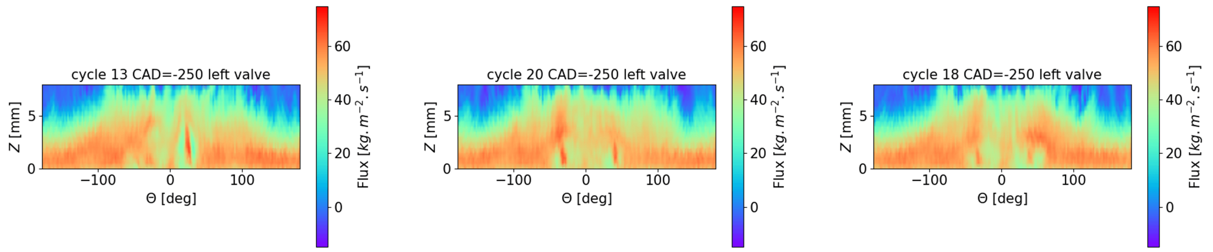

FIGURE 7.42: Instantaneous velocity field in the left valve curtain plane at -250 CAD for the three cycles 13, 20 and 18.

The instantaneous velocity field is then integrated over the height Z to provide the radial distribution of mass flow rate $\dot{m}(\theta)$:

$$\dot{m}(\theta) = \int \rho(\theta, z) U(\theta, z) \vec{n} \mathrm{d}z \tag{7.3}$$

By integrating the mass flow rate $\dot{m}(\theta)$ over time, we can obtain the integrated mass flow distribution $m(\theta)$:

$$m(\theta) = \int_{\phi_1}^{\phi_2} \rho(\theta, z) U(\theta, z) \vec{n} \mathrm{d}z d\phi \tag{7.4}$$

where ϕ represents the crank angle.

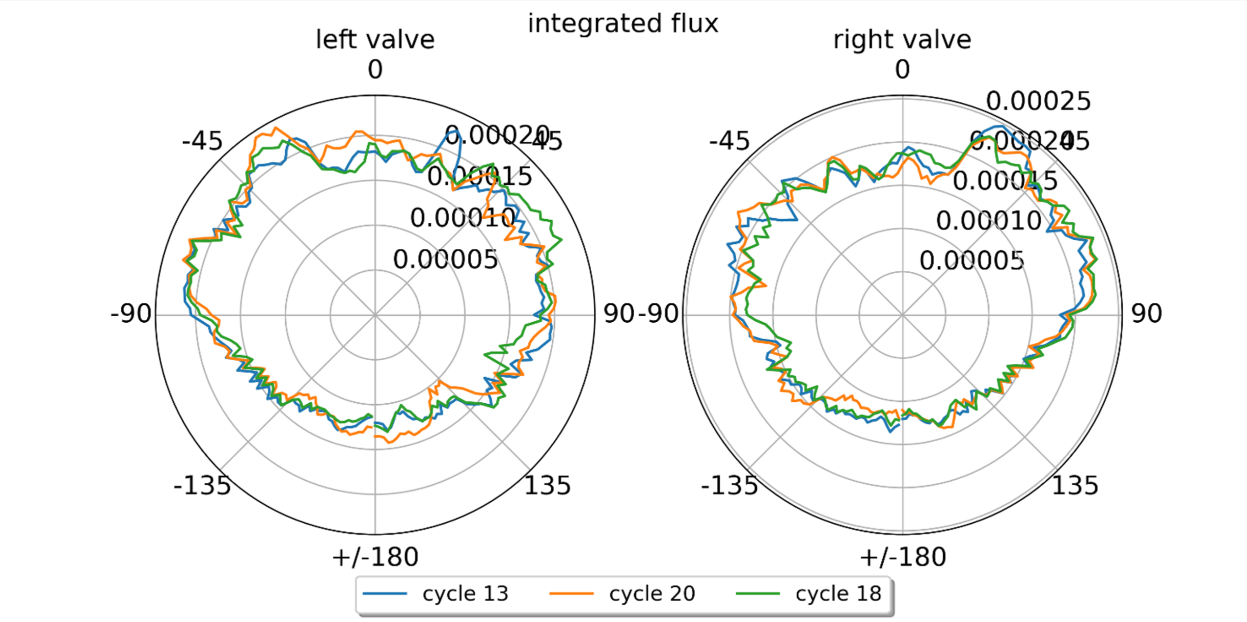

(A) Instantaneous mass flow rate distribution $\dot{m}(\theta)$ at -250 CAD.

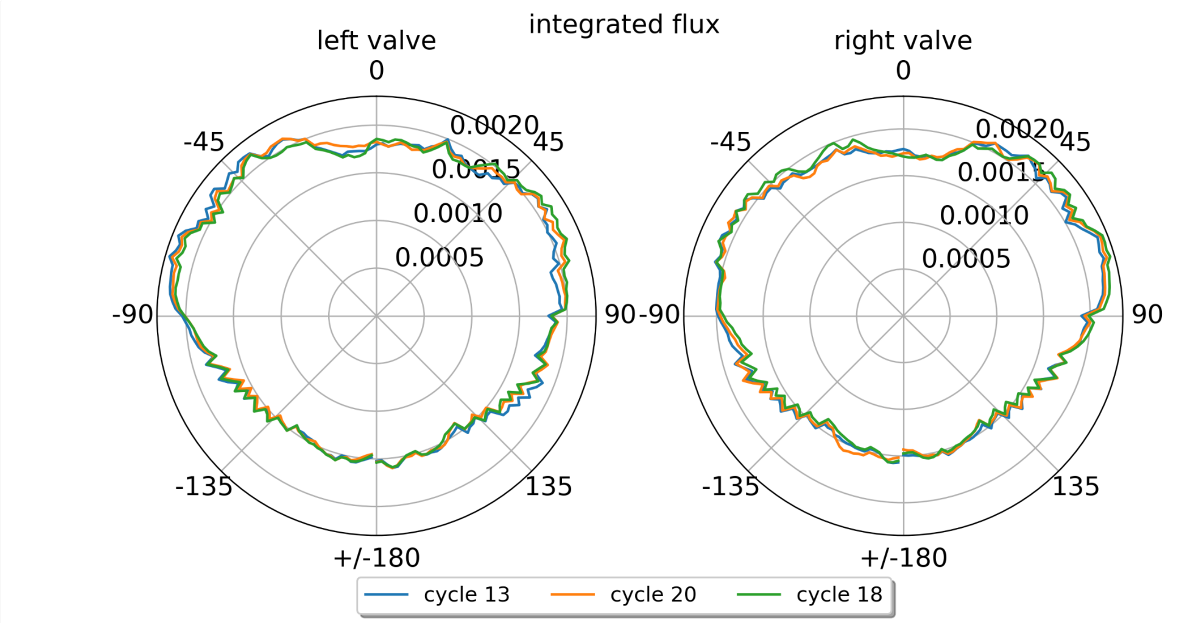

(B) Integrated mass flow distribution $m(\theta)$ from -360 to -250 CAD.

FIGURE 7.43: Comparison of intake mass flow distribution in the radial direction. $\theta = 0$ on the exhaust side and $\theta = +/-180$ on the intake side.

In Figure 7.43, we compare the instantaneous mass flow rate $\dot{m}(\theta)$ at -250 CAD and the integrated mass flow distribution $m(\theta_1, \theta_2)$ from -360 to -250 CAD around the two intake valves. From the instantaneous radial distribution, we can observe that differences exist in all the directions, in regions between the two valves and also those close to the liner. The integrated mass flow distribution also shows some differences which remain moderate and are not as variable as the generated flow 4 observed before in section 7.4.3.

The radial distribution of mass flow does not show significant CCV. However, it is worth noting that the instantaneous velocity captured in the two valve curtain planes contains both large- and small-scale structures which are not separated in the current analysis but could impact separately or jointly the formation of flow 4. Also, the interaction between the two intake valve jets is not involved but is of great importance in the generation of flow 4. Further analyses are needed for a deeper understanding of the generation of CCV from intake valve jets.

7.5 Summary of main findings

In this Chapter, a root-cause analysis of combustion CCV was addressed. Starting from the two major CCV factors identified in Chapter 6, we aimed to trace their origins back to the compression and intake strokes. We tried to answer all the questions listed in Figure 7.1, and the analysis allowed us to give corresponding answers presented in Figure 7.44 and summarized below.

The study started with the compression stroke. The tumble deformation was highly correlated with two CCV factors at spark timing: the tumble deformation led to different large-scale flow patterns at spark timing, which led to different turbulence generations near the spark. Γ_{3p}, local tumble ratio $\mathbf{TR}$ and bivariate 2D EMD were used to characterize the tumble evolution during the compression stroke. The same type of tumble deformation presented in the motored case study was found. The tumble deformation was triggered even in the first half of compression, suggesting the origin of such deformation could be determined even earlier.

This hypothesis was proved by analyzing the flow state at BDC: the tumble's shape formed at BDC was a determinant factor for the tumble's evolution during the whole compression stroke. A tumble presenting a certain level of distortion (quantified by $|CTR|$) at BDC was more likely to experience a significant deformation which led to a flow pattern switching. Further analysis revealed that the distortion was mainly caused by the flow deviation over the piston, which was caused by the impact of the primary flow on the exhaust side of the piston, for which significant CCV were captured.

We continued our study on the intake flow characterization. Based on a 3D visualization of the primary flow, it was noticed that its shape near the piston also presented CCV, which led to the different behaviors of the flow deviation over the piston. The CCV of the flow at spark timing was thus traced back to the flow state during the intake stroke. The analysis in the tumble plane with bivariate EMD also highlighted the complexity of the primary flow, which was formed gradually during the intake stroke. An important part remained on identifying dominant flows during the intake stroke, for which trivariate 3D EMD was performed on the velocity field at -250 CAD. Several dominant flows were identified, especially side flow 3 and central flow 4. The interaction between flow 3 and flow 4.α resulted in the formation of the primary flow on the exhaust side. On the intake side, the secondary flow was formed similarly by flow 2 and flow 4.β. Flow 4, generated by the interaction between intake valve jets, presented significant CCV around flow 4.α and flow 4.γ. More 2D planes were added to characterize the evolution of the different dominant flows. It was found that the interaction between flows 3 and 4.α resulted in significant CCV in the shape of the primary flow. The variability of the primary flow on its shape was linked with the flow deviation over the piston. Therefore, we concluded that the CCV of the in-cylinder flow were principally brought by flow 4 generated by the interaction between intake valve jets.

In the end, a multivariate linear regression model was used to highlight the combined effects of dominant flows on the CCV synthetically. With four independent flow features representing different mechanisms as input variables, the model could correctly predict the combustion behavior based on a linear combination of input parameters. However, the lack of convergence with 35 LES cycles could mislead our interpretation of certain results. Also, this analysis was based on a strong assumption of linearity, whereas the in-cylinder phenomena were highly nonlinear.

We also attempted to link the observed CCV of the primary flow and the CCV in the intake port. No evident relation was found, but the results could be misleading due to the simplicity of the linear correlation. In the future, it could be beneficial to investigate further the variability of the intake flow.

Through this study, we tried to build a cause-and-effect chain to explain the origins of the CCV sources related to internal aerodynamics. The tumble motion during the compression stroke was carefully investigated, and we could identify its link with the flow development during the intake stroke. The major CCV source was found to be the central flow 4 resulting from the interaction of the intake valve jets. The multivariate linear regression analysis also concluded that the interaction between large-scale dominant flows was responsible for the CCV during the overall in-cylinder flow development. It should also be mentioned that our analysis of the intake flow development was focused on the large-scale LF part of the flow, while the impact of the turbulence was not involved in the current study, which could be improved in future work.

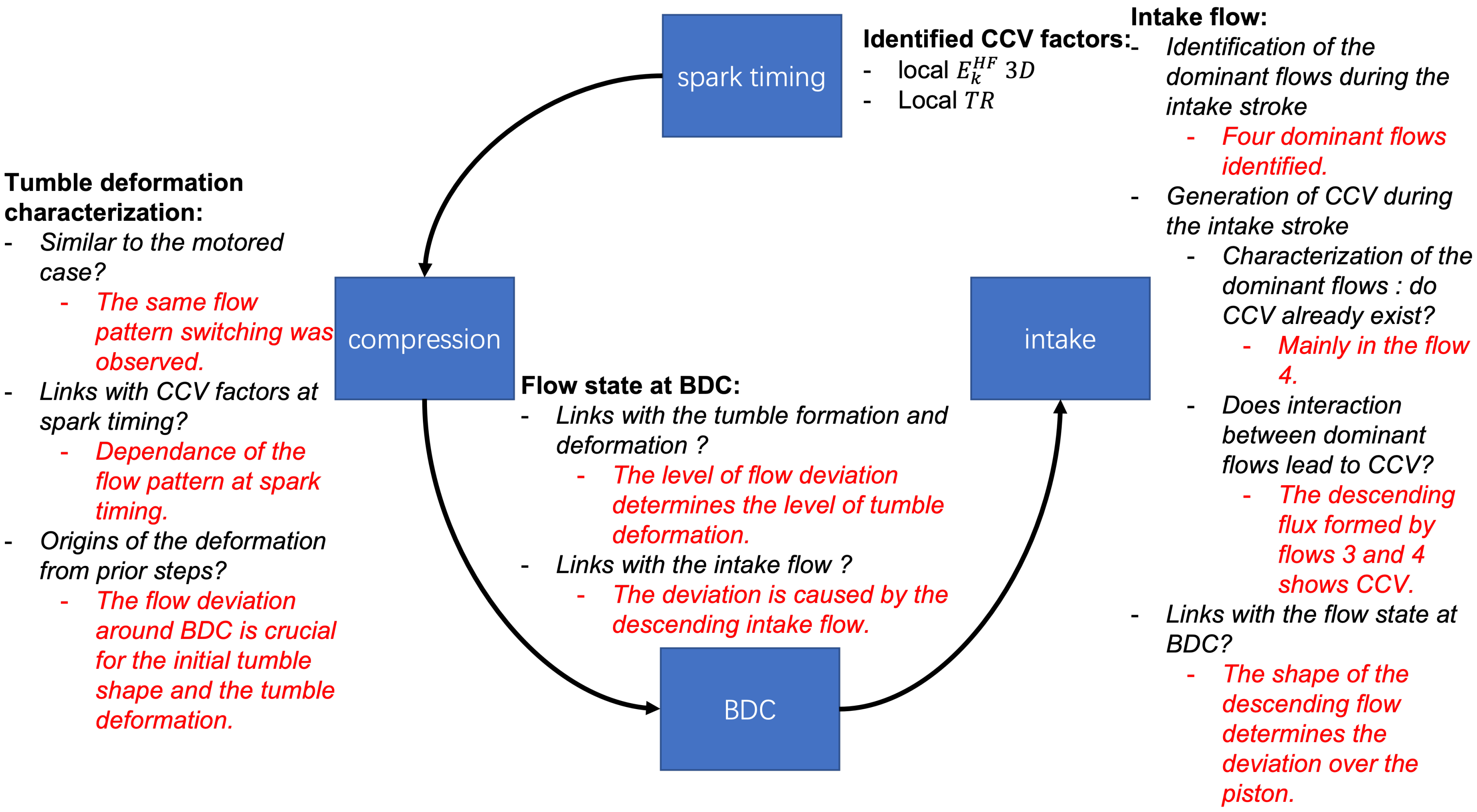

Identified CCV factors:
- local E_k^{HF} $3D$
- Local TR

Intake flow:
- *Identification of the dominant flows during the intake stroke*
  - *Four dominant flows identified.*
- *Generation of CCV during the intake stroke*
  - *Characterization of the dominant flows : do CCV already exist?*
    - *Mainly in the flow 4.*
  - *Does interaction between dominant flows lead to CCV?*
    - *The descending flux formed by flows 3 and 4 shows CCV.*
- *Links with the flow state at BDC?*
  - *The shape of the descending flow determines the deviation over the piston.*

Flow state at BDC:
- *Links with the tumble formation and deformation ?*
  - *The level of flow deviation determines the level of tumble deformation.*
- *Links with the intake flow ?*
  - *The deviation is caused by the descending intake flow.*

Tumble deformation characterization:
- *Similar to the motored case?*
  - *The same flow pattern switching was observed.*
- *Links with CCV factors at spark timing?*
  - *Dependance of the flow pattern at spark timing.*
- *Origins of the deformation from prior steps?*
  - *The flow deviation around BDC is crucial for the initial tumble shape and the tumble deformation.*

FIGURE 7.44: Results of the cause-and-effect chain investigation and answers to related questions are listed in Figure 7.1.

CHAPTER 8

Towards uncertainty quantification in engine simulations

Contents

8.1 Context of the work 194

8.2 LES modeling 195

8.2.1 Closure of the Favre-filtered momentum equation 195

8.2.2 Wall shear stress modeling 195

8.3 Turbulent pipe flow 196

8.3.1 Presentation of the test-case 196

8.3.2 Simulation setup 196

8.3.3 Results of the first run 197

8.4 Uncertainty and sensitivity analysis on pipe flow simulation 198

8.4.1 Methodology 199

8.4.2 Design of experiments 201

8.4.3 Surrogate modeling 202

8.4.4 Sensitivity analysis 203

8.4.5 Data calibration 204

8.4.6 Final tuning of model parameters 206

8.5 Summary of main findings 207

In section5.4.3, a sensitivity analysis was conducted to evaluate qualitatively the impact of boundary conditions on the prediction of in-cylinder flow obtained by LES. The results emphasized the importance of a correct choice of boundary conditions which were usually provided by experimental measurements. However, uncertainties associated with experimental measurements were rarely considered in numerical modeling, especially in SI engine simulations. In this Chapter, we aim to develop an uncertainty quantification (UQ) methodology to be coupled with LES. The developed methodology is applied to a turbulent pipe flow case for validating its implementation and evaluating its applicability to SI engine simulations. This work was the subject of a conference proceedings paper entitled *Uncertainty and Sensitivity Analysis in Turbulent Pipe Flow Simulation* [176], exposed at the 14th WCCM-ECCOMAS Congress.

8.1 Context of the work

During the last few decades, supported by the rapid development of computational capacity and the improvement of mathematical modeling, significantly increased usage of numerical simulation tools like Computational Fluid Dynamics (CFD) for the analysis and design of numerous engineering applications can be observed. The use of CFD in automobile engineering has become more common, especially the Large-Eddy Simulation (LES), for its ability to reproduce the numerous coupled phenomena in internal combustion engines. However, in such numerical simulations, uncertainties can arise from different simulation parameters, including material properties, initial and boundary conditions, physical models, and numerical resolution, which question the results' quality and eventually disturb the associated analysis [177]. The aim of applying numerical approaches to fluid dynamics problems is to obtain high-quality results in terms of accuracy, reliability and robustness [178, 179]. To assess the accuracy, reliability and robustness of numerical simulations, approaches based on verification and validation (V&V) [180] are commonly applied [181]. Verification means investigating the errors in the numerical modeling and its solution, while validation aims to quantify the accuracy of the numerical solutions compared to reference experimental data. To obtain reliable results, it is necessary to study the impact of various uncertainties on the final solution. A possible approach is the application of Uncertainty Quantification (UQ) tools, which allows propagating uncertainties related to different factors (inputs and parameters, ...) of a simulator (*i.e.*., the computational code) to its outputs.

Uncertainty is defined as the lack of certainty in a numerical model output which may be caused by incomplete knowledge or lack of knowledge, incomplete modeling or data, uncertain or variable factors in the numerical model, etc. Two types of uncertainties can be identified: epistemic (bias) and aleatoric (random) uncertainties. The treatment of each type of uncertainties requires appropriate mathematical and statistical tools [182]. A common strategy in the UQ framework is to consider the uncertainties to be random to make probabilistic methods applicable [182].

The use of UQ in CFD application has attracted attention from various domains, typically in nuclear engineering, where CFD is more and more used as a tool for design and safety issues and related uncertainties that need to be well-controlled [183–186], and also in aerospace applications [187] and aircraft design [188]. UQ has been introduced in experimental research [189] in automobile engineering, while numerical work with UQ is still challenging on real systems like internal combustion engines. Therefore our motivation is to develop a feasible UQ methodology for engine CFD applications.

UQ methods can be divided into two categories: intrusive and non-intrusive. In intrusive approaches, the stochastic description of the parameter is integrated within the numerical formulation, which may exhibit algorithmic difficulties [190]. In contrast, non-intrusive approaches [191–194] are sampling based, and the simulator is used as a black box. Therefore they are usually used in CFD applications. The most known non-intrusive UQ method is the Monte Carlo sampling based which is straightforward to implement. However, it requires a large number of simulator runs to achieve accurate statistical results due to its low convergence rate and becomes untractable for CFD applications. One technique is to replace the CFD code with surrogate models characterized by fast response time. Only a limited number of simulations is enough to construct surrogate models that approximate the relationship between input and output vectors. Further UQ analysis can entirely rely on these surrogate models. A popular surrogate model in UQ is based on Gaussian Processes (GP) which allows flexible approximations with an intrinsic control of estimation errors [195].

The present study aims to develop a non-intrusive CFD-UQ methodology based on existing UQ techniques to systematically quantify accuracy, robustness and sensitivity of CFD simulations with respect to variation of different numerical and computational parameters. The analysis is based on surrogate models of Quantities of Interest (QoIs) extracted from solutions and chosen for the UQ study. Its application to engine simulations remains challenging as the engine flow is strongly non-stationary and complex, and uncertainties can come from not only physical models used in simulations for which parameters are not always known and can be case-dependent but also from boundary conditions obtained from experimental measurements for which uncertainties are not well evaluated. This methodology is applied for validation purposes on a relatively simple case: a turbulent pipe flow, which features typical engine flow conditions in intake and exhaust ports.

The structure of this Chapter is as follows: in section 8.2, basic concepts of LES modeling are described, and in section 8.3, a detailed description of the test case used for evaluating the CFD-UQ methodology is provided. Finally, section 8.4 presents the results of the UQ analysis.

8.2 LES modeling

In LES, filtered Navier-Stokes equations are resolved. The Favre-filtered momentum equation for compressible flows can be written as follows [196]:

$$\frac{\partial \overline{\rho}\tilde{u}_i}{\partial t} + \frac{\partial \overline{\rho}\tilde{u}_i\tilde{u}_j}{\partial x_j} = -\frac{\partial \overline{p}}{\partial x_i} + \frac{\partial \overline{\tau}_{ij}}{\partial x_j} - \frac{\partial}{\partial x_j}\left(\overline{\rho}(\widetilde{u_i u_j} - \tilde{u}_i\tilde{u}_j)\right) \tag{8.1}$$

where $\overline{\tau}_{ij}$ is the viscous shear stress tensor and $\overline{\rho}(\widetilde{u_i u_j} - \tilde{u}_i\tilde{u}_j)$ is the unresolved subgrid stress tensor τ_{ij}^{SGS}. τ_{ij}^{SGS} that needs special modeling to close the eauqtion, therefore subgrid stress model is necessary in LES.

8.2.1 Closure of the Favre-filtered momentum equation

The Smagorinsky SGS model is chosen for SGS modeling in this study. It is the simplest model and has been proven to perform reasonably well [132]. The basic principle of such a model is to account for the additional diffusivity inherited from the turbulent flow structures that are smaller than the filter size by adding explicitly in the conservation equations an additional, non-physical viscosity, called turbulent or eddy viscosity ν_t. It assumes that it is possible to express the subgrid stress tensor τ_{ij}^{SGS} in a similar way to the shear stress tensor $\overline{\tau}_{ij}$ following:

$$\overline{\tau}_{ij} = 2\overline{\rho}\nu(\tilde{S}_{ij} - \frac{1}{3}\delta_{ij}\tilde{S}_{kk}) \tag{8.2}$$

$$\tau_{ij}^{SGS} - \frac{1}{3}\delta_{ij}\tau_{kk}^{SGS} = 2\overline{\rho}\nu_t(\tilde{S}_{ij} - \frac{1}{3}\delta_{ij}\tilde{S}_{kk}) \tag{8.3}$$

where $\tilde{S}_{ij}$ is the strain rate tensor computed as $\tilde{S}_{ij} = \frac{1}{2}(\frac{\partial \tilde{u}_i}{\partial x_j} + \frac{\partial \tilde{u}_j}{\partial x_i})$.

Using the Boussinesq hypothesis [132], the eddy viscosity ν_t is modeled as $\nu_t = (C_s\Delta)^2\sqrt{2\tilde{S}_{ij}\tilde{S}_{ij}}$, where Δ is the filter size of LES and C_s the Smagorinsky constant. The value of C_s is not universal and depends on the flow's nature. A typical value of C_s is 0.18 which is determined from the homogeneous isotropic turbulence. In practice, its value may vary from 0.1 to 0.23 [197].

8.2.2 Wall shear stress modeling

When applying a wall-function boundary condition, the wall-normal velocity is set to zero, and the wall shear stress is imposed. The friction velocity u_τ is obtained by solving the logarithmic law of the wall iteratively:

$$u^+ = \frac{1}{\kappa}\ln y^+ + B,\; y^+ > 30 \tag{8.4}$$

where $u^+ = \tilde{U}/u_\tau$ and $y^+ = yu_\tau/\nu$. $\tilde{U}$ is the tangential velocity at the center of the first near-wall cell, ν is the kinematic viscosity and u_τ is the friction velocity defined from the wall shear stress τ_w as $u_\tau^2 = \tau_w/\rho$. τ_w is then used to estimate the local velocity gradient in the momentum equation.

The empirical constants in the logarithmic law, the so-called von Karman constant, κ, and the additive constant, B, are believed to be universal. Nonetheless, there seems to be no consensus about these universal values. According to a review of previous work [198], the value of κ may vary between 0.3 and 0.45, and that of B may range from 4 to 6. Most values are extracted from experimental measurements in which errors can be significant. However, in recent DNS of pipe flows, different values of κ and B are also found for different Reynolds numbers [199, 200].

8.3 Turbulent pipe flow

8.3.1 Presentation of the test-case

The test case chosen for the UQ study is a fully developed turbulent pipe flow at Reynolds number $\text{Re} = 44000$. Direct Numerical Simulation results of the same case obtained by Wu and Moin [199] can be used as reference data for the UQ study. This canonical case has been extensively used in the literature to study the physics of wall-bounded turbulence and develop and test numerical algorithms due to its simple nature. Additionally, the same flow exists in internal combustion engines, in both intake and exhaust ports (typical Re is in the order of 10^4 [160]). UQ study on this case helps us prepare the UQ application for engine cases in the future.

The pipe is of radius $R = D/2 = 5$ mm and length $15R = 75$ mm as recommended in [199]. A flow of air at 300 K and 1 atm is driven by fixed mass flux and is periodic in axial direction z. The corresponding averaged bulk velocity U_b is 69.3 m/s. The pipe wall is isothermal, and its temperature is fixed to 300 K. The pipe flow simulations are carried out using commercial CFD solver CONVERGE V2.4 [201]. For this high Reynolds number flow, WMLES is performed as it gives a good compromise between computational cost and accuracy. The detailed simulation setup is described in the following sections.

8.3.2 Simulation setup

The simulation is performed using a 2^{nd} order Crank-Nicolson scheme for temporal integration and a 2^{nd} order central scheme for spatial discretization. A CFL number based on the convective velocity of 0.3 is used to limit the time step. The Cartesian mesh used is presented in Figure 8.1.

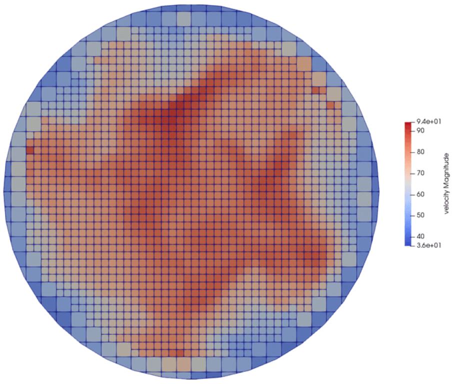

FIGURE 8.1: View of mesh on the transversal section of the pipe.

As we can notice, cells close to the pipe wall are set 2 times larger than those in the inner region, so that center of wall cells is located in the logarithmic region of the boundary layer. Finer grid size is used in outer regions where gradients of the filtered velocity need to be resolved. Turbulent fluctuations are located in the inner region and vanish in the near-wall region.

Starting from initial conditions consisting of a constant velocity U_b which is the bulk velocity such that $Re = U_b D/\nu = 44000$, the flow undergoes a transition and eventually becomes fully turbulent. Then, quantities of interest (QoIs) can be computed for further analysis.

8.3.3 Results of the first run

Using the numerical setup described above, a first run is performed with $\kappa = 0.42$, $B = 5.5$, and $C_s = 0.1$, which are default values in the solver. Figure 8.2 shows the instantaneous velocity field inside the pipe when the flow is fully turbulent. LES well captures detailed turbulent structures of different scales.

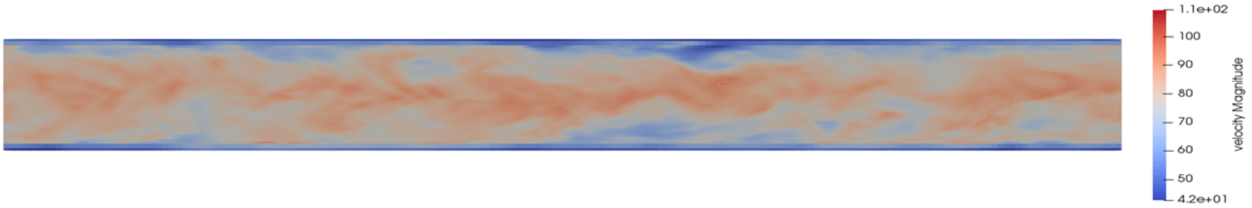

FIGURE 8.2: Snapshot of instantaneous velocity magnitude inside the pipe.

Instantaneous velocity does not permit the characterization of the flow. Therefore the averaged axial velocity $\bar{U}(r)$ in the radial direction r is computed as the averaged flow is axially symmetric. Once the flow becomes fully turbulent, the simulation continues for an additional time of $300R/U_b$, allowing a particle to travel 20 times along the pipe at the bulk velocity U_b. Statistics are collected for each time step during this period. Finally, velocity is averaged over time and the axial direction of the flow for better convergence.

The averaged axial velocity $\bar{U}$ w.r.t normalized wall distance from the wall is presented in Figure 8.3, and the corresponding dimensionless profile is presented in Figure 8.4.

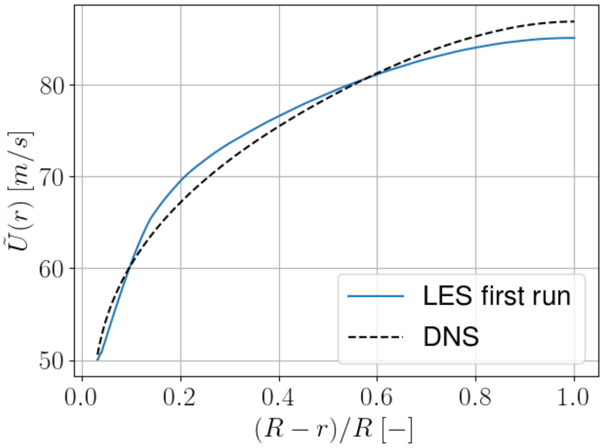

FIGURE 8.3: Mean profile $\bar{U}$.

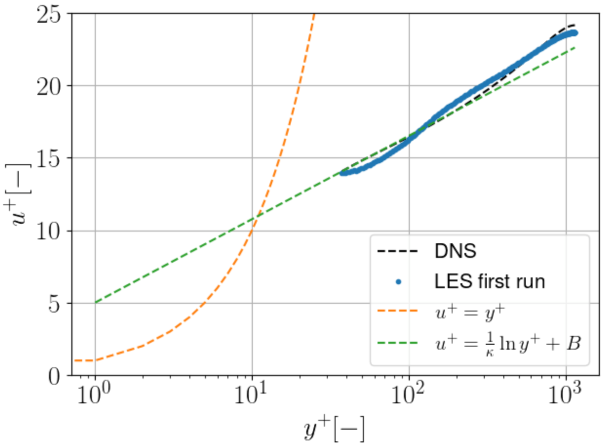

FIGURE 8.4: Dimensionless mean profile $\bar{U}^+$.

The center of the first cell is located at $y^+ = 36$, well inside the log-law region. With the current configuration, the velocity profile is already comparable with that of DNS. Considering DNS data as reference, the relative error of our simulation on $\bar{U}$ can be quantified by a relative error $\epsilon_{\bar{U}}$ defined as $\epsilon_{\bar{U}} = \left|(\bar{U} - \bar{U}_{ref})/\bar{U}_{ref}\right|$. The global error on the profile we have in the first run is 2.1%.

The momentum equation of the mean flow can be written as:

$$\frac{d\bar{\tau}}{dr} = -\frac{d\bar{p}}{dz} \tag{8.5}$$

In the periodic fully turbulent flow, the mean pressure gradient is uniform across the flow, thus the mean shear stress is also constant. Knowing values of $\bar{\tau}$ at the pipe center $\bar{\tau}(0) = 0$ and at the wall $\bar{\tau}(R) = \tau_w$, the mean shear stress $\bar{\tau}$ is obtained as $\bar{\tau}(r) = \tau_w \cdot r/R$.

The total shear stress $\tilde{\tau}_{tot}$ is the sum of 3 contributions:

$$\tilde{\tau}_{tot} = \underbrace{(-\bar{\rho}\nu\frac{d\tilde{u}_z}{dr})}_{\tilde{\tau}_{lam}} + \underbrace{(-\bar{\rho}\nu_t\frac{d\tilde{u}_z}{dr})}_{\tilde{\tau}_{sgs}} + \underbrace{\bar{\rho}\tilde{u}_r\tilde{u}_z}_{\tilde{\tau}_{res}} \tag{8.6}$$

where $\tilde{\tau}_{lam}$ is the filtered viscous shear stress, $\tilde{\tau}_{sgs}$ is the subgrid viscous shear stress, $\tilde{\tau}_{res}$ is the resolved shear stress.

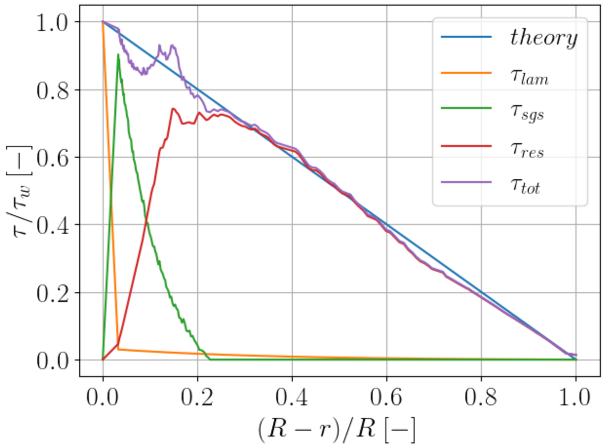

FIGURE 8.5: Shear stress distribution in the wall-normal direction.

The time-averaged shear stress budget is presented in Figure 8.5, and the analytical expression of total shear stress is also plotted for comparison. Far from the wall, the total shear stress, mainly contributed by the turbulent shear stress, follows well the analytical expression. In the near-wall region, the wall shear stress is completely viscous, mainly due to the subgrid stress model. Also, the total shear stress begins to deviate from the analytical expression, which may be related to the jump in cell size in this area which disturbs the estimation of the local gradient and the resolution of the momentum equation.

8.4 Uncertainty and sensitivity analysis on pipe flow simulation

In this section, the CFD-UQ methodology is evaluated on the test case described in the previous section. Only uncertainties from the two physical models employed in LES are studied. Different UQ techniques are applied.

8.4.1 Methodology

Figure 8.6 presents the workflow of the CFD-UQ methodology we used in this study. It can be divided into several parts:

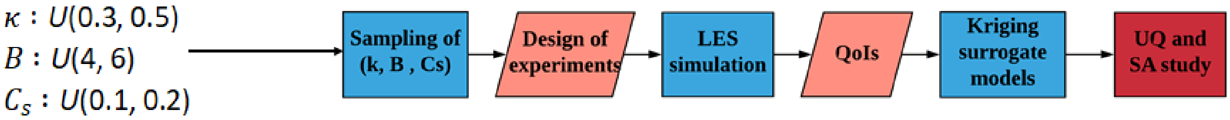

FIGURE 8.6: Workflow of CFD-UQ methodology.

- Based on prior distributions, a sampling of the parameter space is performed using the Maximin Latin Hypercube method [202]. A Design of Experiments (DOE) of N_s samples is then formed.
- LES is then launched for each sample of DOE. Quantities of Interest (QoIs) can be extracted from the simulation results for further study.
- Surrogate models based on Gaussian Processes [195, 203] are built for QoIs extracted w.r.t parameters of interest. LES will not be called anymore.
- Uncertainty and sensitivity analysis are finally carried out using previous surrogate models.

The uncertainty and sensitivity analysis allows us to investigate how model parameter uncertainties can impact simulation results. Different techniques are applied:

- The sensitivity analysis is carried out to quantify the impact of the parameters on simulation results. The variance-based Sobol indices [204] are computed as measures of sensitivity by the RBD-FAST method [205] for its efficiency and reliability.
- Based on experimental data and the prior distribution of model parameters, the data calibration aims to reduce these parameter uncertainties thanks to Bayes' theorem [206]. The resulting posterior parameter distribution (compared to the prior distribution) gives the uncertainty reduction achieved by the data integration.
- The reduction of uncertainties on output parameters is based on the propagation of input parameters' posterior distribution on the outputs via the surrogate models.

In the following, the used UQ techniques are briefly described.

Latin Hypercube Sampling

A Latin Hypercube Sampling (LHS) of size n and dimension d is a sampling D of n points that contain d parameters. Each parameter has n unique values. An example of three LHS for $n = 10$ and $d = 2$ is given in Figure 8.7. It can be seen that the first LHS does not cover the whole parameter space and the area colored in red is not sampled. The second LHS fills much better the parameter space.

The third LHS is generated using the maximin method [207] to properly fill the parameter space, for which the minimum (Euclidean) distance between any pair of points, defined below, is maximal:

$$d(D) = \min_{1 \leq i,j \leq n, i \neq j} \left\| x_i - x_j \right\|^2 \tag{8.7}$$

A certain number of LHS are generated independently and the one with the maximal value of $d(D)$ is taken as the optimal sampling, as shown in Figure 8.7. This allows us to have different parameter

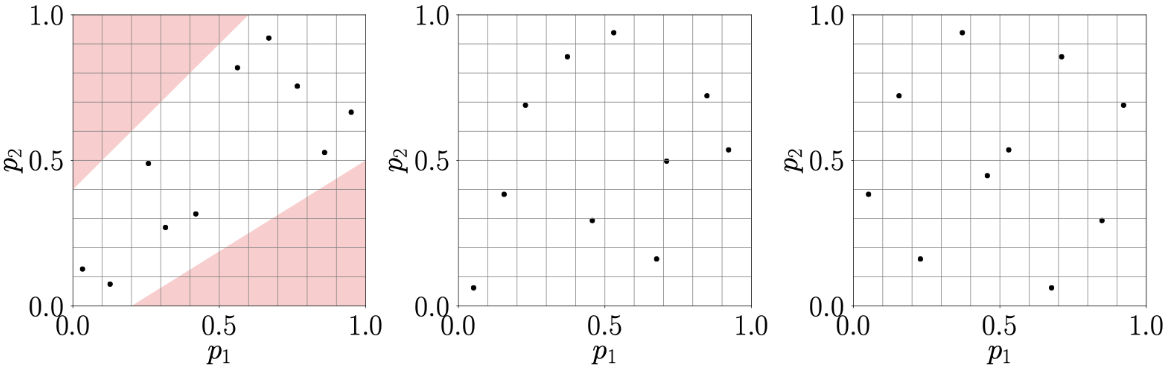

FIGURE 8.7: Example of three LHS randomly generated for $n = 10$ and $d = 2$. The third LHS is obtained using the maximin method [207].

values while still evenly covering the parameter space. While their projective properties are not as good as orthogonal array, they are more space-filling. This makes Latin hypercube sampling widely used for surrogate meta-modeling.

Gaussian processes regression

The Gaussian process (GP) regression, originally in geostatistics and known as Kriging [195], is an interpolation method for which the interpolated values are modeled by a Gaussian process governed by prior covariances. For a set of parameters $x = (x_1, x_2, ..., x_k)$ and the corresponding output function $y(x)$, a GP metamodel is defined as following:

$$\hat{y}(\mathrm{x}) = \sum_{i=1}^{k} \beta_i x_i + Z(\mathrm{x}) \tag{8.8}$$

The first term is a first order polynomial regression and $Z(\mathrm{x}$ represents for a random function with zero mean and variance σ^2. The covariance function $\mathrm{Cov}\left(Z\left(\mathrm{x_i}\right), Z\left(\mathrm{x_j}\right)\right)$ is given by:

$$\mathrm{Cov}\left(Z\left(\mathrm{x_i}\right), Z\left(\mathrm{x_j}\right)\right) = \sigma^2 R\left(\mathrm{x_i}, \mathrm{x_j}\right) \tag{8.9}$$

The correlation function $R(x_i, x_j)$ is to be chosen and is this work the Matérn 5/2 kernel is employed [208]:

$$R(r) = \left(1 + \frac{\sqrt{5}|r|}{\theta} + \frac{5|r|^2}{3\theta^2}\right) \exp\left(-\frac{\sqrt{5}|r|}{\theta}\right) \tag{8.10}$$

where $r = |x_i - x_j|$ and θ a parameter to be fitted to maximize a likehood function.

Sobol indices

The most popular global sensitivity analysis method, Sobol indices [204], is based on the decomposition of variance into additive terms. The function $y(x)$ can be firstly decomposed in the following way:

$$y(\mathbf{x}) = y_0 + \sum_{i=1}^{k} y_i\left(x_i\right) + \sum_{i<j}^{k} y_{ij}\left(x_i, x_j\right) + \cdots + y_{1,2,\ldots,k}\left(x_1, x_2, \ldots, x_k\right) \tag{8.11}$$

Similarly the variance of $y(x)$ can also be decomposed by computing the variance of about expression:

$$\mathrm{Var}(y(x)) = \mathrm{Var}\left(y_0\right) + \sum_{i=1}^{k} \mathrm{Var}\left(y_i\left(x_i\right)\right) + \sum_{i<j}^{k} \mathrm{Var}\left(y_{ij}\left(x_i, x_j\right)\right) + \cdots + \mathrm{Var}\left(y_{1,2,\ldots,k}\left(x_1, x_2, \ldots, x_k\right)\right) \tag{8.12}$$

The above variance decomposition shows how the variance can be decomposed into terms attributable to each input parameter, as well as the interaction effects between them.

The first order Sobol indice is widely used as a sensitivity measure for quantifying the influence of first order effects:

$$S_i = \frac{\mathrm{Var}\left(y_i\left(x_i\right)\right)}{\mathrm{Var}(y(x))} \tag{8.13}$$

Higher order indices S_{ij} can be formed by dividing other terms in the variance decomposition by total variance $\mathrm{Var}(y(x))$. To drastically reduce the computation time while keeping the reliability of the sensitivity index, the RBD-FAST method [205] is used.

Bayesian calibration

The process of finding model parameters such that the model evaluation using this parameter vector agrees with some numerical or experimental observations is called calibration. A typical method is the Bayesian calibration which is a statistical inference method and based on Bayes' theorem [206].

In such an approach, unknown variables (*e.g.* input variables/parameters in model calibration) are treated like random variables. For a model $y(x)$, the parameter vector x is assumed to be distributed according to a prior distribution:

$$x \in P(\mathrm{x}) \tag{8.14}$$

Probability theory can be applied not for finding 'best-fit' parameter, but rather to compute a posterior distribution given the observations D (reference data from experiments or simulations), thus giving access to the uncertainties on the parameters:

$$P(\mathrm{x} \mid D) = \frac{P(D \mid \mathrm{x})P(\mathrm{x})}{P(D)} \propto P(D \mid \mathrm{x})P(\mathrm{x}) \tag{8.15}$$

This formula allows to update prior knowledge about parameter x to posterior distribution $P(\mathrm{x} \mid D)$ given data D, using a so-called likehood function $\mathfrak{L}(\mathrm{x}, D) = P(D \mid \mathrm{x})$.

The posterior distribution of parameters is generally not analytically tractable. The technique called Markov chain Monte Carlo (MCMC) sampling, originally developed by Metropolis et al. [209] and Hastings [210], can be used to resolve the problem. It constructs Markov chains that are guaranteed to produce samples distributed according to the posterior distribution. Posterior characteristics including its distribution can then be estimated using these samples.

In the following parts, we will present the application of our methodology to the pipe flow case, including the generation of the DOE (section 8.4.2), the surrogate modelling (section 8.4.3), the application of the sensitivity analysis (section 8.4.4), and the data calibration (section 8.4.5). Based on the UQ analysis, a tuning of model parameters is also realized and presented in section 8.4.6.

8.4.2 Design of experiments

We focus on the uncertainties introduced by the constant parameters of the SGS tensor and the law-of-the-wall used in LES of pipe flow. Consistently with ranges of values found in the literature, we define for each parameter a prior distribution as follows: $\kappa \in U(0.3, 0.5)$, $B \in U(4, 6)$, $C_s \in U(0.1, 0.2)$.

As no prior information is available, they are supposed to follow a uniform distribution. Based on prior distributions, a DOE of 400 samples is generated. A similar number of samples has been chosen for another study with the same number of parameters, and corresponding surrogate models showed good quality [211]. The spatial distribution of all the samples are presented in Figure 8.8. The generated samples well fill the parameter space.

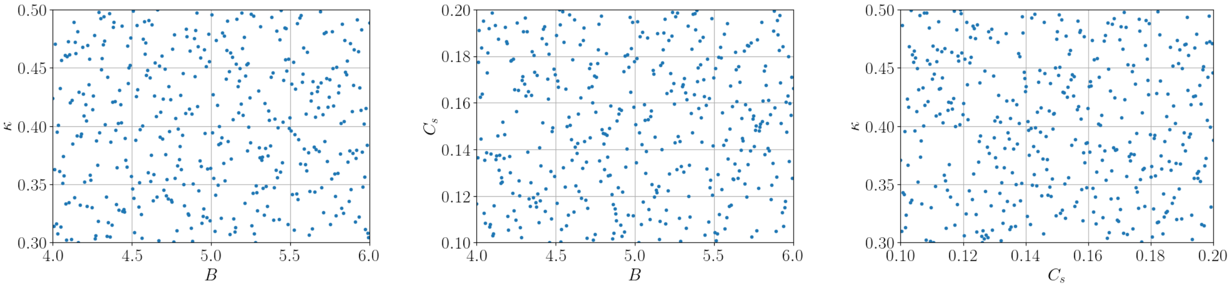

(A) κ, B plan.
(B) C_s, B plan.
(C) κ, C_s plan.

FIGURE 8.8: 2D views of DoE generated using LHS.

8.4.3 Surrogate modeling

LES are then performed for all the samples to compute QoIs defined in section 8.3.3: averaged velocity profile $\bar{U}(r)$ and the averaged error $\epsilon_{\bar{U}}$. The results are presented in Figure 8.9 and Figure 8.10. It can be seen that $\bar{U}(r)$ varies significantly with respect to the three parameters and the corresponding error. The reference curve of $\bar{U}(r)$ lies well inside the variation range. The maximal $\epsilon_{\bar{U}}$ can reach more than 0.15, representing an important deviation compared to the reference data.

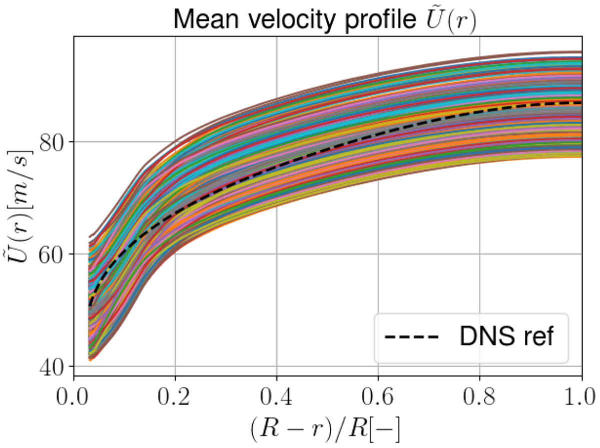

FIGURE 8.9: $\bar{U}(r)$ extracted from LES.

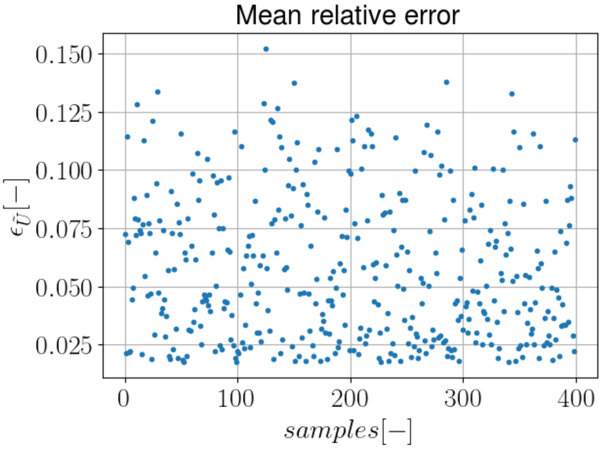

FIGURE 8.10: $\epsilon_{\bar{U}}$ extracted from LES.

Surrogate models based on GP are then constructed for QoIs using all the samples as a training dataset: 1 multivariate model of $\bar{U}(r)$ and one monovariate model for $\epsilon_{\bar{U}}$. Given the high cost of LES, we choose not to set a validation dataset. Instead, the leave-one-out cross-validation is done to evaluate the quality of models, and the corresponding predictivity coefficient Q_2 [212] value is extremely close to 1 for all surrogate models. Obtained models are shown in Figure 8.11 and Figure 8.12, with fixed $C_s = 0.1$.

Figure 8.11 shows us that the response surface of $\epsilon_{\bar{U}}$ is of valley shape. $\epsilon_{\bar{U}}$ is minimized for κ and B located at the bottom of the valley. Additionally, a couple of $\kappa = 0.41$ and $B = 5$ is found in this area and corresponds to values found from pipe flow experiments [213], which confirms our findings from simulations. The response surface of $\bar{U}(r)$ at $r = R/2$ shown in Figure 8.12 is almost

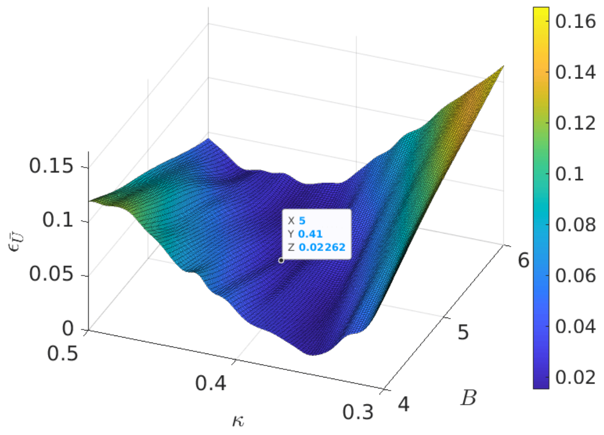

FIGURE 8.11: Response surface of $\epsilon_{\bar{U}}$.

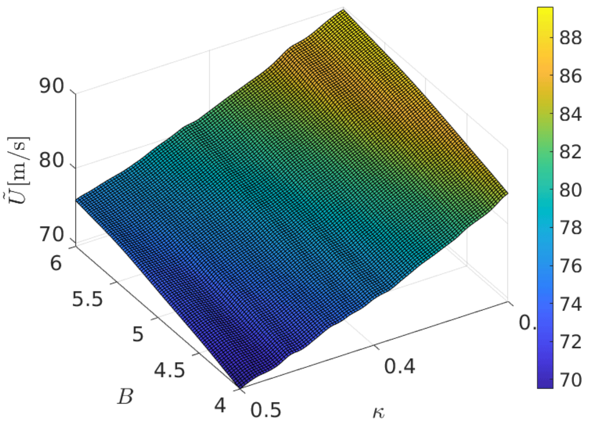

FIGURE 8.12: Response surface of $\bar{U}(r)$ for $r = R/2$.

flat. The impact of κ and B on the velocity at this point is obvious: smaller values of B and larger values of κ lead to lower velocity, and κ seems to have a relatively more important role.

8.4.4 Sensitivity analysis

The sensitivity analysis aims to rank the input parameters according to their impact on the simulated outputs. In this part, variance-based Sobol indices are computed, which allows the quantification of the impact of the three parameters on the QoIs extracted from LES.

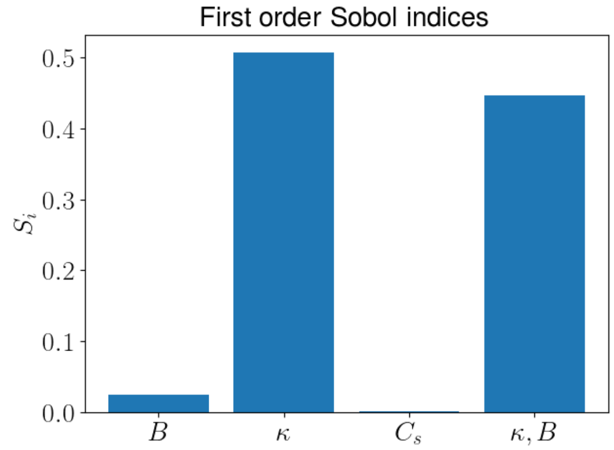

FIGURE 8.13: Sobol indices of $\epsilon_{\bar{U}}$.

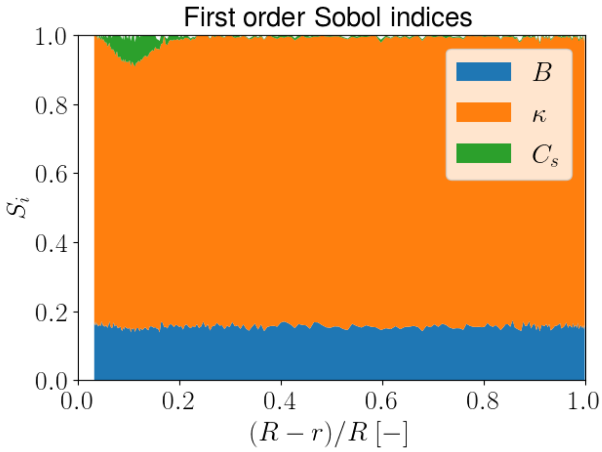

FIGURE 8.14: Sobol indices of $\bar{U}(r)$.

The sensitivity analysis is firstly done for the QoI $\epsilon_{\bar{U}}$. Sobol indices are plotted in Figure 8.13. It is clear that κ is the most influential parameter for $\epsilon_{\bar{U}}$. B alone doesn't have a significant influence but combined with κ, it also plays an important part in the variations of $\epsilon_{\bar{U}}$. Relatively the Smagorinsky constant C_s has little impact on the variations of $\epsilon_{\bar{U}}$.

The same study is then carried out for the QoI $\bar{U}$ to see how the three parameters affect the velocity along the profile at different positions. Sobol indices are computed for each discretization point on the velocity profile, and their values are plotted in Figure 8.14 w.r.t normalized wall distance. From the near-wall region to the pipe center, we observe that κ is still the most critical parameter for $\epsilon_{\bar{U}}$.

The influence of B is relatively less significant and is constant along the profile. C_s remains the least important parameter, but interestingly it does affect $\bar{U}$ in the near-wall region.

As a reminder, the contribution from the subgrid-scale in total shear stress $\bar{\tau}_{sgs}$ is dominant in the near-wall region, as shown in Figure 8.5. Moreover, the region in which C_s has importance coincides with that in which $\bar{\tau}_{sgs}$ is prevalent among all the contributions. This can be explained by the fact that $\bar{\tau}_{sgs}$ depends on the value of C_s as it is proportional to the eddy viscosity modeled by the SGS model. Outside the boundary layer, the mesh is refined so that the contribution of the subgrid-scale model to the total shear stress is negligible compared to the resolved one, as seen in Figure 8.5. The turbulent viscosity given by the Smagorinsky model increases when approaching the wall to reach a value similar to the one obtained by the Prandtl mixing-length model[214]. Therefore, C_s can directly affect the shear stress of flow and the velocity profile, though its impact is relatively weak compared with parameters of the law-of-the-wall model.

We can also compute the momentum thickness θ of the boundary layer using the following formula:

$$\theta = \int_0^R \frac{\bar{U}(y)}{\bar{U}_c}\left(1 - \frac{\bar{U}(y)}{\bar{U}_c}\right) dy \; , y = R - r \tag{8.16}$$

where $\bar{U}_c$ is the velocity at the pipe center. Using the reference $\bar{U}$ from DNS, the thickness θ equals $0.089R$, *i.e.*, $\theta^+ = 106$ in dimensionless scale, which is larger than the dimensionless wall distance of the first wall cells ($y^+ = 35$ in average). The maximal Sobol indice of C_s locates at $0.1R$ which is of the same order of magnitude as θ.

8.4.5 Data calibration

As we have seen in Figure 8.9, $\bar{U}(r)$ varies a lot w.r.t the three parameters whose uncertainties are important. To reduce these uncertainties, a data calibration is applied using the DNS velocity profile as a reference. The result is shown in Figure 8.15.

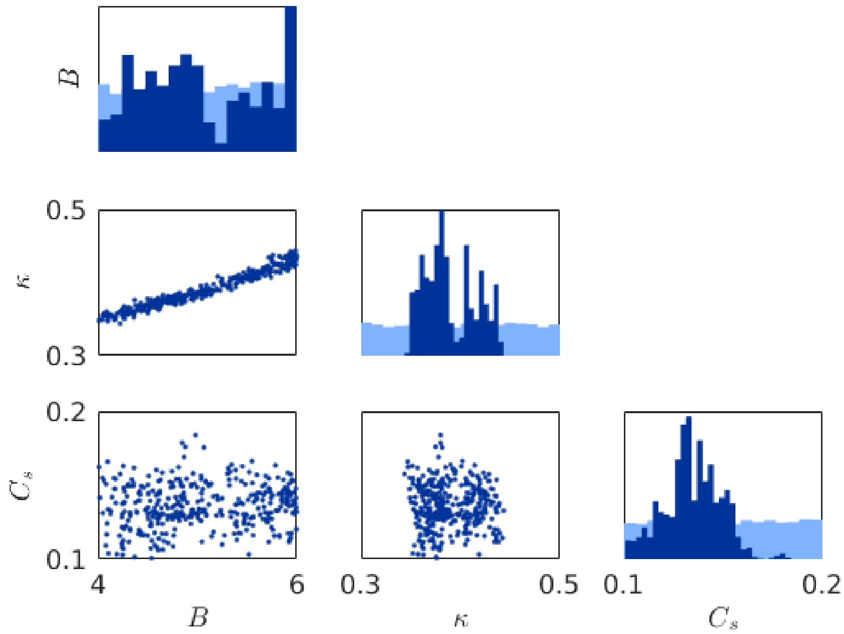

FIGURE 8.15: Prior and posterior distributions of inputs.

Distributions of parameters, both prior (in light blue) and posterior after calibration (in dark blue), are presented on the diagonal. The three other graphs are joint distributions between different couples of parameters. After calibration, uncertainties are primarily reduced for the three parameters, as observed in the posterior distributions. Also, we can observe that these distributions are multi-modal, meaning that several values of the parameters are the most likely to lead to a suitable data calibration: B has two groups of optimal values centered at 4.6 and 5.5, κ also has two groups of optimal values centered at 0.37 and 0.42, Cs has a very likely value at around 0.13. A narrow zone appears on the joint distribution of κ and B, and a strong correlation between κ and B can be identified.

Once prior and posterior distributions of input parameters are available, we can evaluate the corresponding distributions of the QoI $\bar{U}(r)$ by performing uncertainty propagation. Samples are randomly generated based on prior and posterior distributions and then propagated to the output $\bar{U}(r)$ via surrogate model predictions. Then, the corresponding output results are gathered to obtain distributions of $\bar{U}(r)$.

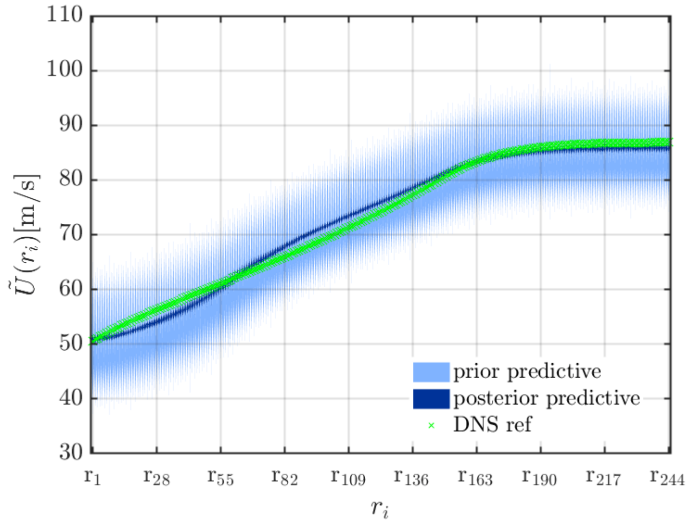

FIGURE 8.16: Uncertainty propagation on $\bar{U}(r)$.

Results are shown in Figure 8.16. The distribution of $\bar{U}(r)$ obtained with prior prediction presents a significant level of uncertainty. The one obtained with posterior prediction shows almost no uncertainty thanks to the reduction of uncertainties by data calibration. Even though uncertainties have been largely reduced on $\bar{U}(r)$, local deviations can still be observed compared to the reference data. This indicates that the current configuration needs other improvements than data calibration to obtain better results.

We have seen that all possible combinations of κ and B allowed in posterior distributions give almost the same velocity profile. The reason can be explained after a straightforward manipulation of the law-of-the wall. Based on the log-law, we can establish a relation between κ and B:

$$B = -\frac{C_1}{\kappa} + C_2, \quad C_1 = \ln y^+ , C_2 = u^+ \tag{8.17}$$

From a LES with $\kappa = 0.41$ and $B = 5.5$ (located in the narrow zone of joint distribution in Figure 8.15), values of C_1 and C_2 can be determined such that $C_1 = \ln(35) = 3.55$ and $C_2 = 14.25$. In Figure 8.17, the curve of Eq. 8.17 is plotted, and it indeed passes through the middle of the joint distribution. Hence, a linear correlation exists between B and $1/\kappa$, allowing the error minimization on $\bar{U}(r)$ of the LES.

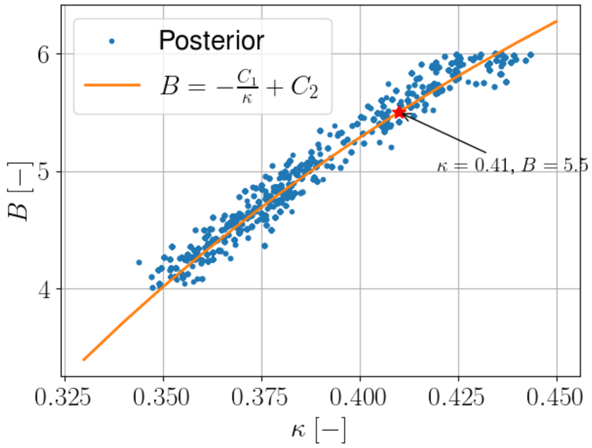

FIGURE 8.17: Joint posterior distribution of κ and B compared with Eq. 8.17.

8.4.6 Final tuning of model parameters

We have seen from the previous UQ analysis that the optimal choice of κ and B is not unique in this particular case. Thus, we only try to propose one possible choice for the three parameters that permits obtaining the optimal velocity profile in the current configuration.

The sensitivity analysis in section 8.4.4 has shown that κ and B are more critical parameters, and therefore their optimal values are first determined. As no uniqueness exists in this case, we now fix the parameters $\kappa = 0.41$ and $B = 5.5$ which are optimal values as shown in Figure 8.17.

To determine the optimal value of C_s, two approaches are possible:

- Performing LES for C_s varying between 0.1 and 0.2 and computing related global error on the velocity profile $\epsilon_{\bar{U}}$.
- Using the surrogate model of $\epsilon_{\bar{U}}$ to predict error corresponding to C_s varying between 0.1 and 0.2.

Both approaches are adopted and the results are compared below.

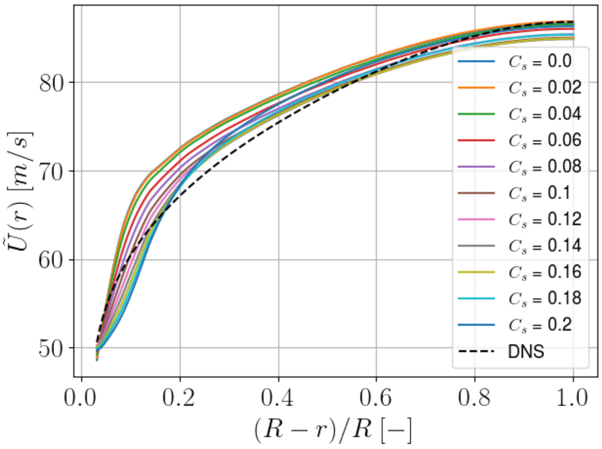

FIGURE 8.18: $\bar{U}$ obtained using LES.

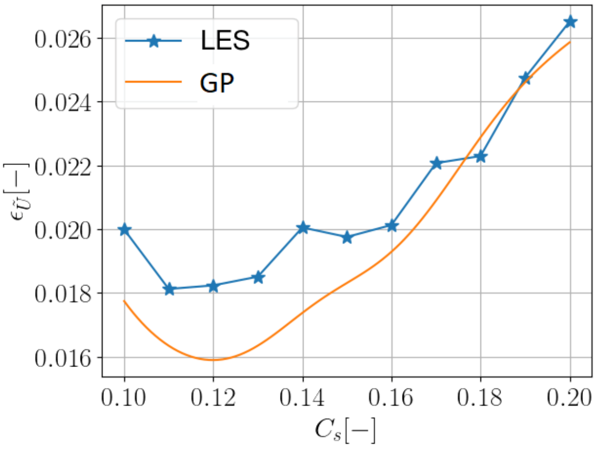

FIGURE 8.19: Comparison of $\epsilon_{\bar{U}}$ from LES and surrogate model.

Results of 11 LES are plotted in Figure 8.18. The variation due to the value of C_s is relatively small, as C_s is the least influential parameter for QoIs. The corresponding error $\epsilon_{\bar{U}}$ from LES is presented in Figure 8.19 and compared with that predicted by the surrogate model of $\epsilon_{\bar{U}}$. Both show a similar evolution trend while deviations between them reach 12%. The minimum is located at 0.11 according to LES and at 0.12 based on the prediction of the surrogate model. In this case, we give more credit to LES results, and the value chosen is 0.11 for C_s, though 0.12 would provide almost the same result.

8.5 Summary of main findings

In this work, a UQ-CFD methodology was presented and applied to the LES of a turbulent pipe flow with wall function for the shear stress. The methodology consists of evaluating uncertainties from the parameters of the simulation models. UQ analysis is based on surrogate models of QoIs from LES to reduce the computational cost generated by numerous LES in the application of UQ techniques. Different capabilities of the developed methodology are illustrated, including sensitivity analysis, data calibration, and uncertainty propagation.

The analysis shows that parameters of the wall model are more critical in the pipe simulation, while the impact of the parameter of the SGS model increases near the wall. With the help of the data calibration, uncertainties are mainly reduced on input parameters and the QoIs $\bar{U}(r)$. A strong correlation is found between parameters of the wall model, which is intrinsic to the model formulation. Following the UQ analysis, an optimal set of parameters is proposed which allows for minimizing the errors on the velocity profile compared to the reference DNS data.

It is worth emphasizing that the proposed methodology, which combines Latin Hypercube sampling, surrogate modeling, sensitivity analysis, and Bayesian data calibration, is general and can be applied to any UQ problem involving complex computer codes. Applying such a methodology to a relatively simple case also allows us to anticipate difficulties when studying more complex cases.

The application of the current methodology to internal combustion engine simulations is envisaged in future work. However, some challenges stand out:

- In this study, a single LES of a pipe flow demands a runtime of 7 hours on 36 CPUs, in total around 250 CPU.hours. 400 experiments are used for building surrogate models, resulting in a total computational cost of 10^5 CPU.hours. For more complex engine simulations, a single engine cycle requires much more computational resources of about 10^4 CPU.hours, which makes the current methodology too expensive to use, even only for surrogate modeling.
- Unlike the pipe flow which is statistically stationary, in-cylinder engine flow is transient and presents variabilities between different cycles. Thus, QoIs extracted from a single cycle may not be representative of the global characteristics of the flow, and values obtained from a certain number of cycles are preferred, which again increases the computational cost of a single experiment.

Therefore, a critical step in our next work is to integrate an adaptative sampling strategy coupled with surrogate modeling with which DOE is not generated once but updated consecutively by adding critical samples to improve the quality of surrogate models efficiently. Also, qualitative studies will be conducted to investigate the primary uncertainty sources in engine simulations and define quantifiable QoIs for UQ analysis.

CHAPTER

9

Conclusions and perspectives

Contents

9.1 Conclusions . . . 209
9.1.1 Development of flow analysis tools . . . 210
9.1.2 Simulation and analysis of the motored case . . . 210
9.1.3 Simulation and analysis of the fired case . . . 211
9.2 Perspectives . . . 212

9.1 Conclusions

The present thesis aimed to understand the role of internal aerodynamics on cyclic combustion variability (CCV) in SI engines. The LES approach was chosen to address the CCV problem due to its ability to capture such a cyclic varying phenomenon. The available number of LES cycles was limited due to the expensive computational cost, but the 3D information in the intake port, the chamber and the exhaust port provided us with a deep insight into the in-cylinder physics. Advanced flow analysis tools were developed and applied for characterizing the evolution of in-cylinder flow in the Darmstadt optical engine and its impact on the combustion process.

The literature review revealed the importance of internal aerodynamics on CCV, however, the impacts of large-scale tumble motion and small-scale turbulence were not decoupled, which motivated us to develop suitable flow analysis tools to separate flow structures of different scales, including EMD for 2D/3D analysis and Γ_3 function for 3D tumble characterization. The developed tools were first applied to LES data of the Darmstadt engine under motored conditions to evaluate their capacity to characterize large-scale flow variations and small-scale turbulent fluctuations. They were then used to identify CCV factors at spark timing in the Darmstadt engine under fired conditions. Starting from the flow state at spark timing which was found crucial for the combustion process, we succeeded in tracing back the origins of identified CCV factors to the intake stroke.

9.1.1 Development of flow analysis tools

The present thesis is a continuation of the previous work by Sadeghi [19], in which the capacity of the 2D EMD method on analyzing tumble-like turbulent flow was evaluated. In this thesis, a significant effort was put into improving 2D EMD for its extensive usage in in-cylinder flow analysis, and for the first time the extension of EMD in 3D to treat LES data.

- Bivariate 2D EMD was only applied to velocity fields in a fixed domain in [19] and was adapted to deal with velocity fields in complex time-varying geometries [1]. A grid stretching strategy was used to satisfy conditions required by the mode combination strategy of 2D EMD. In this work, we proposed an improvement to 2D EMD by replacing the complete decomposition approach with an accelerated one. In the previous version, EMD decomposed an instantaneous velocity field into a finite number of IMF and a residual. They were combined to construct an LF part representing large-scale motion and an HF part containing small-scale fluctuations. In the improved version, the combination was made during the decomposition in each direction. EMD worked like a filtering tool to eliminate small-scale fluctuations from the instantaneous velocity field. Such modification allowed us to get rid of the grid stretching strategy and largely reduce the computational cost of 2D EMD, which facilitated its massive application in the multi-planar analysis of in-cylinder flow.
- Following the acceleration strategy used in 2D EMD, a straightforward extension of EMD in 3D for multivariate data was achieved. Trivariate 3D EMD was first applied to a 3D trivariate velocity field. From the resulted 3D LF and HF parts, we had more insight into the 3D flow characterization of the large-scale motion and the turbulence, both globally and locally. However, the corresponding computational cost was much greater than that of 2D EMD. Hence the massive utilization of 3D EMD seemed difficult.
- An application of spatial-temporal 3D EMD was also made. An artificially generated 2D large-scale motion with a time-dependent rotation center was superposed on a 2D HIT field and served as the test data. Spatial-temporal 3D EMD eliminated fluctuations in both spatial and temporal domains. Nonetheless, the known border effect of EMD seemed to be important in this test case, which was not observed in applications to 2D and 3D velocity fields. Its application to in-cylinder flow was also made and discussed in Appendix C. We could not interpret the results physically, and the methodology was also questionable.

Even with acceleration, the important computational cost of trivariate 3D EMD prevented such a method from being extensively used in 3D flow characterization. In this work, another existing flow analysis tool called the Γ_3 function was chosen to complete the 3D vision of the in-cylinder flow.

- Γ_3 is a vortex detection tool in 3D and was first applied to in-cylinder flow by Buhl et al. [123] to extract the rotation axis of tumble motion, which was retained in this study. With a paralleled implementation realized in this work, we facilitated the computation of Γ_3 in multi-cycle analysis. The distribution of Γ_{3p} was also exploited to visualize the rotational structure at different instants, which provided the possibility to follow the tumble evolution.
- Γ_3 helped indicate if a rotation was organized but did not quantify its intensity. We proposed a quantity called local tumble ratio to characterize the rotation intensity along the rotation axis of the tumble. It allowed a quantitative description of the tumble motion.

9.1.2 Simulation and analysis of the motored case

In the simulation of the motored case, two contributions were made to improve the prediction of LES:

- The overestimation of in-cylinder pressure, commonly reported in previous studies, was caused by the inaccurate prediction of crevice flow. A simplified crevice model was applied to adjust the mass exchange between the crevice and the chamber.
- The importance of boundary conditions on the prediction of the in-cylinder flow field was studied. Different types of inlet conditions and wall modeling were tested. A qualitative sensitivity analysis was conducted to find the best configuration of boundary conditions, emphasizing the important uncertainties in the current LES setup.

Flow analysis tools were applied to all the 25 LES cycles of the motored case:

- 2D EMD and 3D were applied to characterize the large-scale CCV of the flow field in the tumble plane and the small-scale turbulence near the spark plug. Important large-scale CCV associated with the tumble motion were observed.
- Γ_3 and local tumble ratio $\mathbf{TR}$ were used to characterize the tumble evolution in 3D during the compression stroke. A tumble deformation was observed through the 3D visualization of the tumble motion, which led to a flow pattern switching.
- The relation between the large-scale motion and local turbulent level was also investigated. With the limited number of available cycles, a moderate correlation was found between the large-scale tumble motion and the generation of turbulence near the spark region. The same correlation was verified later in the fired case also.

The correct LES prediction on the internal aerodynamics and the successful application of flow analysis tools allowed us to pursue the fired case study. The results of the motored case also constituted an article entitled *On the use of LES and 3D EMD for analyzing cycle-to-cycle variations of in-cylinder tumbling flow* and was submitted to the journal *Flow, Turbulence and Combustion* [215].

9.1.3 Simulation and analysis of the fired case

Based on the LES methodology used in the motored case, the LES simulation of the fired case was carried out by adding combustion modeling.

The validated results against experimental data were first exploited to identify which flow parameters at spark timing were crucial for the ignition phase. EMD was used to extract large- and small-scale flow features in the whole chamber and near the spark region, at spark timing. The analysis showed that the two main CCV factors were the local turbulence near the spark plug and the global tumble motion.

A root-cause analysis was then conducted, explaining how identified flow CCV at spark timing were initiated during the in-cylinder flow development. We attempted to trace their origins back to the compression and intake stroke. To achieve this objective, we divided the overall flow evolution into three phases: the compression stroke, around BDC, and the intake stroke. Starting from the compression stroke, we tried to quantify important flow features in each phase and establish the links between the three phases.

The analysis of the compression stroke revealed the importance of the tumble deformation to the two CCV factors. The origin of the tumble deformation was also discovered by the following study on the flow state at BDC: the flow deviation, caused by the impact of the primary flow on the piston, conditioned the tumble's shape at BDC, which was found to be determinant to the tumble deformation. The last step consisted of characterizing intake flow during the intake stroke. Multiple dominant flows were identified, which allowed us to propose an intake flow division based on the one proposed in [99]. The central flow noted as flow 4, was recognized as the most variable among all the dominant flows. Its interaction with the lateral flow 3 yealding CCV of the primary flow was found responsible for the flow deviation over the piston. A multivariate analysis was made in the end, and the results indicated that the CCV of combustion could be caused collectively by multiple flow mechanisms during the intake stroke.

Through the fired case study, we were finally able to link CCV of the combustion to the flow development during the intake stroke, with several intermediary descriptors of in-cylinder flow at different stages. An article summarizing results obtained in the analysis of the fired case is currently under work and will be submitted later. A similar analysis using EMD and Γ_3 function developed in this thesis was conducted on another engine configuration [26] which is closer to a real industrial engine, and results were presented in the article *ECFM-LES modeling with AMR for the CCV prediction and analysis in lean-burn engines* accepted by the journal *Science and Technology for Energy Transition* [216].

9.2 Perspectives

In this thesis, the development and application of certain flow analysis tools allowed us to investigate the impact of the in-cylinder flow on the combustion process. Nonetheless, some weaknesses can still be identified and could be improved in the future.

Concerning the flow analysis tools developed and applied in this work, some issues were identified during their application and deserve further investigation in the future.

The developed EMD method presents some drawbacks which were not overcome in this work:

- The border effect is a common issue of EMD. In this work, we used the classical border treatment, which did not avoid this problem. Many boundary treatments exist, but none of them is perfect. Thus, all of our EMD results might have been perturbed, which could mislead the corresponding interpretation. In the future application of EMD, attention should be paid to quantifying potential errors brought by the border effect.
- The extension of EMD in 2D and 3D was based on the principle of sequential decomposition: EMD 1D was carried out sequentially on all the lines one after the other direction. Using such an approach, each line's decomposition was independent, resulting in visible discontinuities on extracted LF parts. Increasing the number of realizations NE did not fundamentally resolve the problem. Some extensions of EMD in 2D [161] using 2D interpolation and in 3D [217] using separable filters can be promising alternatives for the current EMD implementation.
- Another downside of the current EMD was the treatment of local discontinuities caused by complex geometries. In this work, local discontinuities were temporally filled by linear interpolation before decomposition. The impact of such a strategy was not evaluated in this work.
- The separation of LF and HF parts remained subjective in this study, though a criterion based on energy content proposed in [130] was retained. Also, the separation criterion was defined identically for all the instants of the engine cycle. It was possible that the definition was not universally suitable and might need adjustment according to the flow state. The question of generality in the application of EMD should be considered.
- The application of spatial-temporal EMD was made in this thesis (cf Appendix C). However, we were not able to give a physical interpretation of the obtained results. Some doubts about the application were also discussed in Appendix C. We look forward to discovering its potential in in-cylinder flow analysis in the future.

Γ_3 also needs to be further improved concerning its computation:

- In this work, the choice of the sub-volume in which Γ_3 was evaluated was not carefully investigated. We simply chose a spherical volume whose radius varied with the total chamber height. However, both its size and shape could impact the results of computation.
- Γ_3 used in this work is Galilean invariant (similar to Γ_2 in 2D), which takes into account local convection. A comparison could be made with the version without consideration of local convection (similar to Γ_1 in 2D) to justify the choice.

The developed analysis tools of in-cylinder flow were applied in a classical gasoline SI engine. The automotive industry and research institutes are currently investigating the potential of hydrogen engines in which the role of internal aerodynamics in the mixing and combustion process needs to be mastered, and our analysis methodology could be applied for this purpose. These analysis tools could also find their place in other contexts:

- The tank filling process [218] remains quite similar to the in-cylinder flow development, and our analysis tools could be used to optimize heat losses and filling rate.
- EMD showed its capacity in characterizing the flow of different scales. Such an ability could help in analyzing any internal or external flows showing a various range of scales, for instance, drag prediction [219] and near-wall flow characterization [220].
- EMD can also be coupled directly with machine learning techniques [221] to extract information of different scales (temporal or spatial) for the prediction of quantities of interest.

Regarding numerical modeling by LES, our methodology allowed a correct prediction of in-cylinder physics but can be further improved. The prediction of internal aerodynamics always presented minor differences compared to LES in the motored and fired cases. The no-slip condition used on intake valve walls was not applied to a well-refined mesh, as the local refinement for a Cartesian mesh was quite challenging. The newly implemented inlaid mesh in CONVERGE [20] seems helpful in improving the wall modeling in LES.

In the studies of motored and fired cases, we relied on linear regression to establish links between flow features and combustion features. A strong assumption of linearity between these features representing complex physical phenomena is imposed. Nevertheless, in-cylinder physics involving turbulence can hardly be considered linear. Despite the few LES cycles, 25 in the motored case and 35 in the fired case, the deep analysis of the flow evolution on both individual and over all cycles using the proposed methodology provided qualitative tendencies and objective conclusions. Some recent studies [222–225] use machine learning techniques to predict engine performance using extracted flow features and other ignition-related factors. However, the classical approach using linear regression can still be helpful by coupling with machine learning techniques [37, 226]: linear regression is used to identify promising CCV factors, which are then used as input parameters of machine learning models to predict the combustion behavior. Statistical approaches like machine learning techniques require sufficiently large data set to obtain satisfying accuracy of the results. For that reason, most of machine learning techniques rely on 2D PIV measurements, which however prevent revealing flow features from the whole 3D flow field (as highlighted by Dreher et al. [224]).

By studying the fired case, we could identify the most variable dominant flow, the central flow 4, which was one of the major CCV sources during the intake stroke. Limited by the time available in the thesis, we did not continue on the characterization of intake valve jets that generated flow 4. Some attempts have been made to explore the potential relation between the radial distribution of intake valve jets and the primary flow, but no clear link was found. To further investigate intake valve jets, adapted analysis tools need to be integrated. A promising choice, the iso-surface of pressure, is presented in [64] and could provide a 3D vision of intake jets, similar to Γ_3 for tumble motion.

The sensitivity analysis of boundary conditions conducted in the motored case study resulted in a relatively optimal numerical setup, and revealed the necessity of an accurate set of boundary conditions for engine simulations. Nonetheless, boundary conditions provided by experimental measurements contains unknown uncertainties. Their impact on the results of simulation should be carefully investigated, which motivated the UQ work presented in Chapter 8. The proposed UQ methodology was coupled with the CFD solver and was successfully applied to an academical test case. The use of surrogate models did help reduce the overall computational cost, but the building of surrogate models demanded also considerable computational resources despite the simplicity of the test case. Engine simulations using LES are of much higher complexity and require huge computational resources. Further improvements in the sampling strategy and choice of QoIs should be carefully considered to make the methodology applicable for engine simulations.

An ANR project ALEKCIA [227] promoted by IFPEN started in 2021, which aimed to develop tools for augmented prediction and analysis of turbulent reactive flows with a focus on real SI engine operations fueled with hydrogen to better capture time-resolved events and increase understanding and control of the origins of undesired behaviors. The current thesis will bring valuable knowledge and tools that will be further consolidated and exploited in this project and also for other applications.

Bibliography

[1] M. Sadeghi, K. Truffin, B. Peterson, B. Böhm, and S. Jay, “Development and application of bivariate 2d-emd for the analysis of instantaneous flow structures and cycle-to-cycle variations of in-cylinder flow,” *Flow, Turbulence and Combustion*, vol. 106, pp. 231–259, 1 2021. DOI: `10.1007/s10494-020-00197-z/figures/25`.

[2] *How many cars are there in the world in 2022? statistics by country.* `https://hedgescompany.com/blog/2021/06/how-many-cars-are-there-in-the-world/`.

[3] *Normes de performance en matière d’émissions de co2 pour les voitures particulières et les camionnettes.* `https://ec.europa.eu/clima/eu-action/transport-emissions/road-transport-reducing-co2-emissions-vehicles/co2-emission-performance-standards-cars-and-vans_fr`.

[4] *Fit for 55 package: Council reaches general approaches relating to emissions reductions and their social impacts.* `https://www.consilium.europa.eu/en/press/press-releases/2022/06/29/fit-for-55-council-reaches-general-approaches-relating-to-emissions-reductions-and-removals-and-their-social-impacts/`.

[5] *Turbulence for international automotive markets in 2021.* `https://www.vda.de/en/press/press-releases/220118_Turbulence-for-international-automotive-markets-in-2021`.

[6] *Internal combustion engine market size, share & trends analysis report by fuel, by end-use, by region and segment forecasts, 2022 - 2030*, `https://www.reportlinker.com/p06291040/?utm_source=GNW`.

[7] Iea, “Global ev outlook.,” 2022.

[8] F. M. Eltoumi, M. Becherif, A. Djerdir, and H. Ramadan, “The key issues of electric vehicle charging via hybrid power sources: Techno-economic viability, analysis, and recommendations,” *Renewable and Sustainable Energy Reviews*, vol. 138, p. 110 534, 2021. DOI: `https://doi.org/10.1016/j.rser.2020.110534`.

[9] R. D. Reitz *et al.*, “Ijer editorial: The future of the internal combustion engine,” *International Journal of Engine Research*, vol. 21, no. 1, pp. 3–10, 2020. DOI: `10.1177/1468087419877990`.

[10] T. Nagasawa *et al.*, “Thermal efficiency improvement of super-lean burn spark ignition engine by stratified water insulation on piston top surface,” *International Journal of Engine Research*, vol. 22, no. 5, pp. 1421–1439, 2021. DOI: `https://doi.org/10.1177/1468087420908164`.

[11] J. Wang *et al.*, “Numerical investigation of water injection quantity and water injection timing on the thermodynamics, combustion and emissions in a hydrogen enriched lean-burn natural gas si engine,” *International Journal of Hydrogen Energy*, vol. 45, no. 35, pp. 17 935–17 952, 2020. DOI: `https://doi.org/10.1016/j.ijhydene.2020.04.146`.

[12] J. B. Heywood, *Internal Combustion Engine Fundamentals*. 2018.

[13] Nasa, *Ideal otto cycle*, `https://www.grc.nasa.gov/www/k-12/airplane/otto.html`.

[14] E. Nicoud, “Quantification de la stabilité de la combustion dans les moteurs essence à injection directe par simulation aux grandes échelles,” Ph.D. dissertation, 2018.

[15] P. Kyrtatos, C. Brückner, and K. Boulouchos, "Cycle-to-cycle variations in diesel engines," *Applied Energy*, vol. 171, pp. 120–132, 2016. DOI: `10.1016/j.apenergy.2016.03.015`.

[16] R. K. Maurya and A. K. Agarwal, "Experimental study of combustion and emission characteristics of ethanol fuelled port injected homogeneous charge compression ignition (hcci) combustion engine," *Applied Energy*, vol. 88, pp. 1169–1180, 4 2011. DOI: `10.1016/j.apenergy.2010.09.015`.

[17] T. Badawy, X. C. Bao, and H. Xu, "Impact of spark plug gap on flame kernel propagation and engine performance," *Applied Energy*, vol. 191, pp. 311–327, 2017. DOI: `10.1016/j.apenergy.2017.01.059`.

[18] N. Ozdor, M. Dulger, and E. Sher, "Cyclic variability in spark ignition engines a literature survey," *SAE Technical Papers*, 1994. DOI: `10.4271/940987`.

[19] M. Sadeghi, "Potential of the empirical mode decomposition to analyze instantaneous flow fields in direct injection spark ignition engine : Effect of transient regimes," Ph.D. dissertation, 2017.

[20] R. K.J., S. P.K., and P. E., *Converge 3.0, convergent science*, 2022.

[21] A. Scholtissek, S. Buhl, D. Hain, and C. Hasse, *Internal combustion engine - cause and effect chain*, 2017. DOI: `10.6084/m9.figshare.5170480.v3`.

[22] D. Freudenhammer, B. Peterson, C. P. Ding, B. Boehm, and S. Grundmann, "The influence of cylinder head geometry variations on the volumetric intake flow captured by magnetic resonance velocimetry," *SAE International Journal of Engines*, vol. 8, pp. 1826–1836, 4 2015. DOI: `10.4271/2015-01-1697`.

[23] J. Bode, J. Schorr, C. Krüger, A. Dreizler, and B. Böhm, "Influence of the in-cylinder flow on cycle-to-cycle variations in lean combustion disi engines measured by high-speed scanning-piv," *Proceedings of the Combustion Institute*, vol. 37, pp. 4929–4936, 4 2019. DOI: `10.1016/j.proci.2018.07.021`.

[24] S. Fontanesi, A. d'Adamo, and C. J. Rutland, "Large-eddy simulation analysis of spark configuration effect on cycle-to-cycle variability of combustion and knock," *International Journal of Engine Research*, vol. 16, no. 3, pp. 403–418, 2015. DOI: `10.1177/1468087414566253`.

[25] F. Nicollet *et al.*, "A piv-guided large-eddy simulation of in-cylinder flows," *Oil & Gas Science and Technology - Revue d'IFP Energies nouvelles*, vol. 72, p. 28, 5 2017. DOI: `10.2516/ogst/2017022`.

[26] O. Benoit *et al.*, "Development of a large-eddy simulation methodology for the analysis of cycle-to-cycle combustion variability of a lean burn engine," *Flow, Turbulence and Combustion*, vol. 108, pp. 559–598, 2 2022. DOI: `10.1007/s10494-021-00278-7/figures/31`.

[27] R. Stiehl, J. Bode, J. Schorr, C. Krüger, A. Dreizler, and B. Böhm, "Influence of intake geometry variations on in-cylinder flow and flow–spray interactions in a stratified direct-injection spark-ignition engine captured by time-resolved particle image velocimetry," *International Journal of Engine Research*, vol. 17, no. 9, pp. 983–997, 2016. DOI: `10.1177/1468087416633541`.

[28] D. Goryntsev, A. Sadiki, M. Klein, and J. Janicka, "Large eddy simulation based analysis of the effects of cycle-to-cycle variations on air–fuel mixing in realistic disi ic-engines," *Proceedings of the Combustion Institute*, vol. 32, pp. 2759–2766, 2 2009. DOI: `10.1016/j.proci.2008.06.185`.

[29] M. Schmitt, C. E. Frouzakis, A. G. Tomboulides, Y. M. Wright, and K. Boulouchos, "Direct numerical simulation of the effect of compression on the flow, temperature and composition under engine-like conditions," *Proceedings of the Combustion Institute*, vol. 35, pp. 3069–3077, 3 2015. DOI: `10.1016/j.proci.2014.06.097`.

[30] J. Koch, M. Schmitt, Y. M. Wright, K. Steurs, and K. Boulouchos, "Les multi-cycle analysis of the combustion process in a small si engine," *SAE International Journal of Engines*, vol. 7, pp. 269–285, 1 2014. DOI: `10.4271/2014-01-1138`.

[31] M. G. Masouleh, K. Keskinen, O. Kaario, H. Kahila, Y. M. Wright, and V. Vuorinen, "Flow and thermal field effects on cycle-to-cycle variation of combustion: Scale-resolving simulation in a spark ignited simplified engine configuration," *Applied Energy*, vol. 230, pp. 486–505, 2018. DOI: `10.1016/j.apenergy.2018.08.046`.

[32] S. Wadekar, P. Janas, and M. Oevermann, "Large-eddy simulation study of combustion cyclic variation in a lean-burn spark ignition engine," *Applied Energy*, vol. 255, p. 113 812, 2019. DOI: `10.1016/j.apenergy.2019.113812`.

[33] M. Schmitt, C. E. Frouzakis, Y. M. Wright, A. G. Tomboulides, and K. Boulouchos, "Investigation of wall heat transfer and thermal stratification under engine-relevant conditions using dns," *International Journal of Engine Research*, vol. 17, no. 1, pp. 63–75, 2016. DOI: `10.1177/1468087415588710`.

[34] M. Schmitt and K. Boulouchos, "Role of the intake generated thermal stratification on the temperature distribution at top dead center of the compression stroke," *International Journal of Engine Research*, vol. 17, no. 8, pp. 836–845, 2016. DOI: `10.1177/1468087415619289`.

[35] M. Schmitt, C. E. Frouzakis, Y. M. Wright, A. G. Tomboulides, and K. Boulouchos, "Direct numerical simulation of the compression stroke under engine-relevant conditions: Evolution of the velocity and thermal boundary layers," *International Journal of Heat and Mass Transfer*, vol. 91, pp. 948–960, 2015. DOI: `10.1016/j.ijheatmasstransfer.2015.08.031`.

[36] M. Sjerić, D. Kozarac, and R. Tatschl, "Modelling of early flame kernel growth towards a better understanding of cyclic combustion variability in si engines," *Energy Conversion and Management*, vol. 103, pp. 895–909, 2015. DOI: `10.1016/j.enconman.2015.07.031`.

[37] L. Zhao *et al.*, "Examining the role of flame topologies and in-cylinder flow fields on cyclic variability in spark-ignited engines using large-eddy simulation," *International Journal of Engine Research*, vol. 19, pp. 886–904, 8 2018. DOI: `10.1177/1468087417732447`.

[38] B. Enaux *et al.*, "Les study of cycle-to-cycle variations in a spark ignition engine," *Proceedings of the Combustion Institute*, vol. 33, pp. 3115–3122, 2 2011. DOI: `10.1016/j.proci.2010.07.038`.

[39] V. Granet, O. Vermorel, C. Lacour, B. Enaux, V. Dugué, and T. Poinsot, "Large-eddy simulation and experimental study of cycle-to-cycle variations of stable and unstable operating points in a spark ignition engine," *Combustion and Flame*, vol. 159, pp. 1562–1575, 4 2012. DOI: `10.1016/j.combustflame.2011.11.018`.

[40] M. Matsuda, T. Yokomori, and N. Iida, "Investigation of cycle-to-cycle variation of turbulent flow in a high-tumble si engine," *SAE Technical Papers*, vol. 2017-October, 2017. DOI: `10.4271/2017-01-2210`.

[41] J. L. Lumley, "Engines: An introduction," 1999. DOI: `10.1017/cbo9781139175135`.

[42] P. Janas, I. Wlokas, B. Böhm, and A. Kempf, "On the evolution of the flow field in a spark ignition engine," *Flow, Turbulence and Combustion*, vol. 98, pp. 237–264, 1 2016. DOI: `10.1007/s10494-016-9744-3`.

[43] J. L. Lumley, "Early work on fluid mechanics in the ic engine," *Annual Review of Fluid Mechanics*, vol. 33, no. 1, pp. 319–338, 2001. DOI: `10.1146/annurev.fluid.33.1.319`.

[44] M. Fogleman, J. Lumley, D. Rempfer, and D. Haworth, "Application of the proper orthogonal decomposition to datasets of internal combustion engine flows," *Journal of Turbulence*, vol. 5, 2004. DOI: `10.1088/1468-5248/5/1/023`.

[45] F. Foucher, L. Landry, F. Halter, and C. Mounaïm-Rousselle, "Turbulent flow fields analysis of a spark-ignition engine as function of the boosted pressure," in *14th International Symposium on Laser Techniques to Fluid Mechanics*, lisboa, Portugal, 2008.

[46] M. Voisine, "Etude expérimentale de l'aérodynamique interne des moteurs : Mise en oeuvre de diagnostics d'analyses spatio-temporels pour un écoulement de rouleau compressé," Ph.D. dissertation, 2010, 1 vol. (201 p.)

[47] A. Robert, "Simulation aux grandes échelles des combustions anormales dans les moteurs downsizés à allumage commandé," Ph.D. dissertation, 2014.

[48] O. Imberdis, M. Hartmann, H. Bensler, L. Kapitza, and D. Thevenin, "A numerical and experimental investigation of a disi-engine intake port generated turbulent flow," *SAE Technical Papers*, 2007. DOI: `10.4271/2007-01-4047`.

[49] F. R. Menter and Y. Egorov, "The scale-adaptive simulation method for unsteady turbulent flow predictions. part 1: Theory and model description," *Flow, Turbulence and Combustion*, vol. 85, pp. 113–138, 1 2010. DOI: `10.1007/s10494-010-9264-5`.

[50] P. R. Spalart, "Comments on the feasibility of les for wings, and on a hybrid rans/les approach," in *Proceedings of first AFOSR international conference on DNS/LES*, Greyden Press, 1997.

[51] S. Buhl, F. Hartmann, S. A. Kaiser, and C. Hasse, "Investigation of an ic engine intake flow based on highly resolved les and piv," *Oil & Gas Science and Technology - Revue d'IFP Energies nouvelles*, vol. 72, p. 15, 3 2017. DOI: `10.2516/ogst/2017012`.

[52] S. Buhl, D. Hain, F. Hartmann, and C. Hasse, "A comparative study of intake and exhaust port modeling strategies for scale-resolving engine simulations," *International Journal of Engine Research*, vol. 19, pp. 282–292, 3 2018. DOI: `10.1177/1468087417707452`.

[53] F. Nicoud, H. B. Toda, O. Cabrit, S. Bose, and J. Lee, "Using singular values to build a subgrid-scale model for large eddy simulations," *Physics of Fluids*, vol. 23, p. 085 106, 8 2011. DOI: `10.1063/1.3623274`.

[54] K. Nishad, F. Ries, Y. Li, and A. Sadiki, "Numerical investigation of flow through a valve during charge intake in a disi -engine using large eddy simulation," *Energies 2019, Vol. 12, Page 2620*, vol. 12, p. 2620, 13 2019. DOI: `10.3390/en12132620`.

[55] J. L. Lumley and G. R. Newman, "The return to isotropy of homogeneous turbulence," *Journal of Fluid Mechanics*, vol. 82, pp. 161–178, 1 1977. DOI: `10.1017/s0022112077000585`.

[56] M. Haussmann *et al.*, "Evaluation of a near-wall-modeled large eddy lattice boltzmann method for the analysis of complex flows relevant to ic engines," *Computation*, vol. 8, no. 2, 2020. DOI: `10.3390/computation8020043`.

[57] M. Schmitt, "Direct numerical simulations in engine-like geometries," 2015. DOI: `10.3929/ethz-a-010349869`.

[58] K. Tang-Wei, Y. Xiaofeng, G. Venkatesh, and C. Zhaohui, "Large eddy simulation (les) for ic engine flows," *Oil & Gas Science and Technology - Revue d'IFP Energies nouvelles*, vol. 69, pp. 61–81, 1 2014. DOI: `10.2516/ogst/2013127`.

[59] A. P. Morse, J. H. Whitelaw, and M. Yianneskis, "Turbulent flow measurements by laser-doppler anemometry in motored piston-cylinder assemblies," *Journal of Fluids Engineering*, vol. 101, pp. 208–216, 2 1979. DOI: `10.1115/1.3448937`.

[60] S. E. Tahry, "Application of a reynolds stress model to engine-like flow calculations," *Journal of Fluids Engineering*, vol. 107, pp. 444–450, 4 1985. DOI: `10.1115/1.3242508`.

[61] D. C. Haworth and K. Jansen, "Large-eddy simulation on unstructured deforming meshes: Towards reciprocating ic engines," *Computers & Fluids*, vol. 29, pp. 493–524, 5 2000. DOI: `10.1016/s0045-7930(99)00015-8`.

[62] J. P. Keskinen, V. Vuorinen, O. Kaario, and M. Larmi, "Large eddy simulation of a piston-cylinder assembly: The sensitivity of the in-cylinder flow field for residual intake and in-cylinder velocity structures," *Computers & Fluids*, vol. 122, pp. 123–135, 2015. DOI: `10.1016/j.compfluid.2015.08.028`.

[63] M. Schmitt, C. E. Frouzakis, A. G. Tomboulides, Y. M. Wright, and K. Boulouchos, "Direct numerical simulation of multiple cycles in a valve/piston assembly," *Physics of Fluids*, vol. 26, p. 035 105, 3 2014. DOI: `10.1063/1.4868279`.

[64] M. Schmitt, C. E. Frouzakis, Y. M. Wright, A. G. Tomboulides, and K. Boulouchos, "Investigation of cycle-to-cycle variations in an engine-like geometry," *Physics of Fluids*, vol. 26, p. 125 104, 12 2014. DOI: `10.1063/1.4903930`.

[65] M. Schmitt, C. E. Frouzakis, Y. M. Wright, A. Tomboulides, and K. Boulouchos, "Direct numerical simulation of the compression stroke under engine relevant conditions: Local

wall heat flux distribution," *International Journal of Heat and Mass Transfer*, vol. 92, pp. 718–731, 2016. DOI: `10.1016/j.ijheatmasstransfer.2015.08.074`.

[66] P. Schiffmann, S. Gupta, D. Reuss, V. Sick, X. Yang, and T. W. Kuo, "Tcc-iii engine benchmark for large-eddy simulation of ic engine flows," *Oil & Gas Science and Technology - Revue d'IFP Energies nouvelles*, vol. 71, p. 3, 1 2016. DOI: `10.2516/ogst/2015028`.

[67] K. Liu and D. C. Haworth, "Large-eddy simulation for an axisymmetric piston-cylinder assembly with and without swirl," *Flow, Turbulence and Combustion*, vol. 85, pp. 279–307, 3 2010. DOI: `10.1007/s10494-010-9292-1`.

[68] P. S. Abraham, X. Yang, S. Gupta, T.-W. Kuo, D. L. Reuss, and V. Sick, "Flow-pattern switching in a motored spark ignition engine," *International Journal of Engine Research*, vol. 16, no. 3, pp. 323–339, 2015. DOI: `10.1177/1468087414565400`.

[69] I. Ko, A. D'Adamo, S. Fontanesi, and K. Min, "Study of les quality criteria in a motored internal combustion engine," *SAE Technical Papers*, vol. 2017-March, March 2017. DOI: `10.4271/2017-01-0549`.

[70] I. Ko, K. Min, F. Rulli, A. D'Adamo, F. Berni, and S. Fontanesi, "Investigation of sub-grid model effect on the accuracy of in-cylinder les of the tcc engine under motored conditions," *SAE Technical Papers*, vol. 2017-September, 2017. DOI: `10.4271/2017-24-0040`.

[71] Y. Xiaofeng and K. Tang-Wei, "Correlation of ccv between in-cylinder swirl ratio and polar velocity profile in valve seat region using les under motored engine condition," *Oil & Gas Science and Technology - Rev. IFP Energies nouvelles*, vol. 72, p. 38, 6 2017. DOI: `10.2516/ogst/2017036`.

[72] S. Y. *et al.*, "An experimental and simulation study of early flame development in a homogeneous-charge spark-ignition engine," *Oil & Gas Science and Technology - Rev. IFP Energies nouvelles*, vol. 72, p. 32, 5 2017. DOI: `10.2516/ogst/2017028`.

[73] G. K. Giannakopoulos, C. E. Frouzakis, P. F. Fischer, A. G. Tomboulides, and K. Boulouchos, "Les of the gas-exchange process inside an internal combustion engine using a high-order method," *Flow, Turbulence and Combustion*, vol. 104, pp. 673–692, 2 2019. DOI: `10.1007/s10494-019-00067-3`.

[74] A. Wu, S. Keum, and V. Sick, "Large eddy simulations with conjugate heat transfer (cht) modeling of internal combustion engines (ices)," *Oil & Gas Science and Technology - Revue d'IFP Energies nouvelles*, vol. 74, p. 51, 2019. DOI: `10.2516/ogst/2019029`.

[75] A. Wu, S. Keum, M. Greene, D. Reuss, and V. Sick, "Comparison of near-wall flow and heat transfer of an internal combustion engine using particle image velocimetry and computational fluid dynamics," *Journal of Energy Resources Technology, Transactions of the ASME*, vol. 141, 12 2019. DOI: `10.1115/1.4044021/956070`.

[76] J. Borée, S. Maurel, and R. Bazile, "Disruption of a compressed vortex," *Physics of Fluids*, vol. 14, p. 2543, 7 2002. DOI: `10.1063/1.1472505`.

[77] O. L. Roy and L. L. Penven, "Compression of a turbulent vortex flow," *International Journal of Heat and Fluid Flow*, vol. 19, pp. 533–540, 5 1998. DOI: `10.1016/s0142-727x(98)10028-0`.

[78] S. Maurel, J. Borée, and J. L. Lumley, "Extended proper orthogonal decomposition: Application to jet/vortex interaction," *Flow, Turbulence and Combustion*, vol. 67, pp. 125–136, 2 2001. DOI: `10.1023/a:1014050204350`.

[79] J. Moreau, J. Boree, R. Bazile, and G. Charnay, "Modification of an experimental model gdi tumbling flow by direct injection," *SAE Technical Papers*, 2003. DOI: `10.4271/2003-01-0064`.

[80] V. Moureau, I. Barton, C. Angelberger, and T. Poinsot, "Towards large eddy simulation in internal-combustion engines: Simulation of a compressed tumble flow," *SAE Technical Papers*, 2004. DOI: `10.4271/2004-01-1995`.

[81] A. Devesa, J. Moreau, T. Poinsot, and J. Helie, "Large eddy simulations of jet / tumble interaction in a gdi model engine flow," *SAE Technical Papers*, 2004. DOI: `10.4271/2004-01-1997`.

[82] M. S. Toledo, L. L. Penven, M. Buffat, A. Cadiou, and J. Padilla, "Large eddy simulation of the generation and breakdown of a tumbling flow," *International Journal of Heat and Fluid Flow*, vol. 28, pp. 113–126, 1 Spec. Iss. 2007. DOI: `10.1016/j.ijheatfluidflow.2006.03.029`.

[83] V. Dugué, N. Gauchet, and D. Veynante, "Applicability of large eddy simulation to the fluid mechanics in a real engine configuration by means of an industrial code," *SAE Technical Papers*, 2006. DOI: `10.4271/2006-01-1194`.

[84] S. Richard, O. Colin, O. Vermorel, A. Benkenida, C. Angelberger, and D. Veynante, "Towards large eddy simulation of combustion in spark ignition engines," *Proceedings of the Combustion Institute*, vol. 31, pp. 3059–3066, 2 2007. DOI: `10.1016/j.proci.2006.07.086`.

[85] O. Vermorel, S. Richard, O. Colin, C. Angelberger, A. Benkenida, and D. Veynante, "Towards the understanding of cyclic variability in a spark ignited engine using multi-cycle les," *Combustion and Flame*, vol. 156, pp. 1525–1541, 8 2009. DOI: `10.1016/j.combustflame.2009.04.007`.

[86] M. Schmitt, R. Hu, Y. M. Wright, P. Soltic, and K. Boulouchos, "Multiple cycle les simulations of a direct injection natural gas engine," *Flow, Turbulence and Combustion*, vol. 95, pp. 645–668, 4 2015. DOI: `10.1007/s10494-015-9625-1`.

[87] O. Pajot, "Etude expérimentale de l'influence de l'aérodynamique sur le comportement et la structure du front de flamme dans les conditions d'un moteur à allumage commandé," Ph.D. dissertation, 2000.

[88] Y. Laurant, "Variabilité aérodynamique d'un moteur à combustion interne pendant la phase d'admission : Vers l'origine des fluctuations cycliques," Ph.D. dissertation, 2008.

[89] Y. Cao, "Sensibilité d'un écoulement de rouleau compressé et des variations cycle à cycle associées à des paramètres de remplissage moteur," Theses, Ensma, 2014.

[90] B. Enaux *et al.*, "Large eddy simulation of a motored single-cylinder piston engine: Numerical strategies and validation," *Flow, Turbulence and Combustion*, vol. 86, pp. 153–177, 2 2010. DOI: `10.1007/s10494-010-9299-7`.

[91] K. Truffin, C. Angelberger, S. Richard, and C. Pera, "Using large-eddy simulation and multivariate analysis to understand the sources of combustion cyclic variability in a spark-ignition engine," *Combustion and Flame*, vol. 162, pp. 4371–4390, 12 2015. DOI: `10.1016/j.combustflame.2015.07.003`.

[92] M. Baumann, F. D. Mare, and J. Janicka, "On the validation of large eddy simulation applied to internal combustion engine flows part ii: Numerical analysis," *Flow, Turbulence and Combustion*, vol. 92, pp. 299–317, 1 2013. DOI: `10.1007/s10494-013-9472-x`.

[93] T. M. Nguyen, F. Proch, I. Wlokas, and A. M. Kempf, "Large eddy simulation of an internal combustion engine using an efficient immersed boundary technique," *Flow, Turbulence and Combustion*, vol. 97, pp. 191–230, 1 2016. DOI: `10.1007/s10494-015-9683-4`.

[94] R. Mittal and G. Iaccarino, "Immersed boundary methods," *Annual Review of Fluid Mechanics*, vol. 37, no. 1, pp. 239–261, 2005. DOI: `10.1146/annurev.fluid.37.061903.175743`.

[95] C. He, W. Leudesdorff, F. di Mare, A. Sadiki, and J. Janicka, "Analysis of in-cylinder flow field anisotropy in ic engine using large eddy simulation," *Flow, Turbulence and Combustion*, vol. 99, pp. 353–383, 2 2017. DOI: `10.1007/s10494-017-9812-3`.

[96] C. Iacovano, A. d'Adamo, S. Fontanesi, G. D. Ilio, and V. K. Krastev, "A wall-adapted zonal urans/les methodology for the scale-resolving simulation of engine flows," *International Journal of Engine Research*, 2021. DOI: `10.1177/14680874211032379`.

[97] C. Iacovano, F. Berni, A. Barbato, and S. Fontanesi, "A preliminary 1d-3d analysis of the darmstadt research engine under motored condition," *E3S Web of Conferences*, vol. 197, p. 06 006, 2020. DOI: `10.1051/e3sconf/202019706006`.

[98] M. Impagnatiello *et al.*, "Systematic assessment of data-driven approaches for wall heat transfer modelling for les in ic engines using dns data," *International Journal of Heat and Mass Transfer*, vol. 183, p. 122 109, 2022. DOI: `10.1016/j.ijheatmasstransfer.2021.122109`.

[99] C. Krüger, J. Schorr, F. Nicollet, J. Bode, A. Dreizler, and B. Böhm, "Cause-and-effect chain from flow and spray to heat release during lean gasoline combustion operation using conditional statistics," *International Journal of Engine Research*, vol. 18, no. 1-2, pp. 143–154, 2017. DOI: `10.1177/1468087416686721`.

[100] F. Nicollet, "Analysis of cyclic phenomena in a gasoline direct injection engine of flow and mixture formation using large-eddy simulation and high-speed particle image velocimetry," Ph.D. dissertation, Technische Universität, Darmstadt, 2019.

[101] C. Funk, V. Sick, D. L. Reuss, and W. J. Dahm, "Turbulence properties of high and low swirl in-cylinder flows," *SAE Technical Papers*, 2002. DOI: `10.4271/2002-01-2841`.

[102] S. H. Joo, K. K. Srinivasan, K. C. Lee, and S. R. Bell, "The behaviourt of small- and large-scale variations of in-cylinder flow during intake and compression strokes in a motored four-valve spark ignition engine," *International Journal of Engine Research*, vol. 5, no. 4, pp. 317–328, 2004. DOI: `10.1243/146808704323224222`.

[103] P. G. Aleiferis, M. K. Behringer, and J. S. Malcolm, "Integral length scales and time scales of turbulence in an optical spark-ignition engine," *Flow, Turbulence and Combustion*, vol. 98, pp. 523–577, 2 2016. DOI: `10.1007/s10494-016-9775-9`.

[104] M. Farge, "Wavelet transforms and their applications to turbulence," *Annual Review of Fluid Mechanics*, vol. 24, pp. 395–458, 1 1992. DOI: `10.1146/annurev.fl.24.010192.002143`.

[105] R. Camussi and G. Guj, "Orthonormal wavelet decomposition of turbulent flows: Intermittency and coherent structures," *Journal of Fluid Mechanics*, vol. 348, pp. 177–199, 1997. DOI: `10.1017/s0022112097006551`.

[106] M. Farge, G. Pellegrino, and K. Schneider, "Coherent vortex extraction in 3d turbulent flows using orthogonal wavelets," *Physical Review Letters*, vol. 87, p. 054 501, 5 2001. DOI: `10.1103/PhysRevLett.87.054501`.

[107] T. Sakurai, K. Yoshimatsu, K. Schneider, M. Farge, K. Morishita, and T. Ishihara, "Coherent structure extraction in turbulent channel flow using boundary adapted wavelets," *Journal of Turbulence*, vol. 18, no. 4, pp. 352–372, 2017. DOI: `10.1080/14685248.2017.1284326`.

[108] P. J. Schmid, "Dynamic mode decomposition of numerical and experimental data," *Journal of Fluid Mechanics*, vol. 656, pp. 5–28, 2010. DOI: `10.1017/s0022112010001217`.

[109] T. Sayadi, J. Nichols, P. Schmid, and P. Moin, "Dynamic mode decomposition of h-type transition to turbulence," *Center for Turbulence Research - Proceedings of the Summer Program*, 2012.

[110] A. Sakowitz, M. Mihaescu, and L. Fuchs, "Flow decomposition methods applied to the flow in an ic engine manifold," *Applied Thermal Engineering*, vol. 65, pp. 57–65, 1-2 2014. DOI: `10.1016/j.applthermaleng.2013.12.082`.

[111] F. Richecoeur, L. Hakim, A. Renaud, and L. Zimmer, "Dmd algorithms for experimental data processing in combustion," *Proceeding of the 2012 Summer Program, Center for Turbulence Research, Stanford University*, 2012.

[112] A. J. Torregrosa, A. Broatch, J. García-Tíscar, and J. Gomez-Soriano, "Modal decomposition of the unsteady flow field in compression-ignited combustion chambers," *Combustion and Flame*, vol. 188, pp. 469–482, 2018. DOI: `10.1016/j.combustflame.2017.10.007`.

[113] A. Chatterjee, "An introduction to the proper orthogonal decomposition," *Current Science*, vol. 78, no. 7, pp. 808–817, 2000.

[114] J. L. Lumley, "The structure of inhomogeneous turbulent flows," *Atmospheric turbulence and radio wave propagation*, 1967.

[115] L. Sirovich, "Turbulence and the dynamics of coherent structures. i. coherent structures," *Quarterly of applied mathematics*, vol. 45, no. 3, pp. 561–571, 1987.

[116] L. Sirovich, "Turbulence and the dynamics of coherent structures. ii. symmetries and transformations," *Quarterly of Applied mathematics*, vol. 45, no. 3, pp. 573–582, 1987.

[117] L. Sirovich, "Turbulence and the dynamics of coherent structures. iii. dynamics and scaling," *Quarterly of Applied mathematics*, vol. 45, no. 3, pp. 583–590, 1987.

[118] M. Fogleman, “Low-dimensional models of internal combustion engine flows using the proper orthogonal decomposition,” Ph.D. dissertation, Cornell University, New York, 2005.

[119] K. Liu and D. C. Haworth, “Development and assessment of pod for analysis of turbulent flow in piston engines,” *SAE 2011 World Congress and Exhibition*, 2011. DOI: `10.4271/2011-01-0830`.

[120] K. Liu, D. C. Haworth, X. Yang, and V. Gopalakrishnan, “Large-eddy simulation of motored flow in a two-valve piston engine: Pod analysis and cycle-to-cycle variations,” *Flow, Turbulence and Combustion*, vol. 91, pp. 373–403, 2 2013. DOI: `10.1007/s10494-013-9475-7`.

[121] H. Chen, D. L. Reuss, and V. Sick, “On the use and interpretation of proper orthogonal decomposition of in-cylinder engine flows,” *Measurement Science and Technology*, vol. 23, p. 085 302, 8 2012. DOI: `10.1088/0957-0233/23/8/085302`.

[122] M. Voisine, L. Thomas, J. Borée, and P. Rey, “Spatio-temporal structure and cycle to cycle variations of an in-cylinder tumbling flow,” *Experiments in Fluids*, vol. 50, 5 2011. DOI: `10.1007/s00348-010-0997-7`.

[123] S. Buhl *et al.*, “A combined numerical and experimental study of the 3d tumble structure and piston boundary layer development during the intake stroke of a gasoline engine,” *Flow, Turbulence and Combustion*, vol. 98, 2 2017. DOI: `10.1007/s10494-016-9754-1`.

[124] S. Roudnitzky, P. Druault, and P. Guibert, “Proper orthogonal decomposition of in-cylinder engine flow into mean component, coherent structures and random gaussian fluctuations,” *Journal of Turbulence*, vol. 7, N70, 2006. DOI: `10.1080/14685240600806264`.

[125] W. Qin, M. Xie, M. Jia, T. Wang, and D. Liu, “Large eddy simulation and proper orthogonal decomposition analysis of turbulent flows in a direct injection spark ignition engine: Cyclic variation and effect of valve lift,” *Science China Technological Sciences 2014 57:3*, vol. 57, pp. 489–504, 3 2014. DOI: `10.1007/s11431-014-5472-x`.

[126] W. Qin, L. Zhou, D. Liu, M. Jia, and M. Xie, “Investigation of in-cylinder engine flow quadruple decomposition dynamical behavior using proper orthogonal decomposition and dynamic mode decomposition methods,” *Journal of Engineering for Gas Turbines and Power*, vol. 141, 8 2019. DOI: `10.1115/1.4042725/374477`.

[127] F. Rulli, S. Fontanesi, A. d’Adamo, and F. Berni, “A critical review of flow field analysis methods involving proper orthogonal decomposition and quadruple proper orthogonal decomposition for internal combustion engines,” *International Journal of Engine Research*, vol. 22, no. 1, pp. 222–242, 2021. DOI: `10.1177/1468087419836178`.

[128] N. E. Huang *et al.*, “The empirical mode decomposition and the hilbert spectrum for nonlinear and non-stationary time series analysis,” *Proceedings of the Royal Society of London. Series A: Mathematical, Physical and Engineering Sciences*, vol. 454, pp. 903–995, 1971 1998. DOI: `10.1098/rspa.1998.0193`.

[129] F. Foucher and P. Ravier, “Determination of turbulence properties by using empirical mode decomposition on periodic and random perturbed flows,” *Experiments in Fluids*, vol. 49, pp. 379–390, 2 2010. DOI: `10.1007/s00348-009-0804-5`.

[130] M. Sadeghi, F. Foucher, K. Abed-Meraim, and C. Mounaïm-Rousselle, “Bivariate 2d empirical mode decomposition for analyzing instantaneous turbulent velocity field in unsteady flows,” *Experiments in Fluids*, vol. 60, 8 2019. DOI: `10.1007/s00348-019-2775-5`.

[131] J Smagorinsky, “General circulation experiments with the primitive equations,” *Monthly Weather Review*, vol. 91, p. 99, 3 1963. DOI: `10.1175/1520-0493(1963)0910099:gcewtp2.3.co;2`.

[132] S. B. Pope, *Turbulent Flows*. Cambridge University Press, 2000. DOI: `10.1017/cbo9780511840531`.

[133] N. Peters, “The turbulent burning velocity for large-scale and small-scale turbulence,” *Journal of Fluid Mechanics*, vol. 384, pp. 107–132, 1999. DOI: `10.1017/s0022112098004212`.

[134] S. Richard, “Simulation aux grandes echelles d’un moteur à allumage commandé - evaluations des variabilités cycliques,” Ph.D. dissertation, 2005.

[135] O. Colin, S. Chevillard, J. Bohbot, P. K. Senecal, E. Pomraning, and M. Wang, "Development of a species-based extended coherent flamelet model (sb-ecfm) for gasoline direct injection engine (gdi) simulations," *ASME 2018 Internal Combustion Engine Division Fall Technical Conference, ICEF 2018*, vol. 2, 2019. DOI: `10.1115/icef2018-9684`.

[136] O. Colin, A. Benkenida, and C. Angelberger, "3d modeling of mixing, ignition and combustion phenomena in highly stratified gasoline engines," *Oil & Gas Science and Technology - Revue d'IFP Energies nouvelles*, vol. 58, pp. 47–62, 1 2003. DOI: `10.2516/ogst:2003004`.

[137] D. Veynante and T. Poinsot, "Reynolds averaged and large eddy simulation modeling for turbulent combustion," *New Tools in Turbulence Modelling*, pp. 105–140, 1997. DOI: `10.1007/978-3-662-08975-0_5`.

[138] O. Colin, F. Ducros, D. Veynante, and T. Poinsot, "A thickened flame model for large eddy simulations of turbulent premixed combustion," *Physics of Fluids*, vol. 12, p. 1843, 7 2000. DOI: `10.1063/1.870436`.

[139] C. Meneveau and T. Poinsot, "Stretching and quenching of flamelets in premixed turbulent combustion," *Combustion and Flame*, vol. 86, pp. 311–332, 4 1991. DOI: `10.1016/0010-2180(91)90126-v`.

[140] O. Colin and K. Truffin, "A spark ignition model for large eddy simulation based on an fsd transport equation (issim-les)," *Proceedings of the Combustion Institute*, vol. 33, pp. 3097–3104, 2 2011. DOI: `10.1016/j.proci.2010.07.023`.

[141] T. Tanaka and D. P. Mandic, "Complex empirical mode decomposition," *IEEE Signal Processing Letters*, vol. 14, pp. 101–104, 2 2007. DOI: `10.1109/lsp.2006.882107`.

[142] M. U. B. Altaf, T. Gautama, T. Tanaka, and D. P. Mandic, "Rotation invariant complex empirical mode decomposition," *ICASSP, IEEE International Conference on Acoustics, Speech and Signal Processing - Proceedings*, vol. 3, 2007. DOI: `10.1109/icassp.2007.366853`.

[143] G. Rilling, P. Flandrin, P. Goncalves, and J. M. Lilly, "Bivariate empirical mode decomposition," *IEEE Signal Processing Letters*, vol. 14, pp. 936–939, 12 2007. DOI: `10.1109/lsp.2007.904710`.

[144] N. U. Rehman and D. P. Mandic, "Empirical mode decomposition for trivariate signals," *IEEE Transactions on Signal Processing*, vol. 58, pp. 1059–1068, 3 Part 1 2010. DOI: `10.1109/tsp.2009.2033730`.

[145] N. Rehman and D. P. Mandic, "Multivariate empirical mode decomposition," *Proceedings of the Royal Society A: Mathematical, Physical and Engineering Sciences*, vol. 466, pp. 1291–1302, 2117 2010. DOI: `10.1098/rspa.2009.0502`.

[146] G. Rilling, P. Flandrin, and P. Goncalves, "On empirical mode decomposition and its algorithms," *IEEE-EURASIP workshop on nonlinear signal and image processing*, vol. 3, pp. 8–11, 2003.

[147] B. M. Battista, C. Knapp, T. McGee, and V. Goebel, "Application of the empirical mode decomposition and hilbert-huang transform to seismic reflection data," *Geophysics*, vol. 72, 2 2007. DOI: `10.1190/1.2437700`.

[148] D. M. Klionski, N. I. Oreshko, V. V. Geppener, and A. V. Vasiljev, "Applications of empirical mode decomposition for processing nonstationary signals," *Pattern Recognition and Image Analysis 2008 18:3*, vol. 18, pp. 390–399, 3 2008. DOI: `10.1134/s105466180803005x`.

[149] F. Wu and L. Qu, "An improved method for restraining the end effect in empirical mode decomposition and its applications to the fault diagnosis of large rotating machinery," *Journal of Sound and Vibration*, vol. 314, pp. 586–602, 3-5 2008. DOI: `10.1016/j.jsv.2008.01.020`.

[150] R. T. Rato, M. D. Ortigueira, and A. G. Batista, "On the hht, its problems, and some solutions," *Mechanical Systems and Signal Processing*, vol. 22, pp. 1374–1394, 6 2008. DOI: `10.1016/j.ymssp.2007.11.028`.

[151] J. L. Sanchez and J. J. Trujillo, "Improving the empirical mode decomposition method," *Applicable Analysis*, vol. 90, no. 3-4, pp. 689–713, 2011. DOI: `10.1080/00036810903569531`.

[152] A. Cicone and P. Dell'Acqua, "Study of boundary conditions in the iterative filtering method for the decomposition of nonstationary signals," *Journal of Computational and Applied Mathematics*, vol. 373, 2020. DOI: `10.1016/j.cam.2019.04.028`.

[153] S. Sandoval, M. Bredin, and P. L. D. Leon, "Using linear prediction to mitigate end effects in empirical mode decomposition," *2018 IEEE Global Conference on Signal and Information Processing, GlobalSIP 2018 - Proceedings*, pp. 281–285, 2019. DOI: `10.1109/globalsip.2018.8646563`.

[154] E. Zivot and J. Wang, "Vector autoregressive models for multivariate time series," *Modeling Financial Time Series with S-Plus®*, pp. 369–413, 2003. DOI: `10.1007/978-0-387-21763-5_11`.

[155] A. Hemakom, V. Goverdovsky, D. Looney, and D. P. Mandic, "Adaptive-projection intrinsically transformed multivariate empirical mode decomposition in cooperative braincomputer interface applications," *Philosophical Transactions of the Royal Society A: Mathematical, Physical and Engineering Sciences*, vol. 374, 2065 2016. DOI: `10.1098/rsta.2015.0199`.

[156] N. E. Huang, Z. Shen, and S. R. Long, "A new view of nonlinear water waves: The hilbert spectrum," *Annual Review of Fluid Mechanics*, vol. 31, no. 1, pp. 417–457, 1999. DOI: `10.1146/annurev.fluid.31.1.417`.

[157] Y. Gao, G. Ge, Z. Sheng, and E. Sang, "Analysis and solution to the mode mixing phenomenon in emd," *Proceedings - 1st International Congress on Image and Signal Processing, CISP 2008*, vol. 5, pp. 223–227, 2008. DOI: `10.1109/cisp.2008.193`.

[158] Z. Wu and N. E. Huang, "Ensemble empirical mode decomposition: A noise-assisted data analysis method," *Advances in Adaptive Data Analysis*, vol. 1, 1 2009. DOI: `10.1142/s1793536909000047`.

[159] N. Rehman, C. Park, N. Huang, and D. Mandic, "Emd via memd: Multivariate noise-aided computation of standard emd," *Advances in Adaptive Data Analysis*, vol. 05, 2013. DOI: `10.1142/s1793536913500076`.

[160] E. Baum, B. Peterson, B. Böhm, and A. Dreizler, "On the validation of les applied to internal combustion engine flows: Part 1: Comprehensive experimental database," *Flow, Turbulence and Combustion*, vol. 92, pp. 269–297, 1 2013. DOI: `10.1007/s10494-013-9468-6`.

[161] Y. Xia, B. Zhang, W. Pei, and D. P. Mandic, "Bidimensional multivariate empirical mode decomposition with applications in multi-scale image fusion," *IEEE Access*, vol. 7, pp. 114 261–114 270, 2019. DOI: `10.1109/access.2019.2936030`.

[162] B. Galmiche, N. Mazellier, F. Halter, and F. Foucher, "Turbulence characterization of a high-pressure high-temperature fan-stirred combustion vessel using ldv, piv and tr-piv measurements," *Experiments in Fluids*, vol. 55, pp. 1–20, 1 2013. DOI: `10.1007/s00348-013-1636-x`.

[163] L. Graftieaux, M. Michard, and G. Nathalie, "Combining piv, pod and vortex identification algorithms for the study of unsteady turbulent swirling flows," *Measurement Science and Technology*, vol. 12, p. 1422, 9 2001. DOI: `10.1088/0957-0233/12/9/307`.

[164] I. Bücker *et al.*, "Stereoscopic multi-planar piv measurements of in-cylinder tumbling flow," *Experiments in Fluids*, vol. 53, pp. 1993–2009, 6 2012. DOI: `10.1007/s00348-012-1402-5`.

[165] M. Gohlke, J. F. Beaudoin, M. Amielh, and F. Anselmet, "Thorough analysis of vortical structures in the flow around a yawed bluff body," *Journal of Turbulence*, vol. 9, 2008. DOI: `10.1080/14685240802010657`.

[166] K. Jaffri *et al.*, "Tumble and swirl quantification within a motored four-valve si engine cylinder based on 3-d ldv measurements," *SAE Technical Papers*, 1997. DOI: `10.4271/970792`.

[167] T. U. Darmstadt, *Darmstadt engine workshop (dew)*, `https://https://www.rsm.tu-darmstadt.de/home_rsm/events_3/darmstadt_engine_workshop/index.en.jsp`.

[168] R. I. Issa, "Solution of the implicitly discretised fluid flow equations by operator-splitting," *Journal of Computational Physics*, vol. 62, pp. 40–65, 1 1986. DOI: `10.1016/0021-9991(86)90099-9`.

[169] M. Namazian and J. B. Heywood, “Flow in the piston-cylinder-ring crevices of a spark-ignition engine: Effect on hydrocarbon emissions, efficiency and power,” *SAE Technical Papers*, 1982. DOI: 10.4271/820088.

[170] A. Misdariis, “Schémas cinétiques réduits et couplage thermique pour les simulations aux grandes échelles du cliquetis dans les moteurs à piston,” Ph.D. dissertation, 2015.

[171] S. Ishizawa, “An experimental study on quenching crevice widths in the combustion chamber of a spark-ignition engine,” *Symposium (International) on Combustion*, vol. 26, pp. 2605–2611, 2 1996. DOI: 10.1016/s0082-0784(96)80094-4.

[172] T. Poinsot and D. Veynante, *Theoretical and numerical combustion*. RT Edwards, Inc., 2005.

[173] F. S., P. S., D. A., and D. S., “Investigation of boundary condition and field distribution effects on the cycle-to-cycle variability of a turbocharged gdi engine using les,” *Oil & Gas Science and Technology - Revue d’IFP Energies nouvelles*, vol. 69, pp. 107–128, 1 2014. DOI: 10.2516/ogst/2013142.

[174] B. Johansson, “Cycle to cycle variations in s.i. engines - the effects of fluid flow and gas composition in the vicinity of the spark plug on early combustion,” *SAE Technical Papers*, 1996. DOI: 10.4271/962084.

[175] M. Leguille, “Étude du cliquetis dans un moteur industriel à allumage commandé par simulation aux grandes échelles,” Ph.D. dissertation, 2018.

[176] Z. Ding, K. Truffin, S. Jay, and D. Sinoquet, “Uncertainty and sensitivity analysis in turbulent pipe flow simulation,” in *14th WCCM-ECCOMAS Congress 2020*, 2021. DOI: 10.23967/wccm-eccomas.2020.185.

[177] A. G. Kravchenko and P. Moin, “On the effect of numerical errors in large eddy simulations of turbulent flows,” *Journal of Computational Physics*, vol. 131, pp. 310–322, 2 1997. DOI: 10.1006/jcph.1996.5597.

[178] P. J. Roache, “Quantification of uncertainty in computational fluid dynamics,” *Annual Review of Fluid Mechanics*, vol. 29, no. 1, pp. 123–160, 1997. DOI: 10.1146/annurev.fluid.29.1.123.

[179] W. L. Oberkampf and T. G. Trucano, “Verification and validation in computational fluid dynamics,” *Progress in Aerospace Sciences*, vol. 38, pp. 209–272, 3 2002. DOI: 10.1016/s0376-0421(02)00005-2.

[180] “Guide: Guide for the verification and validation of computational fluid dynamics simulations (aiaa g-077-1998(2002)),” in *Guide: Guide for the Verification and Validation of Computational Fluid Dynamics Simulations (AIAA G-077-1998(2002))*. DOI: 10.2514/4.472855.001.

[181] W. L. Oberkampf and C. J. Roy, “Verification and validation in scientific computing,” *Verification and Validation in Scientific Computing*, pp. 1–767, 2011. DOI: 10.1017/cbo9780511760396.

[182] R. C. Smith, *Uncertainty Quantification - Theory, Implementation, and Applications*. Siam, 2014.

[183] D Bestion *et al.*, “Review of uncertainty methods for cfd application to nuclear reactor thermalhydraulics,” *NUTHOS 11- The 11th International Topical Meeting on Nuclear Reactor Thermal Hydraulics, Operation and Safety*, 2016.

[184] J. Fokken, B. Krohn, R. Kapulla, B. Niceno, H.-M Prasser, and A. Badillo, “Nea benchmark exercise: Computational fluid dynamic prediction and uncertainty quantification of a gemix mixing layer test,” 2019.

[185] P. J. Wenig, R. Ji, S. Kelm, and M. Klein, “Towards uncertainty quantification of les and urans for the buoyancy-driven mixing process between two miscible fluids—differentially heated cavity of aspect ratio 4,” *Fluids*, vol. 6, p. 161, 4 2021. DOI: 10.3390/fluids6040161.

[186] M. Hassan, J. Xiong, X. Cheng, and D. Liu, “Uncertainty quantification (uq) for cfd simulation of oecd-nea cold leg mixing benchmark,” *Nuclear Engineering and Design*, vol. 393, p. 111 799, 2022. DOI: 10.1016/j.nucengdes.2022.111799.

[187] J. Schaefer, B. Leyde, C. Denham, V. Romero, and S. Schafer, “Approaches for quantifying uncertainties in computational modeling for aerospace applications,” *AIAA Scitech 2020 Forum*, vol. 1 PartF, 2020. DOI: 10.2514/6.2020-1520.

[188] E. N. Tinoco, “Validation and minimizing cfd uncertainty for commercial aircraft applications,” *Collection of Technical Papers - AIAA Applied Aerodynamics Conference*, 2008. DOI: `10.2514/6.2008-6902`.

[189] B. Gainey, J. P. Longtin, and B. Lawler, “A guide to uncertainty quantification for experimental engine research and heat release analysis,” *SAE International Journal of Engines*, vol. 12, pp. 509–523, 5 2019. DOI: `10.4271/03-12-05-0033`.

[190] Q. Wang, “Uncertainty quantification for unsteady fluid flow using adjoint-based approaches,” Ph.D. dissertation, Stanford University, California, 2009.

[191] L. Mathelin, M. Y. Hussaini, and T. A. Zang, “Stochastic approaches to uncertainty quantification in cfd simulations,” *Numerical Algorithms*, vol. 38, pp. 209–236, 1 2005. DOI: `10.1007/bf02810624`.

[192] J. Peter, E. Savin, and I. S. E. Din, “Generalized polynomial chaos and stochastic collocation methods for uncertainty quantification in aerodynamics,” 2018.

[193] S. Rezaeiravesh, R. Vinuesa, and P. Schlatter, “An uncertainty-quantification framework for assessing accuracy, sensitivity, and robustness in computational fluid dynamics,” *Journal of Computational Science*, vol. 62, p. 101 688, 2022. DOI: `10.1016/j.jocs.2022.101688`.

[194] Y. Duan, M. N. Ridao, M. Eaton, and M. Bluck, “Non-intrusive semi-analytical uncertainty quantification using bayesian quadrature with application to cfd simulations,” *International Journal of Heat and Fluid Flow*, vol. 93, p. 108 917, 2022. DOI: `10.1016/j.ijheatfluidflow.2021.108917`.

[195] O. Roustant, D. Ginsbourger, and Y. Deville, “Dicekriging, diceoptim: Two r packages for the analysis of computer experiments by kriging-based metamodeling and optimization,” *Journal of Statistical Software*, vol. 51, pp. 1–55, 1 2012. DOI: `10.18637/jss.v051.i01`.

[196] E. Garnier, N. Adams, and P. Sagaut, “Large eddy simulation for compressible flows,” 2009. DOI: `10.1007/978-90-481-2819-8`.

[197] J. Meyers and P. Sagaut, “On the model coefficients for the standard and the variational multi-scale smagorinsky model,” *Journal of Fluid Mechanics*, vol. 569, pp. 287–319, 2006. DOI: `10.1017/s0022112006002850`.

[198] E. S. Zanoun, F. Durst, and H. Nagib, “Evaluating the law of the wall in two-dimensional fully developed turbulent channel flows,” *Physics of Fluids*, vol. 15, p. 3079, 10 2003. DOI: `10.1063/1.1608010`.

[199] X. Wu and P. Moin, “A direct numerical simulation study on the mean velocity characteristics in turbulent pipe flow,” *Journal of Fluid Mechanics*, vol. 608, pp. 81–112, 2008. DOI: `10.1017/s0022112008002085`.

[200] J. G. M. Eggels *et al.*, “Fully developed turbulent pipe flow: A comparison between direct numerical simulation and experiment,” *Journal of Fluid Mechanics*, vol. 268, pp. 175–210, 1994. DOI: `10.1017/s002211209400131x`.

[201] R. K.J., S. P.K., and P. E., *Converge 2.4, convergent science*, 2017.

[202] M. D. McKay, R. J. Beckman, and W. J. Conover, “Comparison of three methods for selecting values of input variables in the analysis of output from a computer code,” *Technometrics*, vol. 21, no. 2, pp. 239–245, 1979. DOI: `10.1080/00401706.1979.10489755`.

[203] J. P. Kleijnen, “Kriging metamodeling in simulation: A review,” *European Journal of Operational Research*, vol. 192, pp. 707–716, 3 2009. DOI: `10.1016/j.ejor.2007.10.013`.

[204] I. M. Sobol, “Global sensitivity indices for nonlinear mathematical models and their monte carlo estimates,” *Mathematics and Computers in Simulation*, vol. 55, pp. 271–280, 1-3 2001. DOI: `10.1016/s0378-4754(00)00270-6`.

[205] S. Tarantola, D. Gatelli, and T. A. Mara, “Random balance designs for the estimation of first order global sensitivity indices,” *Reliability Engineering & System Safety*, vol. 91, pp. 717–727, 6 2006. DOI: `10.1016/j.ress.2005.06.003`.

[206] M. C. Kennedy and A. O'Hagan, "Bayesian calibration of computer models," *Journal of the Royal Statistical Society: Series B (Statistical Methodology)*, vol. 63, pp. 425–464, 3 2001. DOI: `10.1111/1467-9868.00294`.

[207] M. Stein, "Large sample properties of simulations using latin hypercube sampling," *Technometrics*, vol. 29, no. 2, pp. 143–151, 1987. DOI: `10.1080/00401706.1987.10488205`.

[208] D. Duvenaud, *The Kernel cookbook: Advice on covariance functions*. 2014.

[209] N. Metropolis, A. W. Rosenbluth, M. N. Rosenbluth, A. H. Teller, and E. Teller, "Equation of state calculations by fast computing machines," *The Journal of Chemical Physics*, vol. 21, p. 1087, 6 1953. DOI: `10.1063/1.1699114`.

[210] W. K. Hastings, "Monte Carlo sampling methods using Markov chains and their applications," *Biometrika*, vol. 57, no. 1, pp. 97–109, 1970. DOI: `10.1093/biomet/57.1.97`.

[211] F. Mastrippolito, "Optimisation de forme numérique de problèmes multiphysiques et multiéchelles : Application aux échangeurs de chaleur," Ph.D. dissertation, Université de Lyon, 2018.

[212] T. Hastie, R. Tibshirani, and J. Friedman, *The Elements of Statistical Learning*. Springer New York, 2009. DOI: `10.1007/978-0-387-84858-7`.

[213] M. V. Zagarola and A. J. Smits, "Mean-flow scaling of turbulent pipe flow," *Journal of Fluid Mechanics*, vol. 373, pp. 33–79, 1998. DOI: `10.1017/s0022112098002419`.

[214] L. Prandtl, "7. bericht über untersuchungen zur ausgebildeten turbulenz," *ZAMM - Journal of Applied Mathematics and Mechanics / Zeitschrift für Angewandte Mathematik und Mechanik*, vol. 5, pp. 136–139, 2 1925. DOI: `10.1002/zamm.19250050212`.

[215] Z Ding, K Truffin, S Jay, M Schmidt, F Foucher, and J Borée, "On the use of les and 3d emd for analyzing cycle-to-cycle variations of in-cylinder tumbling flow," *Flow, Turbulence and Combustion*, 2022, Under Review.

[216] G Maio, Z Ding, K Truffin, O Colin, O Benoit, and S Jay, "Ecfm-les modeling with amr for the ccv prediction and analysis in lean-burn engines," *Science and Technology for Energy Transition*, 2022, In Press.

[217] Z. He, J. Li, L. Liu, and Y. Shen, "Three-dimensional empirical mode decomposition (temd): A fast approach motivated by separable filters," *Signal Processing*, vol. 131, pp. 307–319, 2017. DOI: `https://doi.org/10.1016/j.sigpro.2016.08.024`.

[218] E. Ruffio, D. Saury, and D. Petit, "Thermodynamic analysis of hydrogen tank filling. effects of heat losses and filling rate optimization," *International Journal of Hydrogen Energy*, vol. 39, no. 24, pp. 12 701–12 714, 2014. DOI: `https://doi.org/10.1016/j.ijhydene.2014.06.069`.

[219] M. A. Aguirre, S. Duplaa, X. Carbonneau, and A. Turnbull, "Velocity decomposition method for exergy-based drag prediction," *AIAA Journal*, vol. 58, no. 11, pp. 4686–4701, 2020. DOI: `10.2514/1.j059414`.

[220] E. Mäteling and W. Schröder, "Analysis of spatiotemporal inner-outer large-scale interactions in turbulent channel flow by multivariate empirical mode decomposition," *Phys. Rev. Fluids*, vol. 7, p. 034 603, 3 2022. DOI: `10.1103/PhysRevFluids.7.034603`.

[221] Y. Shen, P. Wang, X. Wang, and K. Sun, "Application of empirical mode decomposition and extreme learning machine algorithms on prediction of the surface vibration signal," *Energies*, vol. 14, no. 22, 2021. DOI: `10.3390/en14227519`.

[222] J. Kodavasal, A. A. Moiz, M. Ameen, and S. Som, "Using machine learning to analyze factors determining cycle-to-cycle variation in a spark-ignited gasoline engine," *Journal of Energy Resources Technology, Transactions of the ASME*, vol. 140, 10 2018. DOI: `10.1115/1.4040062/368179`.

[223] A. Hanuschkin *et al.*, "Machine learning–based analysis of in-cylinder flow fields to predict combustion engine performance," *International Journal of Engine Research*, vol. 22, no. 1, pp. 257–272, 2021. DOI: `10.1177/1468087419833269`.

[224] D. Dreher *et al.*, "Deep feature learning of in-cylinder flow fields to analyze cycle-to-cycle variations in an si engine," *International Journal of Engine Research*, vol. 22, no. 11, pp. 3263–3285, 2021. DOI: `10.1177/1468087420974148`.

[225] A. Hanuschkin *et al.*, "Investigation of cycle-to-cycle variations in a spark-ignition engine based on a machine learning analysis of the early flame kernel," *Proceedings of the Combustion Institute*, vol. 38, pp. 5751–5759, 4 2021. DOI: `10.1016/j.proci.2020.05.030`.

[226] J. Kodavasal, A. Abdul Moiz, M. Ameen, and S. Som, "Using Machine Learning to Analyze Factors Determining Cycle-to-Cycle Variation in a Spark-Ignited Gasoline Engine," *Journal of Energy Resources Technology*, vol. 140, no. 10, 2018. DOI: `10.1115/1.4040062`.

[227] Anr, *Augmented prediction and analysis of massive data for the identification of key parameters controlling internal aerodynamics*, `https://anr.fr/Project-ANR-20-CE05-0007`.

Appendices

APPENDIX A

PIV comparison of motored case

The quantitative validation of LES results on the prediction of aerodynamics continues in this appendix with comparisons between LES and PIV at two instants to complete Chapter 5.

Phase-averaged velocity fields at -270 CAD during the intake stroke obtained from LES and PIV are compared in Figure A.1a. The intake flow generated by the interaction between intake valve jets is slightly weaker as predicted by LES. The flow descends also much more deeply on the exhaust side as shown in the PIV field, contrary to the one predicted by LES that the secondary intake flow on the intake side penetrates more in the chamber.

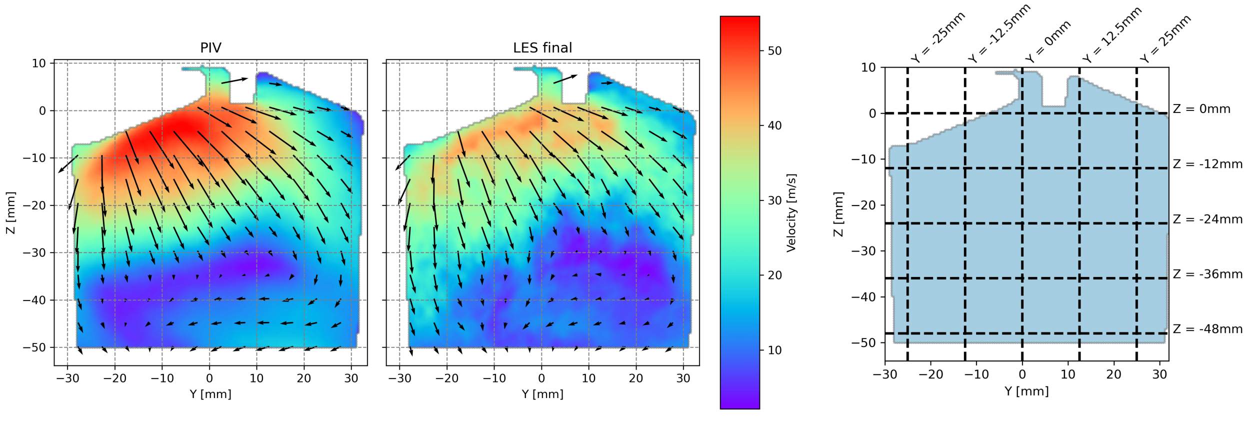

(A)

(B)

FIGURE A.1: (A) Comparison of phase-averagedd velocity between LES and PIV at -270 CAD (B) Sampling lines in tumble plane at -270 CAD for comparison between LES results and PIV measurements.

The comparison of velocity profiles on horizontal sampling lines indicated in Figure A.1b is illustrated in Figure A.2. On the component U_y, LES results match well PIV data except on the line $Z = -48\ mm$ near the piston where U_y is globally smaller cause LES does not capture the arrival of primary intake flow as shown in Figure A.1a. Concerning the component U_z, differences can be observed on the line $Z = -12\ mm$ laying inside the interaction zone and also on lateral sides of the line $Z = -36\ mm$ where primary and secondary intake jets pass through.

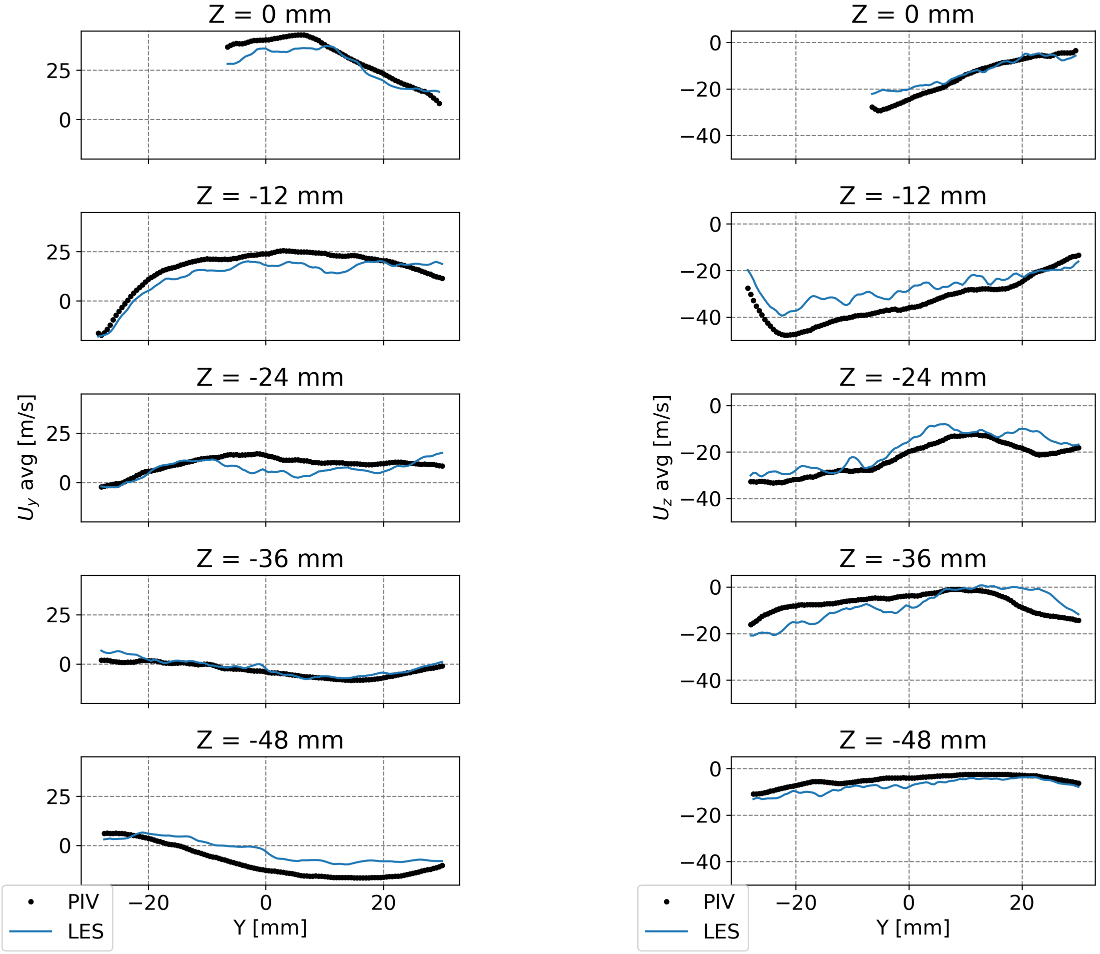

(A) U_y component.

(B) U_z component.

FIGURE A.2: Comparison of 1D profiles over horizontal lines in tumble plane at -270 CAD.

Velocity profiles on vertical sampling lines are compared in Figure A.3 between LES and PIV. Similar to the comparison on horizontal lines, most disparity exists in the region of interaction and on both the intake and exhaust sides where primary and secondary intake flows descend.

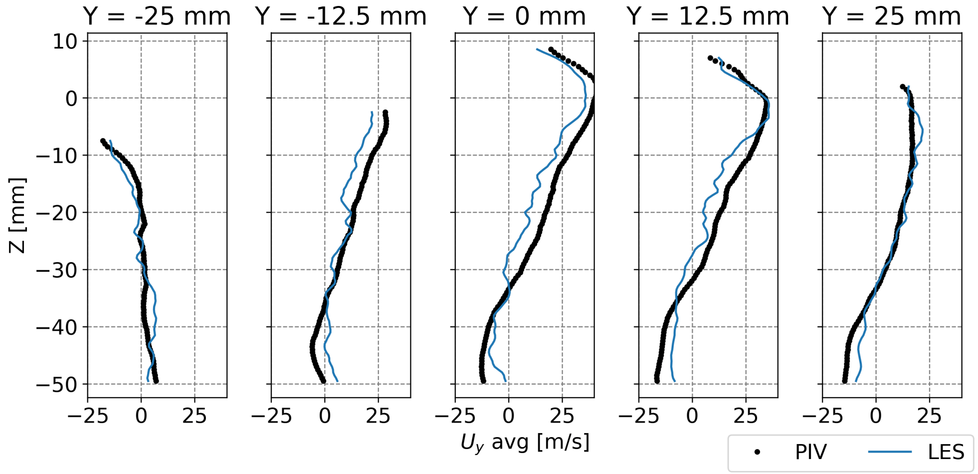

(A) U_y component.

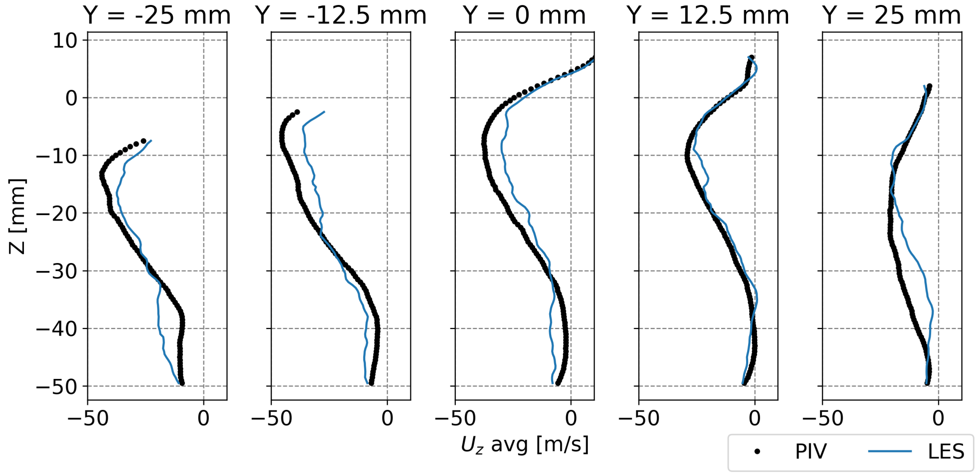

(B) U_z component.

FIGURE A.3: Comparison of 1D profiles over vertical lines in tumble plane at -270 CAD.

Phase-averaged velocity fields at -90 CAD during the compression stroke obtained from LES and PIV are compared in Figure A.4a. The flow pattern is of a classical tumble motion which is moving upward. LES tends to predict a weaker tumble motion than what has been captured by PIV.

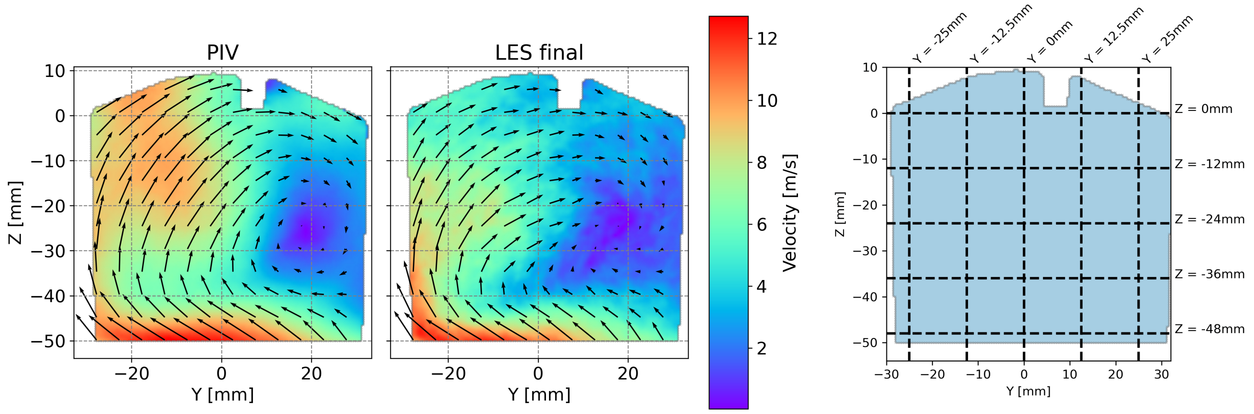

(A) (B)

FIGURE A.4: (A) Comparison of phase-averagedd velocity between LES and PIV at -90 CAD (B) Sampling lines in tumble plane at -90 CAD for comparison between LES results and PIV measurements.

The comparison is also made on horizontal and vertical sampling lines plotted in Figure A.4b. For both horizontal and vertical lines, discrepancies are all located in the region around the tumble front, otherwise, a general accord exists between LES and PIV.

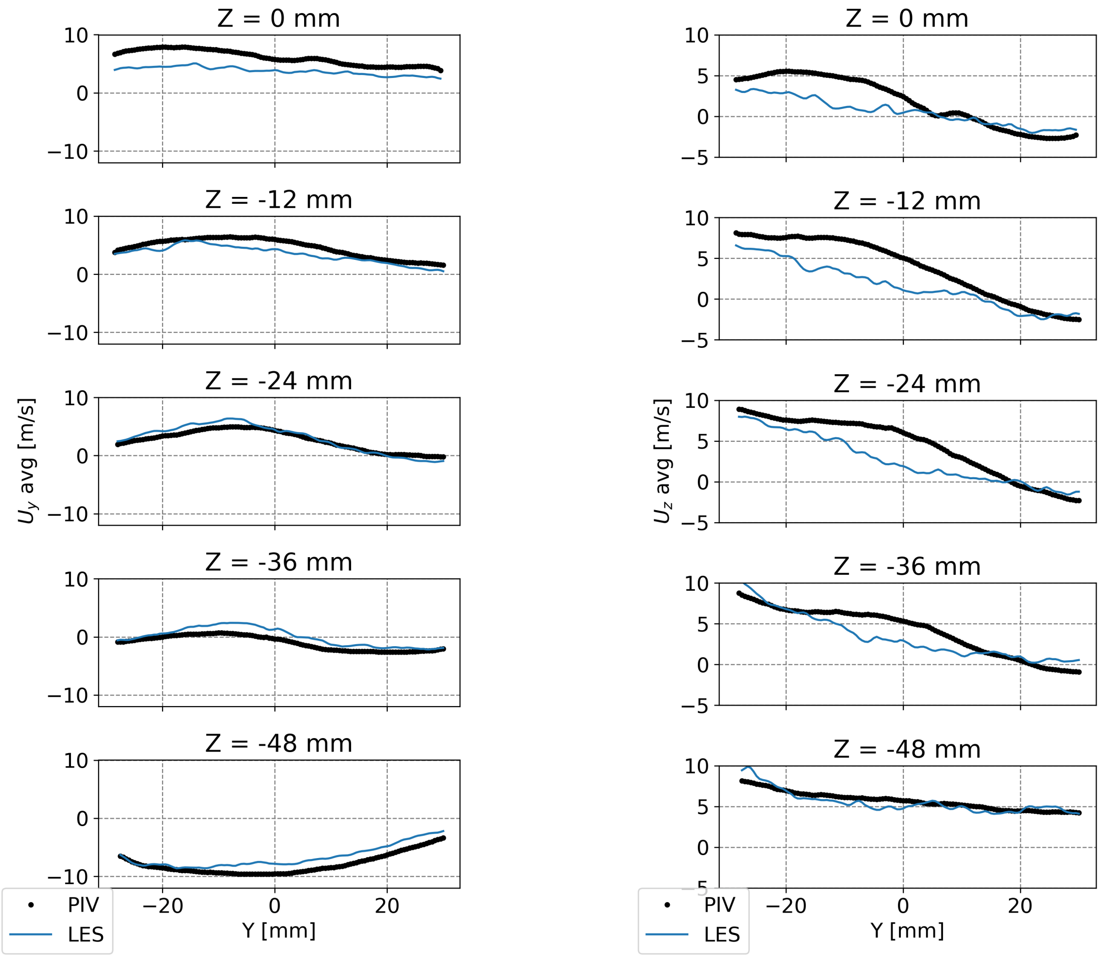

(A) U_y component.

(B) U_z component.

FIGURE A.5: Comparison of 1D profiles over horizontal lines in tumble plane at -90 CAD.

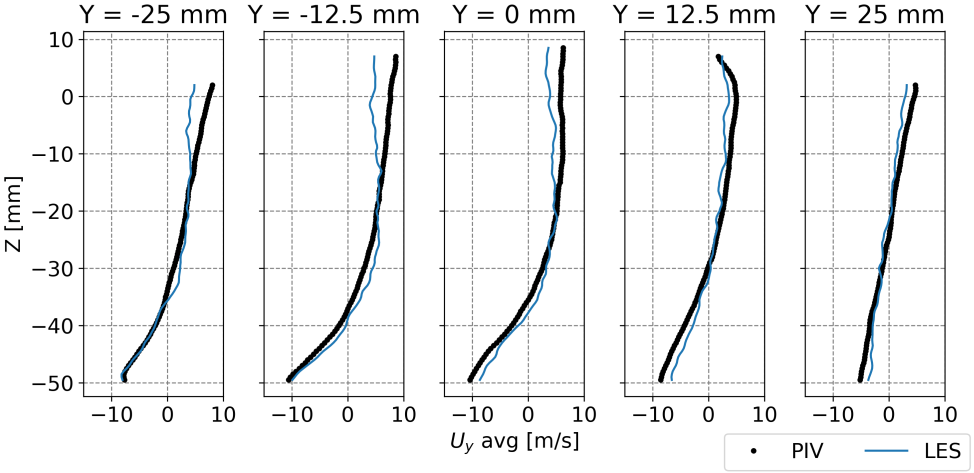

(A) U_y component.

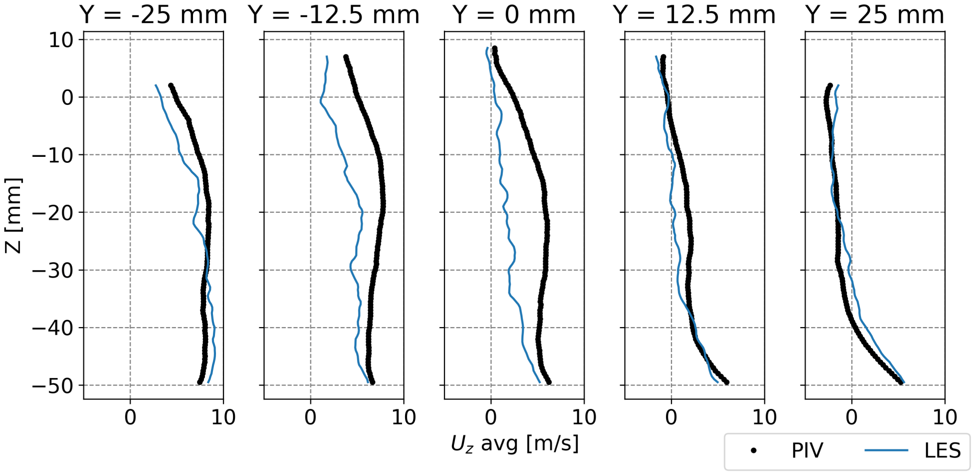

(B) U_z component.

FIGURE A.6: Comparison of 1D profiles over vertical lines in tumble plane at -90 CAD.

Appendix B

PIV comparison of fired case

The comparison between LES and PIV is given in this appendix to complete the validation of LES results presented in Chapter 6. The qualitative validation at two additional instants -270 and -90 CAD is presented.

Phase-averaged velocity field at -270 CAD obtained from LES is compared against PIV data at the same crank angle and the result is presented in Figure B.1. On the contrary to the same comparison made for motored case presented in Appendix A, the flow in region beneath the intake valves predicted by LES is much stronger than that measured by PIV. PIV captures also a descending flow on the exhaust side which penetrates much faster in the chamber and is deviated already over the piston surface, while the same flow structure predicted by LES advances relatively slower. The descending flow on the intake side presents also some differences: the one predicted by LES moves faster towards the piston than that observed by PIV.

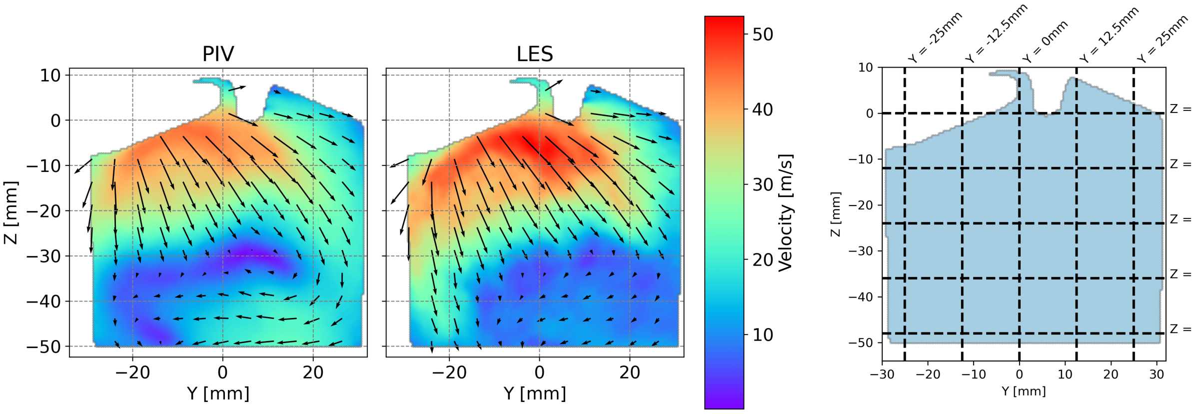

(A)

(B)

FIGURE B.1: (A) Comparison of phase-averagedd velocity between LES and PIV at -270 CAD (B) Sampling lines in tumble plane at -270 CAD for comparison between LES results and PIV measurements.

More detailed comparisons of velocity profiles on horizontal and vertical sampling lines indicated in Figure B.1b are illustrated in Figure B.2 and Figure B.3.

A globally good agreement is achieved between LES and PIV for horizontal lines at $Z = 0$ mm, $Z = -12$ mm and $Z = -24$ mm which lie inside the interaction zone of the in-cylinder flow. For other two lines $Z = -36$ mm and $Z = -48$ mm which are closer to the piston, differences can be observed on U_y and U_z which are caused by the differences between LES and PIV on the prediction/measurement of descending flows.

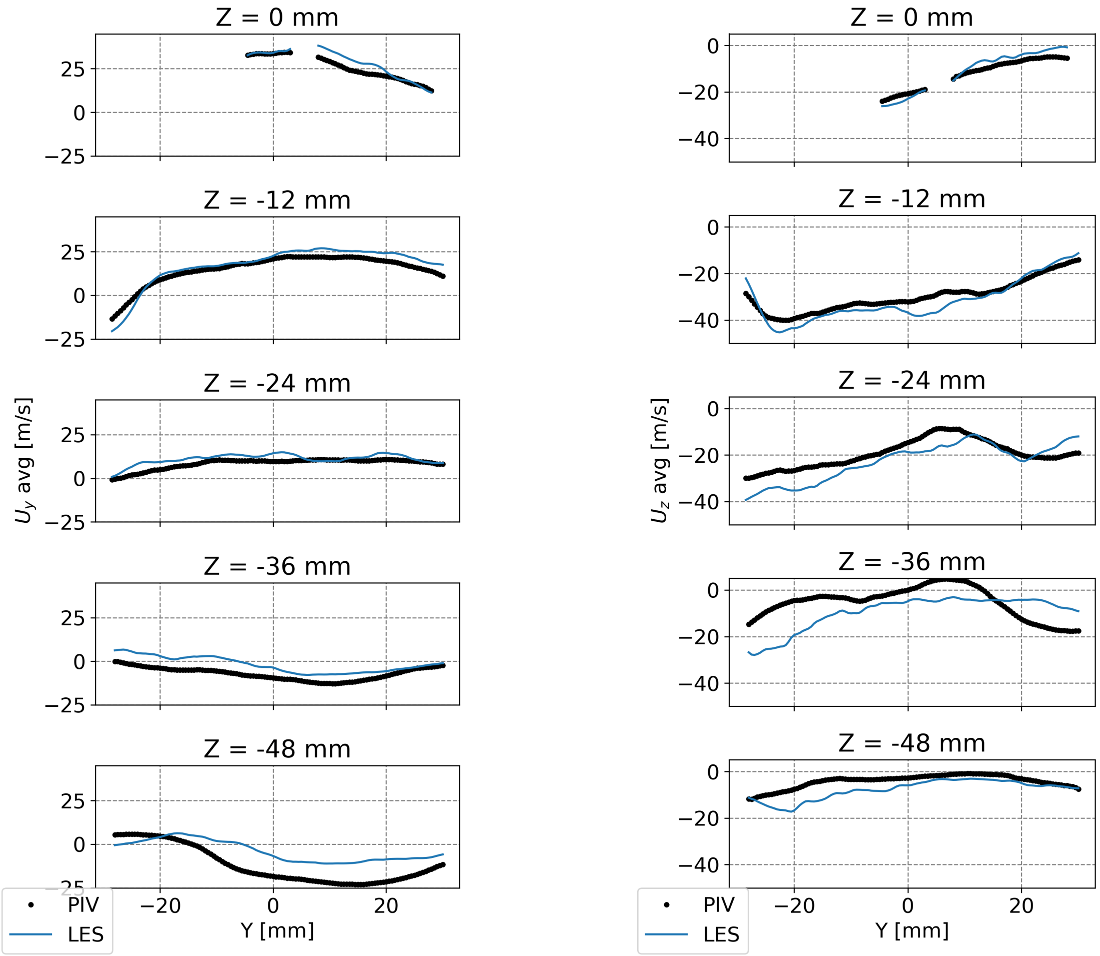

(A) U_y component.

(B) U_z component.

FIGURE B.2: Comparison of 1D profiles over horizontal lines in tumble plane at -270 CAD.

Velocity profiles illustrated in Figure B.3 shows a better accord between LES and PIV. Important discrepancies are located in regions close to the piston, which confirms the observation on the complet 2D velocity field.

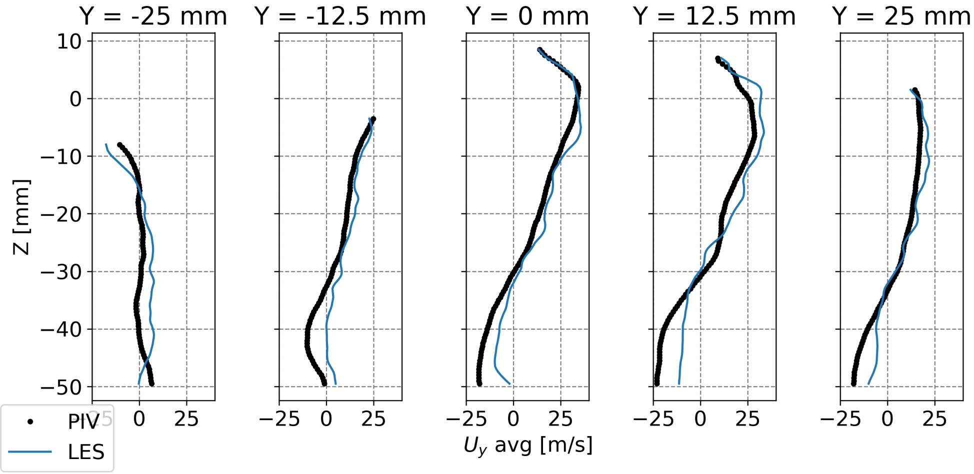

(A) U_y component.

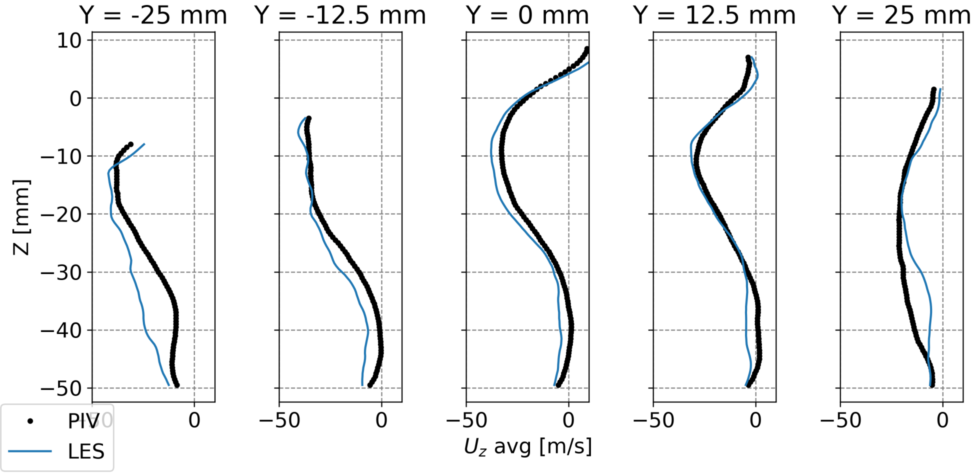

(B) U_z component.

FIGURE B.3: Comparison of 1D profiles over vertical lines in tumble plane at -270 CAD.

Phase-averaged velocity field at −90 CAD obtained from LES and PIV are compared in Figure B.4a. A typical tumble motion can be observed, and LES tends to predict a slightly weaker tumble front (in the upper left aera of the field). The tumble center location remains similar in both LES and PIV cases.

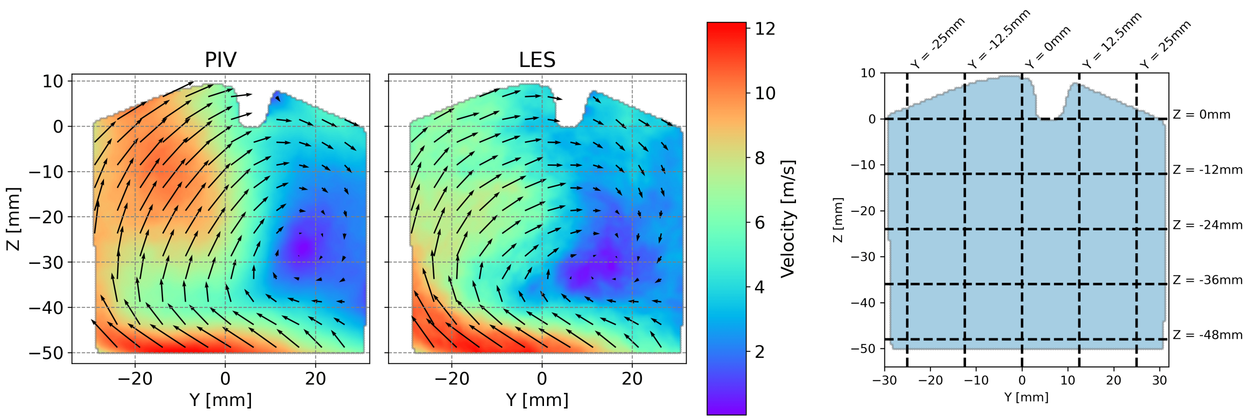

(A)

(B)

FIGURE B.4: (A) Comparison of phase-averagedd velocity between LES and PIV at -90 CAD (B) Sampling lines in tumble plane at -90 CAD for comparison between LES results and PIV measurements.

Comparisons of velocity profiles on horizontal sampling lines indicated in Figure B.4b are illustrated in Figure B.5. Results of LES on the component U_y match well the PIV measurements. Differences on the component U_z are related to the fact that the tumble motion observed by PIV is much stronger that that predicted by LES.

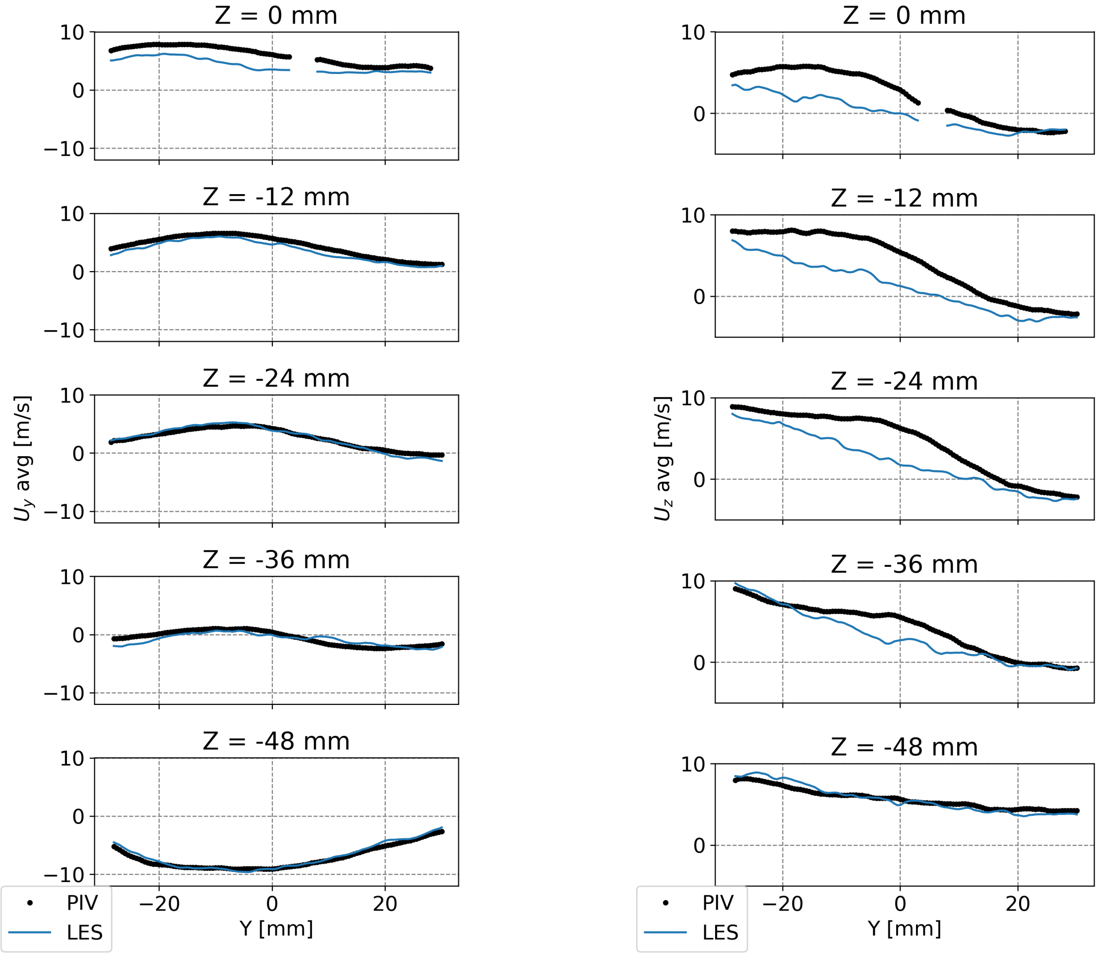

(A) U_y component.

(B) U_z component.

FIGURE B.5: Comparison of 1D profiles over horizontal lines in tumble plane at -90 CAD.

Comparisons of velocity profiles on vertical sampling lines are presented in Figure B.6. Similar to the comparisons made on horizontal lines, the results of the component U_y obtained by LES are satisfying while those of the component U_z exhbits still some disparities compared with PIV data.

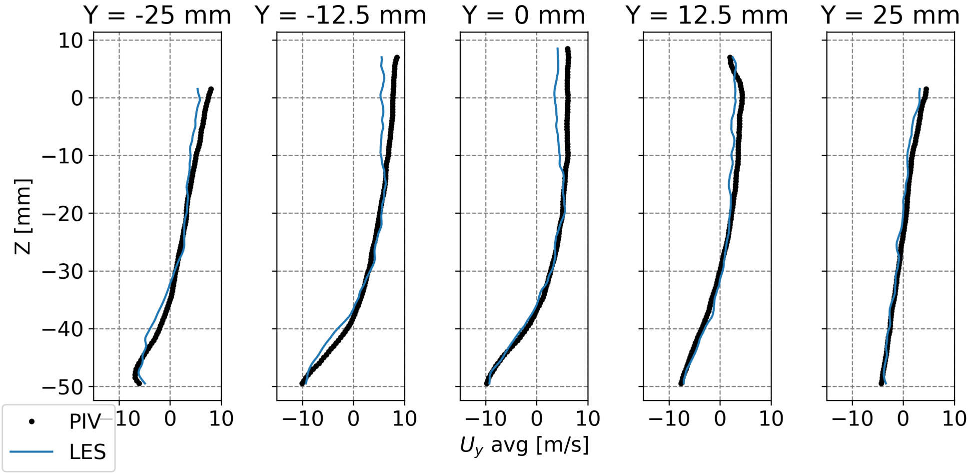

(A) U_y component.

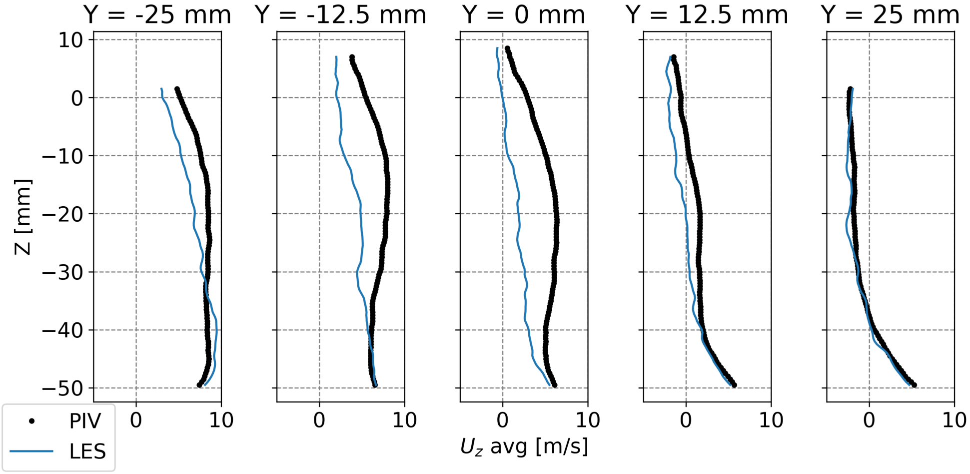

(B) U_z component.

FIGURE B.6: Comparison of 1D profiles over vertical lines in tumble plane at -90 CAD.

APPENDIX C

On the application of spatio-temporal EMD to LES data

In section 4.1.5, we presented the application of spatial-temporal EMD to a simple test case: a mobile large-scale vortex with presence of spatial and temporal fluctuations. In this Appendix, we will illustrate an exemplary application of spatial-temporal EMD to LES data obtained in the work presented in Chapter 7.

C.1 Arrangement of spatio-temporal data

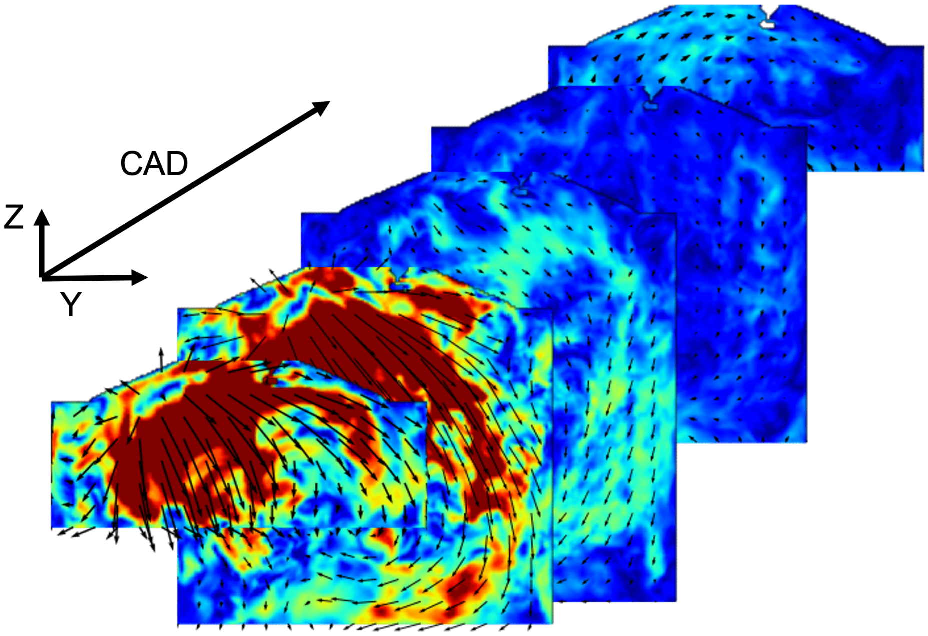

FIGURE C.1: Assembly of 2D velocity fields in the tumble plane into a 3D matrix in the order of crank angle. Only five instants are shown for simplicity.

The velocity fields in the tumble plane are chosen to for testing spatio-temporal EMD. The total 73 2D (in space) velocity fields of crank angle degree from −360 to −22.5 CAD, are arranged in increasing order of crank angle degree into a 3D matrix of spatio-temporal velocity data $U(y, z, CAD)$ containing two dimensions in space Y and Z, and one dimension in time corresponding to the crank angle degree. The arrangement is schematically presented in Figure C.1.

Compared to the test case presented in section 4.1.5, a major difference lies in the shape of the 3D matrix $U(y, z, CAD)$: the size of the tumble plane is affected by the piston motion and the assembled 3D matrix $U(y, z, CAD)$ is not fully filled. Along the temporal direction, each data raw is of different lengths which depend on its location in the Z direction, as shown in Figure C.2.

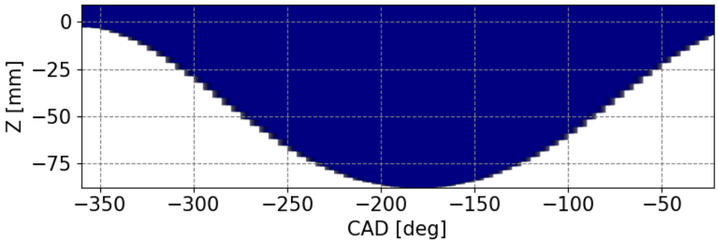

FIGURE C.2: Shape of the 3D matrix containing spatial-temporal velocity data in the tumble plane. The Y direction (depth) is not shown.

C.2 Results of spatio-temporal EMD on LES data

The assembled 3D matrix is of concave shape and no discontinuity is present in the three directions. Therefore, the developed spatial-temporal EMD, based on the principle of sequential decomposition, is still applicable. We carried out spatial-temporal EMD on the data of a single cycle 3, first in space and then in time to extract a spatial LF part which corresponds to the results of 2D EMD applied to each 2D velocity field, and a temporal LF part in which temporal fluctuations are further filtered. The definition of LF part remains identical in each direction: the last IMF mode and the residual form the LF part. The results of such an application is presented in Figure C.3. Figure C.3 compares the obtained LF parts after filtering by EMD in space and time in the plane $Y = 0$ mm. As mentioned before, the LF part in space of the 3D spatial-temporal velocity matrix is equivalent to the assembly of LF parts, extracted by 2D EMD, of all the 2D velocity fields in the tumble plane. After the filtering in space, it can be seen that fluctuations are still visible along the temporal direction, on the components U_y (cf Figure C.3a) and U_z (cf Figure C.3b), principally during the intake stroke (CAD< -220) near the cylinder head ($Z > -10$ mm) due to the high variability of the interaction between the intake valve jets. The filtering in time by EMD allows the elimination of such fluctuations, considered as HF part in time, which could provides a new insight into the temporal evolution of the large-scale motion.

The same comparison is made in the tumble plane at −300,−240 and −180 CAD in Figure C.4. The global flow patterns observed in the tumble plane in the two LF parts differ slightly between each. The filtering in time clearly brings some minor modifications to the LF parts in space, and the resulted HF parts in time indicate regions of significant variations in time. However, a physical interpretation of the obtained LF and HF parts in time seems difficult, which will be discussed in the next section.

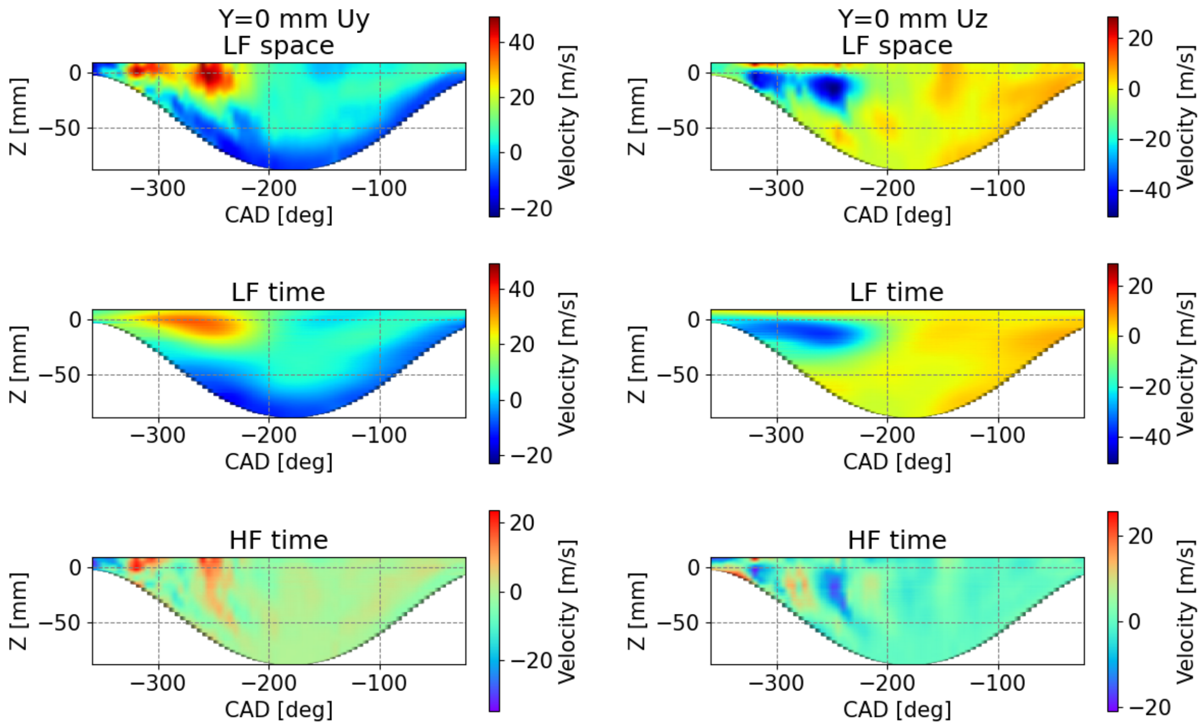

(A) U_y.

(B) U_z.

FIGURE C.3: LF parts after filtering in space and time. Only lines at $Y = 0$ mm is shown.

C.3 Discussions about the usage of spatio-temporal EMD

In this thesis, spatio-temporal EMD was applied to LES data. We noticed some potential problems concerning its pre-processing and also the interpretation of obtained results, which are discussed below:

- The arrangement of the 3D spatio-temporal velocity matrix presented in section C.1 is a straightforward way to handle LES data in a time-varying geometry: the velocity data are organized according to their corresponding coordinates in space and time. However, such an arrangement could be questionable. Taking the line at $Y = 0$ mm and $Z = -50$ mm as an example (cf Figure C.3), the two borders of the line are located in regions close to the piston while its central part remains in the middle of the cylinder around BDC. The line contains thus information gathered from different locations in the cylinder, which might not be of important relevance. A potentially more suitable way is illustrate in Figure C.5, in which the decomposition in the temporal direction takes into account the impact from the piston motion. Each curved line contains information extracted from the same region: the first line stays close to the cylinder head while the last line follows the flow evolution near the piston. Such an arrangement requires also an extra step of interpolation to have the same number of data points in the Z direction for all the instants. A comparison of the obtained LF and HF parts in time with the current method presented in section C.1 will be necessary to evaluate the potential improvements brought by the proposed new method of arrangement.
- In the above application, the definition of the LF part in time is identical with that in space. However, the LF and HF parts in time are not as well defined as those in space. Also,

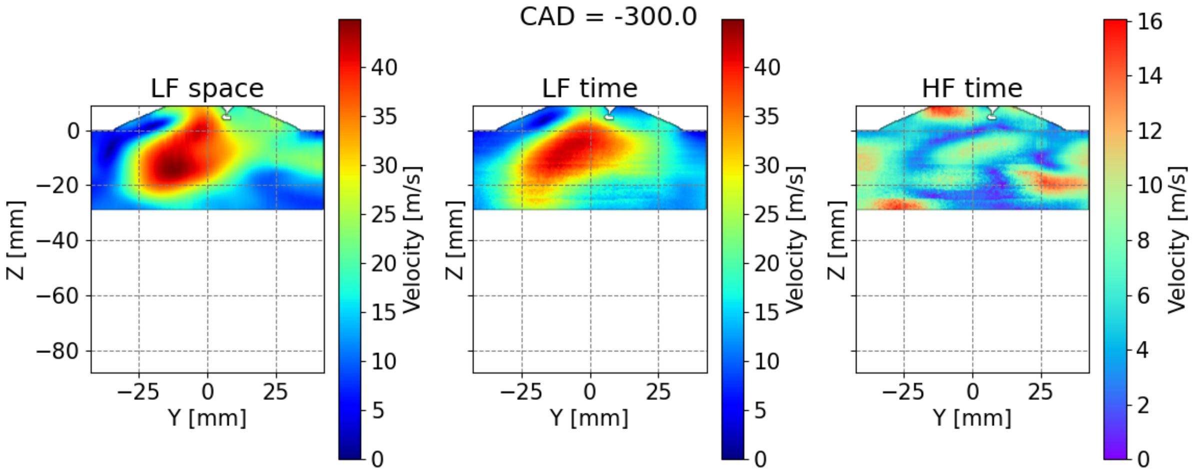

(A) −300 CAD.

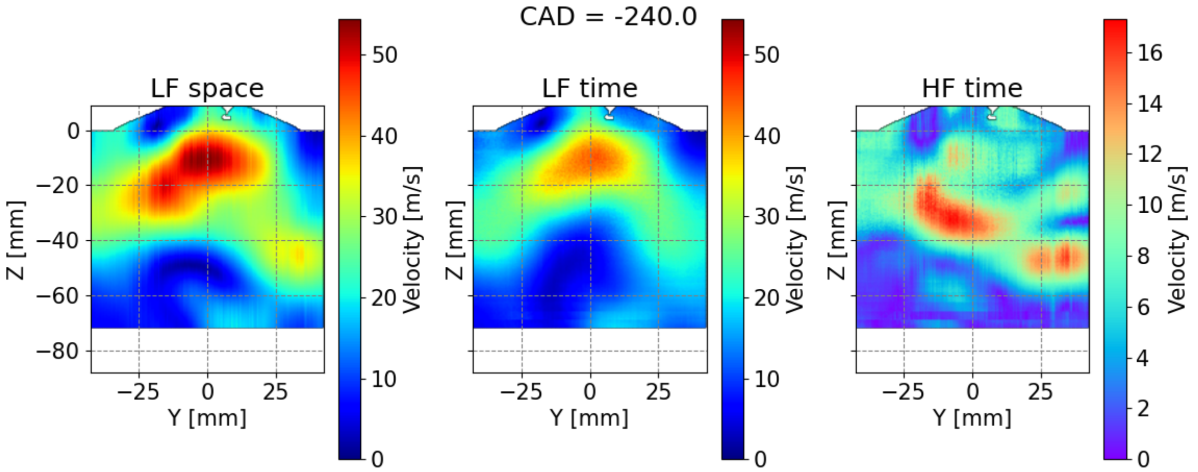

(B) −240 CAD.

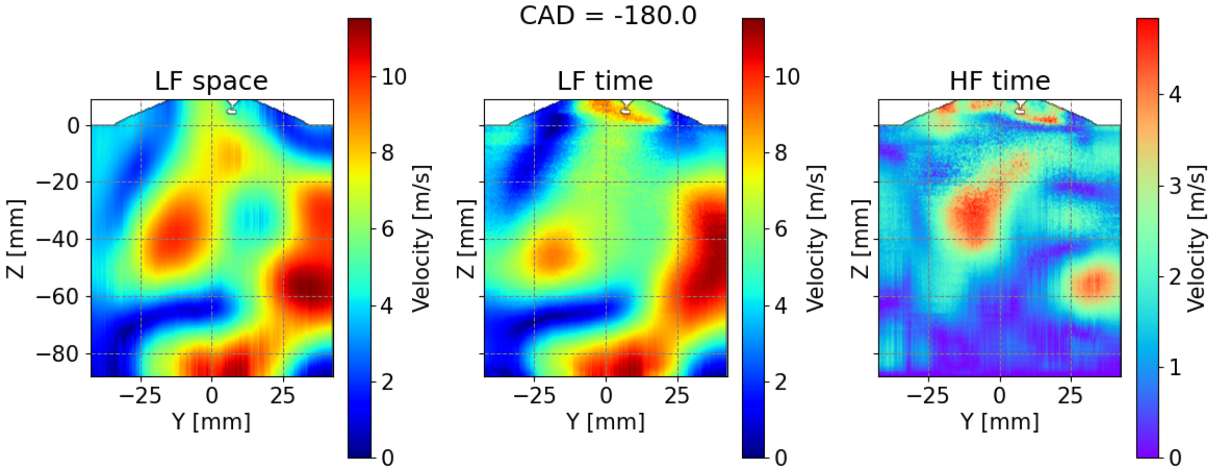

(C) −180 CAD.

FIGURE C.4: LF parts after filtering in space and time in the tumble plane.

the temporal resolution could also impact the results of the decomposition in the temporal direction, but was not carefully investigated in this work.

- By following the spatial and temporal structure of the large-scale eddies and of the turbulence, this decomposition may provide a spatio-temporal characterization of the flow.

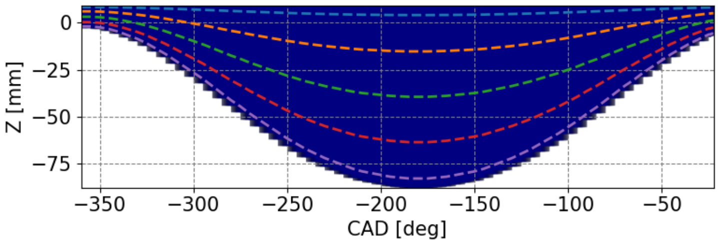

FIGURE C.5: Example of the decomposition in the temporal direction along curved lines.

Due to the problems related to the application of spatio-temporal EMD, in this thesis we did not exploit the results obtained from its application to LES data. Further improvements are required to resolve the listed problems before validating this method.

Zhihao DING

Simulation aux grandes échelles et analyse spatio-temporelle de l'aérodynamique interne moteur

Résumé: Parmi les utilisations possibles de l'hydrogène en tant que futur vecteur d'énergies renouvelables, sa combustion, soit en tant que carburant, soit en tant qu'additif dans un moteur à allumage commandé, est considérée comme un moyen possible d'atteindre les objectifs de réduction totale des émissions (gaz à effet de serre et polluants nocifs) du transport routier. Des stratégies comme la combustion ultra-pauvre ont un énorme potentiel pour améliorer l'efficacité thermique et réduire les émissions de polluants. Cependant, la combustion pauvre est associée à des problèmes tels que les variations cycle-à-cycle (CCV) dans le processus de combustion, ce qui pénalise le rendement moteur et peut conduire à des ratés d'allumage dans certains cycles extrêmes. La compréhension et la réduction des CCV sont un des principaux sujets de recherche en ingénierie automobile. Des études antérieures ont mis en évidence l'importance de l'aérodynamique interne, caractérisée par un écoulement turbulent tourbillonnaire appelé rouleau, comme l'une des principales sources de CCV puisque les structures de l'écoulement, tant à grande qu'à petite échelle, présentent un certain niveau de variabilité. L'objectif de cette thèse est de comprendre plus en détail le rôle de l'aérodynamique interne sur les variabilités de combustion.

Dans ce contexte on s'appuie sur la simulation aux grandes échelles (LES) qui permet de résoudre les tourbillons jusqu'à une certaine échelle. Elle permet également de prédire les phénomènes instationnaires et les variabilités cycliques. Cependant, au vu de la grande quantité de données générée, des outils adaptés sont nécessaires pour identifier le mouvement des grandes structures de l'écoulement et le mouvement fluctuant associé à la turbulence, les deux pouvant être à l'origine des variabilités cycle-à-cycle observées dans un moteur. La méthode proposée ici est basée sur la décomposition en modes empiriques (EMD) qui permet d'extraire les composantes basse et haute fréquence de n'importe quel signal. Dans cette présente étude, la méthode a été étendue pour être appliquée en 2D puis en 3D sur des champs de vitesse issue de résultats LES en géométries complexes. Les avantages de cette méthode sont de n'utiliser qu'un seul champ de vitesse contrairement aux approches plus classiques comme la POD et de ne pas nécessiter de fonction à priori contrairement à des approches de type ondelette ou filtre Gaussien. On peut ainsi traiter n'importe quel champ de vitesse au cours d'un cycle moteur et avoir accès à la variabilité du mouvement d'ensemble entre les cycles ce qui est un apport majeur dans l'analyse et la compréhension des mécanismes physiques conduisant aux variabilités cycliques de la combustion. En outre, cela permet de définir des descripteurs propres à ces composantes haute et basse fréquence ainsi qu'à leur variabilité pour quantifier l'impact des différents phénomènes (jets de soupapes, interactions avec les parois, mouvement du rouleau).

En termes d'application, des simulations LES multi-cycles d'un moteur de recherche installé à TU Darmstadt ont été réalisées sur un cas entraîné et sur un cas réactif. Les techniques EMD développées ont été combinées avec un algorithme d'identification des tourbillons permettant ainsi de mettre en évidence le lien entre la déformation du rouleau pendant la phase de compression et la vitesse de propagation de la flamme. Le rôle des interactions entre certains écoulements dominants pendant la phase d'admission, ainsi que la déviation de l'écoulement sur le piston près du point mort bas ont également été mises en évidence. Ces travaux ont permis le développement d'une technique innovante pour définir de nouveaux descripteurs de l'écoulement turbulent dans des situations fortement instationnaires. Elle ouvre la voie à des analyses encore plus poussées de l'aérodynamique turbulente en vue d'identifier des mécanismes à l'origine de certaines phénomènes indésirables (bruit, émissions, ...) pour les systèmes énergétiques.

Mots clés : Écoulement interne, Variations cycle-à-cycle, Décomposition en modes empiriques, Simulation aux grandes échelles, Turbulence, Mouvement organisé à grande échelle

Large-eddy simulation and spatio-temporal analysis of internal engine aerodynamics

Abstract: Among the possible use of hydrogen as a future vector for renewable energies, its combustion either as a pure compound or as an additive inside a spark-ignited engine is seen as a possible way to reach ambitious goals for road transport total reduction of emissions (greenhouse gas effects and harmful pollutants). Strategies such as ultra-lean combustion have enormous potential to improve thermal efficiency and reduce emissions of pollutants. However, lean burn is associated with problems such as cycle-to-cycle variations (CCV) in the combustion process, which weakens engine performance and can lead to misfires in some extreme cycles. Understanding and reducing CCV are one of the major research topics in automotive engineering. Previous studies have highlighted the importance of internal aerodynamics, characterized by a turbulent rotational flow called tumble, as one of the main CCV sources since both large- and small-scale flow structures present a certain level of variability. The objective of this thesis is to understand in more detail the role of internal aerodynamics on combustion variability.

In this context, we rely on Large-eddy simulation (LES) which allows to resolve the vortices up to a certain scale. It also allows the prediction of unsteady phenomena and cyclic variability. However, due to the large amount of data generated, adapted tools are needed to identify the motion of large-scale structures and the fluctuating motion associated with turbulence, both of which can be at the origin of the cycle-to-cycle variability observed in an engine. The method proposed here is based on Empirical Mode Decomposition (EMD) which allows the extraction of the low- and high-frequency components of any signal. In this study, the method has been extended to be applied in 2D and 3D on velocity fields from LES results in complex geometries. The advantages of this method are the usage of only one velocity field contrary to more classical approaches such as POD and the dispense of a priori function contrary to wavelet or Gaussian filter type approaches. We can thus treat any velocity field during an engine cycle and have access to the variability of the overall motion between cycles, which is a major contribution to the analysis and understanding of the physical mechanisms leading to the cyclic variability of combustion. In addition, it allows to define specific descriptors of high- and low-frequency components and their variability to quantify the impact of different phenomena (valve jets, interactions with the walls, tumble motion).

In terms of application, multi-cycle LES simulations of a research engine installed at TU Darmstadt have been performed on a motored case and a reactive case. The developed EMD techniques were combined with a vortex identification algorithm to show the link between the deformation of the tumble during the compression stroke and the speed of flame propagation. The role of interactions between some dominant flows during the intake phase as well as the flow deviation on the piston near the bottom dead center were also highlighted. This work has allowed the development of an innovative technique to define new descriptors of the turbulent flow in highly unsteady situations. It opens the way to further analysis of turbulent aerodynamics in order to identify mechanisms at the origin of certain undesirable phenomena (noise, emissions, ...) for energy systems.

Keywords: In-cylinder flow, Cycle-to-cycle variations, Empirical Mode Decomposition, Large-eddy simulation, Turbulence, Large-scale organized motion

Laboratoire PRISME
8 rue Léonard de Vinci
45072 Orléans cedex
FRANCE